

MNB

Journal of
**Geophysical
Research**

VOLUME 65 NOVEMBER 1960 NUMBER 11

**THE SCIENTIFIC PUBLICATION
OF THE AMERICAN GEOPHYSICAL UNION**

Journal of Geophysical Research

An International Scientific Publication

OFFICERS OF THE UNION

LYOYD V. BERKNER, *President*
THOMAS F. MALONE, *Vice President*
A. NELSON SAYRE, *General Secretary*
WALDO E. SMITH, *Executive Secretary*

OFFICERS OF THE SECTIONS

Geodesy

CHARLES PIERCE, *President*
FLOYD W. HOUGH, *Vice President*
BUPORD K. MEADE, *Secretary*

Seismology

LEONARD M. MURPHY, *President*
JAMES A. PEOPLES, JR., *Vice President*
BENJAMIN F. HOWELL, JR., *Secretary*

Meteorology

THOMAS F. MALONE, *President*
GORDON E. DUNN, *Vice President*
WOODROW C. JACOBS, *Secretary*

Geomagnetism and Aeronomy

L. R. ALLDREDGE, *President*
C. T. ELVEY, *Vice President*
J. HUGH NELSON, *Secretary*

Oceanography

WALTER H. MUNK, *President*
DONALD W. PRITCHARD, *Vice President*
EUGENE C. LAFOND, *Secretary*

Volcanology, Geochemistry, and Petrology

ALFRED O. C. NIER, *President*
FRANCIS J. TURNER, *Vice President*
IRVING FRIEDMAN, *Secretary*

Hydrology

WALTER B. LANGBEIN, *President*
WILLIAM C. ACKERMANN, *Vice President*
CHARLES C. McDONALD, *Secretary*

Tectonophysics

PATRICK M. HURLEY, *President*
LOUIS B. SLICHTER, *Vice President*
H. RICHARD GAULT, *Secretary*

BOARD OF EDITORS

Editors: PHILIP H. ABELSON and J. A. PEOPLES, JR.

ASSOCIATE EDITORS

1960

HENRY G. BOOKER	WALTER B. LANGBEIN
E. C. BULLARD	ERWIN SCHMID
JULE CHARNEY	HENRY STOMMEL
GEORGE T. FAUST	J. TH. THIJSSSE
DAVID G. KNAPP	A. H. WAYNICK

J. TUZO WILSON

1960-1961

HENRI BADER	T. NAGATA
K. E. BULLEN	FRANK PRESS
CONRAD P. MOOK	A. NELSON SAYRE
WALTER H. MUNK	MERLE A. TUVE

JAMES A. VAN ALLEN

1960-1962

JULIUS BARTELS	L. A. MANNING
V. V. BELOUSSOV	TOR J. NORDENSON
E. G. BOWEN	E. N. PARKER
JOHN E. CHAPPELEAR	GEORGE P. RIGSBY
G. D. GARLAND	WALTER O. ROBERTS
GORDON J. F. MACDONALD	C. N. TOUART

JAMES R. WAIT

This Journal welcomes original scientific contributions on the physics of the earth and its environment.

Manuscripts should be transmitted to J. A. Peoples, Jr., Geology Department, University of Kansas, Lawrence, Kansas. Authors' institutions, if in the United States or Canada, are requested to pay a publication charge of \$25 per page, which, if honored, entitles them to 100 free reprints.

Subscriptions to the *Journal of Geophysical Research and Transactions, AGU* are included in membership dues.

Non-member subscriptions, *Journal of Geophysical Research*..\$30 for back Volume of 1959, \$4 for this issue; \$20 for the calendar year 1960.

Non-member subscriptions, *Transactions, AGU*.....

.....\$4 per calendar year, \$1.25 per copy.

Subscriptions, renewals, and orders for back numbers should be addressed to American Geophysical Union, 1515 Massachusetts Ave., Northwest, Washington 5, D. C. Suggestions to authors are available on request.

Advertising Representative: Howland and Howland, Inc., 230 Park Ave., New York 17, N. Y.

Beginning with the January 1959 issue (Vol. 64, No. 1) the *Journal of Geophysical Research* is published monthly by the American Geophysical Union, the U. S. National Committee of the International Union of Geodesy and Geophysics organized under the National Academy of Sciences-National Research Council as the U. S. national adhering body. Publication of this journal is supported by the National Science Foundation and the Carnegie Institution of Washington. The new monthly combines the type of scientific material formerly published in the bi-monthly *Transactions, American Geophysical Union*, and the quarterly *Journal of Geophysical Research*. The *Transactions, American Geophysical Union* will continue as a quarterly publication for Union business and items of interest to members of the Union.

Published monthly by the American Geophysical Union from 1407 Sherwood Avenue, Richmond, Virginia. Second class postage paid at Richmond, Virginia.

geophysical research

at Hughes Research Laboratories

Basic and applied studies at Hughes Research Laboratories include many and varied geophysical research programs. Among these are:

Upper Atmosphere & Space Physics—basic studies in the plasma physics of the ionosphere, solar-terrestrial relationships, properties of geomagnetically trapped radiation, and analysis of artificially produced ionization effects.

Radiowave Propagation—radar echoes from auroral and other natural ionization, scatter propagation, fading and diversity reception theory, VLF and whistler mode propagation, and microwave and infrared transmission characteristics.

Physical Oceanography—long-range acoustic propagation, specialized phenomena of importance to submarine detection and communications, and commercial applications of oceanography.

If your research interests are related to the above fields, your inquiry is encouraged.

The new facilities of the Hughes Research Laboratories are located in Malibu, California—overlooking the Pacific Ocean. Here scientists and engineers are offered the academic atmosphere which is essential for effective research effort.

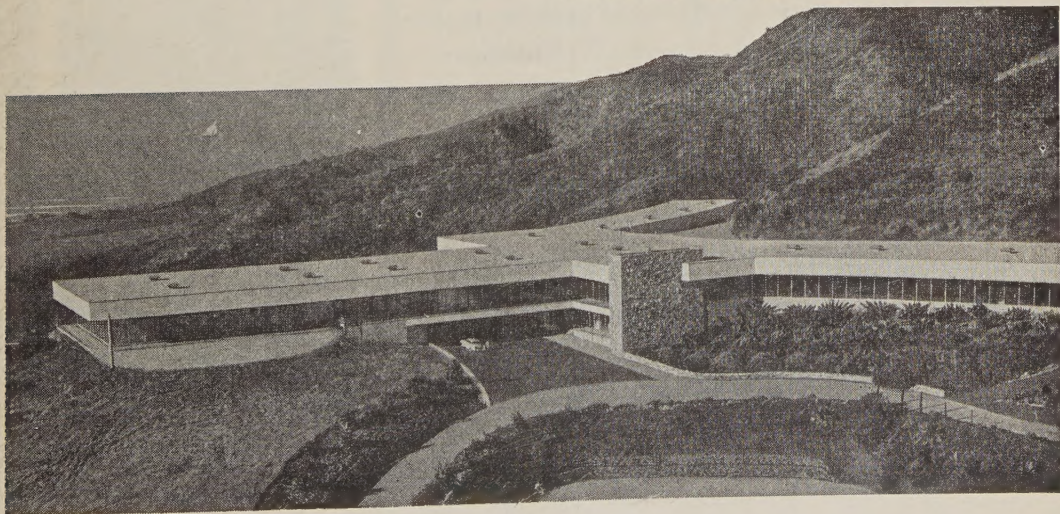
Your inquiry regarding staff openings may be directed in confidence to: Mr. D. A. Bowdoin,
HUGHES RESEARCH LABORATORIES, Malibu 12, California.

Creating a new world with ELECTRONICS

HUGHES

HUGHES AIRCRAFT COMPANY

RESEARCH LABORATORIES



Please mention JOURNAL OF GEOPHYSICAL RESEARCH, when writing to advertisers



"THE NOBLE SCIENCE OF GEOLOGY LOSES GLORY FROM THE EXTREME IMPERFECTION OF THE RECORD"

Darwin

Since the days of Darwin "the noble science of geology" has gained much in glory. Meanwhile an understanding of the environment in which men live has continued to be necessary to his survival. Yet, today, as man seeks to expand from his earth into space, he finds that his knowledge of the earth is in many senses inadequate to the job. Our knowledge of the oceans, of the roots of the mountains, and of the nature of the earth's crust has become, quite suddenly, closely connected to our ability to survive.

The exploration geophysics industry can supply basic scientific methods, necessary techniques, and many of the skilled, experienced personnel to solve these problems in a manner similar to the ways in which this industry has discovered several hundred billion barrels of petroleum in the last twenty-five years. This industry is confident of its ability to contribute significantly to the solution of problems in the Earth Sciences that the Free World faces today.

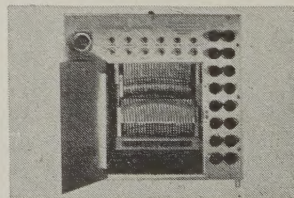
The General Geophysical Company has been a leader in the geophysical industry since 1935. With its large laboratory and over 600 employees with worldwide geophysical experience, General Geophysical Company is prepared to develop special instruments, operate field stations, and interpret geophysical data on many aspects of studies of the earth's crust and the oceans.



EXPERIENCE



PERSONNEL



EQUIPMENT

General
GEOPHYSICAL COMPANY
HOUSTON CLUB BUILDING • HOUSTON, TEXAS

In Canada: 10509 81st Avenue,
Edmonton, Alberta, Canada
General Geophysical Company de France (SARL),
4 Square Rapp • Paris 7, France
General Geophysical Company (Bahamas) Ltd., Libyan Branch
22, Via Vittorio Gadolini, Tripoli Libya
General Geophysical Company (Bahamas) Ltd.
Umm Said, Quatar, Arabian Gulf

A New Look at **VARIAN'S** **MAGNETOMETER FAMILY**

The "Proton Free Precession" types find diverse applications; an "Optical Pumping" instrument extends research capabilities.

The simplicity, ruggedness and absolute accuracy made possible by Russell Varian's "Proton Free Precession" concept has made **proton** magnetometers the world standard in less than a decade. Using this principle, total magnetic intensities are quickly measured, without critical orientation or calibration requirements. Recent application of the "Optical Pumping" concept has enabled Varian Associates to develop a **rubidium vapor** magnetometer, with the highest sensitivity available today. This new instrument measures total magnetic intensities on a continuous basis.



OBSERVATORY

Varian's V-4931 Modular Station Magnetometer (**proton**) is a highly versatile and accurate monitor of the earth's magnetic field. Strip-chart analog records and digital readout are supplemented by printed-tape output which may be engaged, as desired, to provide permanent digital records. The V-4934 Station Magnetometer (**rubidium vapor**) is particularly suitable for measuring and recording geomagnetic micropulsations.



PORTABLE

The Varian M-49, a complete **proton** magnetometer weighing less than 20 lbs., furnishes direct readings in gammas every six seconds. Sensitive to better than ± 10 gammas, it requires no calibration or levelling and is so versatile it can make equally accurate field records from surveys on land, in the air, or over water. Eight plug-in tuner ranges, equally spaced from 19,000 to 101,000 gammas, allow operation throughout the world.



AIRBORNE

The V-4914 Airborne Magnetometer (**proton**) is a rugged, lightweight and compact version of Varian's Station Magnetometer. Sensitivity and accuracy are of observatory quality. Coarse- and fine-scale strip-chart records may be supplemented with punched-tape. The virtually indestructible "bird" contains no mechanical or electronic parts. Varian's V-4914 is easily accommodated in single-engine aircraft. Range: 22,500 to 73,400 gammas.



OCEANOGRAPHIC

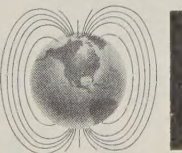
An accessory "fish" towed up to five hundred feet astern of the hydrographic vessel is the sensing adjunct to Varian's V-4931 for oceanographic survey work. Suitable for broad-scale undersea mapping or offshore geophysical exploration, it furnishes information of observatory quality. Analog and digital readout and records, accuracy and operating range are identical to the observatory model.



RESEARCH

Examples of current projects in Varian's research and engineering laboratories include **proton** and **rubidium vapor** miniaturized magnetometers stressed for missile, satellite, and deep-space applications and instruments being developed for specific military applications, such as ASW. Varian's practical contributions to magnetometry are continuing to advance the state of the art.

For further information on magnetometer sales or leases in many countries of the free world — For loan of the Varian 16 mm color and sound movie on **proton** magnetometry — For copies of Varian's new Geophysics Technical Memorandum Series — call, wire or write Instrument Division



VARIAN associates
PALO ALTO 43, CALIFORNIA

NMR & EPR SPECTROMETERS, MAGNETS, FLUXMETERS, GRAPHIC RECORDERS, MAGNETOMETERS, MICROWAVE TUBES, MICROWAVE SYSTEM COMPONENTS, HIGH VACUUM EQUIPMENT, LINEAR ACCELERATORS, RESEARCH AND DEVELOPMENT SERVICES

Please mention **JOURNAL OF GEOPHYSICAL RESEARCH**, when writing to advertisers

GROUND-BASED ANALOG DATA—TRANSMISSION EQUIPMENT

- ▶ **CAPACITY**—1 to 7 channels of low-frequency analog data.
- ▶ **TRANSMISSION CIRCUIT**—a single voice-frequency telephone, radio, or microwave circuit.
- ▶ **TRANSMISSION RANGE**—coast to coast if required.
- ▶ **DEPENDABILITY**—proven, continuous year-round operation.
- ▶ **ECONOMY**—building-block components; ± 100 volt output of discriminator eliminates need of DC amplifier; can use a leased commercial circuit.
- ▶ **COMPONENTS**—FM telemetering multiplexer: output $z=600$ ohms, $8\frac{3}{4}$ " h x 19" w x 15" d; voltage—controlled oscillators: RDB/IRIG subcarrier channels, $\pm 2\frac{1}{2}$ volts input produces $\pm 7\frac{1}{2}\%$ deviation, $4\frac{7}{8}$ " h x $3\frac{7}{8}$ " w x $1\frac{5}{8}$ " d; discriminators: input z —over 1 meg-ohm, output $z=0$ ohms, $5\frac{1}{4}$ " h x 19" w x $16\frac{3}{8}$ " d.



RUGGED SENSITIVE GALVANOMETERS SERIES 2980



- ▶ **PERIODS**—1 to 90 seconds.
- ▶ **SENSITIVITY**— 9×10^{-11} amps/mm/meter typical at 90 seconds.
- ▶ **STABILITY**—new fast-stabilizing design provides extremely small drift.
- ▶ **ADJUSTABLE**—CDRX, sensitivity, leveling, and horizontal light spot position.

SERIES 4100

- ▶ **FREQUENCIES**—1 to 50 cps.
- ▶ **SENSITIVITY**—up to 3×10^{-9} amps/mm/meter.
- ▶ **SUSPENSION**—separate, insulated suspension frame rotates, does not disturb ribbon.
- ▶ **ADJUSTABLE**—air gap, natural frequency, horizontal and vertical light spot position.

FOR INFORMATION WRITE:



THE GEOTECHNICAL CORP.

3401 Shiloh Road • Garland, Texas
P. O. Box 28277 • Dallas, Texas

NEW REPRINT

American Geophysical Union: Transactions

(Reproduced with the permission of the American Geophysical Union)

Now Available

Volumes 13-15, 1932-1934

Volume 13, 1932, paper bound
Volume 14, 1933, paper bound
Volume 15, 1934, paper bound

Previously Reprinted

Volumes 1-12, 1920-1931

(Volumes 3 and 5 were never published)

Paper bound set (in 9 volumes)	\$110.00
Volume 1, 1920, paper bound	5.00
Volume 2, 1921, paper bound	10.00
Volume 4, 1923, paper bound	15.00
Volume 6, 1925, paper bound	5.00
Volume 7, 1926, paper bound	15.00
Volume 8, 1927, paper bound	20.00
Volume 9, 1928, paper bound	15.00
Volume 10-11, 1929-1930, paper bound	20.00
Volume 12, 1931, paper bound	15.00

(Volumes 2, 4, and 6-9 published in National Research Council Bulletin)

Volumes 16-34, 1935-1953, will be reproduced by photo-offset as soon as there is sufficient demand to warrant the undertaking of a reprint edition.

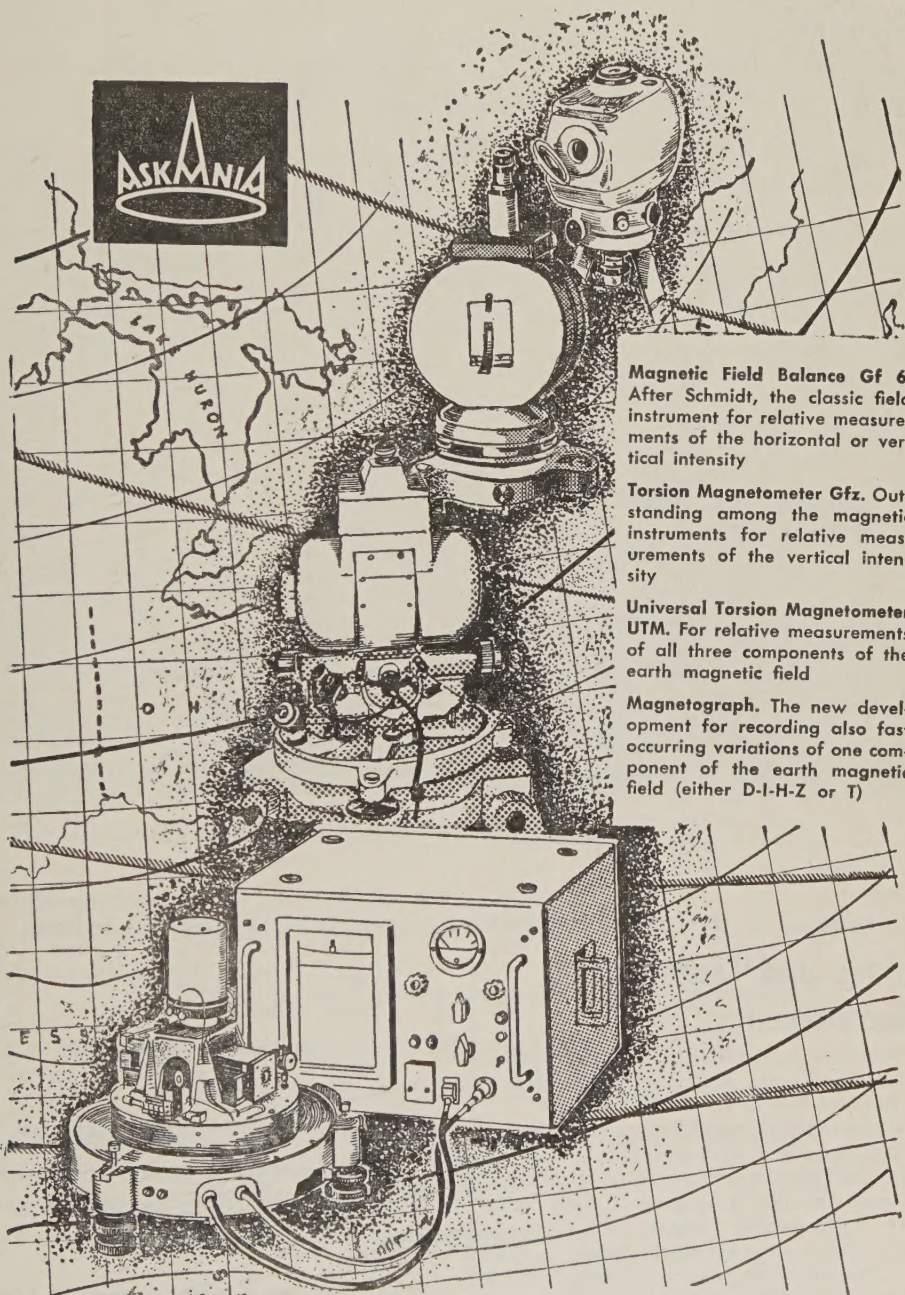


JOHNSON

REPRINT CORPORATION

111 FIFTH AVENUE
NEW YORK 3, NEW YORK

ASKANIA Magnetic Instruments for precise determination of magnetic anomalies



Magnetic Field Balance Gf 6. After Schmidt, the classic field instrument for relative measurements of the horizontal or vertical intensity

Torsion Magnetometer Gfx. Outstanding among the magnetic instruments for relative measurements of the vertical intensity

Universal Torsion Magnetometer UTM. For relative measurements of all three components of the earth magnetic field

Magnetograph. The new development for recording also fast occurring variations of one component of the earth magnetic field (either D-I-H-Z or T)

ASKANIA-WERKE

U. S. Branch Office & Service Dept.

• 4913 Cordell Ave., Bethesda, Maryland

NEW BOOKS FROM INTERSCIENCE

Methods and Techniques in Geophysics

edited by S. K. RUNCORN, *King's College, University of Durham*

Modern advances in physical techniques in this field are presented here by an international group of experts to help fill a relative void in the literature of pure geophysical research. The topics discussed in this first volume include *Measurement of: Temperature Gradient in the Earth, Heat Flow over Land, Gravity at Sea, The Geomagnetic Elements; also Bore-Hole Surveying, Measurements in Paleomagnetism, The Detection of Earth Movements, Earth Currents, Properties of Rocks under High Pressure and Temperature, Latitude and Longitude, and the Secular Motion of the Pole.* An additional volume is in preparation.

Volume 1 387 pages \$10.00

Lead Isotopes in Geology

by R. D. RUSSELL, *University of British Columbia*, and R. M. FARQUHAR, *University of Toronto*

The application of isotopic studies to geophysics has developed rapidly in very recent years, and there is need for this extensive detailed description. The authors, who have contributed much to rock dating by lead isotope determinations, have surveyed the field and given a coherent and up-to-date account of the various ideas that they and other investigators have expressed on the subject. A feature is the very extensive tabulation of lead isotopic abundances, from the authors' own work in Toronto and from other centers of geophysical studies in many parts of the world.

251 pages \$9.00

Methods and Techniques in Geochemistry

edited by A. A. SMALES, *United Kingdom Atomic Energy Research Establishment, Harwell*, and L. R. WAGER, *Oxford*

In this single volume, experts consider the major analytical methods used in geochemistry. Recent advances are discussed, as well as older techniques and their new developments. Each major method, with various related techniques, is treated in a separate contributed chapter, including a discussion of the underlying theory. Thoroughly practical, an early chapter deals with the examination and treatment of the material before analysis begins.

471 pages \$13.50

INTERSCIENCE PUBLISHERS, INC.

250 Fifth Ave., New York 1, N. Y.

ARE YOU A MEMBER of AGU?

If you are a reader or user of either of the publications noted below, you should look into this matter.

Members regularly receive
the monthly

**Journal of
Geophysical
Research**

the quarterly

**Transactions
American
Geophysical
Union**

Members are entitled to special discounts on other publications of AGU such as

- **Geophysical Monograph Series** (Nos. 1 to 5 available)
- **Izvestiya of the Academy of Sciences, USSR; Geophysics Series** for the years 1957, 1958, 1959, and 1960
- **Geodesy and Cartography, USSR, 1959**
- **Annual meeting in Washington** in late April or early May each year
- **Regional meeting in the Pacific Northwest** in autumn
- **Regional meeting in the Pacific Southwest** in winter
- **Others as opportunity permits**

For application forms and other information regarding membership, meetings, and other matters, write to

AMERICAN GEOPHYSICAL UNION

**1515 Massachusetts Ave., N.W.
Washington 5, D. C.**

(An application form is also inserted in the closing pages of this issue.)

We can now measure gravity from the air



Another achievement in gravity measurement from LaCoste & Romberg

Now for the first time, gravity surveys of inaccessible areas can be made from the air, using a LaCoste & Romberg airborne gravity meter. This new meter requires no gyroscopic stabilization platform. Its accuracy is better than 10 milligals.

Commercial airborne surveys are now available from Fairchild LaCoste Gravity Surveys, Inc.

LaCoste & Romberg 6606 NO. LAMAR AUSTIN, TEXAS

Manufacturers of airborne, submarine, shipborne and surface gravity meters for both exploration and geodetic surveys

Please mention JOURNAL OF GEOPHYSICAL RESEARCH, when writing to advertisers

**ANNOUNCING A TRANSLATION OF
GEODESY AND CARTOGRAPHY**

(Geodezia i Kartografiya)

The leading monthly journal of Geodesy and Cartography in the USSR is being translated and published in an English edition, *for the year 1959*, by the American Geophysical Union, aided by a grant from the National Science Foundation.

Subscription price, \$20.00 for the volume of 12 numbers

Send subscriptions to

AMERICAN GEOPHYSICAL UNION

1515 Massachusetts Avenue, N.W.
Washington 5, D. C., U.S.A.

Other publications of the AGU include

- Journal of Geophysical Research** (monthly), \$20.00 per calendar year (approximately 4000 pages anticipated for 1960)
- Transactions** (quarterly), \$4.00 per calendar year (approximately 600 pages anticipated for 1960)
- Geophysical Monograph Series** (occasional volumes), comprising papers too long for the *Journal*, or containing numerous papers of symposia and conferences related to a particular field of interest or project; Number 5 (issued in 1960) *Physics of Precipitation* (Proceedings of the Cloud Physics Conference, Woods Hole, Massachusetts, June 3-5, 1959), 435 pages, \$12.50
- Izvestiya**, Academy of Sciences, USSR, Geophysics series, English edition (monthly), \$25.00 per calendar year, available for 1957, 1958, 1959, and on subscription for 1960

**BULLETIN (IZVESTIYA), ACADEMY OF SCIENCES, U.S.S.R.
GEOPHYSICS SERIES**

Subscriptions for 1960 series now available

This monthly Russian publication, perhaps the leading journal of Geophysics of the U.S.S.R., is being translated and published in an English edition for the year 1960 by the American Geophysical Union. The twelve numbers in Russian cover about 2000 pages. Published with the aid of a grant from the National Science Foundation.

Send subscriptions now to

AMERICAN GEOPHYSICAL UNION

1515 Massachusetts Avenue, N.W.
Washington 5, D. C., U.S.A.

Subscription rates: \$25.00 for the volume of 12 numbers (\$20.00 to individual members of AGU subscribing for personal use)

Numbers will be mailed as issued.

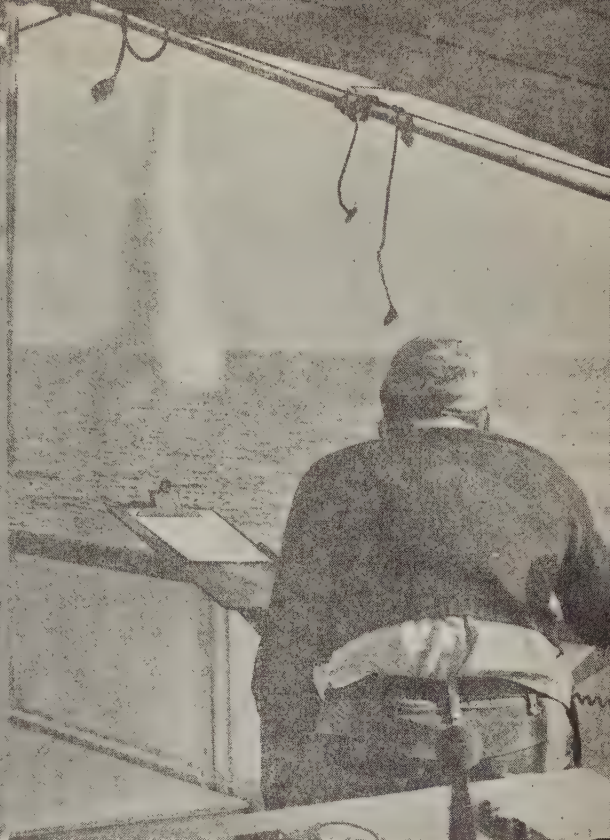
The English edition of this publication for 1957 has been translated and published for the American Geophysical Union by Pergamon Press. This volume may be ordered through the American Geophysical Union at a price of \$25.00. The 1958 and 1959 series are available at a price of \$25.00 for each volume of 12 numbers. Titles and authors of the papers contained in the series have been published in the 1959 and 1960 issues of the *Transactions*, AGU.



TO THE OCEAN'S FLOOR ... AND BELOW

Daily aboard TI's 405-ton, 158-foot SONIC—uniquely a complete sea-going seismic and acoustic investigation center—geoscientists are studying and mapping the structure of the earth below the ocean's floor. Illustrated above is the seismic reflection method, with explosive charges detonated nearby for detailed study of energy travel through water and rock. Technicians aboard the SONIC also record refracted seismic energy, measuring signals through the ocean

floor from charges exploded on land or in water as much as 35 miles away. Similar land-based TI geophysical parties are now working in more than 22 countries of the world.



INNER-SPACE KNOWLEDGE FOR OUTER-SPACE TECHNOLOGY ADVANCED BY TI'S

scientific key to Davy Jones' locker!

At a time when the focus is on outer space—a time when we know more about the moon's surface than we know about 70% of the earth's surface—geophysicists such as this sea-going scientist from Texas Instruments are furthering space-age technology with studies of inner space—the oceans.

He represents one of more than 60 global TI geophysical investigation parties who are applying 30 years' experience in earth sciences to measurement of earth's land and sea physical characteristics. Fundamental to modern defense, earth sciences have extended their traditional role in petroleum exploration to gathering information vital to programs in *underwater warfare, missile accuracy, seismic communications, detection/surveillance of nuclear tests, and design of underground defense structures.*

TI's talent for these "down-to-earth" studies dates back to 1930, when the company was formed as Geophysical Service Inc.—the first independent company to perform seismic reflection surveys for oil exploration. And from GSI's early need for sensitive electronic seismic equipment

came an engineering skill that was applied to Anti-Submarine Warfare systems in World War II, and resulted in TI's Apparatus division becoming a leading ASW equipment manufacturer today. This rare blending of earth sciences knowledge and experience with skills in systems and components gives TI a *unique capability in space-age technology.*

The founding company (GSI) is now the geophysical exploration arm of TI's Geosciences & Instrumentation division, and these capabilities are extended to governmental agencies by the Geosciences department. Designing and manufacturing advanced instruments and systems in wide use by these parties and others is the Instrumentation Product group, with such products as *WORDEN** gravity meters, *EXPLORER** seismograph systems and *seisMAC®* seismic computers.

For more about geosciences at TI, write to Central Merchandising for Bulletin DM-101.

**Trademark of Texas Instruments*

TEXAS  **INSTRUMENTS**
INCORPORATED

HEADQUARTERS: 6000 LEMMON AVENUE, DALLAS 9, TEXAS. **PLANTS:** ATTLEBORO, MASS. • DALLAS, TEXAS • HOUSTON, TEXAS • VERSAILLES, KY. • ELIZABETH SOUTH, AUSTRALIA • ALMELO, HOLLAND • AVERSA, ITALY • BEDFORD, ENGLAND • BONNEVILLE, FRANCE • BUENOS AIRES, ARGENTINA • MEXICO CITY, MEXICO

OFFICES IN 75 PRINCIPAL CITIES OF THE WORLD

Please mention JOURNAL OF GEOPHYSICAL RESEARCH, when writing to advertisers

GEOPHYSICAL MONOGRAPH SERIES

AMERICAN GEOPHYSICAL UNION

1515 MASSACHUSETTS AVENUE, N.W.

WASHINGTON 5, D. C., U.S.A.

Antarctica in the International Geophysical Year—Geophysical Monograph No. 1 (Publication No. 462, National Academy of Sciences—National Research Council); Library of Congress Catalogue Card No. 56-60071; 133 pp. and large folded map of the Antarctic, 1956, 7" x 10", \$6.00. Contains 16 papers by various American authorities on the Antarctic under the headings: General, Geographic and Meteorological, Geological and Structural, Upper Atmospheric Physics, and Flora and Fauna. Map (41" x 41") compiled by the American Geographical Society. Introduction by L. M. Gould.

Geophysics and the IGY—Geophysical Monograph No. 2 (Publication No. 590, National Academy of Sciences—National Research Council); Library of Congress Catalogue Card No. 58-60035; 210 pp., 1958, 7" x 10", \$8.00. Contains 30 papers by leading American authorities under the headings: Upper Atmospheric Physics, The Lower Atmosphere and the Earth, and The Polar Regions. Preface by Joseph Kaplan.

Atmospheric Chemistry of Chlorine and Sulfur Compounds—Geophysical Monograph No. 3 (Publication No. 652, National Academy of Sciences—National Research Council); Library of Congress Catalogue Card No. 59-60039; 129 pp., 1959, 7" x 10", \$5.50. Based on a symposium held jointly with the Robert A. Taft Sanitary Engineering Center of the U. S. Public Health Service in Cincinnati in November, 1957. Contains 23 papers (some as summaries) with discussion. Preface by James P. Lodge, Jr.

Contemporary Geodesy—Geophysical Monograph No. 4 (Publication No. 708, National Academy of Sciences—National Research Council); Library of Congress Catalogue Card No. 59-60065; 96 pp., 7" x 10", 1959, \$5.50. Based on a Conference held at Cambridge, Massachusetts, in December 1958 jointly by the AGU with the Smithsonian Astrophysical Observatory and the Harvard College Observatory. Contains 14 papers by leading authorities, with verbatim discussions on topics ranging from classical geodesy to trilateration by underwater sound to space navigation in the solar system. Edited by Charles A. Whitten and Kenneth H. Drummond.

Physics of Precipitation—Geophysical Monograph No. 5 (Publication No. 746, National Academy of Sciences—National Research Council); Library of Congress Catalogue Card No. 60-60010; 435 pp., 7" x 10", 1960, \$12.50. Based on a Conference held at Woods Hole, Massachusetts, in June 1959. Contains 48 papers by leading authorities, with verbatim discussions on topics ranging from planetary-scale phenomena to microanalysis including hail formation and precipitation control. Edited by Helmut Weickmann.

Postage is to be added to prices shown unless payment accompanies order. Quantity discounts (count each Monograph separately): 5-19 copies, 10%; 20-49 copies, 15%; 50 or more copies 20%.

Purchase Order

TO AMERICAN GEOPHYSICAL UNION

1515 Massachusetts Avenue, N.W., Washington 5, D. C., U.S.A.

Please enter our order for the following:

_____ copies of Geophysical Monograph No. 1, at \$6.00*	\$ _____
_____ copies of Geophysical Monograph No. 2, at \$8.00*	\$ _____
_____ copies of Geophysical Monograph No. 3, at \$5.50*	\$ _____
_____ copies of Geophysical Monograph No. 4, at \$5.50*	\$ _____
_____ copies of Geophysical Monograph No. 5, at \$12.50*	\$ _____

☐ Payment of \$_____ is enclosed.

☐ Please send invoice, adding postage charges.

☐ Enter our standing order for _____ copies of subsequent Geophysical Monographs at the special prepublication rates, e.g., prepublication rate for Monograph No. 4 for non-members was \$4.00, payment in advance, or \$4.75 (plus postage) on invoice.

* List price is net for quantities up to four; see above for discounts on quantity purchases. Special discounts to members.

Typed name _____ Signature _____

Address _____



Western Conducts More Marine Seismic Surveys Than All Other Contractors Combined!

Since 1954, Western Geophysical Company's techniques, instrumentation and professional excellence have won over half of *all* contracts for offshore seismic exploration.

The Western Marine Seismometer, a low-impedance, pressure-sensitive device, is unequalled for high output, low-frequency response, and ruggedness. Western records the entire spectrum from $\frac{3}{4}$ -cps to 10-Kc, plus. Western's high speed cable permits normal production of up to 200 recording locations a day. The story of Western's current activities—"Panorama of a World Wide Organization"—will be sent to you upon request.



Additionally,
Western's land seismic parties
and gravity crews
are at work on four continents

Western

GEOPHYSICAL COMPANY

A SUBSIDIARY OF LITTON INDUSTRIES



Principal Office: 933 NORTH LA BREA AVENUE, LOS ANGELES 38 CALIFORNIA

AFFILIATE AND REGIONAL OFFICES THROUGHOUT THE WORLD

Please mention JOURNAL OF GEOPHYSICAL RESEARCH, when writing to advertisers

SPRENGNETHER LONG PERIOD HORIZONTAL SEISMOMETER

GENERAL SPECIFICATIONS:

- Period Range: 6 to 70 seconds.
- Magnification: Up to 15,000, depending on operating period.
- Damping: Electromagnetic.
- Transducer-moving coils in circular magnetic gaps.
- Coils approximately 500 ohms. or to your specifications.
- Pendulum steady mass weight 22 lbs.

PHYSICAL SPECIFICATIONS:

Length.....25"
Width.....25"
Height.....22"
Net Weight.....90 lbs. approx.
Shipping Weight.....155 lbs. approx.

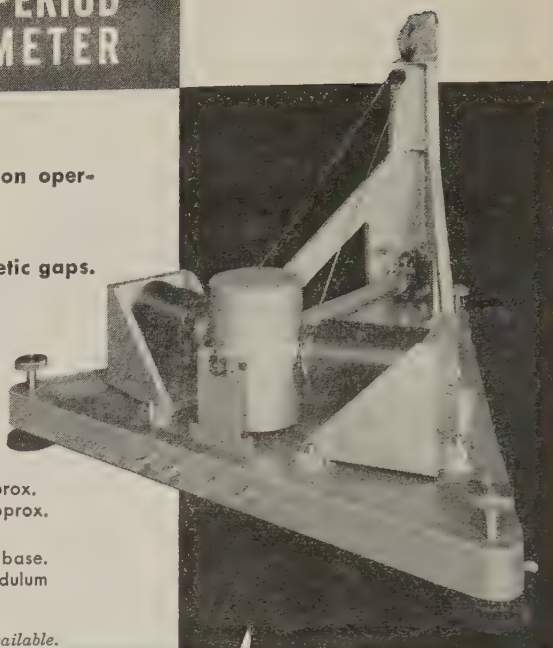
COVER:

Light weight aluminum with rubber gasket seal to base.
Provided with viewing window to observe pendulum centering.

*To compliment this instrument,
a long period vertical seismometer is also available.*

Internationally Known Mfrs. of Seismological, Geophysical Instruments.

W. F. SPRENGNETHER INSTRUMENT CO., INC.
4567 SWAN AVENUE • ST. LOUIS 10, MO.



**WRITE FOR DETAILED
INFORMATION ON THESE
INSTRUMENTS.**

Back issues available . . .

Journal of Geophysical Research • 1959 • Volume 64

Complete set of 12 (2488 pp.)—\$30.00

January (132 pp.) \$2.00	May (98 pp.) \$2.00	September (230 pp.) \$3.00
February (138 pp.) \$2.00	June (110 pp.) \$2.00	October (284 pp.) \$4.00
March (112 pp.) \$2.00	July (168 pp.) \$2.00	November (390 pp.) \$5.00
April (106 pp.) \$2.00	August (268 pp.) \$4.00	December (452 pp.) \$6.00

Scientific Effects of Artificially Introduced Radiations at High Altitudes (74-page
Symposium reprinted from the August issue) \$1.50

International Symposium on Fluid Mechanics in the Ionosphere (202-page Symposium
reprinted from the December issue) \$4.50

Subscriptions to Journal of Geophysical Research, Calendar Year 1960..... \$20.00

AMERICAN GEOPHYSICAL UNION

1515 Massachusetts Avenue, N.W. • Washington 5, D. C.

Note: The former publisher of the *Journal of Geophysical Research* has turned over the stock of back numbers, 1958 and earlier, to Walter J. Johnson, Inc., 111 Fifth Avenue, New York 3, New York.

Journal of GEOPHYSICAL RESEARCH

VOLUME 65

NOVEMBER 1960

No. 11

Balloon Observation of Artificial Radioactivity at the Base of the Stratosphere

H. T. MANTIS AND J. R. WINCKLER

*School of Physics
University of Minnesota
Minneapolis, Minnesota*

Abstract. On two ascents of a series of IGY cosmic-ray balloon flights, layers of radioactivity were observed near the tropopause at Minneapolis, Minnesota. On March 21, 1958, a specific activity of 0.8×10^{-6} disintegrations/cm³ sec was observed and on October 31, 1958, the value was 0.4×10^{-6} . Upper-air trajectories were constructed for the events, and these, together with the mean energy, specific activity, and vertical profiles of the radiation, are consistent with the hypothesis that this radioactivity was produced by Soviet nuclear bomb debris about 1 week old.

During the International Geophysical Year the University of Minnesota launched 85 high-altitude cosmic-ray balloons carrying standardized radiation detectors consisting of a Geiger counter, an ionization chamber, and nuclear emulsions. The balloons also carried a radiosonde transmitter and a 35-mm camera for determining balloon position and obtaining wind information. On two balloon ascents, flights IGY-27 (March 21, 1958) and IGY-54 (October 31, 1958), the radiation detectors showed rates above the normal cosmic-ray level in the vicinity of the tropopause. It is our purpose in this note to present some of the characteristics of this abnormal radiation as determined from the records of the ion chamber and counter and to discuss the evidence that this radiation represents the debris from nuclear explosions. Besides a comparison of the characteristics of the observed radiation with the known properties of bomb debris, additional corroboration of this hypothesis is obtained by a reconstruction of the air trajectories which lead to Asia within a day or two of announced Soviet test explosions. These two observations gain additional significance as the maximum values of artificial radioactivity found in more than 150 measurements of the

vertical radiation profile.¹ Measurements were made so frequently during several series of bomb tests that it is believed these maximum values of the level of radioactivity must have been obtained in a radioactive cloud on its initial traverse around the globe. Decay and dilution in the atmosphere apparently reduce the radioactivity below this observed level in the period between the first and second traverse.

The radiation observations made on both balloon ascents are shown in Figure 1. The pulsing rate of the ion chamber, which is proportional to the rate of ionization produced in argon gas in the thin-walled steel container, and the counting rate of the brass-walled Geiger counter have been plotted as a function of the atmospheric pressure. The details of the instrumentation have been described in a number of publications [Ney and Winckler, 1958; Peterson, Howard and Winckler, 1958; Winckler, Peterson, Arnoldy, and Hoffman, 1958]. The principal feature of the curves of ionization and counting rate shown in Figure 1, the steady increase to

¹ A profile measurement is made during descent as well as ascent of the balloon. The descent occurs almost a day later and frequently represents a sample from a different air mass.

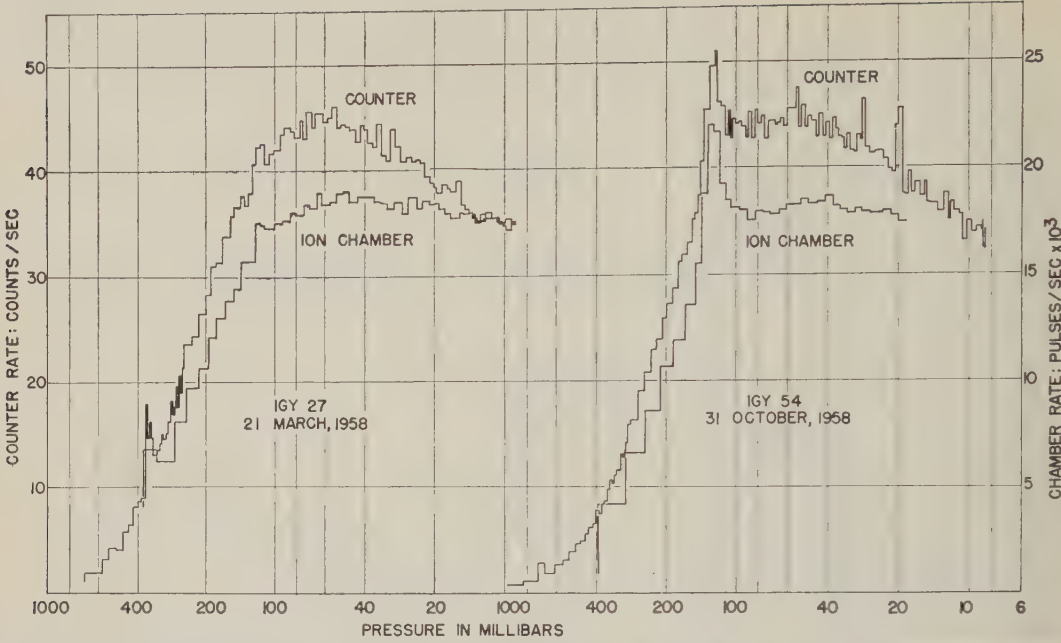


Fig. 1. Balloon soundings for two radioactive clouds. On March 21 the temporary increase in both counter and ion chamber occurs at 350 mb, on October 31 at 140 mb. The main increase in the instruments beginning at 1000 mb and having a maximum at about 60 mb on both flights is due to the normal cosmic-ray background in the atmosphere.

maximum near 60 mb and a slow decrease above this level, is characteristic of the secondary effects produced in the atmosphere by high-energy primary cosmic rays. On each flight, both instruments showed increases in radiation in rather thin layers; on IGY-27 the radiation layer was found at 350 mb just below the tropopause, and on IGY-54 the layer was located above the tropopause at 125 mb. Fluctuations in natural radiation levels of comparable magnitude have not been observed except in association with unusual geomagnetic or solar activity; e.g., the auroral X rays previously reported by Winckler and his co-workers in 1958. The observation made on IGY-27 at 350 mb is almost

certainly *not* a natural cosmic-ray event because the great intensity of cosmic rays required to penetrate to this atmospheric depth would produce some detectable effects at sea level, and none were observed. The absence of such natural causes coincident with these balloon ascents stimulated the search for an alternative explanation and led to this examination of the bomb-debris hypothesis.

Some characteristics of the additional radiation observed on these two flights have been computed from the rates of the radiation detectors, assuming that the increase is caused by γ rays. Values of the peak γ -ray flux, radiation dosage, mean energy, and specific activity in

TABLE 1. Properties of the Artificial Radiation

Flight	Date and Time, GMT	Peak γ -Ray Flux photons/cm ² sec	Average Dosage, microroentgens/hr	Mean Energy, Mev	Specific Activity, disintegrations/ cm ³ sec
IGY-27	0812 Mar. 21, 1958	32	7.3	1	0.8×10^{-6}
IGY-54	1256 Oct. 31, 1958	43	1.0	0.1	0.4×10^{-6}

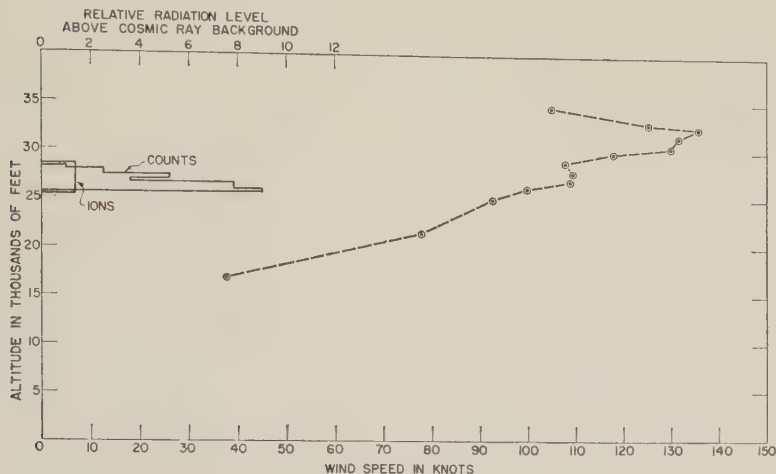


Fig. 2. Vertical profiles of wind and radiation on March 21, 1958 (flight IGY 27). The radioactive layer was concentrated below the jet stream maximum close to what appears to be the remains of an earlier wind maximum.

disintegration/cm³ sec in air at the height of the layer in which the γ rays were observed are given in Table 1.

The flux is determined from the counting rate of the omnidirectional counter and the counter efficiency for γ rays. The radiation dosage is obtained from the ion chamber readings, and the mean energy is calculated from the relative magnitude of the readings of the counter and the ion chamber as described previously by Winckler, Peterson, Arnoldy, and Hoffman [1958]. If the attenuation of γ rays by the surrounding medium, air in this case, is known, the counting rate may be used to compute the specific activity (the rate with which γ rays are emitted per unit volume), for the counting rate is simply a summation over volume of all γ rays emitted in the proper direction, attenuated by the surrounding air. The integral over volume is particularly simple for the omnidirectional counter. The counting rate N will be given by

$$N = IA \int_0^\infty e^{-\mu r} dr \quad (1)$$

where A is the surface area of the counter, μ is the absorption coefficient for air at the pressure of the layer, and I is the specific activity. The specific activity found by evaluating the integral then becomes

$$I = \mu N / A \quad (2)$$

where N is the counting rate corrected for

counter efficiency and μ is given for 0.7-Mev γ rays in air at STP as 0.9×10^{-4} cm⁻¹ [Hirschfelder, 1950, p. 225].

The elimination of natural sources for the observed radiation on flight IGY-27 and the agreement between observed mean energy and the mean energy of fission γ rays is interpreted as being a good means of identification of the radiation as nuclear debris. On flight IGY-54, the observed mean energies of the γ rays were an order of magnitude less, and, because the radiation was observed at higher elevations, the possibility of a natural origin of the radiation cannot be entirely eliminated.

The causes for the occurrence of the debris in a thin layer on flight IGY-27 seemed apparent from the meteorological circumstances in which it was observed. The radiation was found in a secondary wind maximum just below the jet stream level. The vertical wind profile determined from the radio theodolite positions of the cosmic-ray balloon is shown with the profile of radiation excess in Figure 2. A vertical column of debris would be expected to be distorted by the wind profile; the debris arriving earliest and in which the radioactivity would be most intense would be found in a layer at the wind maximum.

The second record showing radioactivity (IGY-54) was obtained in a region of light winds 10,000 feet above the region of maximum wind but the layer in which the radioactivity occurred was equally distinct. Upon reconstruction of the tra-

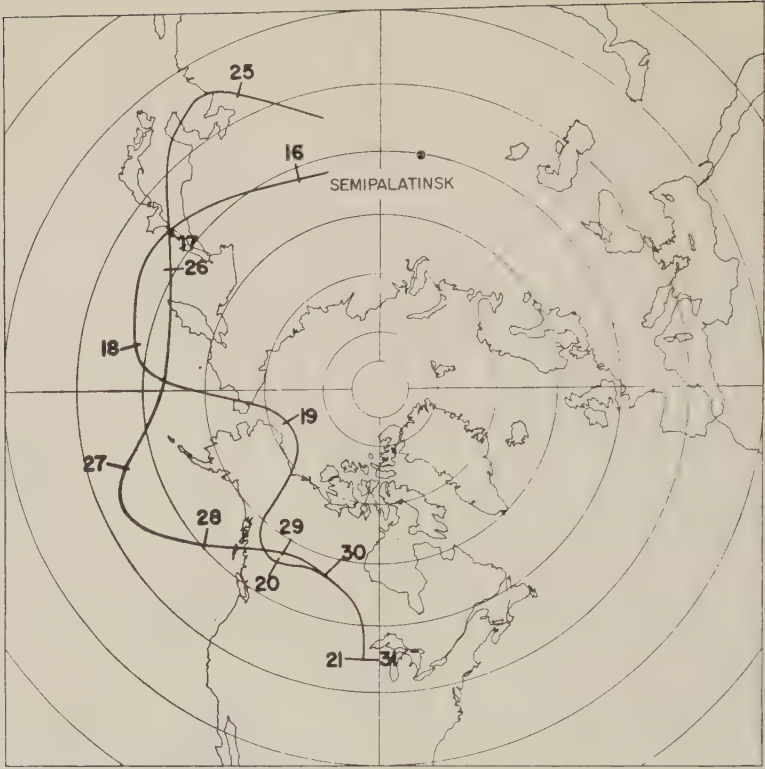


Fig. 3. Estimated trajectories of the air arriving over Minneapolis at the time of the observation of radioactivity on March 21, 1958, and October 31, 1958. The subsequent numbers mark the 0000 GMT trajectory position for that date. The dates and other data on Soviet nuclear explosions as released by the AEC are:

Date	Size	Site
Mar. 15, 1958	< megaton	Siberia
Mar. 14, 1958	< megaton	Arctic
Oct. 25, 1958	large	Arctic
Oct. 24, 1958	large	Arctic
Oct. 22, 1958	large	Arctic

jectory, it was found from the large temperature changes along the trajectory that this air had ascended recently from the tropopause maximum wind level, and it is believed that the layered appearance arises in the same way—a distortion of a vertical column of debris by the mean wind profile.

Air trajectories were reconstructed backwards from the point of observation by using the 12-hourly constant pressure charts nearest the level of the reported radioactivity. The trajectory originating near the jet stream level on March 21, 1958, was constructed from 300-mb charts; it continued to lie within a region of high winds so that it reached the Asiatic mainland in less than 5 days. Successive 24-hour positions on the

trajectory (at 0000 GMT) are indicated by the date on the map (Fig. 3). The trajectory on October 31, 1958, originated near a col in the wind field, and the wind profile made during the descent of this flight was very important in determining the initial leg of the trajectory. After starting this trajectory on 150-mb charts, a temperature change of more than 20°C was observed in the 36 hours preceding the observation of radioactivity. Assuming adiabatic processes, this observation implies that the air ascended from the vicinity of the tropopause—a large-scale upwelling apparently associated with the process of anticyclogenesis in the troposphere below. The remainder of this trajectory was constructed from 200-mb charts; again the

trajectory lay in a region of high winds and, despite its slow start, arrived on the mainland in only 6 days (Fig. 3).

The times of arrival of both trajectories on the Asiatic mainland were periods of frequent Soviet bomb testing. The nearest dates of test explosions as announced by the AEC have also been plotted in Figure 3 along with the location of one of the Soviet test sites, Semipalatinsk. Of the possible explosions that produced the debris, one of the March tests and all the October tests were made at Arctic test sites. The test on March 15 is indicated as having been made at a Siberian site which we have assumed to be Semipalatinsk. The last plotted trajectory positions are less than 1 day's travel time from the Siberian site but probably more than 24 hours from an Arctic site.

As mentioned above, in approximately 150 soundings made with these instruments during 1957 and 1958, only these two observations can be attributed to bomb debris, although this was a period of active testing. It appears that only recent and probably very large detonations produce observable effects. Some process other than the known radioactive decay of bomb debris [Hirschfelder, 1950] alone must be the major cause of the dilution. We have calculated the horizontal diffusion coefficients in the atmosphere, assuming a 'nominal' bomb, and find values of about 10^9 cm²/sec. This is presumably a lower limit, as very probably much larger than nominal bombs were detonated. Other causes of dilution such as precipitation may also be important.

The only other direct measurement of bomb debris in the atmosphere by radiation counters in balloons which has come to our attention is that reported by Ishii [1956]. In a series of flights in 1954 and 1955, specific activity values of about 10^{-10} curies/cm³ were measured. Ishii's values are thus very similar in magnitude to ours.

The successful detection of radioactive debris by the use of instruments with the low γ ray efficiency of the ion chamber and Geiger counter

suggests that improved techniques of γ -ray detection could be used for direct monitoring of artificial radioactivity. Ishii has improved the counter technique by using anticoincident counters to reduce the background from cosmic-ray particle. He must, however, subtract the cosmic-ray photon background which is relatively unknown and certainly not constant throughout the solar cycle. Elimination of the cosmic-ray photon background might be accomplished with a scintillation counter set to detect photons of a definite energy—a γ -ray line from a specific isotope, for example. A counter of this type in conjunction with anticoincident counters should increase the sensitivity of γ -ray detection by a factor of 10^4 , the level apparently required for direct monitoring of older debris.

Acknowledgments. We are indebted to Dr. L. Machta, who called our attention to the identification of Semipalatinsk as a test site in an announcement by the French government, and who provided the unclassified AEC publication on test dates.

This work was supported by the U. S. National Committee for the IGY through the National Science Foundation, by the Office of Naval Research, and by the Geophysics Research Directorate, Air Force Cambridge Research Center.

REFERENCES

- Ishii, Chihiro, Method of Measurement of Radioactive Dusts in the Upper Air by Radiosonde, *Peaceful Uses of Atomic Energy*, Geneva Conferences, 1955, vol. 9, United Nations, New York, p. 747, 1956.
- Hirschfelder, J. O., *The Effects of Atomic Weapons*, Combat Forces Press, Washington, D. C., 456 pp., 1950.
- Machta, L., *Annals of the IGY*, vol. 5, part 5, Pergamon Press, London, 313-323, 1958.
- Ney, E. P., and J. R. Winckler, High altitude cosmic ray measurements during the International Geophysical Year, *Geophysical Monograph No. 2*, American Geophysical Union, 81-91, 1958.
- Peterson, L. E., R. L. Howard, and J. R. Winckler, Balloon gear monitors cosmic radiation, *Electronics*, 31, 76-79, 1958.
- Winckler, J. R., L. Peterson, R. Arnoldy, and R. Hoffman, X-rays from visible aurorae at Minneapolis, *Phys. Rev.*, 110, 1221-1231, 1958.

(Manuscript received July 11, 1960; revised September 1, 1960.)

Balloon Observations of X Rays in the Auroral Zone II

K. A. ANDERSON¹ AND D. C. ENEMARK²

*Department of Physics and Astronomy, State University of Iowa
Iowa City, Iowa*

Abstract. Data from a long-duration balloon flight at 35-km height over the auroral zone during August 1959 showed that only very small fluxes of energetic X rays accompany visible auroras at this latitude. The maximum observed photon flux above 25 keV during a bright aurora was $2.5 \text{ cm}^{-2} \text{ sec}^{-1}$. Much larger fluxes, up to $40 \text{ cm}^{-2} \text{ sec}^{-1}$, preceded two active visible displays by about half an hour. On August 17 and 18 X-ray influxes were observed for several hours during the daytime. From Explorer VI data these are believed to be associated with the filling-up of the outer radiation belt after a geomagnetic storm. The scintillation counter employed permitted a determination of the X-ray energy spectrum at 6 g cm^{-2} depth from 25 to 300 keV on this and several other flights. From an analysis given here the parent electron spectrum is derived and found to be extremely steep. Typically, the ratio of the differential photon intensity at 30 keV to that at 160 keV is 350 to 1. Other balloon flights during August 1959 show that a large loss of electrons having energy $>25 \text{ keV}$ is occurring even on magnetically rather quiet days.

INTRODUCTION

As a result of long-duration balloon flights in the auroral zone it was found in 1957 that moderate fluxes of X rays appear at atmospheric depths of 10 g cm^{-2} in connection with geomagnetic storms [Anderson, 1958]. These X-ray fluxes showed very close association with at least some large storm excursions of the magnetic field. Of particular interest was the observation that a large X-ray burst occurred in time coincidence with the sudden commencement. Subsequent investigations in the auroral zone with scintillation counters having high efficiency for detecting X rays revealed that rather weak, sporadically appearing X-ray fluxes were present 40 to 50 per cent of the total high-altitude monitoring time of about 80 hours [Anderson, 1960]. These photons had roughly the same average energy as the magnetic-storm X rays. The weak X-ray fluxes were found not to be associated with geomagnetic activity, judging from magnetometer records obtained at the site of the balloon launchings (Figs. 1 and 2). Because of the high frequency with which these X rays appear it is reasonable to suppose that they are directly

related to the soft radiation discovered by rocket measurements [Meredith, Gottlieb, and Van Allen, 1955].

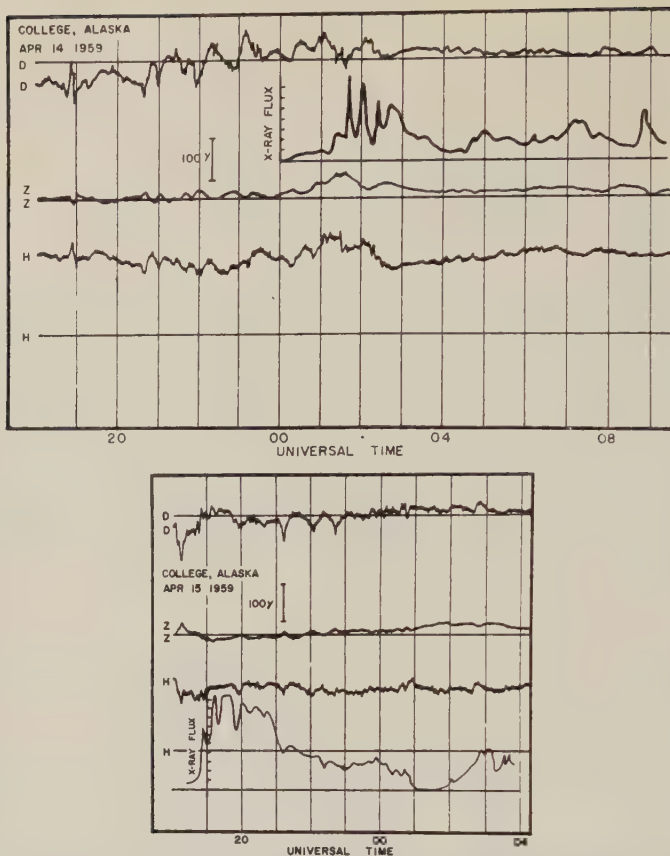
Further observations on auroral-zone X-rays were obtained during several flights made in August 1959 under conditions of geomagnetic activity that ranged from relatively quiet to greatly disturbed. Each of these flights to be described here carried $\frac{3}{4}$ inch by $\frac{3}{4}$ inch sodium iodide scintillation crystals and a four-channel pulse height analyzer which operated over a photon energy region of 25 to 300 keV. Also included in the instrumentation was a 10-inch-diameter Neher-type ionization chamber and a vertically oriented coincidence counter telescope. Such apparatus is capable of distinguishing X rays from other radiations such as electrons and protons without ambiguity.

RESULTS

Flight 990C. The counting rates in the four integral channels of the scintillation counter for this flight are shown in Figure 3. Also indicated there is the position of the Pfozter maximum, or high-energy cosmic-ray transition effect, encountered during the ascent part of the flight, the time at which the balloon reaches its floating altitude and the counting rate due to the high-energy cosmic radiation. Not all this flight is shown, since during its latter part no X rays were present. Sporadic fluxes of X rays were

¹ Now at Department of Physics, University of California, Berkeley, California.

² Now at Bell Telephone Laboratories, Whippany, New Jersey.



Figs. 1 and 2. Examples of quiet-day X-ray fluxes encountered over the auroral zone. The lack of correspondence between prominent ground-level magnetometer features and the X rays observed at high altitude can be seen from these figures.

present a total of 9 out of the 16 hours of data obtained at altitudes greater than 100,000 feet. The effects, relatively small on this occasion, are a great deal less than can be detected by usual techniques employing Geiger counters and ion chambers. The maximum flux, which occurs at about 1640 UT, is approximately 8 photons $\text{cm}^{-2} \text{sec}^{-1}$ above 34 keV. The minimum detectable flux with this scintillation counting apparatus is roughly 0.5 photon $\text{cm}^{-2} \text{sec}^{-1}$.

Flight 992C. From the four-channel counting-rate plot of the scintillation counter presented in Figure 4 it will be noticed that the cosmic-ray background rate slowly rises by about 25 per cent during the course of this flight. This occurred because the balloon was leaky, so that at 1300 UT the atmospheric depth was 8.5 g cm^{-2} , and by the end of the flight it had increased to 15 g cm^{-2} . Data re-

ception ended prematurely on account of a telemetering failure. The features of greatest interest during this flight are the two large X-ray bursts. These quite symmetrical peaks are both less than 3 minutes wide at their half-height and have a relatively small amount of structure, as can be seen from the expanded time scale drawing of the 1730 UT peak in Figure 5. The first of the two peaks occurs in close time coincidence with a sudden magnetic field excursion that amounts to about 500 gammas in the vertical component (Fig. 6). The smaller X-ray fluxes past 1400 UT also occur during times when the magnetometer trace is quite disturbed but not nearly to the same extent as during the first large peak. However, the largest peak encountered on this flight at 1730 UT occurred at a time when the magnetometer trace, though disturbed, is much quieter than during

COUNTS PER SECOND

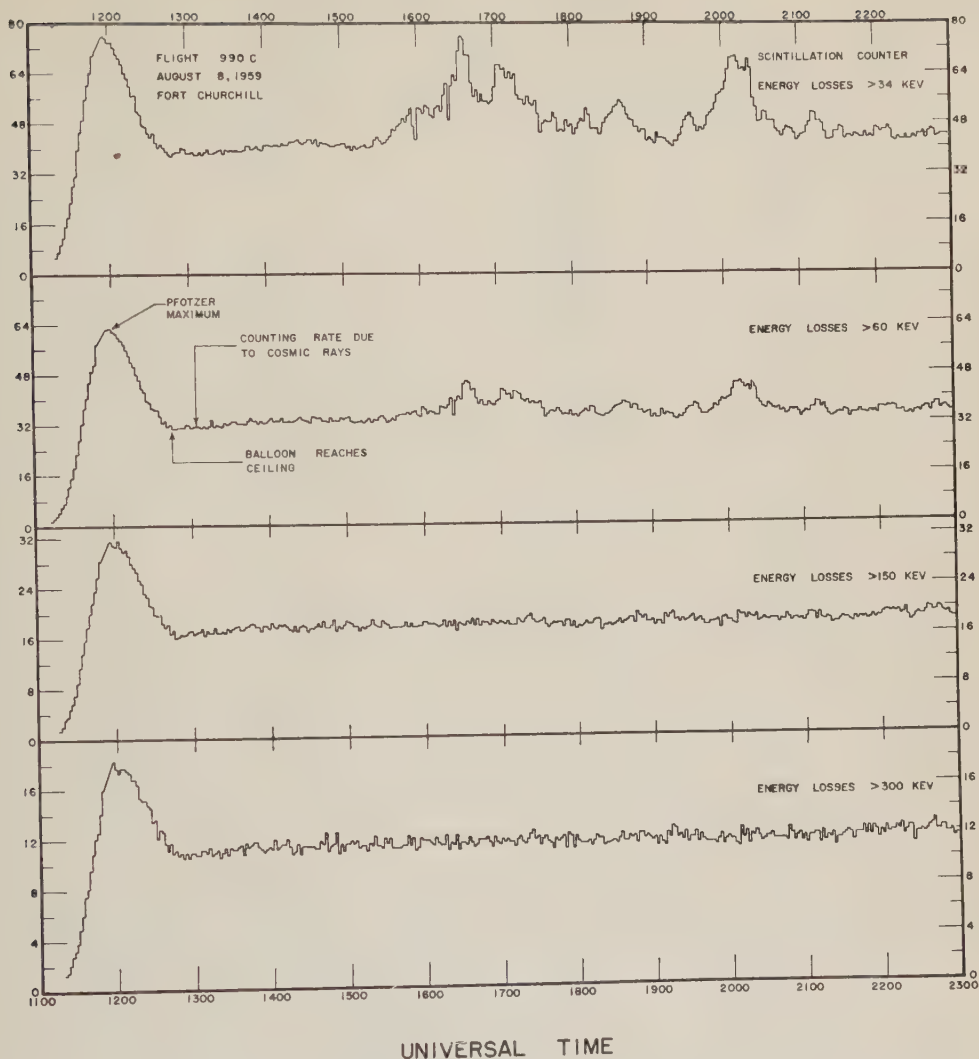


Fig. 3. Counting rates of the four integral channels from the scintillation detector on a flight over Fort Churchill during August 1959. The X-ray effects are seen to begin shortly after 1400 UT on this magnetically quiet day. To obtain local time for this and all other figures involving Fort Churchill flights, subtract 6 hours from Universal Time.

the earlier X-ray activity. The first X-ray peak is associated with approximately 3 db of cosmic noise attenuation at 30 Mc/s, while as shown by the riometer at Churchill the larger peak is related to a considerably smaller effect (Hartz, private communication). The looseness of the correlation between the X rays, riometer, and magnetometer effects may be 'instrumental.' The explanation we have adopted is that the X-ray effects are local and even though they appear at the balloon they may miss the beam

of the riometer antenna. Such an explanation implies that many of the X-ray bursts are connected in a rather incidental way to the large and not very localized geomagnetic field disturbances.

The integral and differential photon spectra as measured at 8.7 g cm^{-2} atmospheric depth during the large burst occurring at 1314 UT are shown in Figure 7.

Flight 993C. This flight provided about 32 hours of high-altitude data, during which time

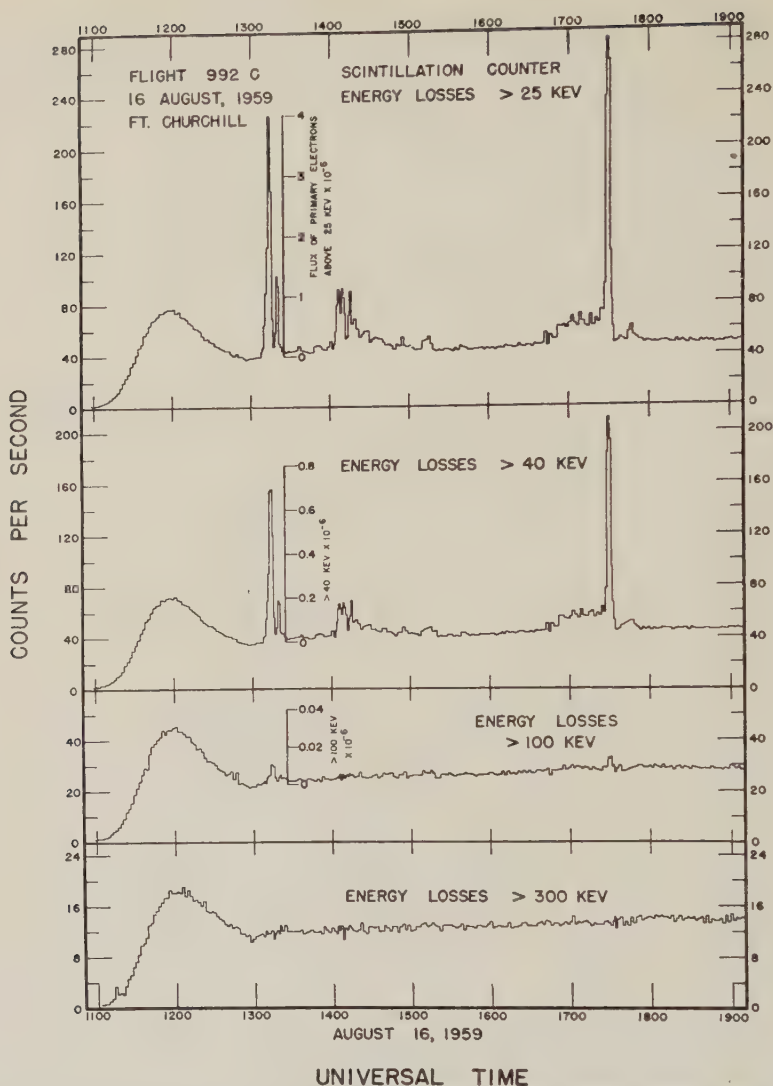


Fig. 4. The four integral channel counting rates during a flight made during very disturbed magnetic conditions. The appearance of the X-ray bursts is very different from the appearance of those in Figure 3, but the total X-ray flux is not strikingly larger. The integral electron fluxes that must have been present above the atmosphere to produce the observed X rays are also shown.

X-ray fluxes could be detected for 17 hours. The balloon remained at high altitude during the night of August 17–18, a time when bright and active auroral forms appeared over Fort Churchill. Figure 8 shows the counting rate due to energy losses in the scintillation crystal greater than 25 kev. The hours of sunset on the balloon are also indicated in this figure. The discriminator circuits are largely free of effects from low temperature during these hours, as can be judged from the constancy of the count-

ing rate due to the energetic cosmic radiation. Just past sunrise at about 1100 UT this rate is seen to increase by a few per cent as the temperature in the instrument gondola returns within the full compensation limits of the circuitry. Large X-ray effects occur shortly after local noon on both days. The smaller X-ray bursts during the night are associated in a manner to be described with active auroral forms occurring directly over the balloon. The detailed appearance of some of the X-ray bursts

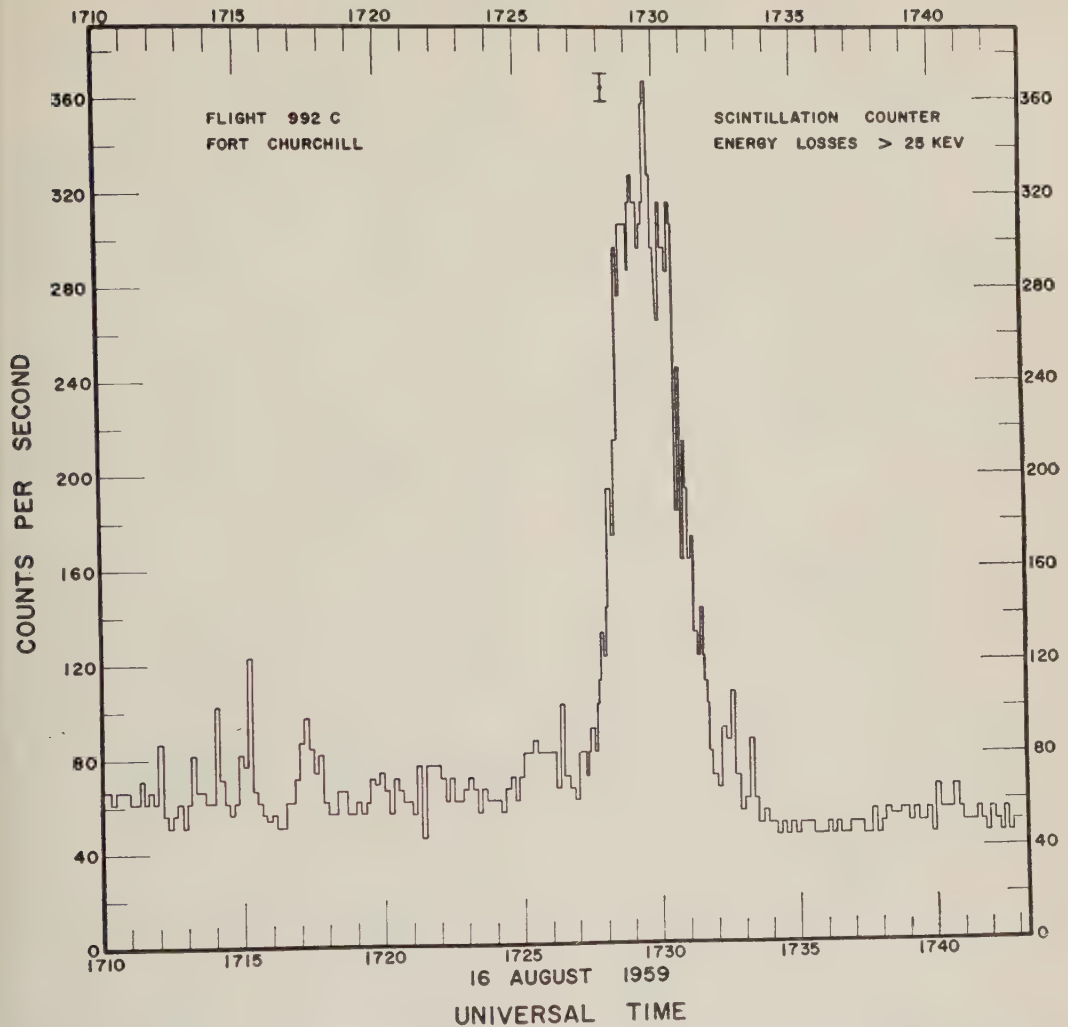


Fig. 5. One of the large X-ray bursts shown in Figure 4 plotted on an expanded time scale. The statistical error for a 10-second sample of data is indicated on the figure.

is shown in Figures 9, 10, and 11. It is seen that the large daytime peaks (Figs. 9 and 11) are very complex and contain structure down to the time scale of 5 seconds used to make the plots. These bursts give the impression of being made up of a rapid succession of smaller bursts piling on top of one another. The 0340 UT burst (Fig. 10) which is considerably simpler, resembles more the large bursts that occurred on flight 992C (Fig. 5). From Figure 12 it can be seen that the night X-ray bursts occur at times of considerable geomagnetic disturbances of a typical auroral character, such as the magnetic bay at 0730 UT. No such con-

nection with geomagnetic activity of even this localized type is exhibited by the larger daytime X-ray fluxes. The rather loose correlation between the X rays and the riometer observations can also be seen from this figure. The nighttime peaks associated with visible auroras have a more definite relation than the daytime bursts to the cosmic noise attenuation observed over Churchill.

The nature of the association of the nighttime X-ray activity with visible auroras is shown in Figure 13. In order to represent this relation auroral photographs have been shown every 10 minutes during the night of August

17-18. These all-sky-camera photographs taken at 1-minute intervals were obtained under excellent sky conditions by the Defence Research Northern Laboratory, Fort Churchill, Canada. The time base is not known with certainty, but the error in positioning the photographs on the Universal Time scale of Figure 13 is not more than ± 4 minutes. This amount of error does not affect any conclusions to be drawn. During this night there were two principal times of visible auroral activity, although less active forms were present during the entire night. These two periods of main auroral activity have been indicated on Figure 13, using the photographs shown there as well as all the intervening

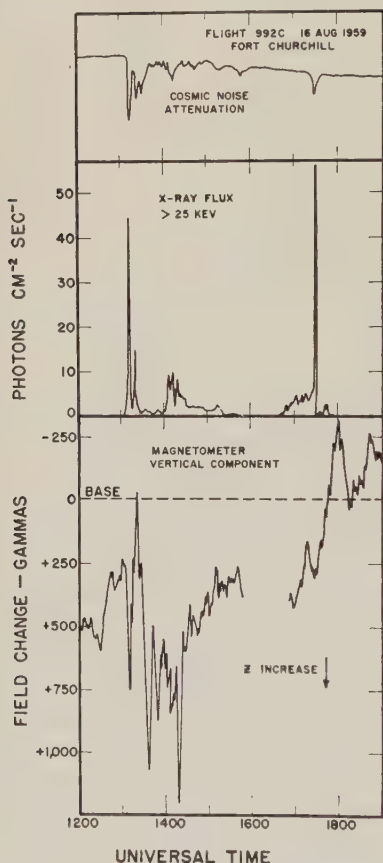


Fig. 6. Relation of the X-ray bursts during flight 992C to ionospheric opacity and the ground-level magnetometer. The relation is seen to be a qualitative one only, since the second and largest X-ray burst is associated with smaller riometer and magnetometer effects.

ones. The brightest and most active display occurred from about 0740 to 0820 UT on August 18, and this corresponds with the time that a sizable magnetic bay was present on the magnetometer record. It will be noticed that the X-ray peaks observed by the balloon apparatus do not coincide with the times of maximum visible auroral activity but instead precede them. The same is true of the smaller X-ray burst at 0340 UT; it occurs at a time of no marked visible aurora but is followed by a period of considerable auroral activity from 0400 to 0540 UT. *McIlwain* [1960] has found by direct rocket measurements that energetic electrons (> 25 kev) were absent in typical auroral forms, including one of intensity III on several occasions during February 1958. He found that lower-energy electrons contributed energy fluxes up to $600 \text{ ergs cm}^{-2} \text{ sec}^{-1}$ and thus concluded that energetic electrons are not responsible for the production of visible effects. The results here clearly support this finding but in addition indicate that energetic electrons are an important feature of the auroras that appear over the auroral zone. It should be noticed, however, that energetic photons were not totally absent during the time the auroral forms became brightest and most active. Small effects are to be seen during both periods of principal auroral activity on the night of August 17-18, and in fact these seem to be quite closely related to the visible auroral features. The largest of these X-ray effects occurring at 0745 UT corresponds to a primary electron flux above 25-kev energy of about $2 \times 10^5 \text{ cm}^{-2} \text{ sec}^{-1}$, and an energy flux of $0.1 \text{ erg cm}^{-2} \text{ sec}^{-1}$. Using the figure for the energy flux obtained by *McIlwain* it is seen that only of the order of 0.01 per cent of the total energy flux is contained in the electron spectrum above 25 kev. This comparison is made for intensity III auroras but not the same auroral display.

Flight 994C. Figure 14 shows the first part of this flight, during which sporadic fluxes of X rays again appeared. The effects are rather small, but the first X-ray feature, encountered from about 1530 to 1730 UT, is of particular interest. It differs from the sharply structured X-ray peaks seen throughout the other flights and has the same general appearance previously seen on two different occasions over Fairbanks, Alaska, during April 1959 [*Anderson*, 1960].

TABLE 1

Flight Number	Launch Time	Data Reception Ends	Instrumentation	
989	1144 UT August 4	0448 UT August 6	1. 10-inch ion chamber 2. G-M tube telescope 3. Single G-M tube	
991	0905 UT August 13	1842 UT August 14	1. 10-inch ion chamber 2. G-M tube telescope 3. Single G-M tube	32.5 hours Above 100,000 foot Altitude (30 km)
995	1403 UT August 22	1316 UT August 24	1. 10-inch ion chamber 2. G-M tube telescope 3. Single G-M tube	

Flight summaries for the three balloon flights that carried only gaseous detectors and observed no counting-rate changes attributable to sporadic auroral-zone X-ray fluxes. All flights were launched from Fort Churchill, Canada.

This peak is again not connected with specific magnetometer features, nor is it accompanied by observable cosmic noise attenuation. The more structured X rays after 1900 UT are associated, but quite loosely, with riometer effects of less than 1 db.

Flights 989, 991, and 995. In addition to the four flights already described in some detail, three other long-duration flights were made during August 1959. These, however, carried

only gaseous detectors, which were several hundred times less sensitive than the sodium iodide scintillation detector. During the flights carrying only the gaseous detectors no counting-rate effects that could be attributed to auroral zone X-ray fluxes were encountered. Counting-rate changes greater than 3 per cent lasting for about 5 or 10 minutes would have been detectable in the ion chamber and Geiger counters. Table 1 gives the dates and times of these flights.

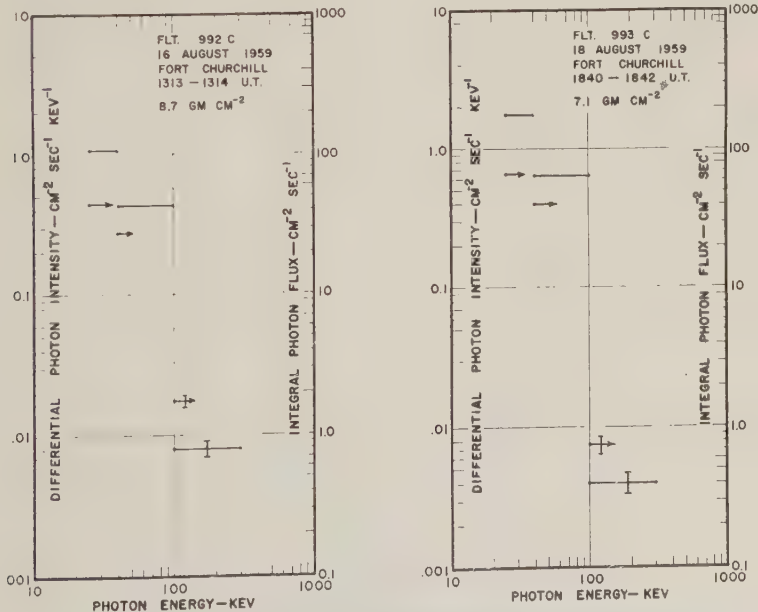


Fig. 7. Integral photon spectra obtained from the scintillation counter during two of the Fort Churchill flights. The derived three-point differential photon intensity spectra are also shown.

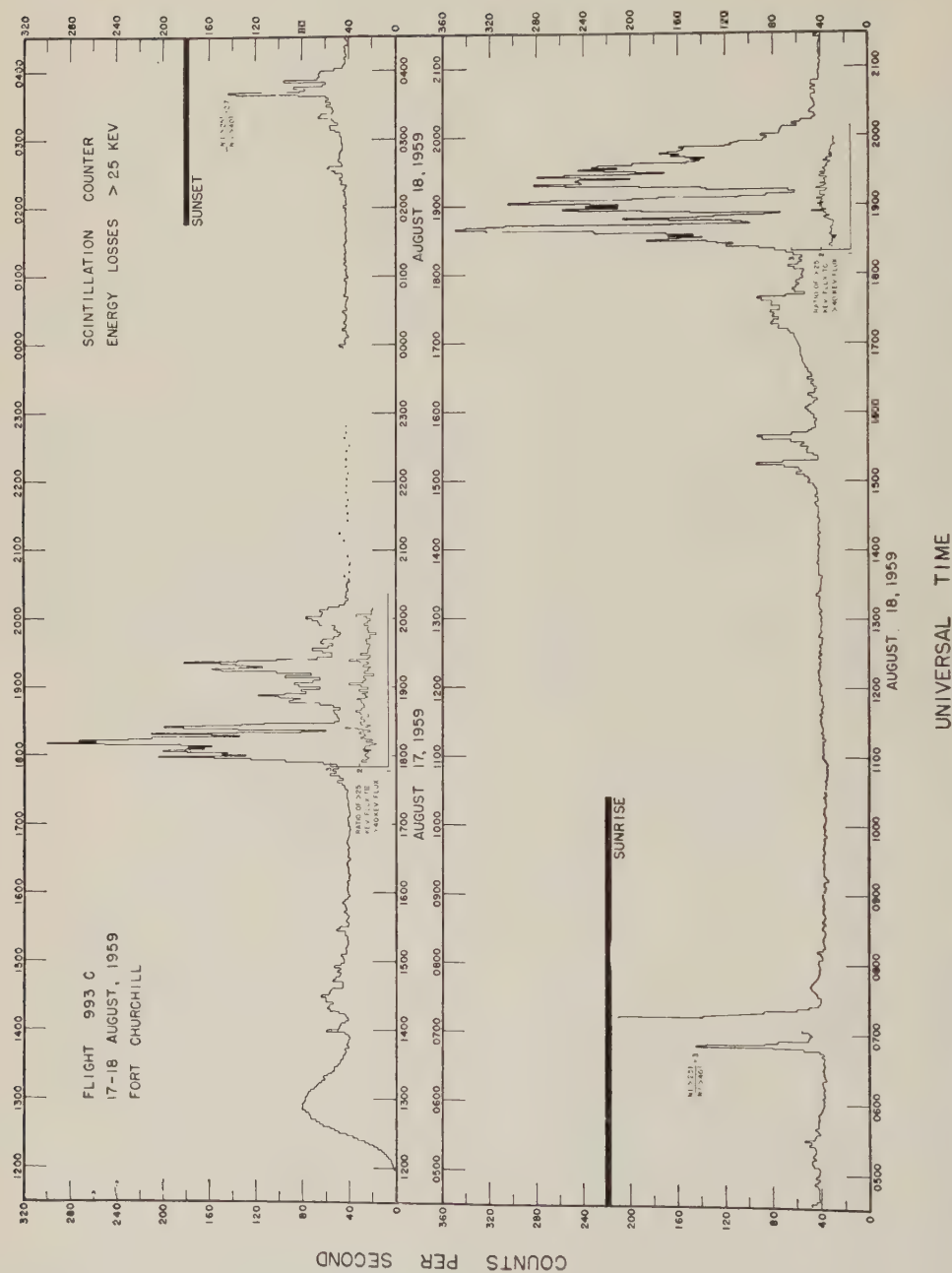


Fig. 8. Counting rate of the scintillation detector due to energy losses greater than 25 kev during a very long balloon flight over Churchill. At no time during this flight did a thin-wall Geiger counter telescope depart from the cosmic-ray rate, showing that very few electrons could have accompanied the X rays.

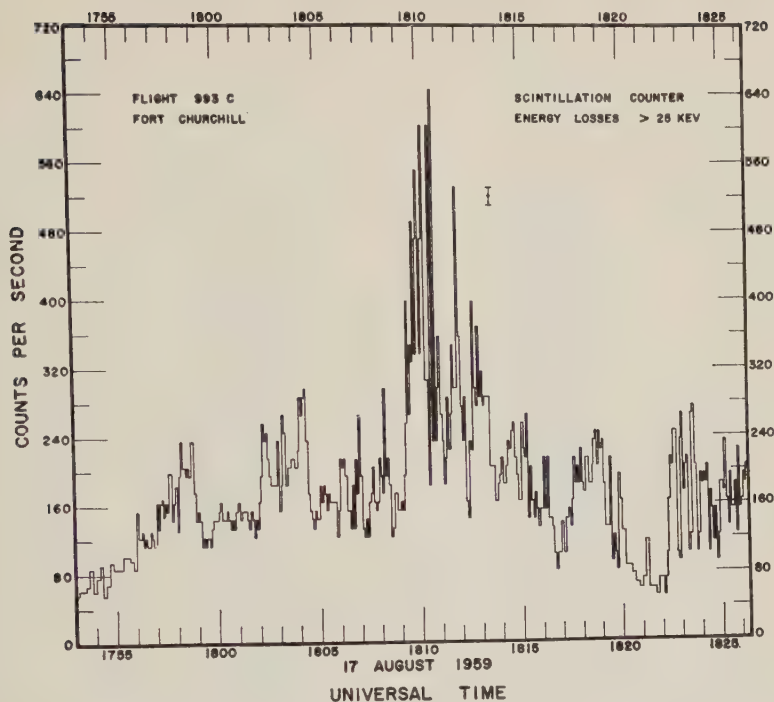


Fig. 9. Detailed appearance of the X-ray bursts during the large daytime influx on August 17. Structure is evident down to a time scale of a few seconds. These X-rays appeared at a time when satellite data showed the outer radiation belt to be filling up with energetic electrons.

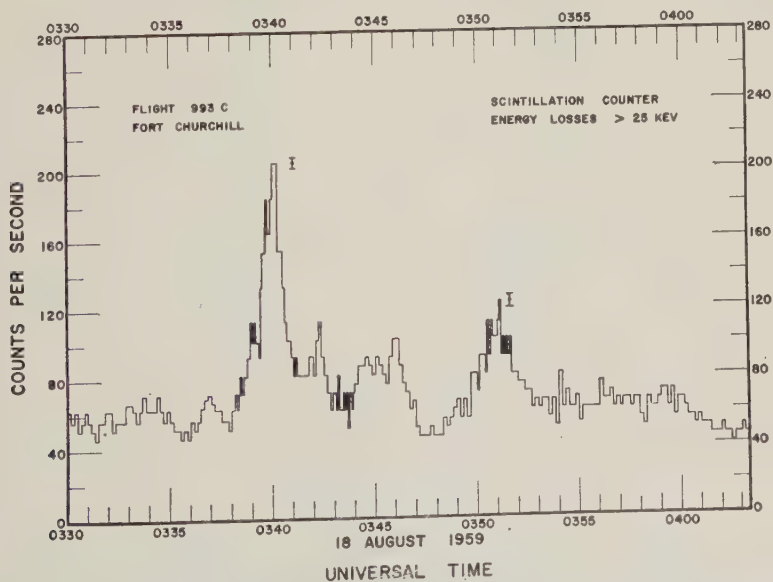


Fig. 10. Appearance of the X-ray bursts which preceded a bright visible aurora by about $\frac{1}{2}$ hour. These have considerably less structure than the X-ray activity shown in Figures 9 and 11.

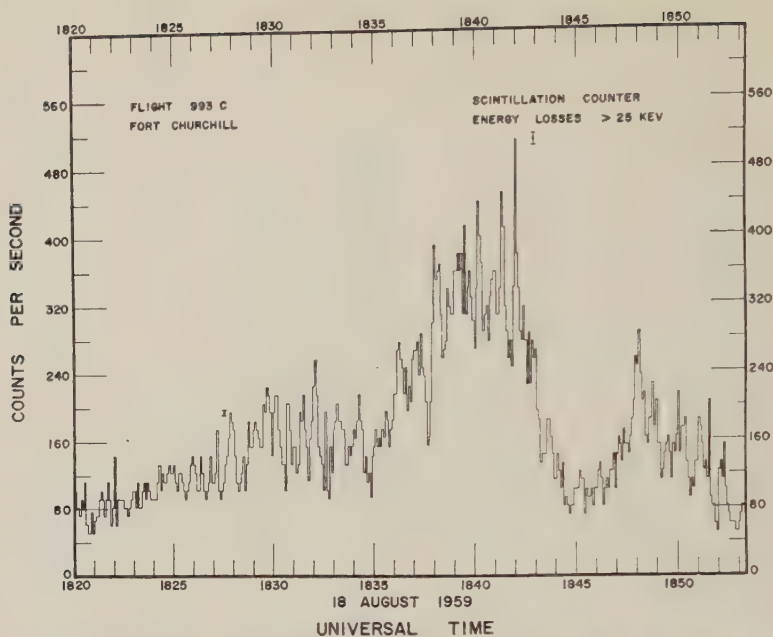


Fig. 11. Detailed appearance of the daytime X-ray activity on August 18. Again at these times the outer radiation belt was filling up with particles. The X-ray bursts have an almost wavelike regularity.

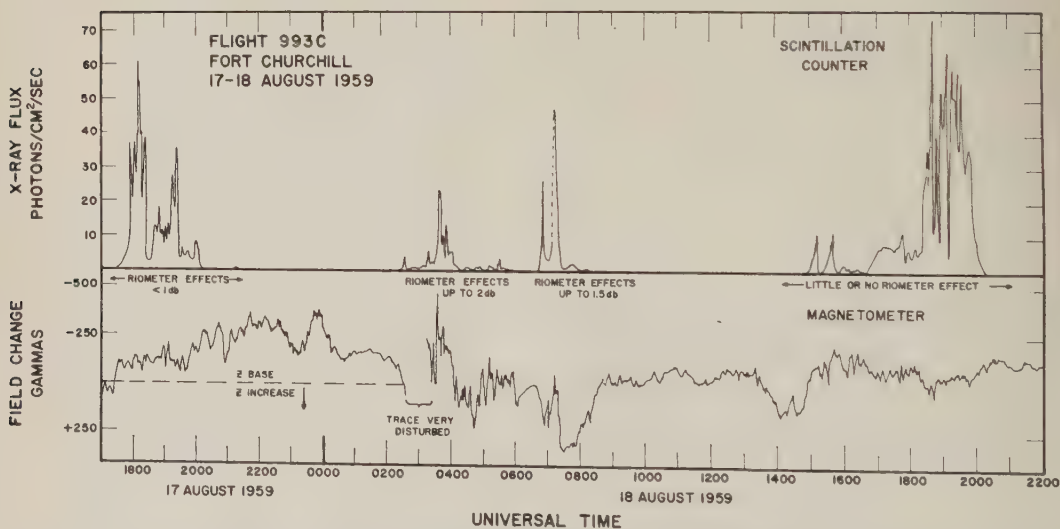
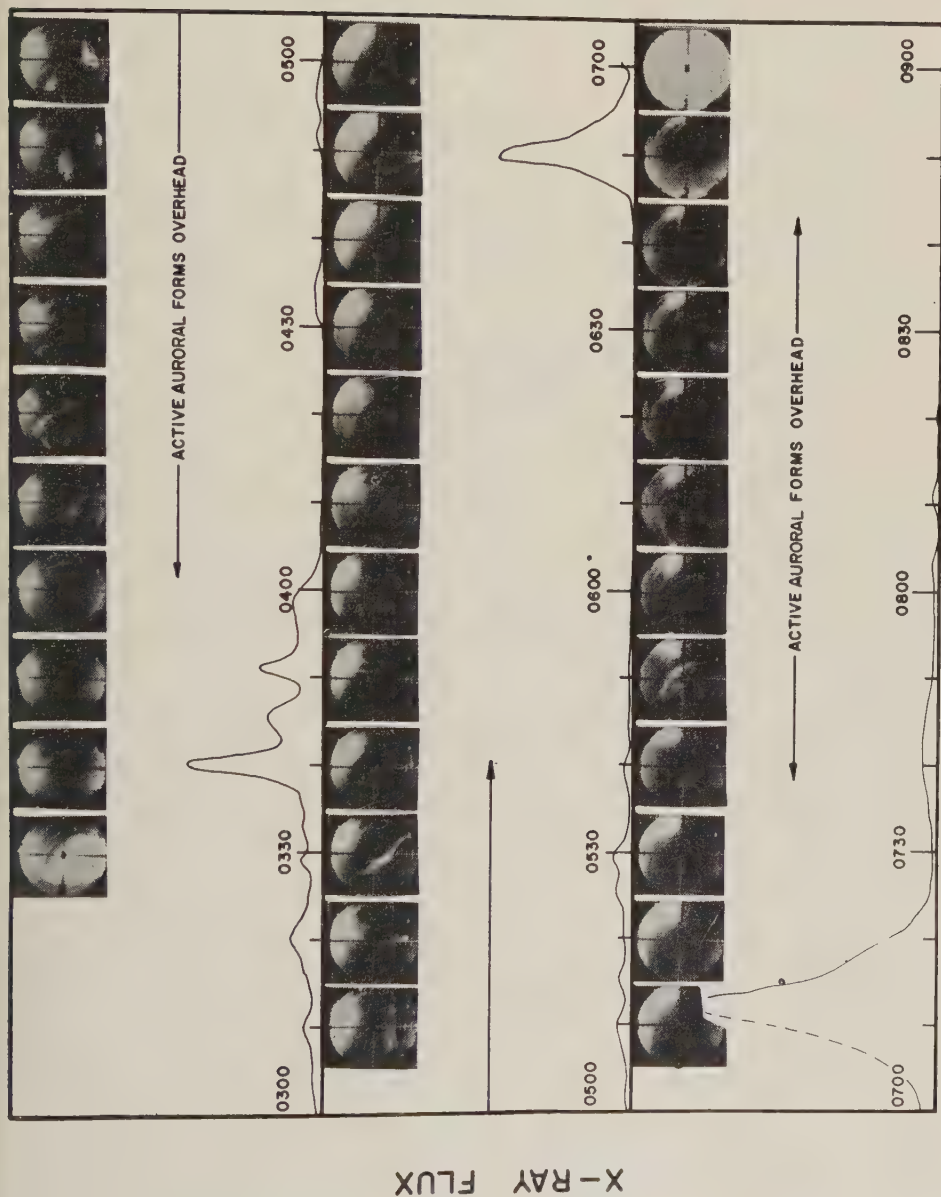


Fig. 12. The large daytime X-ray fluxes on August 17-18 are not associated in any definite way with features on the magnetometer trace. The X-ray activity at about 0100 local time (0700 UT) precedes a magnetic bay of typically auroral character. The nighttime X-ray bursts appear at times of moderate ionometer effects; the greater daytime activity is associated with little or no galactic radio noise attenuation.



UNIVERSAL TIME 18 AUGUST 1959

Fig. 13. The principal x-ray activity that occurred during this night preceded the brightest and most active auroral forms by about $\frac{1}{2}$ hour. At these times the balloon was known to be almost directly beneath the auroral activity.

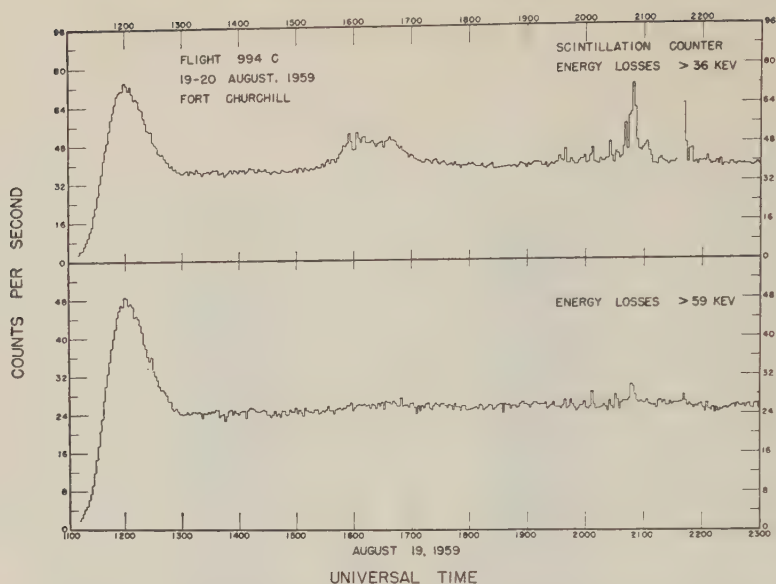


Fig. 14. X-ray activity on a rather quiet day following the magnetic storm of August 16-17.

THE ENERGY SPECTRUM AND FLUX OF PRIMARY ELECTRONS

It is of interest to see what information can be obtained about the form of the energy spectrum and the absolute flux of the parent electrons that give rise to the observed X-ray fluxes. In this analysis the primary data are the three-point differential energy spectra of the energetic photons encountered at balloon levels. Typical examples of such spectra, which can be accurately constructed for time intervals as short as 1 minute, are shown in Figure 7. The first step in the method to derive the electron spectrum is to take into account photoelectric absorption of the photons, and correct the X-ray spectrum as observed at the depth of the balloon to the production layer, which is taken to be the first 0.1 g cm^{-2} of the atmosphere. Then various mathematical forms for the primary electron spectrum are assumed, and, by the use of a range-energy relation and bremsstrahlung formulas, the expected photon spectra just below the production layer are calculated. Finally, these calculated photon spectra are compared with the corrected X-ray spectrum to determine which mathematical expression for the primary electron spectrum provides the best fit.

This method, of course, gives the electron spectrum indirectly, but since X-ray observa-

tions are available from flights made at atmospheric depths from 3 to 8 g cm^{-2} it is believed the X-ray corrections can be made with reliability. Furthermore, it is found that the angular distribution assumed by the photons in the atmosphere does not much affect the form of either the corrected X-ray spectrum or the primary electron spectrum. It is therefore believed that the method gives meaningful results for the shape of the electron spectrum. The absolute flux is not so well determined, since here the angular distribution enters in more strongly. However, the electron fluxes given here are believed to be known within a factor of 3 or 4.

The details of this method of analysis for the electron spectrum have already appeared [Anderson and Enemark, 1960] but will be given here for convenience:

A. *Extrapolation of the X-ray spectrum to zero atmospheric depth.* The following factors have been considered:

1. Photoelectric absorption of the photons. This is the largest correction; it is made using absorption coefficients compiled in the *Handbook of Chemistry and Physics*. The energy dependence of this process is taken into account.
2. The spatial distribution of the X-rays. This is not known from our balloon measurements,

but it is found that the shape of the derived electron spectrum depends very little on the assumed distribution. For example, there is little difference in the final result if the electrons come from a point source or if an isotropic distribution is assumed and the Gold integral used to make the absorption correction. However, the absolute flux of electrons required to produce the observed flux of X rays differs by a factor of 2 between these cases. If the electron sources are localized, some distortion of the electron spectrum would be expected, depending on the relative location of the source and the balloon. This comes about because the photoelectric absorption coefficients depend quite strongly on the photon energy, particularly at the lowest energies measured by our apparatus. Thus when the electron source is at a low zenith angle with respect to the balloon the attenuation of low-energy photons relative to the attenuation of higher-energy photons becomes very great. This effect may be responsible for the rather large variation in the low-energy part of the spectrum between one X-ray burst and another on the same flight and also between X-rays bursts occurring on different flights. This effect can be seen in Figure 18, where a number of photon spectra have been collected.

3. Compton scattering of the X-rays. For the flights at less than 3 g cm^{-2} atmospheric depth this process is ignored because the Compton scattering length is greater than this depth. For flights at depths greater than 3 g cm^{-2} many of the observed X rays will have undergone Compton processes. Even so it is not expected that the observed X-ray spectrum will have been appreciably distorted by this effect. This is because the Compton cross section changes by only 30 percent over the energy region we investigate in addition to the fact that in each collision the photon energy changes by only a few per cent. The effect of the Compton scattering on the spatial distribution of the X rays is of little importance to the form of the electron spectrum.

The measured and corrected X-ray points for a particular time during flight 979, which attained the very high balloon altitude of 41 km, are shown in Figure 15. Also shown there is the correction for one of the large bursts that occurred during flight 992C.

B. *Calculation of the bremsstrahlung spectrum for various assumed electron spectra.* The number of photons produced by an electron of kinetic energy E in passing through a thickness $d\xi \text{ g cm}^{-2}$ of material having radiation length $l_R \text{ g cm}^{-2}$ is

$$\sigma_i(\xi) = \frac{d\xi}{l_R} \int_{\nu=E_a/h}^{\nu=E/h} \frac{d\nu}{\nu} = \frac{d\xi}{l_R} \ln \frac{E}{E_a} \quad (1)$$

Where ν is the frequency of the photon and E_a is the chosen discrimination level. (In practice the discriminator is set by reference to radioactive sources of γ rays with known energy.)

The number of photons having energy above the discrimination level E_a produced by an electron initially of energy E traversing its entire range is

$$N(E_a; E) = \int_{\xi=E/2000}^{\xi=E_a/2000} \sigma_i(\xi) d\xi \quad (2)$$

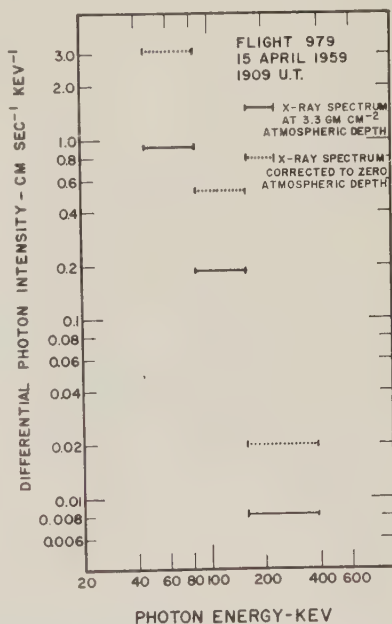


Fig. 15. The X-ray spectrum obtained at a very high balloon altitude over Alaska is seen to contain photons above 160 kev. During the flights at Fort Churchill photons of such high energy have never been observed. The result of correcting for photoelectric absorption of the X-rays is also shown in this figure. The photons are seen to be attenuated by about a factor of 3 from their production level to an atmospheric depth of 3 g cm^{-2} .

The range-energy relation $R = (1/2000)E$ has been used, where R the range is in g cm^{-2} , and the energy E is in kev. Upon integration the last expression becomes

$$N(E_a; E) = \frac{1}{2000l_R} E \left(\log \frac{E}{E_a} - 1 \right) + E_a \quad (3)$$

The differential photon intensity, or number of photons having energy between E_a and E_{a+1} per kilovolt due to a spectral distribution of electrons, $n_e(E)$, is given by

$$n_p(E_{a+1}, E_a) = \frac{\int_{E_a}^{\infty} N(E_a; E) n_e(E) dE - \int_{E_{a+1}}^{\infty} N(E_{a+1}; E) n_e(E) dE}{E_{a+1} - E_a} \quad (4)$$

$n_e(E) dE$ is the number of electrons having energy between E and $E + dE$. If $n_e(E) dE$ is taken to be represented by $KE^{-\gamma} dE$, where K and γ are constants, equation 4 is readily integrated and the following expression is obtained:

$$n_p(E_{a+1}, E_a) = \frac{K}{2000l_R(\gamma - 1)(\gamma - 2)^2} \cdot \left[\left(\frac{1}{E_{a+1} - E_a} \right) \left(\frac{1}{E_a^{\gamma-2}} - \frac{1}{E_{a+1}^{\gamma-2}} \right) \right] \quad (5)$$

$n_p(E_{a+1}, E_a)$ is the quantity to be directly compared with the corrected X-ray spectrum.

The best power-law fit for flight 979 is obtained when $\gamma = 5.0$; for flight 992, when γ is 5.5. However, the best power-law fit is not a particularly good one, since, when two calculated points are matched with two corrected X-ray points, the third point differs by a factor of 2. This means that the exponent, γ , is not constant and is a function of energy. Therefore we have attempted to find a better fit using an electron distribution of the form

$$n(E) dE = Ae^{-bE} dE$$

The best fit to the corrected X-ray measurements made on flight 992 comes when $b = 0.04$ for E expressed in kilovolts. The fit in this case is satisfactory from 25 to 100 kev, but considerable difference between the observed and calculated points at higher energies can be seen in Figure 16.

We have considered the possibility that the simplified range-energy relation used in obtaining equation 5 may introduce large errors in the calculated X-ray intensities. Investiga-

tion showed that the spectral shape should not be greatly affected and that the larger effect would be on the absolute number of electrons required to produce the X-ray effects.

The estimated electron fluxes for flight 992C are shown in Figure 4 and for flight 979 in Figure 17. Because the exponential spectrum used is not the best fit, and since an approximate range-energy relation is contained in equation 3, these electron fluxes may be in error by a factor of 2 from this source. Also, the angular

distribution of the X rays is not known, and this introduces perhaps another factor of 2 uncertainty. Therefore the electron fluxes are probably reliable to within about a factor of 3.

Walt, Chase, Cladis, and Imhof [1960] have reported that measurements made July 7, 1959, with a rocket-borne electron spectrometer in the outer radiation belt yield an electron spectrum having the exponential form given above but with $b = 0.014$. This is in very poor agreement with the much steeper spectrum derived from balloon X-ray measurements. Compared with Walt's spectrum, the one we deduce is very deficient in electrons of higher energy. If both measurements are taken at face value it is worth while noting that the rocket measurements were made at a magnetic latitude of about 48° whereas the balloon experiments were performed at a magnetic latitude greater than 70° . The two sets of measurements might then be reconciled by postulating that electrons of energy greater than about 100 kv do not become trapped as effectively along the magnetic lines joining the auroral zone, or that these higher-energy electrons escape soon after injection, not by entering the atmosphere and stopping but by spiraling out of the lines of force at large radial distances. At the lower latitudes corresponding to the regions of the outer radiation belt nearest the earth where the rocket measurements were made the electrons would be much more firmly bound to the lines of force. Although the electron spectrum we infer cannot be represented very well as a power law because of its rapidly increasing steepness at high energies, it is not too dissimilar from the

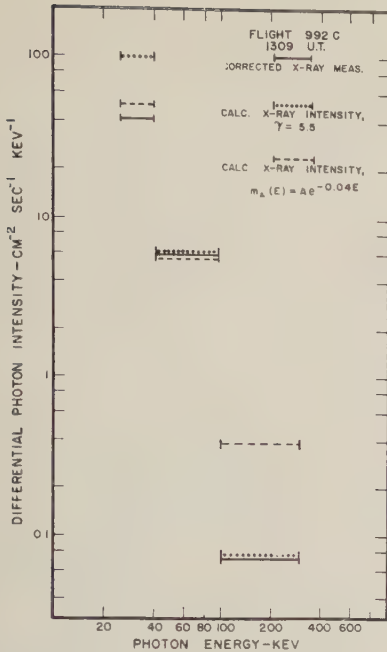


Fig. 16. The expected bremsstrahlung X-ray flux from electron spectra of two different mathematical forms are compared with the corrected photon measurements. The X-ray spectrum high in the atmosphere is seen to require a very steep differential electron intensity spectrum. It must be steeper than $E^{-5.5}$ or $e^{-0.04E}$ when E is in kev.

E^{-5} spectrum reported by Russian workers for trapped electrons in the outer radiation belt. Those measurements refer to a somewhat lower latitude than the present balloon observations.

We next estimate the number of electrons released from the radiation belt along the auroral-zone line of force during one of the large X-ray bursts during flight 992C. At the maximum of the X-ray burst the parent electron spectrum is rather well represented from 25 to 100 kev by

$$N_e(>E) = (A/b)e^{-bE} = 1.1 \times 10^6 e^{-0.04E}$$

And the flux of electrons above 25 kev is found to be

$$N_e(>25 \text{ kev}) = 4 \times 10^6 \text{ cm}^{-2} \text{ sec}^{-1}$$

Using the result that the auroral-zone X rays are present about 40 per cent of the time, and taking an average value for their flux above 25 kev at zero atmospheric depth, the number of electrons lost in the atmosphere during a 1-day period can be found. This number does not de-

pend very much on the magnetic character of the day involved, judging from our experience with a number of balloon flights. It does appear, however, that the magnetic history of the day may be of considerable importance. This daily flux of electrons above 25-kev energy lost in the atmosphere over the auroral zone is of the order of 10^{10} cm^{-2} . This estimate results from an average flux value of $10 \text{ photons cm}^{-2} \text{ sec}^{-1}$ present 40 per cent of the time, values that our measurements show to be rather conservative. From space-probe and satellite observations during 1958 and 1959 it is estimated that the number of electrons trapped in the yoke-shaped volume having a 1 cm^3 base in the auroral zone and running along the lines of force joining a similarly located area in the other hemisphere varies from 10^8 to 10^{11} electrons above about 20 kev. To maintain this daily loss it is apparently necessary to borrow particles from the more intense regions of the outer radiation belt or else to have the acceleration of electrons in the 20- to 200-kev range taking place regularly even in the absence of marked geomagnetic activity. The possibility that particles are injected into the radiation belt from a solar gas cloud at these high energies now seems unlikely [Arnoldy, Hoffman and Winckler, 1960].

DISCUSSION

1. Observations from flights 990C and 994C (Figs. 3 and 14) confirm the earlier findings that rather weak, sporadic fluxes of X rays appear over the auroral zone without apparent relation to features in ground-level magnetometers when the 3-hour K_p values ranged from 1 to 4. During these two flights X rays were present 14 out of 32 hours of high-altitude data, a percentage of 40.

2. The observations made on flight 992C show that some X-ray bursts seen at balloon altitude over the auroral zone are closely connected with geomagnetic-storm activity. This provides confirmation to measurements on this effect first made during the magnetic storm of August 29-30, 1957 [Anderson, 1958]. In the auroral zone the influx of X rays during times of greatly disturbed magnetometer traces and high K_p is not strikingly larger than those times when K_p is moderate or low. Our balloon measurements thus indicate that the more important loss of energetic electrons over the auroral zone

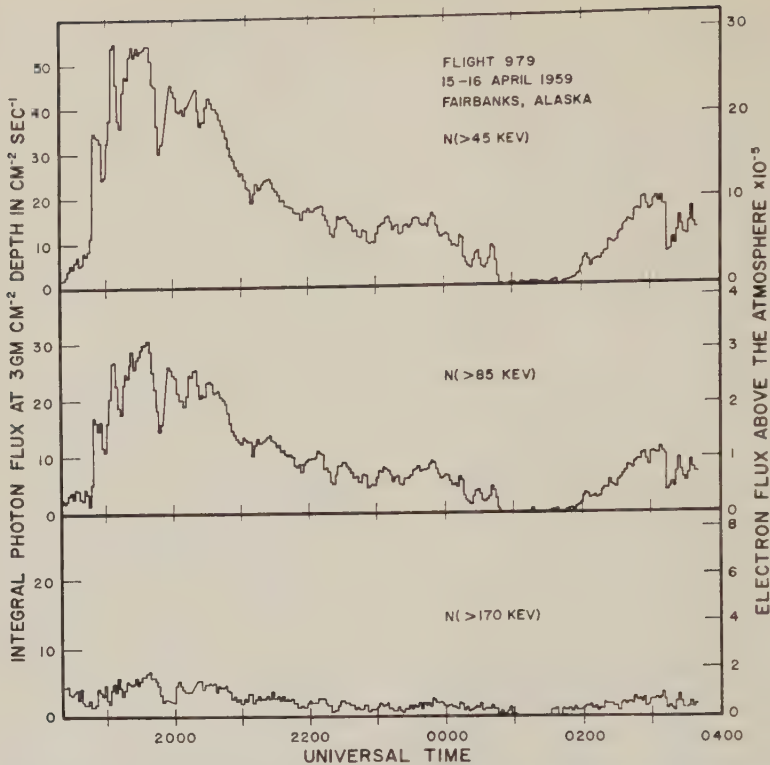


Fig. 17. The integral photon and derived electron fluxes for the very high flight over Alaska during April 1959. The maximum riometer effect at 30 Mc/s corresponded to the peak X-ray flux at 1940 UT and amounted to 1.2 db (Leinbach, private communication).

does not occur during geomagnetic storms but rather in the longer interim periods of magnetic quiet.

3. All the counting-rate effects in excess of the cosmic-ray background observed on the August 1959 series of flights were due to photons within the experimental limits of uncertainty. In particular, there were no detectable electron fluxes entering the detectors. Comparison of the counter telescope with the scintillation counter permits setting a lower limit on the electron flux that could be present but not detectable. In order to produce a count in the vertical counter telescope carried on flight 993 C a particle must have a range greater than 0.1 g cm^{-2} after penetrating the walls of the equipment gondola, which have a stopping power of 0.4 g cm^{-2} . The sodium iodide scintillation crystal is surrounded by about 0.15 g cm^{-2} of material, so that electrons of sufficient energy to enter it can also produce counts in the telescope. During the X-ray influx from 1820 to 1900 UT on August

18 (Fig. 11) there were of the order of 250,000 counts above the 25-kev discrimination level. The total count from the telescope during this 40-minute period was 2400 ± 45 . This was the same within the statistical errors as for the 40-minute period preceding and following the X-ray influx, and was the expected count due to the cosmic-ray background. Therefore, at most 55 counts in the counter telescope during the time of the large X-ray influx from 1820 to 1900 UT can be attributed to electrons. The ratio of X rays having energy greater than 25 kev to electrons of range greater than 0.1 g cm^{-2} (about 350 kev) present inside the instrument gondola at an atmospheric depth of 7 g cm^{-2} exceeds 4500 to 1. Electrons of energy less than roughly 350 kev can enter none of the detectors, and no statements can be made about their flux. We expect to see no photo or Compton electrons in cascade with the X rays, since the flux of photons above 350 kev entering the scintillation detector is negligible.

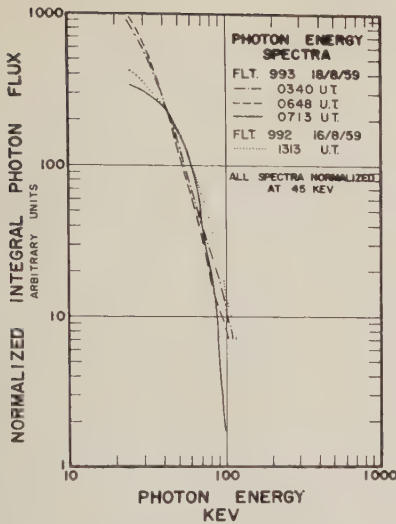


Fig. 18. Photon energy spectra from the Fort Churchill flights are seen to be variable. This probably represents true changes in the parent electron spectrum, but such effects would also be expected if the electrons are discharged from a localized source.

A comparison of the ion-chamber response with the scintillator data leads to the same general conclusion of a lack of electrons accompanying the X-ray flux. However, the limit obtained is not as good as from the analysis involving the counter telescope. Furthermore, the limit refers to electrons above about 1.4 Mev.

4. *Rothwell and McIlwain* [1960] have argued that the magnetic-storm-associated loss of trapped electrons above 20-kev energy from the lower fringe of the outer radiation belt at rather high latitudes was due to enhanced scattering and absorption of the electrons brought about by an expansion of the highest levels of the atmosphere. This presumably occurs when the magnetic storm injects low-energy plasma into the atmosphere, resulting in its heating. The balloon observations during the magnetic storm of August 29–30, 1957 [Anderson, 1958], showed a large particle dumping during the time of the sudden commencement. During the very large storm excursions that followed, the flux of particles incident on the atmosphere was no higher. Therefore, it is not likely that the mechanism of atmospheric heating and expansion by the low-energy plasma is responsible for the major part of the particle dumping at

the time of sudden commencement since the heating and subsequent rise of the atmosphere should not be so immediately effective.

5. The characteristic appearances of the X-ray bursts encountered during the August 1959 balloon flights can be judged from Figures 5, 9, 10, and 11. The bursts accompanying the storm changes in the earth's magnetic field (Fig. 5) and those that precede visible auroral displays are quite symmetrical (Fig. 10), contain rather little structure, and have a width of 2 or 3 minutes. The daytime X-ray activity on August 17 and 18 (Figs. 9 and 11) exhibits a very prominent fine structure. The spikes seen there have widths from 30 seconds down to the resolving time permitted by the pulse scaling, which is about 2 seconds at the highest counting rates. During the daytime X-ray activity on August 18 (Fig. 11) the spacing of the small bursts is to some extent regular, although it is difficult to assign a definite period. The spacing between the spikes varies from 30 to 100 seconds. There is a further difference between the preauroral X rays during the night of August 17–18 and the daytime X-ray activity not associated with magnetometer disturbance of auroral character: The ratio of the number of photons having energy greater than 25 kev to those greater than 40 kev is about 2 to 1; for the preauroral X rays it is substantially higher. This ratio is plotted on Figure 8. The spectrum of the preauroral X rays is thus markedly softer than the daytime flux. These changes in the energy spectrum are mostly brought about by a flattening of the spectrum below about 50 kev.

Simultaneous satellite observations from Explorer VI reported by the University of Minnesota group [Arnoldy, Hoffman, and Winckler, 1960] are of interest to our series of flights in August and also suggest a means of interpreting the markedly different structure between the aurora- or magnetic-storm-associated X rays and the more intense daytime activity. The trajectory of this satellite was such that during the times of interest apogee was nearly 50,000 km and the orbit attained geomagnetic latitudes up to about 40° at these large radial distances. To a fair approximation the same geomagnetic line connects the balloons above Fort Churchill with the satellite Explorer VI at apogee when their longitude is the same.

Early on August 16 but after the sudden

commencement of the magnetic storm on that date and again early on August 17 the Geiger counter aboard this satellite was responding only to the normal cosmic-ray flux when at apogee. At these times the geomagnetic field was very disturbed, K_p reaching 8+ on both these days. As can be seen from Figure 4 our balloon detectors were measuring quite large X-ray bursts at these times on August 16. Also the satellite observations show a very large decrease of intensity in the outer radiation belt during the magnetic storm of August 16-17 and furthermore provide evidence that these particles were dumped into the atmosphere. The discharge of electrons above about 20 kev was shown to be centered around 57° geomagnetic latitude, and their intensity fell rapidly away at latitudes both to the north and south. However, it is likely that the X-ray bursts measured by balloon detectors over Fort Churchill on August 16 represent the comparatively weak high-latitude tail of this dumping.

Although the trapped energetic electron intensity was negligible at radial distances greater than about 40,000 km during the active phase of the storm, the rate of the Explorer VI Geiger counter when near apogee late on both August 17 and 18 was about 100 times the cosmic-ray background, indicating the presence of a considerable flux of trapped electrons above 20-kev energy. Also during these times the outer radiation belt was observed to increase its trapped energetic electron density to values much above the prestorm level. It was just at these times of counting-rate increase near apogee on August 17 and 18 that the large and complex influxes of X rays were measured by our balloon over Fort Churchill (Fig. 8). The origin of the energetic electrons that fall into the atmosphere giving rise to the photons we observe in the balloon-borne detectors is evidently best interpreted as a consequence of the terrestrial acceleration process that is filling up the outer radiation belt at these times. Perhaps as electrons from the low-energy solar plasma are brought to higher energies some of them have inappropriate pitch angles to remain trapped and thus fall into the atmosphere.

6. The observation that, immediately before two bright auroral displays, electrons having very much the same spectrum over the same energy region as electrons trapped in the outer

radiation belt were discharged into the atmosphere is a strong indication that the outer radiation belt plays some role in the auroral-zone, or daily, auroras. The electrons above 20 kev are not responsible for the visible effects, but the conclusion seems inescapable that the outer radiation belt must be involved in a complete and systematic description of the auroral-zone phenomena.

Acknowledgments. This work was assisted by the Office of Naval Research and the Atomic Energy Commission. The field operations were extensively supported by the Canadian Defence Research National Laboratory, Dr. R. Montalbetti, officer in charge. Much logistical help was also provided through the ONR resident representative at Minneapolis, Mr. G. W. Bowers. Raven Industries supplied flight services for most of the balloon launchings. We are also very grateful for the enthusiastic assistance of the following University of Iowa students: Richard Burian, Robert Lamb, and Donald Stilwell.

REFERENCES

- Anderson, K. A., Soft radiation events at high altitude during the magnetic storm of August 29-30, 1957, *Phys. Rev.*, **111**, 1397-1405, 1958.
- Anderson, K. A., Balloon observations of X Rays in the auroral zone I, *J. Geophys. Research*, **65**, 551-564, 1960.
- Anderson, K. A., and D. C. Enemark, Observations of auroral zone X-rays and solar cosmic rays, *Proc. COSPAR*, First International Space Science Symposium, Nice, January 1960.
- Arnoldy, R., R. Hoffman, and J. R. Winckler, Observations of Van Allen radiation regions during geomagnetic storms, *Proc. COSPAR*, First International Space Science Symposium, Nice, January 1960.
- Arnoldy, R. L., R. A. Hoffman, and J. R. Winckler, Solar cosmic rays and soft radiation observed at 5,000,000 km from earth, *J. Geophys. Research*, **65**, 3004-3007, 1960.
- McIlwain, C. E. *Proc. COSPAR*, First International Space Science Symposium, Nice, January 1960.
- Meredith, L. H., M. B. Gottlieb, and J. A. Van Allen, Direct detection of soft radiation above 50 kilometers in the auroral zone, *Phys. Rev.*, **97**, 201, 1955.
- Rothwell, P., and C. E. McIlwain, Magnetic storms and the Van Allen radiation belts: observations from satellite 1958e (Explorer IV), *J. Geophys. Research*, **65**, 799-806, 1960.
- Walt, M., L. F. Chase, J. B. Cladis, and W. L. Imhof, Energy spectra and altitude dependence of electrons trapped in the earth's magnetic field, *Proc. COSPAR*, First International Space Science Symposium, Nice, January 1960.

(Manuscript received August 8, 1960.)

The Cosmic-Ray Equator and the Earth's Magnetic Field

MARTIN A. POMERANTZ AND VASANT R. POTNIS

*Bartol Research Foundation of the Franklin Institute
Swarthmore, Pennsylvania*

AND

ARNE E. SANDSTRÖM

*Fysiska Institutionen, Uppsala Universitet
Uppsala, Sweden*

Abstract. The positions of the cosmic-ray intensity minimum off the west coast of Africa and in the Indian Ocean, respectively, have been determined from measurements obtained with a shipboard neutron monitor during two voyages between Scandinavia and Australia. The cosmic-ray equator is in accordance with the prediction based upon calculations of modified cutoff rigidities at the first location, but differs by 4° at the second. Contemporary observations of zero magnetic dip indicate that the cosmic-ray intensity minimum coincides with the dip equator at 14°W , but differs in geographic latitude by 2° in the vicinity of 60°E .

Introduction. Various approximations have been invoked for representing the effects of the geomagnetic field upon cosmic-ray cutoff rigidities. The maximum precision of comparisons between these representations and the experimental data is attained through the determination of the cosmic-ray equator, defined as the locus of points of minimum intensity.

Theoretical and empirical approximations recently proposed to account for observed discrepancies between cosmic-ray intensity measurements and the predictions based upon the dipole field approximation include shifted dipole [Rose, Fenton, Katzman, and Simpson, 1956; Simpson, Fenton, Katzman, and Rose, 1956], magnetic dip [Rothwell and Quenby, 1958], and dipole plus nondipole [Quenby and Webber, 1959]. Katz, Meyer, and Simpson [1958] have determined an empirical cosmic-ray equator based upon observations with an airborne neutron monitor. Jory [1956] has discussed the effect of quadrupole terms on the cutoff rigidities near the geomagnetic equator, and Kellogg and Schwartz [1959] have computed the location of the cosmic-ray equator using an octopole approximation.

Equatorial crossings of cosmic-ray detectors at various longitudes have been reported by a number of investigators [Rose, Fenton, Katzman, and Simpson, 1956; Rothwell and Quenby,

1958; Katz, Meyer, and Simpson, 1958; Kodama and Miyazaki, 1957; Skorka, 1958; Pomerantz, Sandström, and Rose, 1958; Storey, 1959]. In most cases, the observations have been limited to a single crossing at a particular location. To determine whether the position of the cosmic-ray intensity minimum remains constant or varies with time, an extensive program of repeated crossings of a shipboard neutron monitor was conducted along a route off the west coast of Africa, where the greatest discrepancy between the position of the cosmic-ray minimum and the location of the equator based upon the dipole representation occurs [Pomerantz, Sandström, Potnis, and Rose, 1960]. After four voyages between Sweden and South Africa (eight equator crossings) the equipment was transferred to a ship that followed the same route from Sweden to South Africa on its outbound voyage to Australia, but returned through the Indian Ocean. This provided two crossings east of Africa that are directly comparable with west coast crossings of the equator during the same voyages.

The position of the cosmic-ray intensity minimum determined by the eight earlier crossings had coincided very well with contemporary observations of zero dip at longitude 14°W . It was possible that discrepancies between the dip equator and the cosmic-ray equator previously

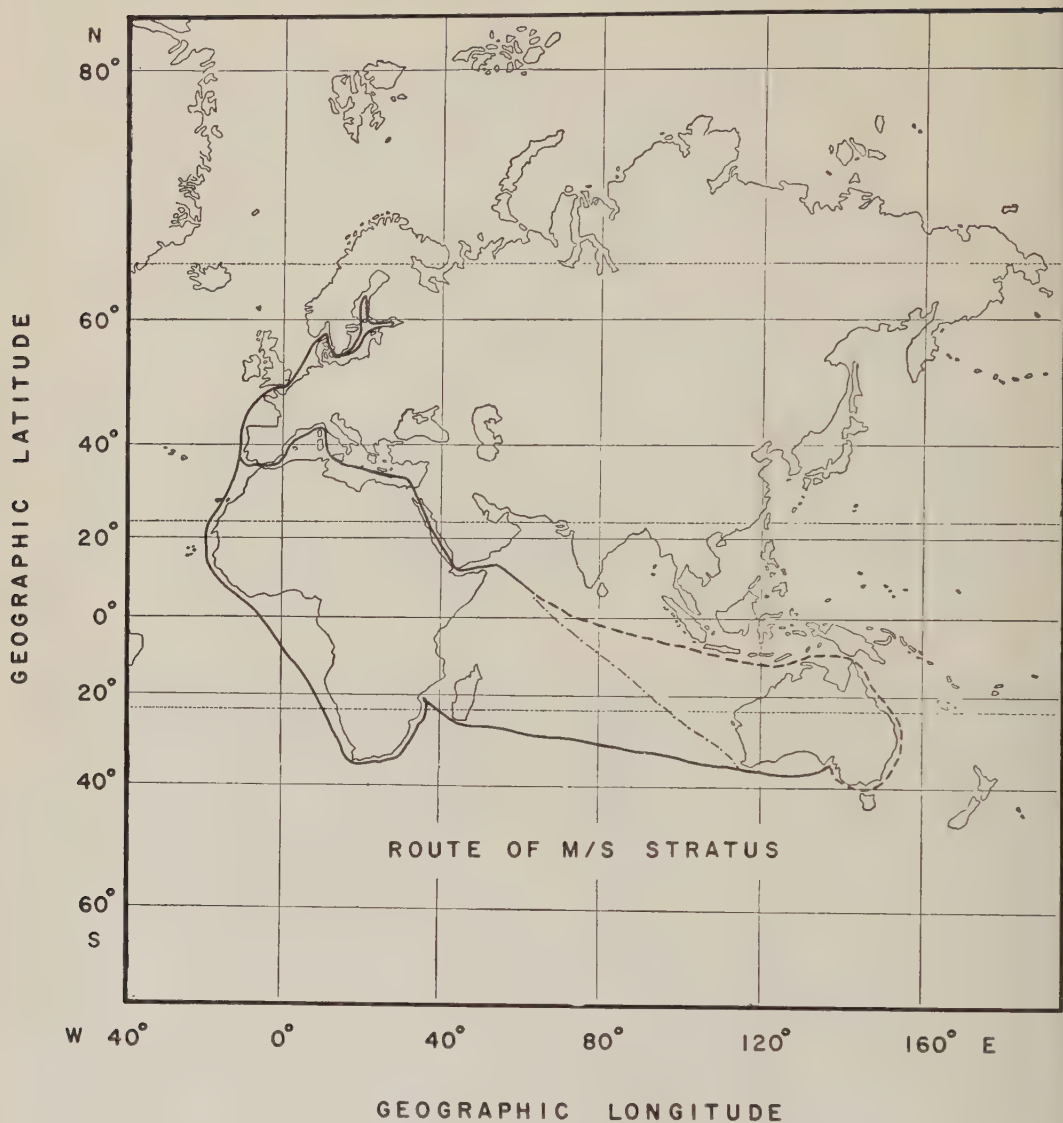


Fig. 1. Routes of shipboard neutron monitor.

noted at other points [Rothwell and Quenby, 1958] were attributable to differences between the real dip and the values obtained from the available charts. The data presented herewith are relevant to this question.

Measurements and Results. Figure 1 shows the routes of M/S *Stratus* during the two voyages between Scandinavia and Australia. During the first voyage (March–August, 1958) the ship followed a route that took it north of Australia. On the second voyage (August 1958–February 1959) it followed the same course to Brisbane,

but returned along a more southerly route through the Indian Ocean.

Following previous practice, the raw hourly counting rates were corrected for variations in the barometric pressure with the usual exponential factor (absorption coefficient $-0.96\%/mm$ Hg). Six-hour intervals have been employed for the curves from which the points of minimum intensity were calculated (Fig. 2). As in the case of the equator crossings off the West African coast [Pomerantz, Sandström, Potnis, and Rose, 1960], the data were normalized for

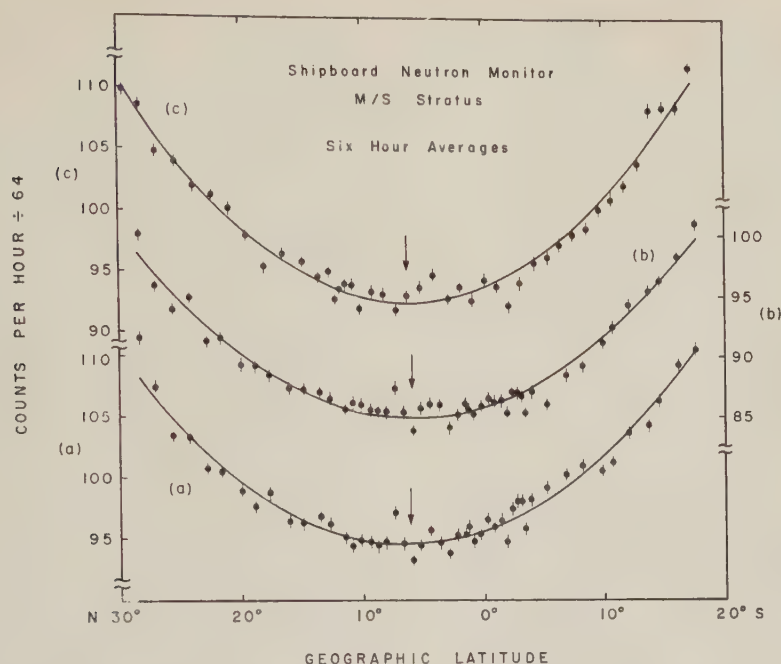


Fig. 2. Counting rates as a function of geographic latitude in the Indian Ocean. (a) July 1958, normalized for world-wide variations with respect to Uppsala; (b) July 1958, normalized with respect to Huancayo; (c) January 1959, normalized with respect to Uppsala. Arrow indicates computed point of minimum intensity.

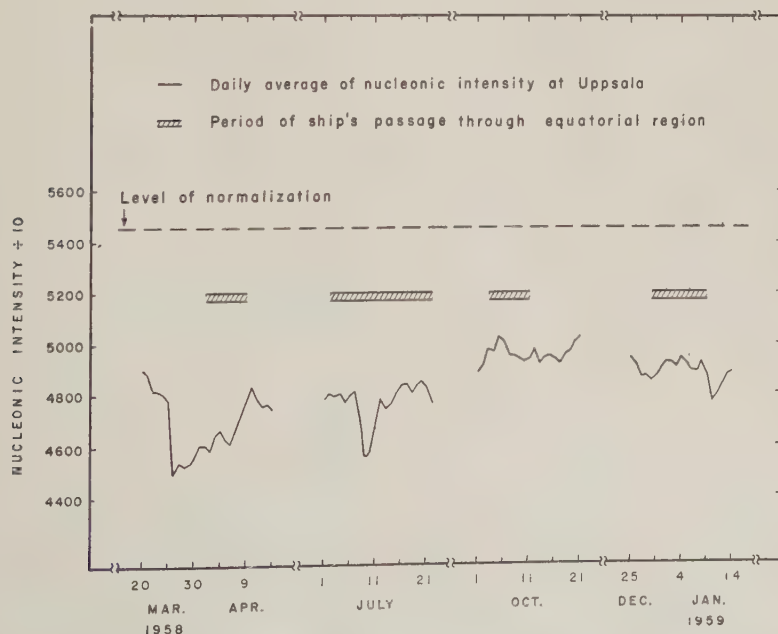


Fig. 3. Daily average of nucleonic intensity at Uppsala during the period of the present observations.

world-wide variations by reference to the Uppsala monitor (Fig. 2 *a, c*). For purposes of comparison, however, they have also been normalized to Huancayo in the case of the first voyage (Fig. 2, *b*). The high density of points is a consequence of the slow rate of change of latitude in the Indian Ocean as compared with the course off West Africa (see Fig. 1).

To determine the position of the cosmic-ray intensity minimum, it is necessary to fit an analytical function to the experimental points. The usual procedure has been to represent the data by a parabola. The validity of fitting a parabola by the least-squares method would be influenced by the presence of an appreciable asymmetry.

For each crossing a machine determination of the function $Y = \sum_0^n a_n x^n$ best representing the points between 30°N and 20°S was performed by the method of least squares. The analysis was carried out for $n = 2$ and $n = 3$. This procedure yields the location of the minimum as determined by the data, precisely and objectively, independently of human judgment. Inasmuch as the locations of the minimum points agree within 0.5° for these two values of n , the effect of any asymmetry is regarded as negligible in comparison with the experimental uncertainties. Consequently, the parabolic approximation $n = 2$ was selected for the evaluation of the data. The computed curves are represented by the solid lines in Figure 2, and the analytically determined points of minimum intensity are indicated by arrows.

As has been pointed out previously [Pomerantz, Sandström, and Rose, 1958], the rigidity-dependence of the amplitude of world-wide variations must be taken into account for a precise normalization of intensity vs. latitude data. Figure 3 shows the daily average intensity of the nucleonic component at Uppsala during the period of the ship's passage through the equatorial region (i.e., geographical latitude 30°N–20°S). On the first voyage of M/S *Stratus*, a Forbush-type decrease occurred during the equator crossing in the Indian Ocean. As is seen in Figure 2, the choice of reference station does not significantly affect the position of the minimum. The computed values of the latter differ by only 0.2°. This confirms previously reported similar results concerning the equator crossings off the West African coast [Pomerantz, Sand-

ström, and Rose, 1960]. Accordingly, the Uppsala monitor has been used as reference station for all determinations of the cosmic-ray intensity minimum as summarized in Table 1.

The mean of the positions of the minimum at 14°W very nearly coincides with the mean for all ten crossings at this longitude (6.7°N). The hydrographer of the U. S. Navy has kindly provided data concerning actual measurements of zero dip in the immediate vicinity of the cosmic-ray intensity minima listed in Table I. The small differences in longitude between the route of the ship and that of the airborne magnetometer were taken into account by a slight extrapolation in the Atlantic Ocean, and by interpolations in the Indian Ocean.

Discussion. The closest previous measurements of the cosmic-ray intensity minimum in the vicinity of the present Indian Ocean crossings were at 53°E and 74°E, respectively [Katz, Meyer, and Simpson, 1958]. The geographic latitudes were 9.5°N and 8.0°N. The corresponding smoothed-out, experimentally determined, cosmic-ray equator differs from the present observations by 2.4° geographic latitude. This may be attributable to a rapid variation of the intensity minimum as a function of longitude, as is qualitatively suggested by the calculations based upon the octopole approximation [Kellogg and Schwartz, 1959]. This region in the Indian Ocean is characterized by relatively small secular variation. In fact, the dip measurement in Table I agrees with the U. S. Navy Hydrographic Office (1955) chart at 60°E, but not at 14°W [Pomerantz, Sandström, Potnis, and Rose, 1960].

In contrast with the situation off the west coast of Africa, the position of the cosmic-ray equator as predicted by the method of Quenby and Webber [1959] differs from the present experimental determination by about 4.0° geographic latitude in this region in the Indian Ocean where the line of minimum intensity predicted on the basis of modified cutoff rigidities is quite flat.

Furthermore, although the dip equator and cosmic-ray minimum coincide at 14°W, they differ in geographic latitude by 2° in the vicinity of 60°E. This discrepancy exceeds the experimental uncertainties. Consequently, the source of the previously noted differences between available experimental results and the dip equa-

TABLE 1. Summary of Determinations of Cosmic-Ray Intensity Minimum by Neutron Monitor Aboard M/S *Stratus*, and of Zero Magnetic Inclination by U. S. Navy Hydrographic Office

Region	Cosmic Ray Intensity Minimum			Zero Magnetic Inclination		
	Date	Latitude	Longitude	Date	Latitude	Longitude
Atlantic Ocean	April 1958	$6.2^{\circ} \pm 0.5\text{N}$	14.0°W	Mar. 1956	$7.0^{\circ} \pm 0.1\text{N}$	14.0°W
	Oct. 1958	$6.9^{\circ} \pm 0.5\text{N}$	14.0°W	Feb. 1957	$7.0^{\circ} \pm 0.1\text{N}$	14.0°W
Indian Ocean	July 1958	$6.2^{\circ} \pm 0.4\text{N}$	63.7°E	Oct. 1959	$8.2^{\circ} \pm 0.1\text{N}$	63.7°E
	Jan. 1959	$6.4^{\circ} \pm 0.4\text{N}$	59.8°E	Oct. 1959	$8.2^{\circ} \pm 0.1\text{N}$	59.8°E

tor representation can not be ascribed solely to secular variations or to uncertainties inherent in the geomagnetic charts.

Acknowledgments. We are very grateful to the Transatlantic Company of Sweden (*Rederiaktiebolaget Transatlantic*) for their exceedingly generous cooperation in accommodating the neutron monitor station aboard M/S *Stratus*. Particular appreciation is expressed to Captain A. Lagerwall for his kind cooperation in making all the necessary arrangements. We wish to thank Olle Ginstrop and Lars Anderson who served as observers aboard the ship during the first and second voyages, respectively. Our appreciation is expressed to the National Geographic Society for sponsoring the field operations. Support was also provided by the U. S. National Committee for the International Geophysical Year as well as by the U. S. Office of Naval Research.

REFERENCES

Jory, F. S., Influence of geomagnetic quadrupole fields upon cosmic-ray intensity, *Phys. Rev.* 102, 1167-1173, 1956.
 Katz, L., P. Meyer, and J. A. Simpson, Further experiments concerning the geomagnetic field effective for cosmic rays, *Nuovo cimento* [10], Suppl. 8, 277-282, 1958.
 Kellogg, P. J., and M. Schwartz, Theoretical study of the cosmic-ray equator, *Nuovo cimento* [10], 13, 761-768, 1959.
 Kodama, M., and Y. Miyazaki, Geomagnetic latitude effect of the cosmic-ray nucleon and meson

components at sea level from Japan to the Antarctic, *Rept. Ionosphere Research Japan*, 11, 99-115, 1957.
 Pomerantz, M. A., A. E. Sandström, and D. C. Rose, Shipboard neutron monitor determination of cosmic-ray equator, *Nuovo cimento* [10], Suppl. 8, 257-261, 1958.
 Pomerantz, M. A., A. E. Sandström, V. R. Potnis, and D. C. Rose, Solar disturbances and the cosmic-ray equator, *Tellus*, 12, 231-235, 1960.
 Quenby, J. J., and W. R. Webber, Cosmic ray cutoff rigidities and the earth's magnetic field, *Phil. Mag.*, 4, 90-113, 1959.
 Rose, D. C., K. B. Fenton, J. Katzman, and J. A. Simpson, Latitude effect of the cosmic-ray nucleon and meson components at sea level from the Arctic to the Antarctic, *Can. J. Phys.*, 34, 968-984, 1956.
 Rothwell, P., and J. Quenby, Cosmic rays in the earth's magnetic field, *Nuovo cimento* [10], Suppl. 8, 249-256, 1958.
 Simpson, J. A., K. B. Fenton, J. Katzman, and D. C. Rose, Effective geomagnetic equator for cosmic-radiation, *Phys. Rev.*, 102, 1648-1653, 1956.
 Skorka, S., Breiteneffekt der Nukleonen-und Mesonen komponente der Ultrastrahlung in Meereshöhe in Indischen und Atlantischen Ozean, *Z. Physik*, 151, 630-645, 1958.
 Storey, J. R., Cosmic-ray latitude survey above 145° east longitude using an airborne neutron monitor, *Phys. Rev.*, 113, 297-301, 1959.

(Manuscript received July 8, 1960; revised August 15, 1960.)

The Secular Variation and the Geomagnetic Theory of Cosmic Radiation

RUTH GALL

*Instituto de Geofísica de la Universidad de México, and
Instituto Nacional de la Investigación Científica, México*

Abstract. This paper discusses the effect of the secular variation of the geomagnetic field on the elements of the eccentric dipole and eccentric dipole-quadrupole models. It studies the migration during the period between 1845 and 1955 of geomagnetically equivalent points and examines the conditions for the invariance of the differential equation of motion of charged particles in the geomagnetic field. Formulas and practical rules are given for adapting calculations of cones, cutoff momenta and energies, and directions of incidence, valid for any arbitrary year to any specific year of observation. Time corrections for the curves of cutoff momenta vs. geomagnetic latitude were calculated for the period 1845-1955 for points of observation distributed over the southern and northern hemispheres.

INTRODUCTION

The trajectories of the cosmic-ray particles in the geomagnetic field are calculated by numerical integration of the differential equation of motion in which the geomagnetic field is represented by some simple model. The elements of any given model such as the directions of the multipoles, their moments, and the position of the geomagnetic center are obtained from the Gaussian analysis of the yearly geomagnetic charts.

Several models of the geomagnetic field have been proposed and studied by different authors. The centered dipole gives the first approximation to the earth's field. A better approximation is given by any of the two models suggested by Schmidt [Bartels, 1936], namely, by the eccentric dipole or the dipole and quadrupole, both eccentric. These two models have been extensively studied by Chargoy [1953], who found that the axes of the eccentric dipole and eccentric quadrupole form an orthogonal system.

The geomagnetic theory of cosmic radiation was developed using the centered dipole model. The Störmer [1955], the allowed, the main [Vallarta, 1948; Lemaitre and Vallarta, 1936a and 1936b], and simple shadow cones [Schremp, 1938], as well as the penumbra, were calculated for the centered dipole field. In order to bring the theory into better agreement with the experimental results, however, the eccentricity of the dipole's location had to be considered [Singer, 1958]. The cutoff momenta were corrected for

eccentricity [Jory, 1956; Webber, 1958]. The longitude effect for 1922 was studied theoretically [Vallarta, 1935].

Several recent papers show the inadequacy of the dipole model to explain the geographic distribution of the experimentally measured intensity of cosmic radiation. [Singer, 1958; Simpson, Fenton, Katzman, and Rose, 1956; Sandström, 1958].

It has been shown that the cosmic radiation intensity is a function of the real local field and is affected by its anomalies [Rothwell and Quenby, 1958]. The effect of the field at the observation point on the shape of the calculated orbits and cones has also been shown theoretically [Gall and Lifshitz, 1956].

In spite of the limitations of any model for representing the actual field, the model used in the geomagnetic theory must be simple enough so that the integration of the differential equation will not be too complex.

The eccentric dipole-quadrupole model has been used in the evaluation of the orbits and cones of the cosmic-ray albedo and of the earth's shadow cones [Gall and Lifshitz, 1958 and 1960]. The quadrupole field becomes important at low latitudes for low-energy particles. (Note: At the geomagnetic equator, at longitude $\varphi = 45^\circ\text{E}$, the quadrupole is 15 per cent of the dipole field.) The models of the centered dipole and zonal quadrupole and of the eccentric dipole and sectorial quadrupole were considered. Corrections to Störmer's theorem and Störmer's

cutoffs were deduced [Jory, 1956]. In this paper we shall limit the discussion mainly to the eccentric dipole and the eccentric dipole-quadrupole models. This last model includes all eight first terms of Gauss's expansion.

The variation of the geomagnetic field with time is known as the 'secular variation.' This variation causes changes in the elements of any given model of the geomagnetic field. In the calculation of the orbits of cosmic-rays particles, the axes of the multipoles are used as the geomagnetic system of reference. Because of the secular variation, these reference systems vary with time. The importance for the geomagnetic theory of studying the secular variation becomes obvious. Analyses of the geomagnetic field models are now available only for a small number of specific years. Moreover, they were performed by various authors by different methods. Consequently, no attempt has been made in this paper to deduce a time function of all the elements of any given model.

The differential equation of motion of a charged particle in the geomagnetic field \mathbf{H} is given by

$$\frac{d^2}{dt^2}(m\mathbf{r}) = \left(\frac{q}{c}\right) \frac{d\mathbf{r}}{dt} \times \mathbf{H} \quad (1)$$

where m is the relativistic mass of the particle and q its charge. In a constant field, v and m are constants of motion.

The dipole and the quadrupole field in geomagnetic coordinates are given by

$$\mathbf{H}_d = M_1 \nabla z / r^3 \quad (2)$$

$$\mathbf{H}_e = 3/2 M'_2 \nabla xy / r^5 \quad (3)$$

where M_1 , M'_2 are the dipole and eccentric quadrupole moments, respectively.

Using the arc as the independent variable, for the dipole we get

$$d^2 \mathbf{r} / ds^2 = C' (d\mathbf{r} / ds \times \nabla z / r^3) \quad (4)$$

and for the dipole and quadrupole

$$d^2 \mathbf{r} / ds^2 = C' d\mathbf{r} / ds \times (\nabla z / r^3 + 3/2 an \nabla xy / r^5) \quad (5)$$

where $C' = (m_1 / pc) (q/a^3)$, $n = m'_2 / m_1$ and m_1 , m'_2 are the reduced dipole and quadrupole magnetic moments, respectively, a is the earth's radius, and p is the relativistic moment of the particle.

Choosing the stormer as the unit of length, the distance in centimeters, r (cm), is given by

$$r(\text{cm}) = r(\text{st})(qM_1/pc)^{1/2} \quad (6)$$

and the differential equation of motion in the dipole field becomes

$$\frac{d^2 \mathbf{r}}{ds^2} = \frac{d\mathbf{r}}{ds} \times \nabla \frac{z}{r^3} \quad (7)$$

In the geomagnetic theory of cosmic radiation the calculations are carried out using the values of the model elements for some arbitrary year. We shall investigate the changes due to the secular variation effect and see whether they do not invalidate the results when applied to some other year. The study is divided into two parts: the variation of the geomagnetic system of reference, and the conditions for the invariance of the differential equation of motion. Practical rules are also given for adapting the calculations valid for an arbitrary year to any specific year of observation.

SECULAR VARIATION AND THE MODELS OF THE GEOMAGNETIC FIELD

The secular variation causes changes in the elements of any model of the geomagnetic field. The changes induced in the eccentric dipole and the eccentric dipole-quadrupole models will now be studied.

Both the dipole and the quadrupole reside at the geomagnetic center $C(X_c, Y_c, Z_c)$, where X_c, Y_c, Z_c are the geographic coordinates. The direction cosines of the dipole axis are given by $\mathbf{OH}_0(x_0, y_0, z_0)$. The geomagnetic z axis of the systems of reference of both models is defined by the dipole axis. The reduced magnetic moment of the dipole is m_1 . The moment and the direction of the axis of the dipole are identical for the centered dipole and for the eccentric dipole of either models studied here. The geographic axis Z and the dipole axis define the geomagnetic meridian, which corresponds to the geographic longitude Φ_0 W. The direction cosines of the two orthogonal axes of the quadrupole are $\mathbf{OH}_1(x_1, y_1, z_1)$ and $\mathbf{OH}_2(x_2, y_2, z_2)$; m'_2 is the reduced moment of the eccentric quadrupole. The geomagnetic equator is the same for both models; its center is at C .

Chargoy and Alvarez [1957] have analyzed the two models for different years. The values

TABLE 1. The Geomagnetic Axes and the Moments of the Multipoles

	Year	1845	1885	1922	1945	1955
OH_1	x_1	-0.9955	-0.9856	-0.9216	-0.8899	-0.8584
	y_1	-0.0581	+0.1363	+0.3632	+0.4285	+0.4881
	z_1	+0.0756	+0.1005	+0.1368	+0.1563	+0.1581
OH_2	x_2	+0.0437	-0.1519	-0.3816	-0.4478	-0.5079
	y_2	-0.9827	-0.9736	-0.9126	-0.8834	-0.8520
	z_2	-0.1802	-0.1703	-0.1467	-0.1385	-0.1268
OH_0	x_0	+0.0847	+0.0747	+0.0715	+0.0739	+0.0728
	y_0	-0.1761	-0.1831	-0.1874	-0.1905	-0.1891
	z_0	+0.9807	+0.9803	+0.9797	+0.9789	+0.9793
	θ_0	11°16'	11°24'	11°35'	11°47'	11°42'
	Φ_0	64°19'	67°49'	69°06'	68°47'	68°57'
	m_1	0.3282	0.3228	0.3159	0.3097	0.3120
	m_2'	0.0212	0.0238	0.0240	0.0219	0.0218
	n	0.0646	0.0737	0.0760	0.0707	0.0699

OH_1 , OH_2 , OH_0 are unit vectors in the direction of the quadrupole and dipole axes; x_i , y_i , z_i are the direction cosines ($i = 1, 2, 0$); θ_0 is the angle between the geographic axis and the dipole axis; Φ_0 is the geographic west longitude of the geomagnetic meridian; m_1 is the reduced dipole moment, m_2' is the reduced moment of the eccentric quadrupole in gauss; $n = m_2'/m_1$.

of the elements for the time interval between 1845 and 1955 are given in Table 1.

From the study of the variation with time of the elements of the models it is deduced that the effect of the secular variation can be represented as a rotation with time of the geomagnetic coordinate system, a displacement of the geomagnetic center C , and a change of the magnitudes of the moments of the multipoles.

We shall first consider the effect of the change of the geomagnetic reference system and later the effect of the change in the magnetic moments.

VARIATION OF THE GEOMAGNETIC REFERENCE SYSTEM; EQUIVALENT POINTS

Consider a point whose geomagnetic coordinates are x, y, z . As the geomagnetic reference system changes with time, this point will migrate in the geographic system of reference. Let $P(X, Y, Z)$ and $P'(X', Y', Z')$ be its positions¹ at times t and t' , respectively. We shall call P and P' equivalent points.

Given the geomagnetic position vector \mathbf{CP} , the geographic vectors of the equivalent points are given by

$$\mathbf{OP}(t) = \mathbf{OC}(t) + \mathcal{Q}(t)\mathbf{CP} \quad (8)$$

$$\mathbf{OP}'(t') = \mathbf{OC}'(t') + \mathcal{Q}(t')\mathbf{CP} \quad (9)$$

The matrix \mathcal{Q} transforms the free geomagnetic into free geographic vector and at any time t is composed of the direction cosines of the axes of the given model of the geomagnetic field. Its columns are the components of unit geomagnetic vectors i, j, k , expressed in geographic coordinates.

For the dipole model the transformation \mathcal{Q} can be represented by two elementary rotations: (a) around the Z axis by Φ_0 angle (matrix \mathcal{B}); (b) around the Y' axis by θ_0 angle² (matrix \mathcal{C})

TABLE 2. The Geomagnetic Center

Year	1845	1885	1922	1945	1955
X_c	-284	-297	-340	-345	-367
Y_c	-6	+60	+115	+150	+205
Z_c	-25	+12	+61	+96	+118
OC	285	305	364	388	436
α_1	175°25'	166°57'	159°14'	152°53'	147°11'
α_2	91°12'	78°39'	71°34'	67°14'	62°0'
α_3	95°2'	87°45'	80°21'	75°40'	74°19'

X_c , Y_c , Z_c are the geographic coordinates in kilometers of the geomagnetic center C ; OC is the distance in kilometers of C from the earth's geographic center; α_1 , α_2 , α_3 are the direction angles of OC .

¹ Lower-case letters will refer to geomagnetic coordinates, capitals to geographic coordinates.

² Here both Φ_0 and θ_0 are positive angles.

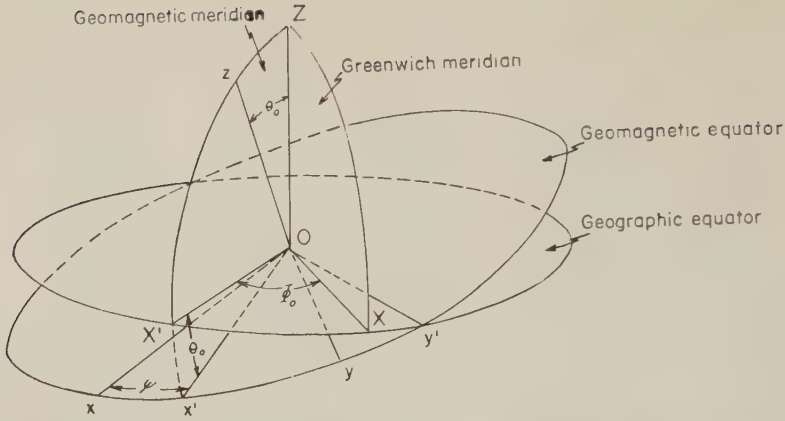


Fig. 1. Schematic representation of the reference systems. X, Y, Z are the geographic axes; x', y', z are the geomagnetic axes for the dipole model; x, y, z are the geomagnetic axes for the dipole-quadrupole model. x lies ψ° west of x' axis. To simplify the figure, the geographic center is drawn to coincide with the geomagnetic.

(see Fig. 1). The x', z axes lie within the geomagnetic meridian.

$$\bar{Q} = \mathcal{BC} = \begin{bmatrix} \cos \theta_0 \cos \Phi_0 & \sin \Phi_0 & \sin \theta_0 \cos \Phi_0 \\ -\sin \Phi_0 \cos \theta_0 & \cos \Phi_0 & -\sin \theta_0 \sin \Phi_0 \\ -\sin \theta_0 & 0 & \cos \theta_0 \end{bmatrix} \quad (10)$$

θ_0 as well as Φ_0 varies little during the 100 years (see Table 1). Averaging over time we get $\bar{\theta}_0 = 11^\circ 37'$, $\bar{\Phi}_0 = 68^\circ 39'$.

The average matrix \bar{Q} of rotation is obtained by substituting these average angles in equation 10

$$\bar{Q} = \begin{bmatrix} 0.3566 & 0.9314 & 0.0733 \\ -0.9123 & 0.3641 & -0.1875 \\ -0.2014 & 0 & 0.9795 \end{bmatrix} \quad (11)$$

For the dipole-quadrupole model the transformation can be represented by three rotations, two of which are given by the matrices \mathcal{B} , \mathcal{C} , and the third, around the axis of the dipole, by an angle ψ (matrix \mathcal{D}). ψ is the angle between the x axes of the dipole and the dipole-quadrupole models (see Fig. 1). The matrix \mathcal{D} is of the same form as the matrix \mathcal{B} . The matrix \bar{Q} is given by

$$\bar{Q} = \mathcal{BCD} = \begin{bmatrix} \cos \theta_0 \cos \Phi_0 \cos \psi & \cos \theta_0 \cos \Phi_0 \sin \psi & \sin \theta_0 \cos \Phi_0 \\ -\sin \Phi_0 \sin \psi & +\sin \Phi_0 \cos \psi & \\ -\sin \Phi_0 \cos \theta_0 \cos \psi & -\sin \Phi_0 \cos \theta_0 \sin \psi & -\sin \theta_0 \sin \Phi_0 \\ -\cos \Phi_0 \sin \psi & +\cos \Phi_0 \cos \psi & \\ -\sin \theta_0 \cos \psi & -\sin \psi \sin \theta_0 & \cos \theta_0 \end{bmatrix} \quad (12)$$

TABLE 3. Rotation of Quadripole Axes with Time

Year	1845	1855	1922	1945	1955
ψ	22°40'	35°30'	43°0'	47°20'	57°20'

ψ is the angle between the X axes of the dipole and the dipole-quadripole models.

The angle ψ for any given year is obtained from the two terms of the matrix, $\sin \psi = -a_{32}/\sin \theta_0$; $\cos \psi = -a_{31}/\sin \theta_0$, where^a $a_{31} = z_2$ and $a_{32} = -z_1$ (see Table 1).

The change in the values of ψ gives the rotation with time of the quadripole axes around the dipole axis. This rotation has already been observed by Chargoy, who studied the migration with time of the points at which the quadripole axes cut the earth's surface [Chargoy and Alvarez, 1957]. This rotation is much faster than that of the geomagnetic meridian plane about the Z axis or about the Y' axis (see Fig. 1 and Table 1).

To the first approximation, we can consider the angles θ_0 , Φ_0 constant and ψ to vary linearly with time:

$$\psi = wt + \psi_0 \quad (13)$$

where $w = 0.268^\circ/\text{year}$.

By substituting $\bar{\theta}_0$, Φ_0 and ψ from (13) into (12), the matrix $\bar{Q}(t)$ for the dipole-quadripole model can be obtained.

The vector \mathbf{OC} (see Table 2) varies rapidly with time; its magnitude almost doubles in 100 years. The change in the direction angles in 100 years is of the order of 22° . Chargoy [1955] found that the point C moves approximately on a plane. It is to be expected that the magnetic center will describe a closed curve. The migration of the point C is, however, too slow to deduce a time function from the data of the last 100 years.

The migration of 36 points distributed over different geomagnetic latitudes and longitudes was studied. The geomagnetic radius for each

of these points was obtained from equation 8 by imposing the condition that the points be situated on the earth's surface in 1945. (Our calculations of albedo orbits and cones were performed using the dipole-quadripole model based on the geomagnetic map for 1945.) The geographic coordinates of the 36 points and of their equivalent points were calculated for the years 1845, 1885, 1922, 1945, and 1955, for both models of the field. The study of migration of the 36 points during the interval of 100 years shows the following:

The geographic latitudes of all equivalent points corresponding to a given point vary little with time. The variation is of the order of a fraction of a degree for the dipole model and of a few degrees for the dipole-quadripole model. The geographic radius of the migrating points varies considerably with time, and for some latitudes and longitudes the change is of the order of 200 km. This change is easily understood in terms of the change of location of the geomagnetic center C with time. The geographic longitude of the equivalent points varies slightly for the dipole field; all 36 points migrate with time toward the west by 2° to 7° . For the dipole-quadripole field, the change in the geomagnetic longitude of the equivalent points corresponding to all 36 points is large; all equivalent points migrate toward the west about 30° in 100 years. This is understood in terms of the rapid rotation of the quadripole axes about the dipole axis.

THE INVARIANCE OF THE DIFFERENTIAL EQUATION OF MOTION

In the previous section the equivalent points were studied for which the spacial part of the differential equation of motion is the same. Lemaitre and Vallarta [1936a] have shown that the acceleration is a function of the coordinates only and does not depend explicitly on the velocity. In order to have the same acceleration at all equivalent points, C' for the dipole model and C'' and n for the dipole-quadripole model must be constant with time (see equations 4 and 5).

The dipole model. The reduced dipole moment m_1 varies with time, its maximum change for 100 years being of the order of 7 per cent. No law of variation of m_1 with time can be deduced from the available data. However, in order to keep C' constant, m_1/pc must be constant. Hence

^a In our calculation of albedo orbits and cones the system $i = \text{OH}_2$; $j = -\text{OH}_1$; $k = \text{OH}_0$ was used. For this system \bar{Q} takes the form:

$$\bar{Q} = \begin{bmatrix} x_2 & -x_1 & x_0 \\ y_2 & -y_1 & y_0 \\ z_2 & -z_1 & z_0 \end{bmatrix}$$

$$\Delta(pc)/pc = \Delta m_1/m_1 \quad (14)$$

The variation of m_1 is compensated by the corresponding variation in the relativistic momentum of the particle.

The kinetic energy of the relativistic particle is

$$\epsilon = (p^2 c^2 + m_0^2 c^4)^{1/2} - m_0 c^2 \quad (15)$$

Hence

$$\frac{\Delta \epsilon}{\epsilon} = \frac{\Delta(pc)}{pc} \left(1 + \frac{m_0 c^2 / \epsilon}{1 + m_0 c^2 / \epsilon} \right) \quad (16)$$

and substituting (14) into (16)

$$\frac{\Delta \epsilon}{\epsilon} = \frac{\Delta m_1}{m_1} \left(1 + \frac{m_0 c^2 / \epsilon}{1 + m_0 c^2 / \epsilon} \right) \quad (17)$$

Equation 17 gives the relative increase of the energy corresponding to the relative increase of the magnetic dipole moment with time. This increase in energy is either equal to or twice the value of the relative change in the dipole moment, according to whether the energy is much larger or much smaller than the rest mass of the particle.

When the Störmer unit of length (stormer) is used (see equation 7), the acceleration is automatically the same for the equivalent points. However, the value of the energy corresponding to a given number of stormers varies, owing to the variation of m_1 .

The results of the present study for an eccentric dipole can be summarized as follows: *The orbits and cones of cosmic radiation defined at the point of observation $P(X, Y, Z)$ for the particle of energy ϵ at the time t are identical to the orbits and cones defined at the point $P'(X', Y', Z')$ for the particle of energy ϵ' at the time t' . The relations between P and P' and ϵ and ϵ' are given by equations 8, 9, and 17, respectively.*

The dipole-quadripole model. The values of n for different years are given in Table 1. Here again not enough data are available to deduce the time function of n . The data of the last 100 years show that the maximum change of n with time is of the order of 15 per cent. H varies with time (see equation 5), and the acceleration will not be the same at the equivalent points even if C' is kept constant. If high precision is required, cones and orbits would have to be

calculated using the model whose values correspond to the year of observation.

The cones calculated for high particle energy using the model for time t can be considered approximately valid for the time t' of observation if $n(t) \cong n(t')$ and if C' is kept constant. At high latitudes or large distances, or both, the quadripole term is negligible and the case reduces to that of the dipole already discussed.

PRACTICAL RULES

The geomagnetic theory provides means for analyzing the intensities of the cosmic radiation. These means consist of different types of cones and the corresponding cutoff energies. The cones and energies are generally calculated for the standard centered dipole model, whose axis is given by $\theta_0 = 11.5^\circ\text{S}$ and $\Phi_0 = 69^\circ\text{W}$, and whose magnetic moment is 8.1×10^{25} gauss cm^3 ($m_1 = 0.3132$ gauss). The cones at any latitude are given in stormers, and the cutoff energies are generally calculated in gev for an observer situated at the earth's surface for a given geomagnetic direction of incidence [Alpher, 1950].

The albedo cones and orbits and the simple shadow cones have also been calculated for an observer on the earth's surface using the dipole-quadripole model based on the 1945 magnetic chart [Gall and Lifshitz 1956, 1958, 1960]. For vertical incidence, the cutoff energies corresponding to Störmer's cone were corrected for eccentricity for the years 1945 [Jory, 1956] and 1955 [Webber, 1958].

In most general terms, the cutoff energies correspond to the main cone for low latitudes and to the forbidden cones, either Störmer's or simple shadow cones, for high latitudes. These general rules vary greatly, however, with the direction of incidence. For instance, for the vertical incidence at the equator the Störmer and the main cutoffs coincide. On the other hand, for the incidence 45°N , there is a heavy penumbra, and the cutoff at the equator is correctly given by the main cone [Vallarta, 1948]. At high latitudes, for the northern and eastern directions, the simple shadow cone cutoff should be taken. (Simple shadow cones have lately been recalculated [Kasper, 1959; Gall and Lifshitz, 1960]. Those previously calculated by Schremp predict a shadow effect larger than the correct one.)

In order to analyze observations taken at any

point P at the time t , time corrections must first be applied to the available cutoff curves [Alpher, 1950]. These corrections will amount to a change with time of the scale of the abscissa corresponding to the geomagnetic latitudes and of the scale of the ordinates corresponding to the cutoff expressed either in stormers or in gev. Care will also have to be taken to interpret correctly a given local geomagnetic direction of incidence, which will vary with time in the geographic system of reference.

The eccentric dipole model. The following quantities should be known for the time t of observation: (a) the location of the geomagnetic center C ; (b) the angles θ_0 , Φ_0 which define the axis of the dipole; (c) the magnetic moment of the dipole.

Let there be a point of observation P whose geographic coordinates are X, Y, Z . In order to find the cutoff for the time t , the geomagnetic coordinates must first be calculated using the following equation:

$$\tilde{G}(t)[\mathbf{OP} - \mathbf{OC}(t)] = \mathbf{CP}(t) \quad (18)$$

$\tilde{G}(t)$ is the transposed matrix \tilde{G} (see equation 10), and

$$\mathbf{CP} = r(t) \times \begin{bmatrix} \cos \lambda(t) \times \cos \varphi(t) \\ \cos \lambda(t) \times \sin \varphi(t) \\ \sin \lambda(t) \end{bmatrix} \quad (19)$$

The geomagnetic latitude of the observation point P corresponding to the standard centered dipole model [McNish, 1936] is given by

$$\sin \lambda_0 = \sin \Theta_0 \times \cos (\Phi_0 + \Phi) \\ \cdot \cos \Lambda + \cos \Theta_0 \times \sin \Lambda \quad (20)$$

Λ, Φ are the geographic latitude and longitude (E) of the point P .

The cutoff should be read off the curve for the time-corrected value of the latitude $\lambda(t)$.

The momentum corresponding to the Störmer unit then has to be corrected for time dependence. For the standard centered dipole model the momentum $(pc)_0$ corresponding to s stormers for an observer at the earth's surface is

$$(pc)_0 = 0.3132 s^2 k \quad (21)$$

where $k = 191.01$ gev/gauss is the conversion factor; the distance is measured in earth's radii.

For the eccentric dipole model at the time t :

$$pc(t) = \frac{m(t)}{r^2(t)} s^2 k \quad (22)$$

The time correction for the eccentric relative to the standard model for the momentum corresponding to s stormers is independent of s and equal to

$$\eta(pc)_1 = \frac{pc(t) - (pc)_0}{(pc)_0} \\ = \frac{m(t)}{0.3132 r^2(t)} - 1 \quad (23)$$

If $(pc)_0$ is the cutoff momentum read off the curve for $\lambda(t)$, the time-corrected cutoff momentum is equal to $[1 + \eta(pc)_1](pc)_0$.

The relative time correction of the cutoff energy is calculated by substituting equation 23 into equation 16.

Last, in order to use the available curves correctly, we must take care of the change with time of the geomagnetic direction of incidence. Let ξ be the zenithal and α the azimuthal angles of incidence in the local geomagnetic system of reference at the time t . The corresponding angles A , and \mathfrak{F} in the local geographic reference system are found by applying the transformation

$$\gamma(t) \begin{bmatrix} \sin \xi & \sin \alpha \\ \sin \xi & \cos \alpha \\ \cos \xi \end{bmatrix} = \begin{bmatrix} \sin \mathfrak{F} & \sin A \\ \sin \mathfrak{F} & \cos A \\ \cos \mathfrak{F} \end{bmatrix} \quad (24)$$

The matrix $\gamma(t)$ transforms local geomagnetic into local geographic coordinates and is a function of $\theta_0(t)$, $\Phi_0(t)$, and of the geographic and geomagnetic latitudes and longitudes of the observation point.

Whenever the cutoff corresponds to Störmer's cone, its value for the point P (λ, φ, r) for the time of observation t and geomagnetic direction of incidence (ξ, α) can be calculated directly from the formula

$$pc(\lambda, r, \xi, \alpha, t) = \frac{\cos^4 \lambda(t) m(t)}{r^2(t)} \\ \cdot k \cdot [1 + (\cos^3 \lambda(t) \sin \xi \sin \alpha + 1)^{1/2}]^{-2}. \quad (25)$$

For the geomagnetic vertical incidence we have

$$(pc)_{\text{vert}} = \frac{\cos^4 \lambda(t) m(t)}{4r^2(t)} \cdot k \quad (26)$$

The time correction for the cutoff for the

eccentric relative to the standard model is given by

$$\frac{(pc)_{\text{vert}} - (pc)_{0,\text{vert}}}{(pc)_{0,\text{vert}}} = \frac{1}{r^2(t)} \frac{\cos^4 \lambda(t)}{\cos^4 \lambda_0} \frac{m(t)}{0.3132} - 1 \quad (27)$$

$(pc)_{0,\text{vert}}$, $(pc)_{\text{vert}}$ are the vertical cutoff momenta for the standard and the eccentric models. The geomagnetic vertical runs along **OP** for the first and along **CP** for the second model.

The dipole-quadrupole model. The cones for the point P and time t can be evaluated using the orbits calculated with the elements of the model valid for the time t' for the equivalent point P' . If point P lies on the earth's surface, $OP = a$, the geographic radius R' of point P' will in general be different from a . The limiting directions of the shadow cone will correspond to the orbits tangent to the sphere of radius R' . This cone for the point P and the time t corresponds to the energy corrected by means of equation 17.

DISCUSSION

The secular variation affects the elements of any given model of the geomagnetic field. The orbits and cones, calculated using a given model and the values of its elements for a specific year, can be valid for another year if proper care is taken to correct the energy corresponding to the orbit or cone. The migration of the point of observation with time must also be taken into consideration.

Owing to the slow variation of the angles θ_0 and Φ_0 and the relatively rapid variation of the angle ψ , a time law for the interval 1845-1955 of the transformation matrix \mathcal{A} for both models could be obtained. However, no time functions could be deduced from the available data for the change with time of C and of the moments of the multipoles. Consequently, all calculations such as the migration of the geomagnetically equivalent points, the time corrections of the cutoff momenta, etc., were performed only for the years for which the values of the elements of the models are available.

The geomagnetic theory provides cutoffs vs. latitude curves for various directions of incidence for the standard centered dipole model. The theory can be applied to the eccentric dipole

model if the curves are corrected for the change with time of (a) the eccentricity, (b) the dipole moment, (c) the axes of the geomagnetic system of reference.

The geomagnetic coordinates, the momenta corresponding to 1 stormer $(pc)_1$, the momenta corresponding to Störmer's vertical cutoff $(pc)_{\text{vert}}$, the percent time corrections for $(pc)_1$ (equation 23) and for $(pc)_{\text{vert}}$ (equation 27), the geographic angles of incidence of the geomagnetic vertical have been calculated for the years 1845, 1885, 1922, 1945, and 1955 for approximately 300 points distributed over the southern and northern hemispheres. The per cent time corrections for 1845 and 1955 have been plotted in Figures 2 to 5. The effect of the secular variation on the cut-off momenta and on the southern-northern asymmetry can be studied from these curves. The time correction of $(pc)_1$ varies between ± 15 per cent, the correction being larger for the northern than for the southern hemisphere in 1955 and larger for the southern hemisphere in 1845. The symmetries of the $(pc)_1$ curves with respect to 0° and 180° geographic longitude for 1845 and to 30° and 150° E for 1955 can easily be understood in terms of the positions of the geomagnetic center C for these years.

The time correction for the Störmer's vertical cutoff is plotted in Figures 4 and 5. Similar curves have been plotted by other authors [Jory 1956; Webber, 1958] for 1945 and 1955. The variation of the dipole moment with time, however, was not considered. The geomagnetic latitude for the eccentric differs little from that for the standard centered dipole model, but for high latitudes this small change in λ amounts to a large change in the vertical cutoff [Dymond, 1952]; the time correction of $(pc)_{\text{vert}}$ reaches values of 50 per cent and more.

The zenithal angle \mathfrak{F} corresponding to the geomagnetic vertical is plotted for the northern hemisphere in Figure 6. For 1845 the values of \mathfrak{F} for both hemispheres coincide; for 1955 they differ by 2° for the longitudes of 30° and 150° E.

Finally, the effect of the secular variation of the geomagnetic field is important in the study of the knee of primary cosmic radiation [Jory, 1956; Dymond, 1952; Meyer and Simpson, 1958]. The secular variation induces a shift in latitude with the corresponding change in the

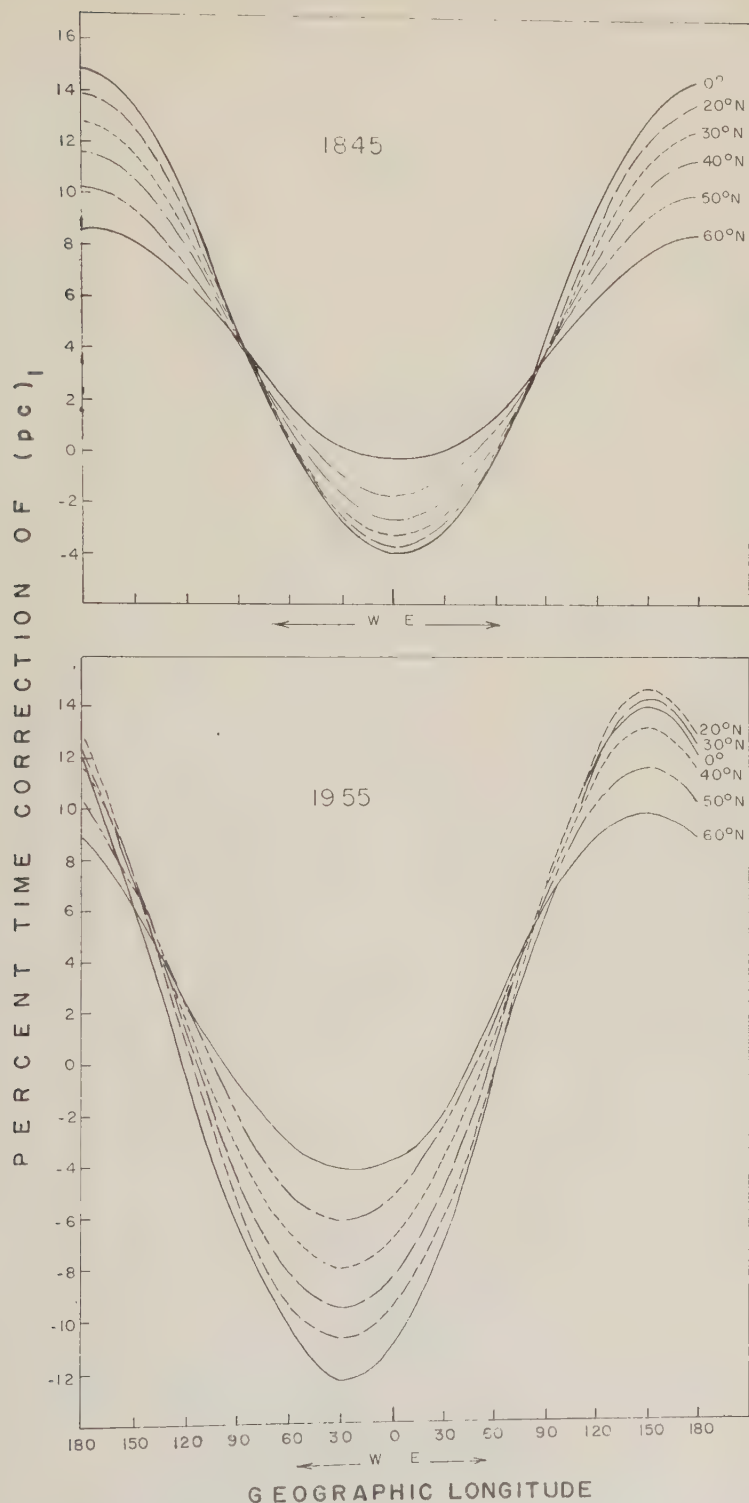


Fig. 2. The per cent time correction of the momentum, corresponding to 1 stormer, is plotted vs. geographic longitude for different geographic latitudes. Northern hemisphere.

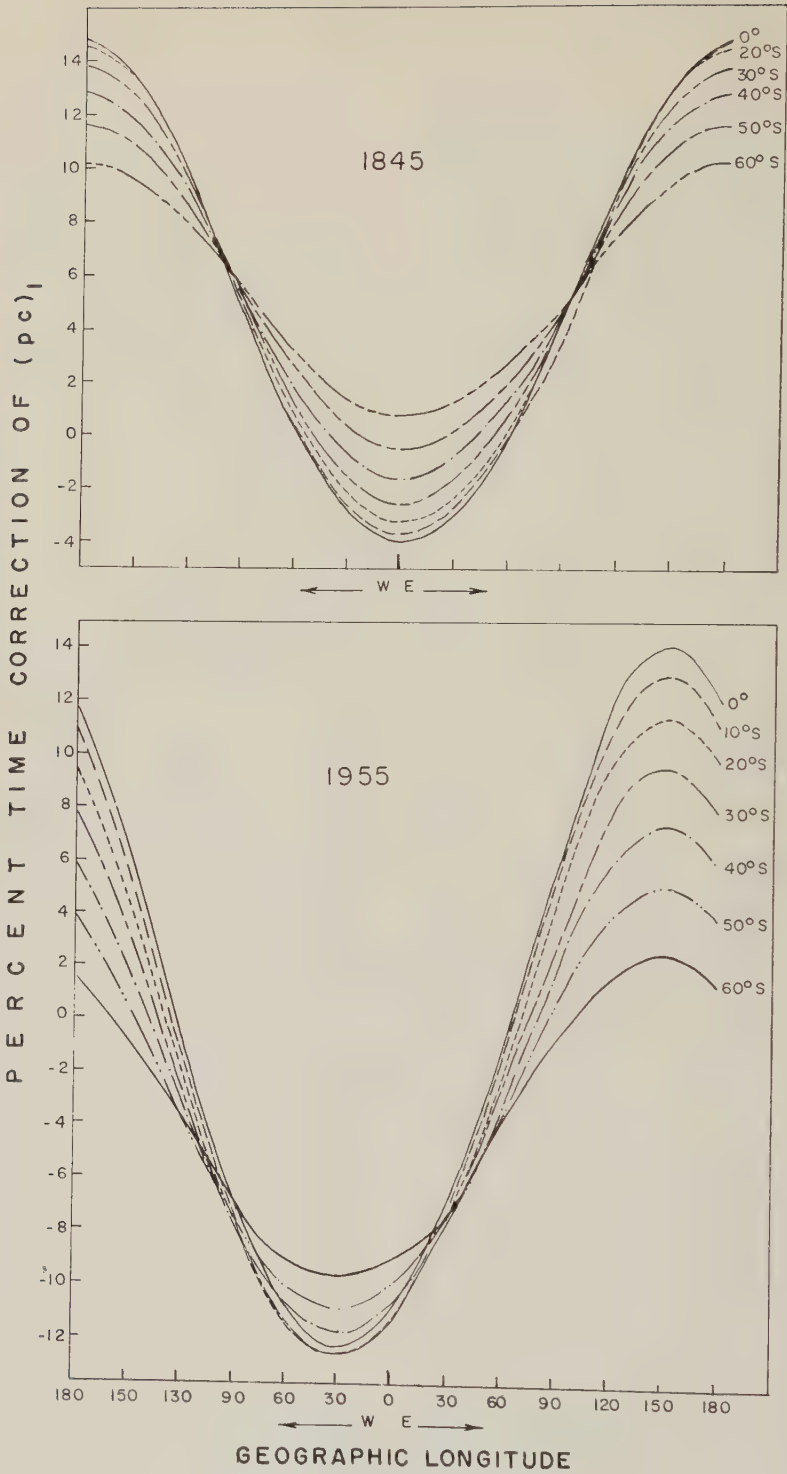


Fig. 3. The per cent time correction of the momentum, corresponding to 1 stormer, is plotted vs. geographic longitude for different geographic latitudes. Southern hemisphere.

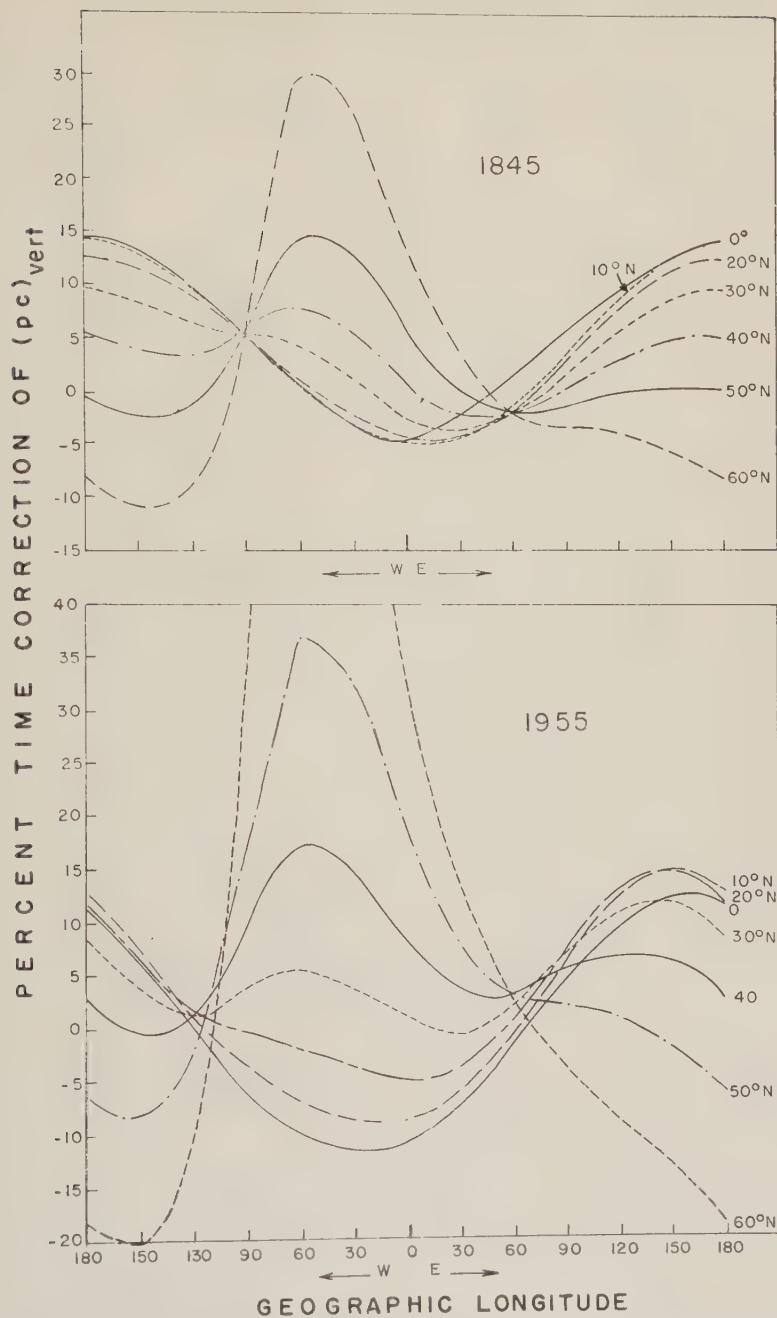


Fig. 4. The per cent time correction of Störmer's vertical cutoff momentum is plotted vs. geographic longitude for different geographic latitudes. Northern hemisphere.

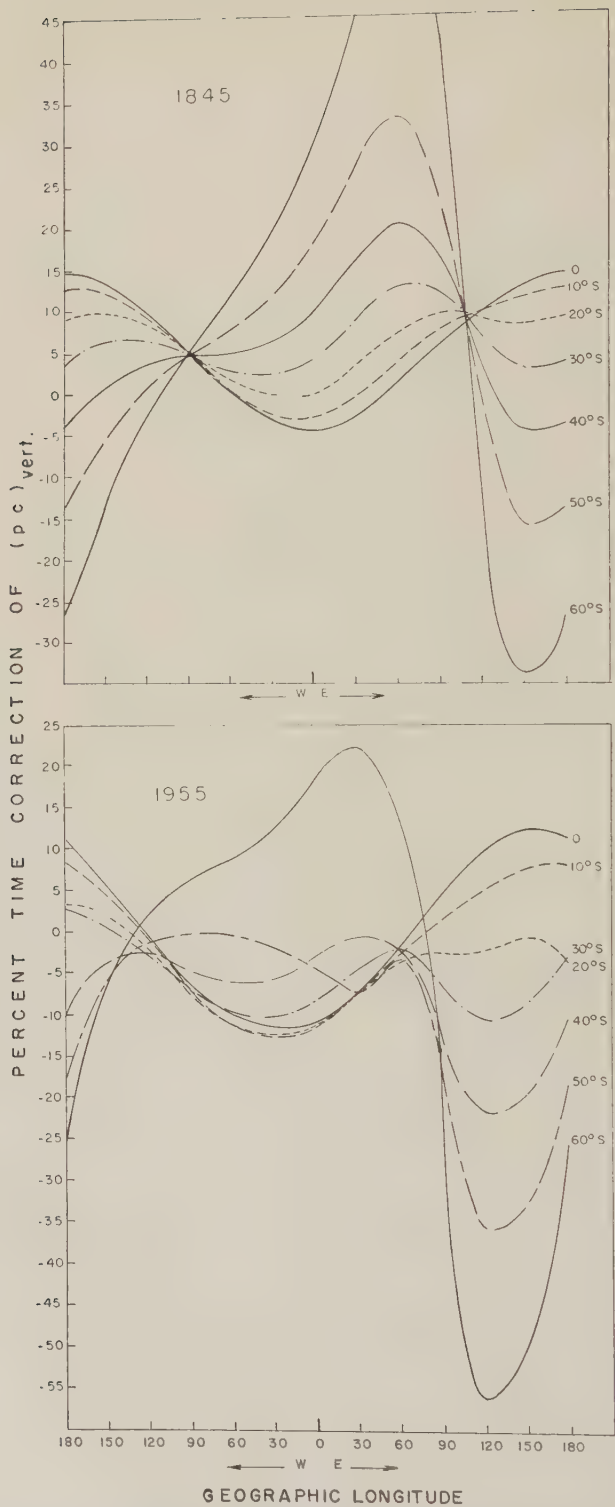


Fig. 5. The per cent time correction of Störmer's vertical cutoff momentum is plotted vs. geographic longitude for different geographic latitudes. Southern hemisphere.

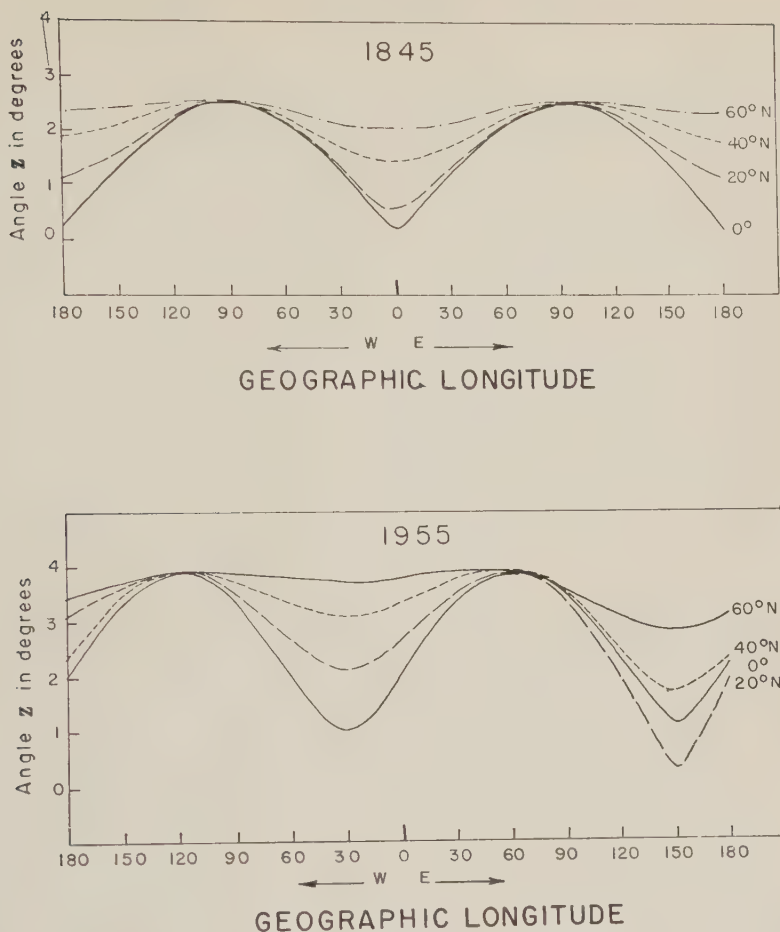


Fig. 6. The geographic zenithal angle Z corresponding to the geomagnetic vertical is plotted vs. geographic longitude for different geographic latitudes. Northern hemisphere.

low-energy cutoff. This shift must first be evaluated before the solar effects on the position of the knee are considered.

Acknowledgments. I wish to thank Professor Manuel Sandoval Vallarta, Anselmo Chargoy, and Mrs. Manuela Garín de Alvarez for interesting discussion on the subject, and Pier Achille Mello for his excellent help in the computations performed with the IBM 650 calculating machine. The calculations were made at the Centro Electrónico de Cálculo of the National University.

I should also like to thank Mrs. Lucila Sánchez de Camacho, José Grapa, Héctor Vázquez, and Eliezer Braum for their collaboration in the analysis of the calculated results, and Mrs. Joan Kruger de Hauff for careful reading of the English text.

REFERENCES

- Alpher, R. A., *J. Geophys. Research*, **55**, 437, 1950.
- Bartels, J., *Terrest. Magnetism and Atmospheric Elec.*, **41**, 248, 1936.
- Chargoy, A., *Rev. mex. fis.*, **2**, 1, 1953.
- Chargoy, A., *Anal. Inst. Geofis.*, **1**, 24, 1955.
- Chargoy, A., and M. Alvarez, *Anal. Inst. Geofis.*, **3**, 137, 1957.
- Dymond, E. G., *Nature*, **170**, 1078, 1952.
- Gall, R., and J. Lifshitz, *Phys. Rev.*, **101**, 1821, 1956.
- Gall, R., and J. Lifshitz, *Nuovo cimento*, [10] **7**, 601, 1958.
- Gall, R., and J. Lifshitz, *Rev. mex. fis.*, **9**, 57, 1960.
- Jory, F. S., *Phys. Rev.*, **102**, 1167, 1956.
- Kasper, J. E., *Nuovo cimento*, [10] **11** (1), 1, 1959.
- Lemaitre, G., and M. S. Vallarta, *Phys. Rev.*, **49**, 719, 1936a.
- Lemaitre, G., and M. S. Vallarta, *Phys. Rev.*, **50**, 493, 1936b.

(Manuscript received August 12, 1960.)

- McNish, A. G., *Terrest. Magnetism and Atmospheric Elec.*, 41, 37, 1936.
- Meyer, P., and J. A. Simpson, *Nuovo cimento*, [10] 8, Suppl. 2, 233, 1958.
- Rothwell, P., and J. Quenby, *Nuovo cimento*, [10] 8, Suppl. 2, 601, 1958.
- Sandström, A. L., *Arkiv Fysik*, 14 (25), 409, 1958.
- Schremp, E. J., *Phys. Rev.*, 54, 158, 1938.
- Simpson, J. A., K. B. Fenton, J. Katzman, and D. C. Rose, *Phys. Rev.*, 102, 1638, 1956.
- Singer, F., *Progress in Elementary Particles and Cosmic Ray Physics*, 4, 239, Interscience Publishers, 1958.
- Störmer, E., *The Polar Aurora*, Oxford University Press, 1955.
- Vallarta, M. S., *Phys. Rev.*, 47, 647, 1935.
- Vallarta, M. S., *Phys. Rev.*, 74, 1837, 1948.
- Webber, W. R., *Nuovo cimento*, [10] 8, Suppl. 2, 532, 1958.

(Manuscript received August 16, 1960.)

The Interaction of the Terrestrial Magnetic Field with the Solar Corpuscular Radiation

DAVID B. BEARD¹

*Lockheed Missiles and Space Division, Sunnyvale, California, and
University of California, Davis, California*

Abstract. In this investigation the terrestrial magnetic dipole field is assumed to exist in an intense stream of protons and electrons emanating from the sun which behaves as a diamagnetic medium terminating the earth's magnetic field at about 7 earth radii on the daylit side and up to perhaps 100 earth radii on the night side of the earth. By detailed examination of particle trajectories the interaction between plasma and magnetic field is shown to occur within a negligibly thin current sheath enveloping the earth. Numerical solutions of the differential equation for the sheath surface reveals an approximately spherical surface on the daylit side giving rise to a more complicated expanding surface on the night side, including a prominent bump of reversed current sheath near the magnetic poles.

1. *Introduction.* The terrestrial magnetic field near the surface of the earth is to fairly good approximation that of a simple magnetic dipole. In a vacuum the terrestrial magnetic field would diminish as the reciprocal of the cube of the distance from the earth's center at large distances from the earth where the dipole approximation would become an increasingly better approximation. The earth, however, is not situated in a vacuum. The principal and most obvious disturbance to the terrestrial magnetic field is assumed to be the intense time-varying neutral flux of energetic protons and electrons constantly emanating from the sun and incident on the earth at all times. Since the excellent studies by Bierman [1953, 1957] of the behavior of comet tails, particularly during sunspot activity, and numerous other observations on such diverse phenomena as scattered polarized light from electrons [Blackwell, 1957], there can be little question of the existence of a solar-originated plasma current whose velocity is roughly 10^8 cm/sec and whose concentration at the position of the earth's orbit is about 50 protons and electrons per cubic centimeter, increasing to possibly 10^4 particles/cm³ during sunspot activity. Several people, notably Chapman and Ferraro [1930, 1931, 1932] Dungey [1958], Johnson [1960], Obayashi [1959], Parker [1958], and Tamao [1959], have suggested that this plasma

flow, or solar wind as Parker has called it, would compress or sweep away the remote daylit part of the earth's magnetic field. This communication discusses a calculation of the position and cause of the electric currents resulting from the interaction between the solar corpuscular radiation and the earth's magnetic field.

The neutral plasma will be deflected by the terrestrial magnetic field—protons curving one way, the electrons curving oppositely. An electric current will result the effect of which will be to cancel any magnetic field causing it. In other words, an electric current sheet resulting from the interaction of the plasma with the magnetic field will in first approximation double a component of the field locally on the side of the sheet away from the sun and will cause the magnetic field to be zero everywhere on the solar side of the sheet (if the solar magnetic field is neglected). This cancellation of a magnetic field acting as a barrier to penetration by a plasma is well known in plasma physics, where a plasma is regarded as a diamagnetic medium.

In the investigation described below the individual charged-particle trajectories are examined in section 2 for the case where the particles are incident along the solar radial line on a thin current sheet enveloping a magnetic field comprised of a magnetic dipole and a field due to the surface sheet current. The differential equation describing the surface sheet is developed in section 3 from standard magnetohydrodynamic principles. The equations are solved approxi-

¹The major part of this work was performed while the author was a consultant to Lockheed Missiles and Space Division.

mately for much of the surface sheet, and the results are presented in section 4. Section 5 briefly discusses the principal conclusions of the calculation at this stage and their significance.

2. Charged-particle trajectories. Electrons and protons with the same velocity will be bent in opposite directions upon encountering a magnetic field with a radius of curvature inversely proportional to their respective masses. Since the positive charge penetrates farther into the magnetic field an electric field will result, due to charge separation. Choosing a right-handed Cartesian coordinate system in which the magnetic field is along the negative Z axis and the Y axis is taken parallel to the surface interaction layer between magnetic field and particles, we may write the particle equations of motion within the layer

$$m\ddot{x} = eE(x) + (e/c)B\dot{y} \quad (1)$$

$$m\ddot{y} = -(e/c)B\dot{x} \quad (2)$$

These equations of motion are readily integrated to give the result

$$v_x^2 = v_{0x}^2 + 2(e/m) \int_{-\infty}^x [E + (v_{0y}/c)B] dx' - (e^2/m^2c^2) \left[\int_{-\infty}^x B dx' \right]^2 \quad (3)$$

$$v_y = v_{0y} - (e/mc) \int_{-\infty}^x B dx' \quad (4)$$

where v_{0x} and v_{0y} are the initial velocity components of the plasma stream at negatively infinite x . Since the resulting electric field prohibits a significant charge separation in the plasma we are considering, we may make the same assumption as *Dungey* [1958] and *Rosenbluth* [1957] in discussing the magnetic pinch from which this treatment is adapted, namely, that the ion and electron densities are everywhere approximately equal. If the initial particle density is N_0 in field-free space, then

$$N = 2N_0v_{0x}/v_x \quad (5)$$

within the surface layer, and therefore the x component of the electron and ion velocities must be approximately equal to prevent charge separation from occurring. Hence

$$\int_{-\infty}^x E(x') dx' \sim -[|e|/(2m_e c^2)] \cdot \left[\int_{-\infty}^x B dx \right]^2 - (v_{0y}/c) \int_{-\infty}^x B dx' \quad (6)$$

$$v_{ix}^2 \sim v_{0x}^2 - (e^2/m_i m_i c^2) \left[\int_{-\infty}^x B dx' \right]^2 \quad (7)$$

where subscripts e and i are used to distinguish electrons and ions.

$$\text{curl } B = 4\pi j \sim 4\pi(2N_0v_{0x}/v_{ix})(e/c)v_{ey} \quad (8)$$

since the electrons are accelerated in the electric field and carry most of the current. The protons are decelerated and penetrate a shorter distance into the magnetic field than they would in the case of no electric field.

The integrodifferential equation for B within the layer resulting from combining equations 4, 7, and 8 may be solved in terms of the boundary conditions that $v_{ix} = 0$ and $B^2 = 16\pi N_0 m_i v_{0x}^2$ at $x = 0$, the inner boundary of the surface layer. (The magnitude of B at $x = 0$ results from the magnetohydrodynamic approximation discussed in the next section.) The solution is a lengthy logarithmic and sinusoidal function which for finite x and v_{0y} is well represented by

$$B \sim (16\pi N_0 m_i v_{0x}^2)^{1/2} \exp(-x/x_0) \quad (9)$$

where $x_0^2 = m_e c^2 / 8\pi N_0 e^2$, $x_0 = 0.3$ km if $N_0 = 50$ electrons/cm³. For $v_{0y} > \sqrt{m_i/m_e} v_{0x}$ the layer is even thinner. Note that the surface layer or current sheath is independent of the plasma kinetic energy and is about a kilometer or less thick, depending on the particle density.

Dr. E. N. Parker, in private discussion with the author, has kindly observed that whereas the electrical conductivity perpendicular to the magnetic field lines is negligible, the conductivity parallel to the field lines is nearly infinite. He suggests that, since the magnetic lines of force are essentially grounded in the ionosphere, no electric field due to charge separation should occur. This interesting possibility should be investigated, but it in no way affects the problem treated here. If Parker is correct, the surface sheath thickness would be given by the curvature of the protons in the magnetic field, $eHv_{0x}/m_i c$, approximately 40 km if v_{0x} is as large as 2×10^8 cm/sec. Since this number is still negligibly small compared with the radius of curvature of the magnetic field lines, the problem is not changed particularly since in this case the protons carry all the current. The currents will be linearly proportional to the radii of curvature of the particles in the magnetic field, so that, since $r = vmc/eH$,

$$H_p/H_e = J_p/J_e = m_p H_e/m_e H_p$$

from which

$$H_p/H_e = \sqrt{m_p/m_e} = J_p/J_e$$

$$r_e = \sqrt{m_e/m_p} r_p$$

where H_p and H_e are the magnetic fields in which the protons and electrons, respectively, move, J_p and J_e are the proton and electron currents, and r_p and r_e are their radii of curvature. A more precise calculation similar to the derivation of equation 9 can be made to show that the current sheath thickness is in Parker's case still much less than even 40 km. In the approximate description given above, the current density would be roughly

$$J_p \sim \sqrt{2x/r_p - x^2/r_p^2}$$

where x is measured from the deepest penetration of the protons. Ninety per cent of the current occurs within 20 km even if v_0 is as large as 2×10^8 km.

Several expected proton trajectories are illustrated in Figure 1. It is important to note that if the electric and magnetic fields are symmetric about a plane perpendicular to the current sheath, and in the direction of the magnetic field at the point of deepest particle penetration, *the particle trajectory must be symmetric about this plane unless the curvature of the magnetic field changes along the short particle trajectory within the field.* (This last reservation is believed significant only near a magnetic pole where the component of the magnetic field parallel to the surface may actually reverse its direction along the particle trajectory.) As a consequence of this assumption, the particle pressure will be perpendicular to the current sheath surface.

As shown in later sections of this paper, the current sheath on the daytime side of the earth is everywhere at a distance from the earth of the order determined by

$$p = B^2/8\pi \quad (10)$$

where p , the particle pressure perpendicular to the current sheath, is approximately 10^{-7} dyne sec under quiet flux conditions of perhaps 30 protons/cm² moving 3×10^7 cm/sec. The corresponding B is 1.5×10^{-8} gauss. In first approximation half of this magnetic field strength is

due to the magnetic field of the earth's dipole, which has a magnitude of 0.75 milligauss at the magnetic equator at a distance of 7.4 earth radii from the center of the earth.

As a consequence of all these considerations of particle trajectories, the particle pressure on the barrier presented to their motion by the earth's field is readily estimated. Since the pressure is proportional to the momentum change of each deflected proton (the electron pressure is, of course, neglected) times the number of protons striking the surface per second,

$$p = (2mv \cos \psi)(Nv \cos \psi) \sim \cos^2 \psi \quad (11)$$

in agreement with an earlier conclusion by Dungey [1958], where N is the number of protons per cubic centimeter in the flux of average velocity v and ψ is the angle of the initial proton velocity vector with the normal to the surface of the current sheet.

3. *Calculations of the current sheath.* A conducting fluid moving in electric and magnetic fields will experience forces expressed by familiar magnetohydrodynamic equations [Spitzer, 1956]

$$\text{grad } p = \mathbf{j} \times \mathbf{B} \quad (12)$$

where \mathbf{j} is the current vector from which the component of \mathbf{j} perpendicular to the magnetic field may be obtained by

$$\mathbf{j}_p = \mathbf{B} \times \text{grad } p/B^2 \quad (13)$$

$$\text{curl } \mathbf{B} = 4\pi \mathbf{j} \quad (14)$$

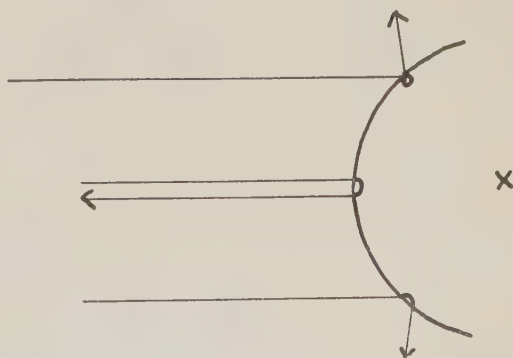


Fig. 1. Illustration of three proton trajectories in the equatorial plane for protons initially traveling in a magnetic-field-free region in the direction of the earth-sun line after they have penetrated a current sheath and been deflected in the magnetic field. Note that the terrestrial magnetic dipole is into the paper, and the magnetic field in which the protons move is up out of the paper.

When equation 14 is substituted in equation 12 there results

$$\text{grad } p = (1/4\pi)(\mathbf{B} \cdot \text{grad})\mathbf{B} - (1/8\pi) \text{grad } B^2 \quad (15)$$

Using the approximation discussed in the previous section that the change in the terrestrial magnetic field over a particle trajectory while in the field is to be neglected, the first term on the right-hand side of equation 15 may be neglected over much of the current sheath because the current sheath is so thin. The rest of the equation is readily integrated so that there results the well-known diamagnetic approximation

$$p + B^2/8\pi = \text{constant} \quad (16)$$

Contrary to customary applications of equation 16, however, the plasma pressure results from a unidirectional plasma flow. The magnetic field in equation 16 is parallel to the current sheath and is approximately twice the component of the terrestrial magnetic field in the plane of the current sheath. As a consequence of the zero divergence of B and equations 13 and 16, the component of the terrestrial field perpendicular to the surface of the current sheath is identically canceled on both sides of the sheath by the magnetic field resulting from the *change* in current along a line of constant longitude and the sum total of all surface currents. (This line of constant longitude is perpendicular to the current in the surface.) Near the poles, p and the component of the terrestrial field in the plane of the current sheath are small; $(\mathbf{B} \cdot \nabla)\mathbf{B}$ in equation 15 and the magnetic field due to all surface currents cannot be neglected even in first approximation. Hence equation 16 is not a good approximation for the polar regions and anywhere along a line extending from the poles toward the night side. This line separates the regions of the sheath surface having opposite currents.

There exists a further approximation in this work which also fails close to the magnetic poles. The current-originated magnetic-field component tangent to the sheath surface is assumed due solely to the local sheath surface current, which is precisely the case for a plane current sheath. In a more precise calculation, the magnetic field due to the curvature of the sheath would have to be subtracted from the assumed value of twice

the tangential component of the earth's dipole in the next highest approximation. The sheath resulting from the zero-order approximation is almost a hemisphere on the daylight side of the earth. As a test of the approximation and a necessary step in calculating the next higher approximation, the contribution of distant current densities has been conservatively estimated by assuming the current sheath to be a hemispherical surface with the positional dependence of the current density given by

$$\mathbf{J} = \mathbf{J}_0 \sin \theta \sin \varphi$$

where θ is the polar angle measured from the earth's dipole vector direction and φ is the longitudinal angle measured from the perpendicular to the earth's orbital radius vector (see fig. 2). The special case of the earth's dipole vector being perpendicular to the earth's orbital radius vector is assumed for calculational simplicity. The two components of the current density vector at the point θ, φ which are tangential and normal to the hemisphere at the angular position θ_0, φ_0 are of interest:

$$J_t = J_0 \sin \theta \sin \varphi \cos(\varphi - \varphi_0)$$

$$J_n = J_0 \sin \theta \sin \varphi \sin(\varphi - \varphi_0)$$

The magnetic-field component tangent to the surface at the angular position (θ_0, φ_0) resulting from the sheath current density is given by the tangential component of the curl of the vector potential

$$B_t = (\text{curl } A)_t = \int_0^\pi \int_0^\pi \left(\frac{J_t}{r^2} \frac{dr}{da} - \frac{J_n}{r^2} \frac{dr}{db} \right) R^2 \sin \theta \, d\theta \, d\varphi$$

where R is the radius of curvature of the hemisphere, a and b are infinitesimal displacements perpendicular to the surface and parallel to the current respectively at the point (R, θ_0, φ_0) , and r is the distance from a point on the surface to the point infinitesimally displaced from (R, θ_0, φ_0) .

$$\begin{aligned} r = & (\sqrt{2} R [1 - \sin \theta_0 \sin \theta \cos(\varphi - \varphi_0) \\ & - \cos \theta_0 \cos \theta - (a/R)(\sin \theta_0 \sin \varphi_0 \\ & - \sin \theta \sin \varphi) - (b/R)(\sin \theta_0 \cos \varphi_0 \\ & - \sin \theta \cos \varphi) + a^2/2R^2 + b^2/2R^2]^{1/2} \end{aligned}$$

B_t was computed numerically using Simpson's rule in steps of 10° for three representative

points on the hemisphere. For $(\theta_0, \varphi_0) = (\pi/2, \pi/2)$ the surface tangential component of the magnetic field due to the curvature of the sheath was -41 per cent of the same magnetic-field component of a plane current sheath at the same position. (The reason for the minus sign is that this additional field due to the curvature is opposite in direction to the planar field. For purposes of comparison the magnetic field of a plane current distribution perpendicular to the plasma flux at distance R from the earth's dipole will be called B_{ref} .) For $(\theta_0, \varphi_0) = (0, \pi/2)$ the tangential component of the magnetic field due to the curvature of the hemispherical current distribution was -18 per cent of B_{ref} . This is roughly equal to the same quantity at $(\theta_0, \varphi_0) = (\pi/12, \pi/2)$, which is the limiting value of θ for which this calculation of the sheath is considered trustworthy. The surface current at $(\pi/12, \pi/2)$ is 26 per cent of its value at $(\pi/2, \pi/2)$, however, so that -18 per cent of B_{ref} is -70 per cent of the field due to the local surface current. Since this additional field contribution is greater near the poles, the surface will have slightly more curvature than a hemisphere and will approach closer to the earth as one moves toward the poles. For $(\theta_0, \varphi_0) = (\pi/2, 0)$ the tangential component of the magnetic field due to the curvature of the hemispherical current distribution was 36 per cent of B_{ref} . In this instance, however, a hemisphere is a very poor assumption, since the first approximation surface is not parallel to the plasma flux at this point but more nearly 23° or so from being parallel. J is about 40 per cent of J_0 , and 36 per cent is too large. Some increased curvature may occur as in the approach to the poles, but it is significantly less in both instances than what would be estimated from a consideration of the fields alone since any increase in curvature is offset by an accompanying decrease in plasma pressure.

Since the true tangential field component is less than twice the earth's field tangential component by the amount calculated above, D , where D varies roughly between 0.4 and 0.7, and since the radius of the sheath $r \sim H^{-1/2}$ we find that if r_0 is the first assumed current sheath distance from the earth the second approximation should amount to

$$r \sim [2/(2 - D)]^{-1/2} r_0 \sim (1 - D/6) r_0$$

so that r may be roughly 7 to 11 per cent less

than what has been estimated in this paper. This approximation converges rapidly and is obtained obviously to second order by computing the field resulting from the first approximation surface as was done above for three representative points and repeating the calculation with this corrected value of the field tangential to the surface. It is expected that the second approximation will be adequate to explore the polar regions and other surface regions having zero current density.

Thus, there exists a surface $[F(r, \theta, \varphi) = \text{constant}]$ on which there is a thin sheet of electrical current such that the magnetic field, \mathbf{B} , outside this surface, is zero, owing to currents and current gradients within the sheet. In spherical coordinates, the terrestrial magnetic field B_* is written

$$B_* = -(M/r^3) \sin \theta \hat{\theta} - (2M/r^3) \cos \theta \hat{r} \quad (17)$$

where M is the magnitude of the earth's magnetic dipole moment, 8.06×10^{25} emu, $\hat{\theta}$ and \hat{r} are unit vectors in the direction of increasing θ and r , respectively, and the earth's magnetic dipole is taken for the coordinate polar axis, and the earth-sun line is chosen to be in the longitudinal plane for which $\varphi = \pi/2$. See Figure 2. The unit vector in the direction of the proton's initial velocity vector is given by

$$\begin{aligned} \hat{v} = & (\sin \lambda \cos \theta - \sin \varphi \sin \theta \cos \lambda) \hat{r} \\ & - (\sin \varphi \cos \theta \cos \lambda + \sin \theta \sin \lambda) \hat{\theta} \\ & - \cos \lambda \cos \varphi \hat{\varphi} \end{aligned} \quad (18)$$

The unit normal vector to the surface $F(r, \theta, \varphi) = \text{constant}$ is given by

$$\begin{aligned} \hat{n}_s = a \text{ grad } F = & a \left\{ \frac{\partial F}{\partial r} \hat{r} + \frac{1}{r} \frac{\partial F}{\partial \theta} \hat{\theta} \right. \\ & \left. + \frac{1}{r \sin \theta} \frac{\partial F}{\partial \varphi} \hat{\varphi} \right\} \end{aligned} \quad (19)$$

where

$$\begin{aligned} a = & \left[\left(\frac{\partial F}{\partial r} \right)^2 + \frac{1}{r^2} \left(\frac{\partial F}{\partial \theta} \right)^2 \right. \\ & \left. + \frac{1}{(r \sin \theta)^2} \left(\frac{\partial F}{\partial \varphi} \right)^2 \right]^{-1/2} \end{aligned}$$

It is useful to note that the increment in F is zero for displacements which occur in the surface, yielding simpler relationships for \hat{n}_s , particularly when one variable (e.g., φ or θ) is held constant. That is, within the surface plane we find that

$$\Delta F \equiv \frac{\partial F}{\partial r} \Delta r + \frac{\partial F}{\partial \theta} \Delta \theta + \frac{\partial F}{\partial \varphi} \Delta \varphi = 0 \quad (20)$$

The unit vector representing the direction of the intersection of plane ($\varphi = \text{constant}$) is given by

$$\hat{P} = k(\hat{\phi} \times \hat{n}_s) = b \left(\frac{\partial F}{\partial r} \hat{\theta} - \frac{1}{r} \frac{\partial F}{\partial \theta} \hat{r} \right) \quad (21)$$

where

$$b = \left[\left(\frac{\partial F}{\partial r} \right)^2 + \frac{1}{r^2} \left(\frac{\partial F}{\partial \theta} \right)^2 \right]^{-1/2}$$

Since \hat{P} lies in the surface, equation 20 applies, and since $\Delta \varphi = 0$, equation 21 may be rewritten

$$\hat{P} = -b' \left(\hat{\theta} + \frac{1}{r} \frac{dr}{d\theta} \hat{r} \right) \quad (21')$$

where

$$b' = \left[1 + \frac{1}{r^2} \left(\frac{dr}{d\theta} \right)^2 \right]^{-1/2}$$

Hence the component of the terrestrial magnetic field that lies in the current sheet surface is given by

$$\hat{P} \cdot \mathbf{B}_s = (b' M / r^3) \left(\sin \theta + \cos \theta \frac{2}{r} \frac{dr}{d\theta} \right) \quad (22)$$

The cosine of the angle between the surface normal and the initial proton velocity vector is

$$\begin{aligned} -(\hat{n}_s \cdot \hat{v}) &= \alpha \left\{ \frac{\partial F}{\partial r} (\sin \varphi \sin \theta \cos \lambda - \cos \theta \sin \lambda) \right. \\ &+ \frac{1}{r} \frac{\partial F}{\partial \theta} (\sin \varphi \cos \theta \cos \lambda + \sin \theta \sin \lambda) \\ &\left. + \frac{1}{r \sin \theta} \frac{\partial F}{\partial \varphi} \cos \varphi \cos \lambda \right\} \quad (23) \end{aligned}$$

The $\cos^2 \psi$, $(-\hat{n}_s \cdot \hat{v})^2$, is proportional to the total momentum exchanged per second by the steady solar plasma flow (i.e., pressure). Hence, equations 22 and 23 are proportional as shown by equation 16 in the approximation where the curvature of the surface is neglected in computing the magnetic effect of the current at any point and $(\mathbf{B} \cdot \text{grad}) \mathbf{B}$ is neglected in comparison with the gradient of the pressure and the square of $\hat{P} \cdot \mathbf{B}_s$ across the surface. Therefore, the differential equation for the current sheath surface, $F(r, \theta, \varphi) = \text{constant}$, is taken to be

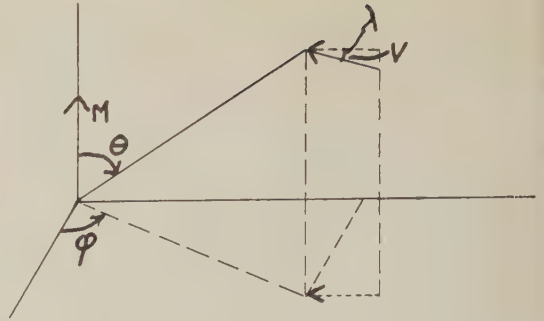


Fig. 2. Illustration of the coordinate system, where M is the earth's magnetic dipole, v is the initial proton velocity vector (parallel to the radius of the earth's orbit), the dashed vector represents the projection of v on the terrestrial equatorial plane, and λ is the solar latitude position with respect to the magnet equatorial plane.

$$\begin{aligned} &\frac{b' M'}{r^3} \left(\sin \theta + \cos \theta \frac{2}{r} \frac{dr}{d\theta} \right) \\ &= \pm \alpha \left\{ \frac{\partial F}{\partial r} [\sin \varphi \sin \theta \cos \lambda - \cos \theta \sin \lambda] \right. \\ &+ \frac{1}{r} \frac{\partial F}{\partial \theta} [\sin \varphi \cos \theta \cos \lambda + \sin \theta \sin \lambda] \\ &\left. + \frac{1}{r \sin \theta} \frac{\partial F}{\partial \varphi} \cos \varphi \cos \lambda \right\} \quad (24) \end{aligned}$$

where

$$\begin{aligned} b' &= \left[1 + \frac{1}{r^2} \left(\frac{dr}{d\theta} \right)^2 \right]^{-1/2} \\ \alpha &= \left[\left(\frac{\partial F}{\partial r} \right)^2 + \frac{1}{r^2} \left(\frac{\partial F}{\partial \theta} \right)^2 \right. \\ &\quad \left. + \frac{1}{r^2 \sin^2 \theta} \left(\frac{\partial F}{\partial \varphi} \right)^2 \right]^{-1/2} \end{aligned}$$

and M' is the terrestrial magnetic dipole moment in units of plasma pressure. The solution of equation 24 is subject to the conditions that ψ can never be less than $\pi/2$, and if ψ is π at $\theta = \varphi = \pi/2$ then p , given by equation 11, is equal to $B^2/8\pi$ by equation 16, where B is twice the terrestrial magnetic field, B_s , in equation 17.

4. *Solution of surface equation.* For the special case $\lambda = 0$, $\varphi = \pi/2$, $\partial F/\partial \varphi = 0$ and equation 24 becomes a simple first-order differential equation in the two variables r and θ . Utilizing equation 20, there results

TABLE 1

Values of α and β as a function of θ , the latitude angle, where α and β are the coefficients in a series expansion of r of the plasma sheath surface as a function of η , the longitudinal angle from the plane containing the earth's dipole and the earth-sun line; $r = 1 + \alpha\eta^2 + \beta\eta^4$ in units of $r_0 = (M^2 8\pi N_0 m_i v^2)^{1/6}$, and η is expressed in radians.

θ	90°	75°	60°	45°	30°	15°
α	0.104	0.102	0.096	0.086	0.068	0.031
β	0.011	0.011	0.010	0.008	0.007	0.004

Let

$$\left. \begin{aligned} A &= [6\alpha \sin^2 \vartheta + 1 - \sin^2 \vartheta \\ &\quad - 2\epsilon_1 \sin^2 \vartheta \cot \vartheta]^{1/2} \\ B &= [-21\alpha^2 \sin^2 \vartheta \\ &\quad - (1 - \sin^2 \vartheta)/3 \\ &\quad + (4 + 50 \sin^2 \vartheta \alpha \\ &\quad - 6 \sin^2 \vartheta) \epsilon_1 \cot \vartheta \\ &\quad - 11\epsilon_1^2 \sin^2 \vartheta \cot^2 \vartheta \\ &\quad - 2\epsilon_2 \cot \vartheta]/2A \\ C &= 3 \sin^2 \vartheta / A \\ D &= 7\alpha + \csc^2 \vartheta - 4\epsilon_1 \cot \vartheta \\ E &= (1 - A) D - 2/3 \\ &\quad + \epsilon_1 \cot \vartheta + 3\alpha A - B \end{aligned} \right\} \quad (34)$$

then there results

$$\left. \begin{aligned} \alpha &= (1/4) \{ 2 + 3 \sin^2 \vartheta \\ &\quad - [(2 + 3 \sin^2 \vartheta)^2 \\ &\quad - 4 \sin^2 \vartheta (1 + 2\epsilon_1 \cot \vartheta)]^{1/2} \} \\ \text{and} \\ \beta &= E/(4 + C) \end{aligned} \right\} \quad (35)$$

The procedure was to start from the boundary condition $r = 1$ at $\varphi = \pi/2$ and evaluate α and β by the use of equation 35 for different ϑ , first assuming $\epsilon_1 = \epsilon_2 = 0$. From the dependence of calculated α and β on ϑ (and therefore r on ϑ), $dr/d\theta$ could be interpolated and thus new values for ϵ_1 and ϵ_2 could be found. With these new values of ϵ_1 and ϵ_2 (no longer = 0) the calculation was made repeatedly, using successive values of ϵ_1 and ϵ_2 , until little improve-

ment in ϵ resulted. Table 1 gives the resultant dependence of α and β in equation 32 on ϑ . Kutta's 3/8 rule was used for $\pi/3 \leq \eta \leq \pi/2$ for $\vartheta = \pi/6$ and for $\pi/12 \leq \eta \leq \pi/2$ for $\vartheta = \pi/2$, and an identical value of r was obtained. Therefore, the series was assumed valid for $0 \leq \eta \leq \pi/2$, i.e., $\pi/2 \leq \varphi \leq \pi$, the entire daylight side.

Using either the series or Kutta's 3/8 rule, we may readily obtain $r(\varphi, \vartheta = 90^\circ)$ since $dr/d\theta = 0$ for this special case. Table 2 gives $r(\varphi, \vartheta = 90^\circ)$.

On the night side of the earth, particularly in some extreme northerly or southerly regions, $dr/d\theta$ changes rapidly with φ and because of its large magnitude plays an important part in the calculation. Different and more precise methods are required and are being attempted with the aid of a high-speed computer for the entire problem. For the special case of $\lambda = 0$, $\varphi = 3\pi/2$, the direction of the current in the sheath reverses near the poles since the direction of the magnetic field underlying the surface changes direction. On the night side for $r \leq 2^{1/3} = 1.26$:

$$dr/d\theta = r \tan \theta (1 + r^3)/(2 - r^3) \quad (36)$$

having the solution

$$\cos \theta \sim (r^3 + 1)/2r^2 \quad (37)$$

or

$$y = r \cos \theta \sim (1 + r^3)/2r \quad (37')$$

For $r \geq 1.26$ the solution is

$$y \sim 1.8/(1 + r^{-3}) \quad (38)$$

Equations 37 and 38 are very approximate in that the constant of integration is determined by matching them to the daylight side solutions across the region of zero surface current, for which the solution has not yet been found precisely.

If $\lambda \neq 0$ the more complicated equation 24 must be used. This case has not yet been examined in careful detail, but the principal effect appears to be that the axis of the current sheath is tilted at an angle from the normal to the plane of the ecliptic roughly one-third of the angle that the terrestrial magnetic dipole vector makes with the normal to the plane of the ecliptic. The nearest distance of the surface to the earth is increased to roughly $(\cos \Phi)^{-1/3} r_0$, where Φ is the angle of the current sheath axis with the normal to the ecliptic plane. The surface is very little changed otherwise from the $\lambda = 0$ case.

TABLE 2

r of the plasma sheath surface in units of r_0 and $|r \cos \phi|$ as a function of ϕ the longitudinal position in the equatorial plane of the earth's magnetic dipole; $180^\circ \leq \phi \leq 270^\circ$ corresponds to the night side of the earth.

ϕ	90	105	120	135	150	180	210	240	270
r	1.000	1.009	1.031	1.068	1.126	1.342	1.842	3.472	∞
$ r \cos \phi $	0	0.261	0.515	0.755	0.976	1.342	1.595	1.736	1.781

In all the foregoing it is implied that the surface sheath trails off to infinity on the night side of the earth. Such an open-ended tail cannot be the case, of course, in an interplanetary environment composed of a radial solar magnetic field entrapped by the corpuscular radiation [Parker, 1958] or especially in a nonzero temperature plasma stream as discussed by Dungey [1958]. The length of the tail would be roughly proportional to the ratio of the radial velocity of the protons to their thermal velocity times the maximum dimension of the current sheath perpendicular to the earth-sun line. That is, the expected length of the tail, L , is roughly given by

$$L \sim (M_p v_0^2 / 2kT)^{1/2} 1.8r_0 \quad (39)$$

If T were 10^4 degrees Kelvin (~ 1 ev), and if v_0 were 3×10^7 cm/sec, L would be approximately $30r_0$. Of course $1.8r_0$ is a slight overestimate for the maximum dimension of the current sheath, which is found by adding the thermal pressure of the plasma on the sheath surface to the radial pressure.

5. *Conclusions.* The interaction between the solar corpuscular radiation and the earth's magnetic field has been investigated, and it is concluded that the earth is encased in a roughly teardrop-shaped, negligibly thin boundary layer



Fig. 3b. Plasma sheath cross section in the plane of the earth's dipole perpendicular to the earth-sun line. The dotted line is a tentative suggested shape.

with sharp indentations at the poles. The sheath surface is pictured in different cross sections in Figures 3a, b, and c. The shape of the surface in the steady-state flux condition assumed throughout this work is smooth and independent of steady flux conditions, being a slightly distorted hemisphere on the daylit side with a point of inflection in the surface occurring at the poles and along a line extending into the night side of the earth, which separates the sheath surfaces having oppositely directed surface currents. As is indicated in Figure 3c, the surface has a valley in it, extending from the poles, if the incident plasma has a finite thermal motion, as it must be assumed to have. The dimensions of the surface sheath are dependent on the incident plasma conditions, however, being given by

$$r_0 = (M^2 8\pi N_0 m_e v^2)^{1/6} \quad (40)$$

where r_0 is the nearest point of the surface to the earth, occurring at the intersection of the sheath surface with the earth-sun line. r_0 would

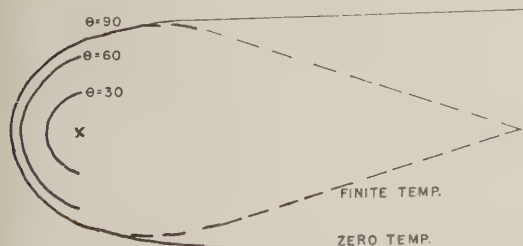


Fig. 3a. Plasma sheath contours viewed in the plane perpendicular to the earth's dipole. The solid lines are for the case of zero temperature for the corpuscular radiation. The dashed lines are for a finite thermal plasma energy.

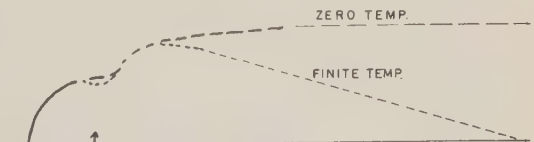


Fig. 3c. Plasma sheath cross section in the plane of the earth's dipole and the earth-sun line. The dashed lines are for tentative presently suggested solutions for the night side for finite and zero plasma thermal energy.

be 7 earth radii if $N_0 = 30$ protons/cc and $v = 3 \times 10^7$ cm/sec.

The Van Allen radiation belts must, of course, be contained within this surface. Auroral particles funnel in along the break in the surface where the surface current is reversed, which makes these regions the most interesting area of solution yet to be completed. Hydromagnetic waves [Dessler, 1959] are generated in this layer and create measurable effects on the terrestrial magnetic field intensity on the surface of the earth. It is interesting to note that in roughing out an equatorial shape to the sheath to match observed magnetic effects Dessler, Francis, and Parker [1960] closely approximated Table 2 of this communication. A turbulent boundary layer caused by short-time variations in the incident solar plasma flux [Parker, 1958] will give a slightly different surface layer in that equation 2 would have to be modified to account for diffuse rather than specular reflection. Turbulence as a function of θ is quickly damped, as may readily be ascertained from an examination of the equations for $dr/d\theta$. Turbulence as a function of θ has been examined by Chapman and Ferraro as discussed in *Chapman and Bartels* [1940]. Flutes discussed by *Rosenbluth and Longmire* [1957] in Project Sherwood applications will not be unstable since the plasma surface is concave on the vacuum or magnetic-field side. Hence fluting is not a mechanism by which plasma will become entrapped in the earth's magnetic field and contribute to Van Allen radiation.

Acknowledgments. Dr. Francis S. Johnson of Lockheed Missiles and Space Division proposed the problem to the author, and contributed a great deal in the way of physical insight throughout the work. Dr. Alex Dessler of Lockheed Missiles and Space Division and Dr. Eugene Parker of the University of Chicago also contributed much in illuminating discussion.

REFERENCES

- Bierman, L., Physical processes in comet tails and their relation to solar activity, *Extrait des Mém. in 8° de la Soc. roy. sci. Liège*, [4] 13, 291, 1953.
- Bierman, L., Solar corpuscular radiation and the interplanetary gas, *Observatory*, 77, 109-110, 1957.
- Blackwell, D. E., The zodiacal light and the nature of the interplanetary gas, *Observatory*, 77, 187-191, 1957.
- Chapman, S., and J. Bartels, *Geomagnetism*, Clarendon Press, Oxford, 1049 pp., 1940.
- Chapman, S., and V. C. A. Ferraro, A new theory of magnetic storms, *Nature*, 126, 129-130, 1930.
- Chapman, S., and V. C. A. Ferraro, *Terrest. Magnetism and Atmospheric Elec.*, 36, 77-97, 171-186, 1931; 37, 147-156, 1932.
- Dessler, A. J., Upper atmosphere density variations due to hydromagnetic heating, *Nature*, 184, 261-262, 1959.
- Dessler, A. J., W. E. Francis, and E. N. Parker, Geomagnetic storm sudden-commencement rise times, *J. Geophys. Research*, 65, 2715-2719, 1960.
- Dessler, A. J., and E. N. Parker, Hydromagnetic theory of geomagnetic storms, *J. Geophys. Research*, 64, 2239-2252, 1959.
- Dungey, J. W., *Cosmic Electrodynamics*, Cambridge University Press, London, 1958.
- Johnson, F. S., The gross character of the geomagnetic field in the solar wind, *J. Geophys. Research*, 65, 3049-3051, 1960.
- Obayashi, T., Entry of high energy particles into the polar ionosphere, *Rept. Ionosphere and Space Research Japan*, 13, 201-209, 1959.
- Parker, E. N., Interaction of the solar wind with the geomagnetic field, *Phys. Fluids*, 1, 171-187, 1958.
- Rosenbluth, M. N., Dynamics of a pinched gas, in *Magnetohydrodynamics*, edited by R. Landshoff, Stanford University Press, Palo Alto, 115 pp., 1957.
- Rosenbluth, M. N., and C. L. Longmire, Stability of plasmas confined by magnetic fields, *Ann. Phys. N. Y.*, 1, 120-140, 1957.
- Spitzer, L., *Physics of Fully Ionized Gases*, Interscience, New York, 105 pp., 1956.
- Tamao, T., Hydromagnetics in the earth's outer atmosphere, *J. Geomagn. Geoelec.*, 10, 143-150, 1959.

(Manuscript received July 22, 1960;
revised August 23, 1960.)

Radiation from Protons of Auroral Energy in the Vicinity of the Earth

W. B. MURCRAY AND J. H. POPE

*Geophysical Institute, University of Alaska
College, Alaska*

Abstract. Some considerations regarding the way in which auroral protons might be expected to radiate as they approach the earth are discussed. The form of the frequency-time curves which might result at the earth's surface from the radiation by such particles are deduced by assuming a reasonable model of the upper ionosphere. It is concluded, at least so far as the frequency-time curves are concerned, that auroral protons are capable of producing the low-frequency electromagnetic phenomenon known as 'Chorus.'

INTRODUCTION

In a recent publication [MacArthur, 1959] it was suggested that some of the audio-frequency electromagnetic radiation of natural origin sometimes known as 'dawn chorus' might be due to protons of moderate to low velocity, such as those associated with the aurora. These incoming protons would radiate at the proton-cyclotron frequency in the whistler mode, for which the index of refraction of the ionosphere is very much greater than 1, so that the Doppler shift is large. This kind of radiation can penetrate the ionosphere and be observed at the ground. Preliminary examination indicated that such a process is possible [Murcray and Pope, 1960] and that a more detailed study is justified.

The suggested mechanism is particularly attractive because it is susceptible to at least semiquantitative treatment. That is, assuming a structure for the free electron distribution in the outer ionosphere and exosphere, it is possible to calculate the shape of the frequency-vs-time curve which would be produced by incoming protons of a given velocity. This curve can then be compared with that seen on the recordings of natural chorus, and eventually conclusions can be drawn as to the possibility that the observed chorus signals actually could have originated in this manner.

EMITTED RADIATION

The auroral spectrum shows $H\alpha$ lines that are Doppler shifted by amounts corresponding to velocities of the order of 10^4 km/sec. Other considerations indicate that protons of con-

siderably higher velocities are present, and it is probably safe to assume the presence of incoming protons of velocities between 10^8 and 3×10^8 km/sec (0.1c) in quite large numbers in the vicinity of the auroral zone during auroral disturbances; that is to say, most of the time. It seems probable that such protons are present to some extent at all times. Associated with these protons should be an equal number of electrons, forming a neutral plasma. Both electrons and protons will spiral about the direction of the magnetic field with their respective cyclotron frequencies.

Of the possible radiations which could originate from this motion, only one, the proton-cyclotron frequency in the extraordinary polarization, is likely to be detected on the ground. This is easily seen by looking at the form of the Appleton-Hartree equations for the index of refraction. The index for propagation along the field reduces to

$$n = \left(1 - \frac{f_0^2}{f^2 \pm f_h f}\right)^{1/2}$$

where f_0 is the plasma frequency and f_h the electron-cyclotron frequency.

For the radiation from the gyrating electrons the frequency f is equal to the cyclotron frequency f_h . In the event of the extraordinary polarization (minus sign) the index becomes infinite, so there can be no radiation of this component in the direction of the magnetic field. The electron radiation in the ordinary mode cannot penetrate the ionosphere because in the ionosphere $f_0 > 2 f_h$ and the medium is

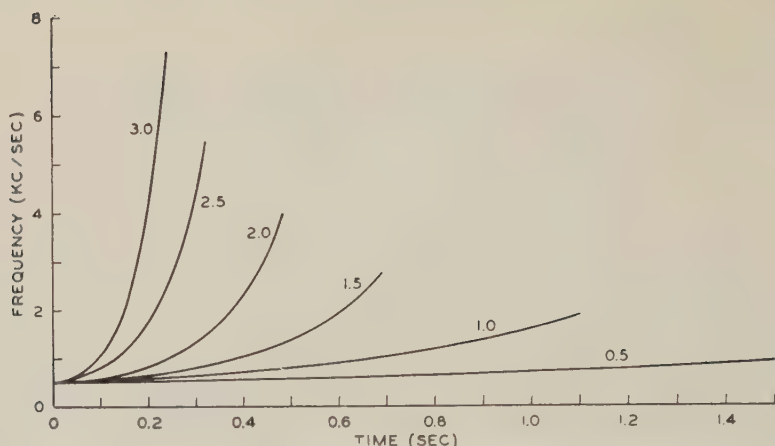


Fig. 1. Calculated dispersion curves for particles of various radial velocities (1000 km/sec).

overdense. The ionosphere also is overdense for transverse propagation of both electron and proton radiations, and for proton radiation in the ordinary mode.

Since the motion is a spiral with a large component along the magnetic field, the effective plane of rotation will be far from normal to the field. This means that there will be a large percentage of the total emission in the direction of the field [see Landau and Lifschitz, 1951]. This proton radiation must necessarily have the extraordinary polarization since the other index is imaginary for the proton-cyclotron frequency.

The Doppler Shift. The equation for the Doppler-shifted frequency emitted by a non-relativistic oscillator is

$$\nu = \frac{\nu_0}{1 \pm \frac{V}{c} n}$$

where

ν_0 is the oscillator frequency.

c is the velocity of light.

n is the phase index of refraction of the medium into which the radiation is emitted.

V is the radial component of velocity of the oscillator relative to the observer.

In this case, the proton is approaching along the magnetic field and the negative sign is used, V being the component of velocity along the field line.

The radiation in this case is into a dispersive medium, so that the use of the index for ν_0 is not appropriate, because the radiation travels

with the velocity of the Doppler-shifted frequency rather than with that of the original frequency. The index of refraction for propagation along the magnetic field in the extraordinary mode, for frequencies much less than the electron cyclotron frequency, is given by

$$n = \left(1 + \frac{80.5N \times 10^6}{f_h \nu}\right)^{\frac{1}{2}}$$

where N is the electron density in electrons cm^{-3} . We are interested only in large values of n , so that $n \simeq A\nu^{-\frac{1}{2}}$ where

$$A^2 = \frac{80.5N \times 10^6}{f_h}$$

The equation for the Doppler shift then becomes

$$\nu = \frac{\nu_0}{1 - \beta A \nu^{-1/2}}$$

where $\beta = v/c$. Solving for ν , one obtains the final equation

$$\nu = \nu_0 + \frac{A^2 \beta^2 \left(1 + \sqrt{1 + \frac{4\nu_0}{\beta^2 A^2}}\right)}{2} \quad (1)$$

for the Doppler-shifted frequency.

THE FREQUENCY VS TIME CURVE AND MODEL UPPER IONOSPHERE

The frequency emitted by the particle will vary as it approaches the earth's surface because the cyclotron frequency will change with the changing magnetic field. The Doppler shift for a particular frequency will also change because

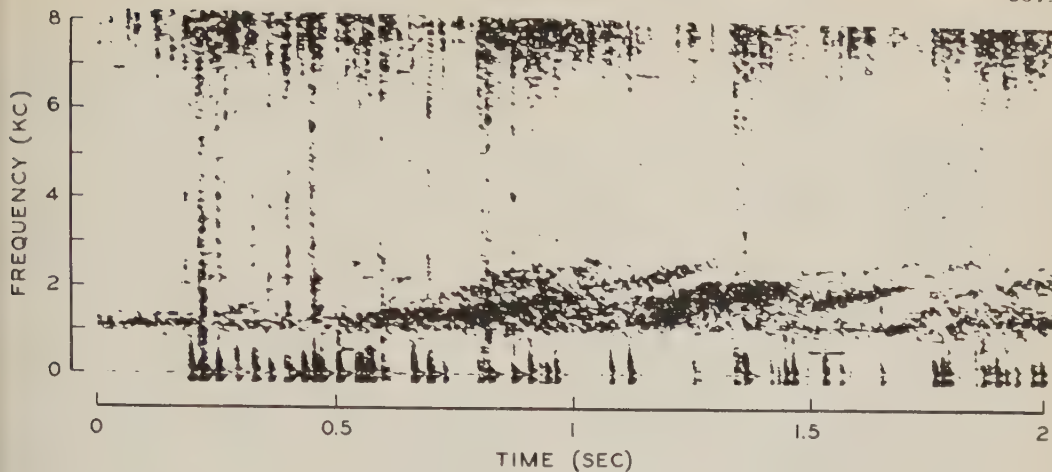


Fig. 2. Sound spectrograph of chorus.

of changes in the ratio N/f_h . There will be a change due to the change in the pitch of the spiral and other factors which tend to reduce V , but this will be ignored for the present and V assumed constant. Since we are concerned with altitudes above 300 km, this is probably not a bad assumption. At each point on the path the particle will produce the frequency given by equation 1 with ν_0 the proton-cyclotron frequency at that distance and the value of A^2 determined by the ratio N/f_h appropriate to the point. This, however, will not be the frequency-time curve observed on the ground because the velocity of the particle is comparable to the velocity of the radiation, and the times of arrival of the various frequency components will be considerably influenced by travel time. It is therefore necessary to correct for this. The travel time is proportional to $\int \mu ds$, where μ is the group index of refraction and for a simple model of electron distribution can be readily computed. The final frequency-time curve which should be received at the ground is computed as follows.

A simple model, believed to be reasonably close to actual conditions, is assumed for the electron-density distribution above the F' region maximum. The frequencies that would be produced along the path are computed as a function of time for a particular particle velocity. The difference in time between the arrival of each particular frequency and the first frequency to arrive is computed, and plotted as the frequency-time curve. Samples of such curves for

particle velocities in the range 500 to 3000 km sec^{-1} velocity passing through the upper ionosphere are shown in Figure 1. The resemblance between each of these curves and a type of signal found in natural chorus is obvious. It is also obvious that one can obtain nearly any type of frequency-time curve desired by the proper distribution of electron density. It seems, however, that most of the curves obtained in chorus observations can be produced by the model used to calculate Figure 1. The model assumed in this calculation is very simple. The maximum electron density is assumed to be 10^6 electron cm^{-3} at 300 km and above the maximum it is assumed to follow an exponential distribution: $N = N_0 e^{-0.002sh}$, where h is the distance above 300 km. It is very close to the model given by Johnson [1959] and is believed to be reasonable for the top of the ionosphere above College, Alaska. The cyclotron frequencies used are those appropriate to the geomagnetic latitude of College. (The electron distribution given applies to the top of the ionosphere and is not intended to be used far out from the earth.)

It should be remarked that the curves of Figure 1 are computed with no allowance for the changing pitch angle as the proton approaches the earth. The pitch angle θ , at a point where the magnetic field has the value B , for a proton of pitch angle θ_0 at the field value B_0 is given by

$$\sin^2 \theta = (B/B_0) \sin^2 \theta_0$$

since the radial component of velocity is propor-

tional to $\cos \theta$, the Doppler shift will be proportional to

$$1 - (B/B_0) \sin^2 \theta_0^{\frac{1}{2}}$$

As a result all the curves of Figure 1 would be flattened somewhat at the high end, the degree of flattening depending upon the value of θ_0 . The particles that seem most promising as sources of chorus are not those that actually mirror in the region, since the combination of flat pitch angle and low radial velocity would mean very little radiation in the direction of the field. Groups of particles coming in at moderate pitch angles would show curves like those of Figure 1 initially, flattening off somewhat in the later portions and fading out in intensity as the number of protons in the group is decreased by absorption. The result might look something like the natural chorus shown in Figure 2.

Chorus Observed at College. Chorus observed at College, Alaska, generally consists of a multitude of randomly occurring rising tones. The frequency range is 2 or 3 kc starting usually at 1 or 2 kc. The individual tones may last 0.2 to 0.5 sec. Other variations sometimes occur, such as descending tones preceding the usual rising component, or the tone may be essentially constant over periods up to possibly 2 seconds. There appears to be no significant difference between the chorus observed at this latitude and the chorus described by Gallet [1959] which is observed at Boulder, Colorado.

The occurrence of chorus correlates with magnetic activity as expressed by K -indices and with the occurrence of aurora. The coefficient of correlation between chorus and auroral indices at College, Alaska, was found to be higher than the coefficient between chorus and magnetic K -indices [Pope, 1959]. This would indicate a closer association between the causes of chorus and luminous aurora than between chorus and magnetic fluctuations. The significance of this in terms of the present hypothesis is not clear.

REGIONS MORE DISTANT FROM THE EARTH

The curves shown in Figure 1 refer to protons of quite low velocities in regions of relatively high electron density. It is evident that audio frequency electromagnetic radiation can also be produced by faster particles in regions

of lower electron densities. Accordingly, it is of some interest to consider what sort of frequency-time curve might come from such regions. Since the cyclotron frequency far from the earth is small, the Doppler shift must be very large if the emitted frequency is to be brought into the range ordinarily observed. At a distance of 1 earth radius from the surface, the cyclotron frequency is about 110 cycles, and if the electron density is still of the order of 10^8 [Johnson, 1959], a velocity of 10^4 km/sec will produce a Doppler-shifted frequency of about 630 cycles, whereas at 2 earth radii from the surface with an electron density of about 400 cm^{-3} a frequency of about 750 cycles is obtained. At this radial velocity, the particles would cover an earth radius in about 0.64 seconds, so that at first glance, it would appear that this might explain some of the events that show a slowly descending tone followed by a quick rise. This is a good example of the need to consider travel times and not only the time of generation, because when travel time is taken into account, the frequency generated at 2 earth radii from the surface will be only about 0.3 sec past the 1 earth-radius point when the frequency appropriate to this point is generated. Since the particles move at nearly the phase velocity in order to generate the frequencies observed, and since the travel times for the radiation are computed from the group velocity, the radiation travel time will be roughly half the particle travel time, the phase index being about twice the group index.

In general it seems that particles with velocities up to about 15,000 km/sec might produce frequency-time curves like those actually observed, the region of generation being fairly close to the earth. As we get farther out from the earth, the amount of confidence we have in the electron densities assumed becomes very small. If irregular distributions of electron density are assumed, it is possible to account for almost anything in the way of a frequency-time curve. It is quite probable that irregular electron distributions do exist, even well down in the ionosphere during magnetic storms, but it would seem more proper to investigate this from the other end; that is, if the present hypothesis should turn out to be correct, there would then be a tool for investigating such distributions.

THE INDEX OF REFRACTION

In the regions of space considered here, and for the frequencies of most interest, the phase index of refraction is given to a very good approximation by

$$n = \left(1 + \frac{80.5N \times 10^6}{f_h \nu} \right)^{\frac{1}{2}}$$

and since $n \gg 1$, this reduces to

$$\frac{9 \times 10^3}{\sqrt{\nu}} \left(\frac{N}{f_h} \right)^{\frac{1}{2}}$$

The group index is equal to nearly $\frac{1}{2}$ the phase index [Storey 1953]. The cyclotron frequency is proportional to the field strength and hence approximately to $(r/r_0)^{-3}$. It is interesting to note that if there is assumed an electron distribution which decreases as $(r/r_0)^{-3}$ [Gallet 1959], the result is a constant index of refraction for frequencies much less than the electron-cyclotron frequency, because the ratio N/f_h is constant leaving $n \propto 1/\nu^{1/2}$. The exponential distribution used in the calculations comes fairly close to this model at moderate distances from the earth, which is the reason for the emitted frequency sometimes increasing and sometimes decreasing as the protons approach the earth. The index of refraction increases or decreases in accordance with the ratio $(N/f)^{1/2}$.

There may be some question as to the propriety of using an index of refraction that takes into account only the influence of electrons, especially in calculations which relate to proton-cyclotron frequencies. It should be remembered, however, that the ions in the *F* region, and for some distance above, probably have a very small percentage of protons, being mainly heavier particles, whereas in the region where the ionized atoms may be largely protons, the frequencies of interest are well above the proton frequency. The contribution of protons to the index of refraction is very small except in the immediate neighborhood of their cyclotron frequency, and the heavier particles, of course, are important only at much lower frequencies, the cyclotron frequency being proportional to e/m .

CONCLUSIONS AND DISCUSSION

The results of the calculations indicate that, so far as the frequency-time curves are con-

cerned, the mechanism proposed by MacArthur is capable of explaining many, if not all, of the varied events classified under the heading 'chorus.' Whether or not the observed events are so produced is, of course, still doubtful. If the hypothesis should be substantiated, however, it promises to be a useful tool in the investigation of the outer ionosphere and exosphere. The study reported here indicates that the radiation may be produced over a wide range of distance from the earth, and, if it is so, produced the form of the frequency time-curve will reflect conditions in the region of origin. The hypothesis is also attractive because it explains the correlation with geomagnetic activity and that chorus is a high latitude phenomenon. It is not immediately obvious that this mechanism explains the diurnal variation [Pope, 1957; Allcock, 1957] but, since it would make the production of chorus dependent upon conditions in the outer ionosphere, there seems at least a possibility that the diurnal variation could be shown to be a consequence of the proton-gyration hypothesis.

The process envisioned by the writers is the approach of a neutral plasma more or less following the field lines. The individual protons and electrons, having components perpendicular to the magnetic field will gyrate at their respective cyclotron frequencies, but, as discussed above, only the protons will radiate. The continuous stream of plasma will produce the background 'hiss.' It is not to be expected that the plasma will be of uniform density, and the more dense regions will produce the stronger signals which are the individual 'chirps' of the chorus. This plasma is diamagnetic and consequently it may be stopped and its motion reversed at some distance from the earth. The stop may be quite abrupt because of the nature of the magnetic field, which would account for the limiting frequency in Figure 3. The outgoing particles would have their radiation Doppler shifted below the cyclotron frequency, so that it would not appear on the record.

It should be noted that the calculated curves shown are based on a model of a quiet ionosphere. During times of magnetic disturbance the character of the ionosphere above the *F* region maximum is drastically changed [Garriot, 1959]. The electron density of the maximum falls by very considerable amounts, though

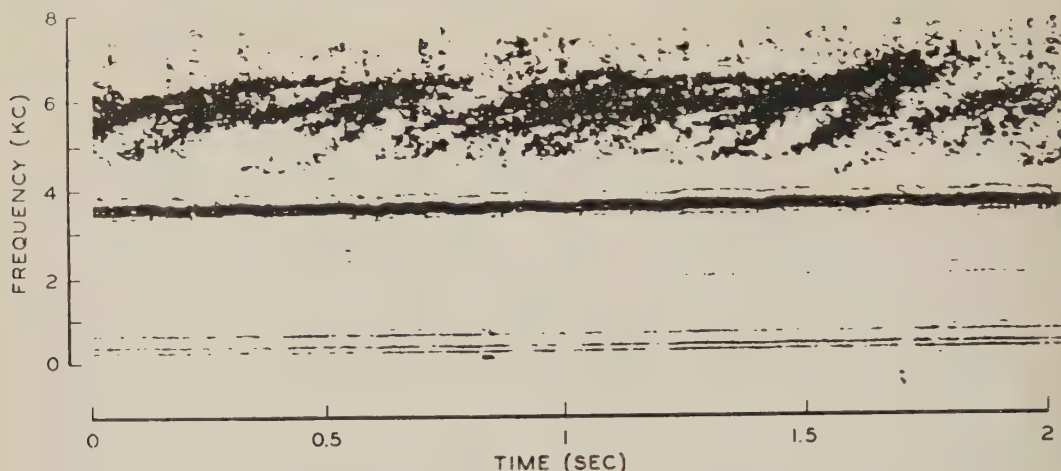


Fig. 3. Sound spectrograph of chorus showing decreasing rate of rise in frequency.

the total electron content changes little, indicating more electrons farther out (a less rapid decrease with height). The frequencies produced under such conditions would be considerably higher than those calculated. A large proportion of the chorus specimens available were observed under these conditions, but because of uncertainty as to the model electron distribution to adopt, calculations have not been attempted for the disturbed ionosphere.

It should be recognized that MacArthur's hypothesis is far from proved, but it is at least plausible, and the semiquantitative treatment above shows no deductions contrary to observation. It remains to devise other tests that may be more conclusive one way or the other, and perhaps to relate specific events to ionospheric conditions in more detail.

REFERENCES

- Allcock, G. McK., A study of the audio-frequency radio phenomenon known as 'Dawn Chorus,' *Australian J. Phys.*, **10**, 286-298, 1957.
- Gallet, R. M., The very low frequency emissions generated in the earth's exosphere, *Proc. IRE*, **47**, 211, 1959.
- Garriot, O. K., Determination of ionospheric electron content and distribution from satellite observations, *NSF Project 32:43, Tech. Rept. 1*, Radio Prop. Lab., Stanford Univ., 1959.
- Johnson, F. S., The structure of the outer atmosphere including the ion distribution above the F-2 maximum, *Lockheed Tech. Rept. LMSD-49719*, Lockheed Aircraft Corp., Sunnyvale, Calif., 1959.
- Landau, L., and E. Lifschitz, *Classical Theory of Fields*, Addison Wesley Press, Cambridge, Mass., p. 214, 1951.
- MacArthur, J. W., Theory of the origin of very low frequency radio emissions from the earth's exosphere, *Phys. Rev. Letters*, **2**, 491, 1959.
- Murcay, W. B., and J. H. Pope, Doppler shifted cyclotron frequency radiation from protons in the earth's exosphere, *Phys. Rev. Letters*, **4**, 5, 1960.
- Pope, J. H., Diurnal variation in the occurrence of 'dawn chorus,' *Nature*, **180**, 433, 1957.
- Pope, J. H., An investigation of whistlers and chorus at high latitudes, *Sci. Rept. 4*, AF 19 (604)-1859, University of Alaska 1959.
- Storey, L. R. O., An investigation of whistling atmospherics, *Phil. Trans. Roy. Soc. London, A*, **246**, 113-141, 1953.

(Manuscript received July 30, 1960.)

The Height of Maximum Luminosity in an Auroral Arc

F. E. ROACH

Boulder Laboratories, National Bureau of Standards
Boulder, Colorado

J. G. MOORE AND E. C. BRUNER, JR.

U. S. Naval Ordnance Test Station
China Lake, California

H. CRONIN

Northeastern University
Boston, Massachusetts

AND

S. M. SILVERMAN

Geophysics Research Directorate, Air Force Research Division
Bedford, Massachusetts

Abstract. The height of maximum luminosity of an auroral arc is estimated from simultaneous observations at three stations in western United States during a night of general auroral activity (November 27–28, 1959). Photometrically this arc is characterized by a selective enhancement of the [O I] 6300 Å line. From twenty-four individual measurements the height is found to be 412 km with a standard deviation of ± 23 km for one observation and ± 5 km for the mean. The geographical position of the arc, its orientation, and its movement during the night are discussed.

Introduction. Recent reports have indicated the frequent occurrence at low latitudes of persistent arcs on the equatorial side of general auroral activity [Barbier, 1958; Roach and Marovich, 1959; 1960]. These arcs are characterized by a considerable enhancement of the intensity of the [O I] 6300 Å line and by no measurable enhancement of the [O I] 5577 Å line. They are restricted to a few degrees of latitude but extend over a considerable longitude approximately along parallels of magnetic latitude.

Barbier [1958] has referred to arcs of the type discussed here as ‘monochromatic’ because the 6300 Å radiation is the only one measurably enhanced. In his eight-color photometry most of the spectral region from about 3300 Å to 7500 Å is covered. In their study of the similar arc of September 29–30, 1957, Roach and Marovich [1959] were observing along a vertical circle that cut sharply across the arc. The enhancement of 6300 Å was pronounced, about 50 times normal night airglow level, but no enhancement at all of the 5577 Å radiation could be detected.

TABLE 1. Coordinates of Observing Stations

Station	Geographic		Geomagnetic Latitude	Magnetic Isoclinic Latitude	Elevation above Sea-Level
	Latitude	Longitude			
Cactus Peak	36°05'N	117°49'W	43.1°	42°	1650 m
Sacramento Peak	32°43'N	105°45'N	41.6°	41°	2760 m
Fritz Peak	39°54'N	105°29'W	48.7°	51°	2749 m

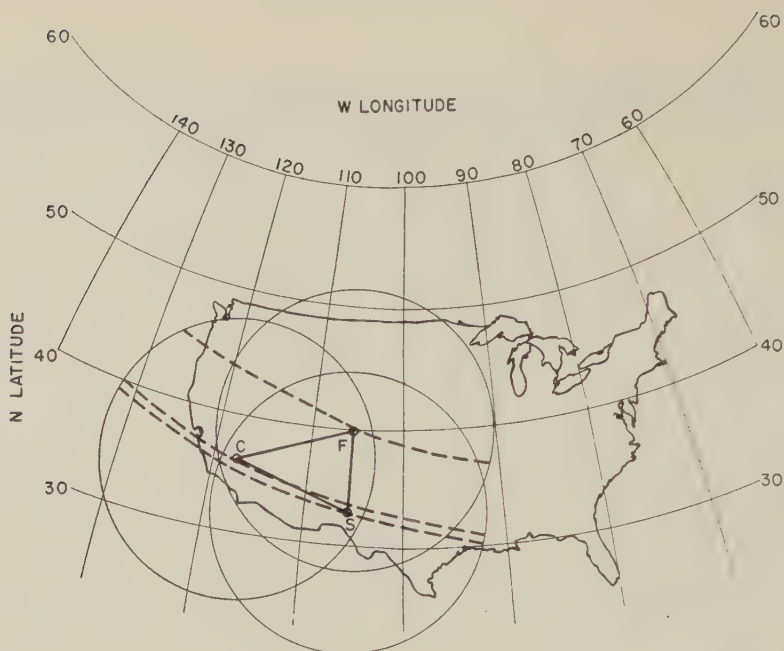


Fig. 1. Location of the stations: Cactus Peak, *C*; Fritz Peak, *F*; and Sacramento Peak, *S*. Circles correspond to region observable down to a zenith distance of 80° for an emission at a height of 410 km. Dashed lines are isoclines through the stations.

Because arcs of this family are usually subvisible, though intense on a physical scale, there is no generally accepted nomenclature to designate them. They should not be confused with auroral activity that includes an enhancement of the 5577 Å radiation such as that referred to in this paper as 'general auroral activity.'

At 23^h 50^m UT (4:50 PM., MST) on November 27, 1959, there was a sudden commencement of a geomagnetic storm followed by magnetic and auroral activity. Visual observers over North America reported auroras, often with definite red coloration during the first half of the night (November 27–28, 1959). Photometric

observations were made at three stations in western and southwestern United States: Cactus Peak (California), Sacramento Peak (New Mexico), and Fritz Peak (Colorado).

Throughout the evening, especially between 05^h and 07^h UT, there was considerable general auroral activity. During this period at the most northerly station (Fritz Peak) it was possible to distinguish an [O I] 6300 Å arc in spite of the competition from the general aurora. At the southerly stations (Cactus Peak and Sacramento Peak) the aurora (including the arc) was low on the northern horizon making it difficult to separate the two features.

Near 07^h UT (midnight MST) the general activity had diminished sufficiently that the photometric [O I] 6300 Å arc could be clearly distinguished at all three stations, making it possible to estimate the height by triangulation.

The method of triangulation. The locations of the three stations are shown on a map of the United States in Figure 1. Parallels of equal magnetic dip (isoclines) going through each station are indicated; also circles included by observations to a zenith distance of 80° by features at a height of 410 km which, as we shall show

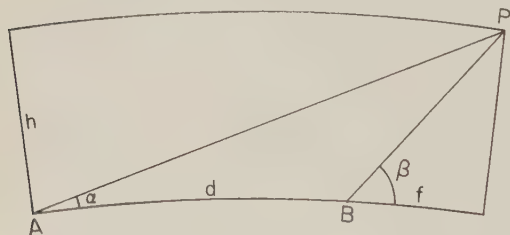
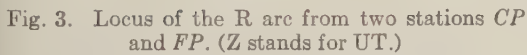


Fig. 2. Position, *P*, of arc with respect to two stations (schematic).



The arc remained to the north of all three stations during the entire night of November 27–28. Figure 2 shows the situation. Obviously a triangulation is possible for two stations, *A* and *B*, by the measurement of the angles α and β . The pair of stations, *FP* and *SP*, is almost exactly on a north-south line (geographic), whereas *CP* is to the west of each. Actually the orientation of the arc is along isoclines and its extent in longitude is such that a triangulation is possible for even the *CP-FP* combination as will now be shown.

Figure 3 is a polar-coordinate plot of the data for *CP* and *FP* from Table 2. The radius is made proportional to the distance from the observer to the arc measured along the earth's surface. (In this method of plotting the arc does not

Fig. 4. Examples of three triangulation attempts: one too high (600 km); one too low (300 km); and one according to the adopted height (430 km).



Fig. 5. Position of the 6300 A arc at 09^h 25^m UT, November 28, 1959, from observations at three stations for an assumed height of 410 km. Triangles, *CP*; open circles, *SP*, closed circles, *FP*.

separation of the two plotted arcs is $(d + f) - f = d$, the base line between the two stations which is 730 km (measured between isoclines).

In deducing the height from such plots it is convenient to scale the outer circle, corresponding to a zenith angle of 80°. In the present example the radius of the outer circle on the working plot was 2.15 inches and d was 1.10 inches. Thus the 80° circle corresponds to $2.15/1.10 \times$

730 = 1427 km, corresponding to a height of 436 km.

Figure 4 illustrates the case for 1045 UT in a somewhat different manner. The observations for the entries of Table 2 are plotted for three assumed heights: (1) one too high (600 km), (2) one too low (300 km), and (3) a height of 430 km corresponding approximately to the triangulation result of the preceding paragraphs.

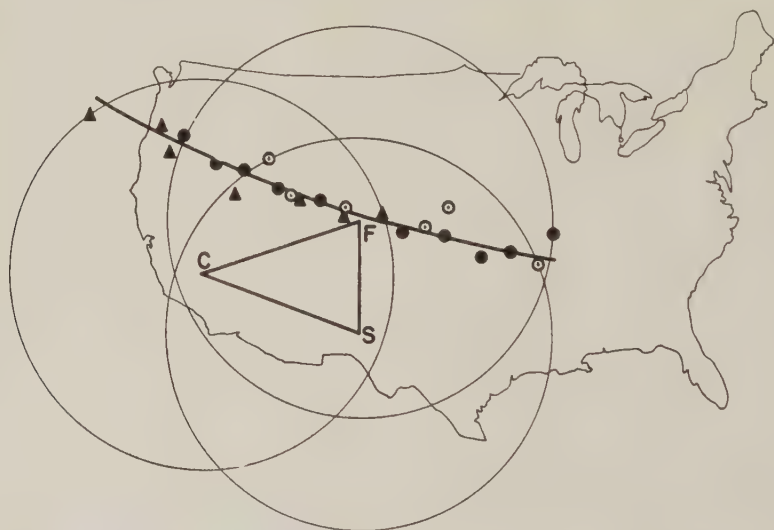


Fig. 6. Position of the 6300 A arc at 11^h 40^m UT, November 28, 1959, from observations at three stations for an assumed height of 400 km.

TABLE 2. Bearing of Arc Maxima in Degrees 1045 UT

Station	Z				
	40	60	70	75	80
FP	97 299	99 297	94 292	94 295	94 297
SP	0	40	68
CP	26	336	332
	..	22	45	61	63
	342	338	317

In Figures 5 and 6 are shown examples of combining the arc positions as observed at all three stations for two other times during the night. It is noted that the arc is followed from a point over the Pacific Ocean across two-thirds of the United States to the vicinity of the Mississippi River. Recalling in one case [Roach and Marovich, 1959] evidence that a similar arc extended from southern France to western United States, we suggest a general property of same may be that they form continuous arcs around the world.

The results. In Table 3 the deduced heights for 24 times during the night are listed. The mean is 412 km. If the scatter is assumed to be random the standard deviation of the mean is

± 5 km and of a single height estimate is ± 23 km.

In Figure 7 a plot of the deduced height versus time is shown. There seems to be a general increase from 375 km to 450 km over the interval 07^h to 10^h UT followed by a decrease to 400 km over the next 2 hours and a rise to 430 km for the last two observations.

The orientation of the arc. The orientation of the arc with respect to dip (isoclinic) latitudes on each of the plots has been estimated. The estimated dip latitudes at the eastern and western extremes are shown in Table 3 together with their differences (east minus west). There is a small tendency for the eastern part of the

TABLE 3

UT	Height, km	Dip Latitude		Difference, E-W	Position North of Fritz Peak, km
		East	West		
0410	(400)*				348
25	(400)	54.0	52.4	1.6	234
0510	(400)	53.1	53.2	-0.1	181
25	(400)	52.0	54.0	-2.0	154
40	(400)				181
55	(400)				194
0640	(400)				208
55	375	53.4	52.4	1.0	147
0710	390	53.9	51.6	2.3	208
25	390	54.1	53.0	1.1	214
40	375	54.0	52.6	1.4	255
55	420	54.0	52.8	1.2	275
0810	410	54.0	52.4	1.6	255
25	390	53.2	52.6	0.6	214
40	400	53.2	52.2	1.0	228
55	440	53.0	52.8	0.2	201
0910	410	53.2	52.6	0.6	221
25	410	54.0	53.1	0.9	255
40	450	54.0	53.0	1.0	281
55	450	53.8	52.9	0.9	208
1010	460	53.4	52.0	1.4	248
25	420	52.3	51.8	0.5	127
40	430	52.0	50.8	1.2	87
55	400	50.8	50.4	0.4	27
1110	400	50.7	50.4	0.3	34
25	400	50.6	50.6	0.0	7
40	400	50.8	50.4	0.4	40
55	400	50.5	51.0	-0.5	54
1210	400	50.9	51.0	-0.1	54
25	430	51.2	51.2	0.0	60
40	430	52.5	51.2	1.3	87
55	(410)	53.2	52.8	0.4	154
1310	(410)	52.0	52.0	0.0	100

* Parentheses indicate that the values of the height were assumed, not measured.

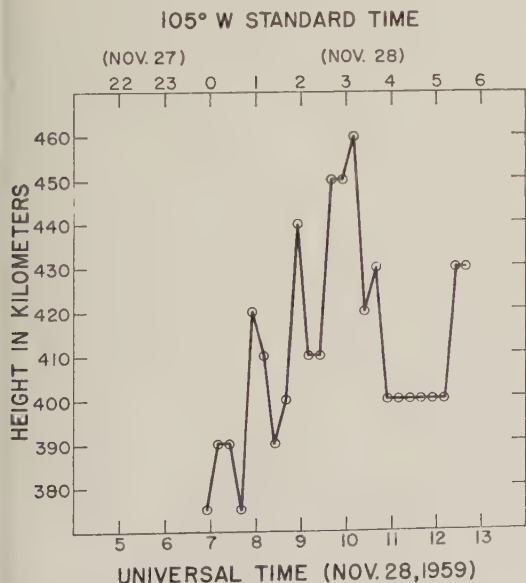


Fig. 7. Variation of the height of the 6300 Å arc with time.

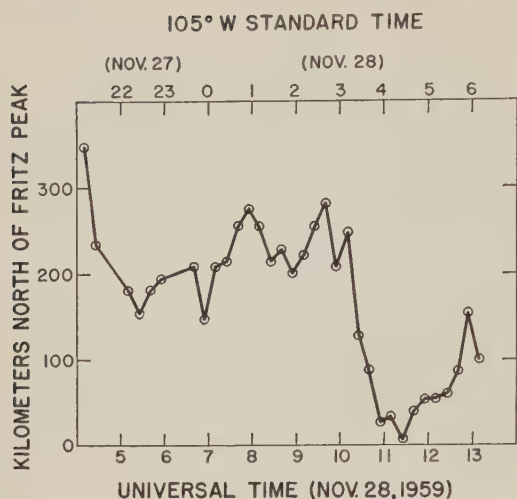


Fig. 8. Variation of the position of the 6300 Å arc with time.

arc to be north of the western part, the mean difference being $0^{\circ}.6$. Because of the difficulties inherent in interpreting our observations over such large distances, we do not consider this difference to be established.

The geographical position of the arc. The distance from Fritz Peak to the arc has been determined for each time and listed in Table 3. A plot of the results is shown in Figure 8. Initially the arc moved rapidly southward (between 0410 and 0525 UT). There then followed

a period during which a slight northerly movement occurred (0525 to 0940 UT). The arc moved rapidly south between 0940 and 1055 UT, remained close to the overhead position with respect to Fritz Peak from 1055 to 1140 UT, and moved slightly northward from 1140 to 1240 UT. The over-all movement for the entire period was southward.

Conclusions. From simultaneous observations at three stations in the United States the height of a monochromatic (6300 Å) arc has been estimated during the night of November 27-28, 1959. From a knowledge of the height it is possible to locate the arc geographically and to measure its movements during the night. Its orientation is approximately along parallels of equal magnetic dip. The variation of the absolute intensity of the arc and its relationship to the general auroral activity will be treated in subsequent communications.

REFERENCES

- Barbier, D., L'Activité aurorale aux basses latitudes, *Ann. géophys.*, **14**, 334-355, 1958.
- Roach, F. E., and E. Marovich, A monochromatic low-latitude aurora, *J. Research NBS*, **63D**, 297-301, 1959.
- Roach, F. E., and E. Marovich, Aurora of October 22/23, 1958, at Rapid City, South Dakota, *J. Research NBS*, **64D**, 205-209, 1960.

(Manuscript received August 10, 1960.)

Some Statistics of Solar Radio Bursts at Sunspot Maximum

A. MAXWELL, W. E. HOWARD, III,¹ AND G. GARMIRE²

*Radio Astronomy Station of Harvard College Observatory
Fort Davis, Texas*

Abstract. This paper discusses the occurrence and intensity of solar radio bursts at four frequencies in the band 100 to 600 Mc/s. The observations cover 4010 hours during a 12-month period at sunspot maximum; the results refer essentially to bursts of intensity great than 10^{-21} mks unit and duration greater than 0.3 second; and the statistical information has been interpreted in terms of the spectral characteristics of the bursts. The experimental data were taken at Fort Davis, Texas, and the analysis shows that at 125 Mc/s burst radiation was recorded for 560 hours, of which 380 hours were of low intensity. At 200 Mc/s the burst radiation covered 350 hours, of which 240 hours were of low intensity. For these two frequencies the bursts occurred mainly in the form of noise storms (spectral type I). At 425 and 550 Mc/s the total times of the solar bursts were much less, being respectively 21 and 23 hours; for the most part, however, this radiation was of high intensity and appeared in the form of continuum radiation (spectral type IV) over a wide frequency range.

INTRODUCTION

The radio emission from the sun is composed of a background thermal emission from the solar atmosphere, and bursts of radiation, sometimes very intense, that originate in localized active areas on the disk. These signals are observed over the complete radio spectrum but are more intense and more variable at the lower frequencies. For receiving equipment on the earth, the low-frequency limit of observation, approximately 10 Mc/s, is set by the critical frequency of the terrestrial ionosphere. the high-frequency limit, approximately 50,000 Mc/s, is set by the absorption of ultra-high-frequency radiation by oxygen and water vapor in the troposphere.

TABLE 1. Equipment Parameters

Frequency, Mc/s	Antenna Collecting Area, m ²	Receiver Noise Figure, db	I-F Bandwidth, Mc/s
125	40	6	0.3
200	38	7	0.5
425	43	8	1.0
550	40	8	1.0

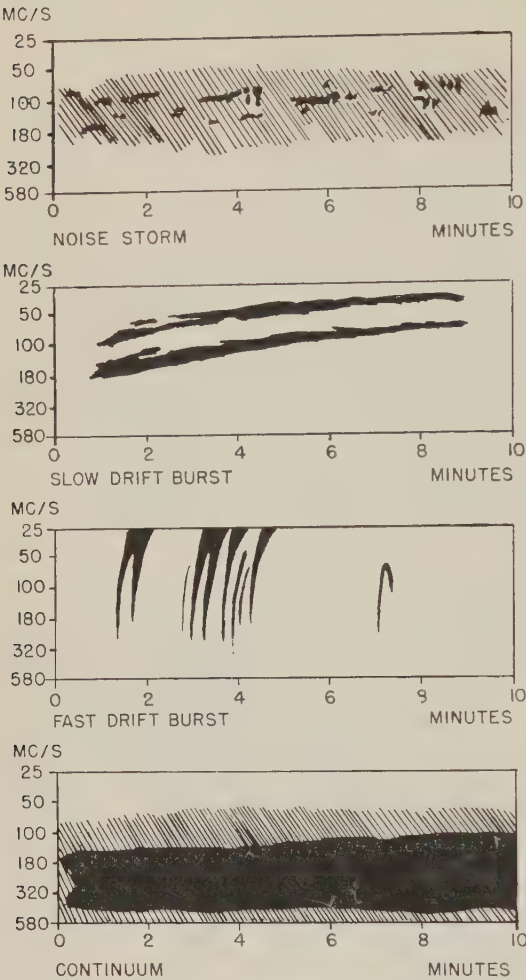
¹ Now at the Observatory, University of Michigan.

² Now at the Department of Physics, Massachusetts Institute of Technology.

TABLE 2. Intensity Levels of Incident Solar Radiation

Frequency, Mc/s	Approximate Intensity Ranges, watts m ⁻² (cps) ⁻¹ × 10 ⁻²²		
	Intensity 1 (faint)	Intensity 2 (moderate)	Intensity 3 (strong)
125	5-40	40-200	>200
200	10-60	60-250	>250
425	20-50	50-200	>200
550	20-50	50-200	>200

This paper describes a detailed investigation of the occurrence of bursts of radio emission from the sun at four frequencies: 125, 200, 425, and 550 Mc/s. The results are derived from data recorded during the period July 1, 1957, to June 30, 1958, which comprised the first 12 months of the International Geophysical Year, and the maximum of the present sunspot cycle. The data have been taken from records of solar bursts made with sweep-frequency equipment at Fort Davis, Texas, and the statistical information has been interpreted in terms of the spectral characteristics of the bursts. The Fort Davis equipment at present covers six octaves of the radio band, 25 to 580 Mc/s and 2.1 to 3.9 KMc/s, but for the period covered by this report the range was only 100 to 580 Mc/s. The station came into operation at the end of August



INTENSITY: STRONG [solid black] MODERATE [hatched]

Fig. 1. Idealized example of the four main spectral types of solar radio bursts. Photographic examples may be seen elsewhere [Swarup, Stone, and Maxwell, 1960].

1956, and had therefore been in operation 10 months before the observing period under discussion. The sweep-frequency equipment and antenna systems have been described in detail elsewhere [Maxwell, Swarup, and Thompson, 1958; Goodman and Lebenbaum, 1958; Jasik, 1958]. Essential parameters are listed in Table 1. Each receiver sweeps a frequency band of approximately one octave, and the sweep rate is 3 times per second. The outputs of the receivers are displayed on intensity-modulated cathode-ray tubes and are recorded photographically.

TABLE 3. Frequency Drift Rate of Slow-Drift and Fast-Drift Bursts

Frequency, Mc/s	Mean Drift Rate of Slow-Drift Bursts, Mc/s per second	Mean Drift Rate of Fast-Drift Bursts, Mc/s per second
125	-0.5	-75
200	-1.5	-150
425		-500
550		-700

The antenna used to detect the solar radio bursts at the four specific frequencies discussed in this paper was a 28-foot steerable paraboloid, which tracked the sun from sunrise to sunset.

For convenience, the solar bursts have been divided into three classes of intensity, and these were assessed visually by reference to the daily intensity calibrations on the receivers. The relation of this intensity scale to the levels of the incident solar radiation in mks units, that is in watts m⁻² (cps)⁻¹, is given in Table 2; minimum intensity values listed in the table indicate minimum detectable levels. For the period under consideration the equipment was in operation for more than 95 per cent of the possible observing time.

THE FOUR MAIN SPECTRAL TYPES OF SOLAR RADIO BURSTS

Noise storms. Noise storms (spectral type I) comprise a series of short-lived bursts more or less randomly distributed in time. They are diagrammatically illustrated in Figure 1. The bursts are generally superimposed on a background of slowly varying radiation, sometimes called a background 'continuum,' which is enhanced above the quiet-sun level. During periods of intense activity hundreds of these bursts occur every hour, and they may continue for a period of several days. Noise-storm activity is often concentrated in one particular band of the spectrum, for example 150 to 250 Mc/s, and may gradually drift into a slightly different band during the course of a day. The bursts are rarely seen at frequencies above 250 Mc/s, although isolated bursts occasionally occur at higher frequencies.

The flux densities of the radiation range from the barely perceptible up to values of the order

of 100 to 1000 times the background thermal radiation, which is of the order 5×10^{-22} watt m^{-2} (cps) $^{-1}$ at 100 Mc/s. The radiation is usually almost completely circularly polarized, the sense of rotation being determined essentially by the polarity of the largest emitting sunspot, right-hand circularly polarized waves being associated with a spot of negative polarity, and left-hand circularly polarized waves with a spot of positive polarity. This radiation corresponds to the ordinary component of magnetoionic theory [Payne-Scott and Little, 1951].

Slow-drift bursts. The regularly defining characteristic of a slow-drift burst (spectral type II) is a narrow band of intense radiation which drifts gradually, and often irregularly, toward lower frequencies. During the sunspot maximum these bursts occurred on the average about 30 times per year, and each lasted for approximately 5 minutes. About 65 per cent of the bursts were preceded by a group of fast-drift bursts, and about 10 per cent were succeeded by an intense, wide-band, continuum radiation. (These radio phenomena, in whole or in part, and in association with a solar flare, constitute the spectral characteristics of the 'outbursts' described in the early literature of solar radio astronomy.) The bursts are generally accompanied by a second harmonic, and the maximum frequency of the fundamental rarely exceeds 150 Mc/s. Observations of their polarization are meager, but existing evidence suggests that the bursts are randomly polarized to a high order, perhaps 95 per cent [Komesaroff, 1958]. The spectral characteristics of the slow-drift bursts suggest that they are caused by the movement of a major disturbance outward through the solar atmosphere. The velocity of this disturbance may be deduced by the application of an appropriate height transformation to the frequency of emissions; it is of the order of 10^8 km/sec.

Fast-drift bursts. Fast-drift solar radio bursts (spectral type III) are characterized by a very rapid drift in the radio emission toward lower frequencies. Their mean drift rate, as a function of frequency, is given in Table 3; it is approximately 100 times that of the slow-drift bursts. Diagrammatic examples of fast-drift bursts are shown in Figure 1, from which it will be seen that individual bursts last only a few seconds and that their duration increases with decreasing

frequency. The fast-drift bursts regularly occur in groups, and groups with more than 10 individual bursts tend to be more intense. Komesaroff [1958], from an analysis of 500 fast-drift bursts, suggests that about half of them have quasi-circular polarization. The origin of the fast-drift bursts is attributed to a disturbance moving outward through the solar atmosphere at a velocity of 10^8 km/sec [Wild, Sheridan, and Neylan, 1959].

Continuum radiation. Solar continuum bursts take the form of an enhancement of radio emission over a wide band of the spectrum. The bursts sometimes cover a band greater than eight octaves, and may drift systematically toward lower or higher frequencies. The radiation is often of high intensity, greater than 10^{-22} watt m^{-2} (cps) $^{-1}$ at 100 Mc/s, is essentially nonfluctuating (in contradistinction to noise storms, which show rapid fluctuations of intensity), and may last for several hours. It often occurs at frequencies higher than the spectral range of noise storms, the upper limit of which rarely exceeds 250 Mc/s. Such polarization measurements as are available (Wild, private communication, 1959) suggest that in the meter band it is wholly circularly polarized. Large-scale examples of continuum radiation are generally designated as spectral type IV and are a fairly common occurrence during the sunspot maximum. At times, the continuum radiation shows evidence of resolving into fast-drift bursts.

The enhanced background radiation that generally accompanies noise storm bursts is at present excluded from the type IV category; in the present analysis, it is considered under the heading of noise storms. Another form of continuum radiation, generally lasting only 1 or 2 minutes, occasionally accompanies fast-drift bursts; this is sometimes known as spectral type V and is probably a short-lived form of the large continuum bursts.

Unclassified bursts. The four main classifications, noise storms, slow-drift bursts, fast-drift bursts, and continuum, account for more than 95 per cent of the phenomena recorded on the films. The few remaining bursts have characteristics that preclude their definite classification in these four main categories; for the most part they are short-lived and isolated in time. It may also be noted that the spectral records preclude any possible confusion of solar

TABLE 4. Monthly Durations of Noise Storm Bursts

Month, and Total Observing Time for Month, hours	Total Times at				
	Intensity	125 Mc/s, hours	200 Mc/s, hours	425 Mc/s, minutes	550 Mc/s, minutes
1957					
July	1	19.3	3.6	1.2	4.2
365 hours	2	9.9	3.6	0	0
	3	1.0	0.2	0	0
August	1	43.8	12.4	1.6	2.0
384 hours	2	7.2	4.2	0.3	0.1
	3	3.5	3.0	6.0	7.0
September	1	76.3	41.2	40.3	44.5
334 hours	2	16.6	8.2	0.1	0.4
	3	14.8	14.6	11.0	5.0
October	1	55.6	38.1	2.6	6.4
305 hours	2	4.0	2.4	0	0
	3	1.6	2.3	0.5	0.4
November	1	20.3	13.0	2.8	0.5
274 hours	2	3.9	2.6	2.0	0.8
	3	13.9	12.4	0.3	0.2
December	1	47.7	31.5	2.8	1.4
283 hours	2	13.2	8.0	2.6	5.8
	3	10.6	4.9	10.0	4.0
1958					
January	1	20.4	19.5	75.6	32.4
289 hours	2	3.9	3.1	15.0	7.8
	3	1.4	0.4	1.2	1.0
February	1	14.3	18.2	0.9	0.1
319 hours	2	10.6	7.0	0.9	0
	3	26.7	6.4	0.1	0
March	1	30.8	20.2	4.0	1.0
336 hours	2	6.9	5.2	0.5	0
	3	8.7	4.8	2.4	0.2
April	1	13.3	8.8	4.9	0.4
342 hours	2	0.1	0.1	0.5	0
	3	0	0	0	0
May	1	12.8	9.7	0	0
383 hours	2	2.4	1.6	1.4	1.1
	3	1.0	0.6	0.2	0
June	1	15.9	8.4	0.2	0
394 hours	2	1.6	0.7	0	0.1
	3	0.1	0.1	0	0
Summary for	1	371 ± 23	224 ± 14	137	93
12 months	2	80 ± 5	47 ± 3	23	16
4010 hours	3	83 ± 2	50 ± 1	32	18
	Total	534 ± 24 hours	321 ± 14 hours	192 minutes	127 minutes

bursts with lightning or man-made interference. Association of the radio bursts with visual solar activity. Noise storms are nearly always associated with sunspot groups, but the fact that many large groups have no associated noise storm suggests that there is some sort of threshold effect. Payne-Scott and Little [1951] have shown that sunspot groups containing no spots of area greater than 400 millionths of the solar

disk are seldom accompanied by recognizable storms; when a group contains a larger spot, a noise storm is observed in two out of three cases. The noise storms show no statistical association with flares, although on rare occasions a significant increase, or decrease, in noise-storm intensity may occur at the time of a flare. Slow-drift bursts are generally associated with flares of large area and intensity, and these are approxi-

TABLE 5. Statistics of Fast-Drift Bursts

Frequency, Mc/s	Average Duration (τ_f), seconds	Proportion of Bursts at Given Frequency, α_f	Proportion of Bursts (β_{fi}) at		
			Intensity 1 (faint)	Intensity 2 (moderate)	Intensity 3 (strong)
125	4.0	0.78	0.46	0.24	0.30
200	3.2	0.56	0.51	0.29	0.20
425	1.6	0.18	0.40	0.30	0.30
550	1.4	0.15	0.44	0.26	0.30

mately uniformly distributed in heliographic longitude across the solar disk. Fast-drift bursts are about 25 per cent associated with flares; the probability of association is increased if the flare is of greater area or height, or is accompanied by a surge or spray. Large bursts of continuum radiation are generally associated with flares of large area and intensity; these flares show a westerly excess on the solar disk of approximately 2:1 [Swarup, Stone, and Maxwell, 1960].

THE OCCURRENCE OF SOLAR RADIO BURSTS

Period analyzed: July 1, 1957 to June 30, 1958. Total observing time: 4010 hours. Frequencies under consideration: 125, 200, 425, and 550 Mc/s. In this section we discuss the total time for which solar radio bursts, of the four spectral types, were observed at four frequencies. The data are subdivided according to the intensity of the bursts, on a scale of 3. The routine summaries of solar radio spectral data published by the Harvard Station in the *CRPL* (Boulder, Colorado) *Monthly Bulletin of Solar-Geophysical Data*, and in the *IAU* (Zurich) *Quarterly Bulletin on Solar Activity*, list solar activity according to spectral types, intensity, and commencing and finishing times. In these summaries certain conventions are used to avoid excessive entries: only the maximum intensity of a burst at any given time is recorded, even though the intensity is often different at different frequencies; noise storms, especially those of intensity 1—, are listed as being 'continuous' in time, provided that one or more bursts occur every 15 minutes. Because of these factors, the total times listed in the published tables represent maximum times for each particular frequency and intensity level. In this paper, however, we consider only the true duration of each spectral type of activity as a function of intensity at the four frequencies given above.

The duration of the bursts has been measured directly from the film records with the exception of the following, which have been calculated statistically: noise-storm bursts and background radiation of intensities 1 and 2 at 125 and 200 Mc/s; fast-drift bursts at all intensities and all four frequencies; unclassified bursts at all intensities at 125 and 200 Mc/s.

The total monthly durations of noise-storm bursts and background radiation are given in Table 4. In most cases, the estimated error for the total figures for each frequency, at each intensity, is less than 10 per cent. The duration of the noise-storm burst and background radiation at 125 and 200 Mc/s, and for intensities 1 and 2, was estimated statistically by the application of a calculated reduction factor to the data of the routine published summaries mentioned above. This factor was obtained by sampling noise-storm activity for approximately every fifth day (or adjacent days when necessary) throughout the 12-month period. The factor was then applied to the recorded monthly totals of the routine analysis to derive the true monthly totals given in the table.

It should be remarked that noise-storm activity of intensity 3 comprises a large number of bursts of intensity 3, but these are not necessarily contiguous. In fact, such noise storms generally contain a large number of sporadic bursts whose intensity varies rapidly between 1 and 3. An analysis, by microphotometer, of a section of a noise storm of high intensity showed that bursts of intensity 3 occupied approximately 10 per cent of time, whereas for approximately 40 per cent of the time the bursts were only of intensity 2, and for the remaining 50 per cent they were of intensity 1.

During the 12-month period under consideration, 32 slow-drift bursts were recorded over the range 100 to 580 Mc/s, of which 30 occurred

TABLE 6. Total Duration of All Types of Solar Bursts, July 1, 1957, to June 30, 1958

Type of Activity	Intensity	Total Times at			
		125 Mc/s, hours	200 Mc/s, hours	425 Mc/s, hours	550 Mc/s, hours
Noise storms (type I)	1	371	225	2.3	1.5
	2	80	47	0.4	0.3
	3	83	50	0.5	0.3
	Total	534	322	3.2	2.1
Slow-drift bursts (type II)	1	0	0	0	0
	2	0.1	0.1	0	0
	3	1.8	0.7	0.1	0.1
	Total	1.9	0.8	0.1	0.1
Fast-drift bursts (type III)	1	4.5	2.9	0.4	0.3
	2	2.4	1.7	0.3	0.2
	3	3.0	1.1	0.3	0.2
	Total	9.9	5.7	1.0	0.7
Continuum (type IV)	1	5.0	12.0	1.8	3.5
	2	3.5	5.3	3.2	5.7
	3	2.8	3.7	11.5	11.3
	Total	11.3	21.0	16.5	20.5
Unclassified	1	0.7	0.2	0	0
	2	0.2	0.1	0	0
	3	0.3	0.1	0	0
	Total	1.2	0.4	0	0
All activity	1	381	240	4.5	5.3
	2	86	54	3.9	6.2
	3	91	56	12.4	11.9
	Total	558	350	20.8	23.4

Total observing time: 4010 hours.

at 125 Mc/s, 23 at 200 Mc/s, 4 at 425 Mc/s, and 2 at 550 Mc/s. Nearly all these bursts were of intensity 3 or greater. The total duration of the slow-drift bursts for the year is given in Table 6. The durations measured from the films had an estimated error of ± 0.1 minute.

The total number of individual fast-drift bursts recorded over the 12-month period was 11,400. Most of these occurred in groups, and the total number of groups was 2828, of which 2450 occurred at one or more of the four frequencies under consideration in this paper. The number of individual bursts in each group ranged from 1 to more than 100. The mean number of bursts per group was 4, and the mode was 1.

The total duration of these bursts, at each of the four frequencies and three intensities, was calculated from the proportion (α_f) of the total number that occurred at frequency f , the duration (τ_f) of an individual burst as a function of frequency, and the proportion (β_{fi}) of bursts of intensity i at frequency f . The total duration

of the bursts, T_{fi} , at frequency f and intensity i , is then

$$T_{fi} = N\alpha_f\tau_f\beta_{fi} \tag{1}$$

The proportion, α_f , of the total number of bursts, N , observed at frequency f was obtained by sampling 1927 individual fast-drift bursts (17 per cent of the total number observed) and studying their distribution with respect to frequency. This sample population consisted of the first 40 groups of bursts in each of the 12 months. The factor α_f was obtained by dividing the number of bursts observed at frequency f by the total number of bursts recorded in the sample. Table 5 gives the value of α_f derived for each of the four frequencies, and the average duration, τ_f , of an individual burst at each of the four frequencies. (Examination of the films shows that the duration of an individual fast-drift burst does not vary significantly with the number of bursts occurring per group.) The proportion β_{fi} , of bursts of intensity i at frequency f was obtained by sampling 529 individ-

TABLE 7. Percentage of Observing Time Occupied by Each Type of Solar Burst, July 1, 1957, to June 30, 1958

Type of Activity	Percentage Time at			
	125 Mc/s	200 Mc/s	425 Mc/s	550 Mc/s
Noise storms (type I)	13.32	8.01	0.08	0.05
Slow-drift bursts (type II)	0.05	0.02	<0.01	<0.01
Fast-drift bursts (type III)	0.25	0.14	0.02	0.02
Continuum (type IV)	0.28	0.52	0.41	0.51
Unclassified	0.03	0.01	<0.01	<0.01
Total per cent	13.93	8.70	0.51	0.58

ual bursts at 125 Mc/s, 308 bursts at 200 Mc/s, 121 at 425 Mc/s, and 117 at 550 Mc/s. The samples were evenly distributed throughout the year, and the intensities were noted for each sample. The numbers of bursts of intensity 1, 2, and 3 were then divided by the total number in the sample, a procedure that gives the proportion of bursts of intensity 1, 2, and 3 at each frequency. These proportions are the factors β_{fi} , which are also listed in Table 5. With each of the factors in equation 1 available, it is thus possible to calculate the total duration of the bursts, T_{fi} , at each of the four frequencies and three intensities. The results are given in Table 6.

Continuum (type IV) activity was recorded on 23 days during the 12-month period. It occurred at least once each month, the maximum number of bursts observed in any one month being 4, during July 1957. The total duration of any occurrence of the continuum bursts, regardless of intensity, was considerably easier to measure than the durations at each intensity. As a consequence, the estimated error in the total times given in Table 6 is 10 per cent, whereas the times for the individual intensity levels are probably accurate only to about 15 per cent. It should be mentioned that, at 125 and 200 Mc/s, it is at times difficult to distinguish between continuum type IV radiation and intense background radiation accompanying noise-storm bursts.

There were 288 unclassified bursts recorded in the frequency range 100 to 580 Mc/s over the 12-month period. Of this number, 150 occurred at 125 Mc/s, 70 at 200 Mc/s, 19 at 425 Mc/s, and 8 at 550 Mc/s. The durations of the unclassified bursts at 125 and 200 Mc/s were calculated by a sampling method. Table 7 shows that

the total time of unclassified activity over the 12-month period was an insignificant fraction of the durations of the four main types of spectral bursts.

DISCUSSION

The set of observations in this paper concerns the maximum of the present solar cycle, which is the greatest in recorded history, the monthly sunspot number for October 1957 reaching the unprecedented value of 254. The data essentially concern solar radio bursts of intensity greater than 10^{-21} watt m^{-2} (cps) $^{-1}$ and duration greater than 0.3 second. From Tables 6 and 7 we note the following main points: (1) Out of a total observing period of 4010 hours, solar radio bursts at 125, 200, 425, and 550 Mc/s covered 558, 350, 21, and 23 hours, respectively. (2) The durations of the noise storms, slow-drift bursts, and fast-drift bursts were drastically diminished at the two higher frequencies. (3) The predominating type of activity at 125 and 200 Mc/s was noise-storm bursts, and about 70 per cent of them were of weak intensity. (4) The predominating type of activity at 425 and 550 Mc/s was continuum bursts, and these were mainly of strong intensity.

The most intense solar radio bursts occur at sunspot maximum, and only when there are large active areas on the disk, but the exact time at which such bursts will occur is at present unpredictable. They have a tremendous intensity range at meter wavelengths, increases up to 1000 times the background thermal level being common. Exceptionally intense bursts can exceed that amount by a further factor of 1000 [cf. *Payne-Scott, Yabsley, and Bolton, 1947*], that is, up to 10^{-16} mks unit at 100 Mc/s. The largest bursts often saturate receiving equipments, and

hence it is generally difficult to obtain an accurate assessment of their maximum intensity. The Fort Davis equipment uses I-F amplifiers with compressed response; the over-all intensity range is of the order of $10^{-6}:1$; and the maximum intensity of the bursts is estimated as approximately 10^{-37} mks unit at 100 Mc/s. Bursts of such intensity generally do not last more than 5 to 10 minutes.

Regarding solar bursts as a form of radio interference, we conclude that the frequencies 125 and 200 Mc/s are more heavily affected than 425 and 550 Mc/s. The data for 125 and 200 Mc/s are generally representative of conditions over the band 50 to 250 Mc/s, and show that noise storms and, to a limited extent, continuum bursts are likely to cause the most trouble. Similarly the data for 425 and 550 Mc/s give an indication of conditions in the band 250 to 1000 Mc/s. At these higher frequencies, the total duration of solar radio activity is reduced by a factor of approximately 20 over that in the lower band, but most of the solar bursts come in the form of continuum radiation of strong intensity, covering a very wide frequency range

and often lasting solidly for periods of several hours.

Acknowledgments. The work described in this paper was supported by financial assistance from the Rome Air Development Center and the Geophysics Research Directorate of the United States Air Force. We wish to thank Dr. A. R. Thompson and Mr. G. Swarup for a number of helpful comments.

REFERENCES

- Goodman, J., and M. Lebenbaum, *Proc. IRE*, **46**, 132, 1958.
 Jasik, H., *Proc. IRE*, **46**, 135, 1958.
 Komesaroff, M., *Australian J. Phys.*, **11**, 201, 1958.
 Maxwell, A., G. Swarup, and A. R. Thompson, *Proc. IRE*, **46**, 142, 1958.
 Payne-Scott, R., and A. G. Little, *Australian J. Sci. Research*, **A4**, 508, 1951.
 Payne-Scott, R., D. E. Yabsley, and J. G. Bolton, *Nature*, **160**, 256, 1947.
 Swarup, G., P. H. Stone, and A. Maxwell, *Astrophys. J.*, **131**, 725, 1960.
 Wild, J. P., K. V. Sheridan, and A. A. Neylan, *Australian J. Phys.*, **12**, 369, 1959.

(Manuscript received June 29, 1960; revised August 24, 1960.)

The Cause of Magnetic Storms and Bays

R. A. DUNCAN

*Upper Atmosphere Section
Commonwealth Scientific and Industrial Research Organization
Camden, N.S.W., Australia*

Abstract. Because of the Hall effect, electric current will circulate anticlockwise around an area of proton precipitation and clockwise around an area of electron precipitation (in the northern hemisphere). This is suggested as the cause of the current systems of magnetic bays and storms. The observed geographical distribution of auroral hydrogen emission, polar black-out, and auroral E ionization is used to suggest that the required pattern of protons and electron precipitation occurs.

From a study of 40 magnetic storms Chapman [1935] derived the mean pattern of magnetic disturbance over the earth and from it a corresponding mean ionospheric current system which could cause it. It has always been difficult to find a possible cause for this somewhat strange current system. Birkeland [1908] noted early that individual magnetic disturbances usually have a simpler form, and recently Nagata and Fukushima [1952; Fukushima, 1953] have emphasized this point. They have derived current systems for individual magnetic bays and for particular moments of storms and shown

that these are simple dipoles, though when averaged the classical maps of Chapman and Vestine are produced.

Ninety per cent of bays correspond to a simple dipole current system with a westward auroral electrojet near the midnight meridian (Fig. 1). In 10 per cent of cases this is accompanied by a similar but weaker eastward auroral zone electrojet on the midday meridian [Fukushima, 1959]. Storms are a series of sometimes overlapping bays plus a general lowering of the geomagnetic field probably due to a ring current outside the ionosphere.

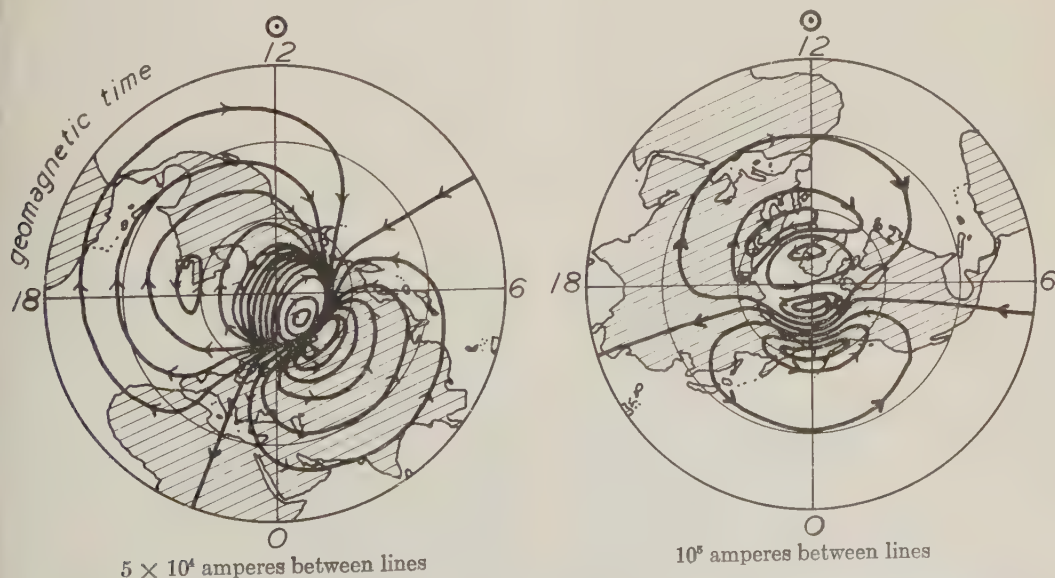


Fig. 1. Left, current system at an instant of a geomagnetic storm [after Nagata and Fukushima, 1952]. Right, current system at an instant during an isolated bay [after Fukushima, 1953].

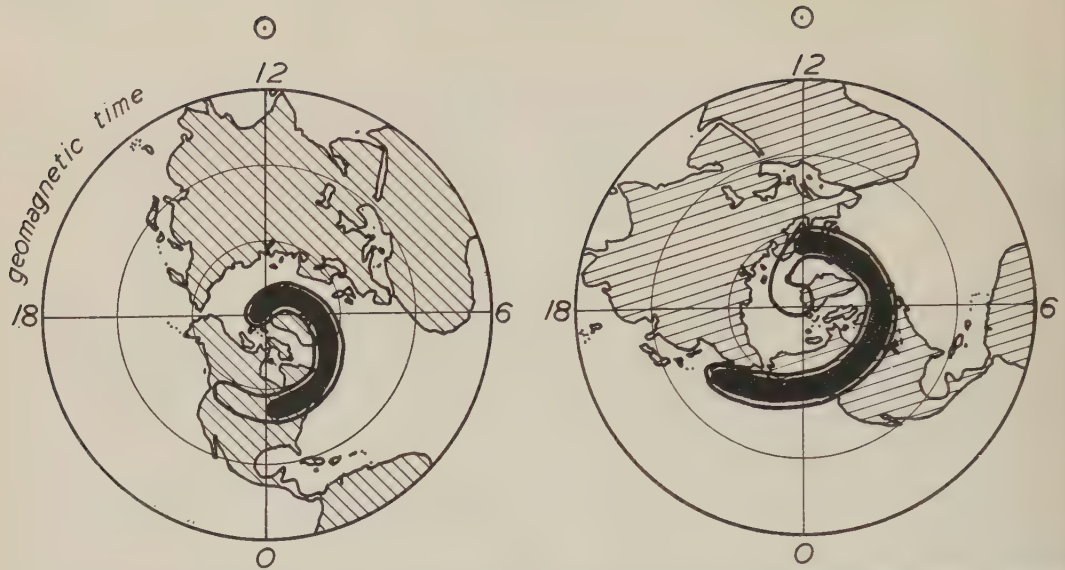


Fig. 2. *Left*, total (black) and partial (outer envelope) blackout pattern 6 hours after storm sudden commencement, September 13, 1957 [Hakura, Takenoshita, and Otsuki, 1958]. *Right*, blackout pattern 10 hours after the storm sudden commencement of February 11, 1958 [Obayashi and Hakura, 1960].

Nagata and Abe [1955] and Obayashi [1959] have shown that the current system of sudden commencements also has the dipole form but in this case centered over the magnetic poles.

In the *E* region, the most highly conducting region of the ionosphere and the probable seat of the currents, Hall conductivity is ten times as great as direct conductivity so that the current flows almost at right angles to the electric field, that is, almost along the equipotentials [Baker and Martyn, 1953]. The current patterns of Figure 1 then would be caused by a positive potential in the center of each anti-clockwise current vortex and a negative in the center of each clockwise current vortex.

It is suggested here that the potentials arise from incoming protons and electrons, the anti-clockwise and clockwise current loops being the impact areas of protons and electrons, respectively.

Independent evidence supports this view. Consider first the strong westward auroral electrojet which flows on the night side of the earth and so can be compared with auroral observations. Our explanation of this requires protons to impact at lower latitudes than electrons. All observers have found this to be true. Vegard and Kvifte [1954] found the average intensity of the hydrogen line $H\alpha$ to be six times greater

at Oslo than at Tromsø. Montalbetti and Jones [1957] from a comparison of auroral spectra at Saskatoon and Churchill concluded that strong $H\alpha$ emission occurs only at the low latitude fringe of the aurora. Gartlein and Sprague [1957] extended observations farther south to Ithaca and showed that the $H\alpha$ is strongest well south of the latitude of active auroral activity. Many workers [e.g., Bless, Gartlein, Kimball, and Sprague, 1959] have shown that magnetic bays occur in the same position and at the same time as auroras.

There is another line of evidence. Hakura, Takenoshita, and Otsuki [1958] plotted maps of ionospheric blackout for instants during the storm of September 13, 1957, and found that the areas of blackout lay on a westward running spiral (Fig. 2). Obayashi and Hakura [1960] gave further examples. Hope [1956] and Nikolski [1957] had earlier noted that a statistical study by Agy [1954] suggested this pattern and that it corresponded to the locus of precipitation of protons calculated by Störmer [1955] and verified by model experiments by Birke-land.

Hagg, Muldrew, and Warren [1959] found the locus of maximum occurrence of auroral *E*-layer ionization to be a spiral emanating from the magnetic pole and running south eastward

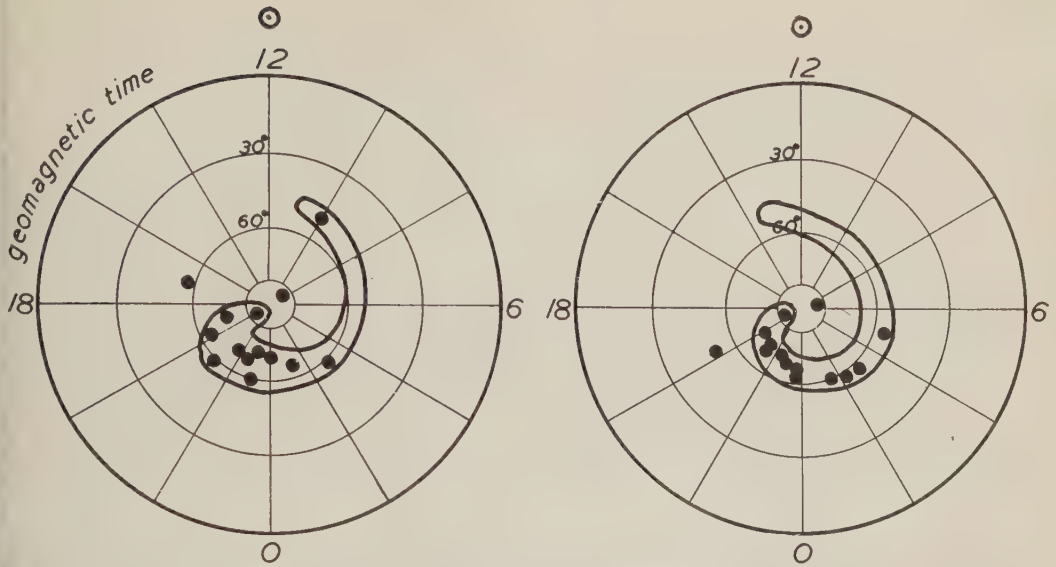


Fig. 3. Geomagnetic times of peak auroral sporadic *E* ionization for various stations [Hagg, Muldrew, and Warren, 1959].

(Fig. 3). This corresponds to Störmer's locus of precipitation of negative particles.

Although these phenomena need further study we shall tentatively accept the interpretation suggested by Störmer's theory. It seems plausible that bombarding protons with their great penetration should augment *D*-layer ionization and thus cause blackouts, while electrons with their lesser penetration should augment the ionization in the *E* layer of the ionosphere.

If, then, we superpose the pattern of proton precipitation (Fig. 2) on the pattern of electron precipitation (Fig. 3) we find that on the midnight meridian we have protons at a lower latitude than electrons, whereas on the midday meridian we have protons at a higher latitude than electrons. This is the pattern needed to explain the observed current system. Daytime electron precipitation seems to be weak, but so is the daytime electrojet.

It remains to be shown that the proton and electron flux is of a magnitude which could explain the observed electric currents. From observations of the auroral Balmer lines Gartlein and Sprague [1957] estimated the incoming proton flux during moderate disturbance ($K = 5$) to be about 10^8 amperes. This estimate involved the doubtful assumption that the aurora was restricted to a point in the sky. Proton precipitation certainly occurs over an appreciable

area and Gartlein later increased his estimate [Bless, Gartlein, Kimball, and Sprague, 1959] to 10^4 amperes. The direct current between the areas of proton and electron precipitation will therefore be 10^4 amperes, but the Hall current—that is the circulating current—will be ten times as great, or 10^5 amperes. This is roughly the magnitude of the current deduced from magnetic disturbance (Fig. 1).

REFERENCES

- Agy, V., Geographical and temporal distribution of polar blackouts, *J. Geophys. Research*, **59**, 499–512, 1954.
- Baker, W. G., and D. F. Martyn, Electric currents in the ionosphere, *Phil. Trans. Roy. Soc. London, A*, **246**, 281–320, 1953.
- Birkeland, K., *Norwegian Aurora Polaris Expedition, 1902–1903*, Oslo, 1908.
- Bless, R. C., C. W. Gartlein, D. S. Kimball, and G. Sprague, Auroras, magnetic bays and protons, *J. Geophys. Research*, **64**, 949–953, 1959.
- Chapman, S., The electric current systems of magnetic storms, *Terrest. Magnetism and Atmospheric Elec.*, **40**, 349–370, 1935.
- Fukushima, N., Polar magnetic storms and geomagnetic bays, *J. Fac. Sci. Univ. Tokyo*, **8**, 294–412, 1953.
- Fukushima, N., Some remarks on the morphology of geomagnetic bays, *J. Geomag. Geoelect.*, **10**, 164–171, 1959.
- Gartlein, C. W., *Proc. Conf. Ionosph. Phys.*, State College, Pennsylvania, July 1950.

- Gartlein, C. W., and G. Sprague, Hydrogen in auroras, *J. Geophys. Research*, **62**, 521-526, 1957.
- Hagg, E. L., D. Muldrew, and E. Warren, Spiral occurrence of sporadic-E, *J. Atmospheric and Terrest. Phys.*, **14**, 345-347, 1959.
- Hakura, Y., Y. Takenoshita, and T. Otsuki, Polar blackouts associated with severe geomagnetic storms on September 13th, 1957 and February 11th, 1958, *Rept. Ionosphere Research Japan*, **12**, 459-468, 1958.
- Hope, E. R., Spiral patterning of solar corpuscular precipitation, *Nature*, **177**, 571-572, 1956.
- Montalbetti, R., and A. V. Jones, H α emissions during aurorae over west-central Canada, *J. Atmospheric and Terrest. Phys.*, **11**, 43-50, 1957.
- Nagata, T., and N. Fukushima, Constitution of polar magnetic storms, *Rept. Ionosphere Research Japan*, **6**, 85-97, 1952.
- Nagata, T., and S. Abe, Notes on the distribution of S.C.* in high latitudes, *Rept. Ionosphere Research Japan*, **9**, 39-44, 1955.
- Nikol'ski, A. P., *Doklady Akad. Nauk SSSR*, **112**, 628, 1957. English translation E. R. Hope. *Canad. Defence Res. Board*, T244R.
- Obayashi, T., Geomagnetic storms and ionospheric disturbances, *J. Rad. Res. Lab. Japan*, **6**, 375-514, 1959.
- Obayashi, T., and Y. Hakura, Enhanced ionization in the polar ionosphere caused by solar corpuscular emissions. *J. Rad. Res. Japan*, **7**, 27-66, 1960.
- Störmer, C., *The Polar Aurorae*, Clarendon Press, Oxford, 403 pp., 1955.
- Vegard, L., and G. Kvifte, Theory and observation of the enhancement of auroral hydrogen lines with increasing distance from the magnetic axis point, *Geofys. Publ.*, **19**, 1-10, 1954.

(Manuscript received August 15, 1960.)

Hydromagnetic Waves in the Ionosphere

W. E. FRANCIS AND ROBERT KARPLUS¹

*Missiles and Space Division, Lockheed Aircraft Corporation
Palo Alto, California*

Abstract. A numerical integration of the hydromagnetic wave equations in the ionosphere has been carried out. Tables and graphs are given for the relations between the field amplitudes above and below the ionosphere and for the power dissipated as a function of altitude. The case of a vertically incident plane monochromatic wave near 45° geomagnetic latitude is treated. The results are used to confirm earlier estimates of ionospheric heating by hydromagnetic waves and to estimate the transit time of extremely low-frequency signals.

1. Introduction. Electromagnetic wave propagation in the ionosphere has been under study for a long time. More recently, attention has been focused on the behavior of very-low-frequency waves (approximately 1 cps) that are associated with many geomagnetic phenomena [Dessler, 1959a; Francis, Dessler, and Karplus, 1960; Fejer, 1960; Kahalas, 1960; and Akasofu, 1960]. These waves are often called magneto-hydrodynamic (MHD) or hydromagnetic waves, because they are accompanied by flow of the conducting medium. Since they are strongly absorbed, they appear to be an important energy source that may affect the ionospheric temperature and density distributions during magnetic storms. Another problem of interest is the propagation through the ionosphere of magnetic-storm effects and of hydromagnetic pulses that have been generated by nuclear explosions at high altitude.

Many authors have considered the propagation of small-amplitude electromagnetic waves in conducting media of various kinds and in the presence of a large static magnetic field. For the problem to be discussed in this paper, the propagation of low-frequency waves in the ionosphere, complications of two sorts have to be considered at the same time [Fejer, 1960]: first, the medium has three components (electrons, ions, and neutral atoms or molecules) that exchange momentum; second, the medium is non-uniform, with density variations occurring over

distances comparable to a wavelength. There are also some simplifying aspects of which we shall take advantage: (1) the static magnetic field is uniform; (2) the pressure is so low that hydrostatic restoring forces and gravitational forces are small compared with electromagnetic restoring forces; (3) the fractional ionization is so small that collisions between electrons and ions can be neglected. We shall further assume that the ionosphere is still and flat and that the wave normal is vertical (i.e., along the ionospheric density gradient). This last restriction makes the integration problem manageable for a high-speed computer.

In section 2 we briefly sketch the derivation of the field equations; in section 3 we describe the methods used for integrating the equations; and in section 4 we present the results, which are applied to two problems in section 5. The Appendix contains a summary of the ionospheric properties we have used. Here we only add that the wave attenuation and the wave absorption are different because the inhomogeneities and electrical properties of the medium give rise to reflection. It will therefore be necessary to calculate the local joule heating to obtain the energy deposition while the ratio of field strengths above and below the ionosphere gives the 'attenuation.' We further observe that the earth is essentially a perfectly reflecting conductor at low frequencies. The energy that is not absorbed, therefore, is reflected. In this paper we calculate only the steady-state field strengths, which exhibit a slight standing wave pattern and may differ considerably from the

¹ Permanent address: University of California, Berkeley.

transient fields associated with sudden field disturbances. Another restriction is related to our choice of ionospheric properties, which correspond to the daytime at sunspot maximum. Finally, we have chosen a magnetic dip angle of 60° which corresponds to a magnetic latitude of about 45° .

2. *Field equations in the ionosphere.* In this section we shall establish the notation and the equations that we shall find convenient. Since Fejer [1960] has discussed the problem and the nature of the approximations in detail we need not do so. We consider simple harmonic time dependence at the angular frequency ω . The medium is then characterized by the three principal values σ_0 , σ_1 , and σ_2 of the conductivity tensor in the presence of the static magnetic field $\mathbf{B}_0 = B_0 \mathbf{e}_0$. The amplitudes of the electromagnetic disturbance are \mathbf{E} and \mathbf{B} , and the current is \mathbf{j} . We neglect the displacement current. Maxwell's equations therefore become (rationalized mks units)

$$\nabla \times \mathbf{E} = i\omega \mathbf{B} \quad (1)$$

$$\nabla \times \mathbf{B} = \mu_0 \mathbf{j} \quad (2)$$

$$\mathbf{j} = \sigma_0 \mathbf{e}_0 (\mathbf{E} \cdot \mathbf{e}_0) + \sigma_1 [\mathbf{E} - \mathbf{e}_0 (\mathbf{E} \cdot \mathbf{e}_0)] + \sigma_2 (\mathbf{E} \times \mathbf{e}_0) \quad (3)$$

We now introduce our model and a coordinate system in which the field quantities and the conductivities depend on x only; the field \mathbf{B}_0 lies in the $x-z$ plane, $(\mathbf{e}_0)_x = \cos \psi$, $(\mathbf{e}_0)_z = \sin \psi$. If we define the auxiliary quantities

$$\sigma_3 = \sigma_1 + \sigma_2^2 / \sigma_1 \quad (4)$$

$$\sigma_1' = \cos^2 \psi + (\sigma_1 / \sigma_0) \sin^2 \psi \quad (5)$$

and

$$\sigma_3' = \cos^2 \psi + (\sigma_3 / \sigma_0) \sin^2 \psi \quad (6)$$

we may express the magnetic field, the current, and the longitudinal electric field quite simply as follows:

$$B_y = \frac{i}{\omega} \frac{dE_z}{dx} \quad B_z = -\frac{i}{\omega} \frac{dE_y}{dx} \quad (7)$$

$$j_y = \frac{\sigma_2}{\sigma_1} E_z \cos \psi + \frac{\sigma_3'}{\sigma_1} \sigma_1 E_y \quad (8a)$$

$$j_z = \frac{\sigma_1}{\sigma_1} E_z - \frac{\sigma_2}{\sigma_1} E_y \cos \psi \quad (8b)$$

and

$$E_z = -\frac{\sin \psi}{\sigma_1'} \left\{ \left(1 - \frac{\sigma_1}{\sigma_0} \right) E_z \cos \psi + \frac{\sigma_2}{\sigma_0} E_y \right\} \quad (9)$$

The longitudinal field $E_z(x)$ is not a dynamical variable and will not be discussed further. The field equation for the transverse components E_y and E_z of the electric field are coupled,

$$\left\{ \frac{1}{\mu_0} \frac{d^2}{dx^2} + i\omega \sigma_1 \frac{\sigma_3'}{\sigma_1'} \right\} E_y(x) + i\omega \sigma_2 \frac{\cos \psi}{\sigma_1'} E_z(x) = 0 \quad (10a)$$

$$\left\{ \frac{1}{\mu_0} \frac{d^2}{dx^2} + i\omega \sigma_1 \frac{1}{\sigma_1'} \right\} E_z(x) - i\omega \sigma_2 \frac{\cos \psi}{\sigma_1'} E_y(x) = 0 \quad (10b)$$

At very high altitude, where the Hall conductivity σ_2 is negligible and the longitudinal conductivity is very large, the equations become uncoupled. The wave that is polarized in the y direction ($E_z = 0$) we shall call the ordinary wave, because its properties are independent of the magnetic field direction; the other wave ($E_y = 0$) we shall call the extraordinary wave. These two modes are coupled by the Hall effect, which is most important near an altitude of 120 km; there the two *circularly* polarized states are almost uncoupled from each other.

3. *Integration of the Equations.* The propagation problem actually extends down to the surface of the earth, which we treat as a perfect conductor at the low frequencies of interest to us. With our choice of coordinate axes, we therefore divide the atmosphere into two regions in this way:

$$x = 0; \text{ surface of the earth} \quad (11a)$$

$$0 < x < d = 80 \text{ km: neutral atmosphere} \quad (11b)$$

$$x = d = 80 \text{ km: discontinuous transition to ionosphere} \quad (11c)$$

$$d < x < D = 550 \text{ km: ionosphere} \quad (11d)$$

$$x = D = 550 \text{ km: upper limit of integration} \quad (11e)$$

The actual variation of composition which has been replaced by a discontinuity at $x = d$ is very rapid compared with the wavelength in

TABLE 1. Real (\mathcal{R}) and Imaginary (\mathcal{I}) Components of the Elements of the Transmission and Reflection matrices T and R vs. incident angular frequency

ω	Ordinary				Extraordinary			
	T_{zz}		T_{yz}		T_{zy}		T_{yy}	
	\mathcal{R}	\mathcal{I}	\mathcal{R}	\mathcal{I}	\mathcal{R}	\mathcal{I}	\mathcal{R}	\mathcal{I}
1	-.3690	-.1193	.2894	-.2022	-.3022	.0849	-.2334	-.1893
3	.0756	.0678	-.0992	.0652	.0913	.0098	.0090	.0754
5	-.0475	-.0323	.0420	-.0517	-.0464	-.0070	.0029	-.0402
7	.0385	.0102	-.0119	.0425	.0279	.0015	-.0008	.0249
9	-.0303	.0057	-.0065	-.0322	-.0176	.0021	-.0019	-.0161
11	.0193	-.0162	.0172	.0197	.0108	-.0037	.0033	.0101
25	-.0045	-.0077	.0076	-.0045	-.0027	.0041	-.0041	-.0027

ω	Ordinary				Extraordinary			
	R_{zz}		R_{yz}		R_{zy}		R_{yy}	
	\mathcal{R}	\mathcal{I}	\mathcal{R}	\mathcal{I}	\mathcal{R}	\mathcal{I}	\mathcal{R}	\mathcal{I}
1	-.4250	.5498	-.0822	.0013	.0712	-.0011	-.5392	.3564
3	.3840	.0925	-.0035	-.0001	.0030	.0001	.1800	.2798
5	-.1442	-.1553	-.0010	-.0350	.0008	.0303	.1100	-.1294
7	-.0002	.1432	-.0271	-.0048	.0234	.0042	-.0764	-.0346
9	.0632	-.0273	.0028	.0021	-.0023	-.0018	-.0166	.0352
11	-.0118	-.0125	.0033	-.0099	-.0028	.0085	-.0120	.0202
25	.0050	-.0026	-.0005	-.0333	.0002	.0276	-.0018	.0002

its vicinity. At the upper limit, the two plane-polarized modes are decoupled and the medium is sufficiently uniform that the solutions are simply harmonic with wave numbers $k^{(o)}$ and $k^{(e)}$ determined by the usual dispersion relation based on the local Alfvén speed V_A ,

$$k^{(o)} = \omega / V_A \quad (12a)$$

$$k^{(e)} = \omega / V_A \cos \psi \quad (12b)$$

We now state the boundary conditions that our solutions satisfy. We know that the electric field vanishes at the surface of the earth and that the tangential component and its derivative are continuous at $x = d$. Since the wavelength in air is extremely long, the fields vary linearly in the air space and their derivative is a constant,

$$E_y(x) = x \cdot \frac{dE_y}{dx} \Big|_{x=d} \quad 0 \leq x \leq d \quad (13a)$$

$$E_z(x) = x \cdot \frac{dE_z}{dx} \Big|_{x=d} \quad 0 \leq x \leq d \quad (13b)$$

The initial condition at the base of the ionosphere therefore satisfies equation 14,

$$\left\{ \frac{1}{E_y} \frac{dE_y}{dx} \right\}_{x=d} = \frac{1}{d} = \left\{ \frac{1}{E_z} \frac{dE_z}{dx} \right\}_{x=d} \quad (14)$$

The second boundary condition that we must introduce is rather arbitrary. Since it is customary to speak of the two plane-polarized modes at high altitude (see equations 12), we have calculated the results for the two situations in which the incident wave at $x = D$ is plane-polarized. The incident fields may be calculated from the total fields as follows:

Writing

$$B_z = ae^{ik^{(o)}x} + be^{-ik^{(o)}x}$$

$$E_y = \frac{\omega}{k^{(o)}} (ae^{ik^{(o)}x} - be^{-ik^{(o)}x}),$$

one finds that

$$be^{-ik^{(o)}x} = [B_z]_{INC} = \frac{1}{2} \left(B_z - \frac{k^{(o)}}{\omega} E_y \right)$$

TABLE 2. Power Incident and Fraction of Incident Power Absorbed vs. Angular Frequency for an Incident Magnetic Field Amplitude of 100γ

ω	Ordinary		Extraordinary	
	$P_{INC} \left[\frac{\text{Watts}}{\text{m}^2} \right] \times 10^3$	P_{ABS}/P_{INC}	$P_{INC} \left[\frac{\text{Watts}}{\text{m}^2} \right] \times 10^3$	P_{ABS}/P_{INC}
1	1.41	0.51	1.22	0.58
3	1.41	0.84	1.22	0.89
5	1.41	0.95	1.22	0.97
7	1.42	0.98	1.22	0.99
9	1.42	1.00	1.22	1.00
11	1.42	1.00	1.22	1.00
25	1.43	1.00	1.20	1.00

and similarly for the extraordinary wave. Therefore,

$[B_z(D)]_{INC} = \frac{1}{2} \left[B_z(D) - \frac{1}{V_A} E_y(D) \right] \quad (15a)$

$[B_y(D)]_{INC} = \frac{1}{2} \left[B_y(D) + \frac{1}{V_A \cos \psi} E_z(D) \right] \quad (15b)$

The incident wave boundary conditions then are these:

Ordinary wave: $\begin{cases} [B_z(D)]_{INC} = 1 \\ [B_y(D)]_{INC} = 0 \end{cases} \quad (16)$

Extraordinary wave: $\begin{cases} [B_z(D)]_{INC} = 0 \\ [B_y(D)]_{INC} = 1 \end{cases} \quad (17)$

We believe that the results in this situation are 'typical' and that it is not worth while to explore other cases that are linear superpositions of ours.

4. Results. The results of the integration contain detailed information about the wave in the ionosphere. There are several ways of expressing this behavior in a compact way. We have chosen to describe the transmission and reflection of the fields by two complex 2 × 2 matrices *T* and *R*, respectively. The fields at the limits of the region we have studied are then related as follows:

$B(d) = T \cdot [B(D)]_{INC} \quad (18)$

and

$[B(D)]_{refl} = R \cdot [B(D)]_{INC} \quad (19)$

Numerical values of the elements of *T* and *R* are given in Table 1.

Since it is not practical to list the values of the field strengths at many points in the ionosphere, we shall summarize the phenomena there by giving the local time average power dissipation *P* as a function of position,

$P(x) = \frac{1}{2} Re [E(x) \cdot j(x)] \quad (20)$

using a 100 γ (1 γ = 10⁻⁸ gauss) incident magnetic field amplitude for each of the two normal modes. The function *P*(*x*) is plotted in Figures 1 and 2 for two values of the incident frequency.

We remind the reader at this point that there is no net flux of energy through the ionosphere in our model, because we have terminated the propagation regions with the perfectly reflecting earth. Conservation of energy therefore implies that the fraction of the incident energy that is not reflected is absorbed. The fraction of the incident power absorbed is given in Table 2. Since the qualitative features are in accord with expectation [Dessler, 1959a; Fejer, 1960], it is

TABLE 3. Phases of the Transmitted Fields vs. Incident Angular Frequency

ω	Ordinary		Extraordinary	
	φ _{xx} , deg	φ _{yz} , deg	φ _{zy} , deg	φ _{yy} , deg
1	198	325	164	219
3	402	506	366	443
5	574	669	549	634
7	735	826	723	812
9	889	979	893	997
11	1040	1129	1061	1152

TABLE 4

Temperature T , neutral number density N_n , ion number density N_i , electron number density N_e , average ionic molecular weight W , ion cyclotron frequency ω_i , electron cyclotron frequency ω_e , ion collision frequency ν_i , and electron collision frequency ν_e vs. altitude above the earth's surface. In this table numbers expressed as N^m signify $N \times 10^m$.

Altitude, km	T , °K	N_n , particles per cm^3	$N_i = N_e$, ions per cm^3	W	ω_i	ω_e	ν_i	ν_e
80	205	4.30^{14}	1.00^3	29.0	1.60^2	8.47^6	2.05^5	3.29^6
90	225	6.70^{13}	2.50^4	29.0	1.60^2	8.43^6	3.24^4	5.42^5
100	280	1.10^{13}	1.22^5	28.4	1.62^2	8.39^6	5.37^3	1.00^5
120	435	6.20^{11}	1.90^5	26.7	1.71^2	8.32^6	3.12^2	7.93^3
140	620	1.45^{11}	2.35^5	25.7	1.76^2	8.24^6	7.44^1	2.66^3
160	780	5.40^{10}	2.55^5	24.7	1.81^2	8.16^6	2.83^1	1.37^3
180	905	2.50^{10}	2.70^5	23.7	1.87^2	8.09^6	1.33^1	8.86^2
200	995	1.28^{10}	2.75^5	23.0	1.91^2	8.02^6	6.94^0	6.46^2
250	1190	3.54^9	3.75^5	21.0	2.04^2	7.84^6	2.01^0	3.97^2
300	1300	1.40^9	3.35^5	19.5	2.16^2	7.66^6	8.25^{-1}	3.83^2
350	1315	6.44^8	3.90^5	18.4	2.23^2	7.49^6	3.91^{-1}	4.20^2
400	1320	3.10^8	4.22^5	17.4	2.31^2	7.33^6	1.94^{-1}	4.43^2
450	1325	1.58^8	4.15^5	16.8	2.34^2	7.17^6	1.00^{-1}	4.32^2
500	1325	8.10^7	4.00^5	16.2	2.37^2	7.01^6	5.26^{-2}	4.14^2
550	1325	4.37^7	3.60^5	16.1	2.34^2	6.86^6	2.86^{-2}	3.73^2

not necessary to present an elaborate discussion of the numerical values at this point.

5. *Applications.* It has been pointed out [Dessler, 1959a and 1959b] that hydromagnetic wave energy dissipated in the ionosphere can represent an important source of ionospheric heating, which can explain, at least in part, the following observed phenomena: (1) the lifting of the ionospheric F region during geomagnetic storms; (2) the irregular orbital acceleration of

satellites; (3) the sudden disappearance of trapped radiation from the Argus nuclear explosion coincident with a geomagnetic storm; (4) the X-ray flux observed at balloon altitudes below the Van Allen radiation belt during geomagnetic storms; and (5) the decrease in intensity at the lower edge of the Van Allen radiation belt during geomagnetic storms [Rothwell and McIlwain, 1960]. (References to observations of the above phenomena, with the exception of item 5, are given in the papers by Dessler [1959a and 1959b]). Some examples of the calculated hydromagnetic heat source are compared in Figures 3 and 4 with the solar ultraviolet heating required to produce the observed ionospheric temperature distribution [Johnson, 1958].

The magnitude of unit incident ordinary and extraordinary wave amplitude transmitted through the ionosphere may be calculated from equation 18:

$$|B(d)|^{(e)} = \sqrt{T_{zz}T_{zz}^* + T_{yz}T_{yz}^*} \quad (21a)$$

$$B(d)^{(e)} = \sqrt{T_{zy}T_{zy}^* + T_{yy}T_{yy}^*} \quad (21b)$$

and the numerical values of the transmission matrix given in Table 1. This result is plotted in Figure 5. From this graph it may be seen that the ionosphere is essentially transparent for frequencies somewhat less than $\omega = 1.0$ and

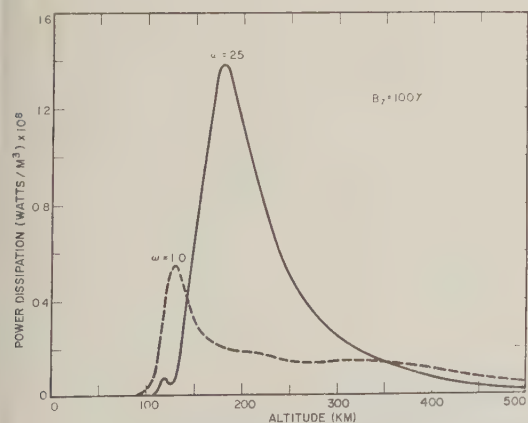


Fig. 1. Power dissipation vs. altitude above the earth's surface for two ordinary waves of 25 rad sec^{-1} and 1.0 rad sec^{-1} incident frequency, each with a 100 γ incident magnetic field amplitude.

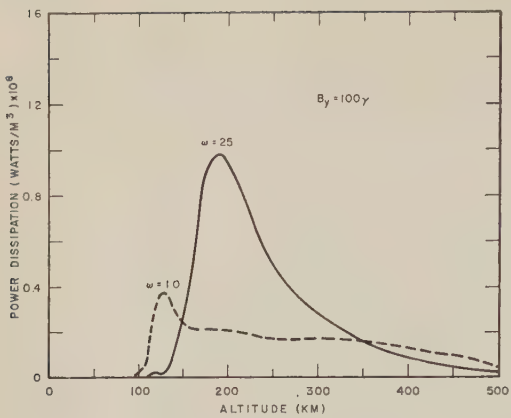


Fig. 2. Power dissipation vs. altitude above the earth's surface for two extraordinary frequency waves of 25 rad sec⁻¹ and 1.0 rad sec⁻¹ incident frequency each with a 100 γ incident magnetic field amplitude.

that the amplitude attenuation is a factor of 10 or more for frequencies above about $\omega = 3.0$. Thus, we may expect that, near 1 cps, the amplitude of magnetic fluctuations above the ionosphere will be many times greater than the amplitude observed at the earth's surface. This result is in agreement with previous qualitative arguments [Dessler, 1958]. An experimental test of the existence of these relatively large-amplitude waves could be made immediately from careful examination of the Vanguard III nuclear

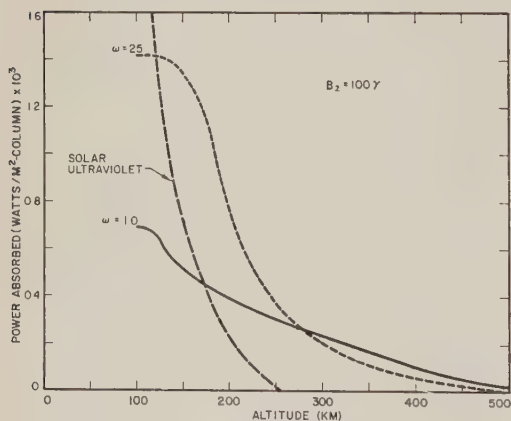


Fig. 3. The total power absorbed by the ionosphere above a certain altitude due to ordinary incident waves of 25 rad sec⁻¹ and 1.0 rad sec⁻¹ frequency each with a 100 γ magnetic field amplitude. The dashed curve indicates the solar ultraviolet power absorption (after Johnson [1958]).

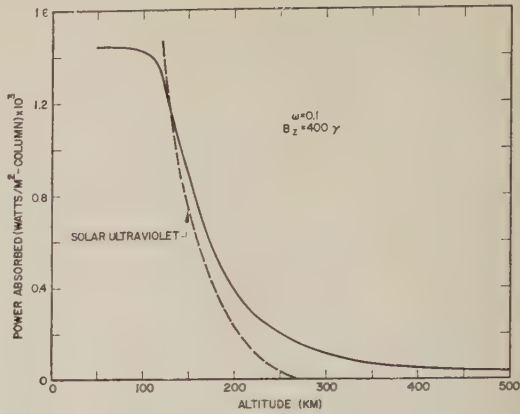


Fig. 4. The total power absorbed by the ionosphere above a certain altitude due to an ordinary incident wave of 0.1 rad sec⁻¹ frequency and a 400 γ magnetic field amplitude. The dashed curve indicates the solar ultraviolet power absorption (after Johnson [1958]).

magnetometer signals (Dessler, private communication).

With the information that is available, it is also possible to calculate the speed with which hydrodynamic signals are transmitted through the ionosphere. This problem has arisen in connection with the Argus experiment, in which a nuclear explosion at an altitude of about 500 km gave rise to magnetic field fluctuations of about 1 cps at ground level. We wish to estimate

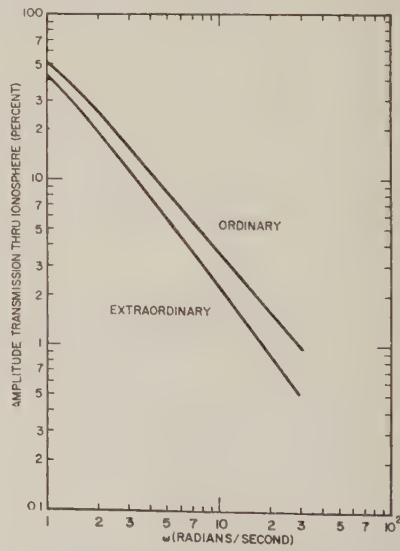


Fig. 5. The per cent of incident wave amplitude, B , transmitted through the ionosphere vs. incident angular frequency.

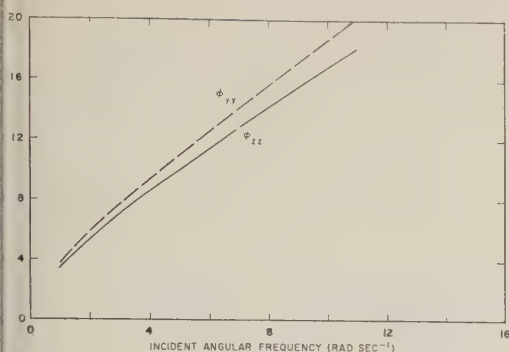


Fig. 6. The phases ϕ_{xx} and ϕ_{yy} of the transmitted fields vs. incident angular frequency. The time delay τ is given by the slope of the line.

the delay between the generation of the signal and its arrival below the detonation point. A more complicated problem is posed by measurements at the point magnetically conjugate to the launch area, where the observed time delay is mostly the result of propagation beyond the ionosphere, guided by the field lines [Grad, 1959; Karplus, 1960]; propagation through the ionosphere makes only a small contribution to the total transit time.

As we have seen, the hydromagnetic signal does not satisfy a wave equation in the lower ionosphere. The signal speed is therefore not a perfectly well-defined concept. We shall interpret it in the sense of a group velocity. That is, we begin with an incident pulse at 550 km such that the simple harmonic components are in phase at $t = 0$. Our calculations give the relative amplitude and phase of each component at 80 km. We therefore ask how much time τ must lapse before the different components are in phase below the ionosphere? This time will be the delay between the maximum field deviation at 550 km and the maximum deviation at 80 km. Because of the attenuation of high frequencies, it is not useful to ask for the time of propagation of a sharp discontinuity in the field strength. If the phase changes of two components differ by $\Delta\phi$ and their frequencies differs by $\Delta\omega$, then τ is given by the ratio

$$\tau = \Delta\phi / \Delta\omega \quad (22)$$

In Table 3, the phases of the transmitted fields are given, as determined from the values listed in Table 1; in Figure 6 the phases in radians are plotted as a function of angular frequency.

It is remarkable that this relationship is almost linear. As a consequence even the broad distribution of frequencies in a fairly sharp incident pulse will be about in phase after propagation through the ionosphere. The time delay, according to equation 22, is given by the slope of the line in Figure 6. It is approximately 1.4 sec for the ordinary wave and 1.6 sec for the extraordinary wave. This transit time is too short to be significant in the propagation of the sudden commencement of magnetic storms.

Acknowledgments. We are indebted to A. J. Dessler for numerous instructive comments.

The work presented in this paper was supported in part by the Propagation Sciences Laboratory of the Air Force Cambridge Research Center under contract AF 19(604)-5906.

APPENDIX

The ionospheric medium is described by the three principal values of the conductivity introduced in equation 3. These may be expressed in terms of the following quantities:

$$\begin{aligned} \omega_e, \omega_i: & \text{electron and ion cyclotron frequencies} \\ \nu_e, \nu_i: & \text{electron and ion collision frequencies} \\ & \text{with neutrals} \\ m_e, m_i: & \text{electron and ion masses} \\ N_e = N_i = N: & \text{density of electrons and ions} \end{aligned} \quad (A1)$$

The formulas for the conductivities are obtained from the equations of motion of ions and electrons. They are

$$\sigma_0 = e^2 N \left\{ \frac{1}{m_e(\nu_e - i\omega)} + \frac{1}{m_i(\nu_i - i\omega)} \right\} \quad (A2)$$

$$\begin{aligned} \sigma_1 = e^2 N \left\{ \frac{\nu_e - i\omega}{m_e[(\nu_e - i\omega)^2 + \omega_e^2]} \right. \\ \left. + \frac{\nu_i - i\omega}{m_i[(\nu_i - i\omega)^2 + \omega_i^2]} \right\} \quad (A3) \end{aligned}$$

$$\begin{aligned} \sigma_2 = e^2 N \left\{ -\frac{\omega_e}{m_e[(\nu_e - i\omega)^2 + \omega_e^2]} \right. \\ \left. + \frac{\omega_i}{m_i[(\nu_i - i\omega)^2 + \omega_i^2]} \right\} \quad (A4) \end{aligned}$$

Some of the numerical values used for the parameters defined in equation A1 are listed in Table 4. We trust that this information is adequate to specify clearly the calculation we have carried out.

Our neglect of electron-ion collisions only has a significant effect on the longitudinal conductivity σ_z at altitudes above 120 km. At these altitudes σ_z is so large that the medium is effectively a perfect conductor. The precise numerical value is therefore immaterial.

REFERENCES

- Akasofu, S., On the hydromagnetic heating connected with geomagnetic micropulsations, *J. Atmospheric and Terrest. Phys.*, **18**, 160-163, 1960.
- Dessler, A. J., Large amplitude hydromagnetic waves above the ionosphere, *J. Geophys. Research*, **63**, 507-511, 1958.
- Dessler, A. J., Ionospheric heating by hydromagnetic waves, *J. Geophys. Research*, **64**, 397-401, 1959a.
- Dessler, A. J., Upper atmosphere density variations due to hydromagnetic heating, *Nature*, **184**, 261-262, 1959b.
- Fejer, J. A., Hydromagnetic wave propagation in the ionosphere, *J. Atmospheric and Terrest. Phys.*, **18**, 135-146, 1960. This excellent paper contains a clear theoretical treatment of the problem we shall discuss and a review with many references to previous work.
- Francis, W. E., A. J. Dessler, and R. Karplus, Attenuation of hydromagnetic waves in the ionosphere, *Bull. Am. Phys. Soc.*, [2] **5** (4), 316, 1960.
- Grad, H., Propagation of magnetohydrodynamic waves without radial attenuation, *The Magnetodynamics of Conducting Fluids*, Stanford University Press, Stanford, California, 145 pp., 1959.
- Johnson, F. S., Temperatures in the high atmosphere, *Ann. géophys.*, **14**, 94-108, 1958.
- Kahalas, S., Magnetohydrodynamic wave propagation in the ionosphere, *Phys. Fluids*, **3**, 372-378, 1960.
- Karplus, R., The radiation of hydromagnetic waves, *Phys. Fluids* (in press), 1960.
- Newman, P. R., Optical, electromagnetic and satellite observations of high-altitude nuclear detonations, part 1, *J. Geophys. Research*, **64**, 923-932 (especially pp. 928-931), 1959.
- Rothwell, P., and C. E. McIlwain, Magnetic storms and the Van Allen radiation belts—Observations from satellite 1958e (Explorer IV), *J. Geophys. Research*, **65**, 799-806, 1960.

(Manuscript received August 22, 1960.)

Electron Densities in the F Region of the Ionosphere from Rocket Measurements

Part 1. Methods of Analysis

JOHN S. NISBET AND S. A. BOWHILL

*Ionosphere Research Laboratory, The Pennsylvania State University
University Park, Pennsylvania*

Abstract. A method is described for analyzing dispersion records from long-range missiles in terms of equivalent electron-density and electron-content profiles above a fixed location. This method takes account of varying horizontal gradients in electron density and the varying local zenith angle of the ray path as a function of range time and height in the ionosphere. Refraction has been considered for both Faraday rotation and range-error measurements, and correction factors are included in the program. Comparisons made between Faraday rotation and range-error measurements and between Faraday rotation measurements at two locations demonstrated the validity of the reduction techniques.

INTRODUCTION

Dispersion measurements on radio waves propagated between a rocket and ground stations can be used to determine properties of the electron-density distribution of the intervening ionosphere. Measurements may be made of the relative dispersion between waves of different frequencies, or, as in the Faraday rotation method, of two modes at the same frequency. Electron density measurements made in the above manner have been described by Seddon [1953] and Jackson and Seddon [1958], Berning [1951], Pfister and Ulwick [1958], and Gringauz [1958]. In these investigations research rockets having substantially vertical trajectories were used.

Long-range military ballistic missiles and satellite launch vehicles have radio links to ground stations for telemetry and tracking purposes, and it was decided to utilize them for making ionospheric measurements. Such rockets are attitude stabilized; their position is accurately known at all times, and they penetrate a region that is very expensive to probe with specially commissioned research rockets. They have large horizontal velocity components, however, and several problems arise that are not present with vertical firings.

Refraction may cause the two signals on which the comparison is based to follow different paths. Horizontal gradients in the ionosphere may cause the vertical electron-density-height profile to be a function of distance along the ray path. Large rockets burn longer, and the height at which it is possible to start an ionospheric measurement may be greater. Inhomogeneities of small horizontal extent make interpretation much more difficult.

Part 1 of this paper will discuss the analysis of such nonvertical high-altitude firings, and part 2 will describe the results of electron-density measurements made in this way.

CHOICE OF THE METHOD

The planning of this experiment was based on the premise that no additional equipment should be installed in the rocket.

In the method described by Berning [1951] the beat frequency of the DOVAP system is measured and compared with the frequency that would be measured if no ionospheric dispersion were present, calculated from the vacuum trajectory. A major disadvantage of this method is the accuracy with which the missile trajectory must be known. In Berning's experiments, the vacuum trajectory was computed from measurements made using the DOVAP system itself, above the burnout altitude of the missile and below the altitude at which ionospheric dispersion could be expected to influence his results. With the larger missiles, which have longer burning times, the margin available is

small. Other, higher-frequency tracking systems were available, however, and they were used in our experiments to determine the position of the missile.

The second method employed the Faraday rotation of the plane of polarization of a wave traveling through the ionosphere in the presence of a stationary magnetic field. This rotation in any given part of the ray path is proportional to the electron density, the length of the path element, and the component of the magnetic field along the ray path. By measuring the total rotation angle at the ground as a function of the missile position, the electron content between the transmitter and the receiver could be calculated, using the known magnetic-field components of the earth.

DESCRIPTION OF THE EXPERIMENT

Frequency dispersion method. The frequency dispersion method employed the difference produced by dispersion in the ionosphere in the apparent position of the missile measured by two tracking systems operating on different frequencies.

DOVAP and UDOP are two such systems, operating on the following principle. A signal is transmitted from a ground station to the missile, where it is doubled in frequency and retransmitted by a transponder unit. At a number of other ground stations the difference between twice the frequency transmitted to the missile and the frequency received from the transponder is compared, to give a Doppler frequency. If the waves are propagated at the velocity of light in vacuo, the slant ranges to each of the receiving stations and hence the position of the missile can be calculated. The phase velocity in the ionosphere differs from the velocity of light in vacuo, and an error is produced in the separation calculated in the above manner. When the ground-based transmitter and receiver are coincident at a point R and the frequencies are sufficiently high compared with plasma and gyro frequencies along the path to the missile at point M , this error is given by the formula

$$\Delta S = \frac{5e^2}{64\pi^2 m \epsilon_0 f_1^2} \int_R^M n \, ds \quad (1)$$

ray path

where

ΔS is the slant range error in meters.

e is the charge of the electron in coulombs.

m is the mass of an electron in kilograms.

ϵ_0 is the dielectric constant of free space.

f_1 is the frequency transmitted to the missile.

n is the electron density along the ray path per cubic meter.

When a corrected vacuum trajectory is available, the range errors may be used to calculate the value of the integral as a function of time. When two tracking systems operating on different frequencies are available, the difference in the range errors may be used in a similar manner.

For missile-tracking purposes, the beat frequencies of the DOVAP and UDOP systems at several sites are recorded on magnetic tapes together with a timing code. Since these measurements are made for each missile that carries a suitable transponder, they were not duplicated. The tapes were processed at the Air Force Missile Test Center by DARE (DOVAP automatic reduction equipment) and FLAC (Florida automatic computer) to provide tables of the accumulated cycle account and its first, second, and third difference at 0.1-second intervals. For the normal flight evaluation of the missile this reduction program was terminated at a low altitude, and these tapes were specially processed by the Computation Laboratory of the Army Ballistic Missile Agency to enable ionospheric studies to be made.

Faraday rotation method. In the ionosphere, the phase velocities of right- and left-hand circularly polarized waves differ for propagation in the direction of a stationary magnetic-field component. A linearly polarized wave may be considered the sum of two such modes, and the effect of this difference in phase velocities is to produce a rotation in the plane of polarization as the wave is propagated through the ionosphere.

When the frequency is sufficiently high compared with the plasma and gyro frequencies, collisions can be neglected, and conditions are such that the longitudinal approximation applies, the rotation of angle A in radians is given by

$$A = \frac{e^3}{8\pi^2 m^2 c \epsilon_0 f^2} \int_R^M n B_L \, ds \quad (2)$$

ray path

where c is the velocity of light in vacuo in

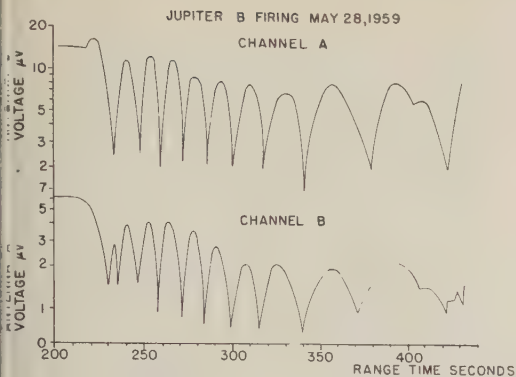


Fig. 1. Signal strength records showing Faraday rotation fading.

meters per second and B_L is the magnetic flux density along the ray path in webers per square meter.

The plane of polarization of the transmitting antennas was determined from polar diagrams, and attitude information was telemetered from the missile. To determine the Faraday rotation angle it was only necessary to measure the plane of polarization of the received wave.

When a plane-polarized wave is rotated with respect to a linearly polarized antenna, the antenna voltage has a sharp minimum each time the planes of polarization are at right angles and a flat maximum when the planes of polarization are aligned. The rotation angle between any two minima or maxima is thus π radians. This was the basic method employed in our measurements of Faraday rotation angle. For early measurements it was necessary to rely on signal strength records produced by other organizations and intended merely for the evaluation of their own telemetry or tracking links with the missile. These records were often of poor quality, and, indeed, on several occasions quasi-circularly polarized receiving antennas had been employed to minimize the effect of fading due to Faraday rotation. The records were made with only one receiving antenna, and thus it was not possible to determine the sense of rotation or to separate out fading patterns due to antenna side lobes.

In May 1959, permission was obtained to install our own receiving equipment at the Ionosphere Research Laboratory's receiver station at Cape Canaveral. Two linearly polarized antennas were used, with the plane of the elements in-

clined at plus and minus 60° from the local vertical. This arrangement allowed separation of rotation fading from signal strength fluctuation due to other effects. It also made possible the determination of the sense of rotation, an important factor in the interpretation of records taken under disturbed ionospheric conditions. Each of the antennas was connected to the input of a DOVAP receiver type 90139 manufactured by the Resdel Engineering Corporation. The signal strength outputs of the receivers were connected to a conventional pen recorder with two channels having a maximum sensitivity of 0.01 volt per millimeter, and a nominal upper frequency limit of 100 cps. An additional event channel was used to record the coded timing pulses that are available at measuring sites throughout the Atlantic Missile Range.

Typical signal strength records showing Faraday rotation fading are shown in Figure 1. The relative times at which the fades occur on the two antennas show that they are due to rotation of the plane of polarization. Faraday rotation

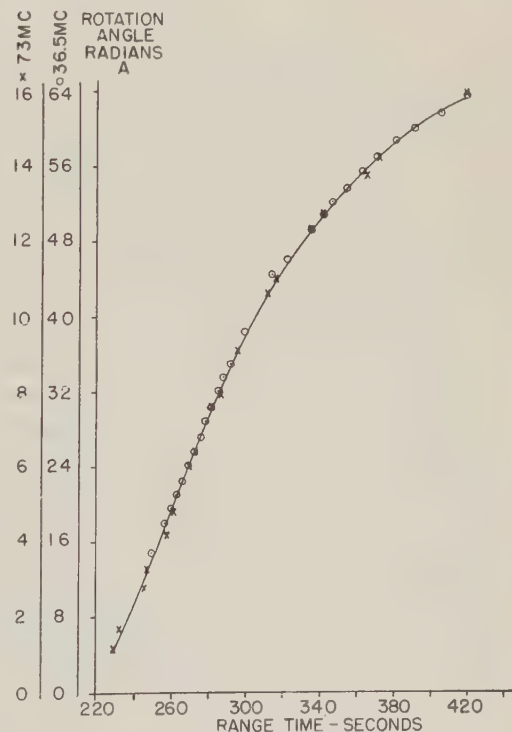


Fig. 2. Rotation angle of plane of polarization for upgoing and downgoing DOVAP waves. Jupiter B firing, May 28, 1959, 02h 35m.

angles computed from this record are shown in Figure 2.

For this flight it was also possible to measure rotation of the upgoing DOVAP signal, on one-half the downcoming frequency, at approximately 36.5 Mc/s, by means of equipment included in the missile for *D*-region electron-density measurements. From equation 2 it can be seen that the Faraday rotation angle is inversely proportional to the square of the frequency. For comparison purposes, upgoing rotation angles have been plotted in Figure 2, on one-quarter the scale used for the downgoing wave, so that the curves should coincide if an inverse-square frequency law was obeyed. This is seen to be the case.

The rotation angles measured are, therefore, consistent with the assumption that they are due to Faraday rotation in the ionosphere. No major systematic departure from the inverse-square frequency relationship is apparent. Such departures would be produced by failure to make correct allowances for rotation of the missile antenna system and refraction in the ionosphere.

ANALYSIS OF THE DATA

Equations 1 and 2 relate the measured range error and rotation angle to integrals evaluated along the ray paths dependent on the electron-density distribution it is desired to determine. If the magnetic field of the earth is assumed to be known, the two methods provide essentially the same information and the analysis can be carried out in the same way. In the following, the somewhat more complicated Faraday rotation analysis will be described.

In the analysis of records from missiles with large horizontal velocities, the ray path along which the integrals of equations 1 and 2 are taken changes continuously with time. It is of interest to obtain the integral of the electron density with height at some fixed location rather than along a varying oblique path.

To enable such an analysis to be made it has been found convenient to consider an ionospheric model consisting of a number of discrete height intervals.

Equation 2 may be written

$$A = \frac{e^3}{8\pi^2 m^2 c \epsilon_0 f^2} \sum_0^p n(h, \psi, \lambda, t) B_L(h, t) \cdot \sec \phi(h, t) \Delta h \quad (3)$$

where

ψ is the longitude of the intersection of the ray path and the incremental layer.

λ is the latitude of the intersection of the ray path and the incremental layer.

ϕ is the local zenith angle of the ray path in the incremental layer.

t is the time.

h is the altitude of the incremental layer.

Values of B_L and $\sec \phi$ may be calculated directly from the trajectory as functions of range time and altitude if, in the first approximation, refraction is neglected.

The electron density in a given incremental layer is a function of latitude and longitude, due to horizontal gradients in the ionosphere, and is a function of time. It is desirable to obtain the electron-density distribution as a function of altitude at some fixed latitude and longitude and time rather than along the ray path, which is oblique and varies with time. For this purpose it is convenient to introduce a function of the horizontal electron-density gradient G . This function is the ratio of the electron-density at the datum latitude and longitude to the electron density at the intersection of the ray path and the incremental layer.

Equation 3 may then be written

$$A = k_1 \sum_0^p n(h) G(h, \psi, \lambda, t) B_L(h, t) \cdot \sec \phi(h, t) \Delta h \quad (4)$$

where

$$k_1 = \frac{e^3}{8\pi^2 m^2 c \epsilon_0 f^2}$$

Below the maximum of the *F* layer, these gradient factors can be calculated from reduced ionograms from a number of swept frequency pulse sounding stations. Above the maximum no information on the gradients is available. It is possible to minimize the effects of this uncertainty by choosing the datum latitude, longitude, and time in the region of the peak of the rocket trajectory. In this way the largest correction factors are applied in the lower regions of the ionosphere where the gradients are known. It is possible to check the assumptions made about horizontal gradients by making measurements at the widely separated stations.

The number of incremental layers may be

chosen to be as large as is consistent with the resolution of the Faraday rotation measurements. The boundaries of the layers are usually chosen as those for which accurate rotation angles are known, such as the altitudes corresponding to times at which minima occurred in the signal strength measurements.

Each rotation measurement introduces an equation with one unknown, the electron density in the incremental layer between the altitude at which it and the preceding measurement were made. The set of equations thus made up a triangular matrix.

$$\begin{aligned} A_1/k_1 &= n_1(GB_L \sec \phi)_{11} \Delta h_1 \\ A_2/k_1 &= n_1(GB_L \sec \phi)_{21} \Delta h_1 + n_2(GB_L \sec \phi)_{22} \Delta h_2 \\ &\vdots \\ A_p/k_1 &= n_1(GB_L \sec \phi)_{p1} \Delta h_1 + \cdots n_p(GB_L \sec \phi)_{pp} \Delta h_p \end{aligned} \quad (5)$$

The general formula for the electron density of the *p*th layer is given by

$$n_p = \frac{\frac{A_p}{k_1} - \sum_{m=1}^{p-1} n_m(GB_L \sec \phi)_{pm} \Delta h_m}{(GB_L \sec \phi)_{pp} \Delta h_p} \quad (6)$$

As an example of the importance of the horizontal gradient terms, Figure 3 shows electron-content profiles deduced from Faraday rotation measurements at Cape Canaveral and at Grand Turk, a tracking station approximately 1500 km downrange. The profiles obtained in an analysis neglecting the effect of the horizontal gradient terms are included for comparison purposes, and it is apparent that the electron-density profiles obtained by differentiating these curves would differ appreciably.

Refraction in the ionosphere causes the ray to deviate from the line-of-sight path assumed in the analysis up to this point, and it is necessary to apply corrections as follows.

In our experiments the lowest frequency used for a firing in the daytime was 108 Mc/s, and at night 36.5 Mc/s. Under these conditions the refractive index did not differ from unity by more than 3 per cent. Departures from line of sight were thus small, and it was found convenient to analyze the data neglecting ray bending and to apply correction factors for the effect later.

A simple slab model ionosphere shown in Figure 4 was used for computing the correction factors; in this model the ionosphere is assumed concentrated in a layer of uniform electron density above a fixed altitude up to the height of the vehicle.

In the analysis neglecting ray bending it is assumed that the ray follows the line-of-sight path *MBR* instead of the actual path *MAR*. An erroneous electron content N_T' is then obtained which can be related to the true electron content of the slab N_T . For Faraday rotation measurements when the departures from the line-of-sight path are small, so that second-order

small quantities can be neglected, this relation can be shown to be

$$\frac{N_T}{N_T'} = 1 - \epsilon \frac{RB \tan \phi_3 (1 + \tan^2 \phi_3)}{RM (V/H) + \tan \phi_3} \quad (7)$$

where V/H is the ratio of the vertical to horizontal components of the magnetic field of the earth and

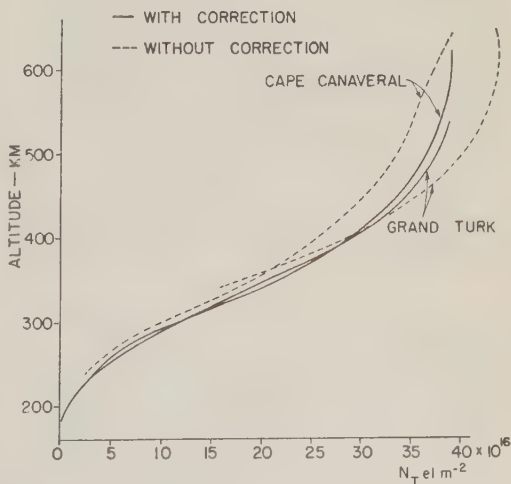


Fig. 3. Comparison of electron column contents with and without corrections for horizontal gradient. Vanguard I firing, March 17, 1959, 07h 15m EST.

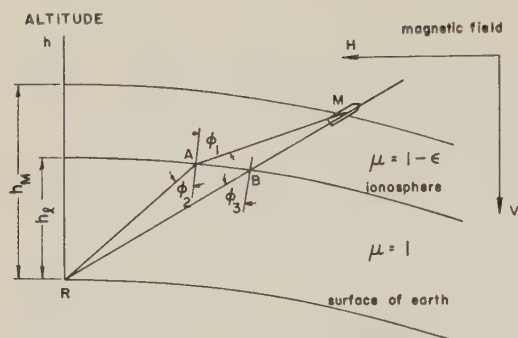


Fig. 4. Ionospheric model for refraction error calculations.

$$\epsilon = 1 - \mu = 1 - \frac{40.32n}{f^2}$$

For methods in which the dispersive range error is measured, refraction on both the upgoing and downgoing waves must be considered. For a measurement using a system similar to DOVAP, in which the frequency is doubled at the vehicle, with the same assumptions as in the Faraday rotation analysis discussed above,

$$N_T/N_{T'} = 1 - 3.4\epsilon(RB/RM) \tan^2 \phi_3 \quad (8)$$

where ϵ is calculated for the downcoming wave.

Using typical values for our experiments of $f = 73$ Mc/s, $\phi_3 = 60^\circ$, $V/H = 4$, $RB/RM = 2/3$ the correction factors amount to 0.61 per cent for the Faraday rotation measurement and 5.2 per cent for the range-error measurement.

The correction factors are thus much larger for the range-error measurement. A comparison of the two methods provides a check on the program for computing the refraction corrections and the magnetic-field components for the Faraday rotation measurements. Figure 5 shows the electron content integrated along the ray path calculated from both Faraday rotation and DOVAP range-error measurements at Cape Canaveral.

DETAILS OF THE COMPUTATION PROCEDURE

Calculations of the ray path parameters B_L and $\sec \phi$ as a function of layer height and range time and antenna attitude were made using final trajectories and missile evaluation reports published by the Computation Laboratories of the Army Ballistic Missile Agency and Air Force Missile Test Center.

Data on the magnetic field of the earth were obtained from two publications of Carnegie In-

stitution of Washington [Vestine, Lange, Laporte, and Scott, 1947; Vestine, Laporte, Lange, Cooper, and Hendricks, 1948]. The values obtained in this way were spot-checked against the more recent spherical harmonic analysis of Finch and Leaton [1957].

Several approximations are involved in the derivation of equations 1 and 2. It has been found convenient to determine several exact values for the refractive indices for the ordinary and extraordinary modes along typical ray paths using a digital computer program described by Mechtly [1959]. These exact values were used to determine correction factors for the approximate formulas.

Equation 1 was based on the assumption that the true vehicle trajectory was known and that the transmitting and receiving antennas were coincident. In practice, the frequencies from two tracking systems operating on different frequencies are more commonly available. The transmitting and receiving sites are usually separated by a considerable distance and are different for the two systems. A program has been developed to enable such measurements to be converted to range differences along a common ray path and hence to range errors for the lower-frequency system.

To determine horizontal gradient correction

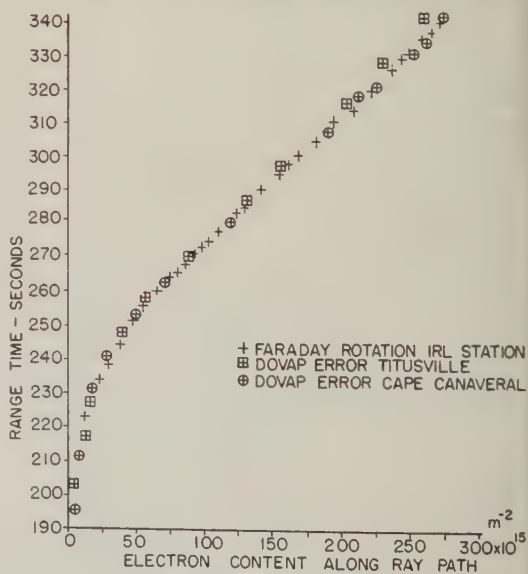


Fig. 5. Electron content integrated along the ray path from Faraday rotation and DOVAP-UDOP comparison. Jupiter B firing, July 9, 1959, 20h 01m.

factors, ionograms from Cape Canaveral, Grand Bahama Island, and San Salvador were used. This chain of stations lies considerably to the south of a typical missile trajectory, and to determine the gradients along the range some further assumptions had to be made. It has been shown by Martyn [1945, 1959] that, for F_2 -region measurements at different stations, agreement may be obtained on a world-wide scale if maximum critical frequencies are related to local time and geomagnetic latitude. In our analyses, the east-west gradient was determined from the variation of the electron density with local time. In the north-south direction, gradients were determined by measuring the differences between electron densities at sounding stations with different geomagnetic latitudes at the same local time.

CONCLUSIONS

The matrix method described is convenient for determining the equivalent vertical electron-density profile from oblique measurements using long-range rockets. It allows for variation in the angles between the ray path and the local zenith and magnetic field, and for altitude-dependent horizontal electron-density gradients.

These factors, of importance in rocket electron-density measurements using missiles with large horizontal velocity components, will doubtless become of greater importance as the altitudes of research rocket measurements increase.

Acknowledgment. The research reported in this paper was carried out under the sponsorship of the Army Ballistic Missile Agency under contract DA-36-061-ORD-577.

REFERENCES

- Berning, W. W., Charge densities in the ionosphere from radio Doppler data, *J. Meteorol.*, **8**, 174, 1951.
- Finch, H. F., and B. R. Leaton, Earth's main field epoch 1955.0, *Geophys. suppl., Monthly Notices Roy Astron. Soc.*, **7**, 314, 1957.
- Gringauz, K. I., Measurements by means of missiles of the electron concentration in the ionosphere using the dispersion interferometer at ultrashort wavelengths, *Doklady Akad. Nauk SSSR*, **120**, 1234, 1958.
- Jackson, J. E., and J. C. Seddon, Ionosphere electron density measurements with the Navy Aerobee-Hi rocket, *J. Geophys. Research*, **63**, 197, 1958.
- Martyn, D. F., Anomalous behavior of the F_2 region of the ionosphere, *Nature*, **155**, 363, 1945.
- Martyn, D. F., The normal F region of the ionosphere, *Proc. IRE*, **47**, 147, 1959.
- Mechtly, E. A., A computer program for obtaining refractive indices and polarizations from the Appleton-Hartree equations and magnetoionic tables for Cape Canaveral, *Sci. Rept. 116*, Ionosphere Research Laboratory, The Pennsylvania State University, University Park, Pa., 1959.
- Pfister, W., and J. C. Ulwick, The analysis of rocket experiments in terms of electron density distributions, *J. Geophys. Research*, **63**, 315, 1958.
- Seddon, J. C., Propagation measurements in the ionosphere with the aid of rockets, *J. Geophys. Research*, **58**, 323, 1953.
- Vestine, E. H., L. Laporte, C. Cooper, I. Lange, and W. C. Hendrix, Description of the earth's main magnetic field and its secular change 1905-1945, *Carnegie Inst. Wash. Publ. 578*, Washington, D. C., 1948.
- Vestine, E. H., L. Laporte, I. Lange, and W. E. Scott, The geomagnetic field, its description and analysis, *Carnegie Inst. Wash. Publ. 580*, Washington, D. C., 1947.

(Manuscript received August 11, 1960.)

Electron Densities in the F Region of the Ionosphere from Rocket Measurements

Part 2. Results of Analysis

JOHN S. NISBET AND S. A. BOWHILL

*Ionosphere Research Laboratory, The Pennsylvania State University
University Park, Pennsylvania*

Abstract. Electron-density distributions in the ionosphere derived from propagation measurements made during seven long-range missile flights are given. These results are compared with measurements derived from variable-frequency pulse soundings and with satellite and rocket measurements described by others. The vertical electron-density gradient was found to vary within quite a large range, being lowest for two firings that took place shortly after sunset and greatest for the one early-morning firing. The equilibrium electron-density variation with height was found to be consistent with the assumption of a Chapman layer, of varying scale height, based on a recent model of the neutral atmosphere derived from satellite retardation measurements.

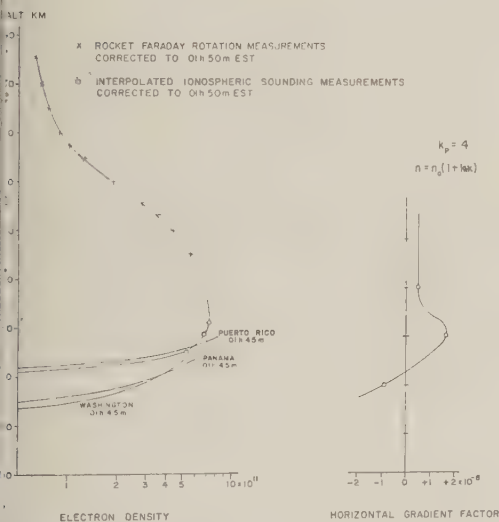


Fig. 1. Electron-density measurements for 01h 50m EST, September 20, 1956.

Introduction. The series of rocket measurements described took place at different times of day over a period of almost 3 years. Since seven out of eight measurements were made in 1958 or 1959 the results correspond to sunspot maximum conditions. All measurements were made at the Atlantic Missile Range, corresponding to a longitude of about 75°W, a geographic latitude of about 28°N, and a geomagnetic latitude of about 0°N.

The electron densities were obtained from propagation measurements between ground stations and long-range rockets by methods of analysis described in part 1.

Results. For five of the firings, those employing Jupiter B missiles, the Faraday rotation measurements were made at the Ionosphere Research Laboratory's receiving site on Cape Canaveral. For four of them it was possible to compare the Faraday rotation and DOVAP error methods of measuring electron content.

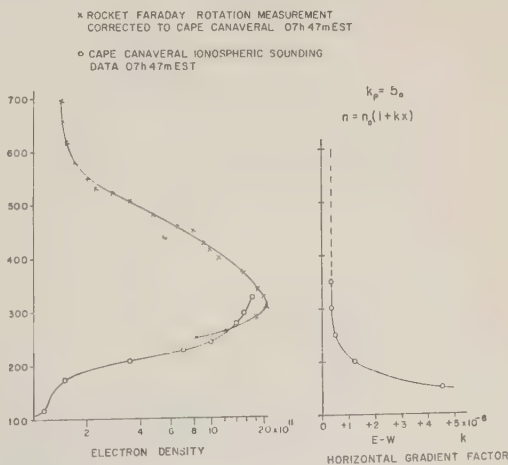


Fig. 2. Electron-density measurements for 07h 47m EST, March 17, 1958.

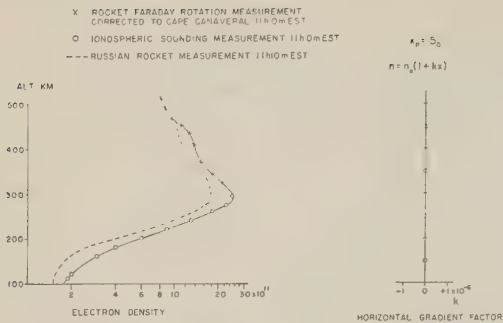


Fig. 3. Electron-density measurements for 11h 0m EST, February 17, 1959.

By the time these measurements were made, the chain of ionospheric sounding stations along the Atlantic Missile Range was in full operation, and better estimates of the horizontal electron-density gradients could be made than were possible for earlier flights.

The records obtained during the launching of the Vanguard I satellite at Cape Canaveral and Grand Turk Island were of excellent quality and showed pronounced Faraday rotation effects. Since the firing took place close to the time of ground sunrise, horizontal gradient effects were large, and a comparison of the results from the two receiving stations provided an excellent check of the methods of analysis and, in particular, of the horizontal gradient correction procedure.

For the remaining two firings, Vanguard II and the Jupiter C launch of September 29, 1956, the Faraday rotation records were of much

poorer quality, and less reliance can be placed on the results. Since the Vanguard II launch was the only record available that approximated noontime conditions, and the Jupiter C altitude greatly exceeded that of the other missiles, their results have been included.

The electron-density profiles determined in each experiment are shown in Figures 1 to 7 with the horizontal electron-density gradient factors used in the analysis.

Comparison with variable-frequency pulse sounding. For each of the electron-density profiles derived from rocket measurements, the corresponding true height electron-density profile reduced from ionospheric sounding measurements is shown on the same graph.

The electron densities derived by the two methods are independent of each other. For Figures 4, 5, 6, and 7 the ionospheric sounding data were only used in the analysis of rocket results to determine the horizontal electron-density gradient. For Figures 1, 2, and 3 they were also used to determine electron contents up to the heights at which it was possible to make Faraday rotation measurements.

For the tests whose results are shown in Figures 5, 6, and 7, ionospheric soundings were made by United States Army Signal Radio Propagation stations. These were reduced to true height profiles by the RCA Range Operations Division at Patrick Air Force Base by a modification of the '10 point method' described by Schmerling [1958], due to Wright and Knecht of NBS.

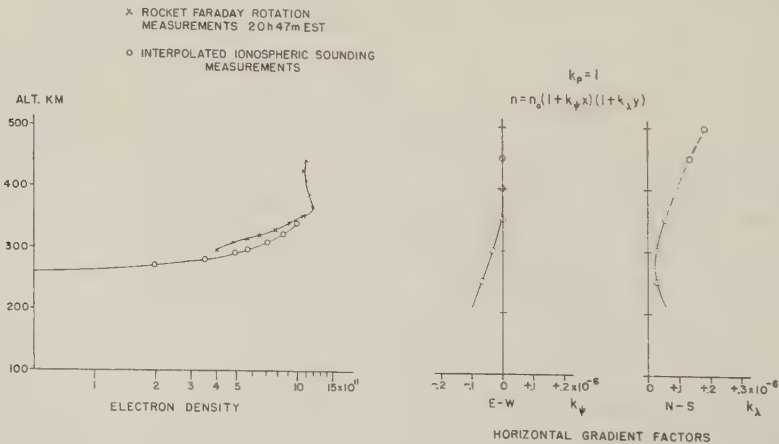


Fig. 4. Electron-density measurements for 20h 47m EST, May 6, 1959.

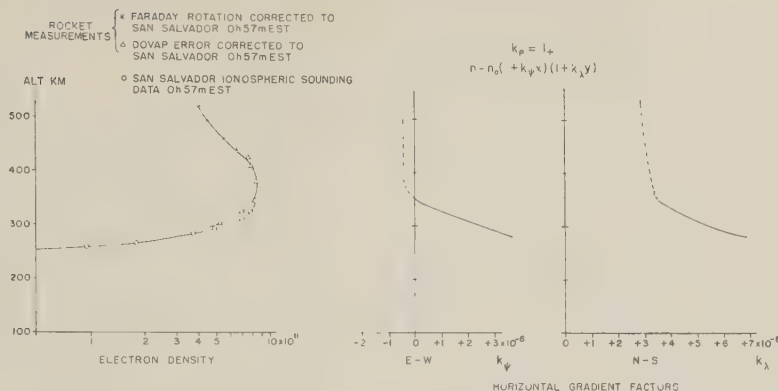
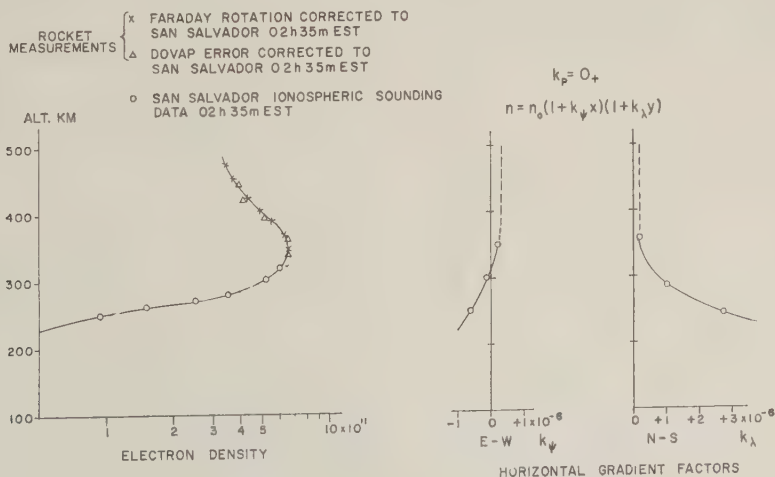


Fig. 5. Electron-density measurements for 0h 57m EST, May 14, 1959.

Fluctuations with periods less than 15 minutes and amplitudes of about 10 km were noticed in the altitude indicated by the reduced ionograms. It is not known whether such fluctuations have an ionospheric origin or are introduced in the scaling or reduction processes. In either event they would be expected to affect the agreement between the missile and ionospheric sounding results. The horizontal gradient factors used to correct rocket measurements over oblique paths to an equivalent vertical electron-density profile cannot take account of such small-scale irregularities.

Since the most complete data are available for the four Jupiter B firings, these will be considered first.

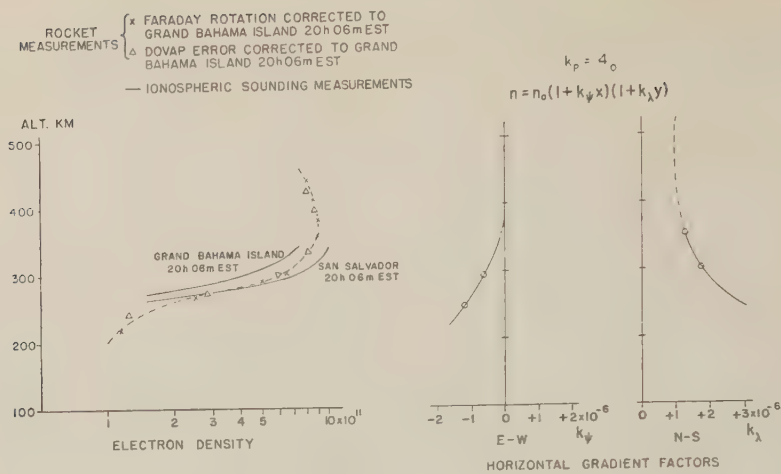
For the tests whose results are shown in Figures 4 and 7, lift-off occurred close to the time of ground sunset. The ionospheric sounding measurements invariably show a greater vertical gradient for electron densities below about $4 \times 10^{11} \text{ m}^{-3}$. The magnitude of this effect appears to be greater than can be accounted for by errors in the horizontal electron-density gradient determinations, and it is presumed to be due to group retardation in the lower layers. The height of the maximum as determined by the rocket measurements is a very uncertain parameter, but the ionospheric sounding method would be expected to give a height and density corresponding to the bottom of the more or less constant electron-density region. Actual heights



MAY 28, 1959

FIGURE 6-

Fig. 6. Electron-density measurements for 02h 35m EST, May 28, 1959.



JULY 9, 1959
FIGURE 7

Fig. 7. Electron-density measurements for 20h 06m EST, July 9, 1959.

and electron densities were found to be lower.

For the tests for Figures 5 and 6, lift-off occurred at 0h 57m and 2h 30m. No marked differences between the heights at lower electron densities were noticed. This is as would be expected, owing to the lower group retardation in lower layers at this time of night. The small Faraday rotation angles and the low quality of the range-error measurements make the check rather unreliable for these two experiments. In the region of the maximum electron density, the two methods are in good agreement for both missiles. It is apparent, however, that the height of the maximum electron density of the layer measured by the rocket is 20 to 40 km greater than would be predicted from the ionospheric sounding measurements.

For the test of Figure 2 lift-off occurred close to the time of ground sunrise. The electron densities measured by the two methods differ by about 15 per cent, but the heights of the electron-density maxima agree quite well. It should be remembered that the electron density is changing very rapidly at this time of day, and departures from the mean gradient factors used to correct the rocket measurements are to be expected. Some departure from the ionospheric sounding profile is also evident at lower altitudes. This is not considered to be significant, in view of the large electron-density gradients and the comparatively poor resolution of the Faraday rotation data in this region.

For Figures 1 and 3, the electron-density profiles from rocket and sounding measurements were not obtained for overlapping height ranges. The contents of the lower layers for the rocket measurements were also based on the sounding measurements. At least, it can be said that the profiles of the upper and lower *F* region, measured by the two methods, are not inconsistent.

A comparison of the electron densities and contents obtained by sounding and rocket measurements thus indicated, in general, quite good agreement. At low electron densities, greater heights were deduced from ionospheric soundings than were indicated by the rocket measurements. For the four most accurate rocket measurements, all of which were made at night, the height of maximum electron density was found to be greater than was indicated by the sounding data.

It should be pointed out that a disagreement on the height of the maximum as measured by the two methods does not necessarily imply a fault in the reduction procedure. From an examination of the DOVAP error records used to determine the profile shown in Figure 7, fluctuations in the electron content along the ray path were noticed which could be interpreted as an irregular structure of the electron-density-height profile. If such irregularities occur, the ionospheric sounder would record the height of the lowest maximum. The rocket Faraday rotation measurements would not resolve this fine struc-

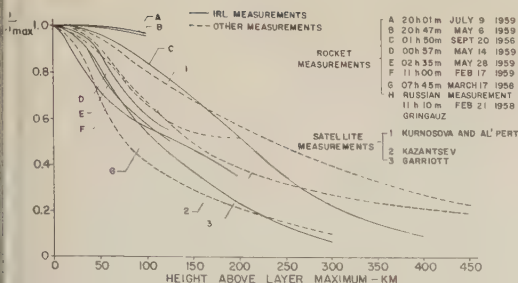


Fig. 8. Normalized electron-density profiles from rocket and satellite measurements.

ture and would indicate a greater altitude for the maximum, defined as the average of the upper and lower altitudes at which the electron density dropped to 0.9 of the maximum value for the layer.

Diurnal variation. Figure 8 shows normalized electron-density-height profiles derived from rocket results. The ratio of the electron density to the maximum electron density of the layer is plotted as a function of height above the maximum. This form of presentation is convenient for comparing results with various ionospheric models, but it is apparent that considerable diurnal and other variations are present.

Normalized profiles for the upper ionosphere derived from satellite measurements by Garriott [1960], Kurnosova and Al'pert [1958], and Kazantsev [1959] are also shown for comparison purposes. The rocket results show a rather wide spread, in general, but, with the exception of the two early-evening firings, lie between the profiles of Kurnosova and Al'pert and those of Kazantsev. The average rate of decrease above the maximum was found to be greater than that obtained by Garriott, perhaps because of the different methods used for the determination of $h_{\text{max}}F_2$.

The main feature observable in the diurnal variation is the percentage vertical gradient of electron density. In order of increasing gradient, the measurements correspond to shortly after sunset, night, midmorning, and shortly after sunrise. The vertical gradients are thus greater at times when the electron density at the maximum is increasing, and less at times when it is decreasing. This suggests that the observed diurnal variation can be explained as a time lag in the upper regions before diffusive equilibrium is reached. Particularly large departures from

the average percentage vertical electron-density gradients were observed for firings at 20h 1m and 20h 47m. As the k_p indices were 4₀ and 1₊, and the profiles measured were quite similar, the layer thickness does not appear to be due to a magnetic-storm effect. For these two tests the missiles were fired shortly after ground sunset, for optical tracking purposes, so that at high altitudes the missile would be sunlit against a dark background. Conditions were such, therefore, that the upper ionosphere was sunlit while the lower levels were in darkness. Since electron contents for the layer measured by moon echoes [Evans, 1957] and satellites [Garriott, 1960] indicate a smooth decrease at around the local time of these firings, the vertical electron-density gradient must increase at altitudes not greatly in excess of the maximum measured in our experiments.

A knowledge of the diurnal changes in electron density and electron column contents over a given height range in the upper ionosphere is of considerable importance in the understanding of the processes that occur there. Such information is not readily available from measurements of the diurnal change in the electron contents above the maximum of the F layer, for the lower boundary of the measurement is itself a variable. Figure 9 shows the electron content measured between 400- and 500-km altitude. A large diurnal change may be observed, which is somewhat different from that for the peak electron density also plotted in this figure. The maximum content appears to occur at around 16 hours, but of course many more measurements would

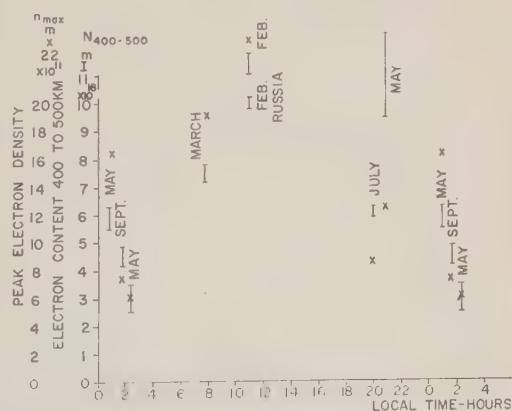


Fig. 9. Electron content from 400 to 500 km and peak electron density as a function of local time.

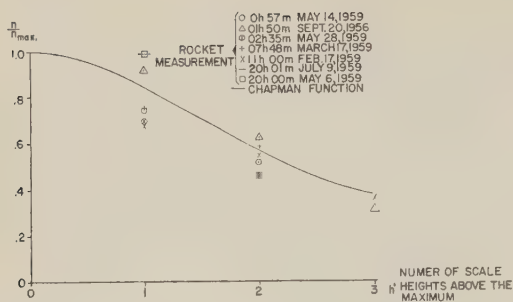


Fig. 10. Electron-density variation with number of scale heights above the maximum.

be required before definite statements could be made about such an effect.

Relation of the results to an atmospheric model. If an atmospheric model is assumed, the relative electron densities shown in Figure 8 may be plotted in terms of number of scale heights above the maximum. This has been done in Figure 10 for the seven rocket measurements, using a recent model of the neutral atmosphere given by Kallman [1959]. The scale height is itself altitude dependent, and an iterative procedure was used to determine the altitudes one, two, and three scale heights above the maximum.

When this form of presentation is compared with that of Figure 9, it is apparent that the spread between measurements at different times of day has been reduced considerably. As an example of this, the relative electron densities at two scale heights above the maximum have a spread of ± 19 per cent of the average value whereas the corresponding spread at 150 km above the maximum is ± 39 per cent.

For comparison purposes the Chapman relation,

$$N = N_{\max} \exp [1 - h' - \exp(-h')]/2$$

where h' is the number of scale heights above the maximum, may be plotted on the same axes. This has been done in Figure 10, and it is apparent that this relation is in reasonable agreement with the mean value of results when allowance is made for experimental inaccuracy and the diurnal variation.

Acknowledgment. The research reported in this paper was sponsored by the Guidance and Control Laboratory of the Army Ballistic Missile Agency under contract DA-36-061-ORD-577.

REFERENCES

- Evans, J. V., The electron content of the ionosphere, *J. Atmospheric and Terrest. Phys.*, **11**, 259, 1957.
- Garriott, O. K., The determination of ionospheric electron content and distribution from satellite observations, part 2, Results and analysis, *J. Geophys. Research*, **65**, 1151-1157, 1960.
- Kallman, H. K., A preliminary model atmosphere based on rocket and satellite data, *J. Geophys. Research*, **64**, 615-623, 1959.
- Kazantsev, A. N., Absorption and electron distribution in F_2 layer determined from measurements of transmitted signals from earth satellites, *Planetary and Space Sci.*, **1**, 130-135, 1959.
- Kurnosova, L. V., and Ia. L. Al'pert, Certain results of research performed using artificial earth satellites, *Priroda*, **n6**, 85, 1958; *Translation Physics Express*, **1**, 32, September 1958.
- Schmerling, E. R., An easily applied method for the reduction of h-f records to N-h profiles including the effects of the earth's magnetic field, *J. Atmospheric and Terrest. Phys.*, **12**, 8-16, 1958.

(Manuscript received August 11, 1960.)

The Geomorphology of Spread F

D. G. SINGLETON

*Physics Department
University of Queensland
Brisbane, Australia*

Abstract. An analysis has been made of reliable spread- F data obtained from IGY f plots for ionosonde stations grouped about longitudes 75°W and 120°E . The temporal variations of occurrence of the frequency-spreading component of spread F are found to change with latitude, these changes having a certain symmetry about the geomagnetic equator rather than about the geographic or dip equators. Four regions with different occurrence characteristics appear: two are regions of high activity, the auroral and equatorial regions; and the other two are regions of lower activity, the middle latitude and polar regions. The season of minimum occurrence in the equatorial region changes from the northern summer solstice in the American zone (75°W) to the southern summer solstice in the Far Eastern zone (120°E). This longitude effect, which led Reber to postulate the existence of a spread- F equator, is shown to be due to the interaction of some form of direct or indirect solar control with the magnetic control of the incidence of the phenomenon.

1. INTRODUCTION

Examination of the literature dealing with the phenomenon of spread F shows that workers in different parts of the world have arrived at seemingly conflicting results, especially in respect to the temporal variations of occurrence of the phenomenon. Several attempts have been made to systemize the occurrence data so as to produce a consistent world-wide picture of the behavior of spread F . The first of these [Reber, 1954, 1956] sought to resolve the problem by postulating the existence of a spread- F equator, a line of demarcation between those places on the earth's surface which experience an occurrence minimum in the northern summer solstice (hereafter referred to as the northern solstice) and those which experience a minimum in the southern summer solstice (hereafter referred to as the southern solstice). More recently Shimazaki [1959] has considered the occurrence of the spread- F phenomenon at a large number of stations throughout the world and has deduced evidence that supports Reber's contentions. Shimazaki, in examining the latitude variation of occurrence, lumped together the data from all his stations. This leads to a considerable scatter of points, which is undoubtedly due to the contamination of the latitude effects by the longitude effects. This paper proposes to re-examine the results using data from stations

within two fairly narrow strips of longitude; in this way it is hoped to isolate the latitude effects and, by comparing the results for the two strips, to make some estimate of any longitude effect.

Section 2 begins by examining the basis of the collection and reduction of the data; section 3 discusses the latitude dependence of occurrence in different seasons in the two zones of longitude. In the light of conclusions reached here, the variations of the diurnal and seasonal distributions with latitude are considered in sections 4 and 5, respectively. The significance of the results obtained is then discussed in section 6.

2. SOURCE OF DATA AND METHOD OF REDUCTION

Selection of stations. Two factors that might reasonably be expected to play a part in the incidence of spread F are the geographic position of the observing station and the magnetic-field situation over the station. Consequently, the two groups of stations listed in Table 1 have been chosen for analysis. The first group, defined by $75^\circ\text{W} \pm 25^\circ$ (hereafter referred to as the American zone), and the second, defined by $120^\circ\text{W} \pm 20^\circ$ (hereafter referred to as the Far Eastern zone), correspond approximately to the regions of longitude for which the deviation between geographic and geomagnetic latitude is a maximum.

TABLE 1. Locations of Stations Whose *f*-Plot Data Have Been Used

Station	Geographic		Geomagnetic		Dip
	Latitude	Longitude	Latitude	Longitude	
American Zone					
Alert	82.6°N	297.4°E	85.0°N	160.0°E	86.1°
Thule, Greenland	76.6°N	291.3°E	87.0°N	355.0°E	87.0°
Resolute Bay, Canada	74.7°N	265.1°E	83.0°N	289.4°E	89.0°
Clyde River, Canada	70.5°N	291.4°E	81.9°N	340.0°E	84.5°
Baker Lake, Canada	64.3°N	264.0°E	73.7°N	315.5°E	86.6°
Churchill, Canada	58.8°N	265.8°E	68.7°N	322.8°E	83.9°
Winnipeg, Canada	49.9°N	262.6°E	59.8°N	322.9°E	77.7°
St. Johns, Canada	47.6°N	307.3°E	58.4°N	21.4°E	72.3°
Ottawa, Canada	45.4°N	284.3°E	56.9°N	351.5°E	75.5°
Ft. Monmouth, U. S. A.	40.3°N	285.9°E	51.0°N	354.0°E	72.0°
Washington, U. S. A.	38.7°N	282.9°E	50.0°N	350.8°E	72.0°
White Sands, U. S. A.	32.3°N	253.5°E	41.2°N	317.0°E	62.0°
Grand Bahama	26.6°N	281.6°E	37.8°N	351.6°E	61.0°
San Juan, Puerto Rico	18.5°N	292.8°E	29.9°N	2.1°E	51.0°
Panama	9.4°N	280.1°E	20.6°N	348.6°E	38.0°
Talara, Peru	4.6°S	278.7°E	6.6°N	350.0°E	13.0°
Chiclayo, Peru	6.8°S	280.2°E	4.4°N	350.2°E	9.0°
Chimbote, Peru	9.1°S	281.4°E	2.2°N	350.4°E	6.5°
Huancayo, Peru	12.0°S	284.8°E	0.6°S	354.0°E	1.0°
São Paulo, Brazil	23.4°S	314.9°E	12.8°S	22.5°N	20.1°
Buenos Aires, Argentina	34.5°S	301.5°E	23.1°S	9.5°E	30.0°
Port Stanley, Falkland Is.	51.7°S	302.3°E	40.4°S	12.8°E	47.0°
Ellsworth, Antarctica	77.7°S	318.9°E	68.9°S	15.0°E	65.0°
Far Eastern Zone					
Wakkanai, Japan	45.4°N	141.7°E	35.2°N	206.1°E	61.0°
Akita, Japan	39.7°N	140.1°E	29.4°N	205.5°E	55.0°
Kokumbunji, Japan	35.7°N	139.5°E	25.4°N	205.5°E	49.0°
Yomagawa, Japan	31.2°N	130.6°E	20.3°N	197.9°E	48.0°
Okinawa, Ryuku	26.3°N	127.8°E	15.2°N	195.7°E	44.0°
Taipei, Formosa	25.0°N	121.5°E	14.0°N	189.0°E	31.0°
Baguio, Philippine Is.	16.4°N	120.6°E	5.0°N	189.3°E	21.0°
Singapore, Malaya	1.4°N	103.7°E	10.0°S	172.7°E	18.0°

Method of obtaining data. In order to compare the occurrence data of one station with those of another it is essential that the two sets of data be derived in the same way; that is to say, similar phenomena at the two stations must be similarly interpreted. The only way of being sure that this condition is fulfilled is to have one observer examine the ionograms from both stations. Where a large number of stations is involved this process becomes prohibitive, not only because of the amount of work entailed but also because of the difficulty of gaining access to all the ionograms involved. Previous workers [Reber, 1954, 1956; Wright, Koster, and Skinner, 1956; Wright and Skinner, 1959; Shimazaki, 1959] have attempted to overcome this difficulty

by utilizing the *F* notations used in conjunction with the published tabulated values of *f_oF₂*. These notations are aimed at giving an estimate of the difficulty in reading *f_oF₂* because of the presence of the frequency-spreading component of spread *F* [Singleton, 1957]. This procedure, however, is likely to lead to some falsification of the data, for the following reasons. The phenomenon is present to some extent during most of the day and night in the auroral and polar regions, and observers there are likely to be overoptimistic about their ability to read *f_oF₂* in the presence of light spreading. On the other hand, observers in the middle-latitude regions, where the spreading phenomenon is rather rare, are likely to be pessimistic about their ability to

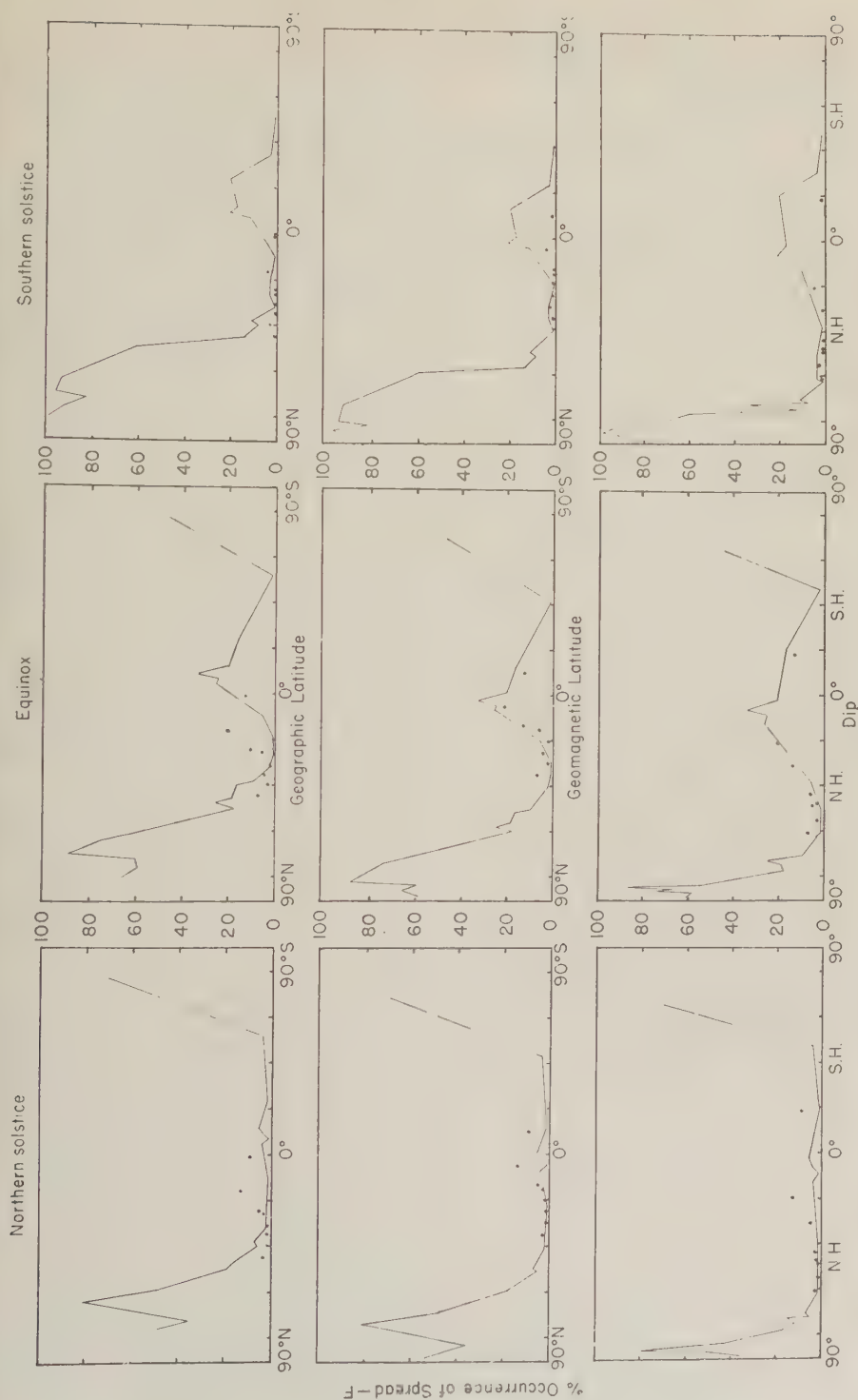


Fig. 1. The variation of the percentage occurrence of the frequency-spreading component of spread F with geographic latitude, geomagnetic latitude, and dip. The full-line curves represent the situation in the American zone; the isolated points give the Far Eastern-zone variation.

read f_oF_2 when light spreading is present. This results in estimates of occurrence which could be low for the higher latitudes and possibly slightly high for the middle latitudes.

Another criticism that may be leveled at the F' -notation method of gaining data is that it is based solely on ionograms made on the hour. That is to say, if the phenomenon appeared shortly after the hour and disappeared a little before the next hour, it would not be recorded in the tabulations even though its presence was evident on the ionograms made between those taken on the hour.

The daily f plots prepared by a large number of ionosonde stations during the IGY offer a very satisfactory compromise between the actual records and the tabulations of f_oF_2 as far as the gathering of frequency-spreading data is concerned. Each f plot [Wright, Knecht, and Davies, 1957] is essentially a plot of the variation of both the o -ray and x -ray penetration frequencies against local time at a particular station. Data from all the ionograms made, not just the hourly ones, are included in the f plots. On these, frequency spreading is indicated by a line parallel to the frequency axis at the appropriate local time. The lower extremity of this line gives the low-frequency boundary of the penetration, and the length of the line indicates the extent of the frequency spreading. Consequently, if the several observers have conformed to the IGY recommendations, the f plots should constitute a concise statement of the frequency-spreading data which is more objective than that obtained from the tabulated values of f_oF_2 .

Method of reduction of data. In computing the occurrence statistics an interval of an hour beginning on the hour was used. If, at any time during an hour, the presence of frequency spreading was indicated on an f plot in the manner mentioned above, that hour was counted as one in the statistics. Hours free of frequency spreading were counted as zero. In the diurnal and seasonal distributions to be discussed in this paper the concept of percentage occurrence is used. This is defined as the ratio, expressed as a percentage, of the number of hours frequency spreading was present to the total number of hours available for analysis at any particular time, for a diurnal distribution; or month, for a seasonal distribution.

3. LATITUDE DEPENDENCE OF THE OCCURRENCE DATA

To determine the main controlling factor in the latitude variation of the occurrence of frequency spreading, the monthly percentage occurrence at each of the American-zone stations has been plotted against its geographic latitude, geomagnetic latitude, and dip. Figure 1 shows the curves that result for July and September 1957, and for January 1958, which represent typical months of the northern solstice, equinox, and southern solstice. The isolated points on these curves represent the eight stations of the Far Eastern zone.

The first point to be made from Figure 1 is that the three American-zone distributions are only symmetrical about the geomagnetic equator. In the geographic plots the only possible axis of symmetry is displaced about 10° to the south of the geographic equator. The dip plots show that in the vicinity of the dip equator there is some semblance of symmetry about this equator. This symmetry, however, is not evident near the dip poles. When the data of the Far Eastern zone are considered in relation to the American-zone distributions, we see immediately the impossibility of the latitude dependence being a geographic one. The Far Eastern-zone geomagnetic and dip variations show much the same properties, as far as symmetry is concerned, as their American-zone counterparts. However, while the scales of the variations for the two zones agree for the equinox plots, this is far from the case in the two sets of solstice plots.

It appears then that a distribution that is symmetrical everywhere can be obtained only in relation to the geomagnetic equator, while in a limited region about the geomagnetic equator a distribution in terms of dip also appears to be symmetric. This suggests some magnetic control of the phenomenon, the nature of which may differ in the vicinity of the equator from that which exists elsewhere.

The general shape of the variation with geomagnetic latitude is also of interest. Three regions of maximum occurrence appear, one between 50° and 80° geomagnetic in both hemispheres and another between 20°N and 20°S geomagnetic. There is a pronounced minimum in the middle-latitude region of 20° to 50° geo-

magnetic in both hemispheres and a weak tendency for another to occur at the poles between 80° and 90° geomagnetic. It would seem convenient, therefore, to divide each geomagnetic hemisphere into four regions, the polar region extending from the geomagnetic pole to 80° geomagnetic, the auroral region from 80° to 50° geomagnetic, the middle-latitude region from 50° to 20° geomagnetic, and the equatorial region within 20° of the geomagnetic equator. In each of these regions, the incidence of frequency spreading is different and, as the following discussion and subsequent papers will show, the phenomenon has different properties.

The range-spreading component of spread F [McNicol, Webster, and Bowman, 1956] has also been shown to vary with geomagnetic latitude [McNicol and Bowman, 1957]. Its percentage occurrence distribution peaks at about 20° and falls off very quickly to small values at the equator, but decays more slowly to small values at 50° . The distributions of the two components of spread F are thus complementary, the range-spreading effect appearing mainly in the middle latitudes, where the frequency spreading effect is not so common. This limited distribution of range spreading and the more universal nature of frequency spreading may explain why many authors [e.g., Briggs, 1958; Wright, Koster, and Skinner, 1956; Shimazaki, 1959] make no mention of the range-spreading effect when discussing spread F .

Attention was drawn earlier to the fact, revealed by Figure 1, that, although the Far Eastern-zone data fitted the American-zone variation with geomagnetic latitude quite well for the equinox, no fit could be obtained for either solstice in the equatorial region. For each of the solstices the general trend of the Far Eastern-zone variation is the same as for the American zone, but the amount of spreading in the equatorial regions of the two zones is different. This implies the existence of a longitude effect, at least in the equatorial region.

In the southern solstice the American-zone equatorial region experiences much more spreading than the Far Eastern zone, whereas the reverse is true in the northern solstice. It will be noted that, for each region of longitude, the solstice that has the largest occurrence is the one for which the sun is on the side of the geographic equator that contains the geomagnetic

equator. This immediately suggests some solar control of the phenomenon, at least in the equatorial region, and it would appear that the longitude effect mentioned above is the result of the conflict between this solar control and the geomagnetic control.

4. DIURNAL DISTRIBUTIONS

The conclusion having been reached that the occurrence of frequency spreading varies with geomagnetic latitude, it will be of interest to examine how the diurnal variations of occurrence change with geomagnetic latitude. Figures 2a, b, and c represent the geomagnetic latitude variations of the American-zone diurnal distributions, for the northern solstice, equinox, and southern solstice. They have been drawn as contours of equal percentage occurrence on a graph of local time against geomagnetic latitude. The contours are based on an interval of 10 per cent. Also the diagrams contain the sunrise and sunset lines at ground level and at 300 km. Because of the lower station density there is some doubt about the authenticity of the contours in the southern hemisphere. Where the station density allows a reasonable estimate of the contours in this hemisphere, they have been included as dashed lines; they have been omitted where such estimates are not possible. In Figures 2a and 2b the points and attached percentages at 69°S indicate the positions the appropriate contours would take up in this region.

From evidence presented in section 3 it seems that there is little solar control of the occurrence of the phenomenon during the equinox; consequently the equinox situation, Figure 2b, will be considered first. The auroral and equatorial regions of high incidence are immediately obvious. In the equatorial region the phenomenon is a night-time one, occurring between 1900 and 0800 hours. The incidence reaches maxima of 80 per cent at 2200 hours at 3°N geomagnetic and 0430 hours at 4°N geomagnetic, the 2200 hours maximum being spread more in both latitude and time. Interestingly, these peaks are not on the geomagnetic equator but displaced from it toward the north, that is toward the geographic equator. The existence of similar maxima to the south of the geomagnetic equator appears unlikely from the data, but the station density is such that this possibility cannot be definitely eliminated. If these southern maxima

do not exist it would appear that there is some solar control in the equatorial region during the equinox.

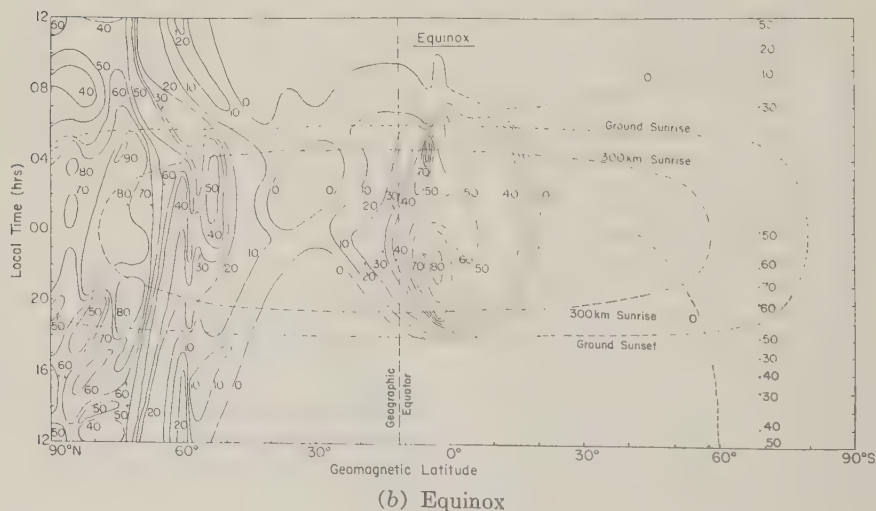
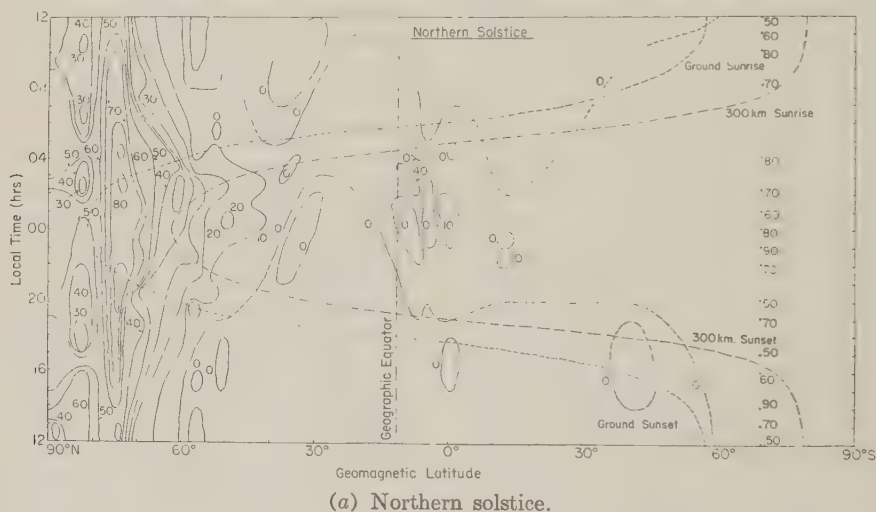
The middle-latitude region experiences little frequency spreading, and the phenomenon is confined to the nighttime hours.

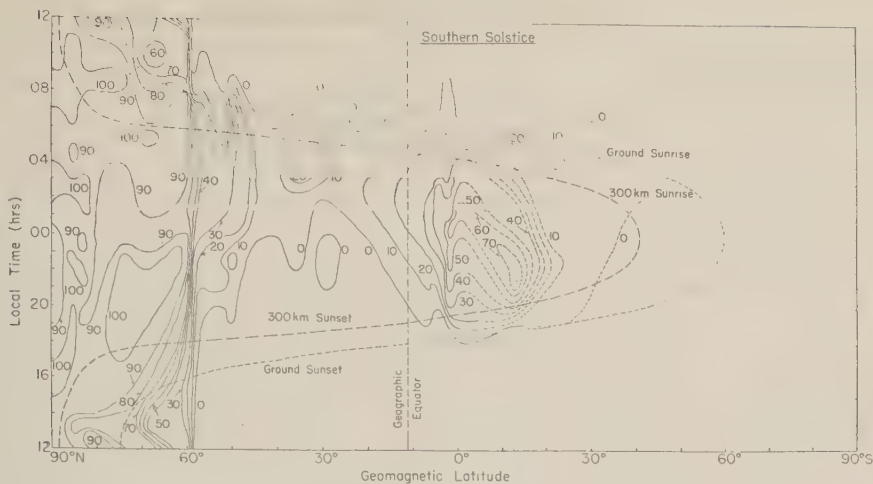
Between 50° and 70° geomagnetic there is a rapid increase in the incidence of frequency spreading. The increase is first noticed about 0200 hours between 50° and 55° geomagnetic, but at higher latitudes it develops into a general increase in occurrence with increasing latitude independently of local time. The maximum occurrence in the auroral region appears between 70° and 80° geomagnetic for all values of local

time and is 90 per cent at 0430 hours at 75° geomagnetic.

Above about 80° geomagnetic the incidence falls off for all values of local time. The drop is most pronounced during the daylight hours, for which the incidence decreases to values as low as 40 per cent at the geomagnetic pole.

Transferring our attention now to the northern solstice situation, Figure 2a, we notice two striking dissimilarities between this and the equinoctial situation. First, there are considerably fewer occurrences in the equatorial regions during the northern solstice; the incidence never reaches the 20 per cent level. Second, whereas in the auroral region the latitude of maximum





(c) Southern solstice.

Fig. 2. The variation of the diurnal distribution of the occurrence of the frequency-spreading component of spread F with geomagnetic latitude.

occurrence is again about 75° geomagnetic in the northern solstice, the decrease in occurrence with increasing latitude above this value is much more pronounced. A minimum is attained at about 82° geomagnetic rather than at the pole itself. The northern solstice is similar to the equinox as far as the rapid rise of occurrence between 50° and 70° geomagnetic is concerned.

On examining the southern solstice diagram, Figure 2c, we find yet another set of circumstances with regard to the situation in both the equatorial and auroral regions. The incidence in the equatorial region reaches the 70 per cent level, which is comparable with the maximum attained in the equinox, but unlike the equinox maximum the southern solstice maximum is south of the geomagnetic equator by some 13° . The southern solstice auroral region comes into being via a very rapid increase in occurrence with latitude at 60° geomagnetic. Here the percentage occurrence increases by amounts of 40 per cent or more over a range of 2° independently of local time. Further, there is little or no decrease in occurrence as one approaches the pole. In this region there are several large areas of time-latitude space corresponding to occurrence at the 100 per cent level.

Looking at the over-all picture presented by the three diagrams of Figure 2 we see that, although the phenomenon is not universally a nighttime one, the areas of major occurrence fall within the ground sunset and sunrise lines.

Occurrences during the daylight hours are found in any quantity only in the auroral and polar regions.

5. SEASONAL DISTRIBUTIONS

Figure 3 displays the variation of the seasonal distribution of occurrence with latitude for the American-zone stations between June 1957 and February 1958. The figure consists of a series of contours of equal percentage occurrence on a graph of months against geomagnetic latitude. An interval of 10 per cent has been used. Again, only the contours justified by adequate station density have been included in the southern hemisphere. The points and attached percentages at 69° S indicate the positions the appropriate contours would take in this region. The dotted line represents the path of the sun during the months considered.

The two regions of maximum occurrence, the equatorial and auroral regions, are immediately obvious. The equatorial region has an occurrence maximum in September, that is, in the equinox, and a minimum in June–July which corresponds to the northern solstice. It will be noted that the equatorial maximum lies a few degrees north of the geomagnetic equator, a result foreshadowed in section 4. Note also the previously mentioned (section 4) submaximum in January at about 13° S geomagnetic. In the equatorial region of the Far Eastern zone an equinoctial maximum is also experienced. The

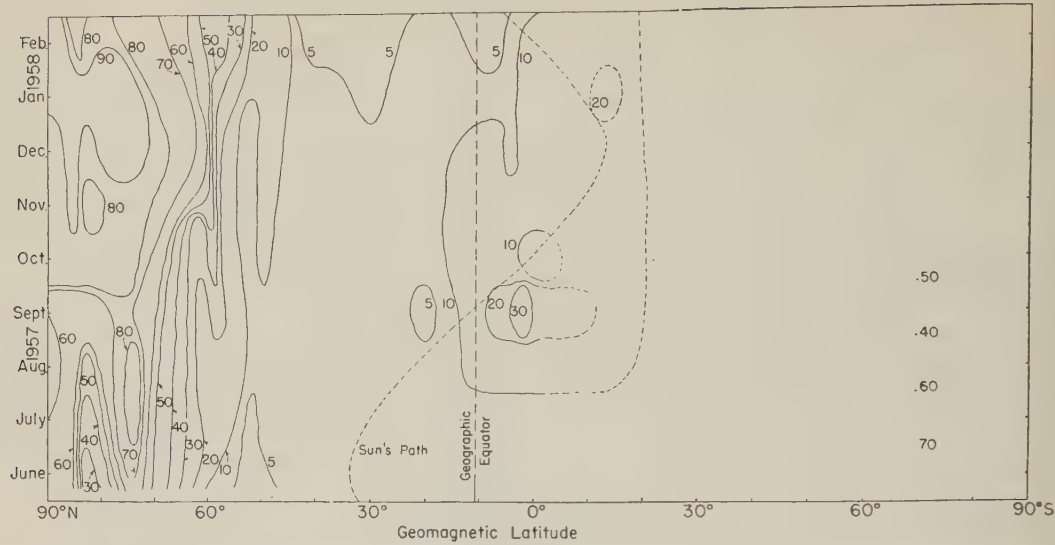


Fig. 3. The variation of the seasonal distribution of the occurrence of the frequency-spreading component of spread F with geomagnetic latitude.

station density in this zone is such that the exact position of this maximum cannot be determined, but it is certainly close to the geomagnetic equator (Fig. 1). In contrast to the American zone, the Far Eastern-zone equatorial region experiences a minimum in the southern solstice.

Generally speaking, the northern auroral region appears to experience a minimum in June, the northern solstice, and a maximum in December-January, the southern solstice. Between 70° and 80° geomagnetic there is a submaximum in July-August followed in September by a slight depression before the main December-January maximum is attained. As we move from the auroral region into the polar region, the July-August submaximum disappears and the region experiences a minimum in June and a maximum in December-January.

The frequency of occurrence in the middle latitudes is so low that a seasonal variation is difficult to detect, but there appear to be some signs of a minimum about February. This is consistent with results for middle-latitude stations reported earlier [Singleton, 1957].

6. DISCUSSION

In connection with the magnetic control of the occurrence of frequency spreading it is of interest to consider the variation of dip with height at different latitudes. Figure 4 illustrates

this variation for each of the geographic latitudes 60°N , 10°S , and 60°S at a longitude appropriate to the American zone, namely 90°W . The dashed curves give the variations of the actual dip with height. These curves are based on the results of a spherical harmonic analysis of the earth's field by Vestine, Laporte, Lange, and Scott [1947]. They show that the dip undergoes a change of several degrees over the height range 0 to 5000 km, but the value of the dip at F -region heights differs from the ground value by only about a degree. The centered dipole approximation to the earth's field suggests that the dip should be constant at the ground value at all heights [Chapman, 1951]. This is illustrated in Figure 4 by the full vertical lines. It is seen immediately that for this longitude the centered dipole approximation represents the actual dip situation for F -region heights only near the geomagnetic equator. At high latitudes the dipole approximation predicts the inclination of the earth's field only at great heights. We have seen that for the high latitudes the geomagnetic distribution of occurrence is symmetrical rather than the distribution based on ground dip. On the other hand, in the equatorial region there is little to choose between the geomagnetic and dip variations of occurrence as far as symmetry is concerned. This suggests that if the property of the field that causes it to control the occurrence of fre-

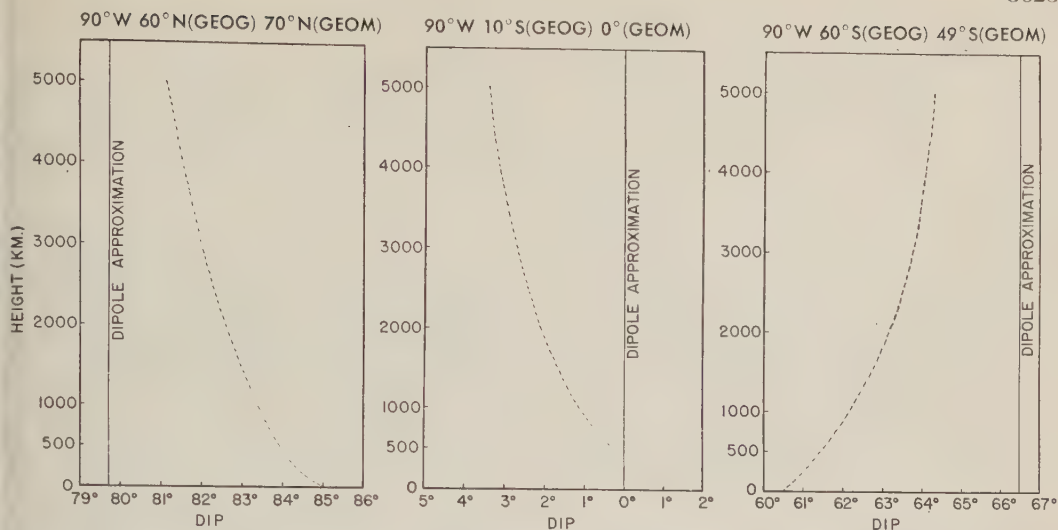


Fig. 4. The variation of dip with height for each of the geographic latitudes 60°N, 10°S, and 60°S at a longitude of 90°W.

quency spreading is the direction of the lines of force, and indeed it is difficult to see what other property could be involved, then in the equatorial region the field in the *F* layer is of importance, whereas at higher latitudes the state of the field at great heights is the important factor.

If this reasoning is accepted the form of the asymmetry of the distribution of occurrence with ground dip in the auroral regions can also be explained. Figure 4 shows that in the northern hemisphere the ground dip is greater than that at great heights but in the southern hemisphere the reverse is true. Consequently, a distribution symmetrical in terms of the dip at great heights will be shifted bodily toward higher values of dip in the northern hemisphere and lower values in the southern hemisphere when plotted against ground dip. Figure 1 shows that this is exactly the nature of the asymmetry of the dip plots. That the geomagnetic latitude and the dip are about equally successful in providing symmetrical distributions in the equatorial region is explained by the fact that the actual direction of the field in the *F* layer is closely approximated here by both the centered dipole and the dip as measured on the ground.

The fact that frequency spreading does experience diurnal and seasonal variations of occurrence implies that the phenomenon is subject to some degree of solar control. The nature of this control is most easily determined for the

regions of maximum occurrence, namely the auroral and equatorial regions.

Examination of the diurnal distributions of occurrence for the auroral regions shows a marked fall-off in percentage occurrence for those times of the day when the ionosphere is sunlit. This point is also illustrated by the seasonal variations which reveal that the incidence is at a minimum in a particular auroral region when the sun is over the same hemisphere as the region and a maximum when the sun is over the opposite hemisphere. This leads to the conclusion that in the auroral regions solar illumination tends to inhibit the occurrence of frequency spreading.

In the equatorial region we find that while the phenomenon is strictly a nighttime one its incidence is at a minimum at the time of the year when the sun is on the side of the geographic equator remote from the geomagnetic equator. That is to say, the incidence is at a minimum when the sun is as far as it can possibly be from the geomagnetic equator, indeed, from the equatorial region. Frequency spreading occurs to any appreciable extent only for that time of the year when the sun is passing over the equatorial region, suggesting that, in the equatorial region, the presence of the sun directly or indirectly promotes frequency spreading but not to the extent of causing daylight occurrences. This is in direct contrast to the

solar-control situation in the auroral region.

The existence of the longitudinal effect in the equatorial seasonal distribution referred to in section 3 can now be seen to be the result of the interplay of the magnetic and solar controls. If the monthly incidence along a particular line of geographic latitude is considered, a nonuniform distribution will be found simply because of the changes in geomagnetic latitude along such a line. On the other hand, if the incidence along a line of geomagnetic latitude is considered, a nonuniform distribution will occur because of the continually changing solar control.

The spread- F equator postulated by Reber is considered to be real and the logical result of the solar and magnetic control of the incidence of frequency spreading. The northern auroral region experiences an occurrence minimum in the northern solstice because it is then sunlit. At this time the equatorial region experiences a minimum only in the vicinity of the American zone. This is the result of the absence of the sun over the part of the equatorial region south of the geographic equator. In the southern solstice similar reasoning shows that minima will occur in the southern auroral region and in the equatorial region in the vicinity of the Far Eastern zone. Consequently, the line of demarcation between places that experience a minimum in the southern solstice and places that experience a northern solstice minimum, i.e., the spread- F equator, will pass south of the geomagnetic equator over the American zone and north of the geomagnetic equator over the Far Eastern zone. This is consistent with the position of the spread- F equator suggested by Reber [1956].

This investigation of the temporal variations of frequency spreading, though demonstrating the existence of magnetic and solar control of its incidence, provides only the following meager facts about the exact mechanisms involved.

1. Some property of the earth's magnetic field is critical. It appears most likely that it is the direction of the lines of force in the F layer in the case of the equatorial region and this direc-

tion at much greater heights in the case of higher latitudes.

2. Solar illumination appears to inhibit frequency spreading in the auroral zone; in the equatorial zone the presence of the sun overhead during the day is associated with a high incidence by night.

These two results appear to suggest that the mechanisms responsible for the production of frequency spreading are different in the two regions of maximum occurrence, the auroral and equatorial regions. A study of how the other properties of the phenomenon vary with latitude could conceivably throw more light on the situation. Such studies are proceeding and will be reported in subsequent papers.

Acknowledgments. I should like to thank Professor H. C. Webster, Dr. J. A. Thomas, and Dr. R. W. E. McNicol for their helpful discussion during the preparation of this paper and Mrs. H. R. Egerton for her aid with the data reduction. Thanks are also due to the IGY Data Center A (CRPL of the NBS) and the Ionospheric Prediction Service for supplying the f -plot data.

REFERENCES

- Chapman, S., *The Earth's Magnetism*, Methuen and Co., London, 1951.
- Briggs, B. H., *J. Atmospheric and Terrest. Phys.*, **12**, 34, 1958.
- McNicol, R. W. E., and G. G. Bowman, *Australian J. Phys.*, **10**, 588, 1957.
- McNicol, R. W. E., H. C. Webster, and G. G. Bowman, *Australian J. Phys.*, **9**, 247, 1956.
- Reber, G., *J. Geophys. Research*, **59**, 257, 1954.
- Reber, G., *J. Geophys. Research*, **61**, 157, 1956.
- Shimazaki, T., *J. Radio Research Labs.*, **6**, 669, 1959.
- Singleton, D. G., *Australian J. Phys.*, **10**, 60, 1957.
- Vestine, E. H., L. Laporte, I. Lange, and W. E. Scott, *Carnegie Inst. Wash. Publ.* 580, Washington, D. C., 1947.
- Wright, J. W., R. W. Knecht, and K. Davies, *Ann. IGY*, **3**, 133, 1957.
- Wright, R. W., J. R. Koster, and N. J. Skinner, *J. Atmospheric and Terrest. Phys.*, **8**, 240, 1956.
- Wright, R. W., and N. J. Skinner, *J. Atmospheric and Terrest. Phys.*, **15**, 121, 1959.

(Manuscript received June 24, 1960.)

The D_1 , D_2 Layers and the Absorption of Radio Waves

G. C. RUMI

Geophysical Institute
University of Alaska
College, Alaska

Abstract. The dependence of nondeviative radio absorption with frequency is analyzed for the case of a dichotomic absorbing region that obeys specific conditions. Selected experimental data are shown to match the theoretical predictions. It is inferred that absorption measurements may be used to study the splitting of the ionospheric D region into two layers.

Introduction. Gardner and Pawsey [1953], and Bracewell and Bain [1952] deduced, from experiments based upon reflection of radio waves, the existence of a D_1 and a D_2 layer in the lower ionosphere. Pfister [1954] obtained a two-layer profile for the D region by combining different observational results. On the other hand, Appleton and Piggott [1954] in a very extensive study on ionospheric absorption deduced that absorption measurements are related to a single layer D region. The present study shows that even absorption measurements may indicate a two-layer structure in the D region of the ionosphere.

1. *Two-layer absorbing region.* In this section the expected behavior of the absorption as function of the frequency for a two-layer absorbing region is discussed.

The absorption coefficient in the D region is given by the well-known formula

$$K = \frac{5.3 \times 10^{-6}}{\mu} \cdot \frac{N\nu}{\nu^2 + (\omega \mp \omega_L)^2} \quad (1)$$

where

K = absorption coefficient.

μ = refraction index.

N = electron density.

ν = electron collision frequency.

ω = operating angular frequency.

ω_L = longitudinal component of gyromagnetic angular frequency.

$+$ is for ordinary component.

$-$ is for extraordinary component.

MKS units are used.

The electron collision frequency in the D region has the value shown in Figure 1 [from Table I, Kane, 1959]. On the basis of (1) and Figure 1 a dichotomic absorbing region should

be characterized by an absorption versus frequency relation similar to the one depicted in Figure 2.

Indeed

$$(\text{absorption})^{-1/2} = \frac{1}{\left[\int_{D_1} K_1 ds + \int_{D_2} K_2 ds \right]^{1/2}} \quad (2)$$

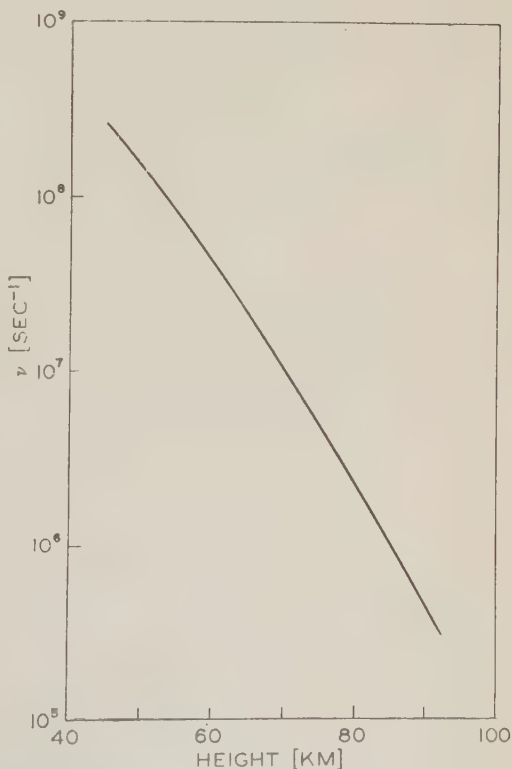


Fig. 1. Electron collision frequency vs. height.

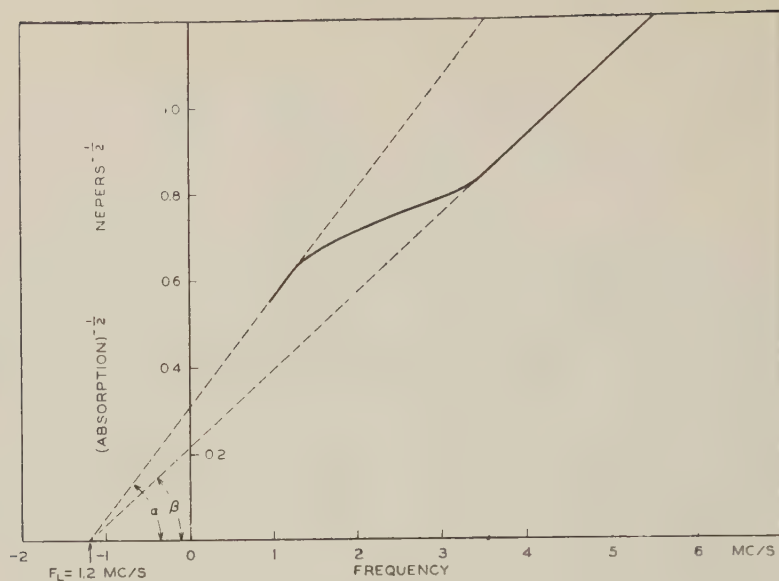


Fig. 2. $(\text{Absorption})^{-1/2}$ vs. frequency curve for two-layer absorbing region.

where the index 1 is for the lower layer D_1 , the index 2 is for the upper layer D_2 , and ds is the elementary path in the layers. At first sight only the ordinary component is considered since it is predominant. The layer D_2 is located above the layer D_1 , where the electron collision frequency is so small in comparison with the frequencies on which the present analysis is centered that it

can be neglected in the expression for the absorption coefficient. Provided that N_1 , ν_1 , N_2 , and ν_2 are such that

$$\int_{D_1} N_1 \nu_1 ds > \int_{D_2} N_2 \nu_2 ds$$

then the expression (2), in first approximation can be written as

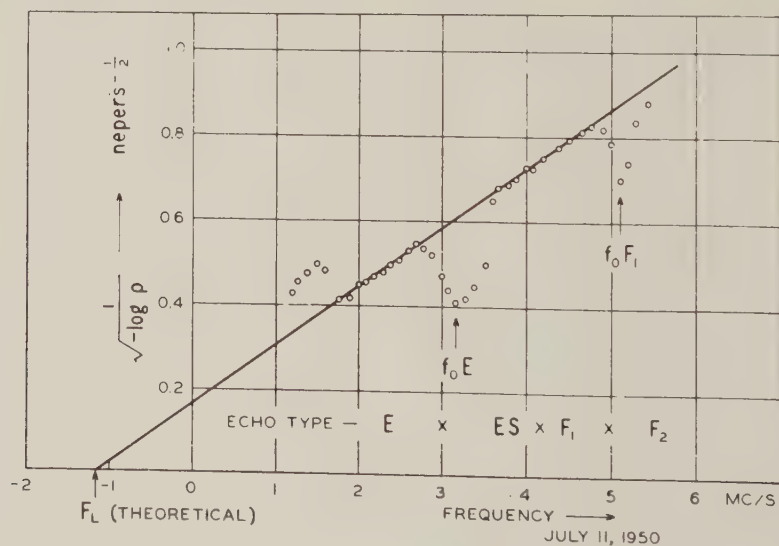


Fig. 3. Plot illustrating the variation of absorption with radio wave frequency; $(|\log \rho|)^{-1/2}$ is shown as a function of frequency f . From Appleton and Piggott.

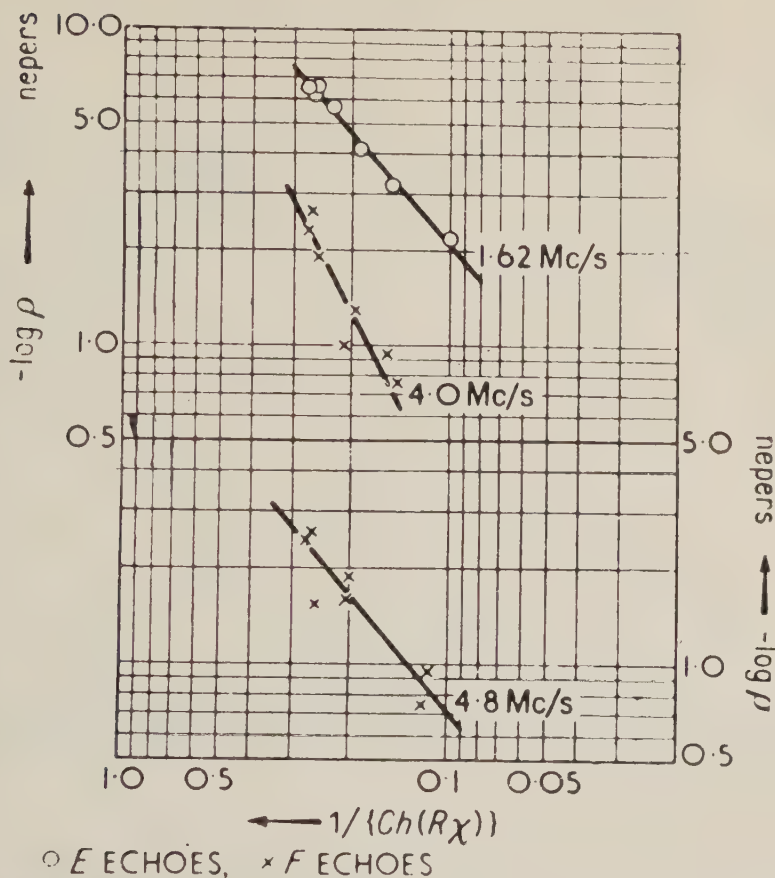


Fig. 4. Logarithmic plots of $|\text{Log } \rho|$ and $1/\text{Ch}(R\chi)$ for 1.6, 4.0, and 4.8 Mc/s on Dec. 17, 1948. From Appleton and Piggott. (For 4.8 Mc/s the scale is on the right side.)

$$(\text{abs})^{-1/2} = \frac{(\omega + \omega_L) \left(1 + \frac{\nu_1^2}{2(\omega + \omega_L)^2} \right)}{\left[C \int_{D_1} N_1 \nu_1 ds \right]^{1/2}} \quad (3)$$

for $(\omega + \omega_L) > \nu_1$

and

$$(\text{abs})^{-1/2} = \frac{(\omega + \omega_L) \left\{ 1 - \frac{(\omega + \omega_L)^2 \int_{D_1} \frac{N_1}{\nu_1} ds}{2 \int_{D_2} N_2 \nu_2 ds} \right\}}{\left[C \int_{D_2} N_2 \nu_2 ds \right]^{1/2}}$$

for $(\omega + \omega_L) < \nu_1$ and $(\omega + \omega_L) > \nu_2$

(4)

where

$$C = \frac{5.3 \times 10^{-6}}{\mu}$$

The graphical representation of (3) is a line whose slope keeps increasing with the frequency until it reaches the asymptotic value

$$\left[C \int_{D_1} N_1 \nu_1 ds \right]^{-1/2}$$

The graphical representation of (4) is a line whose slope keeps increasing as the frequency decreases. It follows that at some intermediate frequency, in the neighborhood of ν_1 , an inversion of curvature takes place; in other words, (2) presents a point of inflection. There the rate of change of the $(\text{absorption})^{-1/2}$ with frequency reaches a minimum. For a D_1 layer located around 70-km height such an inflection should

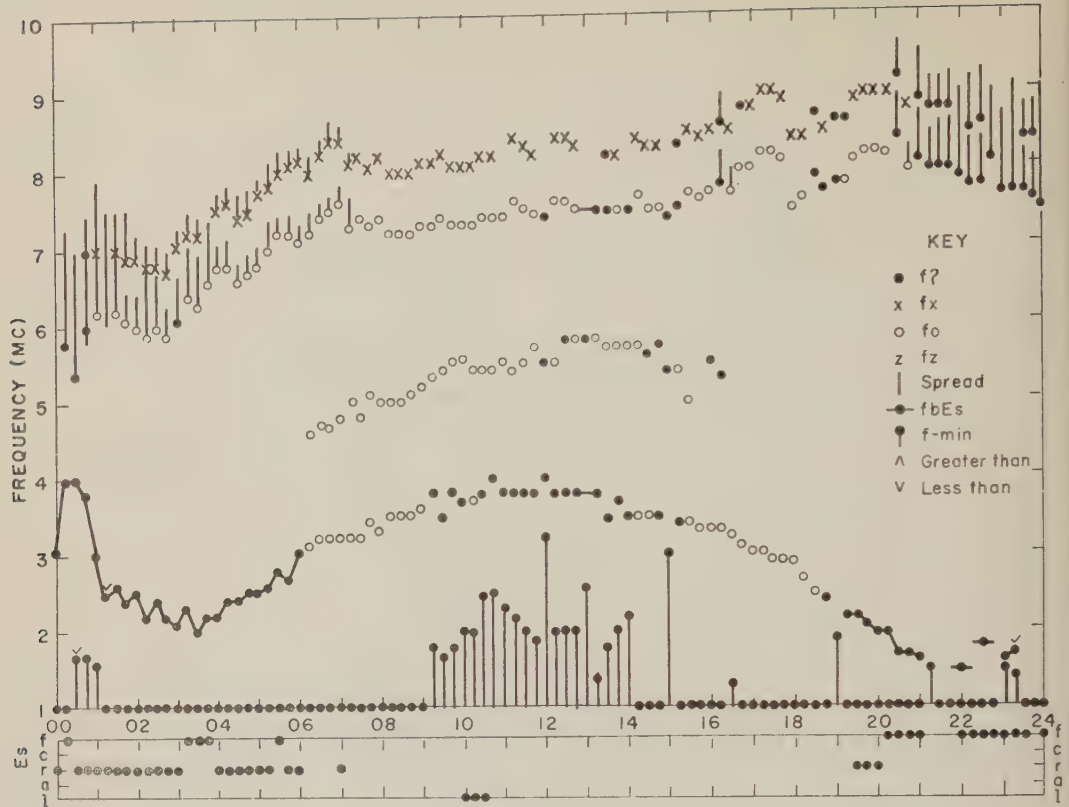


Fig. 5a.

take place, according to Figure 1, in the neighborhood of 2 Mc/s.

It must be noted that (1) and the following are obeying the quasi-longitudinal approximation [Booker, 1935]. In practical cases care must be taken in accepting such an approximation, especially for the D_2 layer. The conclusions reached above are, nevertheless, valid even for the quasi-transversal approximation.

So far it has been shown that, if

$$\int_{D_1} N_1 \nu_1 \, ds > \int_{D_2} N_2 \nu_2 \, ds$$

the diagram of Figure 2 is pertinent to a double-layer D region.

2. *Experimental data and two-layer theory.* This section presents some experimental support for the hypothesis of a dichotomic D region: absorption measurements are shown to be consistent with the theoretical conclusions reached in the preceding section and related to a two-layer D region. Such measurements are illus-

trated in Figures 3 and 4, after Appleton and Piggott [1954].

The method of operation used, the pulse method, requires some remarks. A complete and detailed description of it is given by Piggott [1953]. In this reference various nondissipative phenomena that are responsible for changes in the amplitude of radio waves, and consequently are source of error in absorption measurements, are discussed. Among them the splitting of radio waves in ordinary and extraordinary component is considered. Piggott shows that consequences of practical significance are to be expected when the extraordinary component undergoes an absorption which is of the same order of magnitude of the absorption for the ordinary component. Two cases are contemplated: (a) when the ordinary wave suffers more group retardation than the extraordinary wave; and (b) when the total attenuation is small. In the light of the preceding section a third case should have been considered: namely, (c) when the absorption corresponds to the interval of inflection in Figure 2.

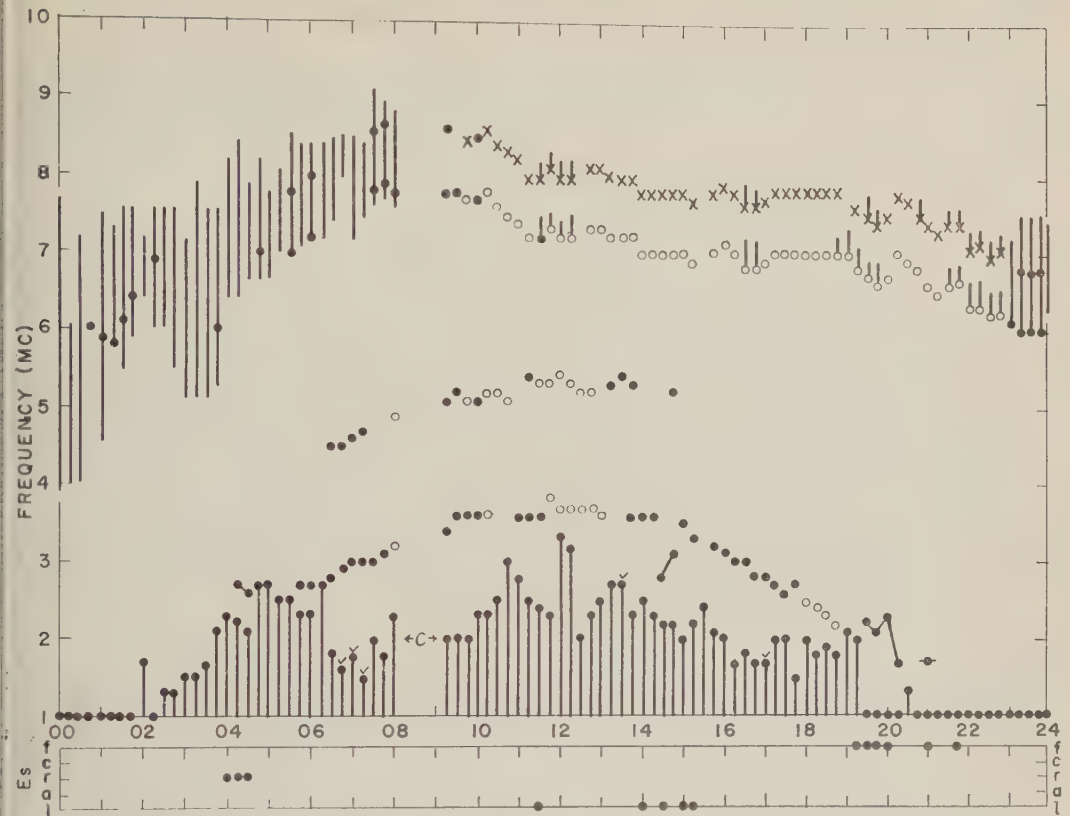


Fig. 5b. May 2, 1958–August 20, 1958: typical F plots for quiet days.

Indeed, such an interval is determined by the predominance of

$$\int_{D_1} \frac{N_1 ds}{\nu_1}$$

in the expression that gives the absorption of the two layers, and where $K_1 \rightarrow N_1/\nu_1$ the ratio of the strength of the ordinary component to the strength of the extraordinary component tends to unity.

This third possibility has not been taken into account and amounts to having neglected a factor that could be even of the order of 2 in the plotting of the experimental data of Figures 3 and 4. One should expect to see, therefore, the section of minimum tangent in Figure 2 to leaven in a bell-shaped curve and the absorption assume the trend of a nonmonotonically decreasing function of the frequency. That is predicted as a result of the dichotomy of the D region.

Figure 3 shows at the lower frequencies such

an apparent irregularity whose origin has not been explained otherwise. The irregularities corresponding to f_oE and f_oF are attributed to deviative absorption. Figure 4 presents the case of absorption on 4 Mc/s that is unexplainably less than absorption on 4.8 Mc/s (deviative absorption has to be excluded since 4 Mc/s was above f_oE). Both situations are interpreted as an experimental evidence of a double-layer D region.

3. f_{min} plots and two-layer theory. The diagram in Figure 2 can be interpreted as the curve of the signal strength at the receiver of an ionospheric sounder (the transmitter is supposed to have a constant emission over the operational range of frequencies).

The threshold of the receiver can be represented on the same diagram as a horizontal line. The intersection between the curve and the horizontal line determines the f_{min} or the minimum detectable frequency. To complete the picture it has to be pointed out that the angles α and β in Figure 2 change according to different electron

contents in the two layers and ν . It follows that even when the electron content changes at a constant rate, the trend of f_{min} should not be regular but discontinuous, in the neighborhood of $\omega \sim \nu_1$.

4. *Examples of f_{min} plots obtained at College, Alaska.* Examples of f_{min} plots obtained at College, Alaska ($64^\circ 51.3'N$, $147^\circ 49.8'W$), are presented in Figure 5. The reader is invited to concentrate his attention on the meridian part of the plots, a time when the absorption is strongly controlled by sunlight, which presents a continuous and regular trend. It is not difficult to recognize that the steplike distribution of f_{min} predicted in accordance with a two-layer absorbing region theory is present in our examples and that the step takes place between 2 and 3 Mc/s.

Conclusion. Experimental results described under sections 2 and 4 check the theoretical predictions presented in sections 1 and 3. These theoretical predictions were based upon the hypothesis of an absorbing region divided into two layers. It is therefore inferred that measurements of radio wave absorption can be used for the detection of the splitting into two layers of the D region of the ionosphere.

Acknowledgments. I am indebted to Mr. R. Parthasarathy for a critical discussion of the paper. This work was supported by the Geophysics Research Directorate, Air Force Cambridge Research Center, Air Research and Development Command, under contract AF 19(604)-3880.

REFERENCES

- Appleton, E. V., and W. R. Piggott, Ionospheric absorption measurements during a sunspot cycle, *J. Atmospheric and Terrest. Phys.*, **5**, 141, 1954.
- Booker, H. G., The application of the magneto-ionic theory to the ionosphere, *Proc. Roy. Soc. London, A*, **150**, 267, 1935.
- Bracewell, R. N., and W. C. Bain, An explanation of radio propagation at 16 kc/sec in terms of two layers below E layer, *J. Atmospheric and Terrest. Phys.*, **2**, 216, 1952.
- Gardner, F. F., and J. L. Pawsey, Study of the ionospheric D region using partial reflections, *J. Atmospheric and Terrest. Phys.*, **3**, 321, 1953.
- Kane, J. A., Arctic measurements of electron collision frequencies in the D -region of the ionosphere, *J. Geophys. Research*, **64**, 133-139, 1959.
- Pfister, W., The morphology of the D - and lower E -layer in the light of solar flare effects, *URSI Comm. III*, The Hague Assembly, 1954.
- Piggott, W. R., The reflection and absorption of radio waves in the ionosphere, *Proc. Inst. Elec. Engrs., London*, **100**, pt. III, 61, 1953.

Note: Etiological considerations about a two-layered D region have appeared in the recent scientific literature: namely,

- Moller, F., VLF propagation effects of a D -region layer produced by cosmic rays, *J. Geophys. Research*, **65**, 1459-1468, 1960.
- Nicolet, M., and A. C. Aikin, The formation of the D region of the ionosphere, *J. Geophys. Research*, **65**, 1469-1483, 1960.

(Manuscript received November 2, 1959;
revised June 15, 1960.)

Scattering of Electromagnetic Waves from a Nondegenerate Ionized Gas¹

JACQUES RENAU

*Cornell Aeronautical Laboratory, Inc., of Cornell University
Buffalo 21, New York*

Abstract. On the basis of a derived Coulomb interaction function, which takes into account the effect of the electrons and the positive ions, we have obtained a rigorous theory of electromagnetic scattering for a nondegenerate ionized gas in thermal equilibrium. Moreover, it is shown that by smearing the positive ions in the background and ignoring the background (a model used by *Pines and Bohm* [1952] and *Akhiezer, Prokoda, and Sitenko*, [1958]) one obtains a scattering cross section incompatible with ionospheric experimental observations [*Bowles*, 1959]. Electromagnetic wave scattering from an ionized gas in nonlaminar flow is also considered. The analysis shows that, if the operating wavelength is much smaller than the smallest eddy size, the mass motion may be neglected and the scattering will be due to the thermal source only. On the other hand, when the wavelength is much greater than the smallest eddy size, the scattering from the nonlaminar fluctuations may dominate the fluctuations from the thermal source if the intensity of turbulence is sufficiently strong. The expected frequency spectrum of the echoes from an ionized gas in turbulent motion is discussed briefly.

INTRODUCTION

It can be shown that, for an ionized gas, the electromagnetic (EM) scattering cross section² per unit solid angle is given by

$$\int_V \sigma(\xi, \alpha) dV = r_e^2 \sin^2 \xi \int_V \int_V \frac{\Delta N(\mathbf{r}) \Delta N(\mathbf{r}')}{r} e^{i\mathbf{q} \cdot (\mathbf{r} - \mathbf{r}')} dV dV' \quad (1)$$

where $\sigma(\xi, \alpha)$ is the scattering crosssection per unit solid angle and per unit volume, the

$$\int_V \sigma(\xi, \alpha) dV$$

is defined as

$$\lim_{R_0 \rightarrow \infty} \frac{R_0^2 |\mathbf{E}_s|^2}{|\mathbf{E}_0|^2}$$

with \mathbf{E}_s the scattered field, \mathbf{E}_0 the incident field, R_0 the distance from the scattering volume element to the observer. V is the total scattering volume.

r_e = classical electron radius = 2.8×10^{-13} cm.

ξ = the angle between the incident electric field \mathbf{E}_0 and the scattered wave propagation vector \mathbf{k}_s .

$\mathbf{q} = \mathbf{k}_s - \mathbf{k}_i$, $|\mathbf{q}| = (4\pi/\lambda) \sin \alpha/2$, with $|\mathbf{k}| = |\mathbf{k}_i| = |\mathbf{k}_s| = 2\pi/\lambda$, and \mathbf{k}_i represents the incident wave-propagation vector.

λ = operating wavelength.

α = angle between \mathbf{k}_i and \mathbf{k}_s . The range of α is $0 < \alpha \leq \pi$.

\mathbf{r} or \mathbf{r}' = position vector of an arbitrary point in the gas from a fixed origin (in the gas). For our purposes, 'gas' implies the space and the particles inside the volume V containing the particles.

$\Delta N(\mathbf{r}) = N(\mathbf{r}) - \overline{N(\mathbf{r})}$, a stochastic variable representing the electron-density fluctuations.

$N(\mathbf{r})$ = the fine-grain electron density for a microscopic distribution in configuration space.

$\overline{N(\mathbf{r})}$ = the (statistical) average of $N(\mathbf{r})$.

Equation 1 is derived with the assumption that single scattering holds; the operating frequency is much greater than the effective collisional³ frequency and the plasma frequency of the gas.

³ So that the permittivity of the ionized gas can be regarded as a pure real quantity.

¹ Section 1 of this paper was submitted to the URSI selection committee during February 1960, and an oral presentation was made at the URSI Conference, Washington, D. C., May 2-5, 1960.

² Radar cross section is ordinarily defined as 4π times the cross section defined here.

The primary problem in the evaluation of equation 1 is the determination of the quantity $\overline{\Delta N(\mathbf{r})\Delta N(\mathbf{r}')}$, which in turn depends upon the temporal variations in charge density due to fluctuations generated by all sources. In order to understand the nature of the sources giving rise to the fluctuations we begin by considering an ionized gas in a volume V with $V^{1/3}$ larger than any length of interest. We shall suppose this system to be in essential isolation (for definition see *Tolman* [1955], p. 498), and will represent it by an ensemble in statistical equilibrium (for example see *Tolman* [1955], p. 55). In the absence of any mass motion, the gas will be nearly in thermal equilibrium, that is, the principle of detailed balancing holds, and the source of the fluctuations will be the thermal motions of the individual charged particles. The 'thermal source' case will be studied in section 1 in a rigorous manner. The case of an ionized gas in mass motion will be studied with much less rigor in section 2. In section 3 the results of these studies will be applied to the ionosphere and compared with the experimental value obtained by *Bowles* [1959].

1. SCATTERING OF EM WAVES FROM AN IONIZED GAS IN THERMAL EQUILIBRIUM (TE)

Pines and Bohm [1952] studied the mean fluctuation amplitude of the Fourier components of the electron density in a gas in thermal equilibrium. They considered the gas as consisting of 'an aggregate of approximately free electrons embedded in a medium of fixed positive charges.' The average density of positive charge was taken to be equal to that of the electrons, but the distribution of the positive ions was assumed uniformly smeared throughout the entire system. It will be shown that smearing positive ions in the system and neglecting to take into account their effect on the distribution of the electron density leads to predictions incompatible with ionospheric experimental observations. (See *Bowles* [1959]).

We now proceed to derive our relations. For charged particles, and in particular for electrons in an ionized gas, it can be shown that

$$\overline{\{\Delta N(\mathbf{r}) \Delta N(\mathbf{r}')\}_{TE}} = \overline{N(\mathbf{r})} [\delta(\mathbf{R}) + \nu(R)] \quad (2)$$

where $R = |\mathbf{r} - \mathbf{r}'|$, $\mathbf{R} = \mathbf{r} - \mathbf{r}'$, $\delta(\mathbf{R})$ is the three-dimensional Dirac delta function, and $\nu(R)$ is the Coulomb-induced interaction function. A

short derivation of equation 2 is given by *Landau and Lifshitz* [1958]; a detailed derivation is presented in Appendix A. We now proceed to derive $\nu(R)$ before introducing equation 2 into the scattering equation 1.

As is shown in Appendix A, $\nu(R)$ by definition is

$$\nu(R) = \overline{N(\mathbf{r}')}\omega(R) = \overline{N(\mathbf{r})}\omega(R) \quad (3)$$

For a dilute, isotropic, and homogeneous ionized gas in thermal equilibrium, $\omega(R)$ satisfies the Debye-Hückel differential equation [*Landau and Lifshitz*, 1958, p. 235, equation 74.25]

$$\left(\nabla^2 - \frac{1}{d^2}\right)\omega(\mathbf{R}) = \frac{4\pi e^2}{KT} \delta(\mathbf{R}) \quad (4)$$

where e is the electronic charge, K the Boltzmann constant, and T the Kelvin temperature. The Debye length d is defined by

$$\frac{1}{d^2} \equiv \frac{4\pi e^2}{KT} \sum_c \overline{N_c} z_c^2 \quad (5)$$

$\overline{N_c}$ here denotes the average density of the kind of charged particles, and $z_c e$ is the charge on a particle of type c . Neglecting the negative ions, but taking into account the positive ions and the electrons, equation 5 reduces to

$$\frac{1}{d^2} \equiv \frac{4\pi e^2 \overline{N(\mathbf{r})}}{KT} (1 + az) \quad (6a)$$

where $a = \overline{zN_+(\mathbf{r})}/\overline{N(\mathbf{r})}$ with $\overline{N_+(\mathbf{r})}$ as the average density of the positive ions and $\overline{N(\mathbf{r})}$ the average density of the electrons. Given that the entire volume of the gas is electrically neutral, then $a = 1$ and

$$\frac{1}{d^2} \equiv \frac{4\pi e^2 \overline{N(\mathbf{r})}}{KT} (1 + z) = \frac{1 + z}{d_0^2} \quad (6b)$$

Considering the Debye length d as a slowly varying quantity, i.e., considering $\overline{N(\mathbf{r})}$ as slowly varying within the scattering volume, the solution to the Debye Hückel differential equation 4 is

$$\omega(R) = -\frac{e^2}{KT} \frac{e^{-1R/d}}{R} \quad (7)$$

Equation 3 then reduces to

$$\nu(R) = -\frac{e^2 \overline{N(\mathbf{r}')}}{KT} \frac{e^{-1R/d}}{R} = \frac{-e^{-1R/d}}{(1+z)4\pi d^2 R} \quad (8)$$

In Appendix B it is shown that $\nu(R)$ expressed by equation 8 is valid⁴ for $R \geq R_{\min}$, where R_{\min} is defined by

$$1 - \frac{e^{-|R_{\min}|/d}}{(1+z)4\pi N(\mathbf{r}') d^2 R_{\min}} = 0 \quad (9)$$

Since $\nu(R)$ approaches zero rapidly for $R \gg d$, we may transform the double integral of equation 1 to relative coordinates, extending one of the volume integrations to infinity. Thus, inserting equation 2 into equation 1, we have

$$\sigma(\xi, \alpha)_{TE} dV = r_e^2 \sin^2 \xi \int_V \left\{ \overline{N(\mathbf{r})} \cdot \int_{V \rightarrow \infty} [\delta(\mathbf{R}) + \nu(R) e^{iqR \cos \theta}] dV' \right\} dV$$

and this relation will hold for any arbitrary scattering volume V . Therefore, we conclude that the scattering cross section per unit angle and per unit volume $\sigma(\xi, \alpha)_{TE}$ is given by

$$\sigma(\xi, \alpha)_{TE} = r_e^2 \sin^2 \xi \overline{N(\mathbf{r})} \cdot \int_{V \rightarrow \infty} [\delta(\mathbf{R}) + \nu(R) e^{iqR \cos \theta}] dV \quad (10)$$

Substituting equation 8 for $\nu(R)$ into equation 10 and carrying out the integration results in

$$\begin{aligned} \sigma(\xi, \alpha)_{TE} &= r_e^2 \sin^2 \xi \left\{ \frac{z}{1+z} + \frac{d^2 q^2}{1+d^2 q^2} \overline{N(\mathbf{r})} \right\} \\ &= r_e^2 \sin^2 \xi \left\{ \frac{z + d_0^2 q^2}{(1+z) + d_0^2 q^2} \overline{N(\mathbf{r})} \right\} \quad (11) \end{aligned}$$

Equation 11 is valid for $0 < dq < \infty$, where, as will be recalled, $q = (4\pi/\lambda) \sin \alpha/2$. Equation 11 is the result we set out to obtain. It will be observed that *Kahn's* [1959] result differs from the simple relationship obtained here.

We note that, when $z \gg 1$, equation 11 reduces to

$$\sigma(\xi, \alpha)_{TE} \approx r_e^2 \sin^2 \xi \overline{N(\mathbf{r})} \quad (11a)$$

for all operating wavelengths, whereas, for singly

ionized gas, $z = 1$ and

$$\begin{aligned} \sigma(\xi, \alpha)_{TE} &= r_e^2 \sin^2 \xi \left\{ \frac{\frac{1}{2} + \frac{d_1^2 q^2}{1 + \frac{d_1^2 q^2}{2}} \overline{N(\mathbf{r})}}{1 + \frac{d_1^2 q^2}{2}} \right\} \quad (11b) \\ &= r_e^2 \sin^2 \xi \left\{ \frac{1 + \frac{d_0^2 q^2}{2} \overline{N(\mathbf{r})}}{2 + d_0^2 q^2} \right\} \end{aligned}$$

where $1/d_1^2$ is given by equation 6 with $z = 1$.

The consequence of 'smearing the positive ions'. Had we smeared the positive ions in the background and ignored the background, i.e. letting $z = 0$ while retaining discrete and fine-grain description of the electrons (hereafter denoted as the smeared model with subscript o to differentiate it from the nonsmeared model), equation 6 defining the Debye length⁵ would have reduced to

$$\frac{1}{d_o^2} \equiv \frac{4\pi e^2}{KT} \overline{N(\mathbf{r})} \quad (6a)$$

In this case equation 11 reduces to

$$\sigma_o(\xi, \alpha)_{TE} = r_e^2 \sin^2 \xi \left\{ \frac{d_o^2 q^2}{1 + d_o^2 q^2} \overline{N(\mathbf{r})} \right\} \quad (12)$$

where the quantity in brackets, when q is replaced by k , represents the Fourier component for a given k of the electron-density fluctuations and corresponds to the results obtained by *Pines and Bohm* [1952], equation A 12, and the results of *Akhiezer, Prok Goda, and Sitenko* [1958], p. 579.

The backscattering cross sections per unit solid angle and per unit volume for both the nonsmeared models of the singly ionized ($z = 1$) gas and the smeared model ($z = 0$) are plotted in figure 1. The abscissa in the upper part of the figure is to be used in conjunction with the solid curve corresponding to the nonsmeared model, and the abscissa in the lower part of the figure is to be used with the broken curve corresponding to the smeared model. It can be seen that, for $\lambda \leq (0.1)4\pi d_1$, $\sigma(\pi/2, \pi)_{TE}$ and $\sigma_o(\pi/2, \pi)_{TE}$ are identical. However, for $\lambda \geq 10(4\pi d_1)$ the results of these two models differ considerably (see section 3).

⁴ In Appendix B we show that R_{\min} is much smaller than the Debye length d for most practical cases. Since eventually $\nu(R)$ will be introduced in equation 1 the error involved in the volume integration by replacing the lower limit R_{\min} by zero is negligible.

⁵ $\frac{1}{d_o^2} = \frac{e^2 \overline{N(\mathbf{r})}}{\epsilon_0 KT}$

in the rationalized mks system.

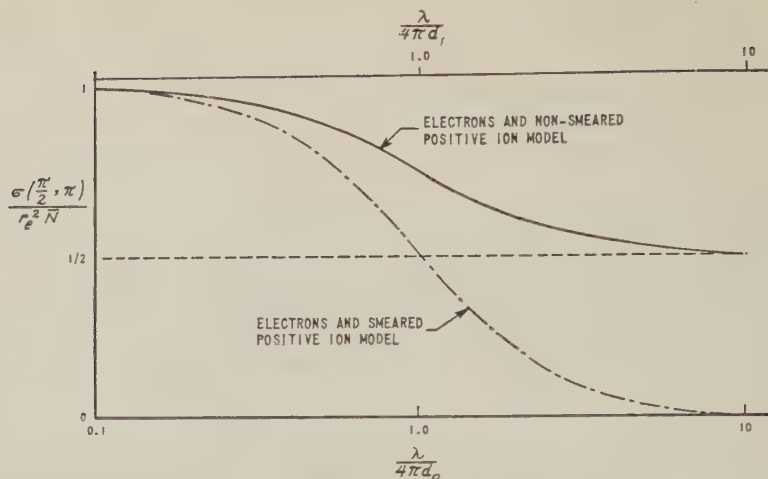


Fig. 1. Scattering of electromagnetic waves from an ionized gas in thermal equilibrium, backscattering case.

Referring to the general scatter relation, equation 11, and for a singly ionized gas ($z = 1$), several cases are of interest:

1. $\lambda \leq (0.1)4\pi d_1 \sin \alpha/2$:

$$\sigma(\xi, \alpha)_{TE} = r_e^2 \sin^2 \xi \overline{N(r)} \quad (13)$$

2. $\lambda \approx 4\pi d_1 \sin \alpha/2$:

$$\sigma(\xi, \alpha)_{TE} = r_e^2 \sin^2 \xi \overline{N(r)}^{\frac{3}{4}} \quad (14)$$

3. $\lambda_p \gg \lambda \geq 10(4\pi d_1)$, with $\lambda_p \equiv$ plasma wavelength:

$$\sigma(\xi, \alpha)_{TE} = r_e^2 \sin^2 \xi \frac{\overline{N(r)}}{2} \quad (15)$$

Note that in this last case the scattered energy is isotropic with respect to the scatter angle α .

Pines and Bohm [1952] and Kahn [1959] show that the electrostatic potential set up by charge density fluctuations in an ionized gas tend to smooth out the large-scale (small-wave-number) components of the density fluctuation spectrum, though, as we have seen, the smoothing is not as drastic as Pines and Bohm concluded. (One of the consequences of our results is that the average Coulomb potential energy associated with each k and for $\lambda \gg 4\pi d$ is not the harmonic oscillator energy $KT/2$ as Pines and Bohm concluded.) This smoothing is responsible for the factor $\frac{1}{2}$ in equation 15. As one approaches scale sizes of the order of Debye length or less (large wave numbers) each electron is surrounded by a cloud of extent d , in which there

is a deficiency of electrons, which is responsible for screening the field of the electron in question, and thus each electron acts 'independently' without restraint from the Coulomb field of other charged particles. This explains the result of equation 13, i.e., $\sigma(\xi, \alpha)_{TE}$ is \bar{N} times the Thomson scattering cross section per electron per unit solid angle. It should be noted that it is the Fourier transform of the Coulomb interaction function $\nu(R)$ that properly accounts for the reduction factor at all scale sizes in $\sigma(\xi, \alpha)_{TE}$. Had we been dealing with a perfect gas (non-interacting particles, e.g. a nonionized gas), $\nu(R)$ for this case would have been equal to zero for all R (quantum effects neglected). This is exactly what we obtain if we let $d \rightarrow \infty$ in $\nu(R)$, equation 8, i.e. when $\bar{N} \rightarrow 0$.

2. SCATTERING DUE TO MASS-MOTION-INDUCED ELECTRON-DENSITY FLUCTUATION

Since our derivation of section 1 establishes the fact that an ionized gas in thermal equilibrium may scatter electromagnetic waves, we are led to scrutinize the mechanism of scattering of EM waves from an ionized gas in non-laminar motion in order to ascertain whether pertinent parameters exist for which scattering from the thermal source in the presence of non-laminar flow becomes of importance.

Consider the ionized gas to be in mass motion in the region of volume V . We shall suppose that this system is in essential isolation and

represent it by an ensemble in statistical equilibrium. In principle we may describe the mass motion of the gas by a coarse-grained kinetic-energy spectrum-function $E(k)$, so that the mass-motion kinetic energy is

$$\int_0^{2\pi/l_{\min}} E(k) dk$$

l_{\min} is defined by observing that this coarse-grained spectrum is invalid for k larger than some $k_{\max} = 2\pi/l_{\min}$ because of the kinematic viscosity of the gas. It will be assumed throughout the rest of this paper that $l_{\min} \gg 4\pi d$.

Let us first consider a gas in mass motion characterized by laminar flow in such a way that the mass motion is not a source of electron-density fluctuations. In this case $l_{\min} \rightarrow \infty$ and the incident electromagnetic waves will still be scattered at all wavelengths because of the electron-density fluctuations arising from thermal motions of the charged particles. The $\sigma(\xi, \alpha)$ appropriate for this case will be equation 11 of section 1.

Now consider a gas in mass motion which is characterized by a nonlaminar flow and in which the mass motion is a source of electron-density fluctuations. At small scale sizes ($\lambda \ll l_{\min}$) the system represented by an ensemble in statistical equilibrium is essentially a gas in thermal equilibrium, and $\sigma(\xi, \alpha)$ expressed by equation 11 will apply once more for values of $\lambda \ll l_{\min}$. At large scales ($\lambda \gg l_{\min}$) the contribution of the large-scale (small- k) Fourier components of the electron-density fluctuations due to the thermal source and the 'mass-motion source' would have been additive if the Navier-Stokes equation describing the flow the of gas could be linearized. However, because of the well-known nonlinearity of the Navier-Stokes equation and for $\lambda \gg l_{\min}$, the nonlaminar mass-motion source and the 'thermal source' will combine in a non-linear fashion to act jointly as a single source of electron-density fluctuations. When the mass motion stops or reduces to a laminar flow, the combined source must reduce to that of a 'thermal source' and electromagnetic scattering should continue to occur even at these large scales since the spectrum of these thermal fluctuations has both small- and large-scale components.

Let us approach this problem from another point of view. We now restrict our attention to mass motion of the gas characterized by turbu-

lent flow, denoted hereafter by subscript T .

Booker and Gordon [1950] considered scattering from a turbulent medium of dielectric constant ϵ and fluctuations $\Delta\epsilon$. They defined a correlation function $C_T(R)$ for this process as follows (The bars denote statistical averages and not space averages as originally used by Booker and Gordon):

$$\overline{\{\Delta\epsilon(\mathbf{r}) \Delta\epsilon(\mathbf{r}')\}_T} = \overline{\{\Delta\epsilon(\mathbf{r} = \mathbf{r}')\}_T}^2 C_T(R) \quad (16)$$

where $R = |\mathbf{r} - \mathbf{r}'|$. Wind-tunnel experiments suggested to them a correlation function of the form

$$C_T(R) = \exp\left\{-\frac{|R|}{l}\right\}$$

with l as the mean eddy size. They then treated in detail the scattering from irregularities in the troposphere where $\Delta\epsilon$ is due to pressure and moisture fluctuations or both.

For a study of scattering from ionospheric gases in turbulent motion (see Booker [1956], for example) one usually relates the electron density and the dielectric constant by⁶

$$\epsilon(\mathbf{r}) = 1 - \frac{e^2 N(\mathbf{r})}{\pi m_e f^2} \quad (17)$$

where f is the operating frequency. In this case equation 16 reduces to

$$\overline{\{\Delta N(\mathbf{r}) \Delta N(\mathbf{r}')\}_T} = \overline{\{\Delta N(\mathbf{r} = \mathbf{r}')\}_T}^2 C_T(R) \quad (18)$$

It is customary to retain the correlation function $C_T(R)$ of equation 16 in equation 18 even though it is not appropriate for the ionosphere, as it fails to account for the changes in electron-density fluctuations due to the Coulomb interaction of the charged particles, nor can it account for the discrete nature of the scatterers.

⁶ The quantities associated with turbulence should be considered coarse-grained, in which case $\epsilon(\mathbf{r})$ and $N(\mathbf{r})$ in equation 17 should have been written $\langle\epsilon(\mathbf{r})\rangle_{l_{\min}}$ and $\langle N(\mathbf{r})\rangle_{l_{\min}}$, where this new notation denotes spatial averages within spheres of radius l_{\min} and centered at \mathbf{r} . By this means the fine-grained electron-density fluctuations are smoothed out. Therefore, $\Delta N(\mathbf{r})_T$ appearing in equation 18 is a stochastic variable defined as

$$\Delta N(\mathbf{r})_T = \langle N(\mathbf{r})\rangle_{l_{\min}} - \overline{N(\mathbf{r})}$$

$\overline{N(\mathbf{r})}$ can be considered equivalent to long-time averaging of $N(\mathbf{r})$.

If we ignore the deficiency of equation 18 and introduce it into equation 1 we then have

$$\int_V \sigma(\xi, \alpha)_T dV = r_e^2 \sin^2 \xi \int_V \left\{ \int_{V \rightarrow \infty} \overline{(\Delta N)_T^2} \right. \\ \left. \cdot \exp \left\{ -\frac{|R|}{l} \right\} e^{i q R \cos \theta} dV \right\} dV$$

Integrating the bracketed part over the scattering volume V with $V^{1/3}$ considered large compared with all lengths of interest,

$$\sigma(\xi, \alpha)_T = r_e^2 \sin^2 \xi \frac{\overline{(\Delta N)_T^2} 8\pi l^3}{\{1 + l^2 q^2\}^2} \quad (19)$$

$\sigma(\xi, \alpha)_T$, expressed in equation 19, is equivalent to the Booker-Gordon result, equation 2v. It is obvious that the derivation of equation 19 is critically dependent upon the correlation function chosen for this process, and for this reason we make no claim of exactness. Hereafter, we will use equation 19, even though it may be inexact, as the term representing scattering from a turbulent ionized gas on a coarse-grain basis in the sense discussed above.

In Appendix A, we show that for a gas represented by an ensemble in statistical equilibrium

$$\overline{\{\Delta N(\mathbf{r}) \Delta N(\mathbf{r}')\}_{\text{total}}} \\ = \overline{N(\mathbf{r})} \delta(\mathbf{R}) + \overline{N(\mathbf{r})} \nu_{\text{total}}(R) \quad (20)$$

For an ionized gas in turbulent motion the exact functional form of $\nu_{\text{total}}(R)$ is not known, although, when the mass motion stops or reduces to a laminar flow, $\nu_{\text{total}}(R)$ must reduce to

$$\nu(R) = \frac{-e^{-|R|/d}}{(1+z)4\pi d^2 R}$$

For a gas in *homogeneous turbulence* we suggest a possible form for $\nu_{\text{total}}(R)$ that is in accord with all the previous discussions. Let

$$\overline{N(\mathbf{r})} \nu_{\text{total}}(R) = \overline{N(\mathbf{r})} \nu(R) \\ + \overline{\{\Delta N(\mathbf{r} = \mathbf{r}')\}_T^2} C_T(R) \quad (21)$$

The fact that $\overline{N(\mathbf{r})} \nu_{\text{total}}(R)$ is expressed in the manner shown could perhaps be justified in the following way. The Coulomb interaction function $\nu(R)$ may still be expressed by that obtained in section 1 because the homogeneous turbulent motion cannot alter the small-scale expression for the average Coulomb interaction between

charged particles in an ionized gas. The correlation function $C_T(R)$ may be considered as accounting for the distribution of noninteracting scatterers among the hierarchy of scale sizes l_{\min} as originally intended in equation 16. Since $\nu(R)$ becomes negligible for $R \gg d$, and $C_T(R)$ is valid for scales sizes larger than l_{\min} , any cross terms between $\nu(R)$ and $C_T(R)$ may be considered negligible compared with the terms that have been kept. $\overline{N(\mathbf{r})} \delta(\mathbf{R})$ in equation 20 takes into account the discrete nature of the individual scatterers of the gas. Note that in equations 20 and 21, if the Coulomb interaction term $\nu(R)$ and the discreteness of the electrons are neglected, we obtain equation 18. On the other hand, when the nonlaminar motion stops or reduces to laminar flow, $l_{\min} \rightarrow \infty$,

$$\Delta N_T = \langle N(\mathbf{r}) \rangle_{l_{\min}} - \overline{N(\mathbf{r})} \rightarrow 0$$

thus the last term of equation 21 drops out and equation 20 leads us back to the results of section 1, with ΔN_{total} reduced to $\Delta N_{TE} = N(\mathbf{r}) - \overline{N(\mathbf{r})}$.

On the basis of these heuristic arguments, then, we introduce

$$\overline{\{\Delta N(\mathbf{r}) \Delta N(\mathbf{r}')\}_{\text{total}}} \\ = \overline{N(\mathbf{r})} \left[\delta(\mathbf{R}) - \frac{e^{-|R|/d}}{(1+z)4\pi d^2 R} \right] \\ + \overline{\{\Delta N(\mathbf{r} = \mathbf{r}')\}_T^2} e^{-|R|/l}$$

into the general scatter equation 1, which leads to the addition of the results in sections 1 and 2, namely

$$\sigma(\xi, \alpha) = \sigma(\xi, \alpha)_{TE} + \sigma(\xi, \alpha)_T$$

Recalling equations 11 and 19 we obtain $\sigma(\xi, \alpha)$ for an ionized gas in turbulent motion

$$\sigma(\xi, \alpha) \\ = r_e^2 \sin^2 \xi \left\{ \frac{z}{1+z} + \left(\frac{4\pi d \sin \alpha/2}{\lambda} \right)^2 \right\} \overline{N(\mathbf{r})} \\ + \left\{ \frac{8\pi l^3 \overline{(\Delta N)_T^2}}{\left[1 + \left(\frac{4\pi l \sin \alpha/2}{\lambda} \right)^2 \right]^2} \right\} \quad (22)$$

Assuming that $\overline{(\Delta N)_T^2} \neq 0$, and for a singly ionized gas ($Z = 1$), various limiting cases of equation 22 are

1. $\lambda_p \gg \lambda \gg 4\pi l \gg 4\pi d_1$ with $\lambda_p \equiv$ plasma wavelength:

$$\sigma(\xi, \alpha) = r_e^2 \sin^2 \xi \left[\frac{\overline{N(\mathbf{r})}}{2} + 8\pi l^3 (\overline{\Delta N})_T^2 \right] \quad (23)$$

2. $\lambda_p \gg \lambda \approx 4\pi l \sin \alpha/2 \gg 4\pi d_1$:

$$\sigma(\xi, \alpha) = r_e^2 \sin^2 \xi \left[\frac{\overline{N(\mathbf{r})}}{2} + 2\pi l^3 (\overline{\Delta N})_T^2 \right] \quad (24)$$

3. $10(4\pi d_1) \leq \lambda \ll 4\pi l \sin \alpha/2$:

$$\sigma(\xi, \alpha) = r_e^2 \sin^2 \xi \overline{N(\mathbf{r})}/2 \quad (25)$$

4. $\lambda \approx 4\pi d_1 \sin \alpha/2 \ll 4\pi l \sin \alpha/2$:

$$\sigma(\xi, \alpha) = r_e^2 \sin^2 \xi 3\overline{N(\mathbf{r})}/4 \quad (26)$$

5. $\lambda \leq (0.1)4\pi d_1 \sin \alpha/2 \ll 4\pi l \sin \alpha/2$:

$$\sigma(\xi, \alpha) = r_e^2 \sin^2 \xi \overline{N(\mathbf{r})} \quad (27)$$

Some of these cases of particular interest in ionospheric studies are discussed in section 3.

3. APPLICATION TO THE IONOSPHERE

At the International Symposium on Fluid Mechanics in the Ionosphere, Cornell University, July 1959, it was concluded that it would be very difficult to have turbulence above about 20 km (see *J. Geophys. Research*, December 1959). In the high ionosphere, experimental evidence seems also to indicate the existence of irregularities, of mean size l increasing with height, but the mechanism producing the irregularities is not well understood. Although the mass motion was characterized as turbulence, we could have ascribed $(\Delta N)_T$ to any mass motion satisfying the correlation function $\overline{N(R)} = \exp \{-|R|/l\}$. This leads us to conceptual reorientation of the mass-motion processes without altering the mathematical expressions describing the cross section. Thus, we will assume that $\sigma(\xi, \alpha)$, equation 22, holds also for the high ionosphere (elongation of irregularities neglected).

For meter wavelengths, and in the high ionosphere, case 3, equation 25, is thought to be appropriate:

$$\sigma(\xi, \alpha) = r_e^2 \sin^2 \xi \overline{N(\mathbf{r})}/2$$

In particular, for backscattering, $\xi = \pi/2$, $\alpha = \pi$

$$\sigma(\pi/2, \pi) = r_e^2 \overline{N(\mathbf{r})}/2$$

which is equal to one-half the quantity proposed by Gordon [1958] on the basis that each electron scatters 'independently.' Cross sections of approximately this value have been measured by Bowles [1959]. For meter wavelengths the scattering cross section per unit volume based on the smeared positive-ion model reduces to

$$\sigma_0(\pi/2, \pi) = r_e^2 \overline{N(\mathbf{r})} (4\pi d_0/\lambda)^2$$

and predicts values approximately 10^4 to 10^6 smaller than those measured by Bowles ($\lambda = 7.5$ meters, $d_0 < 1$ cm in the regions of observation).

For the *D*-region ionosphere the mean size of the irregularities, l , is much smaller than in the high ionosphere. For meter wavelengths, case 2, equation 24 is thought appropriate; for backscattering it reduces to

$$\sigma(\pi/2, \pi) = r_e^2 [\overline{N(\mathbf{r})}/2 + 2\pi l^3 (\overline{\Delta N})_T^2]$$

According to ionospheric observations from the low ionosphere the values of l and $(\Delta N)_T^2$ are such that the second term in brackets dominates the first term.

Doppler spreads of the scattered echoes. It is to be noted that in these derivations we say nothing about the Doppler spread of the echoes. However, our study does lead to an insight into the expected Doppler spreads for the cases $\lambda \leq (0.1)4\pi d$ and $\lambda \geq 4\pi l \gg 4\pi d$. We note that Pines and Bohm give a valid criterion for determining the condition under which each electron moves without restraint from the Coulomb field of the other charged particles. This criterion is

$$(\mathbf{k} \cdot \mathbf{u}_e)^2 \gg 4\pi \bar{N} e^2 / m_e$$

where m_e is the mass of the electron and for a gas with an isotropic distribution at temperature T , and for the case of propagation, reduces to

$$q^2 \gg 12\pi \bar{N} e^2 / m_e \overline{u_e^2} \quad (28)$$

Since locally the gas is essentially in thermal equilibrium, $\overline{u_e^2}$ is obtained from the Maxwellian velocity distribution of the electrons as

$$u_{rms} = (\overline{u_e^2})^{1/2} = (3KT/m_e)^{1/2}$$

With this expression for $\overline{u_e^2}$, equation 28 reduces to

$$q^2 \gg 4\pi e^2 \bar{N} / KT = 1/2 d^2$$

or $qd \gg 1$. But $q = 4\pi/\lambda \sin \alpha/2$, and so the

criterion reduces to

$$\lambda \ll 4\pi d \sin \alpha/2$$

as the condition for the Doppler spread of the scattered echoes to be deduced from

$$\Delta f = 4f(u_{rms})/c \quad \text{electrons} \quad (29)$$

where c is the velocity of light in vacuum.

On the other hand, for the case of $\lambda \gg 4\pi d$, Bowles's experimental results appear to indicate that for 40-Mc/s operating frequency the spread of echoes scattered by the electrons in the high ionosphere ($\lambda = 7.5$ meters, $d < 1$ cm in the regions of observation) is reduced by factor of at least 10 from that predicted by equation 29, and Bowles has tried to justify this reduction by considering the effect of the heavy positive ions on the temporal variation of the density fluctuations. Dougherty and Farley (private communication, 1960) and Fejer (private communication, 1960) have now shown on theoretical grounds the importance of the positive ions in the spectrum of the echo from an ionized gas in thermal equilibrium.

For $\lambda \geq 4\pi l \gg 4\pi d$ and $2\pi l^2(\Delta N)_T \gg \overline{N(r)}/2$, which can occur in the low ionosphere, the echoes are mainly due to the mass motion of the gas. Therefore, the Doppler spread of the echoes will be associated with the velocities of the mass-motion irregularities.

APPENDIX A

Derivation of the Relation between $\overline{\Delta N(r)\Delta N(r')}$ and the Coulomb Interaction Function $\nu(R)$ for the Case of a Nondegenerate Ionized Gas

Consider an ionized gas in a region of volume V . We shall suppose this system to be in *essential isolation* (defined by Tolman [1955], p. 498) and represent it by an ensemble in statistical equilibrium. To specify this ensemble, let us use the function

$$\rho(\mathbf{r}_1, \dots, \mathbf{r}_n)$$

to denote the microscopic distribution function for the position coordinates $\mathbf{r}_1, \dots, \mathbf{r}_n$ of the n electrons present in the volume V . In other words, $\rho(\mathbf{r}_1, \dots, \mathbf{r}_n)$ is just the result of integrating the Liouville density in phase over all coordinates except the position coordinates of the electrons. We shall normalize ρ according to

$$\int_V \dots \int_V \rho(\mathbf{r}_1, \dots, \mathbf{r}_n) dV_1, \dots, dV_n = 1 \quad \text{n integrations} \quad (A1)$$

so that

$$\rho(\mathbf{r}_1, \dots, \mathbf{r}_n) dV_1, \dots, dV_n \quad (A2)$$

is equal to the probability of simultaneously finding electron 1 in dV_1 , electron 2 in dV_2 , etc. ρ has the important property that it is symmetric in the coordinates of the electrons, a property that will be used in this appendix.

The cross correlation of the electron-density fluctuations for the gas is

$$\begin{aligned} \overline{\Delta N(\mathbf{r}) \Delta N(\mathbf{r}')} \\ = \overline{\{N(\mathbf{r}) - \overline{N(\mathbf{r})}\} \{N(\mathbf{r}') - \overline{N(\mathbf{r}')}\}} \\ = \overline{N(\mathbf{r})N(\mathbf{r}')} - \overline{N(\mathbf{r})} \overline{N(\mathbf{r}')} \end{aligned} \quad (A3)$$

where $N(\mathbf{r})$ and $N(\mathbf{r}')$ are the fine-grain electron densities for a particular member of the ensemble at \mathbf{r} and \mathbf{r}' , and the ensemble average (assumed equivalent to long-time averaging) of $N(\mathbf{r})$ at \mathbf{r} is defined by

$$\begin{aligned} \overline{N(\mathbf{r})} = \int_V \dots \int_V N(\mathbf{r}) \\ \cdot \rho(\mathbf{r}_1, \dots, \mathbf{r}_n) dV_1, \dots, dV_n \end{aligned} \quad \text{n integrations} \quad (A4)$$

Similarly

$$\begin{aligned} \overline{N(\mathbf{r})N(\mathbf{r}')} = \int_V \dots \int_V N(\mathbf{r})N(\mathbf{r}') \\ \cdot \rho(\mathbf{r}_1, \dots, \mathbf{r}_n) dV_1, \dots, dV_n \end{aligned} \quad \text{n integrations} \quad (A5)$$

Define the one-electron density function

$$\begin{aligned} P(\mathbf{r}_1) \\ = \int_V \dots \int_V \rho(\mathbf{r}_1, \dots, \mathbf{r}_n) dV_2, \dots, dV_n \end{aligned} \quad \text{n-1 integrations} \quad (A6)$$

and the two-electron density function

$$\begin{aligned} P(\mathbf{r}_1, \mathbf{r}_2) \\ = \int_V \dots \int_V \rho(\mathbf{r}_1, \dots, \mathbf{r}_n) dV_3, \dots, dV_n \end{aligned} \quad \text{n-2 integrations} \quad (A7)$$

Clearly

$$P(\mathbf{r}_1, \mathbf{r}_2) dV_1 dV_2$$

is the joint probability of finding electron 1 in dV_1 and electron 2 in dV_2 . For an isotropic

and homogeneous gas, $P(\mathbf{r}_1, \mathbf{r}_2)$ depends on $\mathbf{r} = |\mathbf{r}_1 - \mathbf{r}_2|$ and not on the absolute positions \mathbf{r}_1 or \mathbf{r}_2 . In order to obtain an expression for $\overline{N(\mathbf{r})N(\mathbf{r}')}$, we shall represent the fine-grain electron density by the Dirac delta function

$$N(\mathbf{r}) = \sum_{i=1}^n \delta(\mathbf{r} - \mathbf{r}_i) \quad (\text{A8})$$

where n , it will be recalled, is the total number of electrons in the volume V . Inserting (A8) into (A4), and interchanging the order of summation and integration,

$$\overline{N(\mathbf{r})} = \sum_{i=1}^n \int_V \cdots \int_V \delta(\mathbf{r} - \mathbf{r}_i) \cdot \rho(\mathbf{r}_1, \cdots, \mathbf{r}_n) dV_1, \cdots, dV_n$$

Using the symmetry property of ρ , integrating over all coordinates of the electrons except \mathbf{r}_i , and introducing equation A6, the above reduces to

$$\begin{aligned} \overline{N(\mathbf{r})} &= \sum_{i=1}^n \int_V \delta(\mathbf{r} - \mathbf{r}_i) P(\mathbf{r}_i) dV_i \\ &= nP(\mathbf{r}) \end{aligned} \quad (\text{A9})$$

By the same token,

$$\begin{aligned} \overline{N(\mathbf{r})N(\mathbf{r}')} &= \sum_{i=1}^n \sum_{j=1}^n \delta(\mathbf{r} - \mathbf{r}_i) \delta(\mathbf{r}' - \mathbf{r}_j) \\ &= \sum_{i \neq j}^n \sum \delta(\mathbf{r} - \mathbf{r}_i) \delta(\mathbf{r}' - \mathbf{r}_j) \\ &\quad + \sum_{i=1}^n \delta(\mathbf{r} - \mathbf{r}_i) \delta(\mathbf{r}' - \mathbf{r}_i) \end{aligned} \quad (\text{A10})$$

Inserting equation A10 into A5 and making use of equation A7,

$$\begin{aligned} \overline{N(\mathbf{r})N(\mathbf{r}')} &= (n^2 - n)P(\mathbf{r}, \mathbf{r}') \\ &\quad + nP(\mathbf{r}) \delta(\mathbf{r} - \mathbf{r}'). \end{aligned} \quad (\text{A11})$$

Recalling equation A9, $nP(\mathbf{r}) = \overline{N(\mathbf{r})}$; and so for the case $n^2 \gg n$ equation A11 reduces to

$$\overline{N(\mathbf{r})N(\mathbf{r}')} = n^2 P(\mathbf{r}, \mathbf{r}') + \delta(\mathbf{R}) \overline{N(\mathbf{r})} \quad (\text{A12})$$

where $\mathbf{R} = \mathbf{r} - \mathbf{r}'$.

We are now ready to express equation A3 in the desired form. For a gas free of external fields

$$\overline{N(\mathbf{r})} = \overline{N(\mathbf{r}')} = n/V$$

and by the relation A9

$$P(\mathbf{r}) = 1/V$$

Similarly, because the correlation will drop to zero for large separation,

$$P(\mathbf{r}, \mathbf{r}') \xrightarrow{R \rightarrow \infty} P(\mathbf{r})P(\mathbf{r}') = 1/V^2 \quad (\text{A13})$$

Let us now introduce the joint probability function $u_{12}(R)$ defined by

$$u_{12}(R) = P(\mathbf{r}, \mathbf{r}')/P(\mathbf{r})P(\mathbf{r}') \quad (\text{A14})$$

With this definition and the above relations it will be noted that

$$u_{12}(R) \rightarrow 1 \quad \text{as} \quad R \rightarrow \infty$$

Using the relation A14 and the results of equation A12, equation A3 can be rewritten as

$$\begin{aligned} \overline{\Delta N(\mathbf{r}) \Delta N(\mathbf{r}')} &= \overline{N(\mathbf{r})} \overline{N(\mathbf{r}')} [u_{12}(R) - 1] \\ &\quad + \overline{N(\mathbf{r})} \delta(\mathbf{R}) \end{aligned} \quad (\text{A15})$$

Letting

$$\overline{N(\mathbf{r}')} [u_{12}(R) - 1] \equiv \overline{N(\mathbf{r}')} \omega(R) \equiv \nu(R) \quad (\text{A16})$$

Equation A15 reduces to

$$\overline{\Delta N(\mathbf{r}) \Delta N(\mathbf{r}')} = \overline{N(\mathbf{r})} [\delta(\mathbf{R}) + \nu(R)] \quad (\text{A17})$$

Equation A17 obtained here appears in the text as equation 2.

Equation A17 is identical to equation 115.3 in *Landau and Lifshitz* [1958]. $\nu(R)$ is related to the probability of simultaneously finding an electron in dV_1 and an electron in dV_2 . The term $\delta(\mathbf{R})$ which appears in (A17) is related to the probability of finding an electron in dV_1 , given that an electron exists in dV_1 . Assuming that the interaction of any two electrons is due to their Coulomb fields only, the $\nu(R)$ of equation A16 is the Coulomb interaction function.

For sufficiently dilute gases the function $\omega(R)$ defined by equation A16 is identical to $\omega_{ab}(R)$ defined by equation 74.22 of *Landau and Lifshitz*. If we now restrict the state of the gas to thermal equilibrium, $\omega(R)$ satisfies the Debye-Hückel differential equation 74.25 of *Landau and Lifshitz*.

APPENDIX B

The Range of Validity of the Coulomb Interaction Function $\nu(R)$

The assumptions leading to the derivation of $\nu(R)$ for an ionized gas in thermal equilibrium restrict the validity of $\nu(R)$ as $R \rightarrow 0$ (quantum effects neglected). To determine the validity

of $\nu(R)$, solve equation A16 for $u_{12}(R)$ in terms of $\nu(R)$

$$u_{12}(R) = 1 - \frac{e^{-|R|/d}}{(1+z)4\pi d^2 \bar{N} R} \quad (\text{B1})$$

and since $u_{12}(R)$ is a probability function its values must never be negative. We therefore let equation B1 hold down to some value of $R = R_{\min}$ such that

$$1 - \frac{e^{-|R_{\min}|/d}}{(1+z)4\pi d^2 \bar{N} R_{\min}} = 0 \quad (\text{B2})$$

in which case

$$\nu(R) = -\frac{e^{-|R|/d}}{(1+z)4\pi d^2 \bar{N}} \quad R \geq R_{\min}$$

$$\nu(R) = -\bar{N} \quad \text{and} \quad u_{12}(R) = 0 \quad R < R_{\min}$$

We wish to show that R_{\min} is much smaller than the Debye length d , and that when $\nu(R)$ is introduced in equation 10 of the text the error involved in the volume integration is negligible when in the R integration the lower limit R_{\min} is replaced by zero. Define R_{\min}' by

$$1 - \frac{1}{(1+z)4\pi d^2 \bar{N} R_{\min}'} = 0 \quad (\text{B3})$$

Equating equations B2 and B3 we obtain

$$R_{\min}/R_{\min}' = e^{-|R_{\min}|/d} \\ \therefore R_{\min} \leq R_{\min}' \quad (\text{B4})$$

Equation B3 gives the following relation between R_{\min}' and d :

$$R_{\min}' = \frac{1}{(1+z)4\pi \bar{N} d^2}$$

where

$$d^2 \equiv \frac{KT}{(1+z)4\pi \bar{N} e^2}$$

Therefore

$$\frac{R_{\min}'}{d} \simeq 10^{-4} \left(\frac{\bar{N}}{T^3} \right)^{1/2} (1+z)^{1/2} \quad (\text{B5})$$

For electron densities as high as 10^{12} electrons cm^{-3} , and for room temperatures and above, $R_{\min}' \ll d$, or, according to Equation B4, $R_{\min} \ll d$.

Acknowledgments. I wish to thank Mr. Harold Camnitz for many valuable technical discussions and for criticism during the conduct of this work. Dr. Walter A. Flood also deserves my thanks for his support and criticism of this paper.

This research was made possible through partial support and sponsorship extended by Wright Air Development Division under contract AF33(616)-6350, and by Cornell Aeronautical Laboratory, Inc., as part of its Internal Research Program.

REFERENCES

- Akhiezer, A. I., I. G. Prokoda, and A. G. Sitenko, *JETP*, **6**, 576, 1958.
- Booker, H. G., *J. Atmospheric and Terrest. Phys.*, **3**, 204, 1956.
- Booker, H. G., and W. E. Gordon, *Proc. IRE*, **38**, 401-412, 1950.
- Bowles, K. L., *Natl. Bur. Standards Rept.* 6070, 1959.
- Debye, P., and E. Hückel, *Physik. Z.*, **24**, 185-206, 1923.
- Gordon, W. E., *Cornell Univ. Research Rept. EE* 376, 1958.
- Kahn, F. D., *Astrophys. J.*, **129**, 205-216, 1959.
- Landau, L. D., and E. M. Lifshitz, *Statistical Physics*, Pergamon Press, London, 1958.
- Pines, D., and D. Bohm, *Phys. Rev.*, **85**, 338-353, 1952.
- Tolman, R. C., *The Principles of Statistical Mechanics*, chapter 6, Oxford University Press, reprints, 1955.

(Manuscript received June 24, 1960; revised August 12, 1960.)

Water Vapor Distribution above 90,000 Feet

DAVID G. MURCRAY, FRANK H. MURCRAY,
WALTER J. WILLIAMS, AND FRANK E. LESLIE

*Department of Physics
University of Denver
Denver, Colorado*

Abstract. The absorptions due to the 6.3- μ band of water vapor were measured for altitudes up to 92,000 ft. On the basis of these absorptions the humidity mixing ratio for the region above 92,000 ft was calculated, the calculated values ranging from 1.5×10^{-4} g/g to 3.4×10^{-4} g/g. The mixing ratio from 40,000 to 92,000 ft was also calculated, yielding values at least an order of magnitude lower than the values obtained above 92,000 ft. It is concluded that at least 20 μ of precipitable water was present above 92,000 ft over Alamogordo, New Mexico, on June 19, 1959.

Introduction. There are few data currently available on the amount of water vapor present in the stratosphere. This lack of information arises because measurements of the small amounts of water vapor present at altitudes above 35,000 ft present difficulties which have precluded taking measurements on a routine basis. Most of the data available have been obtained by experimental soundings that were made with the numerous instruments proposed for obtaining these data. The most reliable data appear to be those obtained by the frost-point hygrometer used by various British groups [Dobson, Brewer, and Cwilong, 1946]. Since this instrument is a manual instrument, the published measurements have been limited to altitudes of less than 50,000 ft.

Barrett, Herndon, and Carter [1949] designed an automatic frost-point instrument which made it possible to make measurements with balloon-borne instruments to altitudes above 90,000 ft. This instrument has been modified and flown a number of times by various groups [Barrett, Herndon, and Carter, 1950]. The reliability of these measurements, which has been questioned, will be discussed in detail later in the paper.

Water vapor has a number of absorption bands in the near-infrared region of the spectrum. Numerous hygrometers have been proposed that will use this absorption in measuring the water vapor present at the higher altitudes. The small amount of water vapor present, per unit volume, requires long path lengths be-

tween the source and the detector to assure that the total water vapor present will be sufficient to obtain a reliable measurement. Such paths are difficult to obtain with a self-contained source, and most instruments use the sun as a source. Since the solar radiation has traversed the atmosphere above the instrument and the absorption depends not only on the water vapor traversed but also on the temperature and pressure environment of the water vapor, the interpretation of the data becomes difficult. However, the fact that the radiation has traversed the atmosphere above the instrument provides a means for estimating the amount of water vapor present at altitudes in excess of those that can be reached by the instrument. Most measurements made by this method have used the water vapor bands at wavelengths less than 3 μ or else were taken from aircraft, so that the spectra used were taken at altitudes of less than 50,000 ft. [Murcray, Brooks, Murcray, and Shaw, 1958; Gates, Murcray, Shaw, and Herbold, 1958; Houghton, Moss, Seely, and Hawkins, 1957; Houghton, Moss, and Chamberlain, 1958; Kiseleua, Neporent, and Fursinkiv, 1959]. Because of the ambiguity of interpretation of such records it is desirable to obtain spectra at altitudes in excess of 50,000 ft. Our group at the University of Denver has been studying the infrared solar spectrum at various altitudes up to 100,000 ft for some time [Murcray, Brooks, Murcray, and Williams, 1960]. These studies were made in the wavelength region less than 5 μ . From the records obtained

on these flights it became evident that in order to get data on water vapor above 50,000 ft it would be advantageous to extend the wavelength region scanned to include the $6.3\text{-}\mu$ band. The spectrometer was therefore changed so that the spectral region scanned included this band. The results obtained on a flight made with this instrument on June 19, 1959, are discussed.

Instrumentation. The spectrometer is a single-pass prism instrument of the Littrow type, with a NaCl prism and a thermistor bolometer used as a detector. The incoming radiation is chopped mechanically at 80 cps, so that the detector output occurs as an a-c voltage. This signal is amplified by means of a narrow band pass preamplifier. The signal is further amplified and the final a-c voltage is synchronously rectified to produce a d-c voltage that varies from 0 to 1.4 volt. The output is recorded on one channel of a 4-channel FM tape recorder. The spectrum from 1 to $10\text{ }\mu$ is scanned in 18 seconds and there is a 1-minute interval between scans. All mechanical rotations are accomplished by means of 400 cps, 115 volt, single-phase synchronous motors. Provision is made to change the gain of the system at selected wavelengths to compensate for the decrease in intensity of the radiation reaching the detector at the longer wavelengths. A complete description of the spectrometer and auxiliary equipment is given in a separate report [Murcray, Brooks, Murcray, Williams, and Leslie, 1960]. The image of the sun is maintained on the slit by means of a biaxial pointing control constructed by Hi-Altitude Instrument Company of Denver, Colorado, and is a modification of one described by Goddard, Juza, Maher, and Speck [1956].

Since the major absorptions occurring in the 1- to $10\text{-}\mu$ region of the solar spectrum are caused by H_2O , a frost-point hygrometer constructed by New York University was also flown with the equipment. The instrument consists of a small mirror in which a bead thermistor is embedded. A beam of light is reflected from this mirror to a phototube. The output of the phototube is compared with the output of a similar phototube that receives its light directly from the lamp. The difference in output of the two phototubes is used to control the current through an induction heater which is

placed around the mirror. The mirror is also placed in contact with a bath of dry ice and ethyl alcohol. Adjustment of the phototube circuits regulates the current through the induction coil so that the mirror can be maintained at the frost point. The resistance of the bead thermistor is monitored, and in this way the temperature of the frost point is determined.

Details of flight. The equipment was flown from Holloman Air Force Base, New Mexico ($32^{\circ}51'\text{N}$ – $106^{\circ}05'\text{W}$), on June 19, 1959. The balloon used was 128 ft in diameter and $800,000\text{ ft}^3$ in volume and was constructed of 2-mil polyethylene. The balloon was inflated with pure helium. The launching occurred at 0550 and the balloon rose at an average rate of 800 ft/min. It reached altitude (92,000 ft) at 0735 and was allowed to float at altitude for an hour. The equipment was separated from the balloon by command from the ground via the telemetering link. It descended on a parachute and landed on rocky terrain southwest of Holloman Air Force Base. In spite of the rough impact the equipment did not suffer any damage.

Data analysis. The equipment operated properly throughout the flight. The seeker locked on the sun when the balloon had reached an altitude of 10,000 ft, and solar spectra were obtained from then until cutoff. A sample of the spectra obtained at altitude is shown in Figure 1. The hygrometer operated properly also, and Figure 2 shows a plot of frost-point temperature versus altitude. The ambient temperature as recorded by the balloon instrumentation and the dew-point from the 0200 rawinsonde run are included on the same plot.

There are some differences between the dew-point and the frost-point plots, presumably due to a change in the water vapor profile during the time interval between the two observations. Rawinsonde data available to the authors indicate that changes of this magnitude during similar time intervals are not uncommon. In spite of the differences, the over-all profiles are quite similar and furnish an additional indication that the frost-point instrument was operating properly.

The detail observed in any spectrum depends on a number of parameters, including the slit width of the spectrometer. In order to be able to use the laboratory data of other workers, it is necessary to find some description of the

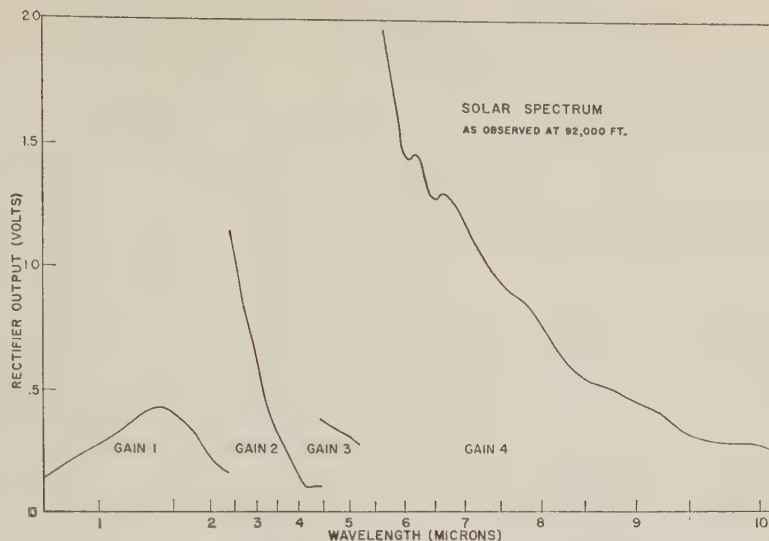


Fig. 1. Solar spectrum as observed at 92,000 ft. Pressure, 12 mm Hg; secant factor, 1.6.

absorption that is independent of the spectrometer used to obtain the spectrum. *Nielsen, Thornton, and Dale* [1944] showed that under certain conditions the quantity $\int_{\nu_1}^{\nu_2} A, d\nu$ is independent of the slit width of the spectrometer. Here A , is the fractional absorption at frequency ν , and ν_1 and ν_2 are the limits of the absorption. This quantity thus provides an excellent parameter for characterizing a band, and is measured in most laboratory studies. In view of this, the quantity $\int_{\nu_1}^{\nu_2} A, d\nu$ was determined from each record for the water-vapor bands at 1.4, 1.9, and 6.3 μ by numerical integration. The altitude at which the spectra were taken was determined from the pressure data supplied by the Air Force telemetry package and the NACA standard atmosphere. The secant factor, which is equal to the secant of the sun's zenith angle corrected for refraction effects, was determined from tables given by *Benford* [1947] and the time at which the record was taken. The time was recorded on tape by means of an analog clock which is part of the balloon instrumentation. These results are summarized in Table 1.

As was mentioned previously, the problem of determining the amount of water vapor traversed from the absorption spectrum is complicated by the fact that the absorption is dependent not only on the amount of water vapor in the path but also on the pressure and temperature environment of the water vapor trav-

ersed. The hygrometer used on this flight was equipped with a bead thermistor that had a resistance greater than 1 megohm when the temperature was -70°C or lower. Because of the method of measuring the resistance it was not possible to determine the frost point with any accuracy when it was less than -70°C . Since the frost point remained less than this value from 40,000 ft up, the hygrometer data can be used only to place an upper limit on the amount of water vapor present above this altitude. Thus, in order to interpret the absorption result, it becomes necessary to make assumptions as to the distribution of the water vapor without the benefit of the hygrometer, except that it should be such that in the region from 40,000 to 92,000 ft the frost point is less than -70°C . In addition, some method must be used to correct for the slant path.

Carpenter, Wright, Quesada, and Swing [1957], using results suggested by *Plass* [1952], arrived at a method for predicting the absorption which radiation will suffer in traversing a slant path in the atmosphere. They showed that for both the Elsasser and Goody models of the absorption band the pressure dependence of the absorption enters through the variation in half width of the individual line. In both cases the absorption can be determined by calculating an equivalent constant pressure path that can be used with empirical relations obtained from laboratory data. The equivalent path is ob-

TABLE 1. Data from Balloon Flight of June 19, 1959

Record No.	Time, MST	Altitude, kilo-feet	Pressure, mm Hg	Se-cant Fac-tor	Observed $\int_{\nu_1}^{\nu_2} A_{\nu} d\nu$			Record No.	Time, MST	Altitude, kilo-feet	Pressure, mm Hg	Se-cant Fac-tor	Observed $\int_{\nu_1}^{\nu_2} A_{\nu} d\nu$		
					1.4 μ	1.9 μ	6.3 μ						1.4 μ	1.9 μ	6.3 μ
19	0559	10.8	496	4.83	689	542	585	123	0743			1.84			67
21	0601	11.6	486	4.69	655	533	645	124	0744			1.83			42
22	0602	12.4	475	4.62			603	125	0745			1.82			48
23	0603	13.2	462	4.55	559	549	634	126	0746	92.0	12	1.81			43
24	0604	14.0	446	4.48			615	127	0747			1.80			58
25	0605	14.4	434	4.42	571	445	546	128	0748			1.79			35
27	0607	16.0	404	4.28	505	411	637	129	0749			1.78			40
28	0608	17.2	391	4.28	429	321	506	131	0751			1.76			43
29	0609	18.0	379	4.16		327	495	132	0752			1.75			36
30	0610	18.8	368	4.11	450	245	497	133	0753	92.2	11.5	1.74			43
31	0611	20.0	354	4.06			465	135	0755			1.72			52
32	0612	20.4	338	4.00		323	430	137	0757			1.71			57
33	0613	21.6	326	3.95			461	139	0759			1.69			60
34	0614	22.4	312	3.90			411	140	0800			1.69			39
35	0615	23.6	298	3.85	270		401	141	0801			1.68			35
36	0616	24.4	288	3.80			413	142	0802			1.67			38
37	0617	25.2	277	3.75			415	144	0804			1.65			37
38	0618	26.4	266	3.71	178		383	145	0805			1.64			49
39	0619	27.6	255	3.67		213	394	146	0806			1.64			39
40	0620	28.0	244	3.62		206		147	0807			1.63			38
41	0621	28.4	237	3.58			396	148	0808			1.62			43
42	0622	29.6	229	3.54		283	371	149	0809			1.62			50
43	0623	30.4	222	3.50	237	146	296	150	0810			1.61			39
44	0624	31.2	214	3.46	154	157	276	151	0811			1.60			38
45	0625	32.0	206	3.42	58	120	205	152	0812			1.59			36
46	0626	32.8	198	3.38			258	153	0813			1.58			50
47	0627	34.0	188	3.34			212	155	0815			1.57			41
48	0628	35.2	179	3.31			174	156	0816			1.56			45
49	0629	36.4	169	3.27			104	157	0817			1.56			34
51	0631	38.0	155	3.20			147	158	0818			1.55			38
52	0632	38.8	149	3.17			81	159	0819			1.54			39
54	0634	40.4	138	3.10			115	160	0820			1.54			36
55	0635	41.2	133	3.07			74	163	0823			1.52			46
56	0636	42.0	126	3.04			57	167	0827			1.49			40
58	0638	45.2	112	2.97			55	169	0829			1.48			46
70	0650	56.8	63	2.67			59	170	0830			1.48			40
71	0651	57.6	61	2.64			62	171	0831			1.47			37
74	0654	59.6	55	2.57			52	172	0832			1.46			36
76	0656	60.8	53	2.53			44	173	0833			1.46			42
88	0708	71.6	30	2.31			46	174	0834			1.45			35
89	0709	72.0	30	2.29			42								
95	0715	77.2	24	2.20			45								
96	0716	78.4	23	2.18			56								
97	0717	79.2	22	2.17			45								
98	0718	80.4	21	2.15			44								
100	0720	82.0	18	2.12			70								
101	0721	82.8	17	2.11			51								
105	0725	86.0	15	2.05			51								
107	0727	88.0	14	2.03			70								
111	0731	91.4	12	1.98			41								
113	0733	91.4		1.95			62								
115	0735	91.6		1.93			60								
118	0738			1.89			57								
119	0739	91.8		1.88			49								
120	0740			1.87			41								
121	0741			1.86			52								
122	0742			1.85			43								

tained by replacing the amount of absorbing gas traversed with an equivalent amount determined from

$$w_e = \int_{h_1}^{h_2} (\alpha/\alpha_s) \rho \, dh$$

where α is the half width of the line, α_s is the half width at the standard pressure, and ρ is the density of the absorbing gas. According to kinetic theory,

$$\alpha = \frac{P}{P_s} \sqrt{\frac{T_s}{T}} \alpha_s,$$

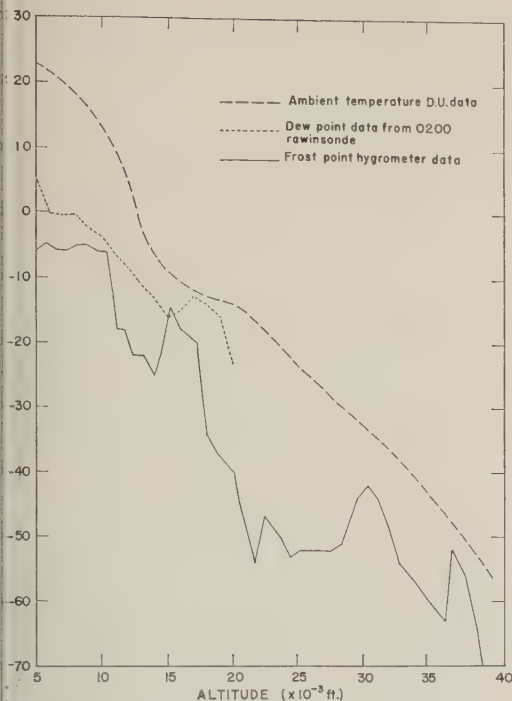


Fig. 2. Comparison of the frost-point hygrometer data and the rawinsonde humidity data for June 19, 1959.

where P and T refer to the pressure and temperature of the gas under consideration and P_s and T_s are the pressure and temperature at standard conditions. If this is substituted into the equation for w_s , we obtain

$$w_s = \int_{h_1}^{h_2} \frac{P}{P_s} \sqrt{\frac{T_s}{T}} \rho \, dh$$

and, if the temperature variation is neglected,

$$w_s = \int_{h_1}^{h_2} \frac{P}{P_s} \rho \, dh$$

which is equivalent to the correction suggested by Curtis and to that used in most meteorological calculations. The assumed relation for α is based on simple kinetic theory and does not include several effects that may be important. The experimental results also indicate that the half width is a more complicated function of pressure than that given above. The empirical data of Howard, Burch, and Williams [1956] indicate that a relation of the type

$$\alpha = \left(\frac{P}{P_s}\right)^n \alpha_s$$

where n is a constant less than 1 that varies from band to band, is a better approximation than the theoretical relation. They also found that the absorption satisfied the following relations

$$\int_{\nu_1}^{\nu_2} A_\nu \, d\nu = C + D \log w + K \log (P + p)$$

for

$$\int_{\nu_1}^{\nu_2} A_\nu \, d\nu > M$$

and

$$\int_{\nu_1}^{\nu_2} A_\nu \, d\nu = c w^{1/2} (P + p)^k$$

for

$$\int_{\nu_1}^{\nu_2} A_\nu \, d\nu < M$$

Here C , D , K , M , c , and k are constants that vary from band to band. The regions for which $\int_{\nu_1}^{\nu_2} A_\nu \, d\nu > M$ are generally referred to as strong fit, and those for which $\int_{\nu_1}^{\nu_2} A_\nu \, d\nu < M$ are referred to as weak fit. The absorptions of interest in this report (above 38,000 ft) all fall into the weak-fit region of the $6.3\text{-}\mu$ band. The data reported in an earlier report [Murcray, Murcray, Williams, and Leslie, 1960] indicate that for the strong-fit region the absorption predicted with

$$w_s = \int_{h_1}^{h_2} \left(\frac{P(h)}{P_s}\right)^n \rho \, dh$$

gives better agreement with the observed data than with the theoretical expression. In view of this, the estimates of the water vapor present at the higher altitudes were made by using both expressions.

Determination of the $\int_{\nu_1}^{\nu_2} A_\nu \, d\nu$ from the spectrum requires a number of operations, each of which can contribute errors. For this reason the errors observed in laboratory studies are of the order of ± 5 per cent of the absorption. Because of the conditions under which these spectra were taken, the probable error is increased to about ± 10 per cent of the absorption. There is also the possibility that on some records the image of the sun might wander so that it would not cover the spectrometer slit while the band was being scanned. This would result

in considerable error in the absorption. Only records that show no evidence of this wandering in the windows were used in this report.

Results. Examination of the data indicates fluctuations in the observed absorptions that are considerably larger than probable error in determining the absorption. It appears that water vapor occurred in concentration centers or clouds. Thus the absorption in the 6.3- μ region of the spectra taken at altitude (92,000 ft) varies from 40 to 60 cm^{-1} around an average value of 44 cm^{-1} . The observed fluctuations are larger than the error in determining the absorption, a fact that is evident on visual inspection of the spectra. Similar results are found at the other altitudes.

Although the observed absorptions indicate that the water vapor was not uniformly distributed, the lack of knowledge of the actual distribution forces us to make this assumption in order to arrive at estimates of the amount of water vapor traversed by the radiation. Starting with this assumption and using the equivalent path concept in conjunction with the laboratory data of *Howard, Burch, and Williams* [1956], we have the following relations:

$$\int_{\lambda_1}^{\lambda_2} A_{\lambda} d\lambda = 356 w_{\lambda}^{1/2} P_0^{-3} \quad \text{for the 6.3-}\mu \text{ band}$$

and

$$w_{\lambda} = \frac{\beta}{P_0^n} \int_{\lambda_1}^{\lambda_2} P^n(h) \rho(h) dh \sec \theta$$

where β is the mixing ratio in g/g, w_{λ} is the equivalent sea level path, and P_0 is taken as 760 mm Hg.

The value for $\int_{\lambda_1}^{\lambda_2} A_{\lambda} d\lambda$ obtained at altitude range from 40 cm^{-1} to 60 cm^{-1} . Calculating w_{λ} from these integrals yields

$$w_{\lambda} = 2.4 \times 10^{-4} \text{ precipitable cm H}_2\text{O for } \int_{\lambda_1}^{\lambda_2} A_{\lambda} d\lambda = 40 \text{ and}$$

$$w_{\lambda} = 5.3 \times 10^{-4} \text{ precipitable cm H}_2\text{O for } \int_{\lambda_1}^{\lambda_2} A_{\lambda} d\lambda = 60$$

The quantity $\int_{\lambda_1}^{\lambda_2} P^n(h) \rho(h) dh$ was determined for $n = 1$ and $n = 0.6$ by numerical integration of the values of $P(h)$ and $\rho(h)$ taken from the ARDC model atmosphere [Minzner and Ripley, 1956]. The value of $\sec \theta$ at the time these records were taken was 1.6. Substituting these values

into the right-hand side of the equation for w_{λ} and using the values of w_{λ} determined from the absorption gives values for β . The limiting values of β are given below for both values of the exponent n .

$$\beta = 1.5 \times 10^{-4} \text{ to } 3.4 \times 10^{-4} \text{ for } n = 0.6 \text{ and}$$

$$\beta = 1.0 \times 10^{-3} \text{ to } 2.2 \times 10^{-3} \text{ for } n = 1$$

If the process is repeated for the absorption observed at 40,000 ft, which ranges from 95 to 145 cm^{-1} , we obtain

$$w_{\lambda} = 1.3 \times 10^{-3} \text{ precipitable cm H}_2\text{O for 95 cm}^{-1} \text{ and}$$

$$w_{\lambda} = 3.1 \times 10^{-3} \text{ precipitable cm H}_2\text{O for 145 cm}^{-1}$$

If a mixing ratio for the region between 40,000 and 92,000 ft is to be calculated, the contribution of the region above 92,000 ft to the equivalent path must be removed. To do this it is first necessary to multiply the equivalent path for the region above 92,000 ft by the ratio of the secants at 40,000 ft and 92,000 ft, respectively. Then these values can be subtracted from the values obtained at 40,000 ft. When this is done we obtain

$$w_{\lambda} = 9.0 \times 10^{-4} \text{ precipitable cm H}_2\text{O}$$

and

$$w_{\lambda} = 2.1 \times 10^{-3} \text{ precipitable cm H}_2\text{O}$$

as the range of values of w_{λ} for the path from 40,000 to 92,000 ft.

The mixing ratio can be calculated as before. It yields

$$\beta = 5.2 \times 10^{-6} \text{ to } 1.2 \times 10^{-5} \text{ g/g for } n = 0.6 \text{ and}$$

$$\beta = 1.2 \times 10^{-5} \text{ to } 3.1 \times 10^{-5} \text{ g/g for } n = 1$$

Thus, it appears that if uniform mixing is assumed, the observed absorptions would be accounted for by a mixing ratio of from 5.2×10^{-6} to 3.1×10^{-5} g/g from 40,000 to 92,000 ft and a mixing ratio of from 1.5×10^{-4} to 2.2×10^{-3} g/g above 92,000 ft.

On the basis of the results obtained on a previous flight [Murcray, Murcray, Williams, and Leslie, 1960] it is felt that the results obtained by using $n = 0.6$ are probably valid. Thus, on the assumption of uniform mixing, there appears to have been from 10 to 22 precipitable microns of water vapor between 40,000 and 92,000 ft on June 19, 1959, at Alamogordo, New Mexico. There also appears to have been between 25 and 55 precipitable microns of water vapor above 92,000 ft. It is interesting to note that if the amount of water vapor present above 40,000 ft is calculated on the basis of the spectra obtained at that altitude only, the total amount of water vapor present above that altitude would be 15 to 36 precipitable microns.

In view of the uncertainty of the pressure correction, the amount of water vapor necessary to account for the observed absorptions was also calculated by assuming that the water vapor existed in a layer rather than being uniformly distributed. Thus, if the layer were assumed to exist at an altitude of approximately 55,000 ft (10 mm Hg), 19 to 44 precipitable microns of water vapor would have been necessary to account for the absorptions observed at 92,000 ft. Because of the pressure dependence of the absorption, the higher the layer is assumed to be the more water vapor there must be to account for the observed absorption.

Conclusions. On the basis of the results obtained on this flight it appears that there was at least 2×10^{-8} precipitable centimeters of water vapor present above 92,000 ft over Alamogordo, New Mexico, on June 19, 1959. It appears that this water vapor was present in concentration centers or clouds. It also appears that the water vapor present between 40,000 and 92,000 ft can be accounted for on the basis of a uniform mixing ratio of 5×10^{-8} g/g, with values higher than this being caused by 'clouds' at higher altitudes.

Comparison with the results of other workers. As was mentioned previously, there is considerable uncertainty at the present time as to the amount of water vapor present above 50,000 ft. The only direct soundings are those made by automatic frost-point hygrometers and a recent measurement made at 27 km with an air-sampling device [Barclay, Elliott, Goldsmith, and Jelley, 1960]. The automatic frost-point hygrometers are theoretically capable of measuring

the frost point down to about 180°K. Some flights that have been made with these instruments indicate the presence of saturated layers and, in some cases, even supersaturated layers in the stratosphere. Since there are a number of condensation nuclei present at these altitudes, the indication of supersaturation has thrown considerable suspicion on all the measurements made with these instruments.

The British have been flying the manual frost-point instrument for a number of years [Brewer, Cwilong, and Dobson, 1948; Brewer, 1949; Dewar, 1951; Dobson, 1950; Farquharson, 1952; Frith, 1951; Bannon, Frith, and Shellard, 1952; Helliwell, Mackenzie, and Kerley, 1957; Murgatroyd, Goldsmith, and Hollings, 1955; Schumacher, 1952; Shellard, 1950]. These flights have been made over a wide range of latitudes at various times of the year. In almost all cases the mixing ratio observed in the lower stratosphere has been in the vicinity of 2×10^{-8} g/g.

The infrared solar spectra obtained by Houghton at 45,000 ft and by Hampson at 47,000 ft and interpreted in much the same way as we have done here (uniform mixing ratios) indicate a uniform mixing ratio of about the same order of magnitude as was observed in the lower stratosphere using the manually operated frost-point hygrometer. These values are also in agreement with the results obtained by the authors on previous flights using the weak bands at the shorter wavelengths. It should be emphasized that, because of the effect of pressure on the absorption and the role it plays in interpreting the data, an order of magnitude change in the mixing ratio at the higher altitudes would be interpreted as a change of less than a factor of 2 in the amount of water vapor traversed when calculated on the basis of uniform mixing from spectra obtained at 45,000 ft.

The only data available to the authors for comparison of the higher-altitude measurements are the frost-point hygrometer flights by Barrett, Herndon, and Carter [1950] and a flight made over England with an air-sampling device [Barclay, Elliott, Goldsmith, and Jelley, 1960].

The values of the mixing ratio at 28 km reported from Barrett's summer flights fall slightly below values calculated from the absorptions at 92,000 ft (28 km). However, the spectral data

indicate the mixing ratio above the point of observation, and Barrett's data show an increasing trend at these altitudes; in fact, his values at 30 km fall inside the range of values calculated from the spectra given by

$$w_s = \frac{\beta}{P_0^{0.6}} \int_{h_1}^{\infty} P_0^{0.6}(h) \rho(h) dh \sec \theta$$

The mixing ratio of 3.7×10^{-5} g/g, measured at 27 km by Barclay, Elliott, Goldsmith, and Jelley [1960] with an air-sampling device, is lower than the values obtained from the summer frost-point hygrometer measurements, but it falls just above the range calculated from the spectral measurements for the region of 40,000 to 92,000 ft. There is no reason to believe that the transition to higher values of the mixing ratio is abrupt so that mixing ratios slightly higher than those calculated could be expected in the upper portions of the 40,000- to 92,000-ft interval. Some variation in the measured values of the mixing ratio is to be expected, since the observations cover a wide range of time and location. There have been several recent flights with frost-point instruments by various investigators, but the results of these are not available to the authors at this time.

It should be re-emphasized that, although calculations in this paper were made on the basis of uniform mixing ratios, and the data indicate (1) that the water vapor was not uniformly distributed, (2) that some of it occurred in concentration centers or 'clouds,' and (3) that some of these 'clouds' existed above 92,000 ft.

Acknowledgment. The research reported in this document was sponsored by the Geophysics Research Directorate, Air Force Cambridge Research Center, under contract AF 19(604)-2069.

REFERENCES

- Bannon, J. K., R. Frith, and H. C. Shellard, Humidity of the upper troposphere and the lower stratosphere over southern England, *Meteorol. Office, Geophys. Memoirs*, 11, no. 88, 1952.
- Barclay, F. R., M. J. W. Elliott, P. Goldsmith, and J. V. Jelley, A direct measurement of the humidity in the stratosphere using a cooled-vapour trap, *Quart. J. Roy. Meteorol. Soc.*, 86, 259-264, 1960.
- Barrett, E. W., L. R. Herndon, Jr., and H. J. Carter, A preliminary note on the measurement of water vapor content in the middle stratosphere, *J. Meteorol.* 6, 367-368, 1949.
- Barrett, E. W., L. R. Herndon, Jr., and H. J. Carter, Some measurements of the distribution of water vapor in the stratosphere, *Tellus*, 2, 302-311, 1950.
- Benford, F., Duration of intensity of sunshine, *Illum. Eng.*, 42, 527-544, 1947.
- Brewer, A. W., Evidence for a world circulation provided by the measurements of helium and water vapor distribution in the stratosphere, *Quart. J. Roy. Meteorol. Soc.*, 75, 351-363, 1949.
- Brewer, A. W., B. M. Cwilog, and G. M. B. Dobson, Measurement of absolute humidity in extremely dry air, *Proc. Phys. Soc. London, A*, 60, 52-70, 1948.
- Carpenter, R. O'B., J. A. Wright, A. Quesada, and R. E. Swing, Predicting infrared molecular attenuation for long slant paths in the upper atmosphere, *Sci. Rept. 1, Geophys. Research Directorate, AFCRC, Baird-Atomic Inc., contract AF 19(604)-2405*, Nov., 1957.
- Dewar, D., First year of upper air observations by ocean weather ships, *Meteorol. Mag.*, 80, 245-253, 1951.
- Dobson, G. M. B., A. W. Brewer, and B. M. Cwilog, Meteorology of the lower stratosphere, *Proc. Roy. Soc. London, A*, 185, 144-175, 1946.
- Dobson, G. M. B., Physics and the atmosphere, *Proc. Phys. Soc. London, B*, 63, 252-266, 1950.
- Farquharson, J. S., Cloud in the stratosphere, *Meteorol. Mag.*, 81, 341-345, 1952.
- Frith, R., Recent work of the meteorological research flight of the Meteorological Office, *Quart. J. Roy. Meteorol. Soc.*, 77, 478-480, 1951.
- Gates, D. M., D. G. Murcray, C. C. Shaw, and R. J. Herbold, Near infrared solar radiation measurements by balloon to an altitude of 100,000 feet, *J. Opt. Soc. Am.*, 48, 1010-1016, 1958.
- Goddard, A., Jr., M. Juza, T. Maher, and F. Speck, Balloon-borne system for tracking the sun, *Rev. Sci. Instr.*, 27, 381-385, 1956.
- Helliwell, N. C., J. K. Mackenzie, and M. J. Kerley, Some further observations from aircraft of frost-point and temperature up to 50,000 ft, *Quart. J. Roy. Meteorol. Soc.*, 83, 257-262, 1957.
- Houghton, J. T., T. S. Moss, and J. P. Chamberlain, An air borne infrared solar spectrometer, *J. Sci. Instr.*, 35, 329-333, 1958.
- Houghton, J. T., T. S. Moss, J. S. Seely, and T. D. F. Hawkins, Some observations of the infrared solar spectrum from a high-flying aircraft, *Nature*, 180, 1187-1188, 1957.
- Howard, J. N., D. L. Burch, and D. Williams, Infrared transmissions through synthetic atmospheres, *J. Opt. Soc. Am.*, 46, 186-190, 237-245, 334-338, 452-455, 1956.
- Kiseleva, M. S., B. S. Neporent, and V. A. Fursinkiv, Spectral determination of water vapor in the upper atmosphere, *Optics and Spectroscopy, Russia*, 6, 522-524, 1959. (Translation of *Optika i Spektrosk.*)
- Minzner, R. A., and W. S. Ripley, The ARDC model atmosphere, *Surveys in Geophys.*, no. 86, *Geophys. Research Directorate, AFCRC*, Dec. 1956.
- Murcray, D. G., J. Brooks, F. Murcray, and C.

- Shaw, High altitude infrared studies of the atmosphere, *J. Geophys. Research*, 63, 289-299, 1958.
- Murcray, D., J. Brooks, F. Murcray, and W. Williams, Atmospheric absorptions in the near infrared at high altitudes, *J. Opt. Soc. Am.*, 50, 107-112, 1960.
- Murcray, D., J. Brooks, F. Murcray, W. Williams, and F. Leslie, Instrumentation for balloon-borne infrared spectral transmission measurements of the atmosphere, *Sci. Rept. 3, Geophysics Research Directorate, AFCRC, Univ. of Denver, contract AF 19(604)-2069*, Feb., 1960.
- Murcray, D., F. Murcray, W. Williams, and F. Leslie, A study of the 1.4μ , 1.9μ and 6.3μ water vapor bands at high altitudes, *Sci. Rept. 4, Geophysics Research Directorate, AFCRC, Univ. of Denver, contract AF 19(604)-2069*, Feb. 1960.
- Murgatroyd, R. J., P. Goldsmith, and W. B. H. Hollings, Some measurements of humidity from aircraft up to heights of about 50,000 ft. over southern England, *Quart. J. Roy. Meteorol. Soc.*, 81, 533-537, 1955.
- Nielsen, J. R., V. Thornton, and E. B. Dale, The absorption laws for gases in the infrared, *Revs. Modern Phys.*, 16, 307-324, 1944.
- Plass, G. N., A method for the determination of atmospheric transmission functions from laboratory absorption measurements, *J. Opt. Soc. Am.*, 42, 677-683, 1952.
- Schumacher, N. J., The Maudheim expedition, 1949-52, II, *Weather*, 7, 327-334, 1952.
- Shellard, H. C., Simultaneous aircraft soundings of temperature and frost point, *Meteorol. Mag.*, 79, 355-356, 1950.

(Manuscript received July 11, 1960.)

Atmospheric Net Radiation Flux during Winter in the Thule Area, Greenland

ROBERT W. FENN AND HELMUT K. WEICKMANN

*U. S. Army Signal Research and Development Laboratory
Fort Monmouth, New Jersey*

Abstract. A brief description of an airborne infrared net radiation receiver (developed in Germany) is given, and the results of radiosonde flights made with this element at Thule, Greenland, during February 1959 are shown.

The outgoing net radiation flux during the arctic winter increases with altitude from 0.05 cal cm⁻²min⁻¹ at the surface to about 0.2 cal cm⁻²min⁻¹ between 15,000 and 20,000 meters. Above 25,000 meters the outgoing net radiation flux again decreases considerably.

Introduction. Infrared radiation is an important factor in the atmospheric heat budget in the Arctic during winter. Radiation fluxes originate from two sources: the thermal radiation flux from the ground and the radiation from gas molecules and from solid and liquid particles in the atmosphere. The difference between the vertical components of these two radiation fluxes is called the net radiation. The vertical divergence of the net radiation flux is a measure of the absorption and emission of radiation in the atmosphere.

Two night ascents of a net radiation radiosonde were made at Thule, Greenland (76°30'N, 68°50'W), on February 14 and 15, 1959. The radiosonde flights were made with a combination of the net radiation radiosonde¹ developed by Pohl [1956] in Germany and the radiosonde MD-317/AMT-12 which is used in the United States.

Theory and instrumentation. The transducer (Figs. 1 and 2) is a pair of sensors, each consisting of two horizontally oriented, blackened plates. One plate is in radiation exchange with the sky and the atmosphere above flight level and the other is in radiation exchange with the ground and the atmosphere below flight level. In one sensor the plate facing up is electrically heated; in the other the plate facing down is electrically heated. In order to guarantee for all four surfaces a uniform conductive heat transfer

with the surrounding air, the receiver rotates around a vertical axis during the ascent by means of a wind vane (Fig. 3). The temperature of each of the four surfaces is measured by a thermistor.

The following energy equations exist for the four surfaces:

$$aD - a\sigma T_1^4 + H - \alpha(T_1 - T_0) - \beta(T_1 - T_2) - \gamma \frac{dT_1}{dt} = 0 \quad (1)$$

$$aU - a\sigma T_2^4 - \alpha(T_2 - T_0) - \beta(T_2 - T_1) - \gamma \frac{dT_2}{dt} = 0 \quad (2)$$

$$aD - a\sigma T_3^4 - \alpha(T_3 - T_0) - \beta(T_3 - T_4) - \gamma \frac{dT_3}{dt} = 0 \quad (3)$$

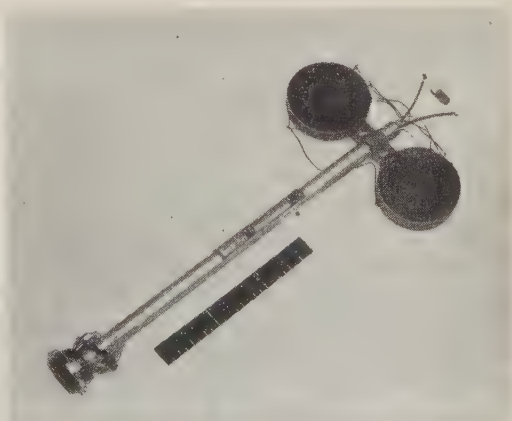


Fig. 1. Receiver for infrared radiation radiosonde.

¹ This net radiation sonde is manufactured by Muenchener Apparatebau fuer elektronische Gerate, Muenchen 23, Germany.

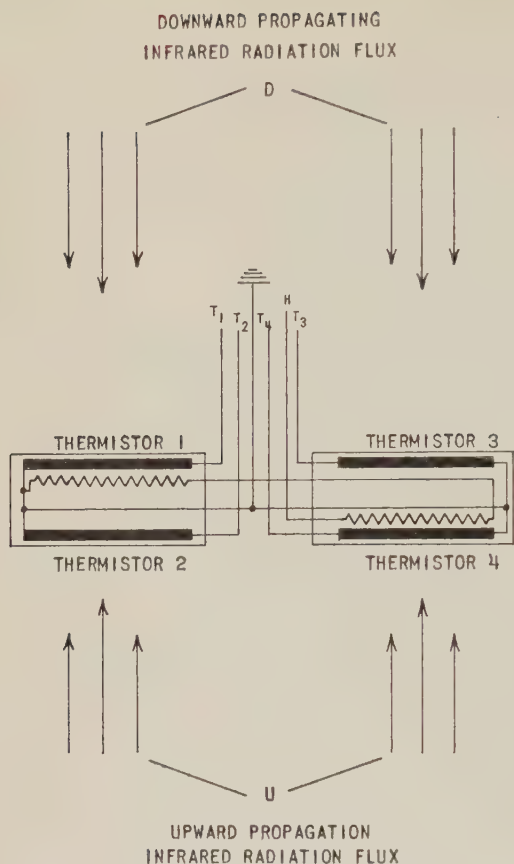


Fig. 2. Schematic of plate arrangement of receiver element.

$$aU - a\sigma T_4^4 + H - \alpha(T_4 - T_0) - \beta(T_4 - T_3) - \gamma \frac{dT_4}{dt} = 0 \quad (4)$$

where

D = downward propagated radiation flux.

U = upward propagated radiation flux.

H = electrical heat input ($\text{cal cm}^{-2} \text{min}^{-1}$).

T_0 = air temperature ($^{\circ}\text{K}$).

σ = Stefan-Boltzmann constant ($\text{cal cm}^{-2} \text{min}^{-1} \text{deg}^{-4}$).

T_i = temperature of surface i ($^{\circ}\text{K}$); $i = 1, 2, 3, 4$.

a = absorption coefficient of the plate surfaces for infrared radiation.

α = heat transfer coefficient from element to air ($\text{cal cm}^{-2} \text{min}^{-1} \text{deg}^{-1}$).

β = heat transfer coefficient with the plates.

γ = heat capacity of one surface ($\text{cal cm}^{-2} \text{deg}^{-1}$).

Because of the small values of $(T_i - T_0)$ compared with T_0 and T_i the terms T_i^4 can be obtained from a binomial expansion:

$$T_i^4 = [T_0 + (T_i - T_0)]^4 = T_0^4 + 4T_0^3(T_i - T_0) + \dots \quad (5)$$

Equations (2) - (1) and (4) - (3) then give

$$\begin{aligned} a(U - D) - H - 4a\sigma T_0^3(T_2 - T_1) \\ - \alpha(T_2 - T_1) - 2\beta(T_2 - T_1) \\ - \gamma \frac{d}{dt}(T_2 - T_1) = 0 \end{aligned} \quad (6)$$

$$\begin{aligned} a(U - D) + H - 4a\sigma T_0^3(T_4 - T_3) \\ - \alpha(T_4 - T_3) - 2\beta(T_4 - T_3) \\ - \gamma \frac{d}{dt}(T_4 - T_3) = 0 \end{aligned} \quad (7)$$

Since the changes of temperature differences with time are small compared with the remaining terms of temperature differences, we get

$$a(U - D) = (\alpha + 4\sigma T_0^3 + 2\beta) \cdot (T_2 - T_1) + H \quad (8)$$

$$a(U - D) = (\alpha + 4\sigma T_0^3 + 2\beta) \cdot (T_4 - T_3) - H \quad (9)$$

and, by dividing these two equations,

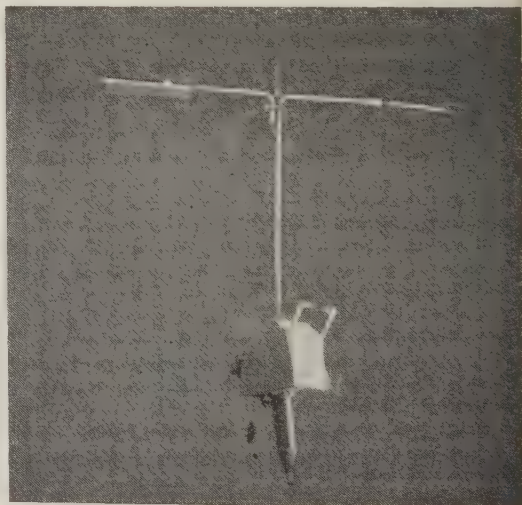


Fig. 3. Radiation radiosonde assembly.

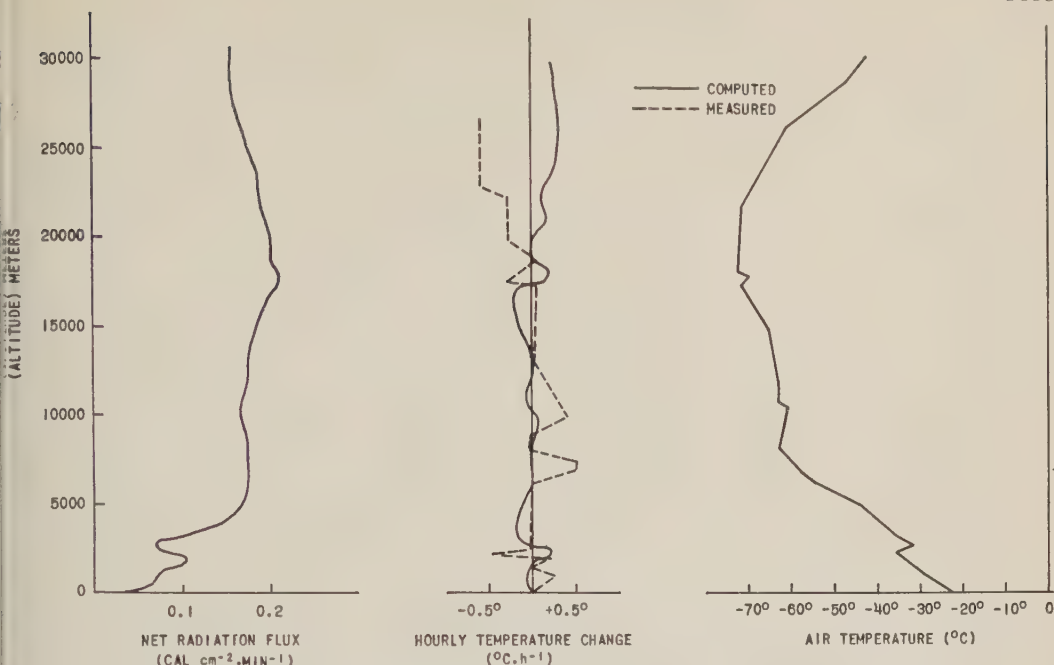


Fig. 4. Results from net radiation radiosonde flight at Thule, February 14, 1959.

$$U - D = \frac{(T_4 - T_3) + (T_2 - T_1)}{(T_4 - T_3) - (T_2 - T_1)} H \frac{1}{a} \quad (10)$$

Equation 10 can be written

$$N = U - D$$

$$= \frac{(T_4 - T_3) + (T_2 - T_1)}{(T_4 - T_3) - (T_2 - T_1)} H + N' \quad (11)$$

N is called net radiation flux. N' is a correction term for (a) deviations of the absorption coefficient from the value 1, (b) different ventilation of the top and bottom side of the plates, and (c) oscillations of the radiosonde package on the balloon. N' varies between ± 10 per cent of N . (Graphs for N' are given by Pohl.)

Since in equation 11 the ratio of temperature differences is dimensionless, we can use scale divisions directly for further computations. However, the thermistors must be calibrated before the flight, since they are not always identical. This correction must be applied to the value of scale divisions.

The amount of heat energy put into the plates is given by the product RI^2 , where R (the resistance of the heater coil for one plate) is approximately 40 ohms, and I is around 75 ma. The heat input in $\text{cal cm}^{-2}\text{min}^{-1}$ is then given by

$$H = \frac{0.239 \times 60}{A} RI^2 \quad (\text{watts})$$

$$= 1.202 RI^2$$

A = surface area of receiving element
($d = 3.9$ cm)

The heating current was supplied by a series of three BA-253 2-volt batteries (water-activated before launching); the current was measured before release. After the flight was completed the entire flight was simulated (with regard to time and temperature) in the laboratory. The batteries were connected to the same load as that during the radiosonde flight and the current through the load was recorded during the simulated flight. The resistance of the heating coil is assumed to be constant over the period of the flight. In this way it is possible to apply at least some correction for changes in heat input during the ascent.

The accuracy of the measurements is mainly determined by the accuracy with which the heating current I (since I enters with the square) and the temperature differences ΔT , can be measured. The accuracy for the temperature difference values in these measurements was about 0.2°C . The value for the error of the

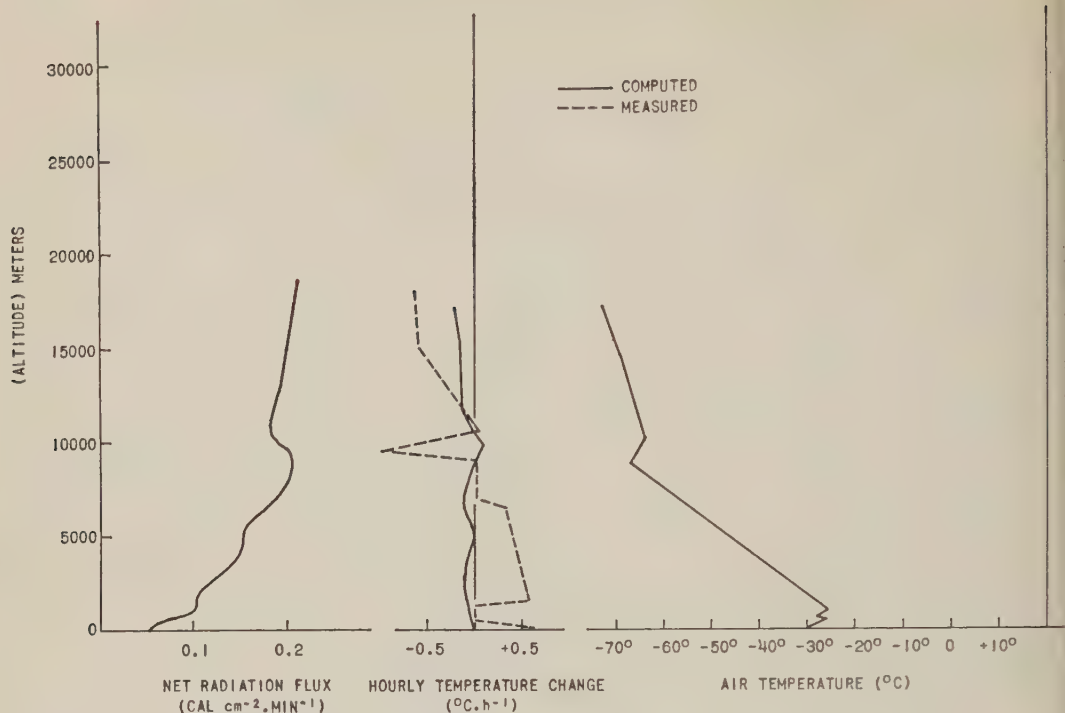


Fig. 5. Results from net radiation radiosonde flight at Thule, February 15, 1959.

heating current must be assumed, despite the above-mentioned correction, to be at least 2 per cent. The total error is approximately 15 per cent. This is the error for the absolute net radiation flux; the error for the radiation flux gradient is somewhat smaller.

As was mentioned before, the net radiation flux can be used to compute the temperature change in the atmosphere due to radiation, since any vertical change of net radiation flux is caused by either absorption or emission of radiation in the particular layer of the atmosphere. The equation of heat diffusion gives

$$\partial N / \partial z = -\rho c_p \partial T / \partial t \quad (13)$$

where

ρ = air density; c_p = specific heat at constant pressure.

z = vertical coordinate.

T = air temperature.

t = time.

With the barometric equation

$$dp = \rho g dz \quad (g = \text{gravity}) \quad (14)$$

we can write

$$\partial N / \partial p = -(c_p / g) (\partial T / \partial t) \quad (15)$$

or

$$\Delta T / \Delta t = -k (\Delta N / \Delta p) \quad (16)$$

If $\Delta T / \Delta t$ is measured in $^{\circ}\text{C/hr}$ and p in mb, k comes out to be $250 \text{ (deg cm}^2 \text{ mb cal}^{-1})$.

The telemetering of the temperature values to the ground was achieved by connecting all transducer elements through a stepping switch to the modulator circuit of the AMT-12 radiosonde, thus allowing the data to be transmitted on the 1680-Mc/s frequency.

Results of the flights. With this instrumentation two radiosonde flights were conducted on February 14 and 15, 1959, at Thule Air Force Base, Greenland. Both flights were made during nighttime. The recorded parameters were the four plate temperatures, air temperature, humidity, and pressure. The flight on February 14 (Fig. 4) was made with a Mylar plastic balloon. The maximum altitude reached was approximately 33 km. The balloon was launched at 1630 hours local time (2130 GCT) and the

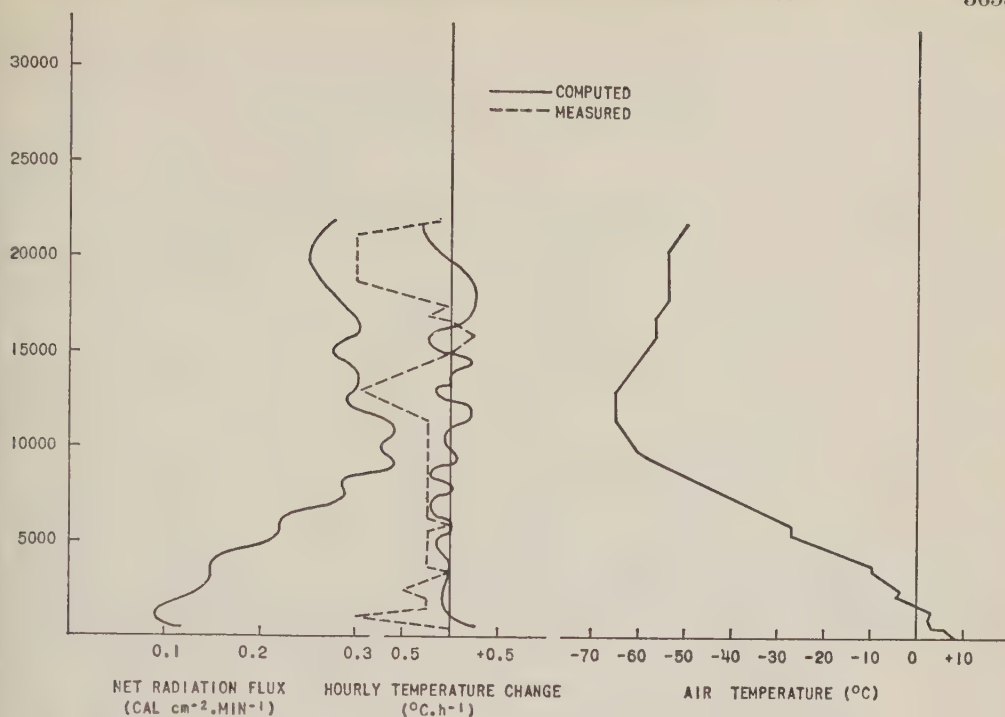


Fig. 6. Results from net radiation radiosonde flight at Fort Monmouth, N. J., November 12, 1959.

total flight time was 130 minutes. The sky was clear except for some very thin cirrus. The net radiation flux, the air temperature, the computed hourly temperature change, and the actual measured temperature change from the regular radiosonde ascent at 1300 and 1900 hours are plotted in Figure 4.

The flight of February 15 (Fig. 5) was also made with a Mylar balloon. At 65 mb the motor switch of the radiosonde stopped, so no data from higher altitudes could be recorded. The balloon was launched at 2140 hours (0240 GCT, February 16) in a clear sky. The actual temperature change as plotted in Figure 5 was obtained from the 3-hour change between 2200, February 15, and 0100, February 16.

For a comparison, in Figure 6 the results of a flight conducted on November 12, 1959, at Fort Monmouth, New Jersey, are shown. The maximum altitude was about 40 mb. The balloon was launched at 1800 hours.

As expected, all ascents show an increasing outgoing net radiation flux with increasing altitude. In the Arctic the net radiation flux increases from around $0.05 \text{ cal cm}^{-2} \text{ min}^{-1}$ at the

surface to about $0.2 \text{ cal cm}^{-2} \text{ min}^{-1}$ between 15,000 and 20,000 meters, and above 20,000 meters it decreases again. (The net radiation flux is defined here as positive if the outgoing radiation is greater than the incoming radiation.) For the flight over New Jersey the maximum value for the net radiation flux was reached at 10,000 to 11,000 meters, and above that it decreased again. The results of these flights show that the net heat radiation flux in the arctic winter is much less than that in temperate zones. For the flight on November 12 in New Jersey the net radiation increased from about 0.1 to $0.35 \text{ cal cm}^{-2} \text{ min}^{-1}$. Pohl [1956] has measured net radiation fluxes in Europe during winter and spring as high as $0.3 \text{ cal cm}^{-2} \text{ min}^{-1}$, and for one flight in June, $0.4 \text{ cal cm}^{-2} \text{ min}^{-1}$. This is not surprising since in the Arctic the temperature of the ground is only -20° to -30°C and therefore the surface radiation is much less. On the other hand, during the arctic winter the heat influx into the atmosphere by air mass exchange is so small that the radiation loss, although much smaller than that in more southern latitudes, results in a considerable cooling of the atmosphere.

If the net radiation flux increases in a certain layer with altitude, this should result in a temperature decrease for this layer, and vice versa. All ascents in the troposphere as well as in the stratosphere show distinct changes of the net radiation flux, which changes must be connected with layers of heating or cooling. Some authors related those variations to the absorption or emission on the top and bottom sides of haze layers. The radiation flux over the Arctic shows a much smoother trend than over the American and European continents, which could be explained by a very homogeneous vertical aerosol distribution over the polar cap. As can be seen from Figures 4 to 6, however, in several cases the actual temperature change is exactly opposite to and much more intense than the expected temperature change due to radiation effects. For inversion zones (flight on February 14, at 2500 meters), this is due to a slight vertical movement of the inversion over the several-hour time interval between the two radiosonde flights from which the temperature change was computed. The momentary value and direction of temperature change obtained from the radiation radiosonde flight, of course, does not have to be the same as the 4- or 6-hour average. Furthermore, such a discrepancy may be due to advective or convective processes opposite to the radiation effect. For instance, on November 12 (Fig. 6), it seems that a general advective cooling was superimposed on the radiation effect.

However, there is one peculiarity in all ascents that must be mentioned: the constant decrease of the net radiation flux in the stratosphere. This decrease of net radiation flux parallel with the vertical temperature increase in the stratosphere was also previously recorded by Pohl and by Roenicke on flights made in Central America (Dr. F. Moeller, private communication). This net radiation flux decrease must be the result of energy absorption, and it causes a temperature increase of the order of 0.2° to 0.3°C per hour. However, other processes of opposite direction must exist to balance this radiation effect. More high-altitude radiosonde flights and rocket measurements will be necessary to study the energy processes in the higher atmosphere.

Acknowledgments. We wish to express our sincere appreciation to Mr. Raymond Bellucci and Mr. John J. Kelly of the U. S. Army Signal Research and Development Laboratory for their advice and help in conducting the radiosonde flights. We are also grateful to the Commander and the personnel of the U. S. Air Weather Service for making available the AN/GMD-1 receiver at their Thule station and for their assistance in making the flights.

REFERENCE

Pohl, Wolfgang, Messungen des ultraroten Strahlungsstromes in der freien Atmosphäre, *Z. Geophys.*, 22, 1-52, 1956.

(Manuscript received December 11, 1959; revised August 25, 1960.)

The Economical Net Radiometer

C. B. TANNER

*Department of Soils, University of Wisconsin
Madison, Wisconsin*

J. A. BUSINGER

*Department of Meteorology, University of Washington
Seattle, Washington*

AND

P. M. KUHN

U. S. Weather Bureau, Madison, Wisconsin

Abstract. The 'economical' net radiometer of Suomi and Kuhn can be used to measure the incoming and outgoing radiation flux density of the total, the solar, and the thermal radiation currents as well as net radiation. This requires at least two radiometers with different spectral absorptions. The theory and errors of the radiometer are developed, and experimental tests of some of the equations are presented.

INTRODUCTION

The 'economical' net radiometer described by Suomi and Kuhn [1958] is being employed increasingly in meteorological, agricultural, and hydrological research. Its usefulness derives from its relatively low cost and the convenience of the measurement (visual reading of thermometers) in the absence of commercial power or recorders. The radiometer with black painted radiation surfaces described by Suomi and Kuhn can be used to determine the total incoming (downward) and outgoing (upward) radiation currents and the net radiation. If surfaces of different spectral absorptions are used, two or more units can be used to separate the currents of solar and thermal (infrared) radiation.

The purpose of this report is to extend the theory [Suomi, Staley, and Kuhn, 1958] of the economical radiometer to both solar and thermal radiation by using simple averages of absorption for wide spectral ranges of radiation. A more precise approach requires the spectral functions to be in the equations, but this complicates the theory unnecessarily. The present approach is sufficiently accurate for general use of the instruments, and the theory is applicable to other radiometers with ventilation shielding. Though the presentation of the radiometer

theory is the primary purpose of this report, the theory is preceded by sections devoted to experimental aspects of the instrument, including data, errors, and potential uses.

PART 1. EXPERIMENTAL PROCEDURE

Description. Figure 1 illustrates two symmetric radiometer units,¹ one facing upward and one facing downward. They are spaced by a distance d_s so that with natural ventilation the entire outside boundary of each unit is at or near air temperature. This construction is referred to as 'single-ended.' When $d_s = 0$, this becomes the radiometer described by Suomi and Kuhn and is referred to as 'standard' construction. As is shown in the section on theory, the single-ended construction simplifies the radiometer equations and data reduction. The radiometer is usually constructed so that d_a is of the order of 1.2 cm, d_d is of the order of 5.0 cm, and the diameter of the radiation surface is 15 to 25 cm—much larger than d_a .

The radiometer is an energy-balance instrument in which the radiation absorbed at the radiation surface is lost by infrared (thermal)

¹ Radiometers may be purchased from Agmet Products Co., P. O. Box 113, Middleton, Wisconsin.

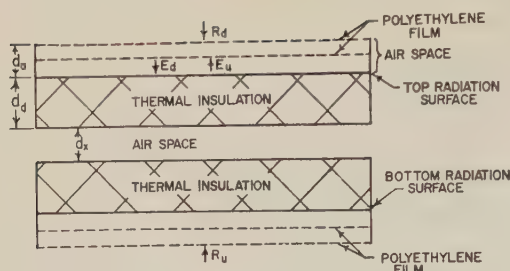


Fig. 1. Schematic of economical radiometer.

radiation and conduction from the surface. Since the radiation loss is a function of the temperature of the radiation surface and the conduction loss is a function of the radiation surface and air temperatures, a measurement of these temperatures gives a measure of the radiation, provided the radiation and conduction properties of the instrument are known.

The purpose of the polyethylene films is to provide protection from natural ventilation, which causes heat losses that cannot be easily assessed, and yet provide a 'window' for both solar and thermal infrared radiation. Polyethylene was chosen because of its low absorption and because the absorption bands of polyethylene do not coincide either with the principal emission (absorption) bands of the atmosphere or with the atmospheric windows; therefore, the upward, the downward, and the net radiation fluxes are not materially affected. This is not true for the mica and Saran windows employed in another shielded radiometer [Fritschen, 1960]. We have employed 0.5-mil-thick, clear polyethylene for reasons discussed later. Polyethylene is by far the most satisfactory film for measurements in the infrared.

Experimental verification of theory. Equation 15, derived in Part 2, is for the single-ended net radiometer with black-painted surfaces *only*. All symbols are defined in Part 2.

In the absence of solar radiation $R_{sn} = 0$, and the equation for the net infrared radiation is simple. The advantage and accuracy of the instrument for thermal radiation measurements have been demonstrated previously [Kuhn, Suomi, and Darkow, 1959]. Therefore, our primary concern is for the case when solar radiation is present.

When solar radiation exists $R_{sn} \neq 0$, and the δR_{sn} term is negligible only when either δ or R_{sn} is small. A small δ is obtained when r_s , ϵ_s , and a_s

are close to r_i , ϵ_i , and a_i , respectively. Because the reflection from the polyethylene depends upon the angle of incidence, r_s will depend upon whether the solar radiation is principally diffused or beamed. Under clear conditions, r_s is large at large angles of incidence (low sun altitudes), found in early morning and late evening, and at high latitudes during the winter. Moreover, r_s at the top will differ from that at the bottom of the radiometer during these times. With thin, clear polyethylene and the black paint we have used, δ is approximately -0.1 , -0.3 , and -0.7 for beam radiation at sun altitudes of 30° , 20° , and 10° , respectively. The only compensating features are that R_{sn} is usually not large at sun altitudes below 20° and that the scattered radiation from the sky is a fairly large portion (30 to 40 per cent) of the solar radiation. At high sun altitudes on clear days $\delta = 0.04$, and on days of complete uniform diffuse radiation $\delta = -0.1$. Tests of (15) were made by comparing $R_n(\text{est}) = (R_n + \delta R_{sn})$ obtained from a black, single-ended economical radiometer with R_n obtained from a ventilated net radiometer [Suomi, 1957] as illustrated in Figure 2. All comparisons were made during clear periods when sun altitudes were greater than 30° . The characteristics of the polyethylene and black paint on the radiation surfaces were known and are listed below.

Polyethylene (2 layers)		Black Paint
$\tau_i = 0.85$;	$\tau_s = 0.83$	$a_{is} = 0.91$
$r_i = 0.135$;	$\epsilon_i = 0.015$	$a_{ib} = 0.85$

It is seen that for these conditions the theory is satisfactory when δ is small.

Equation 15 applies to all similar radiometers² in which the ventilation of the radiation sensors is prevented with a shield that transmits radiation and in which only one 'paint' on the sensor is used. With these radiometers, it is essential that δ be as small as possible. Since low sun altitude greatly affects δ , such instruments are not suitable at low sun altitudes unless δ and R_{sn} are known. This requires more information than can be obtained from a shielded black radiometer alone.

² An example is the net radiometer described by Fritschen [1960], who employed the ventilation shielding proposed by Suomi and Kuhn, [1958].

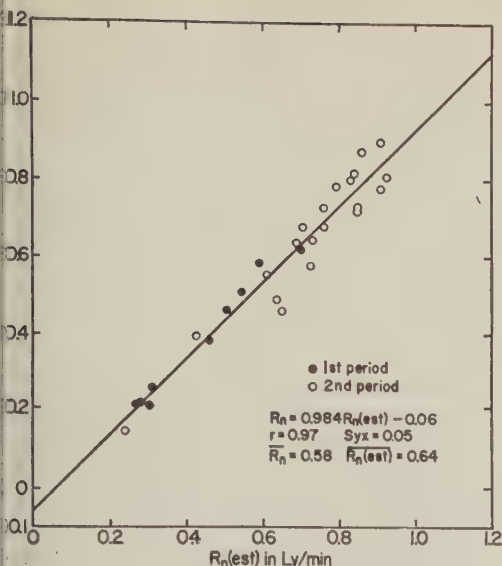


Fig. 2. Net radiation estimates (calculated) from economical radiometer with black surfaces only versus measured net radiation (first period corresponds to data in Figs. 3 and 4).

If we add to the instrument with black surfaces an instrument with white surfaces that reflects the solar radiation selectively, it is possible to derive separate relations for both the solar and infrared (thermal) radiation. This enables us to calculate R_{sd} , R_{sw} , R_{sn} , and R_n (provided τ_s is known). Equations 24 and 19a were derived in Part 2d for R_n and R_{sd} when information is available from both a black and a white unit and where $C_{i,w} = C_{i,b} = C_i$. We used a special lead carbonate paint that did not prove to be stable under solar radiation. However, the paint did not change appreciably until after nine periods of measurements (1 hour each) were completed (these are shown in Figure 3 as the first period). We assumed that $a_{i,w} = 0.85$ (about the same as polished aluminum) and that $a_{i,b} = 0.85$ (the same as black paint). The net radiation computed from (24) is compared with the measured net radiation from [Kusumoto, 1957] radiometer in Figure 3, where $R_n(\text{est})$ is that calculated for the economical radiometers. When only the black-radiometer data are used and the net radiation computed from (15) by assuming that δR_{sn} is negligible, the results for the first period are

$$R_n = 1.03 R_n(\text{est}) - 0.07$$

$$r = 0.99; \quad S_{yx} = 0.02 \text{ ly/min.}$$

The solar radiation computed from (19a) is compared with the measured solar radiation (Eppley pyrliometer) R_{sd} in Figure 4, where $R_{sd}(\text{est})$ is the solar radiation calculated from economical radiometer measurements. An assumption of different white paint characteristics gives an equally good correlation between R_{sd} and $R_{sd}(\text{est})$, but constants in the regression equation change.

Since the equation for R_{sw} is symmetric with (19a) for R_{sd} , except that temperatures for the bottom elements replace those for the top, the albedo of a surface may be found as $\text{albedo} = R_{sw}/R_{sd}$. It is noted that the solar radiation absorptivities of the black and white paints are not required. Some surfaces and their measured albedos are: dry Plainfield sand, 0.25; corn at tasseling stage, 0.16; Lake Mendota in September, 0.07; and clean snow 1 week old, 0.75. Though independent measurements of the albedo with other instruments were not available, the albedos measured with the economical radiometers are reasonable.

It is evident that in sunlight where τ_s is defined the theory of the economical radiometer is satisfactory. Tests of the calculated net radiation indicated that, when an error of 5 to 10 per cent is permissible, the economical radiometer is suitable for general use during daytime conditions of diffuse and beam radiation provided sun altitudes exceed 30° .

Errors. The errors in shielded radiometers may be evaluated in two parts: the radiation properties of the instrument and the heat transmission (conduction) coefficients. With usual construction of the economical radiometer the error in measuring temperatures is unimportant.

When the black unit is used alone to measure total radiation or net radiation, the greatest error results in neglecting δR_{sn} . At sun altitudes greater than 30° , R_{sn} is small only over surfaces with very high albedos. However, at sun altitudes greater than 30° , δ lies in the range of -0.1 for a lower limit (beam radiation at 30° altitude or uniformly diffuse radiation with equal intensity throughout the sky) to 0.04 as an upper limit for normal beam radiation on both surfaces. Under actual conditions there is diffuse (scattered) radiation on clear days at a sun altitude of 30° . Heavy overcasts that create uniform radiation in-

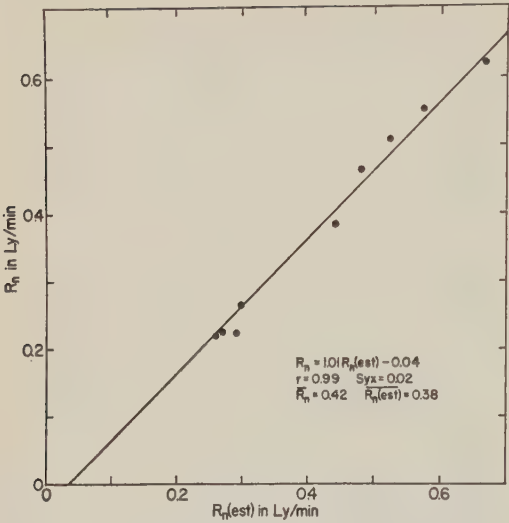


Fig. 3. Net radiation estimates (calculated) from black and white economical radiometer versus measured net radiation.

tensity over the sky do not occur frequently. Thus, δ is usually well within the above maximum limits. Most of the time the error in R_n will be within about 7 per cent. At sun altitudes less than 30° the error is likely to be greater, and we do not recommend the black unit under this condition. Unshielded net radiometers should be used when the altitude of the sun is low.

The change of reflection coefficient of polyethylene with radiation incidence causes the greatest error in assuming δ to be constant. In addition, the radiation reflected from the ground and entering the bottom of the radiometer is diffuse (scattered) whereas that from above is mainly direct under clear skies, with increasing scattered radiation when skies are cloudy. The effect of this difference is much less than that caused by the difference in the infrared and solar characteristics of the instrument (δ) except at high sun altitudes on clear days over a surface with high albedo (> 0.5) where R_{sn} is low.

The a_s of many black paints is greater than a_i . This difference in a_s and a_i can be adjusted to minimize δ for a given radiation incidence, as suggested by *Suomi* [1957], by painting a portion of the sensor white. Another alternative is to measure the R_{sn} and correct (15) accordingly. Correction by either method is poor if δ is large and variable during the period of measurement.

The error in the net radiation estimate when the black and white units are used is somewhat less than that when only the black unit is used, because R_{sn} is evaluated. The error in either R_{sd} or R_{su} is of the order of the error in τ_s . τ_s is about 0.84 when the sun is at an altitude of 90° , 0.81 at 45° , 0.79 at 40° , 0.76 at 35° , and 0.72 at 30° with clear skies; and $\tau_s = 0.73$ with heavy overcast skies or diffuse reflection from the ground. The value of R_s may be obtained within 5 per cent at sun altitudes over 30° , provided the characteristics of the black and white paints are known.

The major practical difficulties that cause error are the accumulation of condensate within the polyethylene films, the accumulation of dirt on the films, and the nonstability of the paints. The films may be changed often to avoid the first and second difficulties. The black paint is stable and a small change in absorptivity is not critical. We have not yet been able to find a satisfactory stable white surface, except ceramics, which have a higher absorptivity for solar radiation than is desirable. Normal paint vehicles darken with age. A promising substitute for white paint is a rear-surfaced mirror. The glass gives high absorption of infrared radiation and the mirror gives high reflection of solar radiation. In addition to the need for stable white paint, it is necessary that $a_{iw} = a_{ib}$, so

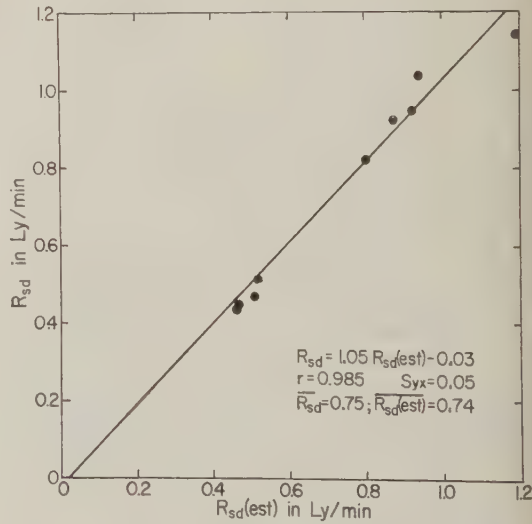


Fig. 4. Solar radiation estimate (calculated) from black and white economical radiometer versus measured solar radiation.

that $C_{iw} = C_{ib}$, if the simplest forms of the equations are to be used.

The main heat conduction errors result from the neglect of heat storage and lag effects, the variation of the transmission coefficient with ventilation, and the change of transmission coefficient with mean temperature. The heat storage can be accounted for as illustrated by *Kuhn and Sapsford* [1960]. The dependence of the transmission coefficient on mean temperature is usually negligible, but if the temperature variations are large it can be accounted for as shown in the conduction theory (Part 2).

When there is little or no wind, free convection is the main means of heat removal at the outer surface of the instrument. The heat transmission from the outer surface to the atmosphere will be less under windless conditions than when there is good ventilation. A careful laboratory test of K for the single-ended instrument showed that the coefficient of heat transmission with no ventilation was about 86 per cent of that obtained when the instrument was force ventilated at 2.25 m/sec (5 mph) and that greater ventilation did not increase the heat transmission appreciably. Since the conduction term usually is of the order of 33 per cent of the total heat balance of the instrument, the net radiation estimate would change only 7 per cent from a nonventilated to a well-ventilated condition. When the diameter of the radiative surface is much greater than either d_a or d_s , the transmission coefficient for the air layer and insulation layer may be calculated satisfactorily from one-dimensional heat flow. Otherwise K is determined by a model test.

In general use, the total of the errors of the instrument will usually result in less than ± 7 per cent error in the net radiation and smaller error in solar radiation (provided a suitable white paint can be found). The relative error may exceed this when the absolute magnitude of the solar radiation is small and at low sun altitude. To achieve reliable performance it is necessary that the films be clean and free from condensation and dirt.

Potential uses. The main advantages of the economical radiometer are that it has possibilities for measuring the separate radiation components and is a relatively inexpensive instrument. Thus, the incident and reflected solar radiation and the albedo can be found. Simi-

larly, the upward and downward thermal radiation currents can be measured. The usefulness of infrared measurements to studies of the upper atmosphere has been clearly demonstrated [*Kuhn, Suomi, and Darkow*, 1959]. The thermal radiation measurement during daytime as well as nighttime hours gives the 'radiation temperature' of the soil surface and of vegetative cover. A measurement of plant temperature should prove advantageous in agricultural research, since plant temperature may differ greatly from air temperature. The surface temperature and radiation measured with the radiometer has been used to advantage by the U. S. Weather Bureau frost protection group for predicting time and severity of freezing on citrus fruits and cranberries.

The radiometer may be so constructed that the radiation element has high thermal mass, thus providing an instrument with a longer time constant. This integrates the radiation. If the temperature is observed at periods about one-half as long as the time constant, complete radiation information is obtained. This greatly facilitates the treatment of data when only average radiation over a period of hours or days is required.

Since the temperature differences between the radiative surfaces are large, standard thermometers may be used. When a high thermal mass can be tolerated, bulb thermographs can be used for recording. The radiometer has the advantage of portability because it does not depend upon sensitive temperature measurements requiring electric-powered recorders. However, temperatures may be measured with thermocouples or thermistors and recorded when desirable. The expressions for $(R_n + \delta R_{en})$ and R_s can be written as $[f(T_1) - f(T_2)]$, where T_1 and T_2 are the temperatures of two radiative surfaces required for a measurement. Separation of the temperature functions permits the construction of either tables or nomograms, so that the quantities required can be found readily.

The economical radiometer can be constructed in many sizes and shapes to fill special needs. For example, small units with fast time constants have been constructed for aerial surveys of surface parameters such as albedo. Long, narrow units can be constructed to span the row-spacing of crops so that the radiation in the

row and interspace can be integrated spatially with a single unit. A heavy copper radiation element with high heat conduction is needed to insure uniform temperature throughout the radiative surface.

Though the primary interest has been in surfaces that are 'black' to infrared radiation but which differ in solar radiation response, surfaces are available which reject the infrared and absorb the solar radiation [Tabor, 1955; Hass, Schroeder, and Turner, 1956]. These may be used to advantage for infrared measurements. For some purposes it may be desirable to have a surface with a high absorptivity or high reflectivity over a rather narrow band of the spectrum, e.g., to study the characteristics of the atmospheric radiation in that band or the photoreactions of plants. The equations for any of these surfaces in the economical radiometer are analogous to those developed here.

PART 2. THEORY

Symbols and Definitions

- B = short notation for black-body function, σT^4 [e.g., $B_t = \sigma T_t^4$; $B_n = B_t - B_b$; $B_{pb} = \sigma T_{pb}^4$].
- C_i = $a_i/[1 - r_i(1 - a_i)]$, short notation for a common constant term that describes the infrared properties of the instrument.
- C_s = $a_s/[1 - r_s(1 - a_s)]$, short notation for a common constant term that describes the solar properties of the instrument.
- E_d, E_u = radiation flux density directed toward and away from the top radiative surface.
- K = coefficient of heat transmission for single-ended radiometer.
 $K = k_a/d_a + k_d/d_s$.
- K_1, K_2 = coefficient of heat transmission constants defined in (32).
 $K_1 = (m_a/2d_a) + (m_d/2d_s)$;
 $K_2 = (n_a/d_a + n_d/d_s)$.
- L_t, L_b, L_n = heat losses in flux per unit area of the top (L_t) and the bottom (L_b) radiative surfaces, respectively, due to conduction and convection in the instrument.
 $L_n = L_t - L_b$.
- R_d, R_u = radiation flux density downward and upward in the atmosphere.
- R_{id}, R_{iu} = infrared radiation component of R_d and R_u .
- R_{sd}, R_{su} = solar radiation component of R_d and R_u .
- R_n, R_{in}, R_{sn} = net radiation flux density of total, infrared, and solar radiation; $R_n = R_d - R_u = R_{in} + R_{sn}$; $R_{in} = R_{id} - R_{iu}$; $R_{sn} = R_{sd} - R_{su}$.
- T_{pt}, T_{pb} = absolute temperature of polyethylene (effective temperature of multiple films) of the top and bottom units, respectively.
- T_t, T_b = absolute temperature of the radiation surfaces of the top and bottom units, respectively.
- a_i, a_s = absorptivity of infrared and solar radiation, respectively, of the radiative surface.
- d_a, d_d, d_s = conduction path lengths in air (d_a) and insulation (d_d) (see Fig. 1); d_s is the effective path length of conduction of insulation in single-ended radiometer; defined by $(k_a/d_a + k_d/d_s) = K$.
- k_a, k_d = thermal conductivity of air (k_a) and insulation (k_d) at a given temperature, approximated by $k_a = m_a T + n_a$ and $k_d = m_d T + n_d$, respectively.
- r_i, r_s = reflection of infrared and solar radiation, respectively, by the polyethylene film(s).
- δ = $(C_s \tau_s / C_i \tau_i) - 1$, where δ reflects the difference between the solar and infrared characteristics of the black radiometer.
- ϵ_i, ϵ_s = absorptivity of the polyethylene film(s) for infrared and solar radiation, respectively.
- τ_i, τ_s = transmissivity of polyethylene for infrared and solar radiation, respectively. $\tau_i = 1 - (r_i + \epsilon_i)$; $\tau_s = 1 - (r_s + \epsilon_s)$.
- Subscripts: d, u indicate downward and upward radiation currents.
 i, s indicate infrared and short wave, respectively.
 t, b indicate top and bottom radiation surfaces, respectively.
 b, w indicate black and white 'paints,' respectively (e.g., T_{tw} and T_{bw} are temperatures of the top white sur-

face and bottom black surface. a_{iw} is the infrared absorptivity of the white surface. C_{sb} is C_s for the black surface).

Energy Balance of Surface for Infrared Radiation Only ($R_s = 0$)

In order to determine what the surfaces of the radiometer are measuring it is necessary to consider their energy balances. Since *only* the infrared is considered, the subscript i has been omitted for simplicity. Assuming that the heat exchange conditions are steady, we may write for the top radiation surface.

$$E_d - E_u = L_t \quad (1)$$

The loss term L_t will be elaborated in a later section. Assuming for the time being that L_t is also the reflectivity r and absorptivity ϵ of the polyethylene and the absorptivity a of the surface are known, we can solve the upward and downward flux densities. The downward flux density can be written

$$E_d = \tau R_d + \epsilon B_{pt} + r E_u \quad (2)$$

For the upward flux density we can write

$$E_u = a B_t + (1 - a) E_d \quad (3)$$

Using equations 1, 2, and 3, it is possible to eliminate E_d and E_u and to solve for R_d . The result is

$$R_d = B_t + \frac{1 - r(1 - a)}{a(1 - r)} L_t + \frac{\epsilon}{1 - r} (R_d - B_{pt}) \quad (4)$$

the last term of the right-hand side R_d appears again. It is seen that the influence of the absorptivity of the polyethylene is small because R_d and B_{pt} are, in this case, of the same order of magnitude. When ϵ is small compared with $(1 - r)$ this last term may be neglected.

In a similar way the expression for R_u can be found for the bottom surface. The net radiation R_n is obtained by solving for $R_n = R_d - R_u$ from

$$R_n = \frac{1 - r}{\tau} \left\{ B_n + \frac{1 - r(1 - a)}{a(1 - r)} (L_t - L_b) - \frac{\epsilon}{1 - r} B_{pn} \right\} \quad (5)$$

The last term is negligible because T_{pt} and T_{pb} are reasonably close to the air temperature, so that $(B_{pt} - B_{pb})$ is small, and because $\epsilon/(1 - r)$ is small. Nevertheless, the influence of the absorptivity of the polyethylene is not entirely negligible (it appears in front of the brackets in equation 5). Writing (5) in shorter notation and neglecting the polyethylene term, we have

$$R_n = \frac{1 - r}{\tau} \left\{ B_n + \frac{(L_t - L_b)}{C(1 - r)} \right\} \quad (6)$$

Solar and Infrared Radiation

When solar (short-wave) radiation also has to be considered, the theory becomes somewhat more complicated because the absorptivity and reflectivity of both the polyethylene and the surface are not constant over the whole spectrum. However, the analysis follows the simpler development of the preceding section (for infrared only). Instead of equations 2 and 3 we now have

$$E_{sd} = \tau_s R_{sd} + r_s E_{su} \quad (7)$$

$$E_{id} = \tau_i R_{id} + r_i E_{iu} + \epsilon_i B_{pt} \quad (8)$$

$$E_{su} = (1 - a_s) E_{sd} \quad (9)$$

$$E_{iu} = a_i B_t + (1 - a_i) E_{id} \quad (10)$$

and instead of (1),

$$E_{sd} + E_{id} - E_{su} - E_{iu} = L_t \quad (11)$$

In this case it is not possible to solve for the net radiation completely with only one instrument because we cannot separate the solar from the infrared radiation. For the top surface the result of combining (7) through (11) is

$$C_s \tau_s R_{sd} + C_i \tau_i R_{id} = C_i (1 - r_i) B_t - C_i \epsilon_i B_{pt} + L_t \quad (12)$$

Symmetric equations exist for the bottom surface, so that by taking the difference of the equations (of the form given in equation 12) for the top and bottom surfaces we have an equation for the net radiation.

$$C_s \tau_s R_{sn} + C_i \tau_i R_{in} = C_i (1 - r_i) B_n - C_i \epsilon_i B_{pn} + (L_t - L_b) \quad (13)$$

For a radiometer with black surfaces

$$C_s \tau_s = C_i \tau_i (1 + \delta) \quad (14)$$

where δ is small and reflects the differences between solar and infrared characteristics of the instrument. Using (14) and neglecting the B_{pt} term as before, we can approximate (13) by

$$R_n + \delta R_{sn}$$

$$= \left(1 + \frac{\epsilon_i}{\tau_i}\right) \left\{ B_n + \frac{L_t - L_b}{C_i(1 - r_i)} \right\} \quad (15)$$

Radiometers with Selective Absorption

The surface of the radiometer described in the preceding sections has high absorption in both the solar and infrared radiation spectra. It is thus *black* to both solar and infrared radiation. If we add to the instrument with black surfaces an instrument with white surfaces, it is possible to derive separate relations for the various radiative fluxes. Since the equations for other selective surfaces are analogous, it will be sufficient to discuss the combination of a black and white radiometer only. Referring to the white and black paint with subscripts w and b , respectively, we can write (12) for the top surface of the black radiometer:

$$C_{sb}\tau_s R_{sd} + C_{ib}\tau_i R_{id} = C_{ib}(1 - r_i)B_{tb} - C_{ib}\epsilon_i B_{ptb} + L_{tb} \quad (16a)$$

$$\text{Albedo} = R_{su}/R_{sd} = \frac{C_{ib}C_{iw}(1 - r_i)(B_{bb} - B_{bw}) + (C_{iw}L_{bb} - C_{ib}L_{bw})}{C_{ib}C_{iw}(1 - r_i)(B_{tb} - B_{tw}) + (C_{iw}L_{tb} - C_{ib}L_{tw})} \quad (18c)$$

and for the top surface of the white radiometer:

$$C_{sw}\tau_s R_{sd} + C_{iw}\tau_i R_{id} = C_{iw}(1 - r_i)B_{tw} - C_{iw}\epsilon_i B_{ptw} + L_{tw} \quad (16b)$$

Similar equations are found for the bottom surfaces:

$$C_{sb}\tau_s R_{su} + C_{ib}\tau_i R_{iu} = C_{ib}(1 - r_i)B_{bb} - C_{ib}\epsilon_i B_{pbb} + L_{bb} \quad (16c)$$

$$C_{sw}\tau_s R_{su} + C_{iw}\tau_i R_{iu} = C_{iw}(1 - r_i)B_{bw} - C_{iw}\epsilon_i B_{pbw} + L_{bw} \quad (16d)$$

Solar radiation. From (16a) and (16b) we can solve for R_{sd} :

$$R_{sd} = \frac{C_{ib}C_{iw}(1 - r_i)}{(C_{sb}C_{iw} - C_{ib}C_{sw})\tau_s}$$

$$\cdot \left\{ (B_{tb} - B_{tw}) - \frac{\epsilon_i}{1 - r_i} (B_{ptb} - B_{ptw}) + \frac{L_{tb}}{C_{ib}(1 - r_i)} - \frac{L_{tw}}{C_{iw}(1 - r_i)} \right\} \quad (17)$$

The equation for R_{su} is similar to (17) if the subscript b , for bottom, is written instead of t . It is noted that the temperature of the inner layer of polyethylene of the radiometers will be midway between the temperature of the radiation surface and air temperature so that $(B_{ptb} - B_{ptw})$ for the inner films will be smaller than $(B_{tb} - B_{tw})$ but may not be negligible in comparison. However, the outer films are both at air temperature and $\epsilon_i/(1 - r)$ is very small so that the polyethylene terms may be neglected. We then have

$$R_{sd} = \frac{C_{ib}C_{iw}(1 - r_i)}{(C_{sb}C_{iw} - C_{ib}C_{sw})\tau_s} \left\{ (B_{tb} - B_{tw}) + \frac{L_{tb}}{C_{ib}(1 - r_i)} - \frac{L_{tw}}{C_{iw}(1 - r_i)} \right\} \quad (18a)$$

$$R_{su} = \frac{C_{ib}C_{iw}(1 - r_i)}{(C_{sb}C_{iw} - C_{ib}C_{sw})\tau_s} \left\{ (B_{bb} - B_{bw}) + \frac{L_{bb}}{C_{ib}(1 - r_i)} - \frac{L_{bw}}{C_{iw}(1 - r_i)} \right\} \quad (18b)$$

$$R_{sn} = R_{sd} - R_{su}$$

$$= \frac{C_{ib}C_{iw}(1 - r_i)}{(C_{sb}C_{iw} - C_{ib}C_{sw})\tau_s} \left\{ (B_{nb} - B_{nw}) + \frac{L_{tb} - L_{bb}}{C_{ib}(1 - r_i)} - \frac{L_{tw} - L_{bw}}{C_{iw}(1 - r_i)} \right\} \quad (18d)$$

It is noted that if $C_{ib} = C_{iw} = C_i$,

$$R_{sd} = \frac{C_i(1 - r_i)}{(C_{sb} - C_{sw})\tau_s} \cdot \left\{ (B_{tb} - B_{tw}) + \frac{L_{tb} - L_{tw}}{C_i(1 - r_i)} \right\} \quad (19a)$$

Albedo

$$= \frac{C_i(1 - r_i)(B_{bb} - B_{bw}) + (L_{bb} - L_{bw})}{C_i(1 - r_i)(B_{tb} - B_{tw}) + (L_{tb} - L_{tw})} \quad (19b)$$

$$= \frac{C_i(1-r_i)}{(C_{sb} - C_{sw})\tau_s} \left\{ (B_{nb} - B_{nw}) + \frac{(L_{tb} - L_{bw}) - (L_{tw} - L_{bw})}{C_i(1-r_i)} \right\} \quad (19c)$$

Long-wave radiation. From (16a) and (16b) we can find the downward infrared flux:

$$R_{iw} = \frac{1-r_i}{(C_{sb}C_{iw} - C_{ib}C_{sw})\tau_i} \left\{ (C_{sb}C_{iw}B_{tw} - C_{ib}C_{sw}B_{tb}) - \frac{\epsilon_i}{1-r_i} (C_{sb}C_{iw}B_{ptw} - C_{ib}C_{sw}B_{ptb}) + \frac{C_{sb}L_{tw} - C_{sw}L_{tb}}{1-r_i} \right\} \quad (20)$$

The equation for R_{iw} is similar to (20), except that subscripts to indicate bottom surface are used.

In this instance the polyethylene can again be neglected to the extent that B_{ptw} is closer to B_{tb} than B_{tw} is to B_{tb} and $\epsilon_i \ll (1-r_i)$. However, neglect of this term should rest in calculations comparing the magnitude of the polyethylene term with the remaining terms, and we will include them in the basic equations).

We can compute the net infrared radiation $R_{in} = R_{id} - R_{iw}$. In this equation the terms for the polyethylene may be neglected, since the B_{ptw} and B_{ptb} are small and $\epsilon_i \ll (1-r_i)$. We then have

$$R_{in} = \frac{(1-r_i)}{(C_{sb}C_{iw} - C_{ib}C_{sw})\tau_i} \left\{ (C_{sb}C_{iw}B_{nw} - C_{ib}C_{sw}B_{nb}) + \frac{C_{sb}L_{nw} - C_{sw}L_{nb}}{1-r_i} \right\} \quad (21)$$

When $C_{ib} = C_{iw} = C_i$,

$$R_{in} = \frac{(1-r_i)}{(C_{sb} - C_{sw})\tau_i} \left\{ (C_{sb}B_{tw} - C_{sw}B_{tb}) - \frac{\epsilon_i}{1-r_i} (C_{sb}B_{ptw} - C_{sw}B_{ptb}) + \frac{C_{sb}L_{tw} - C_{sw}L_{tb}}{C_i(1-r_i)} \right\} \quad (22a)$$

$$R_{in} = \frac{(1-r_i)}{(C_{sb} - C_{sw})\tau_i} \left\{ (C_{sb}B_{nw} - C_{sw}B_{nb}) + \frac{C_{sb}L_{nw} - C_{sw}L_{nb}}{C_i(1-r_i)} \right\} \quad (22b)$$

R_{iw} is similar to (22a), except that subscripts for the bottom surface are used.

Net radiation. From (18) and (21) and from $R_n = R_{sn} + R_{in}$ we find that the net radiation is

$$R_n = \frac{(1-r_i)}{(C_{sb}C_{iw} - C_{ib}C_{sw})\tau_s\tau_i} \cdot \left\{ (C_{ib}C_{iw}\tau_i - C_{ib}C_{sw}\tau_s)B_{nb} - (C_{ib}C_{iw}\tau_i - C_{sb}C_{iw}\tau_s)B_{nw} + \frac{(C_{iw}\tau_i - C_{sw}\tau_s)L_{nb} - (C_{ib}\tau_i - C_{sb}\tau_s)L_{nw}}{(1-r_i)} \right\} \quad (23)$$

If $C_{ib} = C_{iw} = C_i$, it follows that

$$R_n = \frac{(1-r_i)}{(C_{sb} - C_{sw})\tau_s\tau_i} \cdot \left\{ (C_i\tau_i - C_{sw}\tau_s) \left[B_{nb} + \frac{L_{nb}}{C_i(1-r_i)} \right] - (C_i\tau_i - C_{sb}\tau_s) \left[B_{nw} + \frac{L_{nw}}{C_i(1-r_i)} \right] \right\} \quad (24)$$

The energy losses L_i and L_o

The evaluation of the conduction and convection losses from the radiation surface through the air between the polyethylene films and through the insulation materials is a problem of three-dimensional heat flow. The solution for conduction is well known (see *Carslaw and Jaeger* [1959], chap. 6), but it is complicated and is dependent on the temperature differences. In the following discussion, the heat storage of the instruments is omitted and only steady-state losses are considered, though heat storage and lag effects can be accounted for as illustrated by *Kuhn and Sapsford* [1960].

Standard unit. In the standard unit there is conduction through the air layers between the polyethylene films, through the insulation and walls, and through the insulation to the other radiation surface. In order to keep the theory of the standard unit simple, only the case of one-dimensional heat flow is considered. This is a very good approximation for the conduction through the air layers between the polyethylene films, which are thin compared with their horizontal dimensions. Usually the radiometer is constructed so that the heat conducted through

the insulation is of the order of one-third or one-fourth that through the thin air layers so that one-dimensional heat flow is a fairly good approximation for the center part of the radiometer.

The linear problem is simple when the air layers are chosen so that convection is prevented [De Graaf and Van der Held, 1953]. Then we have

$$L_t = (k_a/d_a)(T_t - T_a) + (k_d/d_d)(T_t - T_b) \quad (25a)$$

and

$$L_b = (k_a/d_a)(T_b - T_a) + (k_d/d_d)(T_b - T_t) \quad (25b)$$

The approximation of linear heat flow is best when the air temperature is between the top and bottom temperatures. In this case the error in L will not exceed 2 or 3 per cent. The error is somewhat larger when the air temperature is colder or warmer than both T_t and T_b . For instance, when $T_a > T_t > T_b$, both L_t and L_b will be underestimated by about the same amount.

The result is that in all cases the expressions for net radiation are very nearly correct, because only the difference of the losses L_t and L_b appear.

The influence of the lateral heat losses in the instrument is felt more strongly either when the upward and downward radiation fluxes are considered separately or when the total radiation defined by $R_a + R_u$ is considered. In those cases it may be necessary to make more careful estimates of the errors in L_t and L_b .

Single-ended units. A very simple relation for L_t and L_b is obtained when we use single-ended units instead of the standard instrument. In this case instead of (25a) and (25b) we find for one-dimensional heat flow

$$L_t = (k_a/d_a)(T_t - T_a) + (k_d/d_d)(T_t - T_a) = [(k_a/d_a) + (k_d/d_d)](T_t - T_a) \quad (26a)$$

$$L_b = (k_a/d_a)(T_b - T_a) + (k_d/d_d)(T_b - T_a) = [(k_a/d_a) + (k_d/d_d)](T_b - T_a) \quad (26b)$$

If d_a is large compared with the horizontal dimensions, so that lateral losses are large and one-dimensional heat flow is not approximated, the lateral losses in the single-ended unit can be ac-

counted for by changing d_a to an 'effective' d_a , that is constant when geometry is fixed. Lateral losses increase the constant in front of the temperature difference. The general expression for the losses is then

$$L_t = K(T_t - T_a) \text{ and } L_b = K(T_b - T_a) \quad (27)$$

The constant K is the coefficient of heat transmission for the instrument and can either be calculated or determined experimentally. The loss equations for the single-ended unit are exact regardless of whether T_a is greater or less than T_t and T_b .

Loss terms in radiometer equations. The relations (25) or (27) are applied to the radiation equations depending on which type of instrument is used. For example, combining (25) with (15) gives for the standard instrument for daytime:

$$R_n + \delta R_{sn} = \left(1 + \frac{\epsilon_i}{\tau_i}\right) \left\{ (\sigma T_t^4 - \sigma T_b^4) + \frac{(k_a/d_a) + 2(k_d/d_d)}{C_i(1 - \tau_i)} (T_t - T_b) \right\} \quad (28)$$

When using single-ended units, $(k_a/d_a) + 2(k_d/d_d)$ would be replaced by K .

Loss terms as a function of radiometer temperatures. As was noted previously, the thermal conductivity of air and most thermal insulators is temperature dependent. However, since the thermal conductivity is approximately a linear function of temperature, this can be incorporated in the loss equations. For example, we can write for the single-ended unit

$$k_a = m_a T + n_a; \quad k_d = m_d T + n_d \quad (29)$$

Then the mean k_a and k_d for the top surface is

$$\bar{k}_a = m_a(T_t + T_a)/2 + n_a; \quad \bar{k}_d = m_d(T_t + T_a)/2 + n_d \quad (30)$$

$$L_t = \left\{ \frac{m_a(T_t + T_a)/2 + n_a}{d_a} + \frac{m_d(T_t + T_a)/2 + n_d}{d_d} \right\} (T_t - T_a) \quad (31)$$

so that

$$L_t = K_1(T_t^2 - T_a^2) + K_2(T_t - T_a) \text{ and } L_b = K_1(T_b^2 - T_a^2) + K_2(T_b - T_a) \quad (32)$$

$$= L_t - L_b = K_1(T_t^2 - T_b^2) + K_2(T_t - T_b) \quad (33)$$

ilar expressions may be derived for the standard unit.

If we combine (15) and (18a), respectively, with (33) and (32),

$$+ \delta R_{sn} = \left(1 + \frac{\epsilon_i}{\tau_i}\right) \left\{ (\sigma T_t^4 - \sigma T_b^4) + \frac{K_1(T_t^2 - T_b^2) + K_2(T_t - T_b)}{C_i(1 - r_i)} \right\} \quad (34)$$

$$= \frac{C_{ib}C_{iw}(1 - r_i)}{(C_{sb}C_{iw} - C_{ib}C_{sw})\tau_s} \left\{ (\sigma T_{tb}^4 - \sigma T_{tw}^4) + \frac{K_1(T_{tb}^2 - T_{tw}^2) + K_2(T_{tb} - T_{tw})}{C_{ib}(1 - r_i)} \right. \\ \left. - \frac{K_1(T_{tw}^2 - T_{sw}^2) + K_2(T_{tw} - T_{sw})}{C_{iw}(1 - r_i)} \right\} \quad (35)$$

Equation 35 is greatly simplified if $C_{ib} = C_{iw}$. It is seen that these equations may be written with the T_t and T_b terms separated. For example, (34) may be written

$$+ \delta R_{sn} = \left[1 + \frac{\epsilon_i}{\tau_i}\right] \left\{ \sigma T_t^4 + (K_1 T_t^2 + K_2 T_t)/C_i(1 - r_i) \right. \\ \left. - \left[1 + \frac{\epsilon_i}{\tau_i}\right] \left\{ \sigma T_b^4 + (K_1 T_b^2 + K_2 T_b)/C_i(1 - r_i) \right\} \right\} \quad (36a)$$

$$R_n + \delta R_{sn} = f(T_t) - f(T_b) \quad (36b)$$

Thus, if either tables of $f(T)$ versus T or nomograms are constructed, $(R_n + \delta R_{sn})$ can readily be found. Similar tables can be established for

R_{sa} if $C_{ib} = C_{iw}$. It should be noted that the tables or nomograms can be in terms of either °C or °F rather than absolute values, since the conductivity equations can be written in terms of either °C or °F and σT^4 tables for °C or °F are available [Tanner and Robinson, 1959].

Acknowledgments. This work was supported in part by Army Electronic Proving Ground contract DA-36-039-SC-80282 in cooperation with the Department of Meteorology, University of Wisconsin. We are indebted to Mr. J. Swan, a graduate student in the Soils Department, for his part in collecting the data.

REFERENCES

- Carslaw, H. S., and J. C. Jaeger, *Conduction of Heat in Solids*, Oxford Univ. Press, London, 1959.
- De Graaf, J. C. A., and E. F. M. Van der Held, The relation between the heat transfer and the convection phenomena in enclosed plane air layers, *Appl. Sci. Research*, **3A**, 393-409, 1953.
- Fritschen, L. J., Construction and calibration details of the thermal-transducer type net radiometer, *Bull. Am. Meteorol. Soc.*, **41**, 180-183, 1960.
- Hass, G., H. H. Schroeder, and A. F. Turner, Mirror coatings for low visible and high infrared reflectance, *J. Opt. Soc. Am.*, **46**, 31-35, 1956.
- Kuhn, P. M., V. E. Suomi, and G. L. Darrow, Soundings of terrestrial radiation flux over Wisconsin, *Monthly Weather Rev.*, **87**, 129-135, 1959.
- Kuhn, P. M., and C. Sapsford, A note on the airborne economical radiometer, *Bull. Am. Meteorol. Soc.*, **41**, in press, 1960.
- Suomi, V. E., University of Wisconsin net radiometer, in *Exploring the Atmosphere's First Mile*, **1**, Pergamon Press, New York, pp. 95-98, 1957.
- Suomi, V. E., and P. M. Kuhn, An economical net radiometer, *Tellus*, **10**, 161-163, 1958.
- Suomi, V. E., D. O. Staley, and P. M. Kuhn, Measurement of infra-red radiation divergence to 160 mb, *Quart. J. Roy. Meteorol. Soc.*, **84**, 134-141, 1958.
- Tabor, H., Selective radiation, *Bull. Research Council Israel*, **5A**, 119-133, 1955.
- Tanner, C. B., and S. M. Robinson, Black-body function, *Soils Bull. I*, Soils Dept., Univ. Wisc., 1959.

(Manuscript received April 13, 1960; revised June 29, 1960.)

Infrared Radiometer Soundings on a Synoptic Scale

P. M. KUHN

*Office of Meteorological Research, U. S. Weather Bureau
Madison, Wisconsin*

AND

VERNER E. SUOMI

*Department of Meteorology, University of Wisconsin
Madison, Wisconsin*

Abstract. The results of a direct synoptic measurement of infrared radiation flux obtained in a simultaneous ascent of fifteen radiometersondes are presented. The area covered is central and western United States. Vertical profiles of temperature, humidity, net radiation, and the divergence of net radiation provide patterns of tropospheric and stratospheric radiation. Conclusions as to the level of maximum radiation divergence, cooling effects of clouds, causes of atmospheric instability, principal radiators, importance of water vapor above the tropopause, and tentative conclusions on high-level ozone heating effects are discussed.

INTRODUCTION

Large synoptic scale radiative balances in the atmosphere have already been determined by calculation [Moller, 1956; London, 1957; Broughton, 1954]. Recently, single station measurements of the infrared radiation flux in the troposphere and stratosphere have been obtained by using balloon-borne radiometersondes [Bohl, 1956; Suomi, Staley, and Kuhn, 1958; Kuhn, Suomi, and Darkow, 1959].

Long-wave radiation measurements from above the atmosphere have been under way since October 13, 1959, the date of the launch of the United States' satellite Explorer VII. They are also planned for the meteorological satellite Tiros II.

The purpose of this paper is to present the results of a synoptic measurement of infrared radiation flux obtained from a simultaneous ascent of 15 radiometersondes. The geographical area covered is central and western United States. To the writers' knowledge, this represents the first measurements on a synoptic scale of the divergence of atmospheric infrared radiation flux.

OBSERVATION NETWORK

Radiometersonde measurements were made by 15 cooperating U. S. Weather Bureau upper-stations at 06 UT, July 29, 1959. The balloon-

borne radiometersonde described by Suomi and Kuhn [1958] and Suomi, Staley, and Kuhn [1958] were released on two lines of Weather Bureau upper-air stations. One group was on the line: Point Arguello, California to International Falls, Minnesota. The other formed a line from San Antonio, Texas, to International Falls, Minnesota. In addition to the upward and downward streams of infrared radiation, air temperatures, pressure, and humidity observations were obtained simultaneously. Since all soundings were made at night, no solar energy was involved.

Net radiation R_n is defined as the difference between the upward R_u and downward R_d streams of infrared radiation, positive when directed away from the earth's surface, thus,

$$R_{net} = R_u - R_d > 0 \text{ (cal/cm}^2\text{/minute)}$$

The radiometersonde measures R_u and R_d directly. Details of its theory and construction are given by Suomi and Kuhn [1958].

THE RADIATION DATA

Two sets of cross sections through the atmosphere have been evaluated; one is for the line from Point Arguello, California, to International Falls, Minnesota, and the other is for the line from San Antonio, Texas, to International Falls,

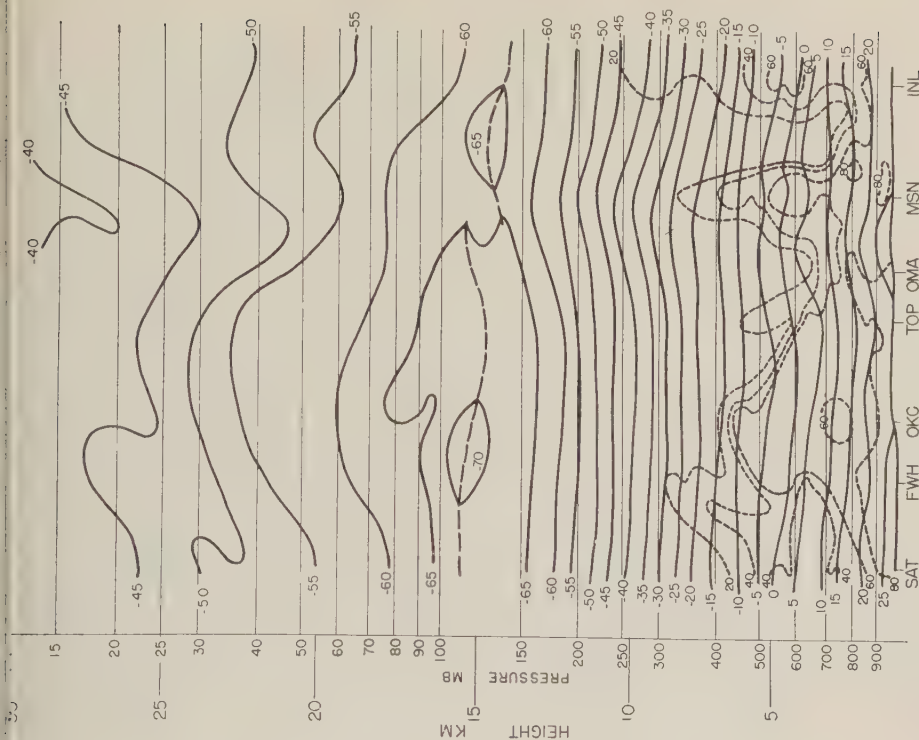


Fig. 2. Atmospheric cross section for 06 UT, July 29, 1959, Las Vegas through International Falls. Solid lines are isotherms; dashed lines are isolines of relative humidity; double line is frontal boundary.

Fig. 3. Atmospheric cross section for 06 UT, July 29, 1959, San Antonio through International Falls. All lines are identified as in Figure 2.

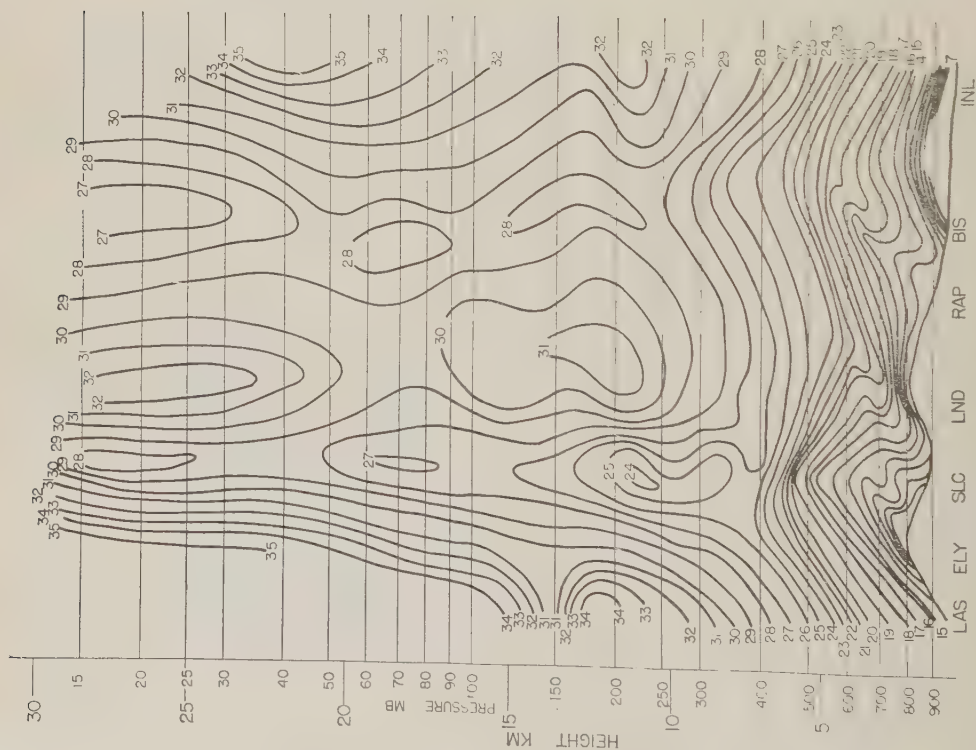


Fig. 4. Atmospheric cross section of net radiation for 06 UT, July 29, 1959, Las Vegas through International Falls. Solid lines are isolines of net radiation in hundredths of calories per square centimeter per minute.

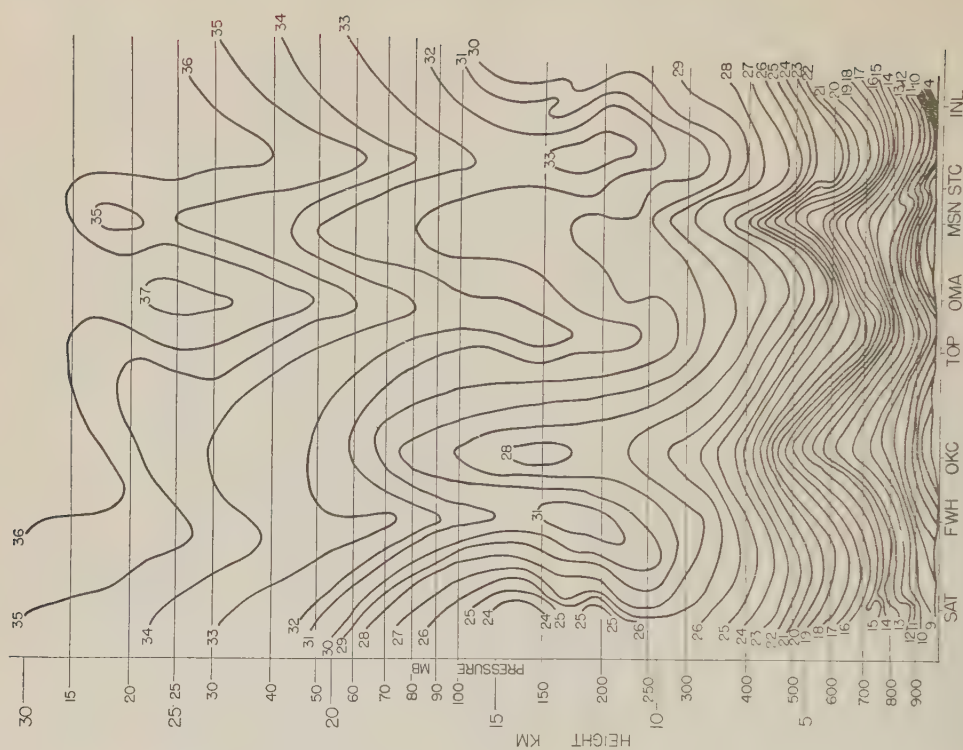


Fig. 5. Atmospheric cross section of net radiation for 06 UT, July 29, 1959, San Antonio through International Falls. All lines are identified as in Figure 4.

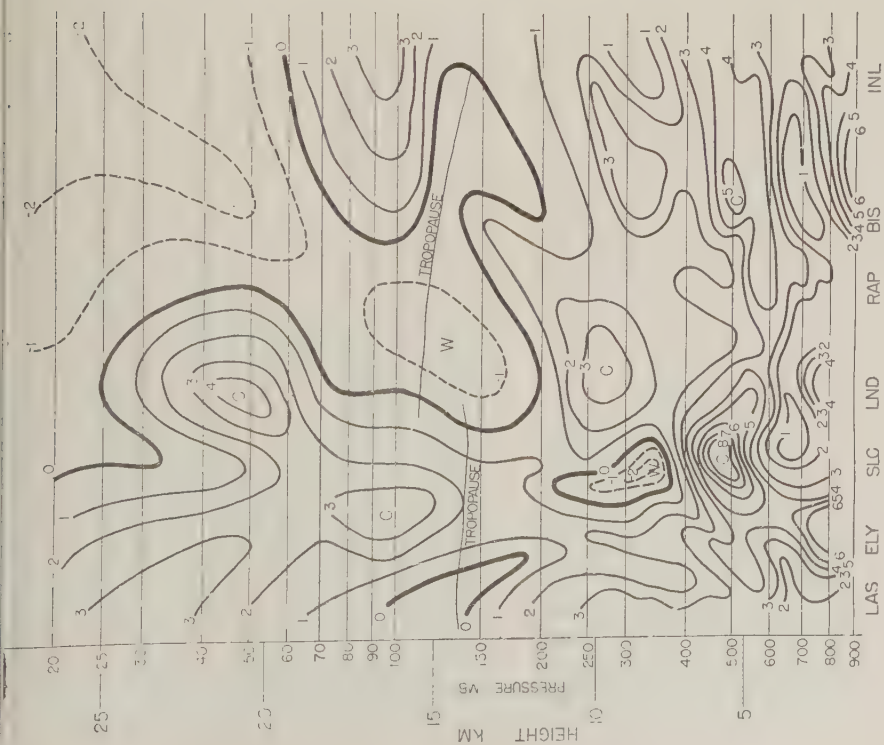


Fig. 6. Atmospheric cross section of net radiation divergence in the vertical for 06 UT, July 29, 1959, Las Vegas through International Falls. Solid and dashed lines are isolines of the vertical divergence of net radiation in hundreds of calories per square centimeter per minute, per 100 millibars. *W* indicates warming and *C* indicates cooling.

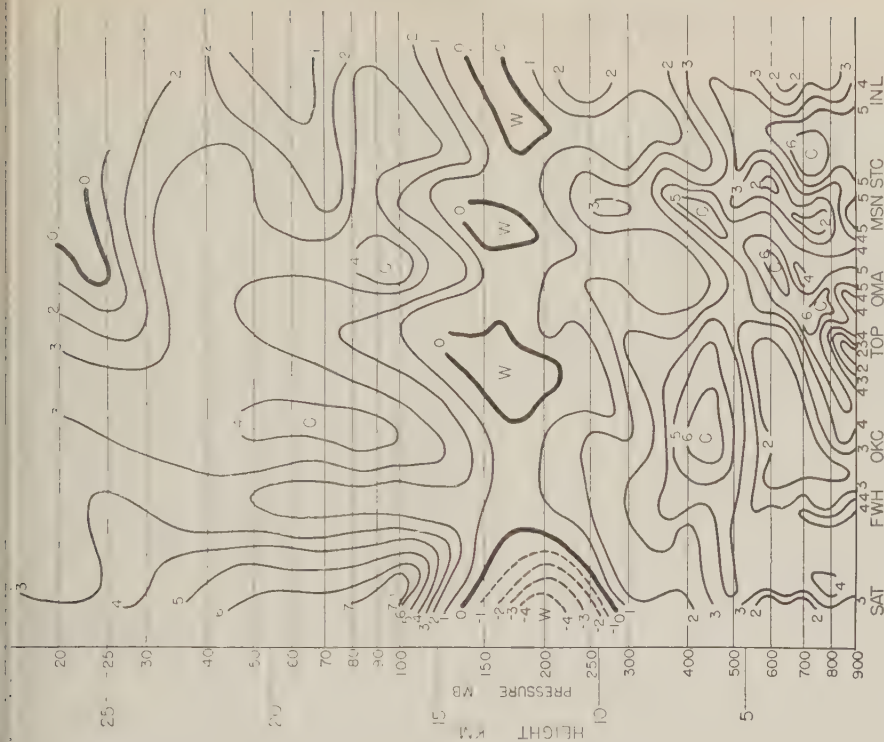


Fig. 7. Atmospheric cross section of net radiation divergence in the vertical for 06 UT, July 29, 1959, San Antonio through International Falls. All lines are identified as in Figure 6. *W* indicates warming and *C* indicates cooling.

Minnesota. Figure 1 is the synoptic surface chart.

The cross sections have been evaluated to show the following data: (1) temperature and humidity profiles (Figs. 2 and 3); (2) net radiation profiles (Figs. 4 and 5); (3) vertical divergences of net radiation expressed in calories per square centimeter per minute per 100 millibars (Figs. 6 and 7).

The data given in (1) and (2) above are from the radiometersonde soundings directly. The data in (3) were obtained by a differentiation with respect to pressure of the data given in (2). The data from (3) can be expressed as a cooling rate from the relationship

$$\frac{\partial T}{\partial t} (^{\circ}\text{C}/\text{day}) = \frac{-g}{C_p} \frac{\Delta R_n}{\Delta p}$$

Values of $\Delta R_n/\Delta p$ corresponding to 0.01 cal $\text{cm}^{-2} \text{ min}^{-1}$ per 100 mb represent cooling rates of 0.6 $^{\circ}\text{C}$ per day; g is the acceleration of gravity in cgs units; and C_p is the specific heat of air .239 cgs. It is possible to perform the mechanics of differentiation with respect to pressure in several ways. One method is to perform the differentiation on each net radiation sounding and from this draw a cross section designating isolines of cooling rates. The other is to prepare cross sections of the atmosphere plotted on a linear pressure scale and then to use graphical differentiation to obtain the cooling rates. The latter procedure was used because it is somewhat easier to interpolate cooling rates between stations. Results were then plotted in turn on a logarithmic pressure scale. This was done for (3) above. Perhaps as experience is gained with this type of analysis the graphical differentiation step will be unnecessary.

DISCUSSION OF RESULTS

Tropospheric radiation. Figures 4 through 7 indicate that the greatest divergence of net radiation in the vertical occurs in the lower half of the troposphere. The average infrared radiation divergence for the complete group of stations from the surface to the 400-mb level is 0.20 cal/ cm^2/min . In contrast, the average divergence from 400 mb to the 15-mb level for the same stations is 0.07 cal/ cm^2/min . In this example 75 per cent of the divergence of net radiation occurred in the lower 7 km of the troposphere.

Here the troposphere was the principal heat sink for the atmosphere.

Radiation cooling, occurring in the lower half of the troposphere and centered at cloud tops or above moist layers, may produce atmospheric instability. Such instability was present at International Falls, Minnesota, St. Cloud, Minnesota, Madison, Wisconsin, Omaha, Nebraska, and Topeka, Kansas, averaging -1 for the Showalter [1953] stability index. This radiational cooling may have played a part in the occurrence of nocturnal thunderstorms on July 29 and again, farther east, on July 30, ahead of the front (Fig. 1), in that part of the cross section where the strongest flux divergence was measured. Since representative radiational cooling can be measured several hours before the outbreak of such storms, a radiational profile may be important as one of the factors in picking out potentially unstable areas.

It is interesting to note that the tropospheric radiational pattern is the controlling feature of the radiational pattern at the top of the flights. This has important implications for infrared measurements made from satellites. Figures 4 and 5 illustrate this feature. In both instances the outgoing net radiation is less over the frontal regions than on either side. This is expected on the basis of cold, high-level, moist, radiating surfaces such as middle clouds. In this group ascent the flux divergence in the lower 400 mb appears to fix the flux pattern at 30 km.

Stratospheric Radiation

Radiators. The radiation balance in the stratosphere depends upon the absorption of solar radiation by ozone and water vapor, and upon the infrared emission by these same radiators, carbon dioxide, and particulate matter.

However, until recently there have been very few direct measurements of stratospheric emission in the infrared. Estimates of infrared stratospheric emission were made by computations based on laboratory measurements of the transmissivities of carbon dioxide, ozone, and water vapor for low pressures and absorber concentrations. The radiometer, on the other hand, measures total radiation for any and all radiators present.

If we can independently obtain the radiative contribution to infrared cooling of carbon dioxide and ozone in the lower stratosphere, the

TABLE 1. Comparison of Measured and Calculated Cooling Rates

Station	25 km			21 km		
	dT/dz , °C/km	$\partial T/\partial t$, °C/day	E^*	dT/dz , °C/km	$\partial T/\partial t$, °C/day	E^*
San Antonio	2.3	-1.8	-0.4	2.0	-3.0	-2.7
Fort Worth	2.0	-1.8	-0.4	1.0	-1.5	-1.2
Oklahoma City	2.0	-1.8	-0.4	1.7	-2.1	-1.8
Las Vegas	2.1	-1.8	-0.4	1.7	-1.5	-1.2
McLean	2.1	-1.8	-0.4	1.6	-2.0	-1.7
Plass [1956a, b]	2.0	-1.4	...	2.0	-0.3	...

* Excess of measured total radiative cooling over computed carbon dioxide-ozone cooling.

Difference between this calculation and the measured total infrared radiation will give the radiative cooling due to water vapor and other absorbers. To have any meaning, the calculated and observed values must have been made from similar temperature and ozone profiles. Fortunately, these soundings are very similar to those used by Plass for his calculated values. Table 1 shows the agreement between Plass's temperatures and ours to be good. Plass's [1956a, b] radiative cooling computations were based on an average ozone concentration at middle latitudes after the NRL rocket measurements [Rocket Panel, 1952] and for the rocket panel temperature profile. Comparing his computations with the measured cooling rates between the tropopause and 21 km, we obtain the excess or deficiency, if any, of the total measured cooling with respect to that due to carbon dioxide and ozone. This necessitates, however, verifying the fact that our temperature profiles, specifically the temperature lapse in this same interval, are the same as those used by Plass.

It can be seen in Figures 6 and 7 that from 21 through 25 km the measured radiational cooling rates over Las Vegas, Nevada, San Antonio, Texas, Fort Worth, Texas, and Oklahoma City, Oklahoma, were equal to or exceeded $-1.8^{\circ}\text{C}/\text{day}$. Plass's computed values of the total carbon dioxide and ozone cooling, calculated with his average ozone and carbon dioxide concentrations, vary from $-0.3^{\circ}\text{C}/\text{day}$ at 21 km to $-1.4^{\circ}\text{C}/\text{day}$ at 25 km. At 25 km the measured cooling exceeds that computed for carbon dioxide and ozone by $-0.4^{\circ}\text{C}/\text{day}$ or more. At 21 km the average measured cooling above Fort Worth, Texas, Las Vegas, Nevada, San Antonio, Texas, and Oklahoma City, Oklahoma, was

$-2.2^{\circ}\text{C}/\text{day}$. Since our measurements were made in deep tropical air, for the most part, and since Plass used the average middle-latitude ozone concentration, the excess of measured over computed warming is, if anything, less than would be expected. Plass's figure for carbon dioxide and ozone cooling is $-0.3^{\circ}\text{C}/\text{day}$ at 21 km. These comparisons are summarized in Table 1.

Since the observed temperature lapses agree essentially with the Rocket Panel profile, the excess total measured cooling ($^{\circ}\text{C}/\text{day}$) in this ascent could be caused by any or all of the following factors: (1) a concentration of ozone below 21 km and above the tropopause; (2) a concentration of ice crystals below 21 km and above the tropopause; (3) particulate matter below 21 km and above the tropopause. Although we cannot positively rule out the first factor, even for a summer situation, the latter two seem more likely. Repeated evidence of haze and cirrus clouds above the tropopause from balloon data support this observation [Grant, 1951; Endlich and McLean, 1957].

The area of large-scale warming occurring from 15 km upward over the Lander, Wyoming-International Falls, Minnesota, line (Fig. 6) suggest another feature. In spite of the steady decrease in the ozone concentration above 22 km, from 0.01 cm/km to 0.0003 cm/km [Plass, 1956a, b], an underneath approach to the high-temperature level near 50 km could result in radiative convergence. However, there is also evidence of drastic departures from the accepted level of maximum ozone concentration at 22 km. This could also produce such warming. In any case, departures from a typical case in the stratosphere are too great to be ignored.

TABLE 2. Reported Sky Conditions for Flights 06 UT July 29, 1959

Station	Pressure, mb	Temperature, °C	Relative Humidity	Sky
Topeka	981.4	25.8	0.81	Clear
Salt Lake City	869.6	23.9	0.28	4/10 Alto cumulus
International Falls	965.1	25.4	0.72	Clear
Omaha	963.8	24.0	0.86	2/10 Stratocumulus
Oklahoma City	969.1	23.9	0.91	Clear
Fort Worth	993.9	26.8	0.79	High thin cirrus
Saint Cloud	972.2	25.2	0.76	Clear
Las Vegas	929.7	30.8	0.10	Clear
San Antonio	986.8	26.0	0.80	9/10 Stratocumulus
Lander	829.0	18.8	0.34	Clear
Ely	808.0	21.8	0.17	1/10 Cumulus
Bismarck*	949.9	25.6	0.16	3/10 Altostratus
Madison	975.7	25.7	0.77	High thin scattered cirrus

* Light rain showers occurred 30 seconds after release.

Stratospheric radiation pattern. As would be expected, the strongest flux divergence occurs immediately above moist or cloud layers. The strongest flux convergence and resulting warming, on the other hand, occur just beneath the base of the clouds or inversions.

The synoptic chart for 06 UT on July 29 (Fig. 1) and the individual temperature and humidity soundings for the stations along the north-south line (Fig. 3) show that moist tropical air was present. The maritime tropical air had persisted along this line for several days prior to the ascent date.

The cross section of Figure 3, showing high relative humidities and warm air distributed as nearly horizontal isotherms to the base of the tropopause, identifies the air mass from San Antonio, Texas, through International Falls, Minnesota, as maritime tropical. A Rossby diagram for any of these stations further substantiates this fact.

On the other hand, the cross section of Figure 2 from Las Vegas, Nevada, through International Falls, Minnesota, indicates drier, cooler, polar air between Salt Lake City, Utah, and Bismarck, North Dakota. Between Lander, Wyoming, and Rapid City, South Dakota, the air is 10°C colder than at any of the stations in the maritime tropical air mass. Humidities are also much lower at Lander and Rapid City. Thus, synoptically, the two contrasting air masses are identified. It is of interest that direct radiation measurements at heights equal to or greater

than 25 km can also be used for such identification.

The contrast between the infrared radiation flux at 25 km over the group of stations in the maritime tropical air and those in the maritime polar air is evident. Those stations in maritime tropical air (Fig. 5) average 0.35 cal/cm²/min for the measured net radiation. The two stations in maritime polar air (Fig. 4) average 0.27 cal/cm²/min net radiation. For the weak frontal situation the radiometersondes detected a 22 per cent difference in the net radiation from one air mass to the other. It is apparent that such differences could be detected over a much wider range with radiation measurements from satellites. Ambiguity can occur, however, in the differentiation of air masses by this technique when net radiation over clouds and over cold clear air masses is compared with surface temperatures at or near cloud-top temperature. Table 2 gives 06 UT reported weather at each station.

From these measurements over two summertime air masses, which did not have strong contrasts, it seems evident that either balloon-borne or satellite-borne radiometers can detect air-mass types. The importance of such detection in areas not covered by surface observations is obvious.

Tropopause radiation patterns. Staley [1957] computed the radiative cooling in the vicinity of the tropopause by means of Brooks' [1950] tabular method. He finds warming centered on

the tropopause relative to the layers above and below. Figure 7 demonstrates a frequently observed feature of infrared radiation profiles in the vicinity of the tropopause. The maximum 'relative' warming occurs from 25 to 50 mb below the tropopause, rather than being centered on the tropopause. A more detailed analysis of measured radiative effects in the vicinity of the tropopause is being prepared by G. L. Darkow of the Department of Meteorology, University of Wisconsin. This result will be reported later. Results of this synoptic ascent indicate that balloon-borne radiation-measuring equipment, though not ranging as wide or as high as satellite equipment, does provide the important vertical details of radiative flux divergence unattainable from satellites. Such measurements on a continuing and seasonal basis should provide important comparisons.

Acknowledgment. This research was supported by contract funds from the Office of Meteorological Research, U. S. Weather Bureau.

REFERENCES

- Brooks, D. L., A tabular method for the computation of temperature change by infrared radiation in the free atmosphere, *J. Meteorol.*, **7**, 313-321, 1950.
- Endlich, R., and G. S. McLean, The Structure of the Jet Stream Core, *J. Meteorol.*, **14**, 543-552, 1957.
- Grant, D. R., R. Frith, and H. C. Shellard, High level cloud photographs, *Meteorol. Mag.*, **80**, 229, 1951.
- Houghton, H. G., On the annual heat balance of the northern hemisphere, *J. Meteorol.*, **11**, 1-9, 1954.
- Kuhn, P. M., V. E. Suomi, and G. L. Darkow, Soundings of terrestrial radiation flux over Wisconsin, *Monthly Weather Rev.*, **87**, 129-135, 1959.
- London, J., A study of the atmospheric heat balance, Final Report, Contract AF 19 (122)-165, Research Division, College of Engineering, New York University, 1957.
- Moller, F., The pattern of radiative heating and cooling in the troposphere and lower stratosphere, *Proc. Roy. Soc. London, A*, **236**, 148-156, 1956.
- Plass, G. N., The influence of the 9.6 micron band on the atmospheric infrared cooling rate, *Quart. J. Roy. Meteorol. Soc.*, **82**, 30-44, 1956a.
- Plass, G. N., The influence of the 15 micron carbon dioxide band on the atmospheric cooling rate, *Quart. J. Roy. Meteorol. Soc.*, **82**, 310-324, 1956b.
- Pohl, W., Messungen des Ultraroten Strahlungsstromes in der freien Atmosphere, *Z. Geophys.*, **22**, 1-52, 1956.
- Rocket Panel, Pressures, densities, and temperature in the upper atmosphere, *Phys. Rev.*, **88**, 1027-1032, 1952.
- Showalter, A. K., A stability index for thunderstorm forecasting, *Bull. Am. Meteorol. Soc.*, **34**, 250-252, 1953.
- Staley, D. O., Some comments on physical processes at and near the tropopause, *Arch. Meteorol. Geophys. u. Bioklimatol., Ser. A*, 25-35, 1957.
- Suomi, V. E., and P. M. Kuhn, An economical net radiometer, *Tellus*, **10**, 160-163, 1958.
- Suomi, V. E., D. O. Staley, and P. M. Kuhn, A direct measurement of infrared radiation divergence to 160 millibars, *Quart. J. Roy. Meteorol. Soc.*, **84**, 134-141, 1958.

(Manuscript received June 29, 1960;
revised August 3, 1960.)



An Improved Technique for Obtaining Atmospheric Ion Mobility Distributions¹

ELDEN C. WHIPPLE, JR.²

*U. S. Naval Research Laboratory and The George Washington University
Washington, D. C.*

Abstract. An improved technique for obtaining atmospheric ion mobility distributions using Blackwood's double-electrode condenser is described, which simplifies both the experimental procedure and the data analysis. Only the current to the second electrode needs to be measured, and it is shown that the mobility distribution can be obtained with one rather than two differentiations of the characteristic curve. Two representative small-ion distributions with good resolution, obtained with this technique, are presented and discussed.

Introduction. The general shape of the ion mobility distribution curve for the atmosphere has been known since the discovery of the three major ion groups: large, intermediate, and small ions, the last being most important to electrical conductivity. Detailed descriptions are scarce, however, because measurement problems such as the small currents involved (10^{-14} amp), the high insulation required, and the necessity for sampling ambient rather than treated air to get a true picture of atmospheric mobilities combine to make a determination of the mobility distribution with good resolution extremely difficult.

[Israel [1933] and Gish [1955] have emphasized the need for direct mobility measurements in the atmosphere. The author believes that the determination of ion mobility distributions should be pursued to answer the question whether clean air is characterized by a 'normal,' that is, an experimentally reproducible distribution under given conditions of ion formation rate. If it is, deviations of distributions from this form would doubtless help to attain a more satisfactory quantitative description of ionic equilibrium in the atmosphere and would throw some light on certain features of meteorology [Serbu and Trent, 1958]. This paper describes an improved technique which simplifies both the experimental procedure and the data analysis involved in obtaining a mobility distribution.

In addition, some representative results are given.

Theory. The usual method for ascertaining mobility distributions has been to determine the current-voltage characteristic of a Gerdien condenser. The second derivative of this curve is then directly proportional to the distribution [Israel, 1931]. This technique has at least two shortcomings. Any experimental errors are magnified in differentiation so that the data must be extremely smooth to give meaningful results after two such operations. In addition, the time required for obtaining a distribution is lengthened by the fact that a current measurement must be made while the applied potential is held constant. Varying the potential continuously causes the ion current to be masked by the larger charging current to the condenser. Thus the applied potential must be changed in steps.

Nolan and Kenny [1952] have pointed out several advantages of obtaining a current-air flow characteristic. Although the air flow can be varied continuously (at a constant applied potential) without introducing undesirable effects, it is still necessary to differentiate the characteristic twice (with respect to the air flow) to obtain the mobility distribution.

Blackwood [1920] introduced the double-electrode condenser to increase the resolving power. He showed that the current-voltage characteristic for the second (smaller) electrode exhibits a peak for each discrete ion group present in the air. It is the purpose of this paper to show that all the values of current obtained on the second electrode of the double-electrode condenser when

¹ Part of this paper is adapted from a Master's thesis presented to the Physics Department of The George Washington University.

² Now with the National Aeronautics and Space Administration, Washington, D. C.

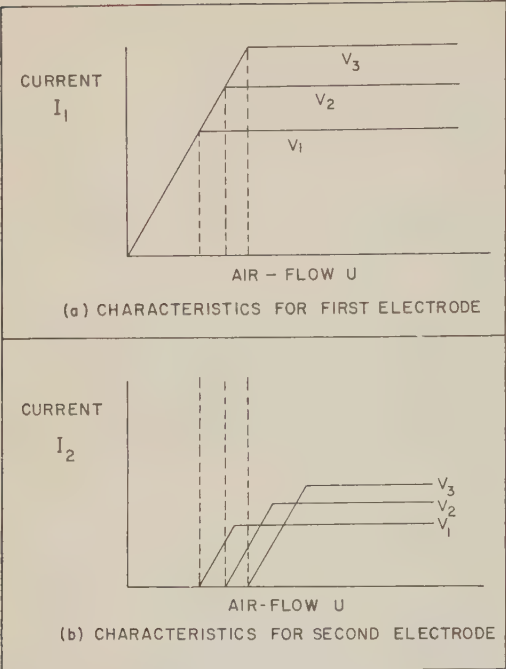


Fig. 1. Current-air flow characteristics for the double-electrode condenser.

either the applied potential or the air flow, or both, are varied, may be reduced to a single characteristic curve. This characteristic curve is a plot of the current-voltage ratio against the ratio of air flow to voltage, and its first derivative is directly proportional to the mobility distribution.

Figures 1 and 2 make it clear that there is a single characteristic curve for a given mobility distribution. Typical current-air flow characteristics for the first electrode where the air is assumed to contain ions of only one mobility k_1 are plotted in Figure 1(a). The values of current for the flat parts are proportional to the applied potentials [Swann, 1914]. The values of the air flow at which the flat parts commence are also proportional to the potentials, since these values correspond to the same critical mobility k_c where current saturation sets in

$$k_1 = k_c = U/4\pi C_1 V \tag{1}$$

where U is the volume rate of air flow, C_1 the effective capacitance of the first electrode, and V the applied potential.

The characteristics for the second electrode are shown in Figure 1(b). They are similar to those of the first electrode in that the values of

the flat parts are proportional to the potentials. In the low air flow region I_2 is zero because all the ions are caught by the first electrode. Ions begin to be collected at the value of the air flow for which $k_c = k_1$, and the current stops increasing at the value for which $k_d = k_1$, where k_d is the critical mobility for the second electrode:

$$k_d = U/4\pi(C_1 + C_2) V \tag{2}$$

Since I_2 is proportional to V in the flat parts of the characteristics it follows that the ratio I_2/V is independent of voltage in this region. Therefore, a plot of I_2/V against U reduces the three curves of Figure 1(b) to one curve in this region as shown in Figure 2(a). Similarly, since corresponding points on the rising parts of the characteristics refer to a given value of k_c , and since, therefore, the air flow values for these points are proportional to the voltages, it follows that plotting I_2/V against U/V reduces the three curves to one curve as shown in Figure 2(b). The presence of ions with different mobilities has the effect of rounding off the sharp angles as shown by the dashed line. However, when plotted in this way there is a single characteristic for a given distribution of mobilities no matter what values of voltage and air flow are used. This is

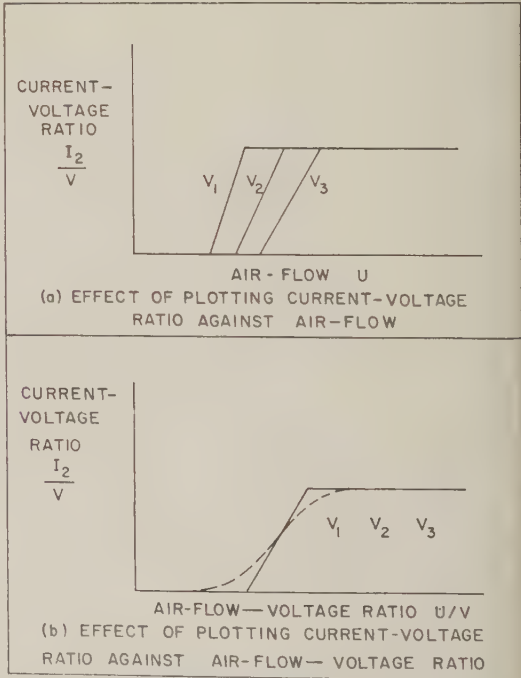


Fig. 2. Characteristic curves for the second electrode of the double-electrode condenser.

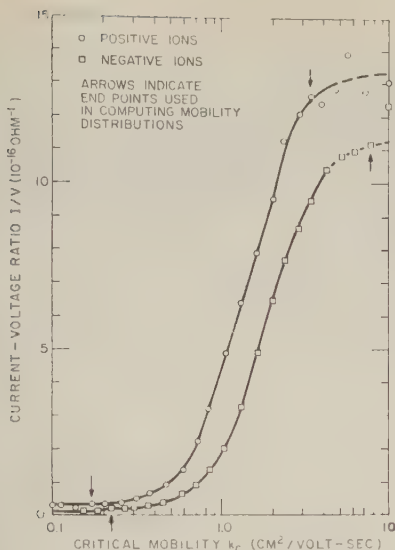


Fig. 3. Experimental characteristic curves obtained with laboratory air.

true not only for the second electrode but also for the first, and therefore for the simple Gerdien condenser as well.

The current to the second electrode of the double-electrode condenser has been given by Misaki [1950]. The ratio I_2/V can be written in the form

$$\frac{I_2}{V} = 4\pi e \left[C_1 k_e \int_{k_d}^{k_s} f(k) dk + (c_1 + c_2) \cdot \int_0^{k_d} k f(k) dk - C_1 \int_0^{k_s} k f(k) dk \right] \quad (3)$$

where e is the magnitude of the electron charge and $f(k)$ is the mobility distribution function. Since U/V is proportional to k_s (and to k_d), I_2/V may be plotted against either of them, merely a change in scale on the abscissa being involved. Differentiating,

$$\begin{aligned} \frac{d(I_2/V)}{dk_e} &= \frac{\partial(I_2/V)}{\partial k_e} + \frac{\partial(I_2/V)}{\partial k_d} \frac{dk_d}{dk_e} \\ &= 4\pi C_1 e \int_{k_d}^{k_s} f(k) dk \end{aligned} \quad (4)$$

Thus, the first derivative gives the number of ions per cubic centimeter between k_d and k_s , and the resolution is determined by the ratio $k_d/k_s = C_2/(C_1 + C_2)$.

Experimental results. Some results obtained by this technique under two different sets of

conditions are shown in Figures 3 through 6. The characteristic curve and resulting small-ion mobility distribution shown in Figures 3 and 4 were obtained in a small sealed room at the U. S. Naval Research Laboratory where there was a considerable amount of pollution in the air. The curves in Figures 5 and 6 were obtained at the NRL Atmospheric Electricity Ground Station near Big Meadows in Shenandoah National Park, Virginia (SNP). This site at an elevation of approximately 3600 feet is well removed from sources of atmospheric pollution.

The procedure was the same in both places, each experimental point on the characteristic curves consisting of a measurement of average current to the small section of the inner cylinder for a period of 2 to 3 minutes with the air flow and applied potential at a given value. The air flow was monitored by a variable area type flowmeter in series with the condenser and was maintained at a rate such that the Reynolds number was less than that for turbulent flow. Electrical shielding was provided at the intake of the condenser so as to reduce external fields. The applied potential was changed by steps for all the points except the bottom one on the positive ($k_s = 0.10$ cm²/volt sec) and the bottom three on the negative curve of Figure 3, which were obtained by lowering the air flow.

The condenser (Fig. 7) has outer and inner

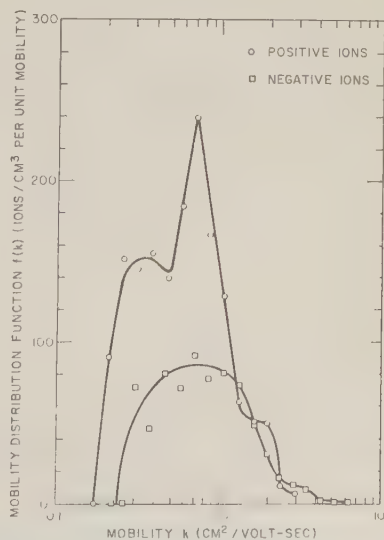


Fig. 4. Small-ion mobility distributions for laboratory air.

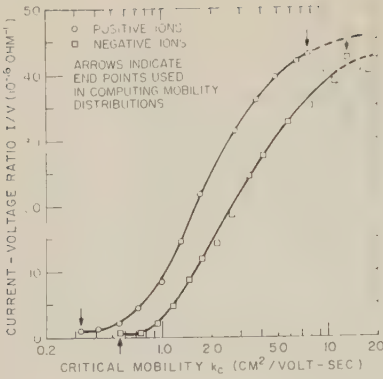


Fig. 5. Experimental characteristic curves obtained with ambient air at SNP.

diameters of 4 inches and $\frac{3}{4}$ inch, respectively. The lengths of the two sections of the inner cylinder are 15 and 3 inches with a $\frac{1}{4}$ -inch insulating spacer between them. Each section has its own stem for support and for electrical contact with an electrometer. The effective capacitances of the two sections were obtained from the following relations between them: their ratio, C_1/C_2 , which was found by measuring conductivity simultaneously on the two sections; and their difference, $C_1 - C_2$, which was computed from the formula for the capacitance of two coaxial cylinders. This assumes that the effective capacitances of the hemispherical caps and the stems are the same for each section. Although the two caps and stems are physically identical, it is possible that those of the second section are not as efficient in collecting ions because of shielding from the air flow. Such an effect was found to be negligible by measuring C_1/C_2 with a reversed air flow. The current was measured with a vibrat-

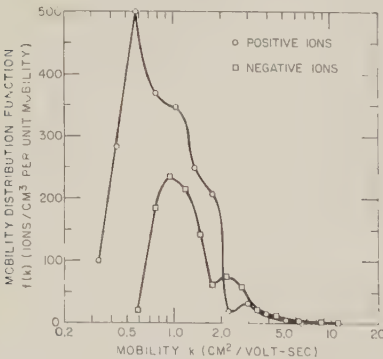


Fig. 6. Small-ion mobility distributions for ambient air at SNP.



Fig. 7. The U. S. Naval Research Laboratory double-electrode condenser.

ing-reed electrometer with an input resistance of 10^{11} ohms and is estimated to be accurate to 2×10^{-10} amp or 1 per cent, whichever error is greater. The currents measured ranged from 155×10^{-10} amp down to 5×10^{-10} amp, the smallest currents occurring at both ends of the characteristic curves, which is the reason for the departure of these points from a smooth curve. The estimated relative accuracy of the points used in computing the mobility distributions ranges from better than 4 per cent in the middle portion of the characteristic curves to 15 per cent at the end points indicated by the arrows. None of the current values have been corrected for diffusion losses.

The distributions were obtained by numerical differentiation between the experimental points of the characteristic curves, as indicated by equation 4. Although differentiation between experimental points magnifies the errors more than differentiation of the smoothed curve, it is believed that any scatter of the points obtained in this way represents the uncertainties of the distribution truly, and that drawing a smooth curve through the points obtained after differentiation is in this case a better averaging process than smoothing the characteristic curve. The derivative $d(I/V)/dk_c$ is assumed to be given by $\Delta(I/V)/\Delta k_c$ and the integral

$$\int_{k_d}^{k_e} f(k) dk$$

is equal to Δn , the number of ions per cubic centimeter between the limits k_d and k_e . The critical mobility k_e at the midpoint of the interval used in the differentiation defines the upper limit, and k_d is related to it by

TABLE 1. Average Mobilities, Ion Densities, and Conductivities

	Laboratory Air		Ambient Air at SNP	
	+	-	+	-
μ , cm ² /volt sec	0.99	1.43	1.36	2.18
n , ions/cm ³	222	141	554	330
σ , 10 ⁻¹⁶ /ohm cm	0.35	0.32	1.21	1.15
σ , measured	0.31	0.35	1.56	1.04

$$k_d = C_1 k_c / (C_1 + C_2).$$

The distribution function $f(k) = dn/dk$ is then given by $\Delta n/\Delta k = \Delta n/(k_c - k_d)$, and is plotted against the mean value $\frac{1}{2}(k_c + k_d)$.

The most striking feature of the distributions is the contrast between the positive and negative both in magnitude and in the sharpness of the peak value. Also of interest are the fairly sharp cutoff at the lower ends of the distributions and the tails extending out to higher mobilities. A larger positive-ion density is a characteristic of air at the earth's surface due to the electrode effect (in fair weather), and seems to persist for some time in the air inside buildings. The difference in peak sharpness may be indicative of a difference in the nature of the positive and negative ions. The high values of $f(k)$ at Shenandoah National Park are undoubtedly due to the relative lack of pollution as compared with laboratory air.

Average mobilities, ion densities, and conductivities computed from these distributions by numerical integration between the experimental points are presented in Table 1. Average values of conductivity measured in the usual way with a simple Gerdien condenser simultaneously with the mobility measurements are presented for comparison in the last row of the table. Their agreement with the computed conductivities indicates the reliability of the mobility distribution measurement. Especially noteworthy is the fact that the average mobilities are always considerably higher than the peak mobilities because of the contribution of the higher-mobility ions in the tails. This is particularly true for the negative ions, with the result that the positive and negative conductivities are in each case roughly equal in spite of the greater number of positive ions.

Other distributions have been obtained but are not presented here. Two distributions obtained in immediate succession, one by varying the potential and the second by varying the air flow, agreed well except that the second $f(k)$ was noisier. This is to be expected, because of the lower accuracy of air flow as compared with the voltage measurements. The high-mobility tails were present whenever the characteristic curve was extended far enough.

It is possible that these tails are partly a consequence of the method of data analysis. It can be shown from equation 4 that if the slope of the characteristic curve is changing slowly the computed $f(k)$ is approximately proportional to $1/k$. However, the tails of the negative-ion distributions that have been obtained are in every case more pronounced than those for the corresponding positive-ion distributions. This must be the result of a real difference in the positive and negative distributions at the higher mobilities.

Conclusion. A reliable method for obtaining mobility distributions with good resolution has been developed that is simpler both in procedure and in analysis of the data than previous techniques. This analysis might also be applied to existing data obtained by other workers like Blackwood and Misaki, who used double-electrode condensers. Two sample distributions obtained under different atmospheric conditions have been presented, demonstrating the validity and usefulness of the method. Distributions obtained under controlled conditions of temperature, pressure, humidity, nuclei concentration, and ionization rate should reveal much about the nature and behavior of atmospheric ions, and distributions obtained under a variety of natural conditions both on the earth's surface at various locations and aloft as a function of altitude should be a valuable contribution to atmospheric electricity.

Acknowledgments. It is a pleasure to acknowledge the encouragement and helpful criticism of both Dr. James H. Kraakevik of Wheaton College, Wheaton, Illinois, formerly of the U. S. Naval Research Laboratory, and Dr. Thomas B. Brown of Harvey Mudd College, Claremont, California, formerly of The George Washington University.

REFERENCES

- Blackwood, O., The existence of homogeneous groups of large ions, *Phys. Rev.*, **16**, 85-101, 1920.

- Gish, O. H., *Proceedings on the Conference on Atmospheric Electricity*, Geophysical research paper 42, Air Force Cambridge Research Center, Bedford, Mass., p. 244, 1955.
- Israel, H., Zur Theorie und Methodik der Grossenbestimmung von Luftionen, *Gerlands Beitr. Geophys.*, 31, 173-216, 1931.
- Israel, H., and L. Schulz, The mobility-spectrum of atmospheric ions—principles of measurements and results, *Terrest. Magnetism and Atmospheric Elec.*, 38, 285-300, 1933.
- Misaki, M., A method of measuring the ion spectrum, *Papers Meteorol. Geophys. Tokyo*, 1, 313-318, 1950.
- Nolan, P. J., and P. J. Kenny, A modified McClelland method for measuring ionic mobilities, *Atmospheric and Terrest. Phys.*, 2, 266-271, 1950.
- Serbu, G. P., and E. M. Trent, A study of the use of atmospheric-electric measurements in forecasting, *Trans. Am. Geophys. Union*, 39, 1034-1042, 1958.
- Swann, W. F. G., The theory of electrical dispersion into the free atmosphere, with a discussion of the theory of the Gerdien conductivity apparatus, and of the theory of the collection of radio-active deposit by a charged conductor, *Terrest. Magnetism and Atmospheric Elec.*, 17, 81-92, 1914.

(Manuscript received June 1, 1960; revised August 12, 1960.)

Internal Gravity-Vorticity Lee Waves over Mountains

LOUIS BERKOFKY

*Geophysics Research Directorate
Air Force Research Division (ARDC)
Bedford, Massachusetts*

Abstract. An atmospheric model consisting of two incompressible and homogeneous layers of different densities, with a constant shear flow in each layer, is examined for existence of lee waves as the fluid flows over a long narrow mountain ridge. The density discontinuity alone is a driving mechanism for the production of lee waves, as is the vorticity discontinuity. The net result is that the introduction of the vorticity discontinuity has an 'interference' effect on the waves produced by the density discontinuity. The results obtained are in good agreement with theoretical conclusions obtained from more complicated models, and with available observations. The results indicate that the actual atmosphere may be replaced by a relatively simple model, which is amenable to rigorous mathematical treatment, and a reasonable solution to the lee wave problem may still be obtained.

Introduction. In steady two-dimensional flow of an incompressible and homogeneous fluid with no internal surfaces of discontinuity, over a corrugation, there will be no lee-wave effect if static stability is neglected, i.e., if there is a rigid horizontal plane at the top of the fluid and the flow is irrotational. The same will be true if there is constant shear (Couette flow) in the basic current.

We may, as Colson [1952] has done, consider two superposed layers, each homogeneous and incompressible, with different densities and a rigid horizontal boundary at the top. The basic current is constant. In such a model, the static stability is introduced through the internal boundary condition and may be considered to be concentrated at the interface. Internal gravity lee-waves, whose existence depends on the discontinuity in density, are then obtained.

Wurtele [1953] considered the problem of an incompressible, homogeneous fluid in which there is a discontinuity in the vorticity of the basic current profile. He found that this mechanism accounts for steady 'vorticity lee-waves,' which present strong analogies with the gravity lee-waves.

Regarding flows of the type mentioned in the first paragraph, Höiland [1951] may be quoted: 'Thus for a unidirectional horizontal velocity through the layer, no distribution of vorticity whatever can give a steady wave system on either side of the corrugation. The shear or the

variation of shear may affect in an important way steady waves produced by other causes. In the systems considered above they can, however, never be responsible for the formation of such waves. Their effect will rather be in a general way to diminish the possibility of formation of steady waves by other properties of the fluid, for instance by a static stability.' This statement suggests the possibility of introducing a shearing effect into the gravity lee-wave model with density discontinuity. The effect of shear on flows with static stability may then clearly be seen.

In this paper, we consider the problem of two incompressible and homogeneous layers, with a rigid horizontal plane at the top. The model is exactly the same as that of Colson [1952], with the important difference that in the present model there is a Couette flow in each layer; i.e., if the shear is different in each layer, there is a discontinuity of vorticity as well as density at the interface (Fig. 1). The flow is steady and frictionless, and the density is constant in each layer. We thus have a model with two mechanisms for maintaining lee waves. It will be shown that with such a model lee waves are permitted which bear a marked similarity to those existing in a model considered by Wurtele [1952], namely, one with continuous Couette flow throughout and constant internal stability. The shear discontinuity has an 'interference' effect which acts to diminish the amplitudes of

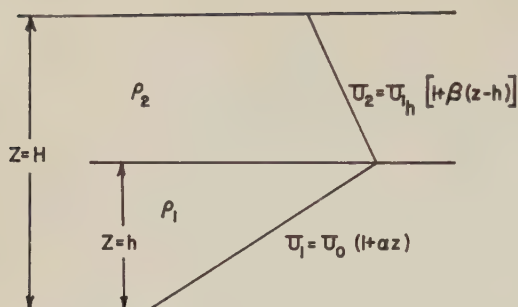


Fig. 1. Two-layer model for gravity-vorticity waves.

the lee waves. The results obtained agree quite well, qualitatively, with observations presented by Yates [1952].

Theory. We consider the model described in the previous paragraph. We neglect the Coriolis force and assume that the problem is one of small perturbations.

If we require that the upper boundary, $z = H$, be rigid, that the bottom streamline be given by the shape of the mountain $g_1(x)$, whose height is small compared to its width, and that the vertical velocity and the pressure be continuous across the interface, we may state the problem in terms of the stream function ψ , as follows [Thompson, 1949]:

Vorticity equation

$$U \frac{\partial}{\partial x} (\nabla^2 \psi) = U'' \frac{\partial \psi}{\partial x} \quad (1)$$

Kinematic boundary conditions

$$\frac{\partial \psi_2}{\partial x} = 0 \quad \text{at } z = H \quad (2)$$

$$\frac{\partial \psi_1}{\partial x} = U \frac{dg_1}{dx} \quad \text{at } z = 0 \quad (3)$$

Continuity of pressure and Bernoulli equation

$$\frac{\partial \psi_1}{\partial z} - \frac{\partial \psi_2}{\partial z} + \left[\frac{U_2' - U_1'}{U} - \frac{g}{U^2} \left(1 - \frac{\rho_2}{\rho_1} \right) \right] \psi = 0 \quad \text{at } z = h \quad (4)$$

Continuity condition

$$\frac{\partial \psi_2}{\partial x} = \frac{\partial \psi_1}{\partial x} \quad \text{at } z = h \quad (5)$$

Here x is the coordinate positive downstream,

z is the vertical component positive upward, H is the total depth of the fluid, h is the height of the interface, $g_1(x)$ is the equation of the terrain, $U = U(z)$ is the undisturbed eastward velocity component, g is the acceleration of gravity, $\nabla^2 = \partial^2/\partial x^2 + \partial^2/\partial z^2$ is the two-dimensional Laplacian operator, subscripts 1 and 2 refer to the lower and upper layers, respectively, ρ is the density, primes denote differentiation with respect to z , and ψ is the stream function satisfying the relations

$$u = -\partial \psi / \partial z \quad (6)$$

$$w = \partial \psi / \partial x$$

In deriving (5), we have made use of the approximate relation

$$\partial \zeta / \partial x = w / U \quad (7)$$

where w is the vertical velocity, and ζ is the displacement of a streamline from its undisturbed position. The equation of the streamlines is therefore

$$\zeta = \psi / U \quad (8)$$

Up to this point, no statement has been made concerning the variation of U with z . We now specialize the problem to the case of a Couette flow in each layer. We consider a linear increase with height of $U(z)$ in the lower layer and a linear decrease in the upper layer, at a distance far upstream from the mountain.

In layer 1:

$$U_1(z) = U_0(1 + \alpha z) \quad (9)$$

In layer 2:

$$U_2(z) = U_{1h}[1 + \beta(z - h)] \quad (10)$$

where U_0 = velocity at $z = 0$, U_{1h} = velocity at $z = h$, i.e., $U_{1h} = U_0(1 + \alpha h)$, α = (positive) shear in lower layer, and β = (negative) shear in upper layer (Fig. 1).

We then get

In layer 1:

$$\nabla^2 \psi = -U_0 \alpha \quad (11)$$

In layer 2:

$$\nabla^2 \psi = -U_{1h} \beta \quad (12)$$

Following a method given by Tsien [1943], we define an undisturbed stream function, ψ_0 , given by $\partial \psi_0 / \partial z = -U_1$, in lower layer,

$\partial\psi_0/\partial z = -U_2$ in upper layer, and introduce the perturbation stream function ψ^* due to the presence of the mountain by writing

$$\psi = \psi_0 + \psi^* \quad (13)$$

so that

$$\nabla^2 \psi^* = 0 \quad (14)$$

In layer 1:

$$\psi_0 = -U_0(z - h) \left[1 + \frac{\alpha}{2}(z + h) \right] \quad (15)$$

In layer 2:

$$Z'' - \delta^2 Z = 0 \quad (23)$$

The boundary conditions on Z are

$$Z_2' - Z_1' + \kappa Z = 0 \quad \text{at } z = h \quad (24)$$

$$Z_1 = Z_2 \quad \text{at } z = h \quad (25)$$

$$Z_2 = 0 \quad \text{at } z = H \quad (26)$$

$$Z_1 = 1 \quad \text{at } z = 0 \quad (27)$$

The condition 27 is chosen so that the integral form of the solution reduces properly to the Fourier integral of $g_1(x)$ at $z = 0$.

We find

$$Z_1(z, \delta) = \frac{\frac{\kappa}{\delta} \sinh \delta(h - z) - \cosh \delta(h - z) - \coth \delta(H - h) \sinh \delta(h - z)}{\frac{\kappa}{\delta} \sinh \delta h - \cosh \delta h - \coth \delta(H - h) \sinh \delta h} \quad (28)$$

$$Z_2(z, \delta) = - \frac{\sinh \delta(H - z)}{[\sinh \delta(H - h)] \left[\frac{\kappa}{\delta} \sinh \delta h - \cosh \delta h - \coth \delta(H - h) \sinh \delta h \right]} \quad (29)$$

$$\psi_0 = -U_0(1 + \alpha h)$$

Finally,

$$\left[z(1 - \beta h) - h + \frac{\beta}{2}(z^2 + h^2) \right] \quad (16)$$

$$\psi_{1,2}^*(x, z) = \frac{U_0}{\pi} \int_0^\infty Z_{1,2}(\delta, z) d\delta$$

The boundary conditions on ψ^* are

$$\frac{\partial \psi_2^*}{\partial x} = 0 \quad \text{at } z = H \quad (17)$$

$$\frac{\partial \psi_1^*}{\partial x} = U_0 \frac{dg_1}{dx} \quad \text{at } z = 0 \quad (18)$$

$$\frac{\partial \psi_1^*}{\partial x} = \frac{\partial \psi_2^*}{\partial x} \quad \text{at } z = h \quad (19)$$

$$\frac{\partial \psi_2^*}{\partial z} - \frac{\partial \psi_1^*}{\partial z} + \kappa \psi^* = 0 \quad \text{at } z = h \quad (20)$$

where

$$\kappa = \frac{g(1 - \rho_2/\rho_1)}{U_0^2(1 + \alpha h)^2} - \frac{(\beta - \alpha) + \alpha\beta h}{1 + \alpha h} \quad (21)$$

The problem now consists of the differential equation 14 and the boundary conditions 17, 18, 19, and 20. To solve this system, we seek solutions of the type

$$\psi^*(x, z) = Z(z) \cos \delta(\xi - x) \quad (22)$$

where δ is a wave number, and ξ is a phase angle' measured in the x direction. Therefore

$$\int_{-\infty}^{\infty} g_1(\xi) \cos \delta(\xi - x) d\xi \quad (30)$$

If we choose as a mountain profile

$$g_1(\xi) = \frac{Aq^2}{q^2 + \xi^2} \quad (31)$$

where A is the height of the crest and q is the half-width, then

$$\psi_{1,2}^*(x, z) = \frac{U_0 A q}{h}$$

$$\text{Re} \left\{ \int_0^\infty Z_{1,2} \left(\frac{u^*}{h}, z \right) e^{ix(u^*/h) - q(u^*/h)} du^* \right\} \quad (32)$$

where $u^* = \delta h$, and Re means 'real part.'

We may now use *Scorer's* [1949] method to evaluate (32). Carrying this through, we find

$$\psi_{1,2}^*(x, z) = U_0 A q \left\{ \frac{(h - z)[\kappa(H - h) - 1] - (H - h)}{h[\kappa(H - h) - 1] - (H - h)} \right\} \cdot \text{Re} \left(\frac{q + ix}{q^2 + x^2} \right) \pm \frac{U_0 A q \pi i}{h} \quad (33)$$

· (sum of residues due to poles on real axis)

$$x > 0$$

$$x < 0$$

$$\psi_2^*(x, z) = \frac{U_0 A q}{h} \left[-\frac{(H - z)}{\kappa h(H - h) - H} \right] \cdot \operatorname{Re} \left(\frac{q + ix}{q^2 + x^2} \right) \pm \frac{U_0 A q \pi i}{h} \quad (34)$$

· (sum of residues due to poles on real axis)

$$x > 0$$

$$x < 0$$

The lee-wave numbers u_0^* are the poles of the integrand, and the residue at u_0^* is

$$L_0 = \frac{U_0 A q}{h} e^{-q(u_0^*/h) + ix(u_0^*/h)} \cdot \frac{f_z(u_0^*)}{f_0'(u_0^*)} \quad (35)$$

where

$$f_z(u_0^*) = \kappa h \sinh \frac{u_0^*}{h} (h - z)$$

$$\psi_1^*(x, z) = \frac{U_0 A q^2}{q^2 + x^2} \left[\frac{(h - z)(\kappa h - 1) - h}{h(\kappa h - 1) - h} \right] - \frac{2 U_0 A q}{h} \cdot \frac{e^{-q(u_0^*/h)}}{u_0^*} \sin \left(x \frac{u_0^*}{h} \right) \cdot \left[\frac{(\kappa h - u_0^* \coth u_0^*) \sinh \frac{u_0^*}{h} (h - z) - u_0^* \cosh \frac{u_0^*}{h} (h - z)}{\left(\frac{\kappa h - 2}{u_0^*} \right) \cosh u_0^* - 2 \sinh u_0^*} \right] \quad x > 0 \quad (40)$$

$$- u_0^* \cosh \frac{u_0^*}{h} (h - z)$$

$$- u_0^* \coth \frac{u_0^*}{h} (h - z) \sinh \frac{u_0^*}{h} (h - z) \quad (36)$$

$$f_0'(u_0^*) = \kappa h \cosh u_0^*$$

$$- u_0^* \sinh u_0^* - \cosh u_0^*$$

$$- \coth \frac{u_0^*}{h} (H - h) \sinh u_0^*$$

$$- u_0^* \coth \frac{u_0^*}{h} (H - h) \cosh u_0^*$$

$$+ \frac{u_0^*}{h} (H - h) \operatorname{csch}^2 \frac{u_0^*}{h} (H - h) \sinh u_0^*$$

(37)

for the lower layer, with corresponding expressions for the upper layer.

u_0^* is the value of u^* which, in both layers, satisfies

$$\kappa h \sinh u_0^* - u_0^* \coth u_0^*$$

$$- u_0^* \coth \frac{u_0^*}{h} (H - h) \sinh u_0^* = 0 \quad (38)$$

To simplify matters, we let $H = 2h$ in (38). Then

$$\frac{\tanh u_0^*}{u_0^*} = \frac{2}{\kappa h} \quad (39)$$

In general, $2/\kappa h < 1$, so that u_0^* is real. Note that in any given situation, h and κ are fixed, so that, according to (39), only one pole, resulting in only one value of u_0^* , exists.

Observations of fluid flow over corrugations, as well as airflow over irregular terrain, show that there is no disturbance at great distances upstream from the obstacle. We therefore obtain the 'practical' form of the solution, i.e., one in which the disturbance vanishes for large negative x , by adding $U_0 A q \pi i L_0/h$ to the solution. We finally obtain

$$\psi_1^*(x, z)$$

$$= \frac{U_0 A q^2}{q^2 + x^2} \left[\frac{(h - z)(\kappa h - 1) - h}{h(\kappa h - 1) - h} \right],$$

$x < 0$ (41)

$$\psi_2^*(x, z) = -\frac{U_0 A q^2}{q^2 + x^2} \left[\frac{H - z}{\kappa h(H - h) - H} \right]$$

$$+ \frac{2 U_0 A q \pi}{h} \cdot \frac{e^{-q(u_0^*/h)}}{u_0^*} \sin \left(\frac{x u_0^*}{h} \right)$$

$$\frac{u_0^* \sinh \frac{u_0^*}{h} (h - z)}{\sinh u_0^* \left[\left(\frac{\kappa h - 2}{u_0^*} \right) \cosh u_0^* - 2 \sinh u_0^* \right]},$$

$x > 0$ (42)

$$\psi_2^*(x, z) = -\frac{U_0 A q^2}{q^2 + x^2} \left[\frac{H - z}{\kappa h(H - h) - H} \right],$$

$$x < 0 \quad (43)$$

The solution for the total stream function may be obtained by adding (15) to (40) and (41) and (16) to (42) and (43).

The velocity components may be obtained by differentiating (40), (41), (42), and (43) in accordance with (6).

From (39), we obtain the value of the critical velocity, given by $2/\kappa h = 1$. We obtain

$$U_{hc}^2 = \frac{gh(1 - \rho_2/\rho_1)}{2 + \left(\frac{\beta - \alpha + \alpha\beta h}{1 + \alpha h} \right)h} \quad (44)$$

Colson [1952], in the model with no shear, obtained

$$U_{hc}^2 = (gh/2)(1 - \rho_2/\rho_1) \quad (45)$$

In the model considered here, α is positive and β is negative, so that the denominator of (44) is always less than 2, if $\alpha, \beta \neq 0$. It is then seen that \tilde{U}_{hc} in the shear model is greater than U_{hc} in the no-shear model. This means that larger values of the basic current are permissible at the interface in the shear model than in the no-shear model, consistent with the observed existence of lee waves. For example, in a model with $U_0 = 3$ m/sec, $U_1 = 27$ m/sec, $U_2 = 3$ m/sec, $h = 4$ km, $1 - \rho_2/\rho_1 = 0.02$, the critical velocity in the shear model is 58 m/sec and that in the no-shear model is 20 m/sec. It is known from observations that lee waves exist with interface values of about 30 m/sec, which already exceeds the critical velocity in the no-shear model. It must therefore be concluded that although lee waves exist in the no-shear model, the density discontinuity by itself does not adequately describe the actual situation.

Results. To obtain a more quantitative comparison between the two models, we have adjusted Colson's solution so as to exclude the upstream waves. In that case, the solution for the perturbation stream function is of exactly the same form as (40)–(43) above, but the following important differences in parameters are noted:

1. Colson's solution has as a factor the quantity U , the constant basic current, where we have

U_0 , the value of the basic current at the ground.

2. The κ 's are different. Denoting ours by κ and Colson's by κ_c ,

$$\kappa = \frac{g(1 - \rho_2/\rho_1)}{U_0^2(1 + \alpha h)^2} - \frac{(\beta - \alpha) + \alpha\beta h}{1 + \alpha h} \quad (21)$$

$$\kappa_c = \frac{g(1 - \rho_2/\rho_1)}{U^2} \quad (46)$$

In view of (39) the lee wave number u_0^* is therefore different in each case.

By differentiating (40)–(43) and the corresponding equations in the no-shear model with respect to x , we obtain expressions for the vertical velocities in each case. If we let $A = 0.4$ (4 km), $q = 2.5$ (4 km), $h = 1$ (4 km), $H = 2$ (4 km) = height of homogeneous atmosphere, $U_0 = 3$ m/sec, $U_1 = 27$ m/sec, $U_2 = 3$ m/sec, $1 - \rho_2/\rho_1 = 0.02$ (corresponding to a temperature inversion of 6.0°C), then in the shear model:

$$\alpha = 8(4 \text{ km})^{-1} \quad u_0^* = 1.21$$

$$\beta = -8/9(4 \text{ km})^{-1} \quad U_{hc} = 58 \text{ m/sec}$$

$$\kappa = 2.89$$

and, in the no-shear model:

$$\alpha = \beta = 0 \quad U = \frac{U_0 + U_1}{2} = 15 \text{ m/sec}$$

$$\kappa = 3.49$$

$$u_0^* = 1.61 \quad U_{hc} = 20 \text{ m/sec}$$

The two solutions for w are shown in Figure 2. The solid curves are for the shear case, the dashed curves for the no-shear case. Upward-pointing arrows mean upward vertical motion; downward-pointing arrows mean downward vertical motion. One is immediately struck by the large differences, both in amplitude and phase, between the two solutions. Note that in the no-shear case the amplitudes are larger while the wavelength is smaller than in the shear case.

The total effect of the shear in the basic current thus seems to be a lengthening of horizontal scale. All other conditions being the same, introduction of shear into the no-shear model has the effect of stretching the waves in the latter model horizontally, thereby decreasing their amplitudes and increasing their wavelengths.

The reason for the larger amplitudes in the

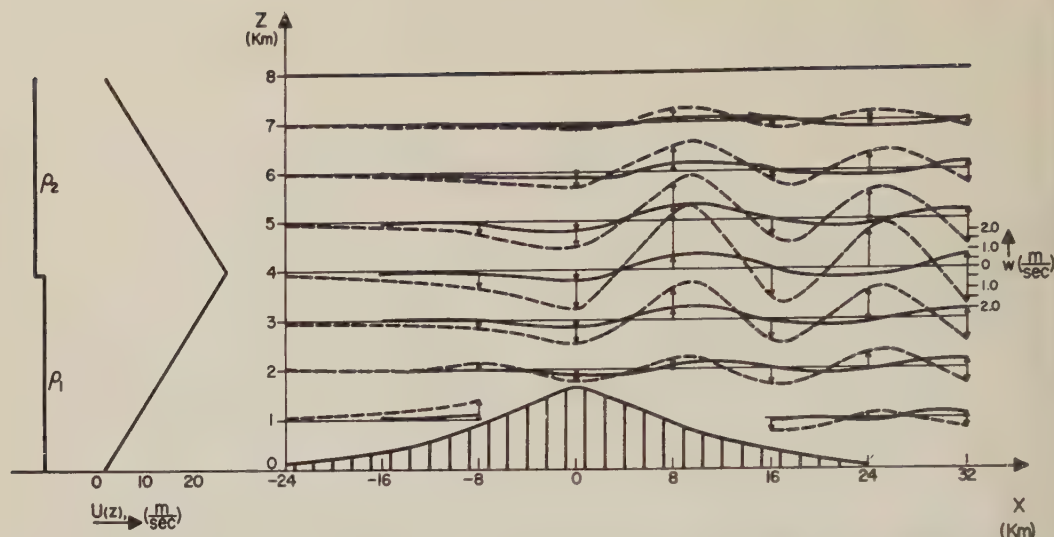


Fig. 2. The solutions for the vertical motion. Solid lines, shear case; dashed lines, no-shear case.

no-shear case is that the calculation was carried out for a constant basic current of 15 m/sec, which is not too far from the critical velocity of 20 m/sec. The fact that the introduction of shear increases the critical velocity, thereby resulting in smaller-amplitude lee waves at the same mean basic current as in the no-shear case, shows that the shear has the effect of 'interfering' with the no-shear waves. In nature, supercritical cases seem to be rare; yet, as pointed out previously, lee waves are observed to exist with interface values up to 30 m/sec, which exceeds the critical velocity for the no-shear case. In this regard, the shear has the desirable effect of yielding more realistic results.

From the few observations of vertical velocities available, all that can be said about the amplitudes in both models is that the values are of the correct order of magnitude. The positions of the vertical velocity maxima and minima in the shear model agree better with Wurtele's [1952] results computed from a model with constant shear and constant stability throughout than do these positions in the no-shear model.

We may obtain additional evidence substantiating the importance of shear by making a rough qualitative comparison with the observational data given by Yates [1952]. The flights he described were often launched from hills 460

meters high, which is about $\frac{1}{3}$ the height of the mountain considered here. The experience has been that waves are possible with any lapse rate which is not too unstable but that a wind shear is a more important factor. For example, Flight 10 was made when the wind shear was about the same as that used in the present calculations, but there were isothermal layers at 1500 to 2500 meters and 3000 to 4300 meters, instead of sharp inversions. The wavelength of the observed waves was 21 km, and the computed wavelength for no-shear model was 16 km.

Conclusions. It has been shown that it is possible for lee waves to exist in a two-layer model with a density discontinuity and a shear discontinuity at the interface. To a great degree, these resemble the lee-wave solutions obtained in a model with density stratification and constant shear. It therefore appears permissible to replace the continuously stratified model with a two-layer model, in which the stability may be regarded as being concentrated at the interface. Such a model has the advantage of mathematical simplicity. Even with a constant basic current, the two-layer model with a density discontinuity leads to lee-wave solutions. The shear discontinuity introduces a more realistic feature into the no-shear model and leads to results which seem to be in somewhat better agreement with existing observations.

REFERENCES

- Colson, D., Internal gravity waves over a long narrow mountain ridge, Paper presented at O.S.T.I.V. Conference in Madrid, 1952.
- Höiland, E., Fluid flow over a corrugated bed, in *Fifth Rept., Sierra Wave Project* [Contract AF 19(122)-263 Air Force Cambridge Research Center], 1-33, September 1951.
- Scorer, R. S., Theory of waves in the lee of mountains, *Quart. J. Roy. Meteorol. Soc.*, 76, 41-55, 1949.
- Thompson, P. D., The propagation of small surface disturbances through rotational flow, *Ann. N. Y. Acad. Sci.*, 51, 463-475, 1949.
- Tsien, H. S., Symmetric Joukowski airfoils in shear flow, *Quart. Appl. Math.*, 1, 130-148, 1943.
- Wurtele, M. G., Two new models in the study of lee waves, 1, Couette flow with internal stability, Paper presented at O.S.T.I.V. Conference in Madrid, 1952.
- Wurtele, M. G., The initial-value solutions of two classical lee-wave problems, Ph.D. thesis, Univ. Calif., Los Angeles, pp. 23-33, February 1953.
- Yates, A. H., Wave flights in Great Britain, Paper presented at O.S.T.I.V. Conference in Madrid, 1952.

(Manuscript received July 22, 1960.)

A Low-Frequency Microbarograph¹

WM. G. VAN DORN

*Scripps Institution of Oceanography
La Jolla, California*

Abstract. A sensitive band-pass microbarograph has been designed to assist in the interpretation of records of surface water waves of low frequency made at isolated Pacific island stations. The instrument employs a hydraulic resistance-capacitance filter network to attenuate high-frequency gusts and the atmospheric tide. Sensitivity can be adjusted to as little as 0.1 millibar full-scale, but the recorder normally operates at the much lower sensitivity of ± 5.0 mb at oceanic stations, with a resolution of ± 0.05 mb (± 50 dynes/cm²).

An example is cited of a one-to-one correspondence between barometric pressure and sea surface elevation during the passage of an anomalous barometric disturbance.

Introduction. During the summer of 1960 the Scripps Institution of Oceanography will install three permanent recording stations at Wake, Johnston, and Canton islands in the mid-Pacific for the continuous monitoring of low-frequency water surface waves [Van Dorn, 1960]. While temporary stations of this type were used in the past to study waves from nuclear explosions and submarine earthquakes it was found that the great abundance of signals in the low-frequency spectrum were undoubtedly associated with barometric fluctuations in the lower atmosphere. In particular, the passage of typhoons within several hundred miles of these stations resulted invariably in long-period forerunners which preceded the ordinary wind waves by one or two days. It soon became obvious that interpretation of the sea-wave records depended for the most part on a knowledge of the local meteorological situation, and to a much more refined degree than was possible from the data available from local weather stations. Although much pioneering work of this nature has been carried out by Donn [1958] and Gossard and Munk [1955], it was believed that a microbarograph specifically designed to have the same spectral response characteristics as the long-wave recorder would greatly simplify the work of analysis of data.

Accordingly, essentially the same components utilized in the latter instrument were adapted to the device described below, resulting in a remarkably simple, thermally stable unit, the out-

put from which can be recorded simultaneously with the water waves at similar amplitude levels and with perfect time synchronization.

Description of the microbarograph. A schematic diagram of the microbarograph is shown in Figure 1, and Figure 2 shows its construction details. It consists of a lower cylindrical plexiglass chamber 4 inches in diameter filled with silicone oil (Dow Corning DC-200, 1000 centistokes viscosity) connected through a capillary restriction to an identical upper chamber half full of oil and open to the atmosphere. The lower chamber also connects through another capillary to one side of an electric pressure transducer (Statham P5-0.2 psid). The other side of the differential transducer is open to the atmosphere. The lower chamber is also filled to a depth of about $\frac{1}{4}$ inch with mercury, which is in direct connection with a 1-inch diameter cylindrical glass flask evacuated and closed at its upper end and elevated about 30 inches above the base so as to produce a Torricelli vacuum above the mercury. In essence, the lower chamber and the elevated flask comprises an ordinary mercury barometer, the position of which is sensed by the pressure transducer. Within the region of interest in the barometric frequency spectrum the response is unity and the phase-shift zero. Response to frequencies outside this region is governed by low- and high-pass filters, which act to attenuate gusts and the barometric tides, respectively. Battery power (1.3 volts d-c) and signals are transmitted via a 4-conductor electric cable to a control panel containing balancing and calibrating networks, and recorded

¹ Contribution from the Scripps Institution of Oceanography, new series.

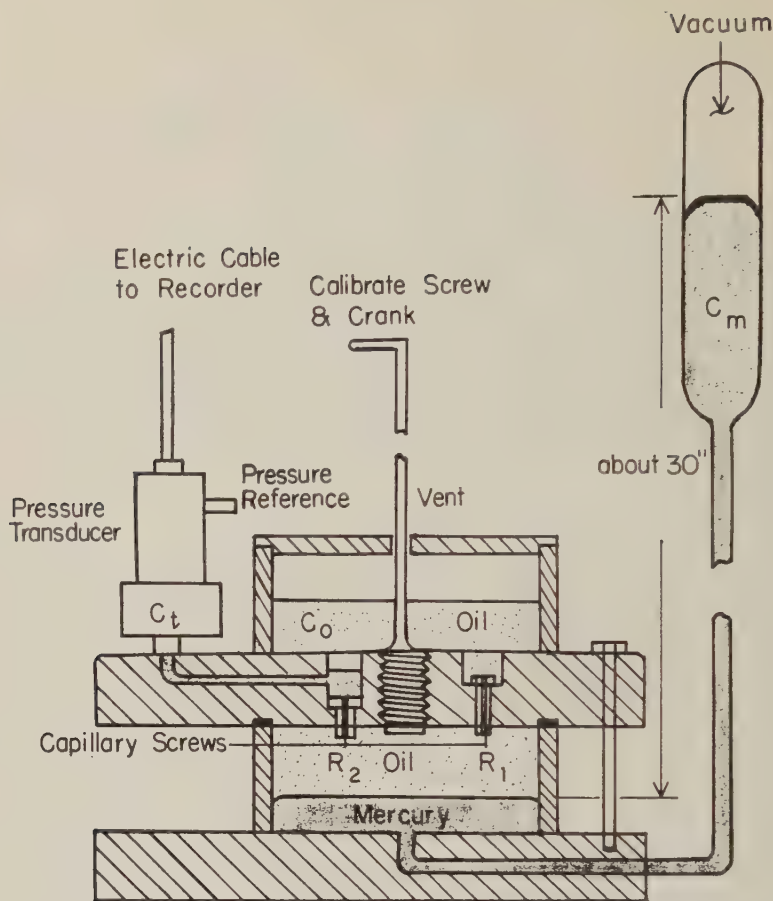


Fig. 1. Schematic drawing of the microbarograph. The abundant use of plexiglass facilitates machining, assembly, and inspection. The mercury flask and its stem are pyrex glass and are filled under vacuum.

TABLE 1. Circuit Constants for the Hydraulic Filter

Symbol	Component	Length, cm	Radius, cm	Circuit Constant (at 25°C)*
R_1	Capillary	1.59	0.080	7.40×10^5 dyne sec/cm ⁵
R_2	Capillary	0.935	0.046	5.26×10^5 dyne sec/cm ⁵
C_m	Mercury flask	20	1.27	3.46×10^{-4} cm ³ /(dyne/cm ²)
C_t	Transducer bellows			8.78×10^{-6} cm ³ /(dyne/cm ²)
C_o	Upper chamber	7.5	5.08	8.23×10^{-2} cm ³ /(dyne/cm ²)

* Using 1000 centistoke (9.73 poise) silicone oil.



Fig. 2. The microbarograph in its wooden supporting rack. The 4-wire electric cable (not shown) connects to the upper end of the transducer.

on a Leeds and Northrup 10-millivolt Speedomax strip-chart recorder.

The dynamical frequency response of this system and its theory of operation are virtually identical with that already described [Van Dorn,

1960], except that the low-pass capacitance C_2 , instead of being a mercury manometer, makes use of the compliance of the small bellows within the transducer itself. Figure 3 shows both the amplitude response of the microbarograph to a constant amplitude sine-wave input of variable frequency and its equivalent electrical analog circuit. Table 1 gives the circuit constants and the dimensions of the pertinent components.

Initial calibration of the microbarograph is accomplished in the laboratory by filling the upper (reference) opening of the transducer with oil and connecting it by a short plastic tube to the upper chamber. Then a brass cylinder is raised and lowered sinusoidally into the upper chamber by a pulley system coupled to a variable-frequency sine generator. In the field, calibration is accomplished by advancing a calibrating screw between the upper and lower chambers by one revolution through a long crank arm extending through the top of the wooden rack which supports the various components. Advancing the screw imparts a steplike increase in pressure to the lower chamber, corresponding to a sudden reduction in atmospheric pressure in normal operation.

In the field the rack-mounted instrument (Fig. 4) is lowered into a vertical well and in an area far away from the dynamical pressure effects induced by the presence of buildings, etc. The well is equipped with an airtight lid, and atmospheric pressure is admitted through an omnidirectional diffuser, consisting of a short vertical length of 1-inch pipe through which a multiplicity of $\frac{1}{8}$ -inch holes are drilled in staggered rows. Atop the diffuser is a sun shield, and thermal stability is further insured by filling the space above the rack with a plastic-encased kapok pillow, such that diurnal ambient temperature fluctuations within the well are reduced to about 1 per cent of their surface values. Thermal sensitivity of the system arises from differential rates of thermal expansion of the silicone oil and the lower chamber walls. This effect was minimized by the choice of plexiglass for the wall material, and laboratory tests indicate that even without the benefit of additional thermal insulation the system is stable to less than 1 per cent of its full-scale sensitivity over a 10°C diurnal variation but shows small signals from alternating exposure to darkness and direct sunlight.

Field experience. A prototype model of the

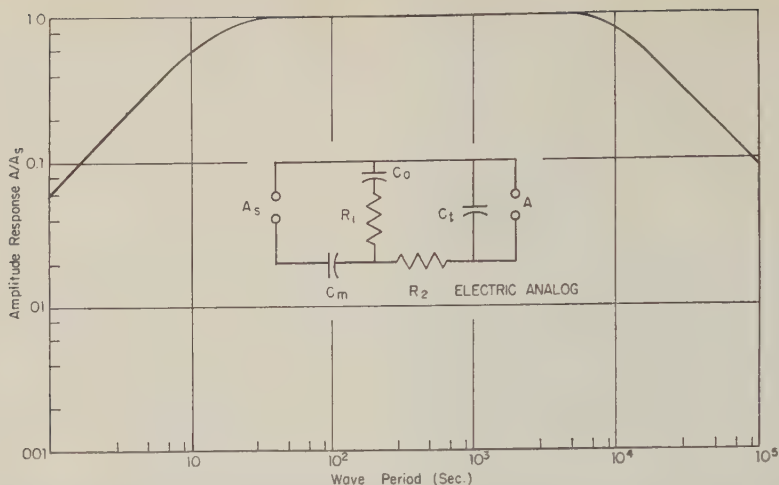


Fig. 3. Frequency response of the microbarograph to a unit sine-wave input, and the electrical analog of the hydraulic filter. The effective band width is easily adjusted by varying the capillaries R_1 and R_2 .

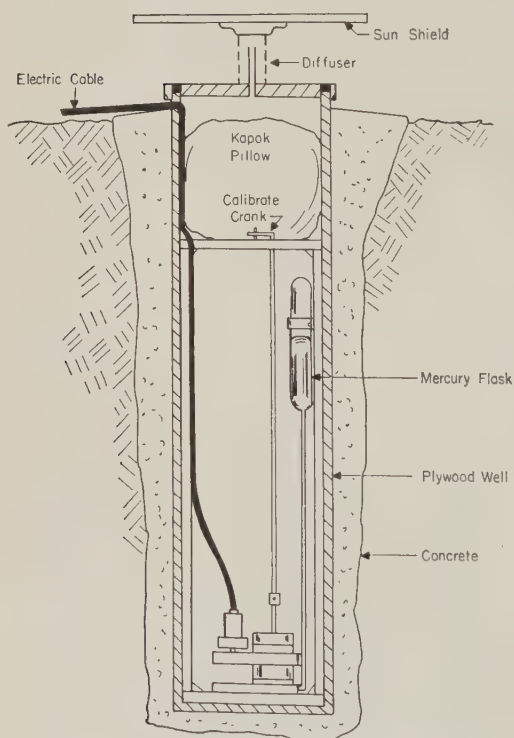


Fig. 4. Schematic drawing of the microbarograph rack installed in its well. The wooden well is coated with fibreglas outside, and serves as a shipping container before installation.

low-frequency microbarograph was installed on Marcus Island in January 1958, together with three long-wave recorders—one on each side of the triangular island—and a wind speed and direction recorder. The signals from all these instruments were recorded against time on a single six-channel Speedomax recorder. The objective for this station was to study the influence of the island on surface water waves approaching from various directions.

It soon became apparent that barometric fluctuations associated with the passage of local disturbances were often reflected by corresponding depressions and elevations of the water surface at all three wave recorders. Since the wave recorders are insensitive to barometric pressure changes, such coherence can only be due to atmospheric coupling. An excellent example of this coherence is shown in Figure 5, which is a direct tracing from the original record for February 26, 1958. In the top curve the microbarograph exhibits at the beginning of the sample quasi-periodic fluctuations of 10–20 minute period and amplitudes of the order of 0.5 mb superimposed on the diurnal atmospheric tide. Such a record is typical during the seasons of strong trade winds with bands of scattered cumulus clouds and occasional intense rain squalls. Suddenly two deep barometric depressions appear, separated by an interval of about 22 minutes, and bounding an unusually high peak; over-all maximum pressure change was 2.8 mb, and it occurred within

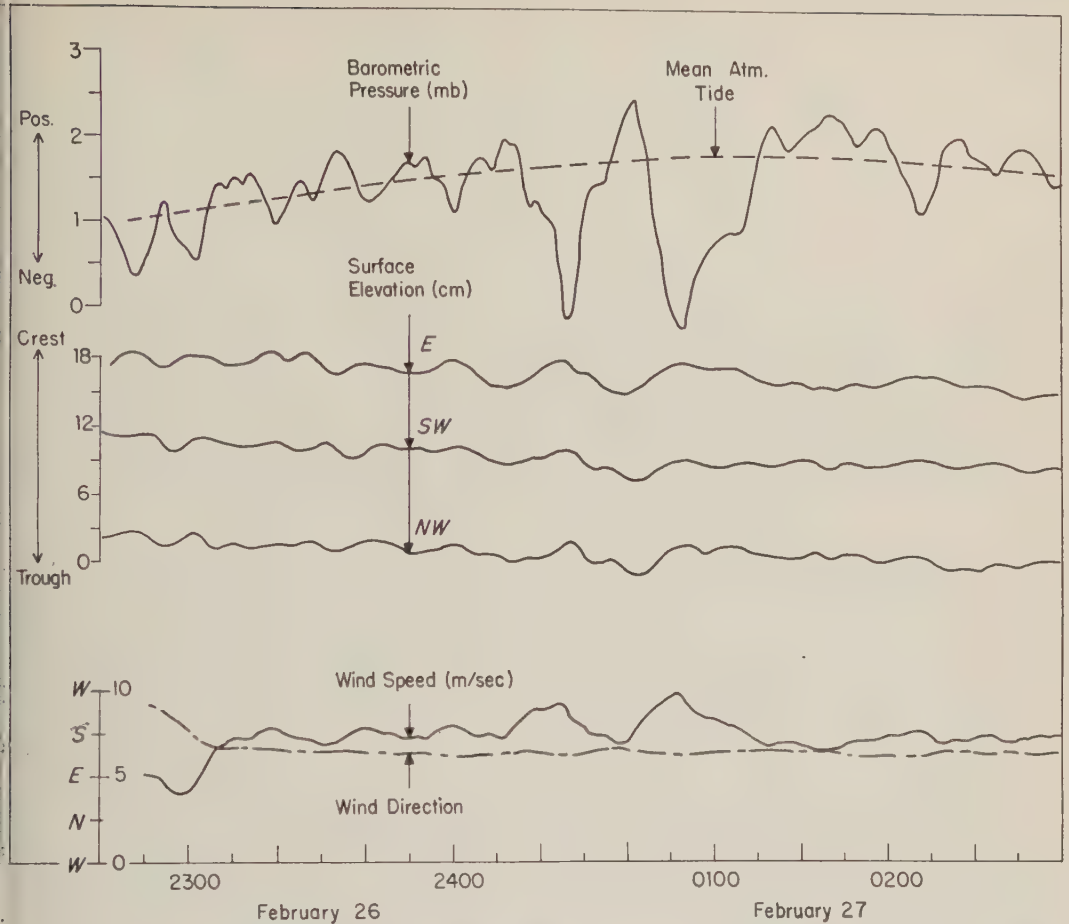


Fig. 5. Record sample from Marcus Island, showing passage of double pressure-jump, as construed from combined records of microbarometric pressure, sea level at three stations, and wind speed and direction.

8 minutes. Following this unusual disturbance the trace returns to normal activity. Corresponding to the barometric changes, the sea surface was elevated and depressed anomalously by about 3 cm, or by roughly the amount of the barometric change at all three stations. Two clear maxima occurred in the wind speed at the time of the depressions, and there was virtually no change in the wind direction.

Reconstruction of the probable sequence of events which resulted in this meteorological singularity² is possible through analysis of the above record and consideration of Figure 6, which

² Although some coherence between the sea level and barograph records was almost always present, only two such extreme examples were observed in 3 months of records at Marcus Island.

shows the outline of Marcus Island and the geographical distribution of the instrumentation. The long-wave recorders were installed near the center of each leg of the triangular island. The anemometer and microbarograph were located on the east side of the island near the east long-wave station. The prevailing wind had been blowing at about 7.5 m/sec from ESE for about 2 hours. The first barometric depression, preceded by a relatively minor pressure increase, was accompanied by an increase in wind speed to 10 m/sec. The disturbance propagated unchanged in form across the island with the mean wind speed and in the prevailing wind direction, as evidenced by the displacement in time of the long-wave records at the SW and NW stations and the nearly identical anomalous sea-level

Estimates of Bowen's Ratio by the Heat Budget Measurements of a Cornfield¹

J. F. GERBER² AND W. L. DECKER

*Department of Soils, University of Missouri
Columbia, Missouri*

Abstract. Estimates of Bowen's ratio, which is the ratio of the amount of heat transferred as sensible heat to that transferred as latent heat from a surface, were made from a 10-acre cornfield during the summer of 1959. These estimates were based on a heat budget technique which partitioned the energy used in evaporative processes, sensible heat transfer to the atmosphere, and heat exchange to the soil. The cases investigated could be divided into two groups. One group of ratios was associated with wet soil surfaces, and the modal value of the ratio was 0.05. The second group of ratios was associated with dry soil surfaces, and a modal of 1.65 was noted. Under practical agronomic conditions the larger values of the ratio are advantageous, since this condition provides for a more economical use of water.

Introduction. Bowen's ratio is the ratio of sensible to latent heat exchange at the surface. Since sensible heat transfer is usually from the surface to the atmosphere, heat movement from the surface is considered positive. Similarly, latent heat transfer is most frequently from the surface to the atmosphere through evaporation, and it is also positive. If the transfer of either heat component is into the surface, it is regarded as negative. Bowen's ratio, B , is commonly written as

$$B = Q/LE \quad (1)$$

where Q is sensible heat transfer and LE is latent heat transfer.

Bowen [1926] proposed that the solution of the ratio of sensible to latent heat transfer could be obtained by assuming that the coefficients of eddy conductivity of vapor and heat were equal. It must be clear that the coefficients of eddy conductivity are not constant, but that their ratio is constant. By this assumption, Bowen was able to show, both theoretically and practically, that the ratio of sensible to latent heat exchange over a lake was described by the following equation:

$$B = 0.46(T_s - T_a)/(e_s - e_a) \quad (2)$$

where T_s and T_a are the surface and air tem-

perature in °C and e_s and e_a are the vapor pressure of the surface and the air in mm of mercury.

Estimates of Bowen's ratio have been made from measurements of the temperature, wind, and humidity profiles. In some studies interest has been focused upon the measurement of the eddy coefficients rather than upon the actual values of Bowen's ratio. Rider and Robinson [1951] made measurements over a short grass cover in England. They concluded that the ratio of the eddy coefficients for vapor and heat were constant, which confirmed Bowen's approach.

Halstead [1953] developed an aerodynamic technique for computing the flux of sensible and latent heat. Bowen's ratio computed from values of sensible and latent heat using this technique has been reported by Mather and Hacia [1959] and Mather and Thorntwaite [1958] and ranges from 0.5 to 4 at Point Barrow, Alaska, and from 0.26 to 0.075 at Centerton, New Jersey. The type of surface represented by these two locations was apparently different. The surface at Point Barrow appeared to be either a dry bare soil or soil with sparse tundra vegetation, whereas the Centerton location provided a grass cover.

Values of Bowen's ratio obtained from measurements of temperature, wind, and humidity profiles in the Lake Hefner studies [*U. S. Geological Survey*, 1954] range from -20.20 to +31.50. These extremely variable values were obtained for daily periods. When periods of 5,

¹ Contribution from the Missouri Agricultural Experiment Station, Journal Series No. 2162.

² Now at Department of Fruits Crops, University of Florida, Gainesville, Florida.

10, and 20 days were used, the values were less variable, ranging between -1.5 to $+1.5$. From May to December the values varied from -0.5 to $+0.5$ and were predominantly positive. Surface water spray, radiative diffusivity, and atmospheric stability were shown in the Lake Hefner studies not to introduce a consistent error. It was concluded in the Lake Hefner report that the Bowen ratio is sufficiently accurate for computing evaporation by the heat budget technique.

Experimental procedures. Estimation of Bowen's ratio was performed by the evaluation of the heat budget of a cornfield. The heat budget may be written as

$$H = Q + LE + S \quad (3)$$

where H is the net radiation.

S is the heat stored in the soil.

LE is the latent heat of evaporation.

Q is the sensible heat transferred to the air.

All other terms, such as photosynthesis and heat of reactions, are ignored. Equation 3 is true if fractional heating of the crop is ignored, and if there are no horizontal losses or gains of heat. To reduce the effects of horizontal exchange of heat, the heat budget was evaluated near the center of a 10-acre cornfield.

The net radiation was measured by a ventilated net radiometer which was located 1 meter above the top of the crop. The changes in the heat stored in the soil were obtained from two heat flow transducers placed 4 cm below the soil surface. The evapotranspiration was obtained by the water balance technique. In this method the measurement of all additions and losses of liquid water, both at or below the surface, are required. The net increase of liquid water together with the change in the soil moisture content is a measure of evapotranspiration. Changes in the soil moisture were obtained by the neutron-scattering technique. Surface applications of water from rainfall and irrigation were measured, and runoff from the area was obtained through a rated flume. The subsurface drainage was assumed to be negligible.

The heavy clay pan associated with the B horizon of the Mexico silt loam soil used in this experiment prevents the ready exchange of water by subsurface drainage. Soil-moisture

measurements indicated no significant change from day to day in the soil-water content in the layer of soil from $3\frac{1}{2}$ to 5 feet below the surface. This negligible change in the water content of the deeper layer of soil indicated either no movement of water or a steady state in water movement. If the acceptance of negligible movement is in error and drainage was occurring, then the estimates of Bowen's ratio will be larger than those indicated.

The transfer of sensible heat to the atmosphere was obtained by the algebraic summation of the heat budget from equation 3. It is realized that precise estimates of Q are not obtained, since all the errors in the other determinations plus the neglected terms are cast into the Q term.

Results. The values of Bowen's ratio for the cornfield are shown in Figure 1, in which the data are segregated into two groups. This grouping is related to the conditions of the soil surface, i.e., whether it was wet or dry. Estimates of the evapotranspiration from the heat budget [Gerber and Decker, 1960] showed the same segregation.

There is a large difference in the modal value of Bowen's ratio for a wet soil surface as compared with a dry soil surface, being approximately 0.05 and 1.65, respectively. Small negative values of the ratio were present during periods when the sensible heat transfer was negative. It will be noted that the negative values were observed only when the soil surface was wet.

Discussion. Although negative values of Bowen's ratio were not obtained from the work of Mather and Hacia [1959] and Mather and Thornthwaite [1958], the Lake Hefner report [U. S. Geological Survey, 1954] contains a sizable quantity of negative ratios. Since for the cornfield negative values were observed only when the soil surface was wet, it is suggested that sensible heat flow into the surface occurs only when the heat requirement is high because of the evaporation of a large amount of water. It should be noted, however, that the occurrence of negative values of Bowen's ratio was always accompanied by increasing maximum air temperatures, so these negative ratios may be related to warm air advection.

Bowen's ratios were always small when the soil surface was wet. These small values were due to the concurrent transfer of a small quan-

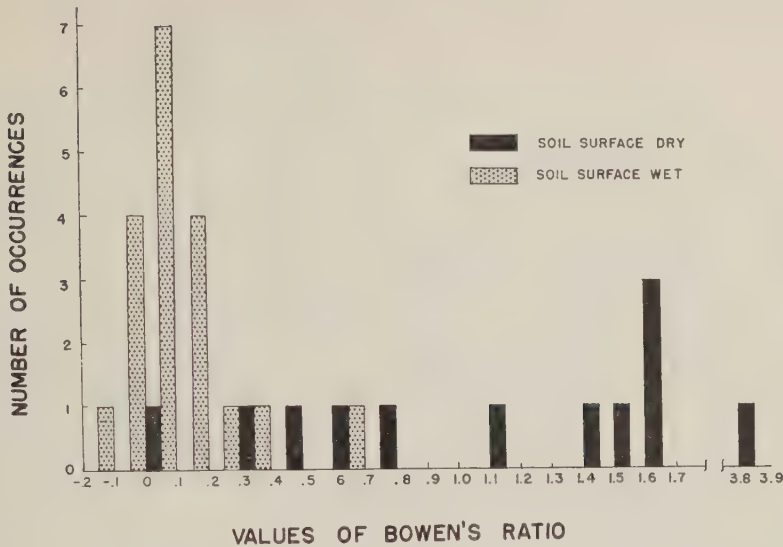


Fig. 1. Bowen's ratio computed from the heat budget.

city of sensible heat and a relatively large amount of latent heat. The mean transfer of sensible heat was 75 cal/cm² when the soil surface was wet and 164 cal/cm² when the soil surface was dry. At the same time, the transfer of latent heat was about twice as great when the surface was wet as when it was dry.

It is possible that the negative values as well as the small values of Bowen's ratio are, in fact, zero. The computation of B by the heat budget is done by the following equation:

$$B = \frac{Q}{LE} = \frac{H - S - LE}{LE} \\ = \frac{H - S}{LE} - 1 \quad (4)$$

where

B is Bowen's ratio.

Q is the sensible heat transfer.

LE is the latent heat transfer from the water balance.

H is the net radiation.

S is the heat stored in the soil.

All the errors in the estimation of each component are then reflected in the estimates of Q by the heat budget technique. Assuming no error due to subsurface drainage, H , S , and LE were measured with the same precision for all periods. Therefore, the percentage of error is the

greatest for small values of Q and is smallest for large values. For this reason, Bowen's ratio will have the greatest percentage of error when Q or LE is small.

The large values of Bowen's ratio observed when the soil surface was dry are due to the transfer of sensible heat and the small exchange of latent heat. The extreme value of the ratio was due to a very small transfer of latent heat. This large value occurred after a cold air mass invasion toward the end of the season when the plants had begun to dry.

Conclusions. The ratio of Q/LE , Bowen's ratio, is small when the surface is wet. This is due to the small amount of sensible heat transferred to the air. For water conservation large values of Bowen's ratio are beneficial to crops if evapotranspiration is sufficient for normal plant growth and development. The curtailment of evapotranspiration causes more of the net heat at the surface to go into the sensible heating of the air. Since the value of potential evapotranspiration is the amount of water used when the plant is grown under high moisture conditions, it is likely that the amount of evapotranspiration which is agronomically advisable may be overestimated if the potential evapotranspiration is used. If the soil surface is maintained dry, the value of Bowen's ratio may be increased and thereby the heat budget advantageously modified.

Acknowledgment. This research was partially supported by the U. S. Weather Bureau, contract Cwb-9563.

REFERENCES

- Bowen, I. S., Heat losses by conduction and by evaporation, *Phys. Rev.*, **27**, 779-787, 1926.
- Gerber, J. F., and W. L. Decker, A comparison of evapotranspiration as estimated by the heat budget and measured by the water balance from a corn field, *Final Rept., contract Cwb-9563*, Soils Dept., Univ. Missouri, Columbia, Mo., 1960.
- Halstead, M. H., The fluxes of momentum, heat and water vapor in micrometeorology, *Publications in Climatology*, **7**, 326-358, 1953.
- Mather, J. R., and H. Hacia, Investigations of the heat and water balance at Centertown, New Jersey, May-July, 1959, *Publications in Climatology*, **12**, 5-47, 1959.
- Mather, J. R., and C. W. Thornthwaite, Microclimatic investigations at Point Barrow, Alaska, 1957-1958, *Publications in Climatology*, **9**, 63-230, 1958.
- Rider, N. E., and G. D. Robinson, A study of the transfer of heat and water vapor above a surface of short grass, *Quart. J. Roy. Meteorol. Soc.*, **77**, 375-401, 1951.
- U. S. Geological Survey, Water-Loss Investigations, Lake Hefner Studies, *U. S. Geol. Survey Prof. Paper* 269, 1954.

(Manuscript received June 4, 1960; revised August 12, 1960.)

The Exceptional Advances of the Muldrow, Black Rapids, and Susitna Glaciers

AUSTIN S. POST

7375 Champagne Point Road, Kirkland, Washington

Abstract. Muldrow Glacier in Alaska advanced extremely rapidly during the winter of 1956-1957, with surface movements of ice amounting to over 6.6 km. This flow was accompanied by a pronounced lowering of the surface of the upper portion of the glacier by 170 m, or more, with a corresponding rise in surface ice levels in the terminal portion; the net exchange of ice is roughly computed to be equal. No other glacier in the region showed evidence of a similar movement during the same period. However, the Black Rapids Glacier in 1937, the Yanert in 1942, and the Susitna in 1953 did make advances of a similar nature. Unusual medial moraines indicate that at least two of these glaciers have previously alternated between stagnation and sudden, brief movements. No evidence was found to suggest short-term climatic conditions favorable to large snow accumulation on these glaciers prior to their advances. Correlation between local earthquakes and these ice movements is also lacking. Evidence does indicate that these advances result from critical dynamic conditions met with in certain glacier systems favoring long periods of stagnation followed by sudden displacements of ice.

INTRODUCTION

In the winter of 1956-1957, the Muldrow Glacier, after many years of quiescence and slow retreat, suddenly and unexpectedly made a spectacular advance, with ice movements down the glacier amounting to 6.6 km (4.1 mi) taking place in a few months. A similar short-lived movement was witnessed in the Black Rapids Glacier in 1936-1937, and in 1952 or 1953 the Susitna Glacier made a like movement.

These advances apparently are not a normal reaction to climatic changes and may have significance to our understanding of the mechanism of glacier flow.

All these glaciers are located in the Alaska Range in central Alaska. Among the many glaciers present, those described in this report are conspicuous only because of these known advances and unusual surface features displayed.

MULDROW GLACIER

This glacier is located on the northern slope of the Alaska Range in Mt. McKinley National Park. Heading in the summit snows of Mt. McKinley, 6193 m (20,320 ft), North America's highest peak, the glacier, about 63 km (39 mi) in length, descends abruptly to an elevation of about 6000 m (6600 ft), then more gradually to its terminus at 762 m (2500 ft). It is joined by its largest tributary, the Traleika, at an elevation

of 1737 m (5700 ft) and by another major branch, the Brooks Glacier, at an elevation of 1646 m (5400 ft). Below the junction of the Traleika the glacier is quite uniform in gradient and width, which averages $2\frac{1}{2}$ km ($1\frac{1}{2}$ mi). The upper portion of the glacier flows in a northeasterly direction for a distance of 42 km (26 mi). Here an abrupt 90° angle occurs and from this point the glacier trends northwesterly to the terminus. The general setting has been described by Griffiths [1952].

Conditions before Advance

For a period of at least 50 years the lower portion of the glacier has been wasting away with little or no movement taking place. Photographs taken in 1916 [Griffen] show debris-laden ice in the terminal area. Others taken since 1950 indicate that vertical wastage of as much as 200 m (660 ft) has occurred during this period. Aerial views in 1936 [Washburn] of that portion of the glacier above the bend showed conditions essentially similar to those in 1952. At that time the glacier above the bend was characterized by lanes of rather smooth, uncrevassed ice and large, irregular moraines (Fig. 1). Photographs taken from McGonagall Pass near the juncture of the Traleika and Muldrow in 1916 [Capps] and 1956 [Mills] show little change.

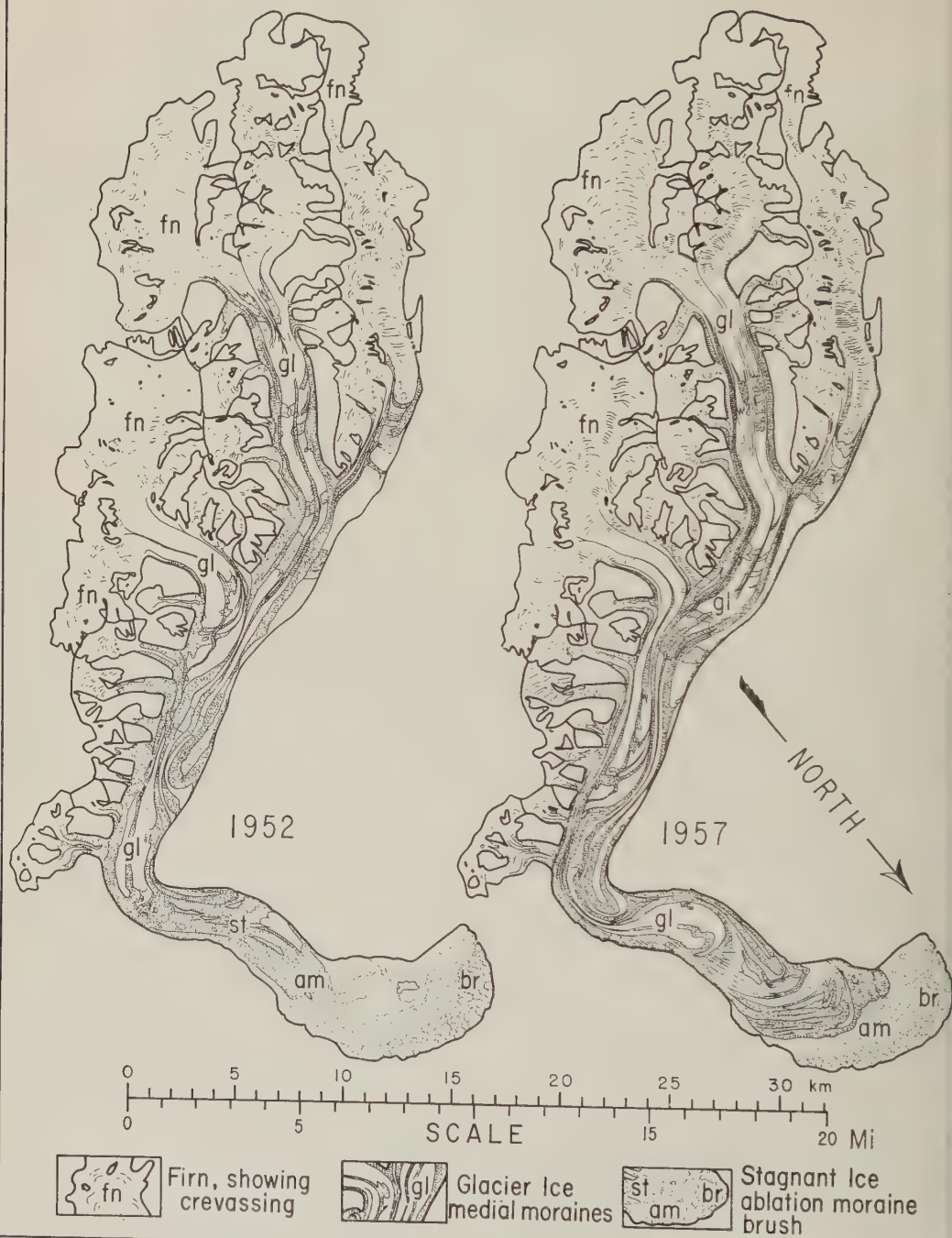


Fig. 1. Maps showing Muldrow Glacier before and after advance. Surface features in early 1954 were essentially the same as in 1952. The advance had reached its maximum by July 1957, as photographs taken in that month and repeated in September show no discernible change.

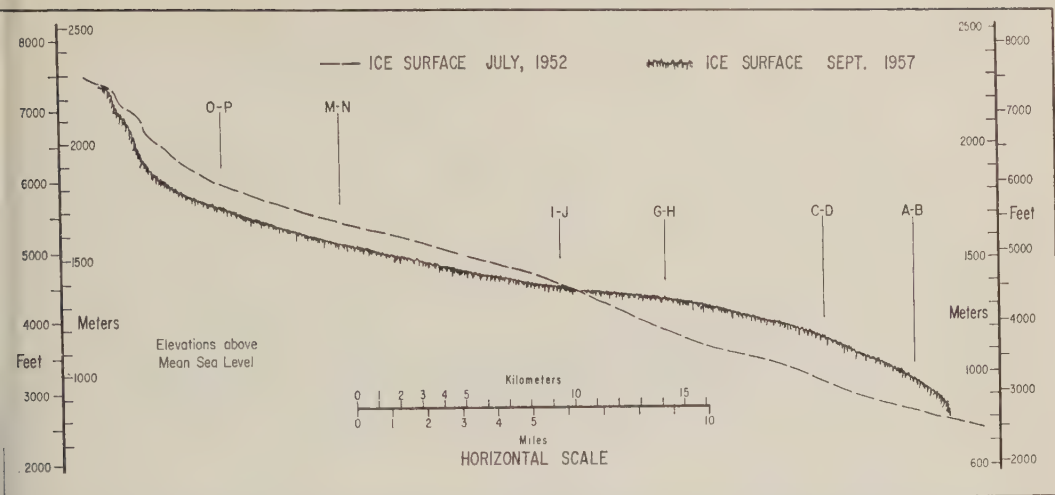


Fig. 2. Horizontal profile, Muldrow Glacier. The glacier above 2300 meters, where no discernible change took place, is not shown.

Early Phases of Advance

Although no one actually seems to have seen the beginning of the advance of the glacier, personal observations and photographs kindly furnished to the author by various persons who had been in the vicinity in 1956 have brought out certain pertinent facts. Photographs by Viereck taken near the right-angle turn in the lower glacier on July 16 show that below this point the glacier was almost unchanged from former years. Views up-glacier from the same point disclose notable shearing in the form of crevassed and broken ice, particularly along the northern margins several kilometers farther up the valley, and what may be a wave of advancing ice extending completely across the glacier at a greater distance. In the immediate vicinity of the right-angle bend, the ice, although not seriously disturbed, shows some marginal crevasing and a convex profile, both of which are indications of activity. Mills (private communication), leader of a mountain-climbing party on the Traleika Glacier that year, definitely witnessed early phases of the actual movement. By his description, the Traleika Glacier was badly crevassed when the group ascended that branch of the Muldrow in late May 1956, and had become almost impassable by July 6. About 6 km (4 mi) up the Traleika the surface level had dropped an estimated 15 m (50 ft) in this 6-week interval. During this same period, the Muldrow Glacier above its confluence with the

Traleika had remained almost unchanged.

It appears that extensive down-valley movements were lowering the ice surface of the upper Traleika before July 6 and that the effects of such movements were just beginning to be manifest on July 16 at the right-angle bend 32 km (20 mi) down the glacier.

Early in the spring of 1957, National Park officials first noted that the lower glacier had advanced and many reports followed describing the glacier as totally changed, including several excited tales of the upper glacier having 'collapsed,' or 'fallen in.' This area was visited by several interested scientists: Péwé [1957] and Millett (unpublished manuscript, 1960) both reported their observations. In July the author made several aerial photo-reconnaissance flights over the area. In September the U. S. Navy obtained excellent aerial photographs.

As very little change took place after detailed observations were begun in June 1957, practically all the movement of ice in the glacier below the 90° bend took place in a period not exceeding 9 months.

Nature of Changes

Lower glacier. Views from the Denali Highway in 1957 disclosed that the lower glacier had been completely transformed since last observed in the fall of 1956. Where formerly the glacier had been a hardly recognizable moraine-covered mass almost concealed behind massive lateral

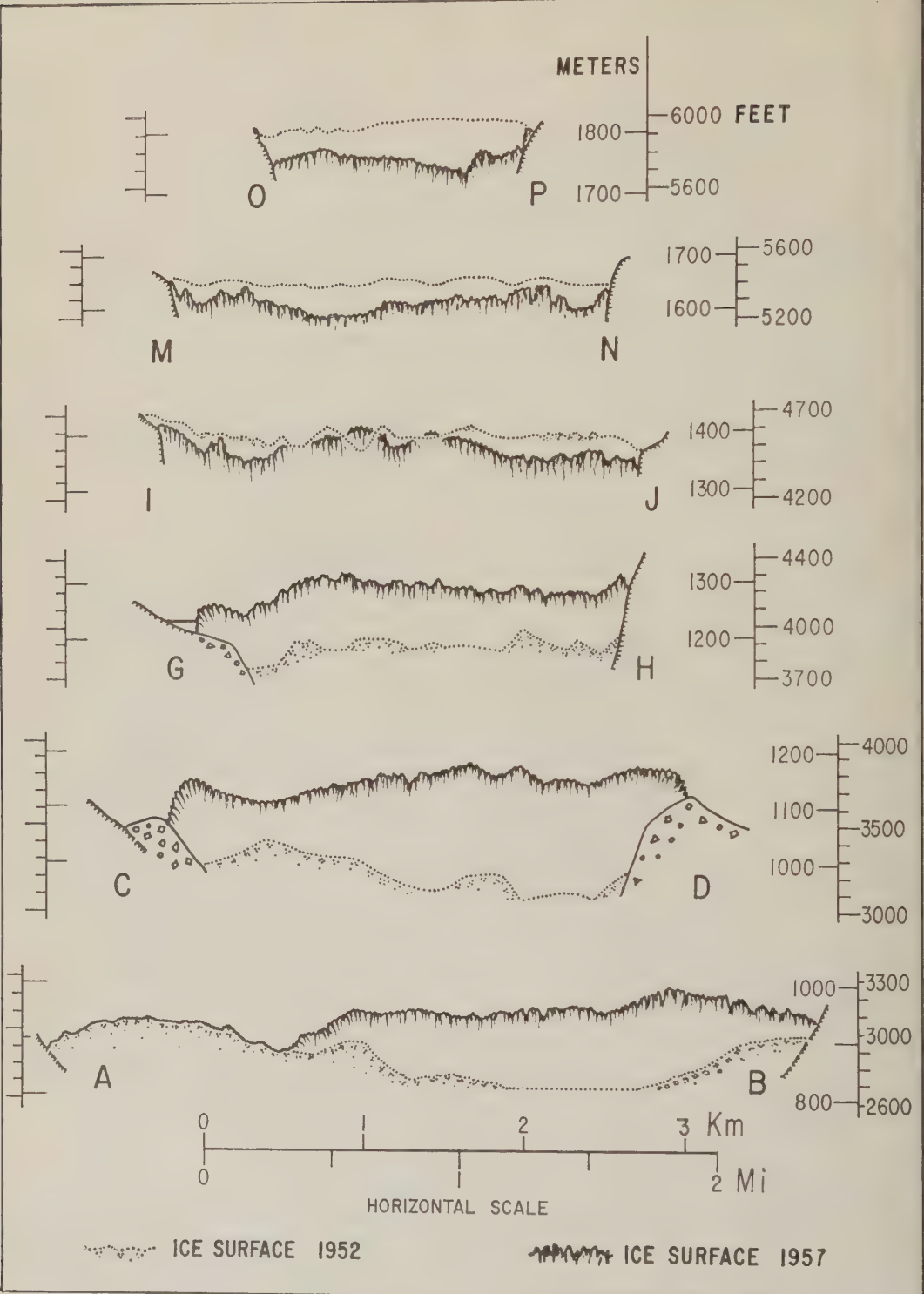


Fig. 3. Six cross profiles, Muldrow Glacier, showing changes in surface levels between 1952 and 1957. Positions of these profiles are shown on Fig. 5.

moraines, fantastically broken seracs of blue ice now rose conspicuously. Closer examination disclosed that the ice advancing down-glacier had

overridden and incorporated much of the nearly stagnant lower portion of the glacier but did not completely cover all of an area of relic, ablation-moraine-covered ice dating from an older advance, judged from vegetational development to be nearly one hundred years old, or even older (Viereck, private communication). On the eastern side of the advancing glacier this brush-covered ice was compressed and pushed into large ridge-like 'rolls.' Margins of the glacier, formerly concave below the lateral moraines, now rose vertically 50 m (160 ft) or more above the point of contact with the moraine, in most places towering high above its crest. This condition was present as far up-valley as the right-angle bend (see Fig. 2; also, Fig. 3, Profiles A-B, C-D and G-H). Streams from bordering mountains which formerly had drained through notches in the lateral moraine were dammed by the glacier and had formed lakes from which the water now escaped through old channels between the moraines and mountain slopes.

Middle portion of the glacier. Above the right-angle bend the rise of the surface of the glacier became progressively less pronounced and was negligible at cross profile I-J (Fig. 3). For 25 km (16 mi) beyond this point the surface was lower than before (Figs. 2 and 3, Profiles M-N and O-P). This lowering of the ice surface was present in all three major tributaries but was most pronounced in the upper trunk glacier and especially noticeable on the Traleika, which furnished the major portion of the ice involved in the advance. Movement of this tributary amounted to nearly 5.5 km (3.4 mi) against 1.8 km (1.1 mi) for the Brooks and 2 km (1.2 mi) for the upper Muldrow (Fig. 4). Most of the smaller, steeply descending tributaries had been greatly altered by this lowering of the main glacier's surface. The least affected were left hanging, their point of contact with the main glacier being marked by a sheer ice cliff as much as 61 m (200 ft) high. The majority of these branches, however, had made large movements and their formerly rather smooth surfaces had become steep cascades of shattered ice blocks.

Hanging 'stranded' lateral moraines, ice fringes, and the sheared-off lateral tributaries clearly indicate that the changes in this portion of the glacier were due almost entirely to a down-valley shift of the ice accompanied by a pronounced lowering of the glacier surface of as

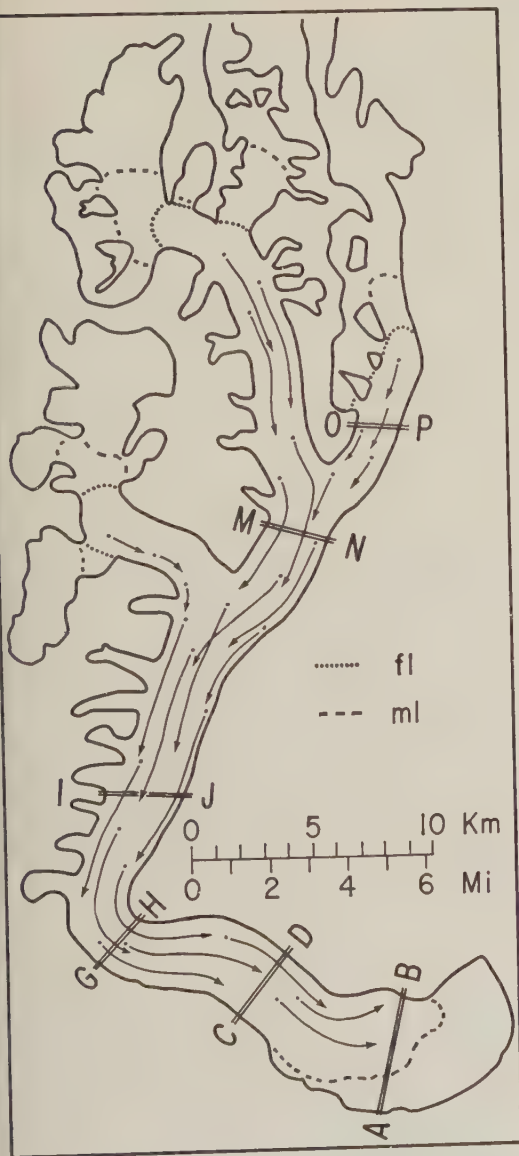


Fig. 4. Map showing surface-movement vectors, Muldrow Glacier. Dots indicate positions of identifiable objects on the glacier in 1952 photographs; arrows indicate positions of same features after advance. The solid line connecting these points shows the inferred path of movement. Locations of cross profiles are shown; fl = firn line; ml = approximate limits where changes in surface levels occurred. Horizontal profile (Fig. 2) extends up center of glacier from broken line below A-B to broken line above O-P.

TABLE 1

Accumulation Area	Km ²	Mi ²
Traleika Gl.	93.5	36.0
Brooks Gl.	54.5	21.0
Upper Muldrow Gl.	46.0	18.0
All other branches	15.0	6.0
Total	209.0	81.0
Ablation Area		
Lower Muldrow	104.0	40.0
Lower Traleika	31.0	12.0
Brooks Gl.	14.0	5.5
Upper Muldrow	12.5	5.0
Relic, stagnant ice, Muldrow Termini	22.5	9.0
Total	184.0	71.5

much as 61 m (200 ft), or more (see Fig. 3, cross profile *O-P*). Sheared marginal remnants of ice, which in places appeared to have been thrust down-valley slightly before being left stranded by the lowering of the main glacier surface, suggest that the down-valley motion may have begun before the lowering.

The movement throughout the affected portion of the glacier appears to have taken place in such a way that, although crevassed and broken into a fantastic mass of ice pinnacles, the main surface features consisting of medial moraines and avalanche debris remained clearly recognizable (Fig. 1). One feature noted was that large areas of heavily debris-encumbered ice frequently remained at a higher level than the adjoining clean ice. The medial moraine extending from the juncture of the Muldrow and Traleika glaciers was a notable example of this, rising above the clean ice on either side almost vertically approximately 30 m (100 ft), and forming a weirdly pinnacled, continuous wall for a distance of several kilometers.

Upper glacier. Where the larger tributaries become narrow and the gradient steepens near the head of the main valleys, the amount of lowering of the ice surface rapidly diminished. Above such points, including at least three-quarters of the accumulation area of the glacier, no discernible change of surface levels took place.

Areas and Volume of Ice, Muldrow Advance

The 1957 firn limit occurred at about 2100 m

(7000 ft) above sea level and is considered to be about the maximum altitude the snowline rises on the glacier. The areas in different branches above and below the firn limit are given in Table 1.

Although the Muldrow Glacier covers approximately 393 sq km (152 sq mi), the portion of the glacier affected by the advance was only about 167 sq km (64 sq mi) (Fig. 4). Of this, 67 sq km (26 sq mi) is located below cross profile *I-J* in the area into which ice advanced, and 100 sq km (38 sq mi) is the area in which loss of volume occurred. The loss of ice from the upper glacier and the gain by the lower glacier appears to be equal within the accuracy of available data. If an average surface lowering above profile *I-J* of 45 m (150 ft) is assumed, probably a minimum figure, the net exchange of ice from the upper to the lower glacier is calculated to be about 3.3 km² (0.8 mi²).

BLACK RAPIDS GLACIER

In the winter of 1936-1957 the Black Rapids Glacier, located 290 km (180 mi) east of the Muldrow, advanced approximately 4.8 km (3 mi) in 3 months. Eyewitness accounts of the terminal advance have been published [*Hanse*, 1937; *Moffit*, 1942]. Apparently no extensive studies or examination of the glacier above the terminal areas were made. Photographs taken in 1942 [*Washburn*] show hanging lateral remnants of ice in the upper portion of this glacier, indicating that this advance was accompanied by a lowering of the ice surface near the head of the glacier.

SUSITNA GLACIER

This glacier flows in a westerly direction from névés contiguous to the Black Rapids Glacier. *Washburn* photographed this glacier in 1942, and vertical photography [USGS] taken in 1954 shows that the glacier had advanced, probably in 1952 or 1953, with ice movements of 4 km (2.5 mi) or more, again with a pronounced lowering of the surface of the upper glacier.

YANERT GLACIER

Aerial photographs taken by *Washburn* in 1942 showed that this glacier, 96 km (60 mi) west of the Black Rapids Glacier, was chaotically crevassed, apparently owing to a rapid ad-

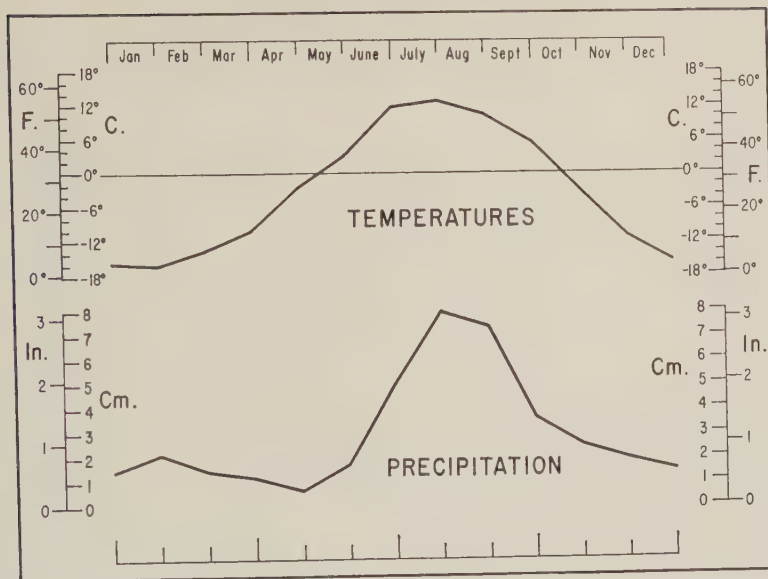


Fig. 5. Mean monthly temperatures and precipitation at McKinley Park Station (elevation 700 meters).

vance then taking place. The U. S. Geological Survey photographs taken in 1952 show this glacier to have been almost free of crevasses.

CONCLUSIONS

It has definitely been determined by examination of aerial photographs and by personal observation that all the above advances took place without contemporary movement of any other glacier in the immediate vicinity.

Unusual Surface Features

The glaciers discussed above have similar, although unusual, medial moraine patterns. These consist of large bulb-like loops in the moraines which frequently extend almost from one side of the glacier to the other. Nearly identical loops may be seen to repeat at intervals. Somewhat similar moraine patterns are found on a very few other valley glaciers in Alaska, one being the West Fork Chulitna. These moraine loops are probably caused by intrusion of fast-moving tributaries into the slower main stream. The moraine loops are displaced down the valley by advances of the trunk glacier. When the movement of the trunk glacier ceases, new ice bulbs are formed by the tributaries. Aerial photographs (USAF and USGS) of the Black Rapids Glacier in different years show deformation of this nature taking place.

Significant Aspects

The glaciers covered in this report have a number of features in common:

1. All have a fairly long, narrow main stem of relatively low gradient (slope in the middle reach averaging about 30 m/km (120 ft/mi). All but the Yanert, which has one, have three or more major tributary valley glaciers. Normally, a reach 8 km (5 mi) or more in length at the terminus is virtually stagnant and covered with debris.
2. Each advance, with the possible exception of that of the Yanert, of which little is known, was preceded by a long period (at least several decades) of inactivity in which the glacier was very inactive and thinning in its terminal regions.
3. As a result of the advance, the surface level in the middle reaches of the trunk and tributaries is lowered. The surface in the terminal area rises, and active ice overrides stagnant, debris-covered ice, but no net change in mass occurs. The surface changes in elevation may amount to 60 m (200 ft) or more.
4. Surface features are displaced down-glacier by several kilometers but otherwise are little distorted by the advance.
5. Similar advances apparently have occurred in the past, and, in some cases at least, this may be a periodically recurring phenomenon.

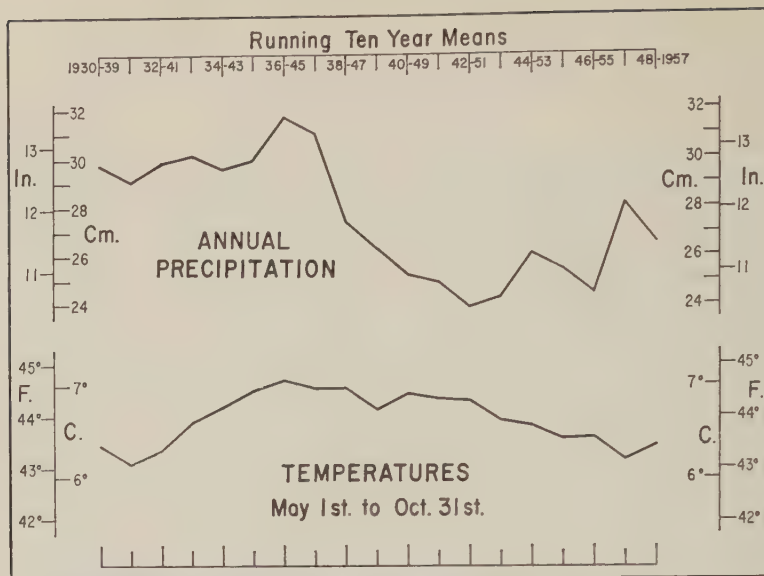


Fig. 6. Running 10-year means, annual precipitation, and May 1 to October 31 temperatures at McKinley Park Station.

Possible Causes

Glaciers are known to be very sensitive to climatic variation, so it is only natural to look first to this as the direct cause of these advances. Attempts to correlate the recent glacial history at the Black Rapids Glacier with other glaciers [Péwé, 1953] imply acceptance of climatic variations as the direct cause of the advance of this glacier. However, the advance of glaciers in the Yakutat Bay area in the very early 1900's was ascribed to abnormal avalanching of snow due to earthquakes [Tarr and Martin, 1914], an idea which has gained widespread acceptance. The possibility that a cycle of advance may be caused directly by wastage of a glacier was mentioned by Forel and Richter in the 19th Century [Russell, 1899] and has been reported recently [Streiff-Becker, 1957; Desio, 1954], but apparently it has not been accepted generally by workers in the field of glacier dynamics.

Climatic variation. No records have been kept which directly indicate weather conditions on the Muldrow or other glaciers described in this report. The general climatic pattern, however, is indicated from records kept since 1930 at McKinley Park Station, located approximately midway between the Muldrow and Black Rapids glaciers.

Figure 5 shows the mean monthly tempera-

tures and precipitation at McKinley Park Station for the 27-year period of record previous to the Muldrow advance. It will be noted that the bulk of the precipitation occurs during the summer months. Cool summer temperatures and a resultant lowering of the firn line would result in a large increase in the area of snow accumulation in the glacier basin. Figure 6 shows the running 10-year mean for May 1 through October 31 temperatures at McKinley Park Station and the annual precipitation over the 27-year period of record. From this, no clear indication of any general climatic change favoring glacier growth is apparent.

Despite this, the possibility of very local increases in snow accumulation must be considered. It will be noted that:

1. Contiguous glaciers (Susitna and Black Rapids firn) did not behave similarly at the same time. In fact, the change revealed by extensive crevassing at the head of the Susitna Glacier in 1954 was remarkable. The crevassing began only a few hundred meters from a point in a common firn from which similar crevassing due to ice moving in the opposite direction occurred during the Black Rapids advance in 1937. During this interval a complete reversal of the dynamic condition of the two glaciers took place.

2. Glaciers in the Alaska Range advanced at

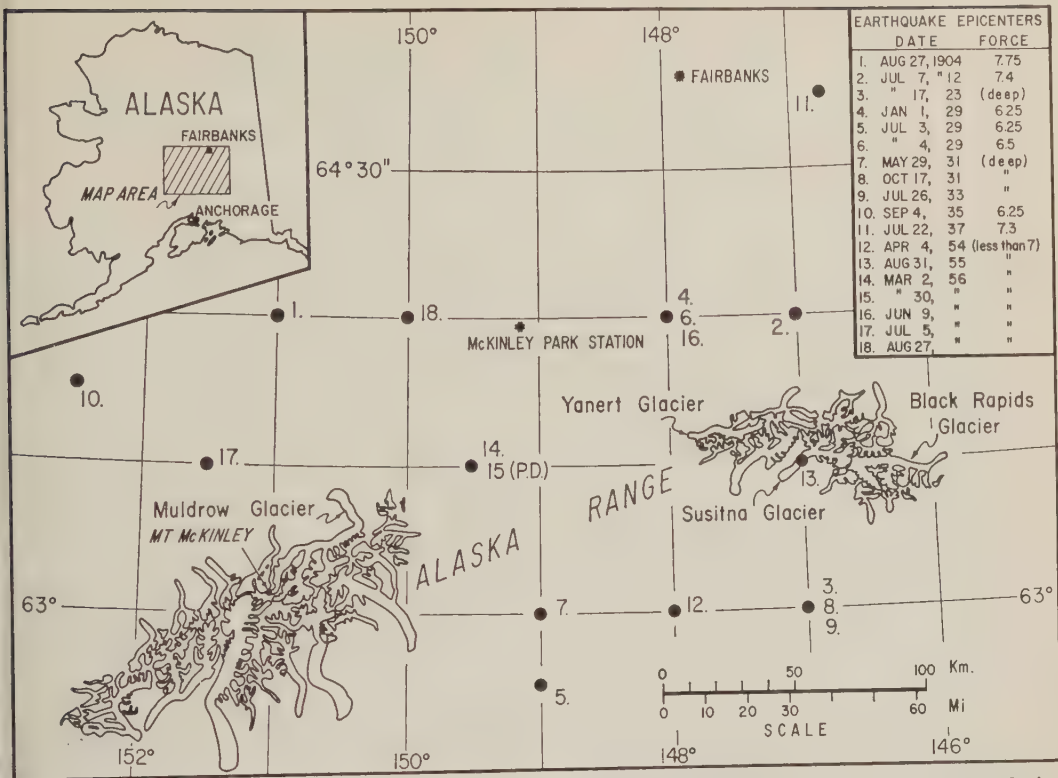


Fig. 7. Map showing locations of recorded earthquake epicenters in central Alaska, and their relation to the Muldrow, Susitna, and Black Rapids glaciers.

widely different intervals in time. Advances cycled completely in a matter of months; therefore these would not seem to be delayed responses to a suitable general climatic variation.

3. In at least one known case (Muldrow), the amount of ice in the terminal advance equaled the amount of ice depleted in upper reaches without any corresponding 'refilling' of the accumulation basin. There was no discernible net addition of mass to the glacier. Indications are that the Black Rapids and Susitna advances were essentially the same as that of the Muldrow. Therefore, even if a localized, sporadic distribution of climatic changes had occurred, it could not have done more than act as a trigger.

Earthquakes. All these glaciers occupy valleys which are believed to follow a major fault line. With but few exceptions, other glaciers situated farther east and farther west and occupying portions of this same fault system show at least some erratic surface features, while on nearby glaciers in valleys not associated with the fault such features generally are absent.

The advance of the Muldrow was not the result of ice being dislodged from surrounding mountains, because the steeper, upper portions of the glacier were unaffected and no extensive recent avalanching was observed anywhere in the basin.

Figure 7 shows the plotted positions of epicenters and the intensity and dates of all recorded earthquakes in this part of the Alaska Range. No direct relationship between these shocks and the various glacier advances is evident, although the earthquake of March 2, 1956, centering 50 km (30 mi) northeast of the Muldrow, or the March 30 shock for which no epicenter was plotted, should be considered as possible triggering mechanisms.

The possibility that earthquakes forming a shock wave within a glacier would result in a catastrophic advance has been proposed by A. E. Harrison (private communication).

No earthquakes have been recorded which show any relationship to the Black Rapids, Susitna, and Yanert advances. Moffit [1942]

stated without elaboration that earthquakes did occur in the vicinity of the Black Rapids in 1936 and 1937. The fact that nearly all the glaciers in the Alaska Range which display erratic flow characteristics are located along the same fault system does suggest a possible connection in triggering such advances, a connection which would bear more detailed investigation.

Dynamic conditions. Most evidence, including published earthquake records, suggests that the advances were not due to any pervasive external cause but were the result of unstable dynamic conditions in the particular glacier systems. The mechanism indicated is that of an ice 'reservoir' forming in the middle portion of each glacier and being filled over a period of years with ice which flows in from tributaries while the stagnant lower terminal portion of the glacier is being reduced by ablation. When certain critical conditions are reached the glacier becomes unstable and a sudden brief movement of the ice takes place. This movement so depletes the reservoir area that when the ice comes to rest virtual stagnation occurs in the lower glacier and the process is repeated.

Acknowledgments. This study was undertaken as a part of IGY Project 4.11 under the sponsorship of the American Geographical Society of New

York. The U. S. Navy, U. S. Geological Survey, Boston Museum of Science, University of Washington, Ohio State University, and the National Park Service are thanked for their cooperation. Dr. Mark F. Meier and Mr. Edward R. LaChapelle rendered valuable assistance.

REFERENCES

- Desio, Ardito, An exceptional glacier advance in the Karakoram-Ladakh region, *J. Geol.*, 2, 383-385, 1954.
- Griffiths, T. M., Glacial geomorphology on the Mt. McKinley massif, Alaska, *Proc. 8th General Assembly, 17th Congr., Intern. Geograph. Union*, Washington, D. C., 331-336, 1952.
- Hance, J. H., The recent advance of Black Rapids Glacier, *J. Geol.*, 45, 775-783, 1937.
- Moffit, F. H., Geology of the Gerstle River District, Alaska, *U. S. Geol. Survey Bull.* 926-B, 146-157, 1942.
- Péwé, T. L., Multiple glaciation in Alaska, *U. S. Geol. Survey, Circ.* 289, 13 pp., 1953. (Abstract), *Bull. Geol. Soc. Am.*, 1908, 1957.
- Russell, I. C., *Glaciers of North America*, Ginn & Company, Boston, 157, (210 pp.), 1899.
- Streiff-Becker, R., Glacier advances apparent and real, *J. Glaciol.*, 3, 151, 1957.
- Tarr, R. S., and L. Martin, *Alaska Glacier Studies*, National Geographic Society, Washington, D. C., 180-197, (498 pp.), 1914.

(Manuscript received May 23, 1960; revised August 12, 1960.)

Modification of the Theory of Leaky Aquifers

MAHDI S. HANTUSH¹

*New Mexico Institute of Mining and Technology
Socorro, New Mexico*

Abstract. The theory of leaky aquifers as currently known involves among other things the assumption that the storage in the semipervious layers is small and may therefore be neglected. Frequently, however, the semipervious beds, although of very low permeabilities, may yield significant amounts of water from storage. The present paper deals with flow systems in which the storage in the semiconfining layers is taken into consideration. The more general solutions thus obtained describe the actual flow system more exactly.

INTRODUCTION

Commonly, a shallow sand is confined above by a semipervious clay or silt that reaches to the ground surface and in which the ground water is replenished continuously by rainfall. In other cases, a semipervious confining layer is over- and/or underlain by other aquifers whose hydraulic conductivities are large. Water thus ponded at the ground surface, or accumulated in the over- and/or underlying aquifers, supplies in part the leakage induced by lowering the hydraulic head in the artesian sand. Under such conditions, the hydraulic head in the strata supplying the leakage may effectively remain uniform.

Strictly speaking, the actual flow in such systems is three-dimensional. However, with certain assumptions whose validity has been verified [Hantush and Jacob, 1955a], the flow can be treated as two-dimensional, augmented or diminished in the direction of the flow by the downward or upward leakage. These assumptions are: (1) The head in the layer supplying the leakage is constant; (2) the permeability contrast in the semipervious layers and in the artesian sand is very great, so that the flow is vertical in the semiconfining beds and horizontal in the artesian sand; and (3) the storage in the semipervious layers is neglected.

Based upon these assumptions, several flow systems involving semiconfined aquifers which may gain or lose water through adjacent semipermeable strata have been analyzed by Jacob

[1946], Hantush and Jacob [1954, 1955b, 1955c], and Hantush [1955, 1956, 1957, 1959]. The results of these analyses have proved successful in practical applications wherever the conditions imposed by the theory approach those met in the field.

In many cases, the artesian sand is confined above and/or below by semipervious elastic clay or silt that yields significant amounts of water from storage. In fact, in certain cases, the water released from storage in these semipermeable layers is much more significant in amount than that released from storage in the shallow semiconfined sands.

In this paper the analyses of problems in which the storage in the semipervious confining layers is taken into consideration are presented. All other assumptions remain the same.

It should be remarked that rigorous solutions can be obtained for the actual nonsteady three-dimensional flow in layered aquifers, as well as solutions for flow systems in which the condition of vertical leakage is removed. These solutions, however, are very difficult to evaluate numerically and are therefore not presented here.

ANALYSIS

Statement of the problem. The problem is to determine the drawdown distribution in the vicinity of a steady well draining an elastic artesian aquifer confined by semipervious elastic strata. The discharge of the well is supplied by the reduction of storage in the aquifer and by leakage from the semipervious layers. The leakage is obtained from the reduction of storage in the semipervious elastic beds or from other bodies of water over- and/or underlying the

¹ On leave from the College of Engineering, University of Baghdad, Iraq.

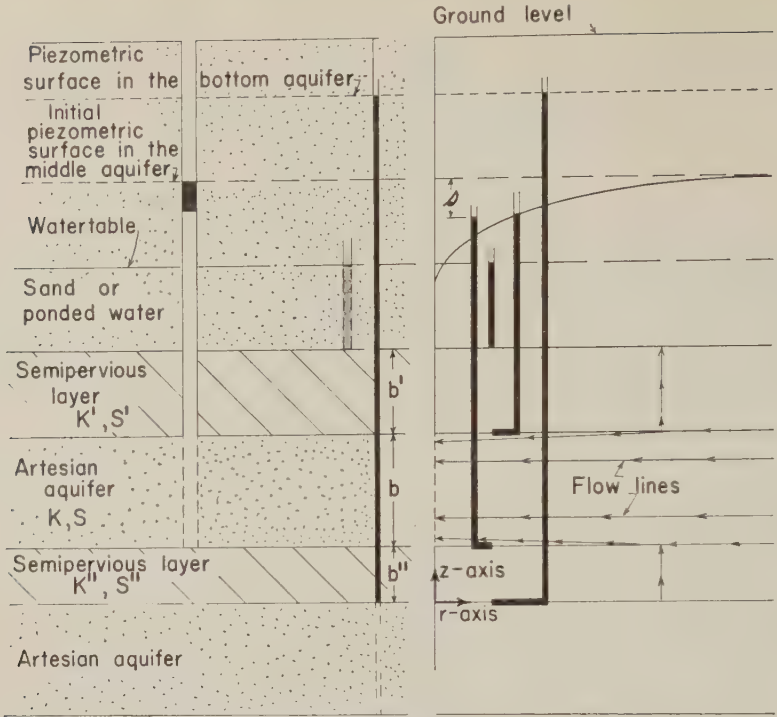


Fig. 1. Diagrammatic representation of a leaky aquifer.

semipervious beds, or from both sources. The hydraulic conductivities in the semiconfining layers are very small compared with that in the main aquifer, so that the flow is vertical through the semiconfining beds and horizontal in the main aquifer; in other words, the completely refracted leakage may be considered to be uniformly distributed throughout the horizontal flow in the main aquifer (Fig. 1).

Notation and definitions. The following is a list of the major symbols and their definitions.

	Dimension		
b, b', b''	Thickness of stratified layers L	$n = T\lambda^2/S$	T^{-1}
$B = \sqrt{Tb'/K'}$	L	Q	Constant well discharge L^3T^{-1}
$\text{erf}(x)$	The error function of (x)	q_L	Rate of leakage added to main aquifer L^3T^{-1}
$\text{erfc}(x)$	The complementary error function, or $[1 - \text{erf}(x)]$	r	Horizontal radial distance, measured from center of the well to any observation point in the field L
h	Hydraulic head (piezometric head) at any time and at any point in the main aquifer L	$s = h_0 - h$	The drawdown of the piezometric surface at any time and at any point in the main aquifer L
		$H(u, \beta)$	
		$= \int_u^\infty \frac{e^{-y}}{y} \text{erfc}(\beta \sqrt{u}/\sqrt{y(y-u)}) dy$	
		K	Hydraulic conductivity of main aquifer LT^{-1}
		K', K''	Vertical hydraulic conductivities of semipervious layers LT^{-1}
		$K_0(x)$	The zero-order modified Bessel function of the second kind —

s_1, s_2

Drawdowns of piezometric surfaces at any time and at any point (r, z) in the semipervious layers L

$$\nu = K/S_s = T/S$$

$$L^2 T^{-1}$$

$$\nu' = K'/S_s' = K'b'/S'$$

$$L^2 T^{-1}$$

$$\nu'' = K''/S_s'' = K''b''/S''$$

$$L^2 T^{-1}$$

$$\left. \begin{aligned} S &= bS_s; \\ S' &= b'S_s'; \\ S'' &= b''S_s'' \end{aligned} \right\}$$

Storage coefficients of the main and of the semipervious layers, respectively —

Specific storage of the main and semipervious layers, respectively. (It is the volume of water a unit volume of the aquifer releases from storage under a unit head decline.)

$$L^{-1}$$

Time at which pumping started

$$T$$

Time since pumping started

$$T$$

Coefficient of transmissivity (transmissibility) of the main aquifer

$$L^2 T^{-1}$$

$$u = r^2/4\nu t$$

Total volume withdrawn during pumping

$$L^3$$

Total volume withdrawn from leakage during pumping

$$L^3$$

$$W(u) = \int_u^\infty \frac{e^{-y}}{y} dy$$

The well function for nonleaky aquifers

$$W(u, v) = \int_u^\infty \frac{dy}{y}$$

$\exp(-y - v^2/4y)$ The well function for leaky aquifers

Vertical coordinate

$$L$$

$$\alpha = r \sqrt{K'/b'T + K''/b''T}$$

$$\beta = (1/4)r\lambda$$

$$\delta_1 = 1 + (S' + S'')/3S$$

$$\delta_2 = 1 + (S' + S'')/S$$

$$\delta_3 = 1 + (S'' + S'/3)/S$$

$$\lambda = \sqrt{\frac{K'/b'}{T} \cdot \frac{S'}{S}} + \sqrt{\frac{K''/b''}{T} \cdot \frac{S''}{S}} \quad L^{-1}$$

Differential equations of motion. The general differential equation of ground-water flow in an elastic aquifer is given by

$$\frac{\partial^2 h_n}{\partial x^2} + \frac{\partial^2 h_n}{\partial y^2} + \frac{\partial^2 h_n}{\partial z^2} = \frac{1}{\nu_n} \frac{\partial h_n}{\partial t} \quad (1)$$

and that in an elastic artesian aquifer which is confined by semipervious elastic layers of relatively low permeabilities is approximated by

$$\frac{\partial^2 h}{\partial x^2} + \frac{\partial^2 h}{\partial y^2} + \frac{\nu_z(b'') - \nu_z(b + b'')}{T} = \frac{1}{\nu} \frac{\partial h}{\partial t} \quad (2)$$

$$\nu_z(x, y, z, t) = -K_n \frac{\partial h_n}{\partial z}$$

where $h(x, y, t)$ and $h_n(x, y, z, t)$ are the hydraulic heads in the main aquifer and in the semipervious layers, respectively, and z_n represents the values of z at the bottom and at the top of the aquifer (see figs. 1 and 2 for the origin of the coordinate system).

If $h_0(x, y, t_0)$ and $h_{on}(x, y, z, t_0)$ represent the initial distribution of the hydraulic heads in the main aquifer and in the semipervious layers, respectively, and if $s(x, y, t)$ and $s_n(x, y, z, t)$ are the respective drawdowns caused by removing water from the main aquifer starting at the instant t_0 , and, if one recalls that h_0 and h_{on} are solutions of (1) and (2), then in terms of the induced drawdowns (1) and (2) become, respectively,

$$\frac{\partial^2 s_n}{\partial x^2} + \frac{\partial^2 s_n}{\partial y^2} + \frac{\partial^2 s_n}{\partial z^2} = \frac{1}{\nu_n} \frac{\partial s_n}{\partial t} \quad (3)$$

$$\frac{\partial^2 s}{\partial x^2} + \frac{\partial^2 s}{\partial y^2} + \frac{\nu_z(b + b'') - \nu_z b''}{T} = \frac{1}{\nu} \frac{\partial s}{\partial t} \quad (4)$$

$$\nu_z(x, y, z, t) = K_n \frac{\partial s_n}{\partial z}$$

where $s = h_0 - h$, $s_n = h_{on} - h_n$, and t is time since the instant t_0 .

Flow systems and boundary-value problems. The flow systems are those of a steady well draining an artesian aquifer over- and underlain by semipervious layers. The semipervious layers are (case 1) under- and overlying two other aquifers in which the hydraulic heads remain uniform; (case 2) under- and overlying two impermeable layers; or (case 3) one layer is overlying an impermeable bed and the other is underlying an aquifer in which the hydraulic head remains uniform.

The flow in these systems, being vertical in the semipervious layers and purely radial in the main aquifer, can be described by the following boundary-value problems.

Case 1.

$$\left. \begin{aligned} \frac{\partial^2 s_1}{\partial z^2} &= \frac{1}{\nu'} \frac{\partial s_1}{\partial t} & (a) \\ s_1(r, z, 0) &= 0 & (b) \\ s_1(r, z', t) &= 0 & (c) \\ s_1(r, z_1, t) &= s(r, t) & (d) \end{aligned} \right\} \begin{array}{l} \text{Upper} \\ \text{semipervious} \\ \text{layer} \end{array} \quad (5)$$

$$\left. \begin{aligned} \frac{\partial^2 s}{\partial r^2} + \frac{1}{r} \frac{\partial s}{\partial r} + \frac{K'}{T} \frac{\partial}{\partial z} s_1(r, z_1, t) & & (a) \\ - \frac{K''}{T} \frac{\partial}{\partial z} s_2(r, b'', t) &= \frac{1}{\nu} \frac{\partial s}{\partial t} & \\ s(r, 0) &= 0 & (b) \\ s(\infty, t) &= 0 & (c) \\ \lim_{r \rightarrow 0} r \frac{\partial}{\partial r} s(r, t) &= -\frac{Q}{2\pi T} & (d) \end{aligned} \right\} \begin{array}{l} \text{Main} \\ \text{aquifer} \end{array} \quad (6)$$

$$\left. \begin{aligned} \frac{\partial^2 s_2}{\partial z^2} &= \frac{1}{\nu''} \frac{\partial s_2}{\partial t} & (a) \\ s_2(r, z, 0) &= 0 & (b) \\ s_2(r, 0, t) &= 0 & (c) \\ s_2(r, b'', t) &= s(r, t) & (d) \end{aligned} \right\} \begin{array}{l} \text{Lower} \\ \text{semipervious} \\ \text{layer} \end{array} \quad (7)$$

Case 2. Same as case 1, the conditions (5c) and (7c) being replaced respectively by

$$\frac{\partial}{\partial z} s_1(r, z', t) = 0 \quad (5c_2)$$

$$\frac{\partial}{\partial z} s_2(r, 0, t) = 0 \quad (7c_2)$$

Case 3. Same as case 1, the condition (7c)

being replaced by

$$\frac{\partial}{\partial z} s_2(r, 0, t) = 0 \quad (7c_3)$$

where $z_1 = b'' + b$, and $z' = b'' + b + b'$.

EQUATIONS OF DRAWDOWN AND RATE OF INDUCED LEAKAGE

The results of solving the above boundary-value problems and those of the special cases derived therefrom are presented below. Readers who wish to follow the details of deriving these solutions are referred to the Appendix.

For the cases represented in Figure 2, the solutions are obtained for the two ranges of the time t as indicated below (see list of symbols for the notation used).

For t less than both $b'S'/10K'$ and $b''S''/10K''$. In this range the solutions for the three cases are the same and are given by

$$s = \frac{Q}{4\pi T} H(u, \beta) \quad (8)$$

$$q_L = Q[1 - e^{u^2} \operatorname{erfc}(\sqrt{nt})] \quad (9)$$

$$V_L = V[1 - 2/\sqrt{n\pi t} + q_L/Qnt] \quad (10)$$

where

$$\beta = (1/4)r\lambda; \quad u = r^2 S/4Tt; \quad n = T\lambda^2/S$$

$$\lambda = \sqrt{\frac{K'/b'S'}{T}} + \sqrt{\frac{K''/b''S''}{T}}$$

and where $H(u, \beta)$ is an infinite integral, a few values of which are given in Table 1.

For large values of time K'' . In this range of time the solutions for the three cases are:

Case 1. In this case, the lower limit of t may be taken as the larger of the two values of $5b'S'/K'$ and $5b''S''/K''$.

$$s = \frac{Q}{4\pi T} W(u\delta_1, \alpha) \quad (11)$$

$$q_L = Q[1 - (1/\delta_1) \exp(-\nu t \alpha^2/r^2 \delta_1)] \quad (12)$$

where

$$\delta_1 = 1 + (S' + S'')/3S,$$

$$\alpha = r\sqrt{\frac{K'/b'}{T} + \frac{K''/b''}{T}}$$

and $W(u\delta_1, \alpha)$ is the well function for leaky

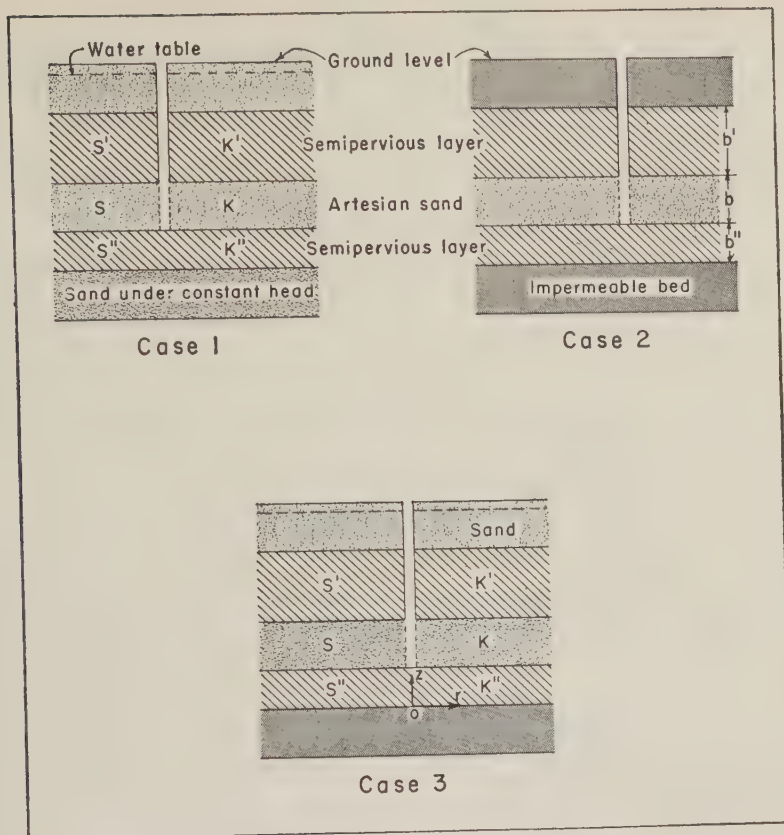


Fig. 2. Schematic representation of three flow systems in a leaky aquifer.

aquifers that was obtained and tabulated by Hantush [1955, 1956]. The expression for V_L can be readily obtained by integration with respect to t from the lower limit of the time range to any time t .

Case 2. For t greater than both $10b's'/K'$ and $10b''s''/K''$, the required expressions are

$$s = \frac{Q}{4\pi T} W(u \delta_2) \quad (13)$$

$q_L = Q(S' + S'')/(S + S' + S'')$ (14)
where $\delta_2 = 1 + (S' + S'')/S$, and $W(u\delta_2)$ is the exponential integral, or what in the field of hydrology is commonly known as the well function.

Case 3. In this case, the larger of the two values of $5b'S'/K'$ and $10b''S''/K''$ can be taken as the lower limit of the time range, in which case the required expressions are

$$s = \frac{Q}{4\pi T} W\left(u \delta_3, r\sqrt{\frac{K'}{b'}}\right) \quad (15)$$

$$q_L = Q[1 - (1/\delta_3) \exp(-\nu K't/b'T \delta_3)] \quad (16)$$

where $\delta_3 = 1 + (S'' + S'/3)/S$.

The value V_L can be obtained by simple integration with respect to t between the lower limit of the time range and any value of t .

An expression for the drawdown in the intermediate range of t is not given for any of the three cases listed above. Values of $s/Q/4\pi T$ are plotted against values of u or t on semilogarithmic paper, with u or t on the logarithmic scale. A smooth curve joining the two branches of the curve thus obtained is then constructed by inspection; from this, values of $s/Q/4\pi T$ in the intermediate range of time can be estimated. The procedure is employed when computing for q_L and V_L in the intermediate range of time.

TABLES OF FUNCTIONS

To make use of the above solutions, tabular values of functions $W(x)$ and $W(x, y)$, and $H(u, \beta)$ should be available. The functions $W(x)$ and $W(x, y)$ have already been tabulated

for a wide range of the parameters involved [Wenzel, 1942; Wisler and Brater, 1951; Hantush, 1955, 1956]. The function $H(u, \beta)$ has not been available previously in tabular form. Sufficient tabulation for all practical purposes, obtained through the use of an IBM computer is shown in Table 1.²

The function $H(u, \beta)$ can be approximated by

$$H(u, \beta) \approx W(u)$$

$$- \frac{4\beta}{\sqrt{\pi u}} (0.2577 + 0.6931 \exp(-u/2)) \quad (17)$$

for $u \geq 10^4 \beta^2$, and by

$$H(u, \beta) \approx (1/2) \ln 0.044/\beta^2 u \quad (18)$$

for $u \leq$ than both $10^5/\beta^2$ and $10^{-4}\beta^2$

SOLUTIONS FOR SPECIAL CASES

From the above general solutions, solutions for special flow systems can be obtained. These are:

Nonleaky aquifer. If K' and K'' are made equal to zero in the solutions of any one of the three above cases, the resulting flow system is that of a nonleaky artesian aquifer. Thus the limit of (8), as K' and K'' go to zero, will give the drawdown distribution; this, as should be expected, is the Theis formula:

$$s = \frac{Q}{4\pi T} W(u) \quad (19)$$

Leaky aquifer without storage in the semiconfining bed. If K'' , S' , and S'' are taken as zero in the flow system of case 1 or case 3, the resulting flow system is that of an artesian aquifer resting on an impermeable bed and semiconfined from above by a semipervious layer in which the storage is negligible. Thus the limit of (11) or

(15), as K'' , S' , and S'' go to zero, will give the drawdown formula, which, as should be expected, is that of Hantush and Jacob [1955b]:

$$s = \frac{Q}{4\pi T} W(u, r/B) \quad (20)$$

where $1/B^2 = (K'/b')/T$.

Other special cases. Formulas for other special cases can also be found by giving special values for the parameters involved (see Figs. 4, 5, and 6).

SUMMARY AND DISCUSSION

A more general theory than has previously been known for the flow in leaky aquifers has been developed. An additional parameter (storage in the semipervious layers) has been introduced. The effect of storage in the semipervious layers on the induced drawdown is depicted in Figures 3 to 8. If the ratio of the storage coefficients of the semipervious layer to that of the main aquifer is small ($S'/S \leq .01$), the effect of storage in the semipervious layers on the drawdown is very small in flow systems such as those shown in Figures 5 and 6. In that case, the limiting drawdown formulas, namely those of Hantush and Jacob [1955b] and Theis [1935], will describe fairly accurately the flow in the respective flow systems. For relatively larger values of S'/S , the drawdown deviates considerably from that given by the limiting formulas mentioned above.

Observational drawdown trends such as those shown in Figures 3 and 6 have previously been attributed to variation of formation coefficients during the early period of flow. Although this may be true in part, it may as well be due to the effect of storage in over- and/or underlying semipervious strata, as has been demonstrated by the present theory. The same general trend of time-drawdown variation may be caused by the flow toward a well which partially penetrates the water-bearing strata. Whereas, in the absence of elastic semipervious water-saturated strata, the first explanation is logical, the second explanation is more likely to be true if these strata are present, provided that the pumped well completely penetrates the aquifer.

Semilogarithmic time-drawdown curves of a flow system such as that shown in Figure 5 have more or less the same general trend as the curves

²For a more detailed table of values of the function

$$H(u, \beta) = \int_u^\infty \frac{e^{-y}}{y} \operatorname{erfc} \frac{\beta \sqrt{y}}{\sqrt{y(y-u)}} dy$$

Document 6427 may be ordered from Chief, Photoduplication Service, Auxiliary Publication Project, Library of Congress, Washington 25, D. C. Remit \$2.25 for microfilm (35 mm) or \$5.00 for photocopies. Advance payment is required. Make checks payable to Chief, Photoduplication Service, Library of Congress.

Table I Values of the function $H(u, \beta) = \int_0^{\infty} \frac{e^{-y}}{y} \operatorname{erfc} \frac{\beta \sqrt{y}}{\sqrt{y(y-u)}} dy$

β	(-3)					(-2)					(-1)					(0)					(1)					(2)				
	1	2	3	4	5	1	2	3	4	5	1	2	3	4	5	1	2	3	4	5	1	2	3	4	5					
1 (-6)	11.9842	11.4237	10.5908	9.9259	9.2469	8.3395	7.6497	6.9590	6.0463	5.3575	4.6721	3.7756	3.1110	2.4671	1.6710	1.1361	0.6879	0.2498	0.1688											
2 (-6)	11.5355	10.7811	10.0216	9.3567	8.6946	7.7804	7.0991	6.4102	5.7012	5.0141	4.3312	3.4412	2.7857	2.1568	1.3944	0.8995	0.5045	0.3013	0.1830											
3 (-6)	11.2593	10.7764	10.0006	9.3561	8.6875	7.7864	7.3024	6.6100	5.4996	4.8136	4.1327	3.2474	2.5984	1.9801	1.2409	0.7725	0.4143	0.1620												
4 (-6)	11.0568	10.5980	9.8419	9.2047	8.5399	7.6412	6.9547	6.2663	5.3567	4.6716	3.9922	3.1109	2.4671	1.8571	1.1361	0.6879	0.3516	0.63(-4)												
5 (-6)	10.8958	10.4566	9.7174	9.0666	8.4251	7.5284	6.8427	6.1543	5.2459	4.5617	3.8836	3.0055	2.3661	1.7593	1.0574	0.6256	0.3091	787(-4)												
6 (-6)	10.7618	10.3389	9.6145	8.9894	8.3310	7.4362	6.7512	6.0637	5.1555	4.4719	3.7951	2.9199	2.2844	1.6877	0.9948	0.5770	0.2768	662(-4)												
7 (-6)	10.6466	10.2379	9.5267	8.9069	8.2512	7.3581	6.6737	5.9867	5.0790	4.3962	3.7204	2.8478	2.2158	1.6246	0.9432	0.5375	0.2511	568(-4)												
8 (-6)	10.5455	10.1493	9.4400	8.8200	8.1619	7.2704	6.6066	5.9200	5.0129	4.3306	3.6558	2.7875	2.1568	1.5706	0.8995	0.5045	0.3020	494(-4)												
9 (-6)	10.4573	10.0702	9.3618	8.7414	8.1206	7.2306	6.5474	5.8611	4.9545	4.2728	3.5989	2.7309	2.1050	1.5234	0.8617	0.4763	0.2127	436(-4)												
1 (-5)	10.3739	9.9987	9.3203	8.7142	8.0657	7.1771	6.4944	5.8085	4.9024	4.2212	3.5481	2.6822	2.0590	1.4816	0.8285	0.4519	0.1978	388(-4)												
2 (-5)	9.8197	9.5097	8.9045	8.3135	7.7010	6.8128	6.1453	5.4623	4.5598	3.8827	3.2162	2.3660	1.7632	1.2170	0.6203	0.3091	0.1166	346(-4)												
3 (-5)	9.4815	9.2084	8.6504	8.1015	7.4884	6.6159	5.9406	5.2597	4.3598	3.6858	3.0241	2.1850	1.5905	1.0716	0.5256	0.2402	818(-4)													
4 (-5)	9.2358	8.9878	8.4646	7.9346	7.3250	6.4677	5.7951	5.1660	4.2165	3.5468	2.8889	2.0588	1.4815	0.9730	0.4518	0.1878	623(-4)													
5 (-5)	9.0422	8.8128	8.3171	7.8031	7.2072	6.3523	5.6821	5.0045	4.1090	3.4394	2.7848	1.9622	1.3943	0.8994	0.4024	0.1685	494(-4)													
6 (-5)	8.8822	8.6674	8.1943	7.6941	7.1068	6.2576	5.5896	4.9344	4.0196	3.3519	2.7002	1.8841	1.3244	0.8412	0.3645	0.1468	406(-4)													
7 (-5)	8.7457	8.5428	8.0888	7.6007	7.0212	6.1773	5.5113	4.8364	3.9442	3.2781	2.6259	1.8199	1.2684	0.7934	0.3341	0.1300	342(-4)													
8 (-5)	8.6266	8.4336	7.9962	7.5100	6.9466	6.1076	5.4434	4.7697	3.8789	3.2163	2.5677	1.7629	1.2169	0.7330	0.3090	0.1166	292(-4)													
9 (-5)	8.5209	8.3364	7.9134	7.4361	6.8804	6.0459	5.3834	4.7108	3.8214	3.1583	2.5138	1.7139	1.1739	0.7182	0.2875	0.1056	253(-4)													
1 (-4)	8.4258	8.2487	7.8386	7.3603	6.8208	5.9906	5.3297	4.6581	3.7700	3.1082	2.4658	1.6704	1.1359	0.6878	0.2698	963(-4)														
2 (-4)	7.7901	7.5563	7.3276	6.9321	6.4190	5.6226	4.9747	4.3315	3.4334	2.7819	2.1397	1.3977	0.8992	0.5044	0.1688	494(-4)														
3 (-4)	7.4110	7.2885	7.0135	6.5663	6.0500	5.4035	4.7655	4.1286	3.2379	2.5937	1.9778	1.2401	0.7721	0.4111	0.1229	315(-4)														
4 (-4)	7.1193	7.0401	6.7840	6.4561	5.9971	5.2459	4.6161	3.9645	3.0999	2.4617	1.8285	1.1352	0.6875	0.3314	0.1631	260(-4)														
5 (-4)	6.9273	6.8775	6.6254	6.2934	5.8561	5.1223	4.4996	3.8527	2.9333	2.3601	1.7604	1.0540	0.6252	0.3089	0.1461	205(-4)														
6 (-4)	6.7533	6.6705	6.4517	6.1596	5.7369	5.0023	4.4040	3.7612	2.9005	2.2778	1.6846	0.9937	0.5765	0.2766	0.161(-4)															
7 (-4)	6.6050	6.5284	6.3047	6.0447	5.6043	4.8313	4.2028	3.6818	2.8314	2.2087	1.6212	0.9420	0.5370	0.2416	0.147(-4)															
8 (-4)	6.4774	6.4048	6.2100	5.9439	5.5501	4.8573	4.2523	3.6167	2.7702	2.1492	1.5670	0.8962	0.5040	0.2300	494(-4)															
9 (-4)	6.3640	6.2952	6.1097	5.8519	5.4513	4.7598	4.1598	3.5575	2.7146	2.0971	1.5196	0.8603	0.4758	0.2125	436(-4)															
1 (-3)	6.2624	6.1969	6.0193	5.7727	5.4001	4.7290	4.1337	3.5045	2.6550	2.0506	1.4776	0.8271	0.4513	0.1976	388(-4)															
2 (-3)	5.9033	5.8411	5.6515	5.4203	5.2203	4.9139	4.5184	3.7598	2.9416	2.1736	1.5825	0.9652	0.4812	0.2384	0.1084	166(-4)														
3 (-3)	5.1948	5.1500	5.0465	4.8837	4.6949	4.4683	4.1643	3.4904	2.5832	1.9599	1.4272	0.8752	0.4561	0.2394	0.11(-4)															
4 (-3)	4.9135	4.8788	4.7819	4.6396	4.4632	4.3962	3.8859	3.2750	2.0253	1.4656	0.9658	0.4496	0.1970	0.10(-4)																
5 (-3)	4.6951	4.6649	4.5786	4.4474	4.2231	3.7415	3.2483	2.6891	1.9250	1.3767	0.8915	0.4001	0.1677	493(-4)																
6 (-3)	4.5165	4.4990	4.4099	4.2888	4.0794	3.6214	3.1436	2.5957	1.8437	1.3054	0.8327	0.3620	0.1460	404(-4)																
7 (-3)	4.3655	4.3400	4.2666	4.1536	3.9544	3.5185	3.0542	2.5165	1.7754	1.2460	0.7843	0.3315	0.1292	340(-4)																
8 (-3)	4.2347	4.2109	4.1421	4.0357	3.8488	3.4282	2.9762	2.4478	1.7166	1.1953	0.7435	0.3064	0.1158	290(-4)																
9 (-3)	4.1194	4.0969	4.0320	3.9313	3.7531	3.3478	2.9068	2.3870	1.6651	1.1512	0.7083	0.2852	0.1047	252(-4)																
1 (-2)	4.0163	3.9950	3.9334	3.8373	3.6669	3.2752	2.8443	2.3325	1.6193	1.1122	0.6775	0.2670	0.1163	955(-4)																
2 (-2)	3.3937	3.3250	3.2818	3.1333	2.9889	2.7829	2.4227	1.9714	1.3239	0.9677	0.4914	0.1653	0.087(-4)																	
3 (-2)	2.9872	2.9354	2.9007	2.7462	2.6052	2.4884	2.1680	1.7579	1.1570	0.7353	0.3965	0.107(-4)																		
4 (-2)	2.6711	2.6611	2.6316	2.5842	2.4955	2.2691	1.9841	1.6056	1.0416	0.6467	0.3357	0.131(-4)																		
5 (-2)	2.4590	2.4502	2.4243	2.3826	2.3005	2.1007	1.8401	1.4872	0.9540	0.5812	0.2923	0.155(-4)																		
6 (-2)	2.2874	2.2795	2.2563	2.2188	2.1478	1.9265	1.7217	1.3908	0.8818	0.5298	0.2593	0.140(-4)																		
7 (-2)	2.1436	2.1365	2.1154	2.0812	2.0164	1.8458	1.6213	1.3088	0.8255	0.4880	0.2332	0.131(-4)																		
8 (-2)	2.0203	2.0138	1.9944	1.9630	1.9031	1.7448	1.5343	1.2381	0.7758	0.4530	0.2119	0.124(-4)																		
9 (-2)	1.9126	1.9066	1.8886	1.8595	1.8039	1.6559	1.4577	1.1760	0.7327	0.4230	0.1941	0.106(-4)																		
1 (-1)	1.8112	1.8116	1.7949	1.7677	1.7157	1.5768	1.3893	1.1207	0.6947	0.3970	0.1789	0.091(-4)																		
2 (-1)	1.2193	1.2159	1.2059	1.1895	1.1579	1.0714	0.9497	0.7665	0.4603	0.2452	0.1219	0.059(-4)																		
3 (-1)	0.9033	0.9010	0.8940	0.8825	0.8603	0.7986	0.7103	0.5739	0.3390	0.1729	0.089(-4)																			
4 (-1)	0.7006	0.6999	0.6936	0.6850	0.6663	0.6218	0.5543	0.4482	0.2619	0.1296	0.061(-4)																			
5 (-1)	0.5584	0.5570	0.5510	0.5463	0.5333	0.4969	0.4436	0.3591	0.2083	0.1006	0.026(-4)																			
6 (-1)	0.4533	0.4522	0.4490	0.4437	0.4333	0.4041	0.3613	0.2927	0.1688	0.079(-4)																				
7 (-1)	0.3729	0.3720	0.3694	0.3651	0.3567	0.3330	0.2980	0.2415	0.1386	0.04(-4)																				
8 (-1)	0.3099	0.3092	0.3070	0.3035	0.2967	0.2770	0.2481	0.2012	0.1151	0.029(-4)																				

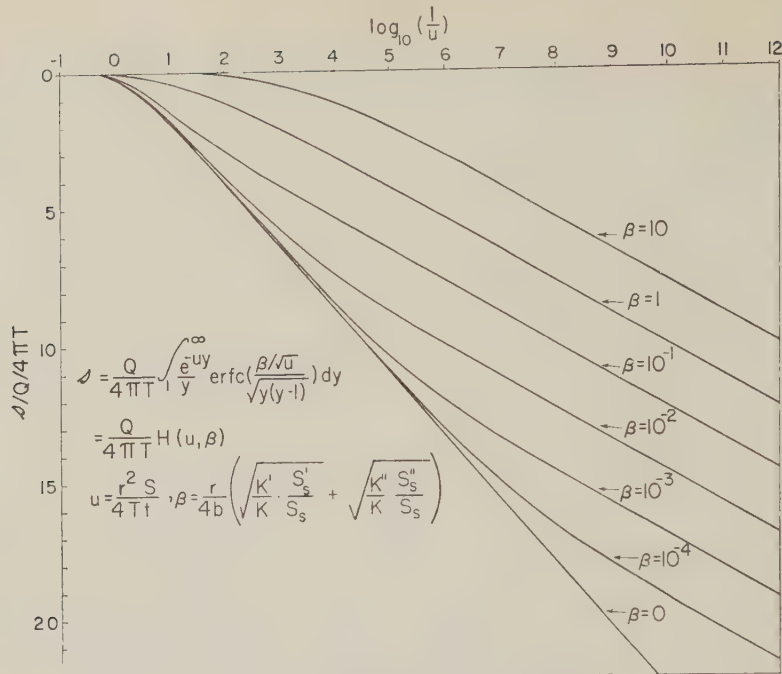


Fig. 3. Type curves of the function $H(u,\beta)$.

artesian aquifer over- and/or underlying thick elastic semipervious layers.

APPENDIX

Integral transforms. In solving the boundary-value problems presented in this paper, the theory of integral transforms is followed. The transforms used are those of Hankel and Laplace.

Hankel transform of order zero. The Hankel transform of order zero, $H[f(r)]$ or $F(\alpha)$, of a function $f(r)$ is defined as

$$H[f(r)] = F(\alpha) = \int_0^\infty r J_0(\alpha r) f(r) \, dr \tag{21}$$

and its inversion formula [Watson, 1944] is

$$H^{-1}[F(\alpha)] = f(r) = \int_0^\infty \alpha J_0(\alpha r) F(\alpha) \, d\alpha \tag{22}$$

Integration of (21) by parts twice yields

$$H\left[\frac{1}{r} \frac{d}{dr} \left(r \frac{df}{dr}\right)\right] = -\alpha^2 F(\alpha) + \left[r J_0(\alpha r) \frac{df}{dr} + \alpha r J_1(\alpha r) f(r)\right]_{r=0}^{r=\infty} \tag{23}$$

Laplace transform. The Laplace transform, $L[f(t)]$ or $\bar{f}(p)$, of a function $f(t)$ is defined as

$$L[f(t)] = \bar{f}(p) = \int_0^\infty e^{-pt} f(t) \, dt \tag{24}$$

Integration of (24) by parts yields

$$L\left[\frac{d}{dt} f(t)\right] = p\bar{f}(p) - f(0) \tag{25}$$

The inversion formula of the Laplace transform is not used in the present development and is therefore not given here. Instead, pairs of transforms which are needed are given below. Extensive tables of Laplace, Hankel, and other integral transforms are found in the literature [Bateman, 1954; Churchill, 1944; Campbell and Foster, 1957].

The following is a list of relations that are referred to in the development of the solutions presented in this paper:

$$L^{-1}\left[\frac{A}{p}\right] = A \tag{26}$$

$$L^{-1}[e^{-bp}\bar{f}(p)] = \begin{cases} 0 & 0 < t < b \\ f(t - b) & t > b \end{cases} \tag{27}$$

$$L^{-1} \frac{1}{p(b + \sqrt{p})} = \frac{1}{b} [1 - e^{bt} \operatorname{erfc}(b\sqrt{t})] \tag{28}$$

$$L^{-1}\left[\frac{e^{-k\sqrt{p}}}{p}\right] = \operatorname{erfc}(k/2\sqrt{t}) \tag{29}$$

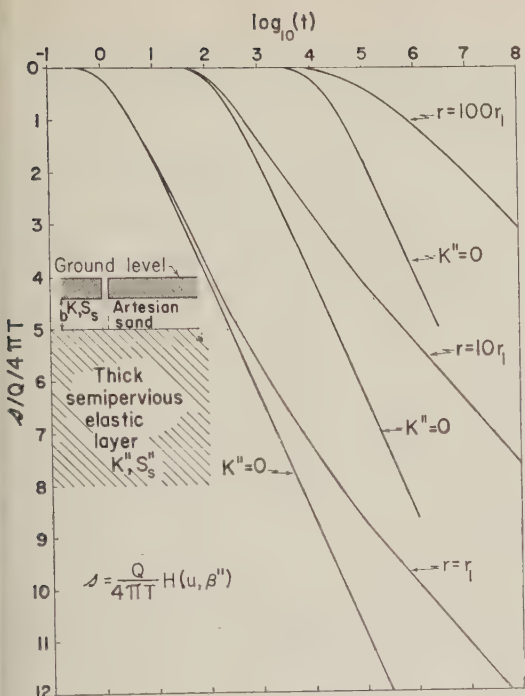


Fig. 4. Time-drawdown variation due to a steady well draining an aquifer overlying an infinitely thick semipervious layer.

$$L^{-1} \left[\frac{ap + b}{p(p + c)} \right] = \frac{b}{c} + \frac{ac - b}{c} e^{-ct} \quad (30)$$

$$H^{-1} \left[\frac{1}{\alpha^2 + k^2} \right] = K_0(kr) \quad (31)$$

$$2K_0(x) = \int_0^\infty \frac{dy}{y} \exp(-y - x^2/4y) \quad (32)$$

$$\int_0^\infty x K_0(x) dx = 1 \quad (32a)$$

Solution of the boundary-value problem of case 1. The boundary-value problem representing the flow system of case 1 (Fig. 1) is given by (5), (6), and (7).

Let $\bar{s}(r, p)$, $\bar{s}_1(r, z, p)$, and $\bar{s}_2(r, z, p)$ be the Laplace transforms, with respect to t , of $s(r, t)$, $s_1(r, z, t)$, and $s_2(r, z, t)$, respectively. Also, let $F(\alpha, p)$, $F_1(\alpha, z, p)$, and $F_2(\alpha, z, p)$ be the Hankel transforms with respect to r of $\bar{s}(r, p)$, $\bar{s}_1(r, z, p)$, and $\bar{s}_2(r, z, p)$, respectively.

If we first apply the Laplace transform to (5), (6), and (7), using conditions (25), (26), (5b), (6b), and (7b); and then apply the Hankel transform to the resulting equations,

using (23) with the Laplace transforms of (6c) and (6d), we can finally double transforms (5), (6), and (7), respectively, to the following:

$$\left. \begin{aligned} \frac{\partial^2}{\partial z^2} F_1(\alpha, z, p) &= \frac{p}{\nu} F_1(\alpha, z, p) \quad (a) \\ F_1(\alpha, z', p) &= 0 \quad (b) \\ F_1(\alpha, z_1, p) &= F(\alpha, p) \quad (c) \end{aligned} \right\} \quad (33)$$

$$\begin{aligned} -\alpha^2 F(\alpha, p) + Q/2\pi T p \\ + \frac{K'}{T} \frac{\partial}{\partial z} F_1(\alpha, z_1, p) \\ + \frac{K''}{T} \frac{\partial}{\partial z} F_2(\alpha, b'', p) = \frac{p}{\nu} F(\alpha, p) \end{aligned} \quad (34)$$

$$\left. \begin{aligned} \frac{\partial^2}{\partial z^2} F_2(\alpha, z, p) &= \frac{p}{\nu''} F_2(\alpha, z, p) \quad (a) \\ F_2(\alpha, 0, p) &= 0 \quad (b) \\ F_2(\alpha, b'', p) &= F(\alpha, p) \quad (c) \end{aligned} \right\} \quad (35)$$

The solutions of (33) and (35) are readily obtained:

$$F_1 = F \cdot \frac{\sinh(z' - z) \sqrt{p/\nu'}}{\sinh b' \sqrt{p/\nu'}} \quad (36)$$

$$F_2 = F \cdot \frac{\sinh z \sqrt{p/\nu''}}{\sinh b'' \sqrt{p/\nu''}} \quad (36)$$

from which

$$\begin{aligned} \frac{\partial}{\partial z} F_1(\alpha, z_1, p) \\ = -F \sqrt{p/\nu'} \coth b' \sqrt{p/\nu'} \end{aligned} \quad (37)$$

$$\begin{aligned} \frac{\partial}{\partial z} F_2(\alpha, b'', p) \\ = -F \sqrt{p/\nu''} \coth b'' \sqrt{p/\nu''} \end{aligned} \quad (38)$$

Substituting (37) and (38) into (34) and solving for F yields

$$\begin{aligned} F = \frac{Q}{2\pi T} / p \left[\alpha^2 + \frac{p}{\nu} \right. \\ + \frac{K'}{T} \sqrt{\frac{p}{\nu'}} \coth b' \sqrt{\frac{p}{\nu'}} \\ + \left. \frac{K''}{T} \sqrt{\frac{p}{\nu''}} \coth b'' \sqrt{\frac{p}{\nu''}} \right] \end{aligned} \quad (39)$$

Using (31) to obtain the inverse Hankel

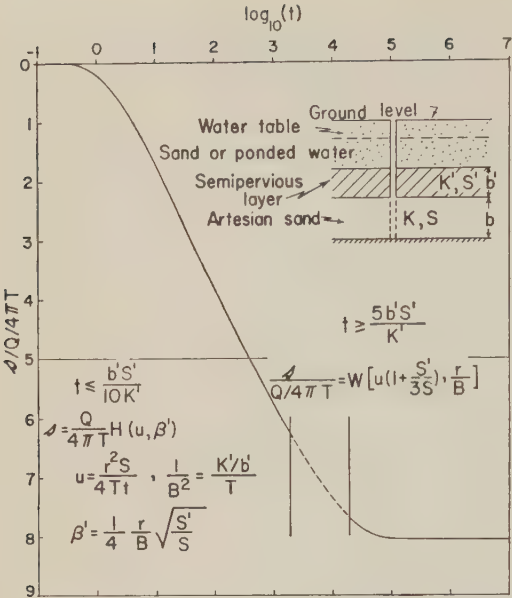


Fig. 5. Time-drawdown variation due to a steady well in the flow system shown in the figure.

transform of (39) and then making use of (32) yields

$$\bar{s}(r, p) = \frac{Q}{2\pi T p} K_0(\gamma r) = \frac{Q}{4\pi T p} \int_0^\infty \frac{dy}{y} \exp[-y - (\gamma r)^2/4y] \quad (40)$$

where

$$\gamma = \left[\frac{p}{\nu} + \frac{K'}{T} \sqrt{\frac{p}{\nu'}} \coth b' \sqrt{\frac{p}{\nu'}} + \frac{K''}{T} \sqrt{\frac{p}{\nu''}} \coth b'' \sqrt{\frac{p}{\nu''}} \right]^{1/2} \quad (41)$$

An exact solution that is the inverse Laplace transform of (40) can be obtained. The solution, however, is complicated and is difficult to evaluate numerically. Instead, approximate solutions, one for sufficiently short periods of time and the other for sufficiently long periods, will be obtained. These two asymptotic solutions will be used to interpolate graphically for the intermediate range of time. The derivation of these asymptotic solutions follows.

Solution for short time periods. The parameters (t and p) in the Laplace transformation are inversely related. Thus, as t becomes small, p becomes large. The solution for short time

periods corresponds to that obtained from (40) if p becomes large. As p increases, the arguments of the hyperbolic cotangents in (41) approach unity. Thus, for $b''p/\nu'' \geq 10$ (of the order $b''/\nu'' \geq 10t$) and $b''p/\nu'' \geq 10$ (of the order $b''/\nu'' \geq 10t$), the hyperbolic cotangents may be replaced by unity without appreciably changing the value of (40). Making this approximation, (40) can be written as

$$\bar{s}(r, p) = \frac{Q}{4\pi T} \int_0^\infty \frac{e^{-y}}{y} \bar{g}(p) dy \quad (42)$$

where

$$\bar{g}(p) = \exp\left(-\frac{r^2 p}{4\nu y}\right) \frac{\exp\left(-\frac{r^2 c^2}{4y} \sqrt{p}\right)}{p} \quad (43)$$

and

$$c^2 = (K'/\sqrt{\nu'} + K''/\sqrt{\nu''})/T$$

The required solution is given by the inversion of (42), which is

$$s(r, t) = \frac{Q}{4\pi T} \int_0^\infty \frac{e^{-y}}{y} L^{-1}[\bar{g}(p)] dy \quad (44)$$

Through the use of (29) and (27), the inverse Laplace transform of $\bar{g}(p)$ is

$$L^{-1}[\bar{g}(p)] = 0 \quad 0 < t < r^2/4\nu y \\ = \operatorname{erfc}\left(\frac{r^2 c^2/4y}{2\sqrt{t - r^2/4\nu y}}\right) \quad t > r^2/4\nu y \quad (45)$$

Finally, with the substitution of (45) into

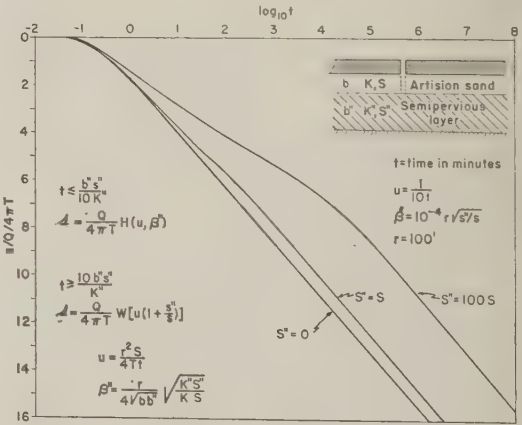


Fig. 6. Time-drawdown variation due to a steady well in the flow system shown in the figure, for different values of specific storage.

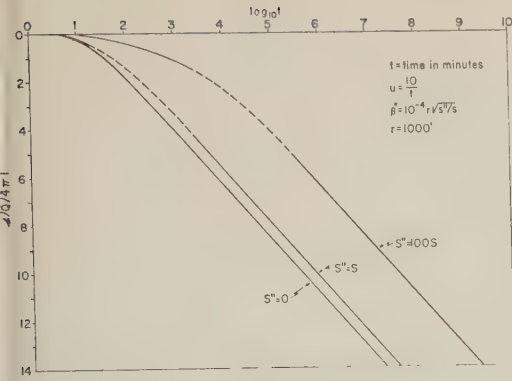


Fig. 7. Time-drawdown variation due to a steady well in the flow system of Figure 6, at a more distant observation well.

(44) and with mathematical reduction, the solution is

$$s = \frac{Q}{4\pi T} \int_u^\infty \frac{e^{-y}}{y} \operatorname{erfc} \left(\frac{\beta \sqrt{u}}{\sqrt{y(y-u)}} \right) dy \quad (46)$$

$$= \frac{Q}{4\pi T} H(u, \beta) \quad (46a)$$

which is valid in the range where the value of t is less than the smaller of $b^2/10v'$ and $b'^2/10v''$. The values of β and u are as defined previously (see list of symbols).

Solution for long times. For large values of t (small values of p), the terms containing the hyperbolic cotangents may be replaced by their approximate values through the relation $x \coth x \approx 1 + x^2/3$, whenever $x^2 < 0.20$. Thus, for $b^2 p/v' < 0.2$ (of the order $b^2/v' < 0.2t$) and $b'^2 p/v'' < 0.2$ (of the order $b'^2/v'' < 0.2t$), (40) may be approximated by

$$\bar{s}(r, p) = \frac{Q}{4\pi T} \int_0^\infty \frac{\bar{g}_1(p)}{y} \cdot \exp[-y - \alpha^2/4y] dy \quad (47)$$

where

$$\bar{g}_1(p) = \frac{1}{p} \exp \left(-\frac{r^2 \delta_1}{4vy} p \right) \quad (48)$$

and where α and δ_1 are as defined previously (see list of symbols).

By a process similar to that used in obtaining (46) from (42), equation (47) may be reduced to

$$s = \frac{Q}{4\pi T} \int_{u, \delta_1}^\infty \frac{dy}{y} \exp[-y - \alpha^2/4y] \quad (49)$$

$$= \frac{Q}{4\pi T} W(u \delta_1, \alpha) \quad (49a)$$

which is valid in the range where the value of t is greater than the larger of $5b^2/v'$ and $5b'^2/v''$.

Rate of induced leakage. The percentage of well discharge that is derived from leakage is obtained as follows:

Substituting (39) into (37) and (38) and then using (31) to find the inverse Hankel transform of the resulting expressions yields

$$\frac{\partial}{\partial z} \bar{s}_1(r, z_1, p) = -\frac{Q}{2\pi T} \frac{\coth b' \sqrt{p/v'}}{\sqrt{v' p}} K_0(\gamma r) \quad (50)$$

$$\frac{\partial}{\partial z} \bar{s}_2(r, b'', p) = \frac{Q}{2\pi T} \frac{\coth b'' \sqrt{p/v''}}{\sqrt{v'' p}} K_0(\gamma r) \quad (51)$$

The Laplace transform of the rate of leakage q_L is given by

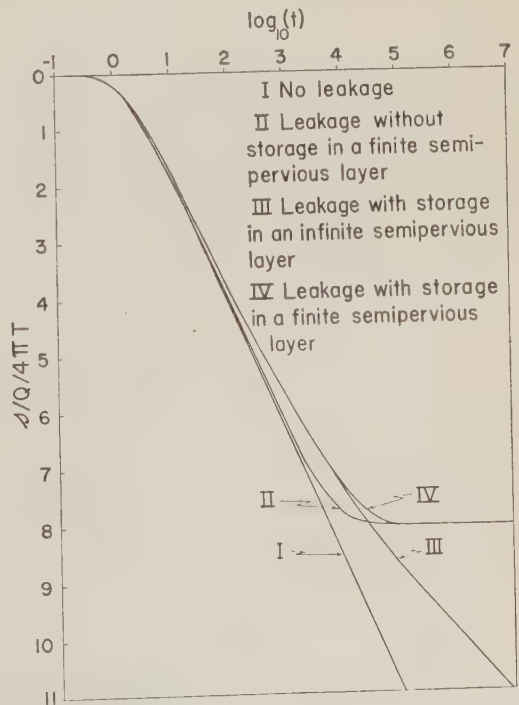


Fig. 8. Comparison of time-drawdown variation in a leaky aquifer with and without storage in the semipervious layers.

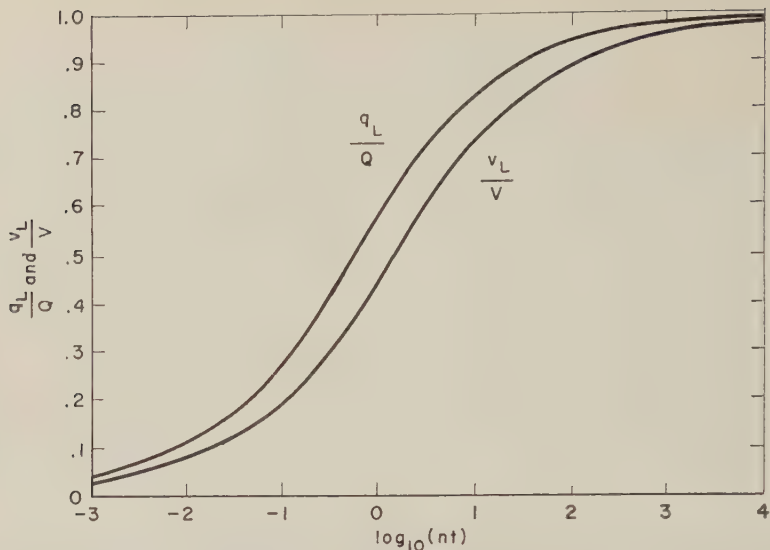


Fig. 9. Variation (with time) of percentage of well discharge derived from storage in the semipervious layers. ($n = (\sqrt{K'S_s'} + \sqrt{K''S_s''})^2/S^2$)

$$\bar{q}_L(p) = \frac{Q}{2\pi T} \int_0^\infty 2\pi r \left[-K' \frac{\partial}{\partial z} \bar{s}_1(r, z, p) + K'' \frac{\partial}{\partial z} \bar{s}_2(r, b'', p) \right] dr \quad (52)$$

Rate of leakage during short time periods. For $b'^2/v' \geq 10t$ and $b''^2/v'' \geq 10t$, the hyperbolic cotangents in (50) and (51) can, as discussed previously, be replaced by unity. With this approximation, substituting (50) and (51) into (52), performing the integration with respect to r through the use of (32a), and then obtaining the inverse Laplace transform by means of (28), results in

$$q_L = Q[1 - e^{nt} \operatorname{erfc}(\sqrt{nt})] \quad (53)$$

where n is as defined previously (see list of symbols).

The total volume of leakage during a continuous operation of the well within the range of time indicated is obtained by integrating (53) with respect to t from 0 to t . The result is

$$V_L = V \left[1 - \frac{2}{\sqrt{\pi nt}} + \frac{1}{nt} (1 - e^{nt} \operatorname{erfc}(\sqrt{nt})) \right] \quad (54)$$

where $V = Qt$ is the total volume of water with-

drawn during a period t of continuous well operation within the range of time specified above.

Rate of leakage during long time periods. For $b'^2/v' \leq 0.2t$ and $b''^2/v'' \leq 0.2t$, the hyperbolic cotangents in (50) and (51) may, as has been discussed above, be replaced by their approximate values, using the relation $x \coth x \approx 1 + x^2/3$. If the process leading to (53) is repeated and (30) is used instead of (28), the final result is

$$q_L = Q[1 - (1/\delta_1) \exp(-vt\alpha^2/r^2 \delta_1)] \quad (55)$$

where the symbols are as previously given.

The solutions to case 2 and case 3 that are given in the text are developed in a process similar to that used above. In this process, the approximations $\tanh x \approx x$ and $\tanh x \approx 1$ are used for $x^2 < 0.10$ and $x^2 > 10$, respectively.

REFERENCES

Bateman, H., *Tables of Integral Transforms*, McGraw-Hill Book Co., New York, 1954.
Campbell, A., and R. M. Foster, *Fourier Integrals for Practical Applications*, D. Van Nostrand Co., New York, 1957.
Churchill, R. V., *Modern Operational Mathematics in Engineering*, McGraw-Hill Book Co., New York, 1944.
Hantush, M. S., *Preliminary Quantitative Study of the Roswell Ground-Water Reservoir*, New Mexico Institute of Mining and Technology, 1955.

- Hantush, M. S., Analysis of data from pumping tests in leaky aquifers, *Trans. Am. Geophys. Union*, 37, 702-714, 1956.
- Hantush, M. S., Nonsteady flow to a well partially penetrating an infinite leaky aquifer, *Proc. Iraqi Sci. Soc.*, 1, 10-19, 1957.
- Hantush, M. S., Nonsteady flow to flowing wells in leaky aquifers, *J. Geophys. Research*, 64, 1043-1052, 1959.
- Hantush, M. S., and C. E. Jacob, Plane potential flow of ground water with linear leakage, *Trans. Am. Geophys. Union*, 35, 917-936, 1954.
- Hantush, M. S., and C. E. Jacob, Steady three-dimensional flow to a well in a two-layered aquifer, *Trans. Am. Geophys. Union*, 36, 286-292, 1955a.
- Hantush, M. S., and C. E. Jacob, Nonsteady radial flow in an infinite leaky aquifer, *Trans. Am. Geophys. Union*, 36, 95-100, 1955b.
- Hantush, M. S., and C. E. Jacob, Nonsteady Green's functions for an infinite strip of leaky aquifers, *Trans. Am. Geophys. Union*, 36, 101-112, 1955c.
- Jacob, C. E., Radial flow in a leaky artesian aquifer, *Trans. Am. Geophys. Union*, 27, 198-205, 1946.
- Theis, C. V., The relation between the lowering of the piezometric surface and the rate and duration of discharge of a well using ground-water storage, *Trans. Am. Geophys. Union*, 16, 519-524, 1935.
- Watson, G. N., *Theory of Bessel Functions*, Macmillan, New York, 1944.
- Wenzel, L. K., Methods for determining permeability of water-bearing materials, *U. S. Geol. Survey Water Supply Paper* 887, 87-98, 1942.
- Wisler, C. O., and E. F. Brater, *Hydrology*, John Wiley & Sons, New York, ch. 7, 1951.

(Manuscript received June 18, 1960.)

Correlations between Soil-Moisture Depletion, Solar Radiation, and Other Environmental Factors

FOREST W. STEARNS

*Southern Forest Experiment Station
U. S. Department of Agriculture
Vicksburg, Mississippi*

AND

CHARLES A. CARLSON

*U. S. Army Engineer Waterways Experiment Station
Corps of Engineers
Vicksburg, Mississippi*

Abstract. To extend the usefulness of a soil-moisture prediction method, solar radiation, temperature, and other environmental factors were studied in relation to moisture loss in the surface 12 inches of soil. Data were obtained in an upland meadow on loessial soil near Vicksburg, Mississippi. Comparisons were made only for drying periods, and only when soil moisture was in the wetter half of its range.

Highest correlations of single factors with moisture loss were obtained with soil temperature and evaporation-pan data ($r = 0.79$ each), and with solar radiation ($r = 0.76$). Values for air temperature, vapor pressure deficit, humidity, and wind were progressively lower. Correlations with soil temperature or evaporation-pan data were somewhat improved by the addition of other factors in combination. Highest correlation was obtained with a site-derived depletion curve ($r = 0.85$) from the previous year.

Introduction. For several years the U. S. Forest Service, in cooperation with the Corps of Engineers, U. S. Army, has been studying soil-moisture regimes with reference to soil strength and vehicular movement. A close relationship between trafficability and moisture content of the surface-to-12-inch layer was demonstrated some years ago by the Army Mobility Research Center of the U. S. Army Engineer Waterways Experiment Station, Vicksburg, Mississippi. The subsequent cooperative research resulted in a reasonably accurate method for estimating the moisture content of the surface layer [Dortignac and Lull, 1951; Carlson, Reinhart, and Horton, 1956; Carlson and Horton, 1959].

The Vicksburg method is designed for estimating soil moisture over the entire range from wettest to driest conditions throughout the year. In the development of the method, rainfall data and detailed soil-moisture records were used to establish accretion relations which account for variation in net water gains with difference in storm size, antecedent soil-moisture content, and other factors. If the accretion relations thus de-

rived are used, some of the discrepancies which accrue when accretion is assumed to equal storage capacity alone are eliminated. From the inter-rain portions of the same moisture records, depletion curves were plotted by season to include water losses from evapotranspiration and from drainage to deeper soil layers. Thus, the method provides a direct estimate of the net accretion and depletion for a limited soil layer for all seasons. Blaney and Criddle [1950], Thornthwaite et al. [1954], Penman [1956], and van Bavel [1956] have developed other methods for determining depletion relationships for the entire root zone of soils at or near field capacity, and they usually assume that accretion equals rainfall until the moisture deficiency is satisfied.

The correlations that form the main subject of this paper were developed for examining the relationships between meteorological measures and soil-moisture loss, as estimated by the Vicksburg system, and to aid in extending the system into diverse climatic areas. The findings also pertain to evapotranspiration theory. As correlations of climatic factors with soil-moisture de-

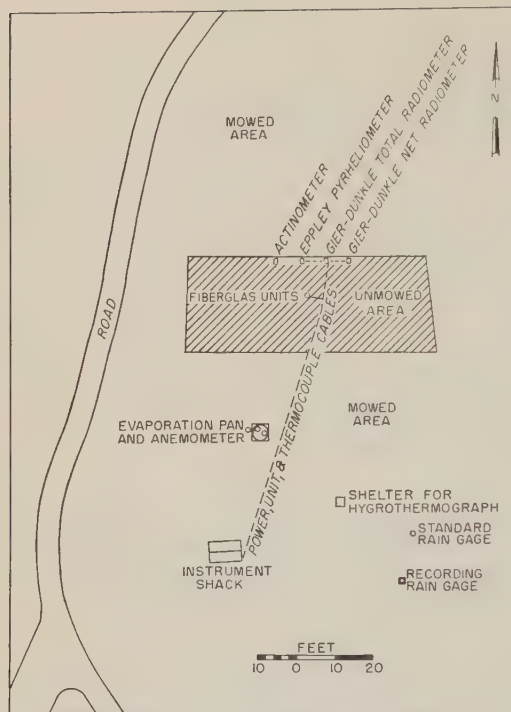


Fig. 1. Site layout. Radiometers were 5 feet above ground, on posts.

pletion necessarily become poorer with increasing soil-moisture tension, only depletion periods during which the soil-moisture content was in the upper half of the total moisture range were used.

Study area and experimental methods. A site was established in a level upland meadow at Vicksburg. The soil, a Memphis silt loam of loessial origin, had fair to good internal drainage and complete cover of Johnson grass, hogweed, goldenrod, and other weedy species.

Data were obtained throughout 1954. Soil moisture was recorded with fiberglas electrical resistance units installed 1.5, 4.5, 7.5, and 10.5 inches below the surface and individually calibrated in place [Reinhart, 1953]. Other instrumentation included four types of radiometers, a standard Class A evaporation pan, precipitation gages, an anemometer, and a hygrothermograph (Fig. 1). The Eppley pyr heliometer provided the longest set of uninterrupted readings, and its data were used in most comparisons.

Relationships between soil-moisture loss and environmental factors were tested first on a daily basis. Correlations were low and nonsig-

nificant, partly because daily moisture loss was small—an average of 0.072 inch. Three-day periods gave markedly better results. Correlations of moisture loss with solar radiation, for example, had coefficients r of 0.20 and 0.76 for 1- and 3-day periods, respectively. Sequences longer than 3 days were not tested because only drying periods were used for comparisons and rain fell on an average of every 3 days. Crabb [1950] and others have also found better trends with radiation data analyzed as a moving sum or as an average for a period of days, rather than as daily totals.

As a result of the many restrictions only thirty 3-day periods were available for comparison. The majority of these fell during winter and spring, low moisture levels ruling out otherwise usable periods from June to mid-November. A concurrent soil-moisture record for depths to 48 inches indicated that most of the depletion during these 30 periods occurred in the surface-to-12-inch layer.

Relative humidity was read at 2-hour intervals from 10 A.M. to 4 P.M.; the readings were averaged for the day and then summed for each 3-day period. For vapor pressure deficit values, temperatures were averaged for times corresponding to humidity measurements. The vapor pressure deficit for the day was determined from these averages, and the three daily values were summed for each period.

Air temperature mean represented the daily mean temperature summed over 3 days. Air temperature sum was the hourly temperature summed over 3 days. Air temperature maximum values, the sums of three daily maxima, were dropped from consideration when their correlations proved to be lower than those for the other expressions of air temperature. Soil temperature was calculated as the sums of temperatures at depths of 1.5, 4.5, 7.5, and 10.5 inches for the first and third day of each period.

Average environmental conditions for drying days are summarized in Table 1.

Single-factor relationships. In linear regressions with single environmental factors (Table 2), both soil-temperature and evaporation-pan losses showed close correlation with the measured moisture loss. These factors are integrating expressions in that they reflect not only air temperature and solar radiation during any 3-day period but also heat exchange and other

TABLE 1. Average Environmental Conditions for Depletion Days, 1954

Month	Data Obtained at Site							Data from Waterways Exp. Sta. Weather Station*			
	Drying Days, no.	Soil Moisture Loss, inches	Radiation (Eppley), langleys	Air Temp.		Relative Humidity, per cent	Vapor Pres. Deficit, mm. Hg.	Evap. Pan Loss, inches	Daily Wind Movement, miles	Monthly Mean Temp., °F.	Rainfall per Month, inches
				Max. °F.	Mean °F.						
Jan.	10	0.04	224	55	42	57	4.45	0.05	16.4	49	5.83
Feb.	13	.06	388	69	53	44	8.58	.12	21.3	56	3.25
Mar.	12	.07	456	68	56	50	7.53	.17	40.5	57	2.78
Apr.	13	.13	549	82	68	61	9.89	.19	25.6	68	6.03
May	11	.11	611	76	63	53	10.61	.20	14.5	66	6.32
June	3	.12	718	85	69	45	15.30	.25	13.4	80	1.60
Nov.	3	.02	275	66	52	50	8.43	.06	9.1	53	2.48
Dec.	13	.02	248	62	47	47	6.38	.06	19.0	47	1.79

* Mean temperature for July was 83°F, for August 84°F, for September 76°F, and for October 66°F; rainfall in inches for these months was 1.53, 1.00, 4.97, and 2.92, respectively.

effects for several days preceding. Soil temperature, in particular, influences the rate both of evaporation and of water movement through the soil and into and through roots. The temperature of moist soil is a relatively stable parameter which reflects the energy available for evapotranspiration more accurately than does the more variable air temperature. Correlation with soil temperature would, of course, have been much lower if periods of comparison had not been limited to those in which the soil was moist. Under drier conditions less energy would be utilized in evapotranspiration and soil temperatures would show greater change.

Total incident solar radiation as measured by the Eppley pyrheliometer was also well correlated with soil-moisture loss. Air temperature sum showed slightly better correlation with moisture loss than did air temperature mean. Vapor pressure deficits had a somewhat lower correlation, relative humidity showed a very weak relationship, and wind showed a negligible one. The square, cube, or logarithm of the single factors did not alter the correlations appreciably, either separately or in combination.

A correlation between air temperature sum and soil temperature revealed a coefficient of $r = 0.89$. Nevertheless, Table 2 indicates that air

TABLE 2. Correlations of Measured Moisture Loss with Single Environmental Factors

Factor	Function of the Factor					Multiple Correlation Coefficients of Third-Degree Polynomial, R
	Linear, r	Square, r	Cube, r	Logarithm, r		
Soil temperature	0.79*	0.79*	0.78*	0.80*		0.80*
Solar radiation	.76*	.75*	.72*	.71*		...
Air temperature						
Mean	.60*	.60*	.59*	.59*		.61*
Sum	.64*	.63*	.62*66*
Vapor pressure deficit	.52*	.54*	.51*	.41†		...
Relative humidity	.21	.17	.11
Wind	.07	.05	.04
Evaporation from pan	.79*	.78*	.74*85*

* Significant at the 0.01 level.

† Significant at the 0.05 level.

TABLE 3. Correlations of Measured Moisture Loss with Combinations of Factors

Combinations of Factors	Multiple Correlation Coefficient, R^*
Air temp. mean, solar rad.	0.77
Air temp. mean, solar rad., evap. from pan	.80
Air temp. mean, soil temp.	.81
Air temp. mean, soil temp., air temp. sum	.82
Air temp. mean, soil temp., solar rad.	.83
Air temp. mean (X , X^2 , X^3), soil temp. (X , X^2 , X^3), air temp. sum (X , X^2 , X^3)	.84
Soil temp., solar rad.	.82
Soil temp., solar rad., wind, rel. humidity	.82
Soil temp., solar rad., wind, rel. humidity, air temp. mean	.84
Soil temp., solar rad., wind, rel. humidity, air temp. mean, evap. from pan	.84
Soil temp., solar rad., evap. from pan	.83
Air temp. sum (X , X^2 , X^3), solar rad. (X , X^3), vapor pressure deficit	.79

* All values significant at the 0.01 level.

temperature sum, if used individually, will not yield an estimate of soil-moisture loss nearly as well as will soil temperature. Air temperature mean or sum accounts for only 36 or 41 per cent, respectively, of the variability in soil-moisture loss when these correlations are expressed as coefficients of determination r^2 , whereas soil-temperature or evaporation-pan loss was associated with 62 per cent of the variability.

Drinkwater and Janes [1958] also reported correlations between evapotranspiration and single environmental factors. The level of correlation varied from year to year during the 3 years of their study. In 1954, for example, correlation with pan evaporation was $r = 0.63$; with average temperature it was $r = 0.47$ for a 7-day period. The higher correlations at Vicksburg are based on the exclusive use of 3-day drying periods, and lack the complications introduced by daily watering and plant-tank interactions.

Potential evapotranspiration calculated by the Thornthwaite formula shows a correlation of $r = 0.62$ with actual moisture loss. This is in agreement with the result when air temperature was directly correlated with moisture loss (Table 2).

Combinations of factors. Multiple regressions were calculated to determine whether groups of factors would materially improve correlations (Table 3).

The inclusion of soil temperature in a group of factors improved correlation. Air temperature alone contributed little to most combina-

tions. The best correlations resulted from combinations which, in some measure, represented the components of the energy balance approach, i.e., soil and sensible heat flux and incident radiation. The addition of the square and cube functions of temperature measures improved correlations only slightly. The most promising combination, excluding soil-temperature and evaporation-pan values, gave the same result ($r = 0.79$) as the latter two when used as single factors (Table 2). The combination of soil temperature and solar radiation appeared to provide correlations as useful as combinations of a greater number of variables.

Correlations involving radiation. The four radiometers gave essentially equivalent results (Table 4). In correlations with moisture loss, solar (Eppley or actinometer) and total (Gier-

TABLE 4. Comparison between Radiation Measurements with Different Instruments and between Radiation Measurements and Soil-Moisture Loss

Radiometer	Correlation Coefficients*	
	Eppley	Soil-Moisture Loss
Eppley		0.72
Net exchange	0.97	.68
Total	.96	.73
Actinometer	.99	.72

* Frequent shutdown with the net and total instruments reduced to 21 the number of periods for comparison.

Dunkle) radiation were slightly superior to net radiation. The very high correlation between instruments indicated that the trends of solar, total, and net radiation were similar, although the relative amounts varied from day to day for any two instruments. Similar high correlations (clear days $r = 0.98$, cloudy days $r = 0.97$) between net and solar radiation have been reported by Shaw [1956]. Under the conditions of the Vicksburg study, solar radiation (Eppley) appears to be as useful an index of the energy available for evapotranspiration as is net radiation.

The actinometer is promising for field use. It is sufficiently accurate for moisture-loss studies; it needs no recording potentiometer and requires little maintenance.

As Halstead and Covey [1957] pointed out, apportionment of the components of net radiation into latent, soil, and sensible heat flux is the critical part of the energy balance approach. Results of this study substantiate the importance of the soil-heat component, particularly during winter and spring.

Tanner [1960] reported a considerably higher correlation ($r = 0.94$) of net radiation with moisture loss. His data, calculated daily for an irrigated alfalfa-brome grass stand near Hancock, Wisconsin, relate primarily to the summer season. The maintenance of high moisture conditions and a lesser amount of advective heating and cooling probably account for the higher correlation at Hancock than at Vicksburg.

That seasonal changes in plant cover did not substantially influence the amount of radiant energy reaching the soil was apparent from the high correlation between soil temperature and radiation. The coefficient of 0.81 for this correlation was appreciably better than that for either the air temperature mean or air temperature sum with radiation, $r = 0.66$ and 0.67 , respectively. Advective heating and cooling help to weaken the correlation between radiation and air temperature.

Pan evaporation showed a high correlation ($r = 0.91$) with solar radiation (Eppley), an indication that the relative amount of sensible heat loss from the pan was similar throughout the period. Wind and relative humidity showed no relationship to radiation: r values were 0.09 and -0.08 .

A summation of incoming and outgoing radi-

TABLE 5. Correlations with Depletion Curve Values and Environmental Factors

Combination of Factors	Correlation Coefficient*
Measured moisture loss versus:	
Loss by derived depletion curve	0.85
Loss by derived depletion curve, solar radiation, soil temperature, and evaporation from pan	.89
Loss by derived depletion curve versus:	
Solar radiation	.72
Air temperature-mean	.50
Air temperature-sum	.54
Soil temperature	.80
Evaporation from pan	.72

* All values significant at the .01 level.

ation was derived from total and net radiation measurements. The correlation with moisture loss was $r = 0.73$, as good as the correlation with other radiation values (Table 4). This value, together with the fact that correlations with moisture loss were slightly better for Eppley and total than for net, suggests that conventional measurements of net radiation may not assay all spectral components affecting evapotranspiration.

Correlations with depletion-curve values. As stated earlier, the system of soil-moisture prediction evolved at Vicksburg depends upon empiric accretion and depletion relationships. Seasonal depletion curves [Carlson, Reinhart, and Horton, 1956], developed for specific sites from measured moisture contents during several drying cycles, are used to calculate the water left in the soil at any given number of days after a rain.

Values from depletion curves derived in 1953 correlated somewhat better with moisture loss measured in 1954 (Table 5) than did any single meteorologic factor or combination of factors listed in Table 2. Correlation was slightly improved when several factors were combined with the depletion curves. Moisture losses, as estimated by depletion curves, correlated well with solar radiation, soil temperature, and evaporation. The better results with depletion curves indicate that, under natural drying conditions, factors other than meteorologic ones are also involved, e.g., drainage and the loss of moisture from the soil under high stress conditions. Any

fundamental study of moisture loss from soil throughout its natural range must of necessity include such factors.

In trafficability prediction, depletion must be estimated at all ranges of moisture from above field capacity to below the wilting point. Experience suggests that at the extremes of the moisture range the superiority of depletion curves over environmental factors would be even greater than appeared under the conditions of this study. Estimates with the curves might be further improved by the addition of selected environmental factors. When various functions of the six best single meteorologic factors were used in conjunction with the loss estimates based on the depletion curve, a correlation of $r = 0.94$ was obtained. Thus meteorologic factors may be helpful in choosing curves for application in areas for which depletion data are not available.

Acknowledgments. The Signal Corps, U. S. Army, furnished the radiometers and recording potentiometers and personnel to assist in the calibration and maintenance of the equipment. Field measurements and computations were performed by the staffs of the Vicksburg Research Center and the Army Mobility Research Center. Howard W. Lull of the U. S. Forest Service gave valuable guidance in the initial phases of the study.

REFERENCES

- Blaney, H. F., and W. D. Criddle, Determining water requirements in irrigated areas from climatological and irrigation data, *U. S. Soil Conservation Serv. SCS-TP-96*, 48 pp. 1950.
- Carlson, C. A., and J. S. Horton, Forecasting trafficability of soils Report Number 5, Development and testing of some average relations for predicting soil moisture, *Tech. Mem. 3-331*, Waterways Exp. Sta., U. S. Army Corps of Engineers, 1959.
- Carlson, C. A., K. G. Reinhart, and J. S. Horton, Predicting moisture in the surface foot of soil, *Soil Sci. Soc. Am. Proc.*, **20**, 412-415, 1956.
- Crabb, G. A., Jr., Solar radiation investigations in Michigan, *Mich. Agr. Exp. Sta. Tech. Bul.* **222**, 153 pp., 1950.
- Dortignac, E. J., and H. W. Lull, Progress Report 1, The development of methods for predicting soil moisture content. U. S. Forest Service, in cooperation with the U. S. Army Engineers Waterways Experiment Station, 1951.
- Drinkwater, W. O., and B. E. Janes, Discussion of "Relation of potential evapotranspiration to environment and kind of plant," *Trans. Am. Geophys. Union*, **39**, 972-974, 1958.
- Halstead, M. H., and W. Covey, Some meteorological aspects of evapotranspiration, *Soil Sci. Soc. Am. Proc.*, **21**, 461-464, 1957.
- Penman, H. L., Estimating evaporation, *Trans. Am. Geophys. Union*, **37**, 43-50, 1956.
- Reinhart, K. G., Installation and field calibration of fiberglass soil-moisture units, *U. S. Forest Serv. South. Forest Exp. Sta. Occas. Paper* **128**, pp. 40-48, 1953.
- Shaw, R. H., A comparison of solar radiation, *Bull. Am. Meteorol. Soc.*, **37**, 205-206, 1956.
- Tanner, C. B., Energy balance approach to evapotranspiration from crops, *Soil Sci. Soc. Amer. Proc.*, **24**, 1-9, 1960.
- Thornthwaite, C. W., et al., Estimating soil tractionability from climatic data, *Publications in Climatology VII*, 369-447, Johns Hopkins University Laboratory of Climatology, 1954.
- van Bavel, C. H. M., Estimating soil moisture conditions and time for irrigation with the evapotranspiration method, Agricultural Research Service, *USDA 41-11* (North Carolina Agr. Exp. Sta.), 16 pp., 1956.

(Manuscript received April 28, 1959; revised July 5, 1960.)

Operational Characteristics of the Laterals near the Edge of a Tile Drainage System¹

BEN L. GROVER,² JAMES T. LIGON, AND DON KIRKHAM

*Iowa State University
Ames, Iowa*

Abstract. A two-dimensional scale model was used in a study of the effect of an undrained area, adjacent to a drained area, on the operation of laterals near the edge of a tile drainage system. The discharge from the outside lateral only was increased owing to the undrained area, but no effect of the undrained area on the water table between any of the laterals was observed, except for a negligible effect in a region within less than one-fourth of a lateral spacing from the outermost tile. Furthermore, the effect was discernible only when the water table had fallen to almost complete flatness at the level of the drains.

INTRODUCTION

To obtain a mathematical solution for a tile or ditch drainage problem, we usually assume that the portion of the drainage system analyzed is so far removed from the undrained area that any effects of the latter area are negligible. This assumption implies that the solution obtained will be applicable only to those lateral tile lines or ditches which have many laterals on either side of them. However, in the design of an actual field drainage system we also need to know the operational characteristics of those laterals which are located near the edges of the system.

This paper presents the operational characteristics of the two outside laterals of a tile drainage system as obtained by the use of a scale model [Grover and Kirkham, 1956] having glass beads as porous material and glycerol as fluid. The beads and glycerol are used to allow a scaling of the capillary fringe as found in the field, a scaling which cannot be accomplished with models using sand and water.

PROCEDURE

The glass bead-glycerol model was initially designed to represent a drainage system in which

the drained area of interest would not be influenced by undrained areas. In such a system the operational characteristics of each tile were supposed to be the same as those of any other tile. The model as used here was modified (Fig. 1) so that it would represent the laterals at the side of a drainage system. This was done by (a) making a small depression in the surface of the glass beads at one end of the model, (b) keeping this depression filled with glycerol, and (c) operating only tiles from the center of the model to the end opposite the depression, laterals A, B, and C as shown in the schematic diagram (Fig. 1).

Part of the symbols used in this paper are presented in Figure 1. Other symbols used are as follows: tile length L , conductivity K , rate of discharge Q , dimensionless discharge Q/KLd , porosity of the porous medium f , elapsed time from the instant the tiles were opened t , and a dimensionless time function $(tK/a)^{1/2}$. Space coordinates were taken so that y was in the vertical direction and x in the horizontal direction perpendicular to the tiles. The center of the coordinates was at the center of a tile.

The model, as set up with ponded glycerol maintained in the depression at the left, represents a ponded surface condition adjacent to a drainage system. Therefore, any effect the simulated undrained area to the left of lateral A had on the drained area between tiles A and C would be more pronounced than in actual practice, because in actual practice the drainage would lower the surface of saturation for a relatively

¹ Joint contribution from the Departments of Agronomy and Agricultural Engineering, Iowa State University. Journal Paper J-3878 of the Iowa Agricultural and Home Economics Experiment Station, Ames, Iowa, Project 1003.

² Now at University of California Citrus Experiment Station, Riverside, California.

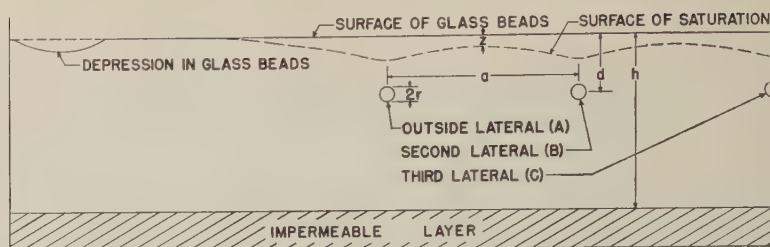


Fig. 1. Schematic diagram of model showing physical arrangement and symbols used for various dimensions.

greater distance beyond the outside lateral than it would in the model. In other words, the model shown in Figure 1 gives results that are on the safe side for drainage design.

In the model the tiles were 50 cm apart and 12 cm above the impermeable layer. For practical interpretation, 1 cm on the model may be taken as 1 foot in the field. The material below the tiles could be varied so as to simulate layered soils with different values of conductivity K in the different layers. The symbol K_1 was used for the conductivity of the surface layer and the symbol K_2 for the conductivity of the sublayer. The value of d could be varied by changing the depth of the glass beads above the tiles.

The data on the shape of the surface of saturation were obtained as photographs. The individual photographs were mounted together and then rephotographed to show the lowering of the water table with time. The locations of the tiles were marked by white spots on the front of the model. A grid on the face of the model has horizontal lines 2 cm apart and vertical lines 1 cm apart.

In the present work four geometries were used, two in which the porous material was homogeneous and two in which the porous medium consisted of two layers having different permeabilities, with the top of the sublayer at $y = -2r$. In the latter cases, $K_1/K_2 = 20$.

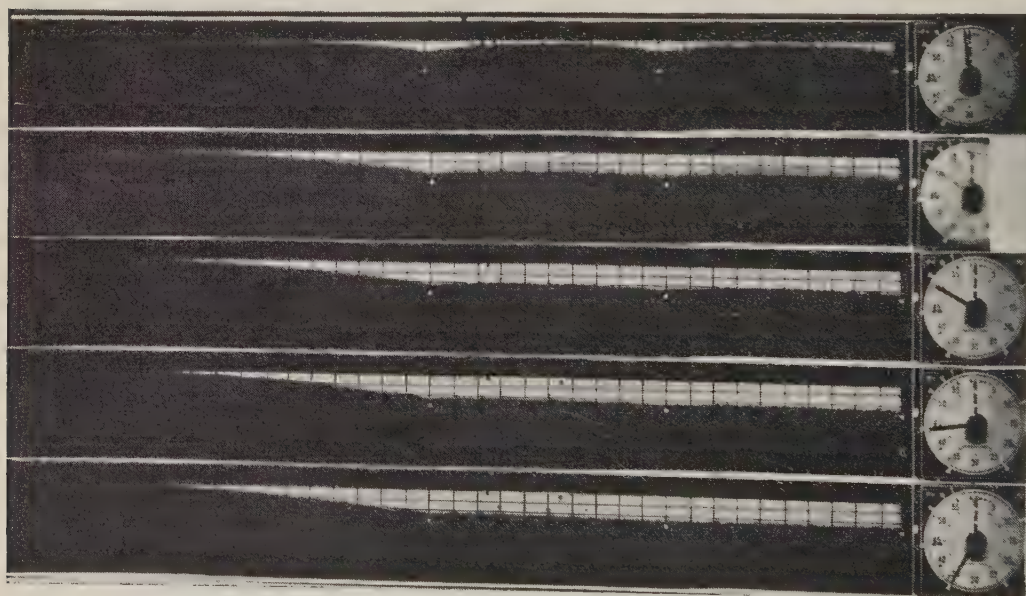


Fig. 2. Succession of photographs of the model showing the change of shape and height of the surface of saturation with time for a homogeneous porous medium with $d = 6$ cm, $h = 18$ cm, and $a = 50$ cm. The boundary between the light and dark areas is the surface of saturation. The locations of the tiles are marked by white spots on the face of the model.

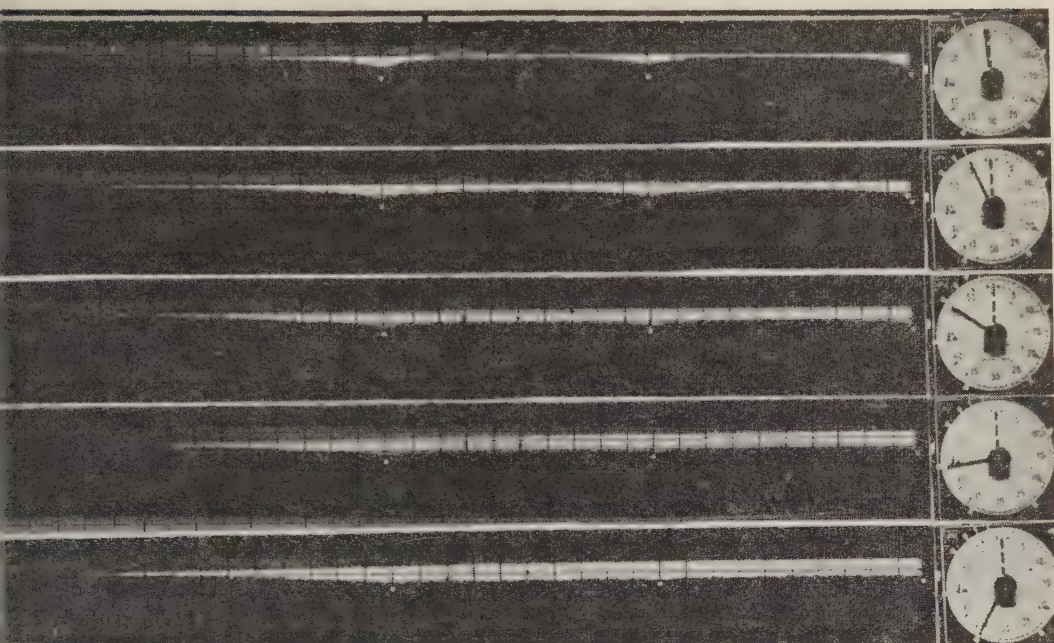


Fig. 3. Same as Figure 2 except that $d = 4$ cm and $h = 16$ cm.

Values of $d = 4$ and 6 cm were used in the homogeneous system, and $d = 6$ and 8 cm in the two-layer system.

RESULTS

The results will be given in two parts, (a) location and shape of the surface of saturation and (b) discharge from the tiles. Tile discharges are given for the times at which photographs were taken, zero time being the instant the tiles are opened, when the water table is at the surface of the beads.

Shape of water table. The data on surface of saturation are presented as photographs rather than in tabular form because of the difficulty in obtaining precise numerical values from the photographs. However, the interested reader can scale values from the photographs.

Figure 2 shows the location of the surface of saturation at successive time intervals for a homogeneous porous medium with $d = 6$ cm and $h = 18$ cm. Remember that for practical interpretation the centimeter values of d , h , etc., may be interpreted as feet. In the photographs the areas above the surfaces of saturation appear much lighter than the areas below. Note that the clock runs counterclockwise, so that the number indicated by the solid black hand, which is the

minute hand, when subtracted from 60, gives the time in minutes since the tiles were opened. The second hand is the striped hand, and the photographs were all taken with the striped hand at, or nearly at, zero seconds. In Figure 2 the top photograph shows the condition at $60 - 59 = 1$ minute after the tiles were opened. The third photograph from the top shows the water table at $60 - 50 = 10$ minutes after the tiles were opened. The second photograph is a double exposure, but the water table and times for both exposures are discernible.

Examination of the dark-light interface in the photographs (Fig. 2) shows that there is no observable difference in the height and shape of the surface of saturation between laterals B and C (see Fig. 1) and between laterals A and B until the drawdown is practically complete; and then the water table is less than $\frac{1}{2}$ cm higher just to the right of tile A as compared with tile B or C . This difference appears to diminish to zero within one-fourth of a tile spacing from lateral A .

Figure 3 shows the surface of saturation at successive time intervals for a homogeneous porous medium with $d = 4$ cm and $h = 16$ cm, 2 cm of beads having been removed from the top. Again no water-table differences due to the

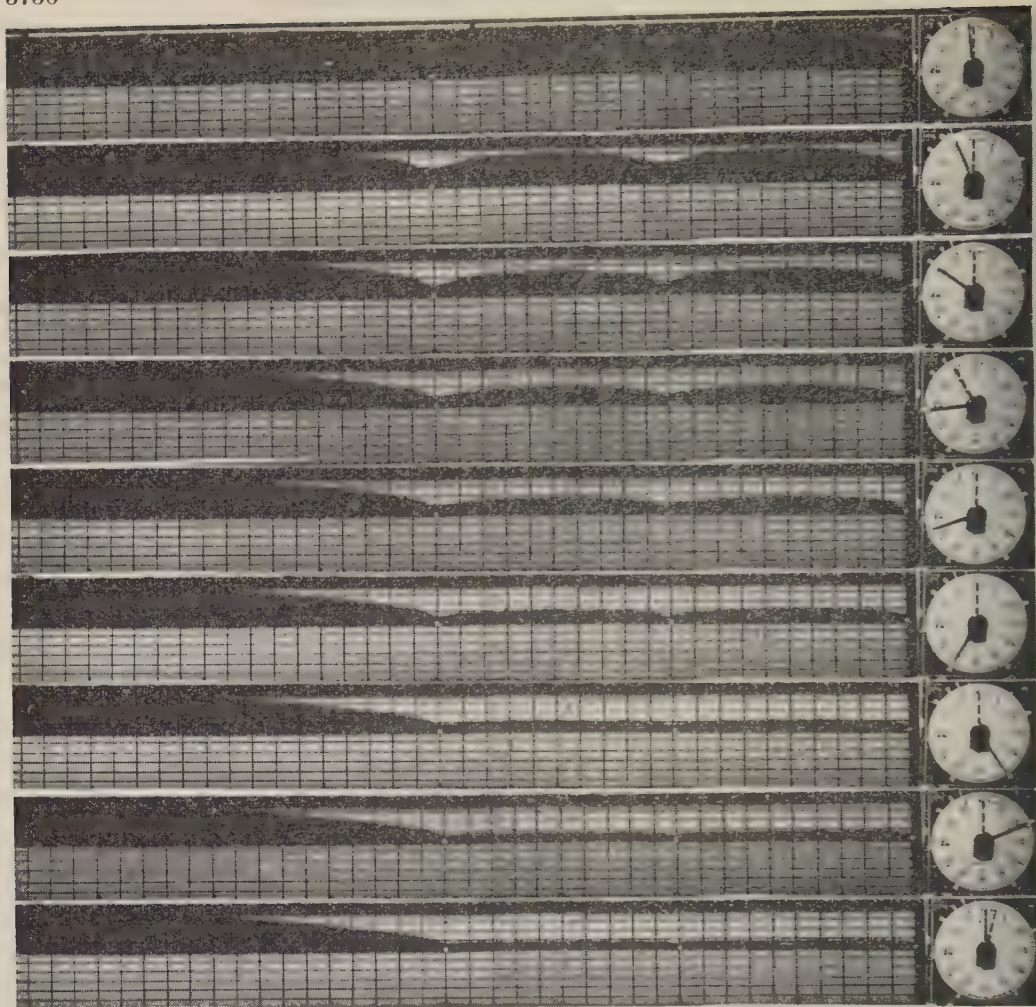


Fig. 4. Same as Figure 2 except that the porous medium is composed of two layers with different permeabilities, the bottom layer being less permeable ($K_1/K_2 = 20$), and $d = 8$ cm and $h = 20$ cm. Note the difference in shading of the layers of beads at their interface just below the tiles.

undrained area are apparent to the right of the first tile line except very near that line, and this small difference appears only after drainage is nearly complete between the tiles. Again this difference disappears within a distance of one-fourth of a tile spacing from lateral A.

Figure 4 shows a two-layer system with the conductivity of the surface layer 20 times greater than that of the subsurface layer. When both are saturated with glycerol, as is nearly the case in the top photograph of the figure, the surface layer composed of 2-mm beads appears much darker than the subsurface layer composed of 0.5-mm beads. In this geometrical ar-

rangement, $d = 8$ cm and $h = 20$ cm. Although the surface of saturation moved downward more slowly in this case, there appears to be no difference in its height or shape between laterals A and B and between laterals B and C.

Similar results (photographs not shown) for water-table height and shape were obtained for a two-layer system with $d = 6$ cm and $h = 11$ cm. Again no significant effect of the undrained area on the water table between tile lines could be detected.

Discharge data. The discharge data are presented in the form of plots of dimensionless discharge Q/KLd versus the dimensionless time

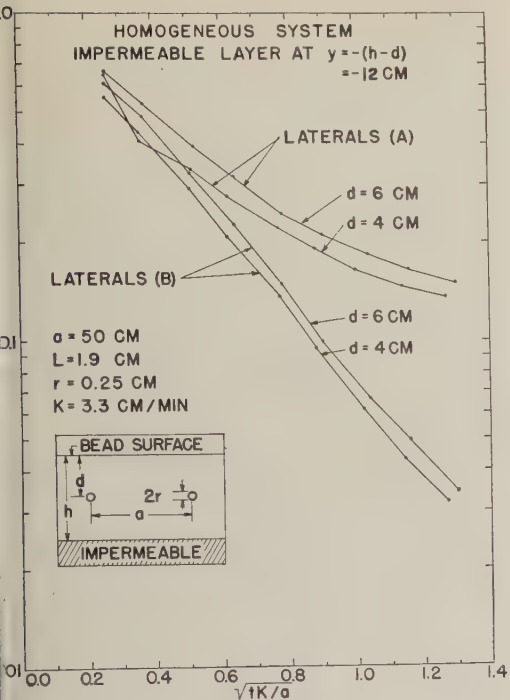


Fig. 5. Dimensionless discharge Q/KLd versus the dimensionless time function $(tK/a)^{1/2}$ for the geometries indicated. Tiles A and B are the outside and the next to the outside tile lines of a system. For $d = 4$ cm, $h = 16$ cm; and for $d = 6$ cm, $h = 18$ cm.

function $(tK/a)^{1/2}$. The data for both the homogeneous systems of Figures 2 and 3 are shown in Figure 5. Here the impermeable layer is at $y = -12$ cm and there are two different depths, $d = 4$ cm and $d = 6$ cm, corresponding to $h = 16$ and 18 cm. Initially the discharge is nearly the same for laterals A and B. Theoretically A will carry more than B but the added amount would be imperceptible [Kirkham, 1949]. The discharge from lateral B drops off at a much faster rate than that from lateral A. In all cases the dimensionless discharge plot of lateral B follows approximately a straight line, as does a lateral at the center of a system [Grover and Kirkham, 1959] which is far removed from the influence of an external undrained area.

Figure 6 shows the data for a two-layer system with the interface at $y = -2r = -0.5$ cm, $d = 6$ cm, and $h = 18$ cm. Corresponding water tables for these data are not shown. Lateral X, referred to in this figure, represents a tile far removed from edge effects; the data for it were

obtained in a separate run in which the discharge from a tile at the center of the system was used. Notice that in the discharge for laterals A and B the drainage period was not allowed to proceed long enough for a wide divergence between discharge values to develop, but separation of values does become apparent near the end of the run, thus showing an increased influence of the undrained area. The difference in discharge between laterals B and X is small and is a constant throughout the drainage period. This small difference could be due to difference in temperature or some other variable of the two independent runs. If this discharge difference were due to the proximity of lateral B to the undrained area, the difference would be expected to change with time, as with laterals A and B, rather than remain constant.

In Figure 7 the data for a two-layer system with $d = 8$ cm and $h = 20$ cm are presented. The divergence between the discharges of laterals A and B becomes quite pronounced as time progresses, but the water-table heights (Fig. 4)

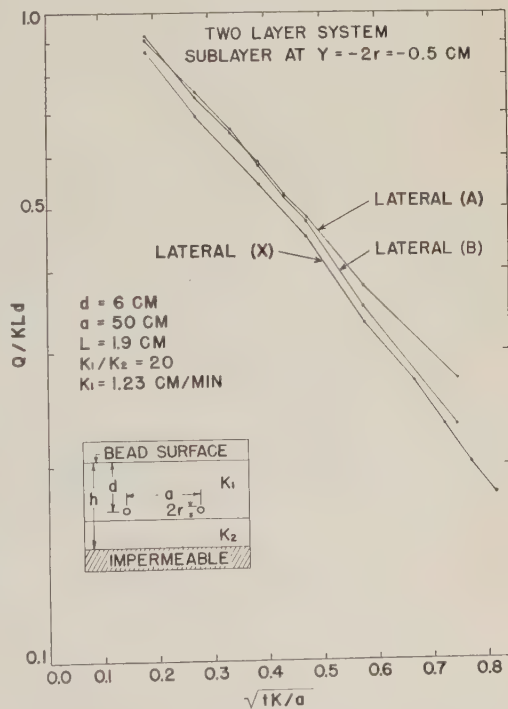


Fig. 6. Same as Figure 5 except $d = 6$ cm and $h = 18$ cm. Lateral X represents a central tile line of a large system. Data for X were taken in an independent run.

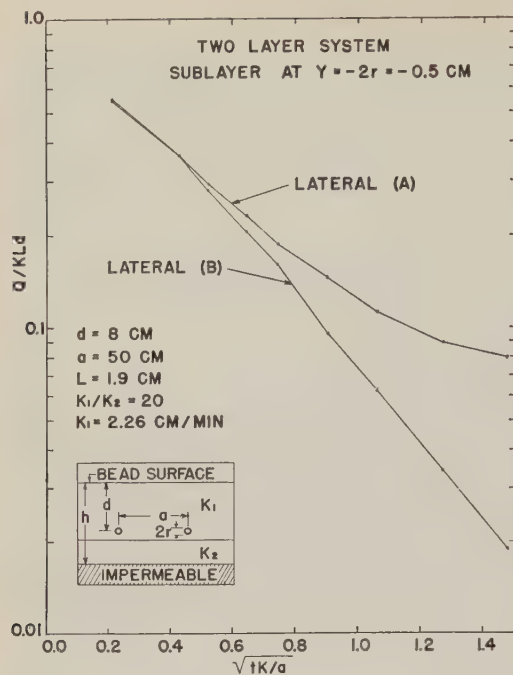


Fig. 7. Same as 6 except that $d = 8$ cm. and $h = 20$ cm and data for tile X are not shown.

are the same. It should be noted, however, that the discharges are approximately the same near the beginning of the run.

CONCLUSIONS

The data presented above indicate that the surface of saturation between the two outside tiles of a drainage system will have, except for a small difference, negligible in practice, the same shape and height as the surfaces between any other two adjacent tiles of a drainage system as long as all the tiles flow without back pressure. A further conclusion is that the discharge from the laterals near the side of a drainage system, except for the outside lateral, will be the same as the discharge from those near the center. The

discharge from the outside lateral is the same as the discharge from those near the center of the system during the early part of the drainage period, but it remains at a higher value as the fluid surface is lowered between the tiles. This implies, in practice, that the outer laterals should have larger capacities than the inner ones if the inner ones are designed to be running full when the surface of saturation is below the soil surface. If the inner drains are designed to be running full when there is ponded water, the outer drains need be no larger than the inner ones because for ponded water they will be flowing at essentially the same rate, as is clear from Figures 5, 6, and 7.

This study indicates that in experimental work the single tile or ditch lateral at the edge of a drained test area should be an adequate guard against foreign ground water and that the whole area between the two outer laterals, except that within a distance of about $\frac{1}{4}$ of a tile spacing of the outer tile, can be used for water table measurements without corrections being made for effects of the undrained area.

REFERENCES

- Grover, B. L., and Don Kirkham, Falling water tables of drained land by glassbead glycerol model, Annual Meetings, American Society of Agronomy, Nov. 12-15, 1956. Abstracted in *Agronomy Abstracts*, pp. 3-4, 1956. (Complete publication to appear elsewhere.)
- Grover, B. L., and Don Kirkham, Nonsteady state tile drainage, Annual meetings, American Society of Agronomy, Nov. 16-20, 1959. Abstracted in *Agronomy Abstracts*, p. 46, 1959. (Now being prepared for enlarged publication.)
- Kirkham, Don, Flow of ponded water into drain tubes in soil overlying an impervious layer *Trans. Am. Geophys. Union*, 30, 369-385, 1949.

(Manuscript received May 26, 1960; presented at the Pacific Southwest Regional Meeting of the American Geophysical Union, Los Angeles, Calif. February 4-5, 1960.)

Singularity Distributions for the Analysis of Multiple-Fluid Flow through Porous Media

G. DE JOSSELIN DE JONG¹

*Institute of Engineering Research
University of California, Berkeley, California*

Abstract. In Part 1 the simultaneous flow of fluids of different properties is treated by substituting these fluids by one hypothetical fluid and applying singularities at those points where the properties of the actual fluids change. Their magnitude is chosen so that the specific discharges in the hypothetical fluid are everywhere identical to the specific discharges in the actual fluids. The flow in the hypothetical fluid can be determined by potential theory from the transformed boundary conditions and the influence of the singularities.

For the determination of the discharge a stream function is used which contains singularities in the form of vortices. For the determination of the fluid pressures a multiple-fluid potential is defined which contains singularities in the form of source and sink distributions. The stream and the potential functions each combine with auxiliary, many-valued functions to form complex potentials. These permit solutions in the form of one integral in complex variables, valid for any point in the entire field, irrespective of the fluid present. The solution for the transition zone between fluids as well as the abrupt interface is elaborated.

In Part 2 the two-dimensional example of an infinite, confined aquifer with an initial vertical interface between two fluids of different specific weight is elaborated, giving as a result the movement of the fluids in the entire field at the first moment and a first approximation for the rotation of the interface around the center as a function of time.

These results are verified by a parallel plate model and an electric resistance model. In the latter model the vortices are replaced by sources for the tracing of streamlines and by source-sink combinations forming doublets for the potential lines.

NOTATION

	Time dependent coefficient describing inclination of interface in example
$[L]$	Breadth of stream channel
$[L]$	Half height of aquifer
$[L]$	Slot width of parallel plate model
$[L]$	Thickness of two-dimensional aquifer
$[L]$	Thickness of two-dimensional electric resistance model
$i = \sqrt{-1}$	Imaginary unit
$[Amp L^{-2}]$	Electric current density vector
$[L^2]$	Specific permeability of aquifer
	Integer number
$[L]$	Coordinate perpendicular to the interface
$[FL^{-2}]$	Pressure in the fluids
$[LT^{-1}]$	Specific discharge
$[LT^{-1}]$	Specific discharge components in s, n, x, y directions
q_s, q_n, q_x, q_y	Continuous, discontinuous components of q on interface
$[LT^{-1}]$	Complex specific discharge
$\bar{q} = q_x - iq_y$	Coordinate along the interface
$[L]$	Time
$[T]$	Mean velocity of the fluid
$[LT^{-1}]$	Horizontal coordinate
$[L]$	

¹ Since August 1960 at Technische Hogeschool, Delft, The Netherlands.

y	[L]	Vertical coordinate
$z = x + iy$	[L]	Complex coordinate
A, dA	[L ²]	Area
A, B, C, D, E, F		Points on boundary
E	[Volt]	Electric potential
E^*	[Volt]	Electric potential in current supply system
I	[Amp]	Electric current
Im		Imaginary part of complex expression
J, K		Intersection points of interface and boundary
M		Center point of interface in example
N		Image of M in ζ plane
P		Arbitrary running point
P_t		Arbitrary running point in ζ plane
Q	[L ³ T ⁻¹]	Discharge in aquifer
S	[L]	Contour or path of line integral
V, W		Unspecified functions of x and y
α		Inclination of interface to horizontal
β		Auxiliary variable
γ	[FL ⁻³]	Specific weight of fluid
δ''	[L]	Doublet distance
ϵ		Porosity of aquifer
$\zeta = \xi + i\eta$		Complex coordinate of transformation
κ	[T ⁻¹]	Strength of source per unit area
λ''	[LT ⁻¹]	Strength of doublet per unit area
μ	[FTL ⁻²]	Dynamic viscosity of fluid
ρ	[Ohm L]	Specific electric resistance
ψ		Exterior angle BP_tE
ω	[T ⁻¹]	Strength of vorticity in x, y plane per unit area
Θ	[L ² T ⁻¹]	Multiple fluid potential
Λ''	[L ⁴ T ⁻¹]	Doublet discharge
Φ	[L ² T ⁻¹]	Auxiliary function
Ψ	[L ² T ⁻¹]	Specific discharge stream function
$\Omega = \Phi + i\Psi$		Complex specific discharge potential
<i>Subscripts</i>		
0		Point, where a singularity is present, or point of interface containing a singularity
I		Part of complex potential accounting for singularities
II		Part of complex potential accounting for boundary conditions
1, 2		Pertaining to fluid 1, 2 (1 is light, 2 is heavy)
μ		Potential functions convenient for the study of viscosity influences with electric resistance analogy
<i>Superscripts</i>		
'		Inversion for electric resistance model (tracing of stream lines)
''		Doublets in electric resistance model (tracing of potential lines)

PART 1. DERIVATION

Introduction. In the study of ground-water flow a theory of the interaction between different fluids needs to be developed so that any arbitrary boundary value problem may be solved rigorously. Many hydrologists have de-

voted their attention to this subject, because in several fields of hydrology important problems are created by the presence of two fluids. The solutions obtained, however, are mainly limited to cases which yield certain geometrical approximations. It is the purpose of this

paper to describe a method which permits the determination of the behavior of two or more fluids, for any form of distribution over a field with arbitrary boundary conditions.

Badon Ghijben [1888] and afterwards *Herzberg* [1901] stated the hydrostatic equilibrium for a fresh water lens floating on top of salt water in a porous aquifer. Since then several authors have considered the more relevant case that either one of the two fluids or both are in movement. The first to have given a correct account of how the movement of the fluids influences the behavior of the interface seems to have been *Lorentz* [1913]. His discussion of the seeping of salt water under a well was later investigated experimentally by *Muskat* [1937]. *Hubbert* [1940] established a general description of the flow of two fluids at either side of a steady interface between fluids. By application of these considerations to a stationary oil deposit above an underlying body of flowing water, the tilt of the interface was derived for a one-dimensional flow system [*Hubbert*, 1953]. *Edelman* [1940] determined the shape of the interface between moving fresh water and stationary salt water in a dune area adjacent to the sea by use of a graphical flow net analysis. A mathematical solution was obtained for the case in which vertical flow components could be ignored, adopting the Dupuit-Forchheimer assumption. *Todd and Huisman* [1959] applied *Edelman's* method for determining the influence of recharge and pumping operations to limit overdraft in the drinking water supply area of Amsterdam.

If only one fluid is in motion, the hodograph method can be applied because the interface is circular. Applications of this technique for particular solutions have been carried out by *Harder, Simpson, Lau, Hotes, and McGauhey* [1953], *Kidder* [1956a, b], *Glover* [1959], and *Ferry* [1959]. When both fluids are moving, the interface, when mapped into the hodograph plane, takes the form of an unpredictable curve, so that the mapping procedure cannot be applied. An approximate method based on the Dupuit-Forchheimer assumptions was developed for one case by *Dietz* [1953].

Model studies provide the only means of studying the location and movement of interfaces for general problems involving movement of both fluids. A parallel plate model has been

employed for this purpose by *Santing* [1951], and sand models have been used by *Harder, Simpson, Lau, Hotes, and McGauhey*, [1953] and *Keulegan* [1954].

None of the publications indicated above contains a mathematical method by which the correct computation of the movement of both fluids as derived from given boundary conditions can be made. The first work which suggested a solution to this problem was an unpublished study by *Edelman* in 1957, 'Grondwaterstroming van een niet homogene vloeistof.' In this study he introduced a concept which proved inspiring for the development of the present theory: the replacement of the two fluids with their own characteristics by one hypothetical fluid with the same properties over the entire field. In this hypothetical fluid a row of sources coinciding with the position of the interface takes care of the change in properties of the two fluids. *Edelman* determined the source distribution in such a way that the velocity field created by these sources is equal to the real velocity distribution in one of the two fluids. The velocities in the other fluid can be obtained from the velocities created by the sources by the addition of a fictitious velocity. This concept was developed only for a horizontal interface, and the absence of sources along a vertical interface was inferred without further proof.

The present work [*de Josselin de Jong*, 1959] was based on this concept of replacing the two different fluids by one hypothetical fluid and of introducing the different fluid properties by singularities along the interface. In determining the character of the singularities, however, the aim was a singularity distribution that would directly create the actual velocity distribution in both fluids. By this approach the treatment of the two fluids becomes equivalent, and because of this equivalency the extension to more fluids can be made without further complications. The present theory shows that it is possible to meet these requirements with two kinds of singularities, vortices or sources and sinks. The choice of the kind to use depends on the objective of the study. If the objective is the determination of the discharges, it is convenient to introduce vortices. If the pressure in the fluids is to be determined, it is more convenient to use the sources and sinks. Furthermore, in the present study any inclination of the interface and

the case of a gradual transition zone are considered, as well as the introduction of boundary conditions.

The important advantage of the singularities is the possibility of solving any boundary value problem involving two or more fluids by application of the established methods of potential theory for the solution of boundary value problems of one fluid. Although the singularity method is completely general with regard to differences of fluid properties, the present work deals mostly with the influence of differences in density only. The effect of differences in viscosity can also be represented in terms of singularities, as indicated, but the procedure is not amenable to mathematical treatment. How an electric analogy can be used to account for viscosity differences in connection with singularities for the density differences will be shown at the end of Part 2.

Physical assumptions and basic equations. This study is concerned with the behavior of miscible fluids filling the pores of a porous medium. The distribution of the fluids over the aquifer is given as initial information, and the value of the specific weight γ and the dynamic viscosity μ is known as a function of position.

The geometry of the pore space is the same, irrespective of the prevailing fluid; therefore, the specific permeability k is identical over the entire field. Both fluids obey Darcy's law while flowing through the porous medium, as all velocities remain in the laminar region.

For the derivation of the formulas the transition zone between two fluids will be considered. Such a zone exists between two miscible fluids. To simplify the mathematical treatment of a special case, which will serve as a demonstration of the method, the transition zone will be reduced to an abrupt interface. Such an interface will not occur in reality, because of effects of dispersion and miscibility. Changes in permeability created by entrapment of fluids and pressure jumps resulting from surface tension differences, both occurring with immiscible fluids, will be ignored in this study. For the sake of simplicity only the two-dimensional case will be treated here, because the third dimension adds no important differences.

Two basic assumptions are inherent in the following derivation. One is that there shall be continuity of incompressible fluids; thus, no

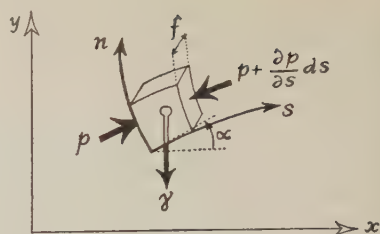


Fig. 1. Coordinate system.

gaps can exist in either fluid or at the interface. The second is that the pressure distribution in the interior of the system shall be continuous. This condition, in which the occurrence of steps in pressure is avoided, is dictated by equilibrium conditions.

It is convenient to consider only those variables which possess magnitudes to be determined independently of the fluid properties. The variables are pressure in the fluid p and specific discharge q (q is ϵ times the mean velocity \bar{v} of the liquid, where ϵ is porosity).

To relate p and q , the forces which drive the fluid through the ground will be equated to the resistance offered by the pore system. Consider in a vertical section of a two-dimensional aquifer of thickness f , a small cube ($ds\ dn\ f$), where s is arc length along an arbitrary but fixed curve, n is the perpendicular to that curve, and α is the direction to the horizontal x coordinate (Fig. 1).

The force acting on the fluid in the s direction consists of a pressure component

$$-(\partial p / \partial s) ds\ dn\ f$$

and a gravity component

$$-\gamma (\partial y / \partial s) ds\ dn\ f$$

By Darcy's law this force is counteracted by a resistance offered by the pore system, which is proportional to q_s , the s component of q . This requires a driving force of magnitude

$$+(\mu / k) q_s ds\ dn\ f$$

The equation for these three forces, after division by the elementary volume, is

$$(\mu / k) q_s = -(\partial p / \partial s) - \gamma (\partial y / \partial s) \quad (1)$$

Similarly, in the n direction

$$(\mu / k) q_n = -(\partial p / \partial n) - \gamma (\partial y / \partial n) \quad (2)$$

the two requirements mentioned above can be written in terms of the variables \mathbf{q} and p . The condition of continuity requires that

$$\text{div } \mathbf{q} = (\partial q_s / \partial s) + (\partial q_n / \partial n) \quad (3)$$

the condition of equilibrium requires that p be a single-valued function containing no jumps. This may be written in two ways:

$$\partial^2 p / \partial s \partial n - (\partial^2 p / \partial n \partial s) = 0$$

$$\text{or } \oint_S (\partial p / \partial s) ds = 0 \quad (4)$$

The contour integral applies to any closed contour S .

Solution with vortices. If the objective is the determination of the discharge \mathbf{q} , it is convenient to introduce a stream function Ψ , whose derivatives are the components of \mathbf{q} according to

$$(\partial \Psi / \partial n) = -q_s, \quad (\partial \Psi / \partial s) = +q_n \quad (5)$$

Ψ is merely a function which generates the specific discharge without the material properties or μ being involved. Therefore, its influence on the fluid motion is equivalent to whatever fluid is present and may therefore be considered to be related to the hypothetical fluid.

Introduction of (5) into the continuity equation (3) shows that

$$-(\partial^2 \Psi / \partial n \partial s) + (\partial^2 \Psi / \partial s \partial n) = 0 \quad (6)$$

which implies that Ψ is a single-valued function without jumps.

The condition of equilibrium may be used in the contour integral form of (4). Writing (1) as a similar contour integral results in

$$\oint_S (\mu/k) q_s ds = \oint_S (\partial p / \partial s) ds + \oint_S \gamma (\partial y / \partial s) ds$$

Substituting for q_s with (5) and using (4) reduces this to

$$\oint_S (\mu/k) (\partial \Psi / \partial n) ds = \oint_S \gamma (\partial y / \partial s) ds \quad (7)$$

The contour integrals in this equation may be replaced by surface integrals by use of Green's theorem, which in two dimensions has the form

$$\begin{aligned} \oint_S V \frac{\partial W}{\partial n} ds &= - \iint_A \left(\frac{\partial V}{\partial x} \frac{\partial W}{\partial x} + \frac{\partial V}{\partial y} \frac{\partial W}{\partial y} \right) dx dy \\ &\quad - \iint_A V \nabla^2 W dx dy \end{aligned}$$

The surface integral extends over the whole area A enclosed by the contour S . If the quantities V and W , which represent any two functions of x and y , are applied to the Ψ term of equation 7 with $V = \mu$ and $W = \Psi$,

$$\begin{aligned} \oint_S \frac{\mu}{k} \frac{\partial \Psi}{\partial n} ds &= - \frac{1}{k} \iint_A \left(\frac{\partial \mu}{\partial x} \frac{\partial \Psi}{\partial x} + \frac{\partial \mu}{\partial y} \frac{\partial \Psi}{\partial y} \right) dx dy \\ &\quad - \frac{1}{k} \iint_A \mu \nabla^2 \Psi dx dy \quad (8) \end{aligned}$$

To apply Green's theorem to the γ term of (7) it is necessary to convert $\partial y / \partial s$ into an expression involving the partial derivation of n . As s and n are perpendicular in such a way that n makes the same angle with y as x makes with s , $\partial y / \partial s$ is equal to $-\partial x / \partial n$. Therefore the γ term of (7) becomes, with $V = \gamma$ and $W = x$,

$$\begin{aligned} - \oint_S \gamma \frac{\partial x}{\partial n} ds &= + \iint_A \left(\frac{\partial \gamma}{\partial x} \frac{\partial x}{\partial x} + \frac{\partial \gamma}{\partial y} \frac{\partial x}{\partial y} \right) dx dy \\ &\quad + \iint_A \gamma \nabla^2 x dx dy \quad (9) \end{aligned}$$

This reduces to $\iint_A (\partial \gamma / \partial x) dx dy$ because $(\partial x / \partial x) = 1$ and $(\partial x / \partial y) = \nabla^2 x = 0$.

Combining (7), (8), and (9) results in, for any small area A , i.e., for every point of the interior,

$$\nabla^2 \Psi = - \frac{k}{\mu} \frac{\partial \gamma}{\partial x} - \frac{1}{\mu} \left(\frac{\partial \mu}{\partial x} \frac{\partial \Psi}{\partial x} + \frac{\partial \mu}{\partial y} \frac{\partial \Psi}{\partial y} \right) \quad (10)$$

This is known in potential theory to represent a singularity of vorticity ω .

$$\omega = - \frac{k}{\mu} \frac{\partial \gamma}{\partial x} - \frac{1}{\mu} \left(\frac{\partial \mu}{\partial x} \frac{\partial \Psi}{\partial x} + \frac{\partial \mu}{\partial y} \frac{\partial \Psi}{\partial y} \right) \quad (11)$$



Fig. 2. Vortices on interface between two fluids ($\gamma_1 < \gamma_2$), clockwise rotating in points where γ increases in x direction.

The first term on the right side represents the tendency of an interface between two fluids of different specific weight to rotate toward the horizontal position in such a way that the heavier fluid underlies the lighter fluid. This is clarified in Figure 2, where the heavier fluid γ_2 , represented by the darker area, is to the right of the lighter fluid γ_1 . Here $(\partial\gamma/\partial x)$ is positive. At all points of the transition zone between the two fluids, vorticity of negative sign exists, which, according to potential theory, imposes clockwise rotation.

The second term on the right side of (11) describes the vorticity caused by differences in viscosity of the two fluids. For simplicity in the subsequent treatment it is convenient to consider only those cases in which the gravity term dominates the viscosity term. A comparison of their respective contribution to the vorticity may be made by writing (11) as

$$\omega = -\frac{k\gamma}{\mu} \frac{\partial \ln \gamma}{\partial x} - \left(\frac{\partial \ln \mu}{\partial x} q_y - \frac{\partial \ln \mu}{\partial y} q_x \right)$$

In the study of problems of sea water intrusion the properties of fresh water (fluid 1) and salt water (fluid 2) are given approximately by the ratios

$$\gamma_2/\gamma_1 = 1.025 \quad \mu_2/\mu_1 = 1.070$$

The components of the gradients $(\partial \ln \gamma/\partial x)$, $(\partial \ln \mu/\partial x)$, $(\partial \ln \mu/\partial y)$ are therefore of the same order of magnitude, and the relative importance of the terms depends on the magnitude of q with respect to the value of $(k\gamma/\mu)$.

Now $(k\gamma/\mu)$ is the specific discharge for head gradient of 1. In general, such high discharge velocities are not present; in problems of sea water intrusion, gradients in head will be of the order of $(\gamma_2 - \gamma_1)/\gamma_1$, which are small with respect to 1. Therefore, an analysis in which the viscosity differences are ignored is justified in such problems. Because, however, the magnitude of the terms also depends on the orientation of the interface with respect to the horizontal and the vector q , it should be verified that their relative importance is not changed because of the sine of the angles involved.

In those cases in which the variation of μ may be disregarded, equation 11 reduces to

$$\nabla^2 \Psi = -(k/\mu)(\partial\gamma/\partial x) \quad (12)$$

Since the distribution of γ is known, the right hand side of (12) is a known function of position and this relation for Ψ is of the type called Poisson's equation, whose solution in terms of vortices is known from potential theory. The solution can be written as

$$\Psi = -\iint_A (k/2\pi\mu)(\partial\gamma/\partial x) \ln r \, dA \quad (13)$$

where r is the distance between the point of consideration and the point where the vortex of strength $-(k/\mu)(\partial\gamma/\partial x)$ is present. Integration has to be effected over all vortices, i.e., the entire area A , where $(\partial\gamma/\partial x) \neq 0$.

Ψ is regular in the entire field and also at point containing a vortex. This is true because although $\ln r$ becomes infinite for r approaching zero, the product $\ln r \cdot dA$ reduces to zero, since dA is of the order of r^2 .

The magnitude of the vortex at a point of the field depends only on the change in properties of the fluids present at that point. The number of fluids involved in the problem is of no importance, and the method is therefore suitable for computing the flow of several fluids and the zones of gradual transition between them.

Treatment of vortices by complex potential. To adapt this flow problem to a treatment by complex variables the stream function Ψ may be combined with an auxiliary function Φ , so that

$$\frac{\partial \Phi}{\partial s} = \frac{\partial \Psi}{\partial n} = -q_s; \quad \frac{\partial \Phi}{\partial n} = -\frac{\partial \Psi}{\partial s} = -q_n \quad (14)$$

the condition of continuity (3) then gives

$$\nabla^2 \Phi = 0 \quad (15)$$

and from the condition of equilibrium, which has already resulted in (12), it follows that

$$\begin{aligned} \partial^2 \Phi / \partial s \partial n - \partial^2 \Phi / \partial n \partial s &= \nabla^2 \Psi \\ &= -(k/\mu)(\partial \gamma / \partial x) \end{aligned} \quad (16)$$

Equation 16 shows that Φ is not single-valued and therefore has no particular physical meaning. However, the complex combination, to be called 'complex specific discharge potential,'

$$\Omega = \Phi + i\Psi \quad (17)$$

is convenient because the solution (13) can be written as a function of the complex variables $z = x + iy$, as follows:

$$\begin{aligned} \Omega &= (-ik/2\pi\mu) \\ &\cdot \iint_A (\partial \gamma / \partial x)_{z_0} \ln(z - z_0) dA \end{aligned} \quad (18)$$

where z is the point of consideration and z_0 the point containing the vortex. The integration extends over all points z_0 , where $\partial \gamma / \partial x \neq 0$.

The expression (18) gives the correct value for Ψ , since $\ln(z - z_0)$ can be separated into real and imaginary parts as $[\ln r + i\theta]$, where r is the distance between z and z_0 and θ the angle with the horizontal. Therefore, $\ln r$ appears in the imaginary part of Ω in the same way as in (13). The real part of Ω consists of the angles θ and is therefore many-valued. This many-valuedness, however, only reflects on the auxiliary function Φ .

From Ω the movement of the fluid is obtained as the complex specific discharge \bar{q} by taking the derivative with respect to z , because

$$\begin{aligned} \bar{q} = q_x - iq_y &= -\frac{\partial \Phi}{\partial x} - i \frac{\partial \Psi}{\partial x} \\ &= -\frac{d\Omega}{dz} \cdot \frac{\partial z}{\partial x} = -\frac{d\Omega}{dz} \end{aligned} \quad (19)$$

The kind of fluid present at the point z is irrelevant in this computation.

Although Φ is many-valued, its derivatives are single-valued and constitute no difficulties for the determination of \bar{q} . Since the discharge is the objective of the study, the awkwardness of the auxiliary function Φ is of no importance in

the analysis. The expression (18) for Ω and its derivative are therefore usable instruments in the analysis and give correct answers for every point in the entire field, even though the point contains vorticity.

Vortices on an abrupt interface. An abrupt interface may be considered to be the degeneration of a transition zone between two fluids of specific weight γ_1 and γ_2 , respectively. The gradient of γ in the zone tends to infinity as the thickness of the zone approaches zero in such a way that in the limit

$$\lim_{dn \rightarrow 0} (\partial \gamma / \partial n) dn = -(\gamma_2 - \gamma_1) \quad (20)$$

Let s be the coordinate along the interface, and n the normal; then the elementary length ds of the interface corresponds to an area $dA = ds dn$ (shaded part of Fig. 3). The contribution to the complex potential created by this part of the interface is

$$d\Omega = (-ik/2\pi\mu)(\partial \gamma / \partial x)_{z_0} \ln(z - z_0) ds dn$$

where z_0 is the complex coordinate of the center of the area.

If α is the angle of ds with the horizontal x axis, $(\partial \gamma / \partial x)$ is equal to $-\sin \alpha (\partial \gamma / \partial n)$. By use of (20) the complex potential becomes

$$\begin{aligned} d\Omega &= (-ik/2\pi\mu)(\gamma_2 - \gamma_1) \\ &\cdot [(\sin \alpha)_{z_0} \ln(z - z_0) ds] \end{aligned}$$

The term between brackets varies along the interface, so that the complex potential originated by the whole interface is given by

$$\begin{aligned} \Omega &= (-ik/2\pi\mu)(\gamma_2 - \gamma_1) \\ &\cdot \int_s (\sin \alpha)_{z_0} \ln(z - z_0) ds \end{aligned} \quad (21)$$

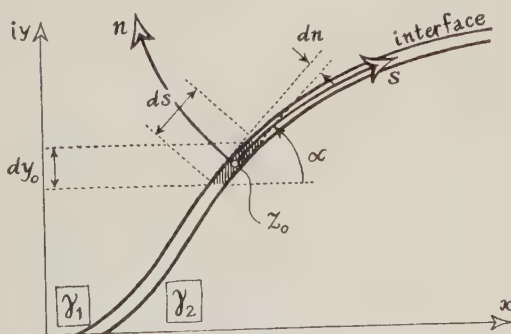


Fig. 3. Interface of infinitesimal thickness dn .

The integral is a line integral running along a line S , which coincides with the interface; the distance ds represents an incremental length along this line and z_0 is any point on the interface. The interface can be represented as a vortex sheet composed of vortex lines. The intersection of this interface with the x, iy plane, which is perpendicular to it, is the line S . As $(\sin \alpha)_s ds$ is equal to dy_0 , the vertical component of ds (see Fig. 3), the strength of the vortex contained in ds is equal to

$$\omega ds = (k/\mu)(\gamma_2 - \gamma_1) d\mu_0 \quad (22)$$

and the complex specific discharge potential may be simplified to

$$\Omega = (-ik/2\pi\mu)(\gamma_2 - \gamma_1)$$

$$\int_S \ln(z - z_0) dy_0 \quad (23)$$

Treatment of a boundary value problem. The foregoing introduction of the stream function Ψ permits the solution of boundary value problems. Besides the knowledge of conditions along the boundary, the position of the interface between the fluids also has to be known in order to specify Ψ over the entire field. Then the motion of the fluids can be derived for a time interval short enough to neglect the displacement of the interface. From the motion of the fluids the movement of the interface, and subsequent positions, each having a different flow pattern, can be determined.

For the computation of Ψ at a given moment it is convenient to treat the influence of the conditions along the boundaries and the velocity created by the interface separately. The superposition principle allows the addition of the particular solutions afterwards.

The boundary conditions are generally given in terms of pressures or discharges. Let s be a coordinate running along the boundary with n perpendicular to it.

If the boundary condition consists of discharge, the component q_n is known, and, from equation 5, $(\partial\psi/\partial s)$ is determined. Integration along s gives the value Ψ for every point along such a boundary.

If the boundary condition consists of pressure, it is possible to determine q_s along that boundary with (1), since p, γ, y are known functions of the coordinate s . The knowledge of q_s , with (5), gives $(\partial\Psi/\partial n)$.

Once the boundary conditions are translated in terms of the stream function Ψ , the solution of the problem can proceed as follows. The actual solution Ψ is broken down into two parts to be called I and II , respectively.

$$\Psi = \Psi_I + \Psi_{II} \quad (24)$$

Part I takes care of the vortices

$$\nabla^2 \Psi_I = -(k/\mu)(\partial\gamma/\partial x) \quad (25)$$

with the solution (13). From this solution the values of Ψ_I and $(\partial\Psi_I/\partial n)$ can be computed along the boundaries. In general, these values will not coincide with the boundary values Ψ or $(\partial\Psi/\partial n)$ required in the problem. The differences $(\Psi - \Psi_I)$ and $[(\partial\Psi/\partial n) - (\partial\Psi_I/\partial n)]$ then constitute new boundary conditions which can be satisfied by part II of the solution.

The quantity Ψ_{II} must satisfy the deficiencies of part I at the boundaries and

$$\nabla^2 \Psi_{II} = 0 \quad (26)$$

over the entire field. The determination of Ψ_{II} constitutes a boundary value problem, with a unique solution to be obtained by known methods of potential theory.

The addition of (25) and (26) shows that the superposition $(\Psi_I + \Psi_{II})$ satisfies the requirement (12). It will prove convenient to use image vortices of opposite sign in order to create values of $\Psi_I = \text{constant}$ along impermeable boundaries so that, for part II of the solution also, these boundaries remain impermeable.

The shear flow at an abrupt interface. A sheet with singularities is known to contain discontinuities. Instead of showing this by evaluating the principal Cauchy value of the integral expression in (23) as the interface is approached from either side, a shorter presentation may be given, using equation 12 as a starting point. Gauss's gradient theorem applied to Ψ for a small rectangle $dsdn$ straddling the interface gives, for a vanishingly small width of dn ,

$$\iint \nabla^2 \Psi ds dn = \int (\partial\Psi/\partial n_1) ds_1 + \int (\partial\Psi/\partial n_2) ds_2 \quad (27)$$

where n_1 and n_2 are the normals to the faces ds_1 and ds_2 pointing toward the exterior of the rectangle. These coordinates are related to n

th a direction (Fig. 3) according to

$$+n = +n_1 \quad +n = -n_2$$

om the surface integral of (12) and the re-
sults of the abrupt interface analysis it follows
at

$$\left[\left(\frac{\partial \Psi}{\partial n} \right)_1 - \left(\frac{\partial \Psi}{\partial n} \right)_2 \right] ds = -\frac{k}{\mu} \iint \frac{\partial \gamma}{\partial x} ds \, dn$$

$$= -\frac{k}{\mu} (\gamma_2 - \gamma_1) \int \sin \alpha \, ds$$

s this applies to any portion of the line s ,
may be written, using (5), as

$$q_{s1} - q_{s2} = (k/\mu)(\gamma_2 - \gamma_1) \sin \alpha \quad (28)$$

his relation shows that there is a disconti-
nuity in discharge parallel to the interface. It
a function of the inclination α and the differ-
ence in specific weights of the fluids on either
le.

The discontinuity is restricted to the dis-
charge parallel to the interface. Perpendicular
it the discharge is continuous, because other-
wise a gap in the fluids would occur and would
olate the continuity principle; hence

$$q_{n1} = q_{n2} \quad (29)$$

he continuous part of the discharge, however,
not restricted to the normal direction. Super-
posed on the discontinuous discharge there
ay be a continuous component parallel to the
interface.

The discontinuous component of the discharge
 q_a in Fig. 4) is created by the vortex at the
point of consideration on the interface. The
continuous component q_o , which can have any
direction with respect to the interface, is created
by all the vortices outside the point of consid-
eration and outside the boundary conditions.

The normal component q_n is responsible for
an advance of the interface, which, for com-
plete displacement of one fluid by the other, is
equal to the mean velocity q_n/ϵ .

Solution with sources and sinks. In problems
of irrotational flow the pressure in the fluid can
be determined from the potential function,
which is defined in the same way as Φ is defined
by (14). Since, however, in this case, Φ is many-
valued, it is an unsuitable function for the deter-
mination of the pressure. If the pressures
are the objective of the study, it is therefore

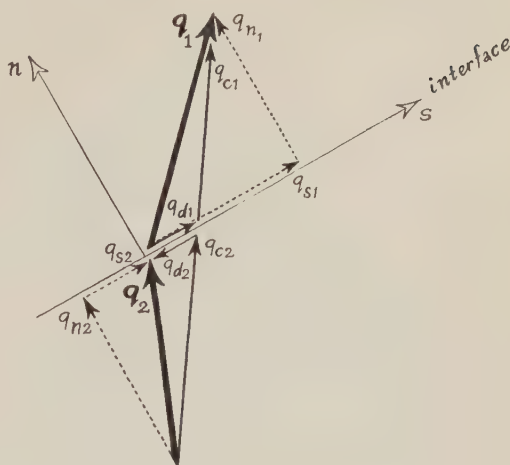


Fig. 4. Discharge discontinuity at an interface.

convenient to introduce a quantity which has
the character of Φ but does not have its many-
valuedness. Let this quantity be called Θ , the
multiple fluid potential, and be defined as

$$(\mu/k)\Theta = p + \gamma y \quad (30)$$

where the values of p , γ , y are those of the
point under consideration. Since all these quan-
tities are single-valued also, Θ is a single-valued
function of position in the entire field.

Taking the derivative in an arbitrary direc-
tion s , it follows for $\mu = \text{constant}$ that

$$(\mu/k)(\partial\Theta/\partial s) = (\partial p/\partial s) + \gamma(\partial y/\partial s)$$

$$+ y(\partial\gamma/\partial s)$$

Application of (1) reduces this to

$$(\mu/k)q_s = -(\mu/k)(\partial\Theta/\partial s) + y(\partial\gamma/\partial s)$$

which may be written

$$(\mu/k)\mathbf{q} = -(\mu/k) \text{grad } \Theta + y \text{grad } \gamma \quad (31)$$

since s is any direction. A comparison with (14)
shows that the relation between Θ and Φ is

$$\text{grad } \Phi = \text{grad } \Theta - (k/\mu)y \text{grad } \gamma \quad (32)$$

where the last term takes care of the many-
valuedness, so that Θ can be single-valued in the
entire field, including the region of vorticity. At
the points, where $\text{grad } \gamma$ is zero, i.e., the points
of no vorticity, the quantities Φ and Θ are the
same.

Application of the condition of continuity (3)
to (31) gives

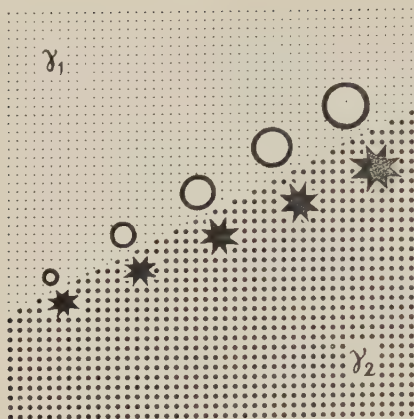


Fig. 5. Doublets on interface between two fluids ($\gamma_1 < \gamma_2$). Doublet strength increases with height of position.

$$\operatorname{div} \mathbf{q} = -\nabla^2 \Theta + (k/\mu) \operatorname{div} [y \operatorname{grad} \gamma] = 0 \quad (33)$$

This is a Poisson's equation showing singularities in Θ of magnitude $(k/\mu) \operatorname{div} [y \operatorname{grad} \gamma]$. Since Θ has the character of a potential in the hypothetical fluid, the singularities may be termed sources for negative and sinks for positive values of their magnitude.

Application of the condition of equilibrium, by using the first expression of (4) and the condition that the function (γy) is single-valued, gives

$$\partial^2 \Theta / \partial s \partial n = \partial^2 \Theta / \partial n \partial s$$

which confirms the single-valuedness of Θ . The solution for Θ can be written in analogy to (13):

$$\Theta = (k/2\pi\mu) \iint_A \operatorname{div} [y \operatorname{grad} \gamma] \ln r \cdot dA \quad (34)$$

Again Θ can be combined with an auxiliary function having the character of a stream function in order to form a complex potential. In this case the stream function is many-valued and unsuitable for the determination of the discharges, but it reduces to Ψ for points of no vorticity. The sources and sinks can be expressed in terms of the complex potential by replacing $\ln r$ in (34) by $\ln(z - z_0)$.

Doublets on an abrupt interface and boundaries. That the expression $\operatorname{div} [y \operatorname{grad} \gamma]$ reduces to a doublet layer if the transition zone reduces to an abrupt interface (Fig. 5), is recognized as

follows. Consider a line n perpendicular to the interface pointing from the γ_2 fluid to the γ_1 fluid (Fig. 3). At the point of intersection with the interface, y is a constant y_0 , and the source distribution is $y_0 \operatorname{div} \operatorname{grad} \gamma = y_0 \nabla^2 \gamma$. Since γ varies in the n direction only, $\nabla^2 \gamma$ is equal to $\partial^2 \gamma / \partial n^2$. Let the interface consist of two infinitesimal bands of width dn at a mutual distance δ'' . Let $(\partial \gamma / \partial n)$ in the region between the bands be constant and equal to $-(\gamma_2 - \gamma_1) / \delta''$, and let $(\partial^2 \gamma / \partial n^2) dn$ in the two bands be equal to $\pm (\gamma_2 - \gamma_1) \delta''$. Then the value of γ will indeed decrease from γ_2 to γ_1 in the region of the interface.

The quantity (34) then becomes

$$\begin{aligned} \Theta &= (k/2\pi\mu) \iint y_0 (\partial^2 \gamma / \partial n^2) (\ln r) dn ds \\ &= [k(\gamma_2 - \gamma_1) / 2\pi\mu \delta''] \\ &\quad \cdot \int_s y_0 [+ \ln r_1 - \ln r_2] ds \end{aligned} \quad (35)$$

where r_1 and r_2 are the distances from the point of consideration to the two sides of the interface. This expression describes a source and a sink at either side of the mutual distance δ'' , their strength being equal to $d\kappa'' = [k(\gamma_2 - \gamma_1) / \mu \delta''] y_0 ds$. If δ'' is allowed to shrink to zero, the $[\ln r]$ term becomes $[\delta'' / r] \cos \phi$, ϕ being the angle between n and the radius r to the point under consideration. This is known to be the potential of a doublet oriented perpendicularly to the interface. The expression (35) therefore represents a doublet layer, containing a doublet of strength.

$$d\lambda'' = \delta'' \cdot d\kappa'' = [k(\gamma_2 - \gamma_1) / \mu] y_0 ds \quad (36)$$

for each line segment ds of the interface.

For the determination of boundary value problems the solution can again be broken down into two parts, Θ_I and Θ_{II} , where Θ_I accounts for the sources and sinks and Θ_{II} satisfies the deficiencies at the boundaries. For boundaries with known pressure, the value of Θ can be computed with (30). For boundaries with discharge information, the value of q_n is known, and from (31) the value of $(\partial \Theta / \partial n)$ can be determined, since $(\partial \gamma / \partial n)$ can be obtained from the γ distribution, which is assumed to be available as initial information. Since either Θ or $(\partial \Theta / \partial n)$ is known along the boundaries, Θ_I

and Θ_{II} can be evaluated with the usual methods of potential theory.

PART 2. MATHEMATICAL EXAMPLE AND EXPERIMENTAL VERIFICATION

Introduction. The application of the foregoing basic results may be demonstrated by an example of a two-fluid system enclosed by impermeable boundaries on all sides. By this disposition the movement of the fluids is due exclusively to the weight differences of the fluids and can be computed by use of the singularity method.

This example is treated mathematically, with the result that the movement of every point in the entire field is given. Since the distribution of the movements is the objective here, the treatment with vortices will be used. From the movements obtained as the solution the initial displacement of the interface can be derived. The subsequent rotation of the interface in course of time cannot be computed rigorously, but an approximate evaluation of the rotation of the center part is developed.

As the singularities permit the application of electric resistance analog models, the potential and streamlines for the same example were determined by the method of electric analogy. In addition to this verification, parallel plate model tests were run in order to obtain photographs of the streamlines traced by particles in the fluids. Both verifications are treated.

Given conditions for the mathematical example. The example consists of a two-fluid system contained in a confined infinite aquifer of thickness $2c$ (Fig. 6). The interface has, at time $t = 0$, a vertical position BME , and it rotates in a clockwise direction from there under the influence of the differences in specific weight of the fluids at either side (fluid 1 is considered to be lighter than fluid 2).

From the two parts of the solution (equation 24), the first part, corresponding to the vortices along the interface, will include images which provide a flow parallel to the boundaries. The second part of the solution then has to satisfy $\nabla^2 \Psi_{II} = 0$ in the interior and $\Psi_{II} = \text{constant}$ along all the boundaries. From potential theory it is known that Ψ_{II} must be constant if it is to satisfy these conditions. If the arbitrary value zero is assigned to the constant, the solution

consists only of the first part, and the suffix I may be omitted in the subsequent treatment.

Movement of the entire field at $t = 0$. Instead of computing Ω from the vortices in the $z = x + iy$ plane of Figure 6, it is more convenient first to introduce a transformation in order to obtain a simpler arrangement of the images than to work with the infinite series necessitated in the z plane. By the transformation function,

$$z = (2c/\pi) \ln \zeta \quad (37)$$

the infinite strip of Figure 6, is mapped into the half plane corresponding to positive real values of $\zeta = \xi + i\eta$ (Fig. 7). The boundaries are mapped into one vertical line, the η axis AF . The interface is transformed into a half circle BME with radius 1. Fluid 1 occupies the region of the half plane inside the circle and fluid 2 the rest of the half plane outside the circle. The images are located on the left half circle BNE and have the opposite sign, in order to make AF an impermeable boundary.

The subscript zero will indicate that the interface is concerned. A line segment dz_0 of the interface contains, according to (22), a vortex of strength

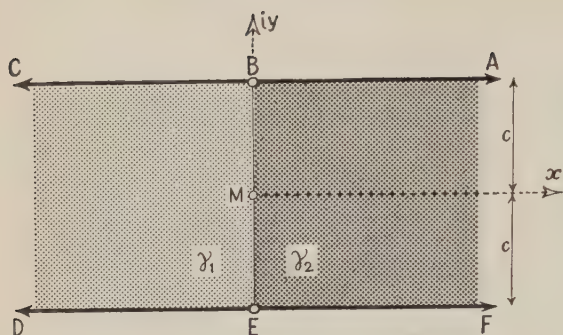
$$(k/\mu)(\gamma_2 - \gamma_1) dy_0 \quad (38)$$

Therefore the vortex strength associated with the line segment dy_0 has to be applied in the transformed field to the line segment $d\zeta_0$ which is the image of dy_0 . Since $x_0 = 0$ is the equation for the interface, a line segment dz_0 is equal to $dx_0 + idy_0 = idy_0$. Application of the transformation (37) gives

$$dz_0 = i dy_0 = (2c/\pi) \zeta_0^{-1} d\zeta_0 \quad (39)$$

which represents dy_0 as a function of ζ_0 . The strength of the vortex associated with the line segment $d\zeta_0$ of the transformed interface is therefore, according to (38) and (39), $[2ck(\gamma_2 - \gamma_1)/i\pi\mu\zeta_0]d\zeta_0$. The complex specific discharge potential in the ζ plane is the integral of the influences of these elementary vortices, each of which is a contribution to the potential of magnitude $d\Omega = (i/2\pi) \ln(\zeta - \zeta_0)$ times the vortex strength in ζ_0 . This gives

$$\Omega(\zeta)_{\text{(vortex part)}} = -\frac{i}{2\pi} \frac{2ck(\gamma_2 - \gamma_1)}{i\pi\mu} \int_{EMB} \ln(\zeta - \zeta_0) \frac{d\zeta_0}{\zeta_0} \quad (40)$$

Fig. 6. Infinite confined aquifer in z plane.

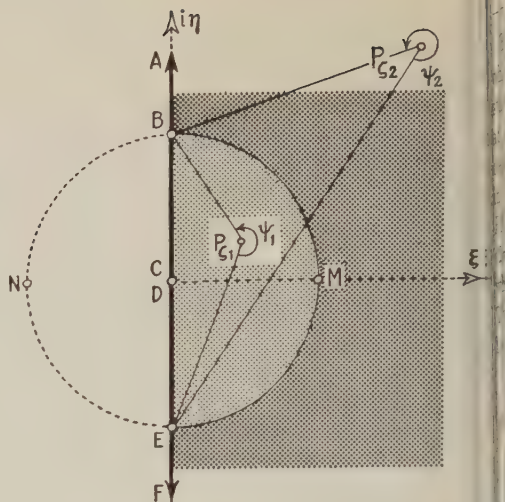
The integration extends over the values of ξ_0 along the half circle EMB , counterclockwise.

The image vortices have opposite sign and the path of integration is the half circle BNE , counterclockwise. If the direction of integration is inverted, a second sign inversion is obtained, giving a value for $\Omega(\xi)$ of the image part, which has the same sign as (40). The result after addition is

$$\begin{aligned}\Omega(\xi)_{\text{total}} &= \Omega(\xi)_{\text{vortices}} + \Omega(\xi)_{\text{images}} \\ &= -\frac{ck(\gamma_2 - \gamma_1)}{\pi^2 \mu} \\ &\quad \cdot \left[\int_{EMB} \ln(\xi - \xi_0) \frac{d\xi_0}{\xi_0} \right. \\ &\quad \left. + \int_{ENB} \ln(\xi - \xi_0) \frac{d\xi_0}{\xi_0} \right] \quad (41)\end{aligned}$$

This integral has no solution in closed form, and, since the aim of the computation is the movement of the fluid, the specific discharge might as well be introduced at this moment because it facilitates the evaluation of the integral. The specific discharge, according to (19), is obtained by a differentiation, and, since it is permissible here to carry this out under the integral sign, (41) yields

$$\bar{q} = -\frac{d\Omega(\xi)}{d\xi} \frac{d\xi}{dz} = -\frac{d\Omega(\xi)}{d\xi} \frac{\pi}{2c} \xi$$

Fig. 7. Transformed infinite confined aquifer in ξ plane.

$$\begin{aligned}&= +\frac{k(\gamma_2 - \gamma_1)}{2\pi\mu} \left[\int_{EMB} \frac{\xi d\xi_0}{(\xi - \xi_0)\xi_0} \right. \\ &\quad \left. + \int_{ENB} \frac{\xi d\xi_0}{(\xi - \xi_0)\xi_0} \right] \quad (42)\end{aligned}$$

Now integration with respect to ξ_0 gives the solution

$$\begin{aligned}\bar{q} &= +\frac{k(\gamma_2 - \gamma_1)}{2\pi\mu} \{ [\ln \xi_0 - \ln(\xi - \xi_0)]_{EMB} \\ &\quad + [\ln \xi_0 - \ln(\xi - \xi_0)]_{ENB} \} \quad (43)\end{aligned}$$

The real part, the x component of the specific discharge, is obtained from $\ln |\xi_0|$ and $\ln |\xi - \xi_0|$, corresponding to the limits B and E . As the interface circle has radius 1, $\ln |\xi_0| = 0$ and

$$q_x = -\frac{k(\gamma_2 - \gamma_1)}{\pi\mu} \cdot \ln \left| \frac{BP_\xi}{EP_\xi} \right| \quad (44)$$

remains. Here P_ξ is the point in the ξ plane corresponding to the point P of consideration in the z plane. The loci of points P_ξ for which (BP_ξ/EP_ξ) is a constant are circles in which the points E and B are inverse points. These circles for equal values of q_x are shown in Figure 8. The imaginary part, the y component of the specific discharge, is obtained from angle (ξ_0) and angle $(\xi - \xi_0)$. The first of these two is the angle swept by the vector ξ_0 , with starting point at the origin, as its end point traces the half circle EMB and ENB . The angles are $+\pi$ and

$-\pi$, respectively, which cancel each other.

There remains, therefore, the angle $(\zeta - \zeta_0)$, which is the angle swept by the vector with starting point on the half circle and end point at the point P_f . The total value of this angle depends on the location of P_f . If P_f is located in fluid 1, the paths of integration BME and BNE pass on either side, giving $(-\psi_1)$ and $(2\pi - \psi_1)$ for the angle swept, respectively, where ψ_1 is the exterior angle EP_fB (Fig. 7). Therefore, the vertical component in fluid 1 will be

$$q_{v_1} = -\frac{k(\gamma_2 - \gamma_1)}{2\pi\mu} [-\psi_1 + (2\pi - \psi_1)] \\ = +\frac{k(\gamma_2 - \gamma_1)}{\mu} \cdot \frac{(\psi_1 - \pi)}{\pi} \quad (45)$$

If P_f is located in fluid 2, the paths of integration both pass on the left side, and the angle swept is for both $(2\pi - \psi_2)$. The vertical component in fluid 2 will therefore be

$$q_{v_2} = -\frac{k(\gamma_2 - \gamma_1)}{\mu} \cdot \frac{(2\pi - \psi_2)}{\pi} \quad (46)$$

On the interface the angles ψ_1 and ψ_2 both have the value $3\pi/2$, so the difference of the parallel discharge at either side of the interface is

$$(q_{v_1} - q_{v_2})_{(\text{interface})} = (k/\mu)(\gamma_2 - \gamma_1) \quad (47)$$

which is the value expected for the shear flow at a vertical interface ($\alpha = \frac{1}{2}\pi$) according to (28).

The expressions (45) and (46) show that on the lines of equal value for q_v the angles ψ_1 or ψ_2 are constants; these lines, therefore are arcs of circles through the points B and E (Fig. 8).

Transformed to the z plane these lines for equal q_s and q_v form the pattern of Figure 9. For each point of the aquifer the specific discharge vector can be determined from the components q_s and q_v , as is shown in Figure 10, where arrows represent the flow in magnitude and direction.

The advance of the interface dx_0/dt at the moment $t = 0$ is equal to the component of the mean velocity perpendicular to the interface; i.e., in this case, the x component of the specific discharge divided by the porosity. From (44) it follows, therefore, that

$$\frac{dx_0}{dt} = \frac{q_x}{\epsilon} = \frac{k(\gamma_2 - \gamma_1)}{\epsilon\pi\mu} \ln \left| \frac{EP_{f0}}{BP_{f0}} \right| \\ = \frac{k(\gamma_2 - \gamma_1)}{\epsilon\pi\mu} \ln \left| \frac{\zeta_0 + i}{\zeta_0 - i} \right|$$

By use of $\zeta_0 \exp(\pi z_0/2c) = \exp(i\pi y_0/2c)$ this reduces to

$$\frac{dx_0}{dt} = \frac{k(\gamma_2 - \gamma_1)}{\epsilon\pi\mu} \ln \left\{ \cot \left[\frac{\pi(c - y_0)}{4c} \right] \right\} \quad (48)$$

Figure 11 shows this velocity as a function of y_0 , an S-shaped curve which is representative of the shape of the interface a small time after $t = 0$.

Displacement of the interface at $t > 0$. As the interface turns, the shape continues to be in the form of an S which is tangent to the impermeable boundaries. For all subsequent positions a different flow pattern applies, because the vortices, which generate the flow pattern, shift position with the interface.

The determination of the advancement of the interface necessitates the computation of the specific discharge component perpendicular to the interface. Also this component changes with the shifting interface. Since an exact mathematical solution of this displacement was not obtained, a first approximation is given here, treating the rotation in the center point of a straight-lined interface.

Let the inclination of the interface with the horizontal be $\alpha = \text{arc cot } a$, so that the interface equation is

$$x_0 = y_0 \cot \alpha = ay_0 \quad (49)$$

Then a line segment dz_0 of the interface is equal to

$$dz_0 = dx_0 + i dy_0 = (a + i) dy_0 \quad (50)$$

A comparison with (39) shows the only difference to be the replacement of i by a factor $(a + i)$. The vortex strength associated with a line segment $d\zeta_0$ becomes, by similar reasoning,

$$+[2ck(\gamma_2 - \gamma_1)/(a + i)\pi\mu\zeta_0] d\zeta_0 \quad (51)$$

The image interface is given by the equation ($m = \text{integer}$)

$$x_0 = a[(4m + 2)c - y_0]$$

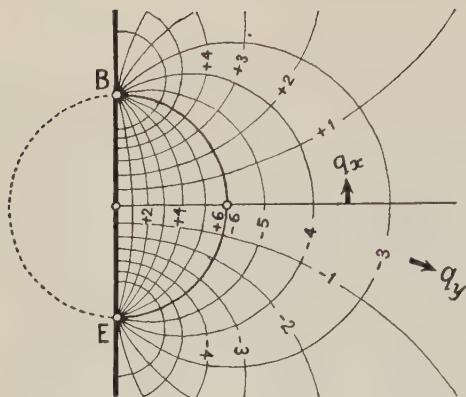


Fig. 8. Lines of constant q_x and q_y in ζ plane.
Values indicate $12 q_x \mu / k(\gamma_2 - \gamma_1)$ and $12 q_y \mu / k(\gamma_2 - \gamma_1)$, respectively.

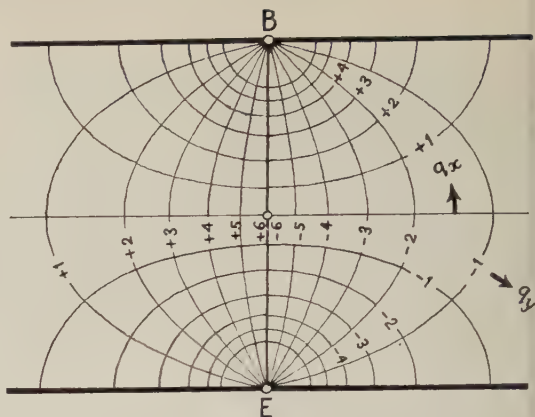


Fig. 9. Lines of constant q_x and q_y in z plane.
Values indicate $12 q_x \mu / k(\gamma_2 - \gamma_1)$ and $12 q_y \mu / k(\gamma_2 - \gamma_1)$, respectively.

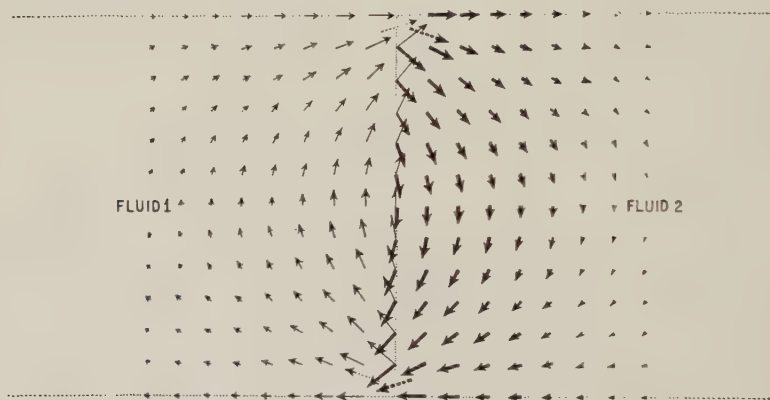


Fig. 10. Discharge vectors at time $t = 0$.

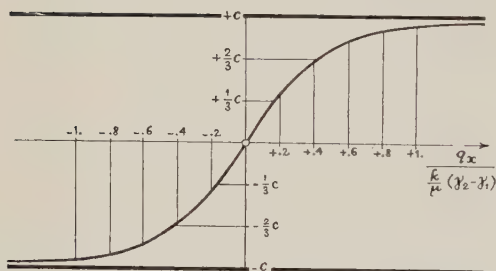


Fig. 11. Distribution of discharge perpendicular to interface.

and a line segment dz_0 of the image interface is

$$dz_0 = dx_0 + i dy_0 = -(a - i) dy_0$$

Since the image vortices have opposite signs, their strength associated with a line segment $d\zeta_0$ of the transformed image interface is

$$+ [2ck(\gamma_2 - \gamma_1) / (a - i)\pi\mu\zeta_0] d\zeta_0 \quad (52)$$

Elaboration of the complex specific discharge potential, as demonstrated previously, gives the complex specific discharge in a form similar to (43):

$$\bar{q} = \frac{k(\gamma_2 - \gamma_1)}{2\pi\mu} \left\{ \frac{i}{a + i} [\ln \zeta_0 - \ln (\zeta - \zeta_0)]_{EMB} - \frac{i}{a - i} [\ln \zeta_0 - \ln (\zeta - \zeta_0)]_{ENB} \right\} \quad (53)$$

where the minus sign for the second term between braces is due to the path inversion from BNE to ENB .

The derivation $(d\bar{q}/dz)$ represents the complex deformation of the fluid and the imaginary part of $[\epsilon^{-1}(d\bar{q}/dz) e^{2i\alpha}]$, the clockwise rotation of a line of fluid particles oriented at an angle

with the horizontal. If computed for the point $z = 0$, it represents the rotation of the interface at the center point M of the confined layer. This rotation is equal to the decrease of the interface inclination α with time, or

$$-d\alpha/dt = \epsilon^{-1} \operatorname{Im} [(d\bar{q}/dz)e^{2i\alpha}]_{z=0} \quad (54)$$

By use of (53) the result for $z = 0$ ($\xi = 1$) is

$$\frac{d\bar{q}}{dz} = \frac{d\bar{q}}{d\xi} \frac{d\xi}{dz} = \frac{k(\gamma_2 - \gamma_1)}{4\mu c} \left\{ -\frac{i}{a+i} \frac{1}{1-\xi_0} + \frac{i}{a-i} \frac{1}{1-\xi_0} \right\}_E^B$$

For the inclined interface the point B corresponds to $z_0 = (a+i)c$ and the point E to $z_0 = -(a+i)c$. Therefore, the integration limits for ξ_0 are, respectively,

$$\xi_0 = e^{\pi(a+i)c/2c} = ie^{\pi a/2c} \text{ and } \xi_0 = -ie^{-\pi a/2c}$$

and

$$\frac{d\bar{q}}{dz} = \frac{k(\gamma_2 - \gamma_1)}{2\mu c(a^2 + 1)} \left[\frac{\sinh(\pi a/2c) - i}{\cosh(\pi a/2c)} \right]$$

By introduction of $\beta = \arccot [\sinh(\pi a/2c)]$ and $a = \cot \alpha$ the expression is simplified to

$$d\bar{q}/dz = [k(\gamma_2 - \gamma_1)/2\mu c] \cdot [\sin^2 \alpha e^{-i\beta}]$$

This value for $d\bar{q}/dz$ used in equation (54) gives

$$d\alpha/dt = -[k(\gamma_2 - \gamma_1)/2\epsilon\mu c] \cdot \sin^2 \alpha \sin(2\alpha - \beta) \quad (55)$$

The right side of (55) being a function of α only, the relation between α and t may be written as

$$t[\epsilon\mu c/k(\gamma_2 - \gamma_1)] = -\int_{(1/2)\pi}^{\alpha} [1/2 \sin^2 \alpha \cdot \sin(2\alpha - \beta)] d\alpha \quad (56)$$

Because of the intricate function relating β to α , a solution of the integral is not available in closed form. The curve of Figure 12 was obtained by numerical step-by-step evaluation of (56), and it represents as the final result of this analysis the decrease of the interface inclination at the center point M with time in a first approximation.

Verification with parallel plate model. To verify the mathematical solution a parallel plate

model test was carried out, with the results as represented in the photographs (Figs. 13 and 14). These pictures show the center part of a 15×60 cm Lucite model, with a slot width of $d = 1$ mm. Since in the beginning the movement is primarily concentrated in the center part, the deviation between this model of limited length and the infinite confined aquifer treated theoretically can be disregarded.

The fluids at either side of the originally vertical interface were, to the left, a glycerine with $\gamma_1 = 1.23$ g/cm³ and, to the right, 60 to 40 per cent mixture of glycerine and phosphoric acid with $\gamma_2 = 1.40$ g/cm³. The viscosity for both fluids at 24°C was $\mu = 0.005$ g sec/cm². Since ϵ , the porosity, is 1 for a parallel plate model, the value of the half-aquifer height c is 7.5 cm, and the specific permeability is $k = d^2/12 = 8.3 \times 10^{-4}$ cm², the factor associated with t in (56) has the value

$$\epsilon\mu c/k(\gamma_2 - \gamma_1) = 265 \text{ sec}$$

The white particles showing in the photographs are flakes of gold leaf, which by their large surface-thickness ratio had a small settling velocity with respect to the motion of the fluid itself. During the 90-sec exposure time the flakes traced lines which are representative of the fluid motion. Figure 13 is therefore the experimental representation of the specific discharge vectors shown in Figure 10. The resemblance of both patterns is apparent.

Figure 13 covers the period $0 < t < 90$ sec, Figure 14 the period $120 < t < 210$ sec. According to the graph (Fig. 12), the inclination of the interface is expected to be approximately $90^\circ > \alpha > 80^\circ$ for Figure 13 and $77^\circ > \alpha > 68^\circ$ for Figure 14. In the pictures the area swept by the interface can be observed as a lighter band, covered by particle tracings of crossing directions. These cross paths are created by the shear flow at the interface and are also present in the analytically obtained flow pattern of Figure 10. In both figures the S-shaped interface predicted by Figure 11 is distinguishable, and the inclination at the center follows the computed values approximately.

Electric analogy. In the electric models, which are particularly appropriate for the plotting of potential lines and streamlines [Malavard, 1956], it is impossible to simulate differences of specific weight directly. However,

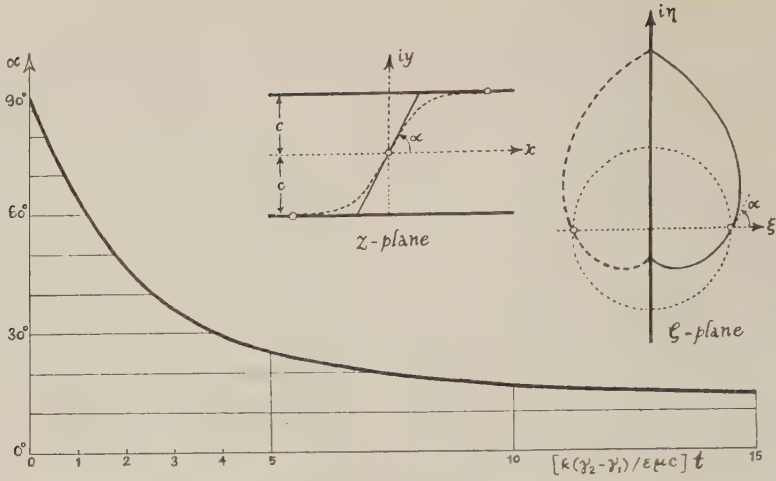


Fig. 12. Slope of rectilinear interface as a function of time.

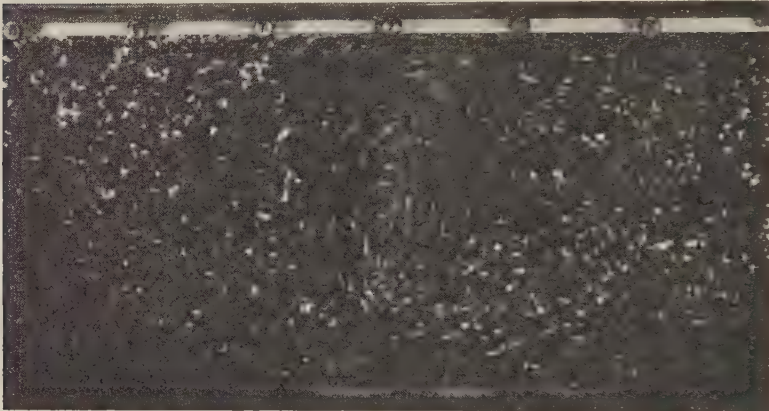


Fig. 13. Photograph of parallel plate model test, with gold leaf flakes tracing streamlines; left side light fluid, right side heavy fluid; exposure time $0 < t < 90$ sec.

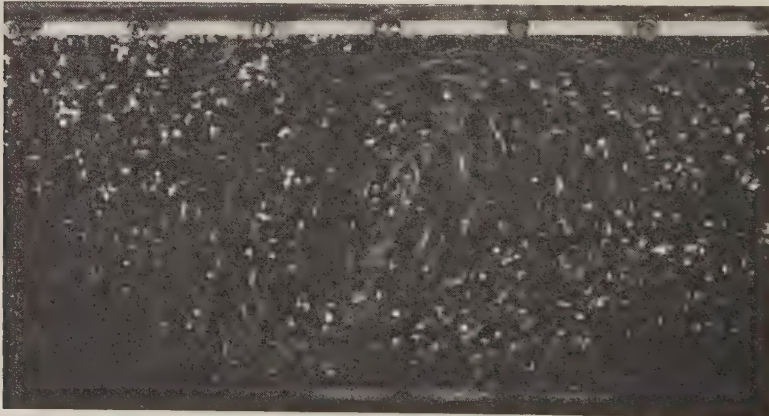


Fig. 14. Photograph of parallel plate model test of Figure 13 at a later stage; exposure time $120 < t < 210$ sec.

by the replacement of the fluids with different properties by the hypothetical fluid and the introduction of property changes by singularities, a concept is obtained which has electric analogies.

In the electric resistance model, where lines of equal electric potential can be traced, sources and sinks can be simulated by electrodes which discharge or withdraw electric current from the model. In this model the electric resistance body with homogeneous specific resistance can represent the hypothetical fluid.

If the multiple fluid potential Θ is to be determined, the strength of the source or sink in the area dA must be proportional to $(k/\mu) \text{div } [y \text{ grad } \gamma] dA$, according to (33). Lines of equal electric potential are then lines of equal Θ , and they are called potential lines. For a gradual transition zone the source-sink distribution is continuous. Exact simulation by a continuous electrode arrangement would give the correct potential lines in the entire field, including the transition zone. In practice, a discrete number of electrodes will be used, giving an eventual distortion of the potential lines. At an abrupt interface the source-sink distribution reduces to a line of doublets whose strength per line element ds , according to (36), is equal to

$$d\lambda'' = [k(\gamma_2 - \gamma_1)/\mu] y_0 ds \quad (57)$$

If the stream function Ψ is to be determined, vortices must be simulated. Actually, vortices have no analogy in the electric resistance model, but this presents no difficulties because the inverted model must be used for tracing the streamlines. With the inversion, where streamlines are simulated by electric potential lines, the vortices are inverted to sources or sinks. For the gradual transition zone the strength of the source in an area dA is $-(k/\mu) (\partial\gamma/\partial x) dA$, according to (12).

For the abrupt interface the strength for a line segment ds corresponding to an elevation increment dy_0 is, according to (22),

$$\kappa' dy_0 = (k/\mu)(\gamma_2 - \gamma_1) dy_0 \quad (59)$$

The correct streamlines would be obtained in the entire field, including a gradual transition, if the exact arrangement of continuous electrodes could be applied.

Since Θ is equal to Φ in the region outside the zone containing the singularities, and since Φ

and Ψ satisfy the Cauchy-Riemann equations (see equation 14), the Θ and Ψ lines form an orthogonal, equilateral grid in this outside region. Inside the gradual transition zone, Θ and Ψ no longer form squares because Θ is unequal to Φ , and therefore the Cauchy-Riemann relations no longer hold between Θ and Ψ .

For completeness it may be mentioned that vortices are encountered in the theory of magnetism, because any wire conducting an electric current creates a magnetic field around it, which, according to the law of Biot and Savart, obeys the same formulas as the potential around the vortex filament. To make a model in which the magnetic analogy is used is difficult from a practical standpoint. The application of boundary conditions, the determination of the flux, and the direct current necessary for the elimination of eddy current losses all create unattractive complications. The elaboration of this type of model is therefore omitted in this study.

Verification with an electric resistance analogy model. In the previous section it was demonstrated how streamlines and potential lines can be determined by means of an electric resistance analogy model. A test by this means was conducted for the vertical interface situation investigated previously by analytic and parallel plate model procedures. Conducting paper was used to simulate the porous medium. Instead of applying the continuous sink and doublet distribution as required theoretically for an abrupt interface, a limited number (10 for the half height c) was used.

For the streamline determination in the inverted model, each sink, according to (59), requires a discharge of

$$Q' = \kappa' f(c/10) = kf(\gamma_2 - \gamma_1)c/10\mu \quad (60)$$

where f is the thickness of the aquifer.

The electric current I flowing through the electric model of thickness f_e is considered representative of the discharge flowing through the aquifer of thickness f . Ohm's law for the current flowing through a stream channel of breadth b , perpendicular to the potential gradient (dE/ds) , with ρ the specific electric resistivity, gives $I = -(bf_e/\rho) (dE/ds)$.

With (5) the discharge through a breadth b in the hydraulic case is $Q = -bf (\partial\Psi/\partial n)$. Because of the inversion d/ds is similar to d/dn ,

and the relation between model and aquifer is

$$(f_e E / \rho) [\text{amperes}] \rightarrow f \Psi [\text{cm}^3 / \text{sec}] \quad (61)$$

The intervals for the streamlines $\Delta \Psi$ were chosen at the arbitrary value of

$$\Delta \Psi = k(\gamma_2 - \gamma_1)c/20\mu \quad (62)$$

By (61), these were simulated by electric potential intervals of magnitude ΔE , according to

$$(f_e / \rho) \Delta E \rightarrow f \Delta \Psi = [k(\gamma_2 - \gamma_1)cf/20\mu] \quad (63)$$

A 500-volt a-c source (E^*) was used to supply current to the point sources. With a 500-k Ω resistance, the current at each source was $E^*/500,000$ [amp] which, according to (60), simulates $k(\gamma_2 - \gamma_1)cf/10\mu$. The resistance of the conducting paper in the model was negligible with respect to the 500 k Ω . Because the conducting paper used in the model has a specific resistivity per unit area of $(\rho/f_e) = 1625 \Omega$, the electric potential intervals to be traced were

$$\Delta E = \frac{1}{2} \times 1625 \times E^*/500,000 \\ = 1.625 \times 10^{-3} E^*$$

A potential divider with 1000 subdivisions was E^* . The intervals ΔE of the streamlines were represented by 39 subdivisions of the potential divider.

For the determination of the potential lines the continuous distribution of doublets was replaced by ten doublets of equal strength. Since, according to (59), the doublet strength increases with height y_0 , the strength distribution is triangular. The ten doublets were therefore placed at heights

$$[2c/3\sqrt{10}] \{ [(m-1)^{1/2} + m^{1/2}] \\ - [(m-1)^{-1/2} + m^{-1/2}]^{-1} \}$$

where m represents the integers from 1 to 10, their positions corresponding to the centers of gravity of the 10 equal subdivisions of the triangle. Each doublet had a strength

$$\Lambda'' = (kf/10\mu)(\gamma_2 - \gamma_1) \int_0^c y_0 dy_0 \\ = (kf/20\mu)(\gamma_2 - \gamma_1)c^2 \quad (64)$$

The doublets were represented by a source and a sink with discharge Q'' at a mutual distance $\delta'' = c/40$, and their strength was $\Lambda'' = Q''c/40$. To meet the requirement (64), the discharges of the sources and sinks were given by

$$Q'' = 2kf(\gamma_2 - \gamma_1)c/\mu \quad (65)$$

The required current for the sources was obtained by replacing the 500-k Ω resistance by smaller one of 250 k Ω . For the sinks a counter phase potential E^* of equal magnitude with 250-k Ω resistance was used. So $E^*/250,000$ [amp] was equivalent to $2kf(\gamma_2 - \gamma_1)c/\mu$.

To obtain potential lines at similar intervals as in (62)

$$\Delta \Theta = k(\gamma_2 - \gamma_1)c/20\mu$$

the electric potential intervals ΔE had to be taken as

$$\Delta E = (\rho/f_e)(f \Delta \Theta / Q'')(E^*/250,000) \\ = 1.625 \times 10^{-4} E^*$$

In Figure 15 the full lines are streamlines and the dotted lines are the potential lines obtained with the electric resistance model. This corresponds to the half-aquifer height, and the streamline pattern is therefore comparable with the upper half of Figure 13. The abrupt change of direction of the streamlines created by the shear flow is again visible.

Because of the replacement of continuous sources and doublet distributions by discrete sources and source-sink combinations, the pattern is distorted along the interface. In Figure 15 the distortion of the streamlines by the discrete sources is shown to the left; the potential distortion by the discrete doublets is shown in Figure 15 to the right.

Outside this region the lines form squares.

Difference in viscosity. If, besides specific weight differences, variations of viscosity also have to be considered, the vortex strength depends on the gradient of Ψ according to (10). This excludes mathematical treatment along the lines developed, but the electric resistance model offers a possibility for determination of the flow characteristics. A slightly different stream function Ψ_u and corresponding multiple-fluid potential Θ_u must be introduced. Their definition is given by

$$\Theta_u = kp + k\gamma y$$

$$\mu q_s = -(\partial \Theta_u / \partial s) + ky(\partial \gamma / \partial s) = -(\partial \Psi_u / \partial n)$$

$$\mu q_n = -(\partial \Theta_u / \partial n) + ky(\partial \gamma / \partial n) = +(\partial \Psi_u / \partial s)$$

Elaboration of the conditions of equilibrium then gives

$$\nabla^2 \Psi_u = -k(\partial \gamma / \partial x)$$

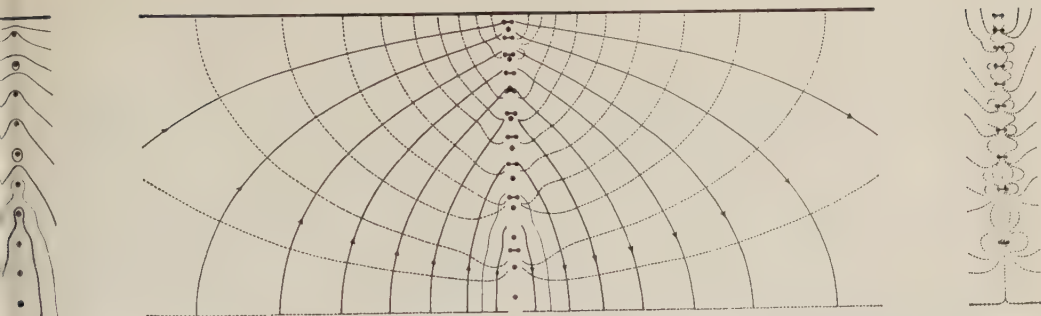


Fig. 15. Result of electric resistance model test, showing lines for constant Ψ (full lines) and constant Θ (dotted lines).

an expression devoid of the μ term. The condition of continuity remains $\text{div } \mathbf{q} = 0$.

In the electric resistance model Ohm's law gives

$$\rho \mathbf{i} = -\text{grad } E$$

where \mathbf{i} is the current density vector, and ρ , the specific resistance, is now a variable function of position. The relation between hydraulic and electric quantities may now be as follows:

For the tracing of potential lines

$$\partial_\mu \rightarrow E; \quad [\mathbf{q} - (ky/\mu) \text{grad } \gamma] \rightarrow \mathbf{i}; \quad \mu \rightarrow \rho$$

For the tracing of streamlines

$$\text{grad } \Psi_\mu \rightarrow -\mathbf{i}; \quad q_n \rightarrow (\partial E / \partial s);$$

$$q_s \rightarrow (-\partial E / \partial n); \quad \mu \rightarrow 1/\rho$$

Application of the conditions of continuity and equilibrium to the hydraulic system gives the following conditions for the electric quantities:

For the case of potential lines

$$-k \text{div} [(y/\mu) \text{grad } \gamma] \rightarrow \text{div } \mathbf{i}$$

$$[\partial^2 \Theta / \partial s \partial n - \partial^2 \Theta / \partial n \partial s] = 0$$

$$\rightarrow [\partial^2 E / \partial s \partial n - \partial^2 E / \partial n \partial s] = 0$$

For the case of stream lines

$$\text{div } \mathbf{q} = 0 \rightarrow [\partial^2 E / \partial s \partial n - \partial^2 E / \partial n \partial s] = 0$$

$$-k(\partial \gamma / \partial x) \rightarrow \text{div } \mathbf{i}$$

These equations show that E is a single-valued function. The values of $\text{div } \mathbf{i}$ indicate a source and sink distribution which differs but slightly from the previous results. In the first case the specific resistance must be directly proportional to the viscosity, in the second case inversely

proportional. As the total resistance in the electric model consists of ρ multiplied by the thickness, it is sometimes more convenient to use a fluid of constant resistivity as conducting material and to vary the layer thickness of the fluid to meet the differences in viscosity.

CONCLUSION

This investigation has shown that it is possible to determine the flow pattern in a porous medium which is saturated by several fluids of different specific weight by the use of singularities. All the fluids are replaced by one hypothetical homogeneous fluid. The motion of the hypothetical fluid will be identical to the movements of the different fluids, for which it is substituted, if singularities are applied at all the points where the original fluids show change in specific weight.

It is proved to be convenient to give the singularities the character of vortices, if the motion of the fluids is to be determined. If the emphasis is on the pressure determination, it is better to use a distribution of sources and sinks. In the case of the vortices, a stream function is the basic variable; in the case of the sources and sinks, it is a multiple-fluid potential. Outside the region of the singularities the potential and stream functions obey the Cauchy-Riemann equations; inside they are not orthogonal.

The magnitude of the singularities is related to the gradients in specific weight. If the initial position of the interface is known, the action of the singularities on the fluids contained within boundaries with known conditions can be determined from potential theory. The solution is given in the form of an integral for which

the region of integration is that part of the aquifer where weight differences are present.

In most practical cases the interface or the mixing zone will have a form which prohibits a mathematically convenient calculation of the integral in closed form. There are, however, methods available for approximation of the integrals involved to any desired degree.

The method requires a knowledge of the position of the interface at a certain moment, and, from that and the known boundary conditions, the subsequent motion of the boundary can be computed from the specific discharge perpendicular to the interface. The displacement of the interface creates a new position of the singularities, with specific discharge changed accordingly, from which a gradual or step-wise movement of the interface can be computed.

A special feature of the singularity distribution is the possibility it offers for the use of the electric resistance model, which is especially useful because it makes possible the direct tracing of potentials and streamlines. Actually, weight differences of fluids have no analogy in electric resistance models, but the hypothetical fluid with homogeneous properties and the singularities applied to this fluid can be simulated by the use of sources and sinks with different distributions for the determination of both potential lines and streamlines.

By introducing a small change in the definition of the potential and stream function, the influence of viscosity differences may also be studied with an electric resistance analogy. Then similar sources and sinks take care of the specific weight variations, but differences in the specific resistance of the model are needed to simulate the viscosity variations.

Acknowledgment. This study was sponsored by the Water Resources Center of the University of California and was conducted in the Hydraulic Laboratory at Berkeley. For the opportunity to study this subject, for various suggestions in the course of the investigation, and for valuable help in the preparation of the manuscript I am especially indebted to Professor David K. Todd, University of California. In the laboratory phases of the study Dr. J. Bear, Technion, Israel, offered his experienced assistance.

REFERENCES

- Badon, Ghijben, W., Nota in verband met de voorgenomen putboring nabij Amsterdam, *Ingenieur, Utrecht*, p. 21, 1888-1889.
- Cooper, H. H., Jr., A hypothesis concerning the dynamic balance of fresh water and salt water in a coastal aquifer, *J. Geophys. Research*, 64, 461-467, 1959.
- Dietz, D. N., A theoretical approach to the problem of encroaching and bypassing edgewater, *Koninkl. Ned. Akad. Wetenschap., Proc., Ser. B* 56, 83-92, 1953.
- Edelman, J. H., Strooming van Zoet en Zout Water, *Rappt. 1940 in zake de watervoorziening van Amsterdam*, Bylage 2, 1940.
- Glover, R. E., The pattern of fresh-water flow in a coastal aquifer, *J. Geophys. Research*, 64, 457-459, 1959.
- Harder, J. A., T. R. Simpson, L. K. Lau, F. L. Hotes, and P. H. McGahey, Laboratory research on sea water intrusion into fresh ground-water sources and methods of its prevention, *Final Rept., Sanitary Eng. Research Lab., Univ. Calif., Berkeley*, 68 pages, 1953.
- Henry, H. R., Salt intrusion into fresh-water aquifers, *J. Geophys. Research*, 64, 1911-1919, 1959.
- Herzberg, B., Die Wasserversorgung einiger Nordseebäder, *J. Gasbeleuchtung und Wasserversorgung*, 44, 815-819, 842-844, 1901.
- Hubbert, M. K., The theory of ground-water motion, *J. Geol.*, 47, 785-944, 1940.
- Hubbert, M. K., Entrapment of petroleum under hydrodynamic conditions, *Bull. Am. Assoc. Petrol. Geologists*, 37, 1954-2026, 1953.
- de Josselin de Jong, G., Vortex theory for multiple phase flow through porous media, *Contrib. 23, Water Resources Center, Univ. Calif., Berkeley*, 80 pp., 1959.
- Keulegan, G. H., An example of density current flow in permeable media, unpublished report of the Natl. Bur. Standards, U. S., June 1954.
- Kidder, R. E., Flow of immiscible fluids in porous media, *J. Appl. Phys.*, 27, 867-869, 1956a.
- Kidder, R. E., Motion of the interface between two immiscible liquids of unequal density in a porous solid, *J. Appl. Phys.*, 27, 1546-1548, 1956b.
- Lorentz, H. A., Grondwaterbeweging in de nabijheid van bronnen, *Ingenieur, Utrecht*, 28, 24-26, 1913 (for English translation see: *Lorentz's Collected Papers*, 4, 59-66, Nyhoff, the Hague, 1937).
- Malavard, L. C., The use of rheoelectrical analogies in aerodynamics, *AGARDograph 18*, NATO Advisory Group of Aeronaut. Research and Develop., Paris, 175 pp., 1956.
- Muskat, M., *The Flow of Homogeneous Fluids through Porous Media*, McGraw-Hill Book Co., New York, 763 pages, 1937.
- Santing, G., Modèle pour l'étude des problèmes de l'écoulement simultané des eaux souterraines douces et salées, *Assemblée Générale de Bruxelles, Assoc. Intern. d'Hydrologie Scientifique*, 2, 184-193, 1951.
- Todd, D. K., and L. Huisman, Ground water flow in the Netherlands coastal dunes, *J. of the Hydrol. Div., Proc. Am. Soc. Civil Engrs.*, 85, no. HY 7, 63-81, 1959.

(Manuscript received June 28, 1960.)

Distribution of Excessive Rainfall Amounts over an Urban Area

F. A. HUFF AND S. A. CHANGNON

*Illinois State Water Survey
Urbana, Illinois*

Abstract. Data recorded over a 10-year period from a network of 11 recording rain gages was used in a study of the distribution characteristics of excessive rainfall amounts over the 10-square-mile urban area of Champaign-Urbana, Illinois. All storms were used in which one or more rain gages recorded an amount equalling or exceeding the 2-year return period value of point rainfall for durations of 30 minutes, 1 hour, 2 hours, 3 hours, 6 hours, 12 hours, and 24 hours.

Factors investigated include: the frequency of excessive rainfall amounts within the area compared with the frequency at a given observation point within the area; the percentage of the urban area experiencing excessive rainfall amounts during individual storms and the frequency distribution of this percentage; the adequacy of a single point to define the frequency distribution of areal mean rainfall within a small area; the frequency with which excessive amounts for 30-minute to 24-hour periods occur within the same storms; and urban influences on the distribution of heavy storm rainfall.

Based on the 10-year sampling period, results indicate that twice as many excessive rainfall amounts occur within a 10-square-mile area compared with the number recorded at specific points; on the average, the percentage of the 10-square-mile area experiencing excessive rainfall amounts increases with increasing storm duration; the majority of the excessive amounts for duration of 30 minutes to 24 hours occur in the same storms; a point rainfall record is a satisfactory index of the areal mean rainfall frequency distribution in a 10-square-mile area; and urban influences, if present, are not of practical significance.

Introduction. A study of the distribution characteristics of heavy rainfall amounts over an urban area has been made with data for the 10-year period 1950-1959 from a network of 11 recording rain gages. This area consists of 10 square miles which constitute the urban area of Champaign-Urbana, Illinois. The urban area and rain-gage network are shown in Figure 1. The urban area is surrounded by extremely flat farm land, noticeably lacking abrupt changes in topography and surface water bodies.

This study was undertaken to obtain a quantitative measure of the frequency of heavy rainfall amounts within a small area compared with the frequency at a given observation point within that area; to determine the percentage of the urban area experiencing excessive rainfall amounts during individual storms and the frequency distribution of this percentage; to evaluate the adequacy of a single point to define the frequency distribution of areal mean rainfall within a small area; to ascertain the frequency with which excessive amounts for 30-minute to 24-hour periods occur within the same storms; and to investigate whether urban influences af-

fect the distribution of heavy storm rainfall.

In the study, all storms were used in which one or more rain gages recorded an amount equalling or exceeding the 2-year frequency of point rainfall for durations of 30 minutes, 1 hour, 2 hours, 3 hours, 6 hours, 12 hours, and 24 hours. These amounts are considered excessive in the urban study. Values of point rainfall frequency were obtained from Illinois Water Survey published data [Huff and Neill, 1959]. Because of the relatively short period of record (10 years), results to date have been based primarily upon an analysis of rainfall amounts equalling or exceeding the 2-year frequency values, with only limited use of 5-year and longer frequency values. The study will be continued in the future as more data are collected on the rain-gage network. However, it is believed that this paper is based upon sufficient data to be of interest and value to those engaged in urban storm sewer design and other small-scale hydrologic design problems.

Point versus areal occurrences. From tabulated data for the 11-gage network, the frequency with which heavy rainfall amounts occurred at

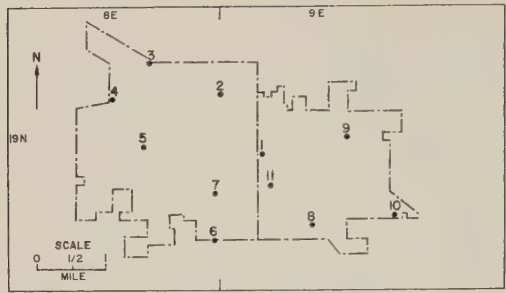


Fig. 1. Boneyard rain-gage network.

a single point in the network was compared with the frequency recorded in the 10-square-mile area. This comparison was made for each storm duration, 30 minutes to 24 hours, and for selected values of recurrence interval. Results are summarized in Table 1 for storms in which the 2-year frequency of point rainfall was equalled or exceeded somewhere in the network.

An over-all mean ratio of 2.0 was obtained for the frequency of areal to individual point occurrences; that is, the results indicate that on the average there are twice as many excessive rainfall amounts observed within a 10-square-mile area as are observed at any particular point in that area in a given sampling period. This ratio might increase slightly if more gages were added to the network, but it is believed that the present concentrated network should miss very

few, if any, occurrences of excessive amounts in the area. Considerable variability is shown between the average ratios for the several storm durations shown in Table 1, but it may be due largely to sampling variations in the relatively short sampling period of 10 years. A slight trend for the average ratio to change with storm duration is indicated, with an over-all mean ratio of 2.2 for 30-minute to 3-hour periods and 1.8 for 6-hour to 24-hour periods. This trend appears logical, since relative variability of rainfall normally decreases with increasing duration [Huff and Neill, 1957]. Consequently, in a given area a single gage is more likely to record a 24-hour excessive rainfall value than a 1-hour value.

Areal extent of heavy rainfall. An investigation was made of the percentage of the urban area experiencing rainfall amounts equalling or exceeding the 2-year frequency value for 30-minute to 24-hour durations in each storm. For each case, an area-depth envelope curve was constructed which showed the amount of area enclosed by any given isohyet in the storm. An example for the storm of May 20, 1959, is shown in Figure 2. These curves provided the data necessary for determining the frequency distribution of the percentage of area experiencing rainfall amounts which equalled or exceeded those for selected recurrence intervals. Table 2 shows the frequency distribution for rainstorms

TABLE 1. Distribution of Rainfall Equalling or Exceeding 2-Year Frequency Values, 1950-1959

Station	Number of Cases for Given Period						
	30 min	1 hr	2 hr	3 hr	6 hr	12 hr	24 hr
1	8	6	10	7	7	9	4
2	9	8	10	10	9	8	4
3	8	9	9	12	8	10	5
4	8	6	11	10	10	10	4
5	9	8	12	11	9	9	4
6	13	12	13	12	10	10	4
7	9	8	13	11	9	10	4
8	12	10	12	9	9	9	2
9	12	7	11	9	8	9	3
10	8	5	10	7	8	10	2
11	10	11	12	12	10	10	4
Median	9	8	11	10	9	10	4
Max.	13	11	13	12	10	10	5
Min.	8	6	9	7	7	9	2
Network total	23	19	20	20	16	13	9
Avg. ratio, network/single gage	2.6	2.4	1.8	2.0	1.8	1.3	2.2

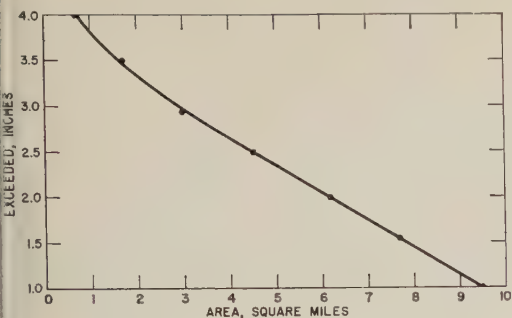


Fig. 2. Area-depth envelope curve, maximum 3-hour rainfall, May 20, 1959.

in which the 2-year frequency value was equalled or exceeded within the network of 10 square miles. Because few samples are available, similar distributions have not been presented for longer recurrence intervals or for the 24-hour, 2-year data. The median values in Table 2 indicate the expected trend for heavy storm rainfall to be more widespread over the network as storm duration increases.

An outstanding example of the variability of rainfall in a severe rainstorm is shown in Figures 3 and 4 for the storm of May 20, 1959. Figure 3 shows the distribution of rainfall for maximum 30-minute to 3-hour periods in the storm, and Figure 4 illustrates the relative intensity of the storm in terms of recurrence interval. In Figure 4, selected isohyets have been drawn and labeled in terms of recurrence interval of point rainfall to which each isohyet corresponds.

The 3-hour maps show that more than 3 inches of rain fell on the west side of the city, while 3 to 4 miles to the east less than 1 inch was recorded. Amounts equalling or exceeding the

TABLE 2. Network Extent of Storms with Recurrence-Interval values of 2 Years or More, 1950-1959

Cumulative Percentage of Storms	Percentage of Network Area Enclosed for Given Durations					
	30 min	1 hr	2 hr	3 hr	6 hr	12 hr
10	100	100	100	100	100	100
25	75	80	85	89	92	95
50	36	43	50	58	69	82
75	16	20	25	30	45	64
90	10	10	10	10	10	10

TABLE 3A. Percentage of Area Experiencing Excessive Rainfall for Various Storm Periods on October 6, 1955

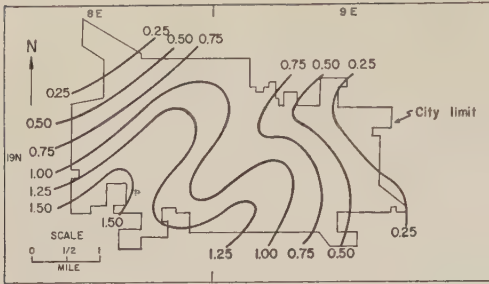
Storm Period	Percentage of Area with Rainfall Exceeding that for Given Recurrence Interval (yrs)			
	2 yr	5 yr	10 yr	25 yr
30-minute	89	59	36	2
1-hour	95	47	31	0
2-hour	95	77	31	0
3-hour	98	92	61	0
6-hour	100	100	90	20
12-hour	100	98	29	0
24-hour	100	41	0	0

100-year frequency were recorded on the west side of the city, while on the east side the rainfall amounts were less than expected once per year (Fig. 4).

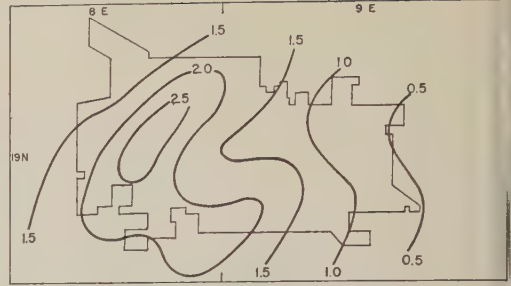
Frequency of excessive amounts in same storms. The frequency with which excessive amounts occurred on the network in the same storms was investigated for 30-minute to 24-hour periods. It was found that the majority of the rainfall amounts equalling or exceeding the 2-year frequency value for the several durations from 30 minutes to 24 hours occurred in the same storms. An example of the occurrence of 2-year or greater frequency values for various durations in the same storm is shown in Table 3 for the storm of October 6, 1955. Amounts were recorded on the network which equalled or exceeded the 2-year and 5-year frequency values for all durations and the 10-year frequency for all except the 24-hour duration. Using station 11 as a point sample, it was found that 2-year or greater frequency values were recorded for all durations. However, as shown by the percentage

TABLE 3B. Recurrence-Interval Values at Station 11 on October 6, 1955

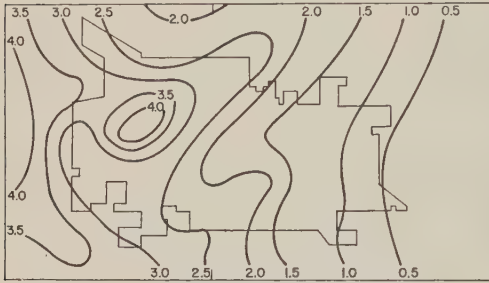
Storm Period	Recurrence Interval, years	Storm Period	Recurrence Interval, years
30-minute	14	6-hour	25
1-hour	9	12-hour	12
2-hour	9	24-hour	7
3-hour	15		



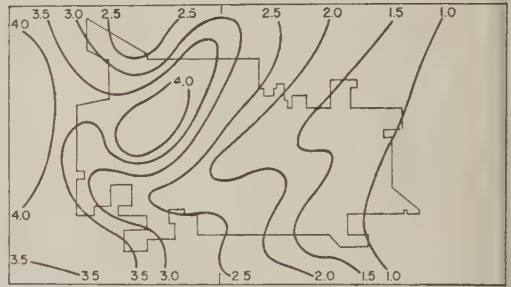
a. MAXIMUM 30-MINUTE RAINFALL



b. MAXIMUM 1-HOUR RAINFALL

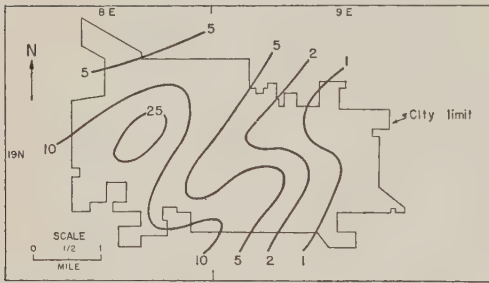


c. MAXIMUM 2-HOUR RAINFALL

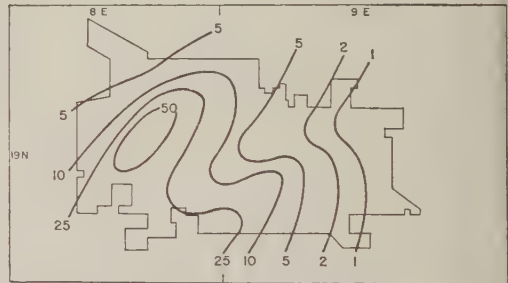


d. MAXIMUM 3-HOUR RAINFALL

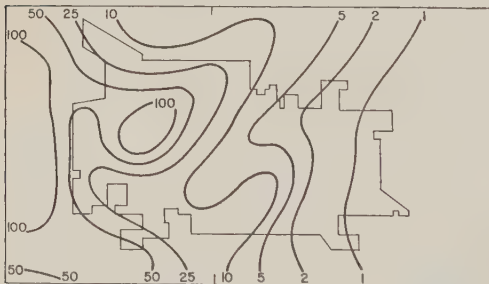
Fig. 3. Rainfall distribution on May 20, 1959.



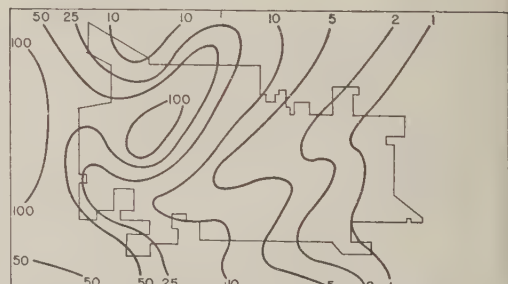
a. AVERAGE RECURRENCE INTERVAL OF MAXIMUM 30-MINUTE RAINFALL



b. AVERAGE RECURRENCE INTERVAL OF MAXIMUM 1-HOUR RAINFALL



c. AVERAGE RECURRENCE INTERVAL OF MAXIMUM 2-HOUR RAINFALL



d. AVERAGE RECURRENCE INTERVAL OF MAXIMUM 3-HOUR RAINFALL

Fig. 4. Variability in storm intensity on May 20, 1959.

TABLE 4. Percentage of All 1- to 24-Hour Excessive Amounts Occurring in Storms with 30-Minute Excessive Amounts

Duration	Number of Cases for Given Recurrence Interval			Percentage of Cases for Given Recurrence Interval		
	2 yr	5 yr	10 yr	2 yr	5 yr	10 yr
30-minute	23	12	8
1-hour	19	9	3	100	100	100
2-hour	20	9	4	95	67	75
3-hour	20	8	4	95	62	75
6-hour	16	7	2	87	71	100
12-hour	13	5	3	92	60	67
24-hour	9	4	1	100	75	100
Durations combined	120	54	25	95	74	82

values in Table 3, all gages did not record values of this magnitude.

Results based upon all storms are shown in Table 4, where the percentage of all 1-hour to 24-hour excessive amounts occurring in storms which also had 30-minute excessive amounts is shown. Combining all durations from 1 to 24 hours, 95 per cent of the 2-year, 74 per cent of the 5-year, and 82 per cent of the 10-year recurrence-interval values came from storms in which 30-minute excessive amounts were also recorded. These results suggest that consideration should be given to the effect of such occurrences in hydrologic design problems.

Areal representativeness of point rainfall. Despite the variability in amounts and areal coverage in individual storms, a point rainfall record within a 10-square-mile area appears to be a satisfactory index of the areal mean rainfall frequency distribution, based on the 10-year sample used here. The relation between the frequency distribution of point rainfall at station 11, a cooperative U. S. Weather Bureau Station, and the frequency distribution of the network mean rainfall was determined. This was accomplished by ranking the point and network mean rainfall data for the sampling period and then determining the relationship between these ranked data. All storms in which an amount equalling or exceeding the 2-year frequency value was recorded within the network were used in the analysis. Relations were obtained for each duration from 30 minutes to 24 hours. Table 5 shows the ratio of areal mean to point rainfall frequency values obtained in this study, and a

comparison with similar values published by the U. S. Weather Bureau [*U. S. Weather Bureau, 1957*]. The two sets of ratios compare very favorably.

Urban effects. An investigation was made to determine whether the spatial distribution of heavy rainfall amounts appeared to be influenced by urban effects. It has been generally accepted that large urban areas have some influence on the intensification and initiation of rainfall in the vicinity, owing to an increase in the concentration of condensation nuclei in the atmosphere from combustion products and/or mechanical and thermal turbulence induced by the city [*Landsberg, 1956*]. Whether a relatively small city such as Champaign-Urbana has appreciable influence on the urban rainfall pattern is highly questionable, but this aspect was studied for indicated effects.

TABLE 5. Relation between Areal Mean and Point Rainfall Frequency Distributions for Area of 10 Square Miles

Storm Period, hours	Ratio of Areal to Point Rainfall	
	Illinois Water Survey	Weather Bureau
0.5	0.92	...
1.0	0.92	0.93
2.0	0.94	0.95
3.0	0.96	0.97
6.0	0.98	0.97
12.0	0.99	0.98
24.0	0.99	0.98

Our efforts to evaluate the urban effect have been based upon the distribution of heavy storm rainfall within the network during the 10-year period, the comparison of this pattern with the annual mean precipitation pattern, the comparison of the urban pattern with that on a rural network, and the determination of the statistical significance of the differences in heavy storms experienced on the urban network during the sampling period. If similar exposure of rain gages is maintained and careful attention given to calibration of the gages and analysis of the gage charts, as was done in this study, the above

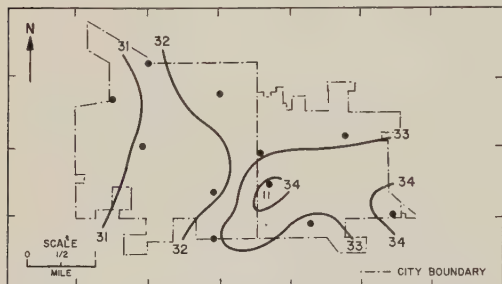


Fig. 5. Annual average precipitation, 1950-1959.

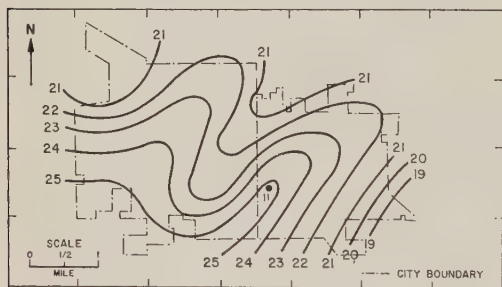


Fig. 6. Total of 1-hour rainfalls in storms with hourly amounts \geq 2-year frequency value at one or more stations, 1950-1959.

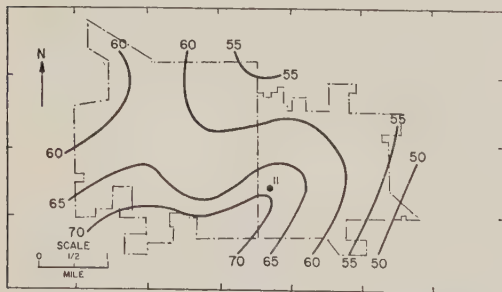


Fig. 7. Total number of 30-minute to 24-hour amounts \geq 2-year recurrence value, 1950-1959.

procedures should reveal natural variations of practical significance. However, the data sample is not suitable for determination of the very small variations which may exist.

Figures 5, 6, and 7, respectively, show the annual mean precipitation pattern for the 10-year period; the rainfall pattern for 1-hour amounts in all storms in which 1-hour values exceeding the 2-year frequency were observed within the network during the 10 years; and the total number of 30-minute to 24-hour amounts equalling or exceeding the 2-year recurrence of rainfall. Similar maps were prepared for each period from 30 minutes to 24 hours, but are not presented here since they show relations similar to those in Figure 6. Figures 5 to 7 show appreciable differences between the annual pattern and the heavy storm patterns. Whereas the annual pattern shows a peak in rainfall in the southeast portion of the area and a low on the western edge of the urban area, the heavy rainfall patterns show a minimum on the east side and a maximum in the south and southwest parts of the urban area. All patterns show a high area in the vicinity of gage 11 in the south-central part of the network. It would appear that if the urban environment were producing significant effects on the heavy rainfall distribution within the 10-square mile area that both the heavy rainfall and annual patterns would show similar characteristics. The prevailing southwesterly winds, the generally west-to-east direction of storm movement, and the heavy rainfall maximum on the southwest side of the city suggest either no significant urban influence or an effect which, contrary to theory, tends to decrease the rainfall intensity across the city.

Although the annual mean pattern shows evidence of a west-to-east increase across the city, in agreement with prevailing winds and most frequent motion of storms, another test strongly suggests that the increase may be due to sampling variations rather than to urban effects. Figure 8 shows the annual mean precipitation pattern on the Panther Creek watershed in north central Illinois for 1950-1959, the same sampling period used on the urban network. The Panther Creek network includes 100 square miles located in a completely rural area 60 miles northwest of the urban network, and the gage density has varied from 4 to 10 square miles per gage during the 10-year period, compared with the urban

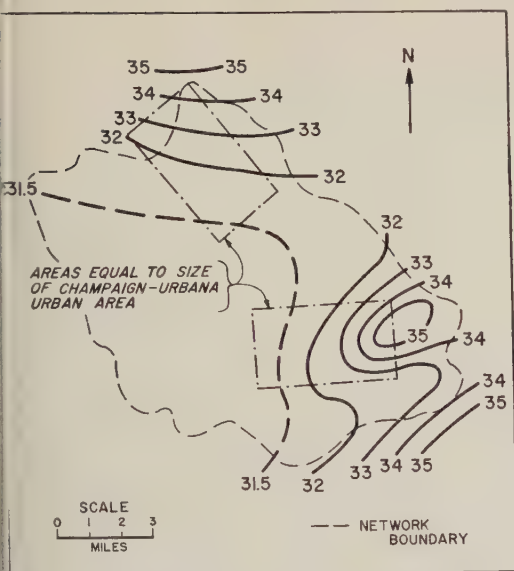


Fig. 8. Annual average precipitation on Panther Creek rain-gage network, 1950-1959.

density of approximately 1 square mile per gage. In Figure 8, a rectangle corresponding approximately to the dimensions of the urban network has been superimposed in two locations where the rainfall gradient is relatively steep for the 10-year period. Within these 10-square-mile rectangles, variations in mean rainfall of approximately 3.5 and 4.0 inches occur. As suggested by Stout [1960], one would expect the urban network with much greater gage density to have sampling variations considerably greater than those within an area of 10 square miles on a less dense network, such as the one on the Panther Creek watershed. Figures 5 and 8 show maximum differences of about the same magnitude on the urban and rural networks. These results suggest, therefore, that the urban differences may merely result from random sampling variations.

Next, an analysis of variance was made using both the number of excessive rainfalls for the 10-year period and rainfall amounts recorded in excessive storms during the 10 years. The variance ratios obtained indicated significance below the 50 per cent level in all cases; thus the tests strongly indicate that the differences in the frequency of excessive rainfall between the 11 gages during the 10-year period and the differences in rainfall amounts between gages in these storms resulted from random sampling variations rather

than from urban influences. The above results were supported by use of the t test and the χ^2 test.

Conclusions. Results of this study, based on a 10-year sampling period, indicate that on the average there are twice as many occurrences of excessive rainfall amounts within a 10-square-mile area as are recorded at specific points within the area. A slight trend for the ratio of areal to point occurrences to decrease with increasing storm duration was noted.

Under average conditions, the percentage of the 10-square-mile area experiencing excessive rainfall amounts increases with increasing storm duration. For the 10-year sampling period, the median percentage for all storms increased from 36 per cent of the area for 30-minute durations to 82 per cent for 12-hour durations.

It was found that the majority of excessive amounts for the various durations occurred in the same storms. Combining all durations from 1 to 24 hours, 95 per cent of the 2-year, 74 per cent of the 5-year, and 82 per cent of the 10-year recurrence-interval values came from storms in which 30-minute excessive amounts were also recorded.

Despite the variability in rainfall amounts and in the areal extent of excessive rates, a point rainfall record appears to be a satisfactory index of the areal mean rainfall frequency distribution in a 10-square-mile area.

No urban influences of practical significance were detected in the excessive rainfall distribution in the urban area during the 10-year sampling period.

REFERENCES

- Huff, F. A., and J. C. Neill, Rainfall frequencies, *Tech. Letter 1*, Illinois State Water Survey, Urbana, Ill., 1959.
- Huff, F. A., and J. C. Neill, Rainfall relations on small areas in Illinois, *Bull. 44*, Illinois State Water Survey, Urbana, Ill., 1957.
- Landsberg, H. E., *The Climate of Towns, Man's Role in Changing the Face of the Earth*, Univ. Chicago Press, Chicago, Ill., 584-603, 1956.
- Stout, Glenn E., Natural variability of storm, seasonal, and annual precipitation, *J. Irrigation and Drainage Div., Proc. Am. Soc. Civil Engrs.*, 86 (IRI), p. 135, March 1960.
- U. S. Weather Bureau, Rainfall intensity-frequency regime, *Tech. Paper 29*, part 1, Washington, D. C., 1957.

(Manuscript received June 30, 1960.)

A Method of Estimating Basin Temperatures in New England and New York

CHARLES D. HOPKINS, JR.

*River Forecast Center
U. S. Weather Bureau
Hartford, Connecticut*

Abstract. A pronounced variability in the rainfall-runoff relations in New England and New York is described. In the belief that these variations are caused by variations in basin temperatures, a method of computing average basin temperatures from station temperatures was sought. To that end, the relationships between station temperatures and elevations and latitudes in New England and New York were investigated. Maximum, minimum, and mean temperatures, averaged for a 22-year period, were used. Correlations were sufficiently high to suggest that a similar study might prove a valuable addition to any climatological atlas. Monthly and seasonal variations in rates of change of temperatures with both elevation and latitude formed very marked patterns. Another finding was that a lapse rate of at least 3.5°F per 1000 feet prevails during melt periods. Testing of the variations of the rainfall-runoff relation showed a strong correlation with basin elevations and latitudes. Since basin elevation and latitude are sufficient to compute average basin temperatures, it was inferred that average basin temperatures can be used, with considerable profit, in the forecasting of runoff.

Assembly of rainfall-runoff data. The Hartford River Forecast Center has developed rainfall-runoff data designed to determine the rainfall-runoff relationships in its area of forecast responsibility, which consists of New England and the Lake Champlain and Hudson River basins. The data for each storm consist of an index of antecedent precipitation, week number or the beginning day of the storm, average storm rainfall, and storm runoff. Only those storms were used which could be assumed to have small, or no, snowmelt or snow accumulations. The total data derived consist of 3738 storms in 63 basins.

From these data, it was intended to develop coaxial relations in the manner described by *Linsley, Kohler, and Paulhus* [1949]. It will be noted, however, that no use was made of the duration of the storm. Experience with this type of relation has shown that knowledge of storm duration is not particularly helpful in reducing the errors in computing runoff. This does not mean, of course, that knowledge of rainfall intensity is not important in determining runoff. But the amount of rainfall and the storm duration do not seem to define adequately rainfall intensity in basins of the size used in this study.

Development of a rainfall-runoff relation.

When the time came to develop rainfall-runoff relations from the data that had been assembled, considerable difficulty was encountered. A relationship that would fit one basin would not fit another, even in the same area. This was a serious complication, since the necessary intention of the work was to develop rainfall-runoff relations that would fit the entire area. If it were necessary to develop a separate rainfall-runoff relation for practically every basin, not only would this be unwieldy for practical application but also it would leave unanswered the question of what rainfall-runoff relations to use in the two-thirds of the area not included in the data.

Finally, by considerable trial and error, a rainfall-runoff relationship was drawn that was an average, more or less, for all basins. The intention was to use such an average relationship as a device with which to measure the variations from one basin to another. The variable used to compare one basin with another was the ratio of total runoff for all storms in a basin as computed by the average relationship to the total observed runoff for the same storms in that basin. This ratio expressed in per cent was termed the forecast bias.

This forecast bias ranged from 45 to 193 per

cent in the various basins, with a standard deviation of 34.4 per cent. This represents a large variation in the rainfall-runoff relations for the various basins. Furthermore, there were large variations in the forecast biases within comparatively small areas between basins that were expected to be comparable.

Causes of the variability in the rainfall-runoff relation. It has been shown by Williams [1940] that there is a strong relation between mean annual water loss and mean annual temperature in the United States east of 95°W. It seems reasonable, therefore, to ascribe some of the variability in the rainfall-runoff relation to differences in temperature.

It has been determined by McAleer and Knox [1948] using Williams' relation between loss and temperature, that the mean annual water loss in New England varies from 18 to 24 inches. This would correspond to mean annual temperatures varying from about 39°F to 51°F.

The decision was made to attempt to derive a method of computing average basin temperatures from temperature station data, in order to test the supposition that temperatures were affecting storm runoffs.

Compilation of temperature data. Monthly temperature data had been compiled for the publication of "Climatic Summary of the United States—Supplement for 1930 through 1952," by the National Weather Records Center, U. S. Weather Bureau, Asheville, N. C., and those unpublished compilations were furnished by that office for the area discussed in this paper.

All monthly maximum, minimum, and mean monthly temperatures were used when 10 years or more of record were available. All stations were excluded, however, which had roof exposures or were on Cape Cod, in metropolitan New York, or on maritime islands.

Stations were selected which had had only one location throughout the 22-year period and which had no more than 12 months of data missing. The missing months were then estimated.

Estimation of missing monthly temperatures was performed as follows: Two to four surrounding temperature stations were selected at which the missing datum had been observed. Common 10-year averages of the particular monthly temperature function were then com-

puted at the station to be estimated and the stations used for estimating, and the 10-year average differences were then obtained. The missing datum was then estimated by adjusting observed temperatures at the estimating stations by the observed average differences and averaging the adjusted temperatures.

Some consideration was given to the possibility of adjusting temperatures at stations where more than one location had been used, but this was abandoned when it became apparent that data sufficient for the study were already available.

The following maximum, minimum, and mean temperatures were then computed for the selected stations: 22-year average, 4 seasonal 22-year averages, and 12 monthly 22-year averages. The seasons were selected as follows: the three coldest months, December, January, and February—winter; the three months of rising temperatures, March, April, and May—spring; the three warmest months, June, July, and August—summer; and the three months of falling temperatures, September, October, and November—fall.

The relation of geography and topography to temperature. Air temperature is a continuous meteorological function. It is reasonable to expect, therefore, that the temperatures throughout an area at a given instant, assuming that no strong frontal system is present, will have relationships with each other which are, in large part, determined by the geography and topography of the area. Furthermore, these relationships should be reflected in the average temperatures for a given period over that area.

It should be pointed out, however, that temperature data in a wooded, hilly area represent the temperatures of the total area badly. None of the temperatures were observed at any but open locations; furthermore, most of the open inhabited area where the observations were made lie in the arable valleys. The wooded and hilly areas, on the other hand, are mostly unrepresented.

The geographic and topographic factors affecting temperatures may be separated into two types, those large-scale variables that do not tend to cancel out over a sizeable area and those small-scale variables that cancel out within fairly short distances. Elevation is a good example of the first type; one parcel of

TABLE 1. Summary of Observed Regressions
Temperatures (44 stations) vs. Elev. (1000 ft.) and Lat. (°)
Average Mean Basin Elevation 930 Feet
Average Mean Basin Latitude 43.52°

	Maximum Temperatures				Minimum Temperatures				Mean Temperatures			
	R_{123}	b_L^*	b_E^\dagger	Aver. T_x , °F	R_{123}	b_L^*	b_E^\dagger	Aver. T_n , °F	R_{123}	b_L^*	b_E^\dagger	Aver. \bar{T} , °F
Annual	.959	-1.849	-3.324	55.54	.902	-2.051	-3.063	33.49	.962	-1.961	-3.193	44.50
Winter	.966	-2.618	-2.289	31.20	.942	-3.323	-3.131	11.50	.966	-2.970	-2.705	21.33
Spring	.954	-1.919	-3.847	53.81	.905	-2.020	-3.240	31.06	.959	-1.975	-3.545	42.44
Summer	.923	-1.045	-3.989	78.56	.826	-1.322	-3.138	54.28	.941	-1.182	-3.566	66.42
Fall	.953	-1.814	-3.143	58.56	.848	-1.521	-2.718	37.12	.944	-1.670	-2.910	47.84
December	.969	-2.633	-2.320	32.41	.938	-2.828	-3.291	14.52	.966	-2.731	-2.801	23.46
January	.926	-2.704	-1.811	30.18	.951	-3.797	-2.688	10.35	.971	-3.291	-2.291	20.24
February	.945	-2.415	-2.689	31.06	.930	-3.365	-3.405	9.60	.957	-2.893	-3.034	20.34
March	.958	-2.216	-3.464	40.46	.919	-2.698	-3.976	19.65	.962	-2.451	-3.716	30.04
April	.960	-2.095	-4.188	53.51	.899	-1.695	-3.117	31.36	.958	-1.899	-3.652	42.43
May	.924	-1.416	-3.943	67.46	.848	-1.674	-2.684	42.18	.936	-1.560	-3.274	54.83
June	.917	-1.161	-3.933	76.21	.844	-1.443	-2.863	51.67	.940	-1.298	-3.384	63.94
July	.911	-1.037	-3.944	80.76	.815	-1.222	-3.273	56.57	.935	-1.124	-3.630	68.67
August	.921	-0.944	-4.081	78.71	.818	-1.317	-3.269	54.58	.937	-1.137	-3.676	66.65
September	.922	-1.402	-3.457	70.74	.827	-1.418	-2.895	47.19	.939	-1.401	-3.181	58.96
October	.939	-1.797	-3.085	59.81	.799	-1.437	-2.523	36.81	.950	-1.617	-2.803	48.31
November	.966	-2.261	-2.869	45.17	.898	-1.699	-2.771	27.38	.962	-1.986	-2.828	36.27

* $b_L = ^\circ\text{F}/^\circ\text{Lat.}$, variation of temperature with latitude.

† $b_E = ^\circ\text{F}/1000 \text{ ft.}$, variation of temperature with elevation.

and will be higher or lower than another. Aspect is a good example of the second; computation of the net vector of aspect over almost any area of fair size will reveal a net aspect of practically zero. Large-scale variables include such items as latitude, elevation, type of cultivation or vegetation, and bodies of water. Some small-scale variables are aspect, slope, and air drainage.

Selection of variables. For the purposes of this study, only large-scale variables needed to be considered, since it seemed that average basin temperatures were needed rather than temperatures at points in the basin. It seemed that the variables selected should be easily measurable, unambiguous, and available for all basins. Elevation and latitude were selected as meeting these requirements; furthermore, they appeared to be a combination of variables that should, together, express some important large-scale effects.

The correlations. The statistical analysis consisted of linear correlations between tem-

perature quantities and station elevation and latitude. There were 44 stations used; degrees of freedom in each of the 51 regressions were, therefore, 41. The results of the regressions are tabulated in Table 1.

Climatological implications. The correlation coefficients shown in Table 1 are surprisingly good when it is realized how many factors were ignored. As might be expected, minimum temperatures, which should be most affected by small-scale local influences, show the poorest correlation. Even so, the poorest correlation coefficient with a minimum temperature is 0.799. The poorest correlation coefficient with a maximum temperature is 0.911, and with a mean temperature, 0.935. This suggests that the unconsidered small-scale effects tend to compensate in the production of mean temperatures.

The quality of the correlations suggests that similar, but perhaps more elaborate studies, might well be part of any climatological atlas. The analogy that comes to mind is the study of normal precipitation made by Spreen [1947]

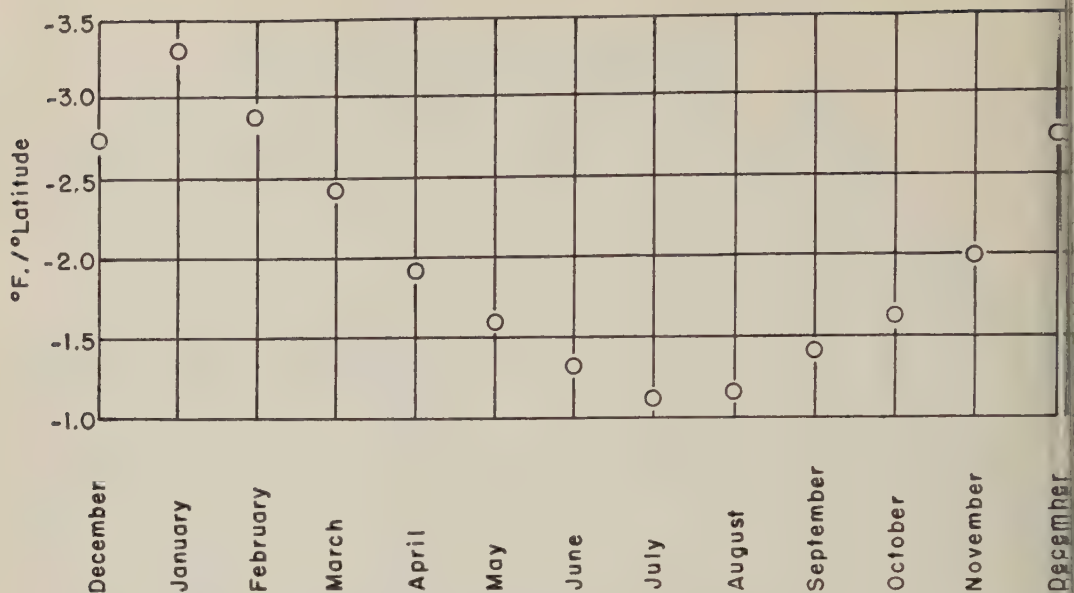


Fig. 1. Rate of change of mean monthly temperature with latitude.

and others. A method of analyzing temperature records for consistency, and perhaps adjusting them, might be developed in order to add to the usable data. A more refined representation of latitude might be used, perhaps a trigonometric function. Certainly, the attempt should be made to add other variables; marine and lake effects, slope, aspect, and air drainage come immediately to mind, and there should be others.

Possible climatological uses of such studies

should be left to others. It would seem, however, that such relationships should make possible the more precise application of climatological temperature data.

The variation in the coefficients for latitude and elevation are marked enough to be worthy of comment. Figures 1 and 2 are intended to present these variations in graphical form; for the sake of clarity, only the coefficients for mean monthly temperatures are shown.

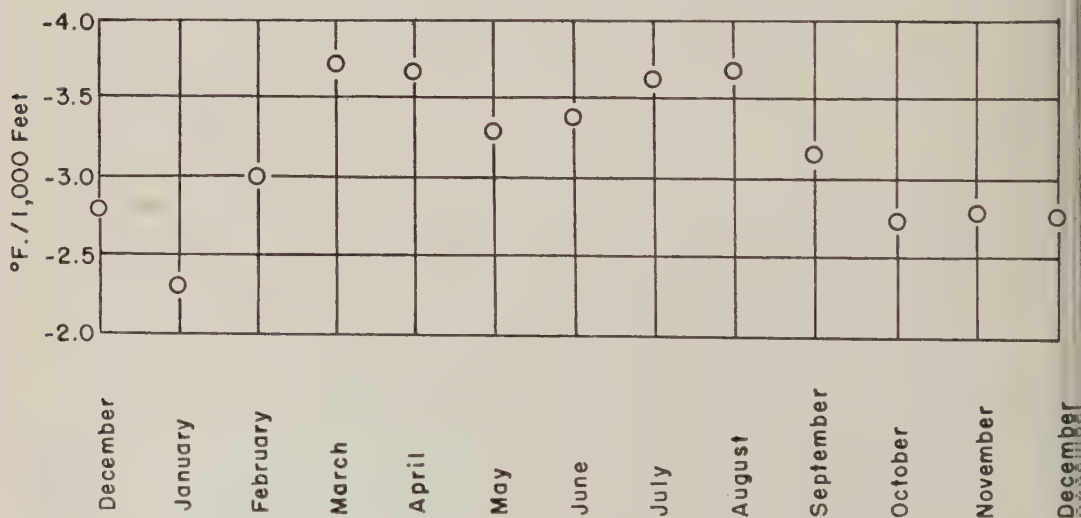


Fig. 2. Rate of change of mean monthly temperature with elevation.

Figure 1 shows that the rate of change with altitude has a very regular pattern from month to month. The rate of change with elevation (Fig. 2) is not as clear. These variations in the coefficients show that the relationships between temperatures in different areas vary according to season.

1 hydrologic implication. Temperatures influence the hydrology of northern regions by affecting the accumulation and ablation of snow. Temperature is certainly one of the important factors influencing the melting of snow. Furthermore, it is available in the field as a body of observations, which is certainly not true of any other variables.

The network of temperature observations in any country is badly biased towards lower elevations. In order to forecast snowmelt in such a region, it is necessary to extrapolate temperature observations by means of an assumed lapse rate. Consideration must also be given to the presence of wooded areas. It is possibly true that, during melting of snow, temperatures are lower in the woods than in the open; it is certainly true that snowmelt is a slower process in the woods.

The results of this study indicate that during the snowmelt season in New England and eastern New York, which is usually March, April, and May, the lapse rate at instrument shelter level varies from 3.3°F to 3.7°F per 1000 feet. This would be averaged at about 3.5°F per 1000 feet. It is well to keep in mind, however, the prevalence of wooded areas at the higher elevations. The effective snowmelt lapse rate might, therefore, be somewhat higher.

The use of temperatures in forecasting runoff. In order to evaluate the possible usefulness

of this temperature study in forecasting runoff, a correlation was computed between (1) basin forecast bias, (2) mean basin elevation, and (3) mean basin latitude. Strong correlations were found, the correlation coefficients being

$$R_{12} = -0.784$$

$$R_{13} = -0.772$$

$$R_{123} = -0.851$$

It is quite feasible to compute average basin temperatures given mean basin elevations and latitudes. Furthermore, the variations in the rainfall-runoff relation are strongly related to mean basin elevations and latitudes. It can be fairly inferred, then, that average basin temperatures can be used with considerable profit in the forecasting of runoff in New England and New York.

A thorough investigation of the use of basin temperatures to forecast runoff will be pursued.

REFERENCES

- Linsley, Ray K., Jr., Max A. Kohler, and J. L. H. Paulhus, *Applied Hydrology*, McGraw-Hill Book Co., New York, p. 421, 1949.
- McAleer, J. B., and C. E. Knox, Annual rainfall and runoff in New England, *Trans. Am. Geophys. Union*, 29, 903-908, 1948.
- Spren, W. C., A determination of *Am. Geophys. Union*, the effect of topography upon precipitation. *Trans. Am. Geophys. Union*, 28, 285-290, 1947.
- Williams, G. R., and others, Natural water loss in selected drainage basins, *U. S. Geol. Survey Water Supply Paper* 846, 1940.

(Manuscript received June 27, 1960; revised August 25, 1960.)

Investigations of the Radioisotopes Be^7 , P^{32} , and S^{35} in Rain Water

RAMA

Tata Institute of Fundamental Research, Bombay, India

Abstract. The concentrations of the radioisotopes Be^7 , P^{32} , and S^{35} in rainfall at Bombay and at Kodaikanal have been measured. The average concentrations in rainfall at Bombay during the period from June 1959 to October 1959 were 2900 atoms/ml of Be^7 , 12 atoms/ml of P^{32} , and about 400 atoms/ml of S^{35} . It is shown that the observed fallout of Be^7 and of P^{32} is almost entirely of cosmic-ray origin; the fallout of S^{35} may possibly contain an appreciable amount of bomb-produced S^{35} .

Introduction. In this laboratory we have been carrying out, over the last few years, a systematic program to measure the concentrations in rainfall of the short-lived radioisotopes P^{32} , P^{33} , and S^{35} . These isotopes are known to be produced in the interactions of cosmic rays with air nuclei. The first experiment on the simultaneous measurement of these four isotopes in rain water was conducted in 1957 by Goel, Narasappaya, Subhakara, Rama, and Zutshi [1959]; the experiment was repeated in 1958 by Lal, Rama, and Zutshi [1960]. The measured fallouts in 1958 were found to be more by 30, 70, and 200 per cent in the case of Be^7 , P^{32} , and S^{35} , respectively, than the values observed in 1957. The excess in the fallout of Be^7 in 1958 over that in 1957 may be considered to be small, but the excess of P^{32} is fairly large and of S^{35} really very large. Further, the observed fallouts of S^{35} and P^{32} in 1958 were found to be in excess of the values to be expected if these isotopes were produced by cosmic rays only. After considering the various factors involved, Lal, Rama, and Zutshi [1960] concluded that the major part of the fallout of S^{35} in 1958 originated in nuclear bomb explosions. This raised the doubt whether part of the fallouts of P^{32} and Be^7 also could have originated in nuclear explosions.

In view of these considerations it was decided to carry out a similar experiment in 1959. The results obtained in the 1959 experiment are reported in this paper and are discussed in relation to the results obtained in earlier years. A significant feature was that no nuclear tests were conducted from November 1958 till the time this experiment was concluded. Therefore, the measured fallouts of Be^7 and of P^{32} (which have short

half-lives) are almost exclusively due to (comparatively recent) cosmic-ray production, since any activity due to bomb explosions would have decayed in the period between cessation of the tests and the present measurements. In the case of S^{35} , which has a relatively long half-life, the bomb-produced activity could not have died down completely during this intervening period.

EXPERIMENTAL PROCEDURE AND RESULTS

The fallouts of Be^7 and P^{32} were measured in rainfall which occurred at Kodaikanal (10°N , 77°E) during the period from November 1958 to October 1959; the fallouts of Be^7 , P^{32} , and S^{35} were measured in rainfall which occurred at Bombay (19°N , 73°E) during the period from June 1959 to October 1959. The results are presented in Tables 1 and 2. The results of all measurements in rainfall at Bombay and Kodaikanal over the past 5 years are summarized in Table 3. The experimental procedures were essentially identical in all these measurements and have been described earlier [Goel and others, 1959].

Discussion. It can be seen that the fallouts of Be^7 , P^{32} , and S^{35} have been fluctuating during the last 5 years. The lowest values in each case were obtained during 1959. The fluctuations, though not enormous, seem significant. The question arises whether such fluctuations can occur if the isotopes are solely of cosmic-ray origin. Recent work has shown that very large changes in cosmic-ray intensity do take place. These are mainly related to phenomena which occur on the sun; thus, following solar flares, very large increases in cosmic-ray intensity have been observed; on other occasions intensity decreases of

TABLE 1. Observations at Kodaikanal

Date of Rainfall	Be ⁷ , atoms/ml	P ³² , atoms/ml	Be ⁷ /P ³²
1958			
Nov. 2	...	17 ± 2	...
Dec. 4	680 ± 100	5.1 ± 0.5	134 ± 25
Dec. 14	730 ± 110	3.2 ± 1.0	224 ± 100
Dec. 24	3700 ± 600
1959			
Jan. 13	550 ± 170	4.7 ± 1.4	117 ± 25
Jan. 14	870 ± 170	4.2 ± 2.0	207 ± 90
Jan. 15	810 ± 400	17 ± 15	...
Jan. 31	1480 ± 170	17.4 ± 3	85 ± 15
Apr. 6	4100 ± 220	16.8 ± 0.6	244 ± 20
Apr. 19	3640 ± 340	19 ± 4	192 ± 30
July 5	750 ± 70	4.4 ± 1.2	170 ± 50
July 13	1570 ± 120	5.7 ± 1.1	276 ± 60
Aug. 12	3880 ± 200	9.5 ± 1.9	409 ± 70
Aug. 26	1190 ± 100	3.5 ± 0.7	340 ± 70
Aug. 31	4080 ± 350	10.4 ± 1.5	381 ± 55
Sep. 24	875 ± 50	6.4 ± 0.9	137 ± 15
Oct. 3	1410 ± 180	3.7 ± 1.5	385 ± 150
Mean	1900 ± 400	9 ± 2	210 ± 60

the Forbush type have been seen. These changes, however, occur mainly in low-energy cosmic rays which are allowed by the earth's magnetic field to enter the atmosphere only at high latitudes. The low-energy particles produce very few interactions which lead to isotope production and any such interactions take place in the high stratosphere. There are, of course, instances of intensity changes in the high-energy component which can reach down through the troposphere to ground level, but these are rare and of short duration. Thus the intensity, in the troposphere, of cosmic-ray particles responsible for isotope production can be considered to be constant when the intensity is averaged over time periods of the order of or greater than the lifetimes of these isotopes. (Since we have measured the concentrations of the isotopes in rainfall, which essentially scavenges only the tropospheric activity, we consider for the purpose of this discussion the tropospheric production alone). It is, therefore, not possible to attribute the observed fluctuations to the changes in cosmic-ray intensity. Some fluctuations could, however, arise from meteorological causes, but these are expected to be small and similar for all the isotopes. Some of the observed large fluctuations have, therefore, to be attributed to some other cause; a possible and likely one is the production of these isotopes

in nuclear bomb explosions. In fact, *Lal, Rama and Zutshi* [1960] had earlier concluded that a major part of the S³⁶ fallout in 1958 was of bomb origin. In view of this, the present experiment of particular interest. No bombs were exploded from October 31, 1958, to the end of 1959; a period of 7 months had therefore elapsed between cessation of the tests and the present measurements (at Bombay). After the cessation of nuclear tests the bomb radioactivity must have reduced both by decay and by the process of fallout. In fact, the concentration in the 1959 rainfall of Sr⁹⁰ (which is produced entirely in nuclear explosions) did drop to a few per cent of that observed in 1958. Sr⁹⁰ has a half-life of 54 days which is almost identical to that of Be⁷; consequently any bomb-produced Be⁷ activity should also have reduced by 1959 to a few per cent of its 1958 value. If one considers decay alone, in the period of 7 months the quantities of bomb-produced P³², Be⁷, and S³⁶ would reduce to 0.003, 6, and 19 per cent, respectively, of their values at the time of cessation of nuclear explosions. The 1958 experiment was carried out when the nuclear tests were in progress. The average concentrations of P³², Be⁷, and S³⁶ in rain water were then 43 atoms/ml, 4300 atoms/ml, and 1500 atoms/ml, respectively. Even if we make the extreme assumption that all this activity derived from nuclear explosions, then decay alone would reduce the bomb activity in rain water in 1959 to a negligible amount of P³², 260 atoms/ml of Be⁷, and 285 atoms/ml of S³⁶. Comparing these values with the ones actually observed in 1959, we arrive at the conclusion that the measured Be⁷ and P³² fallouts in 1959 are essentially free from bomb contributions. Since the S³⁶ fallout in 1958 was mainly of bomb origin and since decay would reduce it only to a value which is comparable to that observed in 1959, it has not yet been possible to measure the fallout of purely cosmic-ray-produced S³⁶. The present measurements of Be⁷ and P³² are the only ones which are certainly free of bomb contamination. We shall, therefore, discuss these observations.

Production and Deposition of Be⁷ and P³²
Lal, Malhotra, and Peters [1958] calculated the rates of production of Be⁷ and P³² by cosmic rays in the earth's atmosphere. They found that the production rates vary considerably with altitude and latitude. However, if one takes the total

TABLE 2. Observations at Bombay

Date of Rainfall	Be ⁷ , atoms/ml	P ³² , atoms/ml	S ³⁵ , atoms/ml	Be ⁷ /P ³²
1959				
June 4	2530 ± 600	13.7 ± 1.4	...	185 ± 50
June 5	4370 ± 200	29.0 ± 1.5	...	151 ± 15
June 22	2640 ± 400	7.5 ± 0.5	2080 ± 100	353 ± 150
June 23	1380 ± 220	10.4 ± 1.5	...	133 ± 20
June 29	1600 ± 220	10.6 ± 1.5	...	151 ± 25
June 29	1960 ± 280	13.0 ± 1.5	...	151 ± 25
July 2	1800 ± 180	11.7 ± 4.0	...	155 ± 50
July 10	3580 ± 220	12.3 ± 0.5	...	291 ± 20
July 13	2840 ± 220	12.0 ± 1.0	565 ± 50	238 ± 30
July 20	1420 ± 200	11.2 ± 0.6	140 ± 35	127 ± 20
July 22	5450 ± 180	24.0 ± 1.0	530 ± 70	226 ± 25
July 31	2760 ± 240	13.6 ± 2.3	90 ± 25	202 ± 30
Aug. 20	9410 ± 340	9.5 ± 0.8	...	990 ± 90
Aug. 22	3020 ± 170	12.1 ± 1.3	430 ± 60	251 ± 25
Aug. 31*	810 ± 60	4.4 ± 0.6	120 ± 30	185 ± 25
Sep. 2*	1670 ± 110	8.6 ± 0.9	...	194 ± 20
Sep. 7*	1930 ± 120	5.7 ± 0.7	75 ± 25	336 ± 50
Sep. 12	2000 ± 110	10.0 ± 0.7	53 ± 20	200 ± 15
Sep. 14	5010 ± 220	13.3 ± 0.7	...	376 ± 20
Sep. 26	...	12.4 ± 1.0
Sep. 28	...	21.7 ± 1.9
Sep. 29	2810 ± 210	17.7 ± 1.1	...	159 ± 15
Oct. 1	1650 ± 140	8.7 ± 0.9	320 ± 150	189 ± 25
Oct. 2	1980 ± 140	8.0 ± 0.6	168 ± 55	248 ± 25
Oct. 4	3120 ± 170	2.7 ± 0.5	228 ± 25	1150 ± 230
Oct. 11	3220 ± 170	12.8 ± 0.7	192 ± 40	251 ± 20
Oct. 13	4150 ± 170	13.6 ± 0.7	...	305 ± 20
Mean	2900 ± 500	12 ± 2	385 ± 80	242 ± 55

The concentrations of Sr⁸⁹ in three samples collected on August 31, September 2, and September 7, 1959, were 180, 155, and 150 atoms/ml, respectively.

duction rate from ground level to the troposphere, it is found to be about the same at all altitudes, within a factor of less than 2. Rainfall is the main mechanism which brings these isotopes to the earth's surface. Since clouds descend very rarely into the stratosphere, the fallout occurs mainly from the tropospheric air. Tropospheric radioactivity will be scavenged by rainfall only if it descends into the troposphere. Very little activity due to Be⁷ and P³² leaks from

the stratosphere to the troposphere since the residence time of these isotopes in the stratosphere is supposed to be large compared with their half-lives. Therefore, rainfall brings to the earth's surface only that part of the Be⁷ and P³² production which is of tropospheric origin. An appreciable fraction of even the tropospheric production decays before it is removed by rainfall. The amount brought down by rainfall can be calculated in the following way:

TABLE 3

Year	Bombay, atoms/ml				Kodaikanal, atoms/ml		
	Be ⁷	P ³²	S ³⁵	Sr ⁸⁹	Be ⁷	P ³²	S ³⁵
1955	2400 ± 700
1956	4200 ± 600	31 ± 7	3100 ± 1500	...	3100 ± 400	...	190 ± 100
1957	3400 ± 600	26 ± 6	500 ± 200	...	1900 ± 400	...	120 ± 60
1958	4300 ± 800	43 ± 8	1500 ± 300	14000 ± 3000
1959	2900 ± 500	12 ± 2	380 ± 80	160 ± 80	1900 ± 400	9 ± 2	...

TABLE 4

Isotope	Geographic Latitude	Atoms/cm ² /yr		
		Tropospheric Production	Calculated Deposition	Observed Deposition
Be ⁷	10°N	6.6×10^5	4.6×10^5	3.3×10^5
	19°N	7.0×10^5	4.9×10^5	2.8×10^5
P ³²	10°N	3700	1500	1600
	19°N	3900	1600	1200

The production of an isotope in the troposphere must be in equilibrium with its fallout and decay, i.e.

$$P = N(1/\tau_F + 1/\tau)$$

where P = production rate, N = equilibrium value of the isotope, τ_F = period of fallout from the troposphere, and τ = mean life of the isotope. This gives the fallout rate

$$F = N/\tau_F = P \tau / (\tau + \tau_F)$$

Taking $\tau_F = 30$ days [Stewart, Osmond, Crooks, and Fisher, 1957] and using Lal, Malhotra, and Peters' calculated production rates for P , we have calculated the fallout rates of Be⁷ and of P³² in the latitudes of Kodaikanal and of Bombay. They are given in the fourth column of Table 4.

To measure the average fallout rate of an isotope on the earth's surface, one must make measurements at a number of places. But a rough estimate may be made from measurements at a single station by multiplying the observed average concentration (atoms/ml) by the average zonal rainfall (~ 175 cm for the Kodaikanal latitude belt and ~ 100 cm for the Bombay latitude belt). The annual fallout rates of Be⁷ and P³² estimated thus for the Kodaikanal and for the Bombay latitudes are given in the last column of Table 4. These values agree well with the values in column 4, which were estimated from Lal, Malhotra, and Peters' [1958] calculations. However, the recent measurements of Lal, Arnold, and Honda [1960] of the production rates of Be⁷ in oxygen and P³² in argon indicate that the calculated rates of production should be raised by a factor of 1.1 for Be⁷ and 1.8 for P³². The agreement between the observed and calculated deposition rates is then good within a factor of 2.

Conclusions. (i) It is shown that the radio-

isotopes Be⁷ and P³² observed in the 1959 rainfall at Bombay and at Kodaikanal are entirely cosmic-ray origin.

(ii) The annual fallout rates of Be⁷ and P³² in tropical latitudes, as computed from the measured concentrations in rain, are about 3×10^5 atoms/cm² and 1.4×10^5 atoms/cm², respectively. These values are compatible with the calculated values of their production in the troposphere by cosmic rays.

(iii) The annual fallout rate of cosmic-ray produced S³⁵ is expected to be less than 4×10^5 atoms/cm²; this is based on the average concentration of 380 atoms/ml of S³⁵ observed in the 1959 rainfall at Bombay. Some part of this activity could be due to bomb-produced S³⁵.

Acknowledgments. I am greatly indebted to Professor M. G. K. Menon for his keen interest and encouragement in this work. I am also grateful to Mr. E. Noronha for his valuable cooperation during the experiments.

REFERENCES

- Goel, P. S., N. Narasappaya, C. Prabhakara, Ramaiah Thor, and P. K. Zutshi, Study of cosmic ray produced short-lived isotopes P³², P³³, Be⁷ and S³⁵ in tropical latitudes, *Tellus*, **11**, 91-100, 1959.
- Lal, D., J. R. Arnold, and M. Honda, Cosmic-ray production rates of Be⁷ in oxygen and P³², P³³, S³⁵ in argon at mountain altitudes, *Phys. Rev.*, **118**, 1626-1632, 1960.
- Lal, D., P. K. Malhotra, and B. Peters, On the production of radioisotopes in the atmosphere by cosmic radiation and their application to meteorology, *J. Atmospheric and Terrest. Phys.*, **12**, 300-328, 1958.
- Lal, D., Rama, and P. K. Zutshi, Radio-isotopes P³², Be⁷, and S³⁵ in the atmosphere, *J. Geophysical Research*, **65**, 669-674, 1960.
- Stewart, N. G., R. G. D. Osmond, R. N. Crooks, and E. M. Fisher, The world wide deposition of long-lived fission products from nuclear test explosions, A.E.R.E. HP/R 2354, 1957.

(Manuscript received June 16, 1960; revised August 31, 1960.)

A Proposed Automatic Standard Magnetic Observatory

L. R. ALLDREDGE

*U. S. Coast and Geodetic Survey
Washington, D. C.*

Abstract. Present-day standard magnetic observatories employ an extensive amount of routine hand labor in determining absolute values of magnetic components and in scaling magnetograms.

An automatic observatory is proposed in which the proton precession magnetometer is used as the detecting element. Two mutually perpendicular pairs of coils control bias fields in a plane perpendicular to the mean magnetic field vector. A preliminary calibration procedure involving reversals of the bias fields and rotations of the coil system eliminates uncertainties in coil geometry. Subsequently, measurements are automatically recorded in digital form so that a value of each magnetic component can be computed with high accuracy once a minute.

The data are automatically handled in a computer to obtain all the statistical output which is typical of standard observatories.

INTRODUCTION

The instrumentation in most standard magnetic observatories has changed very little during the past 50 years. A few important changes, of course, have been made. Some observatories have adopted electromagnetic standards. Some have installed rapid-run magnetographs and a few observatories are beginning to use proton precession magnetometers. None of these innovations have, however, changed the way in which observatory data are handled. Magnetograms are still hand-scaled and the work required to obtain absolute values for base line determinations is tedious and time consuming. One of the main products of an observatory is the statistical output describing the mean hourly, daily, monthly, and annual absolute values of the magnetic field components and the indices. The automatic observatory discussed in this proposal refers to a system which has, as its primary function, the job of automatically producing the statistical output now characteristic of standard observatories.

Many observatories produce quick-run magnetograms. These records are an important part of the work of an observatory even though they do not normally contribute to its statistical output. Successful automation of the more routine work of the observatories will leave more time for productive research activities.

New magnetic measuring devices such as the proton precession, rubidium vapor, and helium

magnetometers yield the absolute value of the total intensity of the magnetic field without any special calibrating devices. Ways have been found to utilize these to obtain the values of the magnetic components in absolute terms. The use of such instruments will make it possible to combine the measurement of magnetic variations and the determination of absolute base-line values into a single integrated apparatus. All these devices produce digital outputs which are readily adapted to automatic data-processing techniques.

It is hoped that the adoption of the proposal made here will make standard magnetograms obsolete. The plan includes the reconstruction of magnetograms from data taken once a minute. If more detail is wanted for research purposes, the quick-run magnetograms could be used.

After the proposal described in this paper was completed, it was brought to the attention of the writer that Paul H. Serson of the Dominion Observatory, Canada, and V. B. Gerard of New Zealand have made informal proposals to accomplish the same results as described here, but in a slightly different manner.

CHARACTERISTICS OF NEW MAGNETOMETERS

During the past 5 years a variety of new magnetometers has come into existence. Those of particular interest to this study belong to a class which yields absolute values of magnetic

field intensity dependent on atomic or nuclear constants. This class of magnetometers measures directly only total field intensity. Without the aid of auxiliary bias fields they cannot be used to obtain component information. In spite of this limitation, they are useful in observatory work. The extra trouble required in using these new instruments to get component data is justified because of the increased accuracy attainable and the ability to combine the measurement of magnetic variations and absolute values into a single integrated apparatus.

The best known and most completely developed absolute total field magnetometer is the proton precession magnetometer [Packard and Varian, 1954]. This instrument employs the well-known proton free-precession principle. Absolute measurements can be made with an accuracy of 0.1γ [Packard, 1960].

The proton precession magnetometer requires a rather strong polarizing field. Only one field determination can be obtained for each polarizing procedure. The resulting slow data rate would be a distinct disadvantage for use in studying rapid time variations but may not limit the use of the instrument in obtaining traditional types of statistical observatory data.

The rubidium vapor magnetometer is not as well developed as the proton precession magnetometer. This magnetometer uses an optical-pumping technique and the precession of atomic magnetic moments. The development has proceeded far enough to make it clear that the self-oscillating type will be capable of recording magnetic field changes as small as 0.01γ .

The value of the rubidium vapor magnetometer as an absolute instrument is not certain at the present time. In the self-oscillating form the output is a smear from four unresolved lines. Changes in light sensitivity or orientation may change the relative population of the energy states involved and hence the absolute calibration. A straight transmission type of system may be more desirable, but here again orientation in the field being measured may have an effect (P. L. Bender, private communication, 1960). Decision on these points must await further developmental work.

Other atomic total field magnetometers which are being developed are the maser nuclear and the meta-stable helium magnetometers. These are not developed far enough to allow proper

assessment of their value as observatory instruments.

At this point it is not really necessary to specify which total field magnetometer should be chosen for use in the automatic observatory being discussed in this paper. The entire new system can be discussed in such a way that any one of a number of magnetometers might be substituted as the indicating instrument. All of them determine magnetic total intensities by measuring a precession frequency or period which is readily digitalized and is hence compatible with automatic data-processing machines. However, in the interest of clarity, the indicating instrument in the following discussion is assumed to be a proton precession magnetometer.

DESCRIPTION OF PROPOSED AUTOMATIC OBSERVATORY

General description. The proposed scheme is patterned after Bacon's [1955] plan, which in modified form was used at ground stations to monitor the earth's field during the project Vanguard magnetic experiment [Heppner, Stolarik, and Meredith, 1958; Shapiro, Stolarik, and Heppner, 1960]. It differs from Bacon's plan by using a larger bias field and a coil reversal procedure to obtain more accurate absolute declination and inclination data and by providing for the automatic processing of the magnetometer output to obtain the final statistical data typical of standard observatories. Although what follows is in the present tense, it should be remembered that it describes a proposed system—not an existing system.

Basically, the design calls for the determination of the amplitude and direction of the magnetic field vector \mathbf{F} through the use of two mutually perpendicular auxiliary bias fields both of which are perpendicular to the mean magnetic field vector, one being in the mean magnetic meridian plane.

The basic geometrical arrangement for the proposed system is illustrated in Figure 1. C_d and C_i represent mutually perpendicular Helmholtz coil pairs used respectively to produce bias fields for the determination of declination and inclination. The proton sample is mounted at the center of the coil system. The rigid coil system can be rotated about the axis $e-f$, which is maintained in a vertical plane. The axis $e-f$

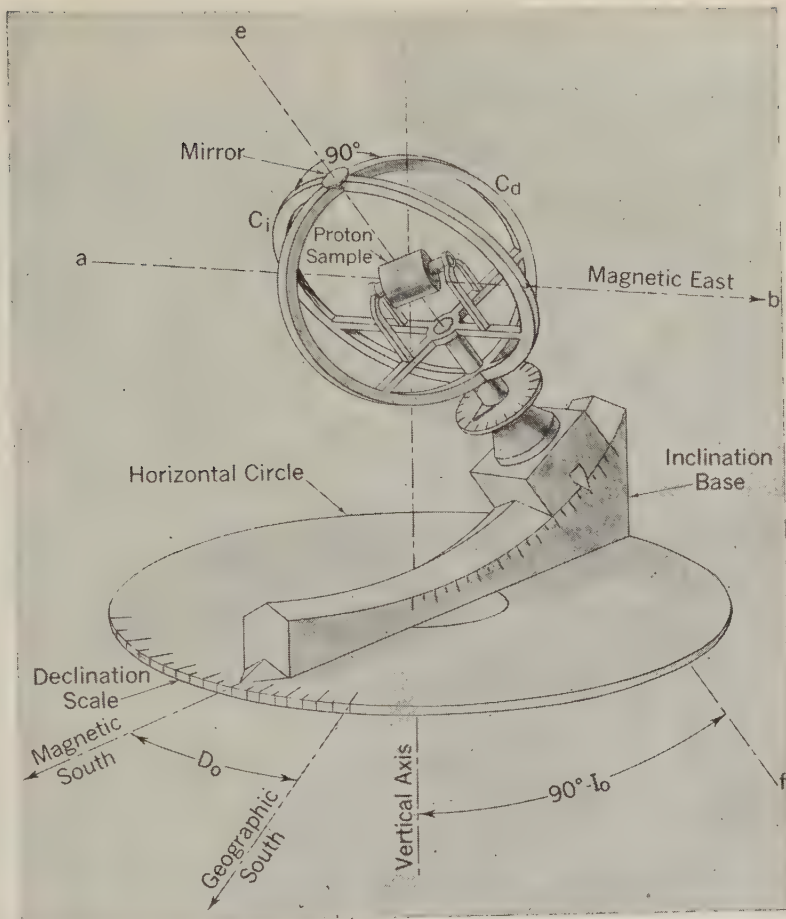


Fig. 1. Coil system for vector proton precession magnetometer (schematic).

can be rotated about the magnetic east-west axis $a-b$. The entire assembly can be rotated in a horizontal plane. Hurwitz and Nelson [1960] have experimentally shown that the gradients within a Helmholtz coil system 97 cm in diameter are sufficiently small to permit a usable signal even when a field as large as 50,000 γ is applied by the coil system. Since in this proposal a bias field of only approximately 15,000 γ is contemplated, a Helmholtz coil system 75 cm in diameter should be adequate. This size is not inconvenient in an observatory instrument.

Initially, rotations are made about the vertical axis and the axis $a-b$ so that the axis $e-f$ coincides as nearly as possible with the mean magnetic field vector \mathbf{F}_0 . After this orientation has been completed, the declination D_0 and inclination I_0 of the axis $e-f$ must be determined accurately. This is done through the use of a mirror, mounted

on the coil system, and an external precision theodolite. The mirror is adjusted perpendicular to the axis $e-f$ by using the motion of a reflected beam of light for an indicator as the coil system is rotated. The theodolite is then positioned so that the telescope axis coincides with the axis $e-f$ by viewing itself in the mirror. The angles I_0 and D_0 are then determined by using standard procedures.

It is anticipated that once D_0 and I_0 have been set and accurately determined, the apparatus is sufficiently stable so that these values will remain constant. They can, of course, be rechecked any time it is thought desirable.

Determination of inclination. At any given moment \mathbf{F} may differ from \mathbf{F}_0 . The differences between the true inclination I and the true declination D and the values of I_0 and D_0 corresponding to the orientation of the axis $e-f$

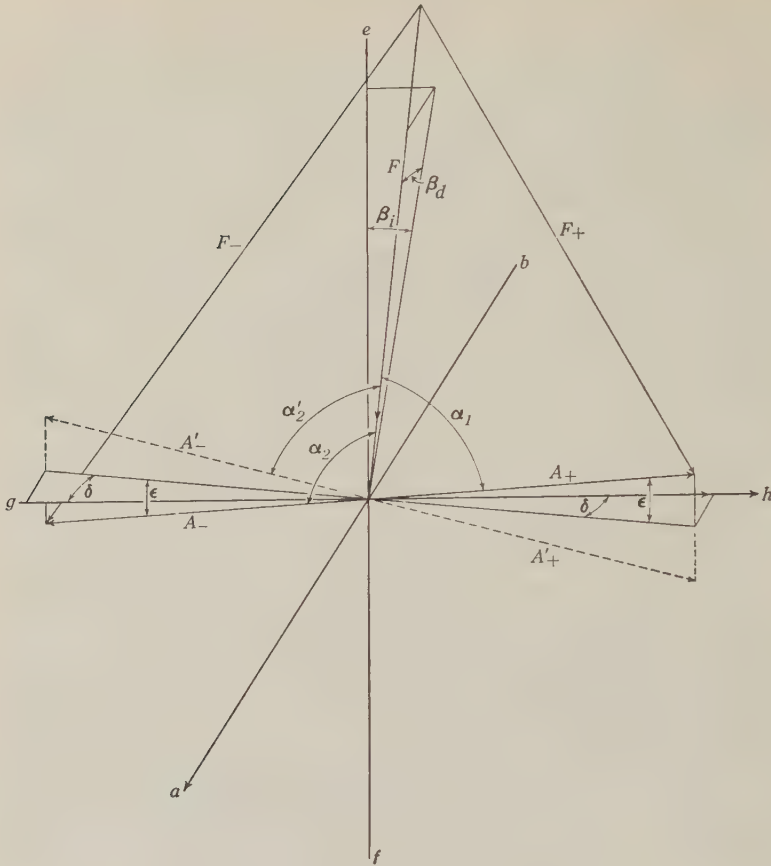


Fig. 2. Determination of inclination.

are determined by use of the auxiliary fields produced by the coils C_i and C_d . This operation would be straightforward if the magnetic axes of the coils were accurately known. In practice the effective axes of the coils must be determined as a part of the calibration procedure if accurate values are to be obtained.

The way in which the instantaneous value of I is obtained can be understood by reference to Figure 2, in which the axes $a-b$ and $e-f$ are the same as in Figure 1 and the axis $g-h$ is perpendicular to the other two. In Figure 2 the plane defined by the axes $e-f$ and $g-h$ represents the mean magnetic meridian plane. The axis $e-f$ still represents the direction of the mean magnetic field vector F_0 . This axis is of course not usually vertical. It has been drawn as vertical in Figure 2 only to simplify the description. The angles β_i and β_d represent departures in I and D from I_0 and D_0 .

A_+ and A_- are equal in amplitude and represent

the bias fields created by positive and negative currents respectively in coil C_i . A'_+ and A'_- represent the same bias fields after the coil frame has been rotated 180° about the axis $e-f$. The angles ϵ and δ represent departures of the bias fields from their designed direction along the $g-h$ axis.

Before any bias field is applied the magnetometer will indicate a magnitude F . When a bias field A_+ is applied the magnetometer will indicate a magnitude F_+ , the resultant of F and A_+ . When the bias field current is reversed the magnetometer will indicate a magnitude F_- . A_+ and A_- are of equal magnitude and are collinear. Using the law of cosines applied to the two large triangles in Figure 2, it can be shown that

$$\alpha_1 = \cos^{-1} \left[\frac{F_-^2 - F_+^2}{2 \sqrt{2} F (F_+^2 + F_-^2 - 2F^2)^{1/2}} \right] \quad (1)$$

$$\cong \frac{\pi}{2} + \frac{F_+^2 - F_-^2}{2\sqrt{2}F(F_+^2 + F_-^2 - 2F^2)^{1/2}} \quad (2)$$

The error in the latter approximation does not exceed 1.5 seconds of arc if α_1 does not deviate from $\pi/2$ by more than 2° . In practice this condition will always apply.

The coil frame is now rotated 180° about the axis $e-f$ and measurements are made of the quantities F_+' and F_-' (which correspond to F_+ and F_- before the coil was rotated). From these measurements α_2' can be computed from

$$\alpha_2' \cong \frac{\pi}{2} - \frac{F_+'^2 - F_-'^2}{2\sqrt{2}F(F_+'^2 + F_-'^2 - 2F^2)^{1/2}} \quad (3)$$

All of the **A** vectors and the axis $e-f$ in Figure 2 are coplanar. Since **F** is in general not in this plane, α_1 and α_2' cannot by themselves precisely determine β_i . From Figure 2 it can be shown that when the series approximations are used for the trigonometric terms and fourth- and higher-order terms are neglected

$$\beta_i = \frac{\alpha_2' - \alpha_1}{2} - \beta_d \delta + \beta_i \left(\frac{\beta_d^2}{2} + \frac{\delta^2}{2} \right) \quad (4)$$

If in practice we take

$$\beta_i = \frac{\alpha_2' - \alpha_1}{2} \quad (5)$$

the error will be approximately equal to $-\beta_d \delta$. In practice this error will be very small, since β_d will seldom exceed 1° even at reasonably high latitudes. This value of β_d would result in an error in β_i of approximately 1 second of arc for each minute of arc for δ . The value of δ cannot be determined by the procedure described here. It is estimated, however, that it can be kept within a limit of a few minutes by careful adjustment of the coil system. This error term gives the interaction between measurements of inclination and declination.

In an automatic system it would be difficult to rotate the coil mechanically to obtain α_1 and α_2' for each determination of β_i , and it is not necessary to do so. Once β_i and α_1 have been determined at a given instant of time, it is anticipated that their sum

$$k_i = \alpha_1 + \beta_i = \pi/2 - \epsilon \quad (6)$$

which is the angle between the bias field **A**₊

and the $e-f$ axis within the approximations already admitted, will remain constant, requiring only occasional rechecking. During subsequent automatic operation only α_1 as obtained from equation 2 need be determined, since the required angle β_i can then be obtained from equation 6.

The final value of inclination is given by

$$I = I_0 + \beta_i = I_0 + k_i - \alpha_1 \quad (7)$$

To insure that k_i remains constant, the coil system and its supporting members will be thermally insulated so that the handling of the instrument will not misorient the coil axis by differential expansion.

A contribution to the error in the determination of α_1 , and hence of I , will come from the uncertainty with which total field values can be measured. This error in α_1 depends on the magnitude of the bias field. The magnitude of the error from this source can be obtained from (2) by assuming that the values of F , F_+ , and F_- can all be measured to an accuracy of $\pm\mu$. The maximum error at a location where F is 50,000 γ for the simplest case of $F_+ = F_-$ is given approximately by

$$\text{error in } \alpha_1 = \frac{\pi}{2} - \cos^{-1} \left[\frac{\mu(1 + \lambda^2)^{1/2}}{5 \times 10^4 \lambda} \right] \quad (8)$$

where λ is the ratio of the bias field intensity to the total field intensity. This error is plotted in Figure 3, where it is seen that, for an error in the measurement of F of $\pm 0.1 \gamma$, a bias field of only $0.3 F$ will keep the error in the determination of α_1 to less than 2 seconds of arc. A value of bias field equal to $0.3 F$ will be tried in the preliminary experiments with this system.

Determination of declination. The measurement of declination is essentially the same as the measurement of inclination. For declination the coils marked C_d in Figure 1 are used to create the needed bias fields in a direction perpendicular to the mean magnetic meridian plane. In the process, the coil system must again initially be rotated through 180° about the axis $e-f$ to obtain a value of β_d in Figure 2. In a manner identical to that used in the inclination problem, once k_d is determined by an equation analogous to (6), β_d can be obtained automatically without further rotation of the coil.

The principal way in which the declination problem differs from the inclination problem is that β_d must be projected down onto the hori-

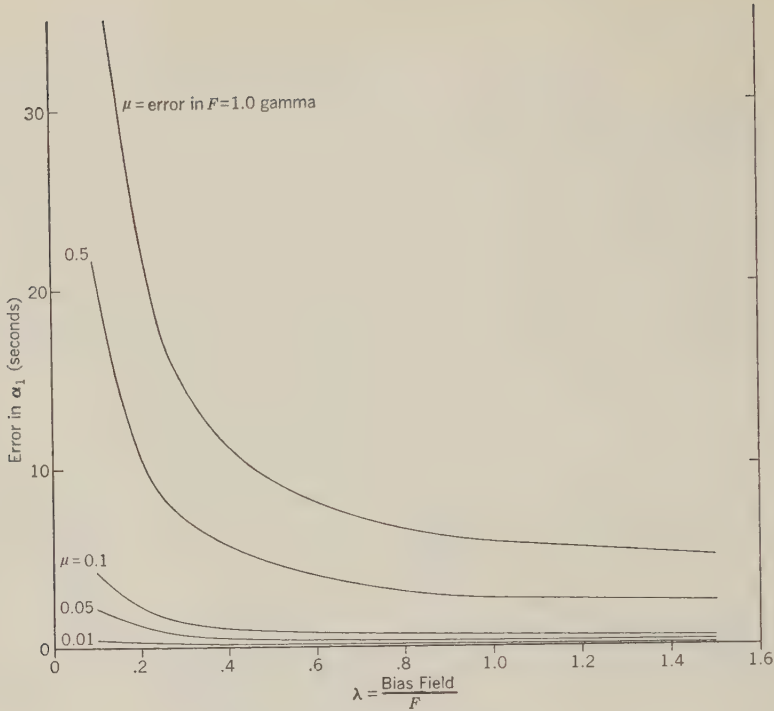


Fig. 3. Error in computing α_1 .

zontal plane. The final value of declination is given by

$$D = D_0 + \frac{\beta_d}{\cos I}$$
$$= D_0 + (k_d - \alpha_1)/\cos I \quad (9)$$

where, of course, α_1 refers to calculations from equation 2 for the case in which the bias fields were created by the declination coils C_d .

The discussion regarding errors in inclination is directly applicable to the declination as well.

Sequence of operation. The heart of the automatic observatory is the digital recording proton precession magnetometer. The instrument as a whole is programmed automatically so as to record variables from which one value of F , (F_+ , F_-) (for inclination) and (F_+ , F_-) (for declination) can be computed each minute.

After the original hand adjustment of I_0 and D_0 and the mechanical coil rotation to obtain the zero calibration have been completed, the automatic program is started which provides for the following sequence of operations:

1. At start of each minute close circuit to C_i , creating resultant field magnitude F_+ to be used in the determination of inclination.

2. Actuate digital counter on the output of the magnetometer and record the number of cycles n_+ corresponding to F_+ . (The meaning of n_+ is described later.)

3. Reverse bias current in C_i , creating the resultant field magnitude F_- .

4. Actuate digital counter and record n corresponding to F_- .

5. Remove bias field.

6. Actuate digital counter and record n corresponding to field magnitude F .

7. Repeat steps 1 to 4 using coil C_d to obtain two additional counts n_+ and n_- to be used to compute declination.

Every operation involving the recording of a number n will require an internal subroutine permitting the polarization of the detecting medium in the proton precession magnetometer. This internal subroutine will also include the retuning of the amplifier if required.

Data recording. The digital output of the magnetometer is recorded on magnetic and paper tape to minimize the data handling and processing work at the central office, which is responsible for processing the output of a group of observatories. With the printed tape output

The observer can quickly determine whether the magnetometer is functioning properly and can write additional notes on the tape if required. The magnetic tape record will provide high-speed 'read-in' to a digital computer.

The proton precession frequency F_p , which is proportional to the magnetic total field, is determined indirectly by measuring the precession period in the following way. A precision counter counts the number of cycles n , from a high-frequency crystal-controlled oscillator with the period t , which elapse while exactly N proton precession cycles are completed. From this information the precession frequency is given by

$$f_p = (N/t)(1/n)$$

and the corresponding magnetic field, using the gyromagnetic ratio of *Bender and Driscoll* [1958], is computed from

$$F \text{ (gammas)} = 23.4874(N/t)(1/n) \\ = \text{constant}/n \quad (10)$$

The constant is known, since N and t are known; and n is the recorded number corresponding to F .

The numbers n corresponding to each magnetic field measured must be recorded to 6 decimal digits to permit the calculation of the magnetic field values to an accuracy of 0.1 γ over a range of 60,000 γ . This can easily be accommodated on standard paper tape. Since five values of magnetic field must be recorded each minute, 7200 entries must be made per day. These data could easily be contained on a 1100-foot roll of paper. Assuming very modest magnetic recording parameters, it is estimated that the data from each observatory for a month could easily be stored on a 1200-foot reel of $\frac{1}{4}$ -inch-wide magnetic tape.

Some key observatories have established the practice of reporting magnetic variation data to leading scientific institutions each day. This requirement is met by making visual strip recordings of the variations in F , I , and D , using the technique described by *Bacon* [1955]. These recordings need not be extremely accurate, since they are used only in the determination of preliminary K indices.

A digital-to-analog converter is used to obtain voltages V_F , (V_+ , V_-) (for inclination), and (V_+ , V_-) (for declination) which are propor-

tional to the digital counts n which correspond respectively to the field strengths F , (F_+ , F_-) (for inclination) and (F_+ , F_-) (for declination). Successive values of V_F are routinely commuted to an F strip recorder. The recorded variations in V_F are inversely proportional to the desired variable ΔF . However, since

$$\Delta F = \frac{\text{constant}}{V_F^2} \cdot \Delta V_F$$

and since V_F^2 will not vary by more than 4 per cent even for a peak variation of 1000 γ , it is clear that the record of ΔV_F may be taken as a record of ΔF for purposes of determining preliminary magnetic indices. It is, of course, necessary to determine the value of the constant properly in relation to the K scale that is used.

To obtain the variations in inclination ΔI , V_+ and V_- (for inclination) are routinely commuted to a differential amplifier so that an output proportional to $V_+ - V_-$ will be recorded. Using equations 2 and 7, and a Taylor series expansion approximation, it can be shown that for any fixed bias field magnitude A ,

$$\Delta I = \frac{\text{const } \Delta(V_+ - V_-)}{F_0(F_0^2 + A^2) + y(A^2 - 2F_0^2)} \quad (11)$$

where y is the component of the magnetic variation along the mean magnetic vector. For y as large as 1000 γ , F_0 equal to 50,000 γ , and $A = 0.3 F_0$, equation 11 indicates that ΔI is proportional to $\Delta(V_+ - V_-)$ to within an accuracy of 3.5 per cent. This is sufficiently accurate for use in the determination of preliminary K indices.

A method of recording ΔD is very similar to that required for ΔI and will not be repeated here.

In using the strip records to obtain preliminary K indices, new K scales must be derived. This will involve a transformation of the old K scales made up for H , Z , and D in such a way as to include the relationship between F , I , D , H , and Z and the calibration constants for the strip charts.

Recordings of only those elements which are found to govern the K indices would be routinely recorded.

COMPUTATIONS

The magnetic tape record is fed directly into a high-speed computer which is programmed to

compute values of each desired magnetic component for each minute and the hourly averages of the components. In addition, the computer will determine the magnetic activity indices by using the following procedures:

(a) For each minute find the average value of a given component over a 3-hour period centered on the minute in question.

(b) Take the difference between the actual value of the component and the average value found in (a).

(c) For each 15-minute period determine the range of the deviations noted in (b), or the largest single deviation, whichever is larger.

(d) In accordance with a predetermined Q scale, assign a Q index to each 15-minute period corresponding to the values found in (c).

(e) For each 3-hour period determine the range of the deviations noted in (b).

(f) In accordance with the predetermined K scale, assign a K index to each 3-hour period corresponding to the values found in (e).

(g) The above steps should be repeated for each component. The final Q and K indices which are retained are the largest found when all components are considered. (In practice some components can be omitted for certain observatories).

After the computation of components is complete, the output cards are fed into an automatic plotting machine such as the electroplotters made by Benson-Lehner Corporation, in which the components are plotted to form magnetograms to a scale suitable for reproduction in the publications of the observatories.

The computations described above provide an output which includes all the statistical type of data now produced and published by standard observatories. It is immediately apparent, of course, that many additional types of correlation or frequency analysis studies can be pursued on the computer once the data is in this digital form.

MAGNETIC ACTIVITY INDICES

The ideas expressed in the computation procedure above for finding magnetic activity indices may be controversial. For this reason further justification of this phase of the proposal is given here.

The K index is intended to be a measure of the effect of solar particle-radiation upon the

earth's magnetic field. The instructions for obtaining K indices indicate that they should be independent of the variations in the magnetic record caused by the solar daily variation Sq , the lunar daily variation L , solar flare effects (s.f.e), and post-storm perturbation represented by a general depression in H [Bartels, 1957].

The instructions on how to recognize s.f.e.'s and prevent their making a contribution to the K index are not clear, and neither are the instructions explicit on how to eliminate the post-storm depression from the K index.

It is frequently found that experienced observers will disagree on the K index that should be assigned for a given time interval. These disagreements often stem from a different choice of the $Sq + L$ curve. Differences among observers are most likely to occur at the start of a magnetic storm. These uncertainties in the determination of the K index represent a subjective element which is not consistent with good scientific work.

The method described in this paper for determining the magnetic activity indices does provide a very definite objective way of obtaining both K and Q indices. This procedure would, of course, not be a practical one if hand-scaling of the records were employed. It should, however, be a straightforward, simple job for a high-speed digital computer already containing values of each component for each minute of time. Admittedly, this method would not eliminate solar flare effects. If this is considered important enough, they can be eliminated by a visual scanning of the final magnetograms. Since the proposed method is based on discrete measurements 1 minute apart, the K indices may be systematically too low during very rare periods which are dominated by very narrow giant pulsations or very rapid storm variations.

The averaging interval suggested in computation procedure (a) should be further investigated. In general, it is clear that the averaging interval should be long compared with the period of K -variation disturbances but short compared with the period of 'non K -variation' disturbances. These two requirements cannot always be met. Compromises are required.

One example of how the averaging period can affect the K indices is illustrated in Figure 4, where samples of H curves for Koror are shown. Superimposed on the regular magnetograms, two

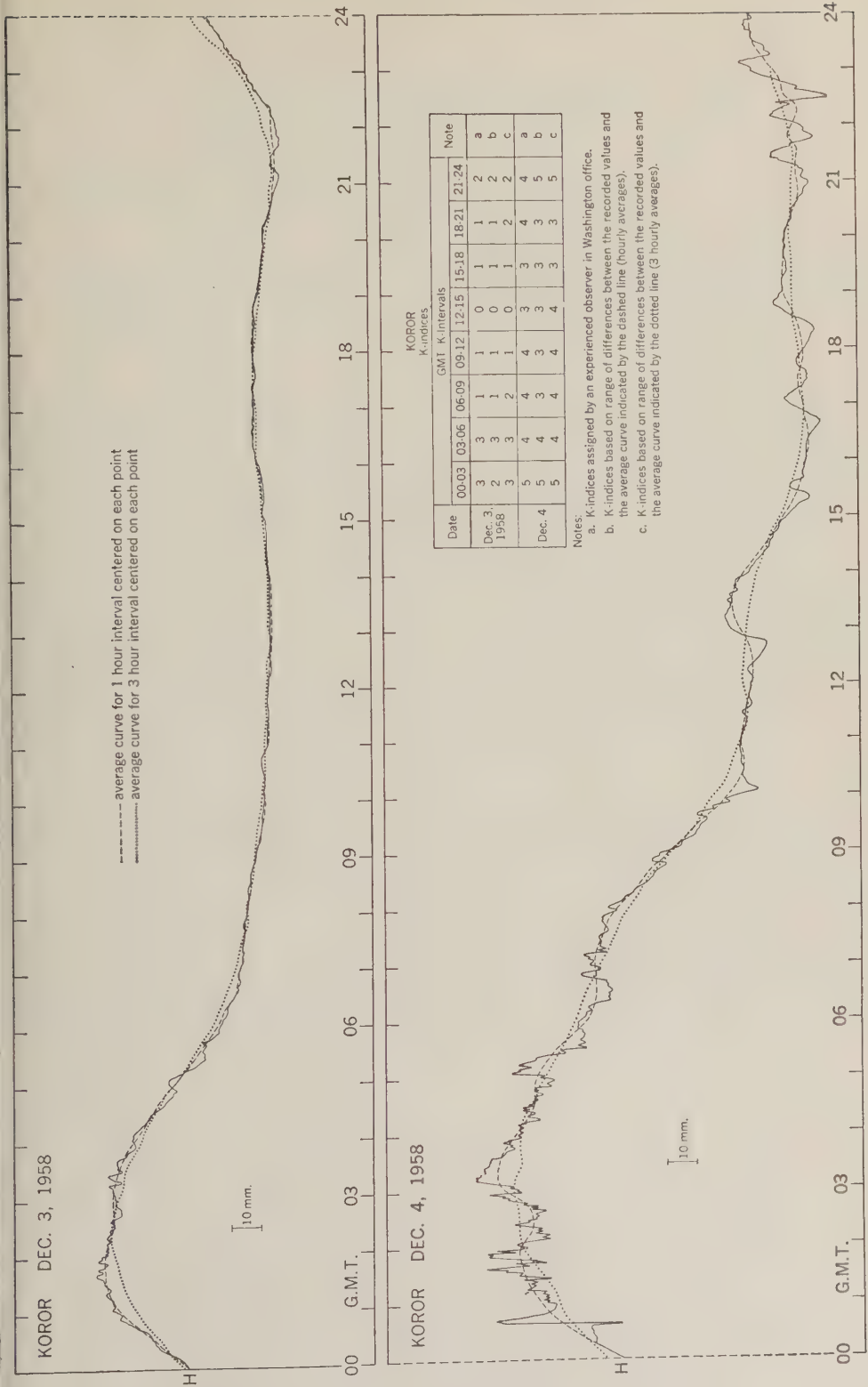


Fig. 4. K scaling for Koror.

different average curves are shown. The one with an hour averaging period follows the recorded value too closely, tending to decrease the K indices. The average curve based on a 3-hour averaging period appears to follow the diurnal curve sufficiently well. A longer averaging period would tend to fall too far below the peak of the diurnal curve producing artificially high K indices during midday at Koror.

A longer averaging period may prove advantageous at other observatories where the ratio of diurnal variations to disturbance variations is smaller than at Koror. Such an example was worked out for Sitka, where it was found that a 5-hour averaging period was preferred to a 3-hour averaging period.

It may be that an averaging period even longer than 5 hours would be better for use at some observatories. A separate study should be made of each observatory to determine the optimum averaging period. The largest averaging period that can be used without producing artificially large K indices during quiet periods should be specified for each observatory.

The Q index described in the computational procedure corresponds quite closely to the Q index used by Bartels [1957]. It should provide an adequate measure of short-term magnetic activity, and is easy to get automatically from the computer.

Since the C figures are not often used in correlation studies, it is probably not worth the trouble to devise a complicated objective way of determining them. It is proposed here that either the C figures be dropped entirely or that a very simple mechanized procedure be adopted starting with the amplitudes of the variations or the K indices themselves.

CONCLUSION

It is concluded that an automatic observatory

as described above will be capable of obtaining with increased accuracy all the statistical outputs from standard observatories. The tedious and time-consuming jobs of hand-scaling the magnetograms and separately determining their base lines will be avoided.

The U. S. Coast and Geodetic Survey has started on an experimental program to test the practicability of such a system.

Acknowledgement. The author would like to thank L. Hurwitz for assistance in the preparation of this paper.

REFERENCES

- Bacon, F. W., Adaptation of a free precession magnetometer to measurements of declination, Master's Thesis, U. S. Naval Postgraduate School, Monterey, Calif., 1955.
- Bartels, J., The technique of scaling indexes K and Q of geomagnetic activity, *Annals of the IGY*, 4, 215-226, 1957.
- Bender, P. L., and R. L. Driscoll, A free precession determination of the proton gyromagnetic ratio, *IRE Trans. on Instrumentation*, 1-7, 176-180, 1958.
- Heppner, J. P., J. D. Stolarik, and L. H. Meredith, A review of instrumentation for the magnetic-field satellite experiment, *Annals of the IGY*, 6, 323-329, 1958.
- Hurwitz, L., and J. H. Nelson, Proton vector magnetometer, *J. Geophys. Research*, 65, 1759-1765, 1960.
- Packard, M., On the comparison of the proton and the rubidium vapor magnetometers as an observatory standard, Abstract submitted for presentation at the IUGG 12th Assembly in Helsinki, 1960.
- Packard, M., and R. Varian, Free nuclear induction in the earth's magnetic field, *Phys. Rev.*, 93, 941, 1954.
- Shapiro, I. R., J. D. Stolarik, and J. P. Heppner, The vector field proton magnetometer for IGY satellite ground stations, *J. Geophys. Research*, 65, 913-920, 1960.

(Manuscript received July 9, 1960.)

The Kernel Function in the Multiple-Layer Resistivity Problem

SEIBE ONODERA

*Geophysical Exploration Laboratory
Kyushu University, Japan*

Abstract. An explicit expression in terms of symmetric auxiliary functions is developed for the kernel function in the integral representation of the potential at the surface of a medium composed of homogeneous, isotropic, horizontal layers. As an example, the explicit form is given for the case of seven layers.

Introduction. A representation of the electric potential by an integral for the n -layer resistivity problem, which concerns the determination of the electric potential due to a point source on the surface of horizontally stratified structure consisting of n layers of different resistivities, was given by *Stefanescu and Schlumberger* [1930]:

$$V(r) = \frac{\rho_1 I}{2\pi} \left\{ \frac{1}{r} + 2 \int_0^\infty K_n(k_i, h_i; \lambda) J_0(\lambda r) d\lambda \right\} \quad (1)$$

where $\rho_1 I/2\pi$ is the strength of a point source, I is the current intensity, r is the surface distance between electrodes, J_0 is the Bessel function of the first kind of zero order, and λ is a parameter. $K_n(k_i, h_i; \lambda)$, called a kernel function, is a function of the resistivity factors k_i , layer-depths h_i , and λ .

In general, the kernel function is expressible in the following forms:

$$K_n(k_i, h_i; \lambda) = \frac{N_n}{\Delta_n} = \frac{N_n}{M_n - N_n} \quad (2)$$

$$M_n = \begin{vmatrix} v_1 & -u_1 & -v_1 & 0 & 0 & 0 & \cdots & 0 & 0 & 0 & 0 & 0 \\ v_1 & p_1 u_1 & -p_1 v_1 & 0 & 0 & 0 & \cdots & 0 & 0 & 0 & 0 & 0 \\ 0 & u_2 & v_2 & -u_2 & -v_2 & 0 & \cdots & 0 & 0 & 0 & 0 & 0 \\ 0 & -u_2 & v_2 & p_2 u_2 & -p_2 v_2 & 0 & \cdots & 0 & 0 & 0 & 0 & 0 \\ . & . & . & . & . & . & . & . & . & . & . & . \\ 0 & 0 & 0 & 0 & 0 & 0 & \cdots & u_{n-2} & v_{n-2} & -u_{n-2} & -v_{n-2} & 0 \\ 0 & 0 & 0 & 0 & 0 & 0 & \cdots & -u_{n-2} & v_{n-2} & p_{n-2} u_{n-2} & -p_{n-2} v_{n-2} & 0 \\ 0 & 0 & 0 & 0 & 0 & 0 & \cdots & 0 & 0 & u_{n-1} & v_{n-1} & -u_{n-1} \\ 0 & 0 & 0 & 0 & 0 & 0 & \cdots & 0 & 0 & -u_{n-1} & v_{n-1} & p_{n-1} u_{n-1} \end{vmatrix} \quad (3)$$

and

$$N_n = \begin{vmatrix} -u_1 & -u_1 & -v_1 & 0 & 0 & 0 & \cdots & 0 & 0 & 0 & 0 & 0 \\ u_1 & p_1 u_1 & -p_1 v_1 & 0 & 0 & 0 & \cdots & 0 & 0 & 0 & 0 & 0 \\ 0 & u_2 & v_2 & -u_2 & -v_2 & 0 & \cdots & 0 & 0 & 0 & 0 & 0 \\ 0 & -u_2 & v_2 & p_2 u_2 & -p_2 v_2 & 0 & \cdots & 0 & 0 & 0 & 0 & 0 \\ . & . & . & . & . & . & . & . & . & . & . & . \\ 0 & 0 & 0 & 0 & 0 & 0 & \cdots & u_{n-2} & v_{n-2} & -u_{n-2} & -v_{n-2} & 0 \\ 0 & 0 & 0 & 0 & 0 & 0 & \cdots & -u_{n-2} & v_{n-2} & p_{n-2} u_{n-2} & -p_{n-2} v_{n-2} & 0 \\ 0 & 0 & 0 & 0 & 0 & 0 & \cdots & 0 & 0 & u_{n-1} & v_{n-1} & -u_{n-1} \\ 0 & 0 & 0 & 0 & 0 & 0 & \cdots & 0 & 0 & -u_{n-1} & v_{n-1} & p_{n-1} u_{n-1} \end{vmatrix} \quad (4)$$

with the notation

$$u_j = e^{-\lambda h_j}, \quad v_j = e^{\lambda h_j}$$

$$p_i = \frac{\rho_i}{\rho_{i+1}}, \quad j = 1, 2, \dots, n - 1$$

Many authors [King, 1933, 1934; Muskat, 1933; Slichter, 1933; Stevenson, 1934; Wetzel and McMurry, 1937; Maeda, 1949, 1950; Flathe, 1955; La Compagnie Générale de Geophysique, 1955; Mooney and Wetzel, 1956] have shown that the kernel function plays an important role in the numerical computation of resistivity curves for the multiple-layer problems. In fact, equation 1 cannot be evaluated until the form of the kernel function is known.

In connection with the expression of the kernel function, there are Maeda's [1949] expression and Flathe's [1955] recurrence formulas. The former is presented by inference and is erroneous; the latter is not well formed as a recurrence formula, and practical calculation is cumbersome for a large value of n .

In the present paper the author starts from the development of the determinants M_n and N_n and deduces the recurrence formulas (7) and (9). By use of these recurrence formulas the general formula for the kernel function can be expressed in the simplest form by introducing the auxiliary symmetric functions.

Derivations of the recurrence formulas. We shall first develop the determinant M_n , which is

of order $2n - 2$. To simplify the calculation, we introduce the following notation:

$$x_j = u_j^2 = e^{-2\lambda h_j} \quad \text{and} \quad y_j = v_j^2 = e^{2\lambda h_j}$$

Then the relation $u_j v_j = x_j y_j = 1$ is valid, and Slichter's abbreviations reduce to

$$a_i = 1 + p_i$$

$$b_i = 1 - p_i$$

and we have

$$k_j = \frac{b_j}{a_j} = \frac{\rho_{j+1} - \rho_j}{\rho_{j+1} + \rho_j}, \quad j = 1, 2, \dots, n - 1$$

where ρ_j is the resistivity of the individual media. Note that

$$1 + k_j = 2/(1 + p_j)$$

Subtracting the first row of M_n from the second and adding the third row to the fourth, the fifth row to the sixth, . . . , the $(2n - 5)$ th row to the $(2n - 4)$ th, and the $(2n - 3)$ th row to the $(2n - 2)$ th, and multiplying the first, second, third, fourth, . . . , $(2n - 5)$ th, $(2n - 4)$ th, $(2n - 3)$ th, and $(2n - 2)$ th row by $u_1, v_1, u_2, v_2, \dots, u_{n-2}, v_{n-2}, u_{n-1},$ and v_{n-1} , respectively, and simplifying, we get

$$M_n = H_n \prod_{j=1}^{n-1} a_j$$

where

$$H_n = \begin{vmatrix} 1 & -x_1 & -1 & 0 & 0 & 0 & \cdots & 0 & 0 & 0 & 0 & 0 \\ 0 & 1 & k_1 y_1 & 0 & 0 & 0 & \cdots & 0 & 0 & 0 & 0 & 0 \\ 0 & x_2 & 1 & -x_2 & -1 & 0 & \cdots & 0 & 0 & 0 & 0 & 0 \\ 0 & 0 & (1 + k_2) y_2 & -k_2 & -y_2 & 0 & \cdots & 0 & 0 & 0 & 0 & 0 \\ \vdots & \vdots & \vdots & \vdots & \vdots & \vdots & \ddots & \vdots & \vdots & \vdots & \vdots & \vdots \\ 0 & 0 & 0 & 0 & 0 & 0 & \cdots & x_{n-2} & 1 & -x_{n-2} & -1 & 0 \\ 0 & 0 & 0 & 0 & 0 & 0 & \cdots & 0 & (1 + k_{n-2}) y_{n-2} & -k_{n-2} & -y_{n-2} & 0 \\ 0 & 0 & 0 & 0 & 0 & 0 & \cdots & 0 & 0 & x_{n-1} & 1 & -x_{n-1} \\ 0 & 0 & 0 & 0 & 0 & 0 & \cdots & 0 & 0 & 0 & (1 + k_{n-1}) y_{n-1} & -k_{n-1} \end{vmatrix} \quad (6)$$

By adding the $(2n - 3)$ th column of (6) multiplied by $k_{n-1} x_{n-1}$ and the $(2n - 2)$ th column multiplied by $(1 + k_{n-1})$ to the $(2n - 4)$ th column, the lower right-hand corner of the determinant becomes

$$\begin{array}{ccccccc} x_{n-2} & 1 & -x_{n-2} + k_{n-1} x_{n-1} (-1) & \vdots & -1 & 0 \\ 0 & (1 + k_{n-2}) y_{n-2} & -k_{n-2} + k_{n-1} x_{n-1} (-y_{n-2}) & \vdots & -y_{n-2} & 0 \\ \cdots & \cdots & \cdots & \vdots & \cdots & \cdots \\ 0 & 0 & 0 & \vdots & 1 & -x_{n-1} \\ 0 & 0 & 0 & \vdots & (1 + k_{n-1}) y_{n-1} & -k_{n-1} \end{array}$$

From this we obtain

$$H_n = H_{n-1} + k_{n-1}x_{n-1}$$

$$\begin{vmatrix} (H_{n-2}) & \vdots & -1 & 0 \\ & \vdots & -y_{n-3} & 0 \\ \cdots & \cdots & \cdots & \cdots \\ x_{n-2} & \vdots & 1 & -1 \\ 0 & \vdots & (1 + k_{n-2})y_{n-2} & -y_{n-2} \end{vmatrix} \quad (6a)$$

where

$$H_{n-1} = \begin{vmatrix} (H_{n-2}) & \vdots & -1 & 0 \\ & \vdots & -y_{n-3} & 0 \\ \cdots & \cdots & \cdots & \cdots \\ x_{n-2} & \vdots & 1 & -x_{n-2} \\ 0 & \vdots & (1 + k_{n-2})y_{n-2} & -k_{n-2} \end{vmatrix} \quad (6b)$$

which is the determinant resulting from deleting the last two rows and the last two columns of of H_n . The second term on the right member of (6a) remains unchanged by multiplying the last column by k_{n-2} and the last row by k_{n-2}^{-1} , and writing $-x_{n-2}y_{n-2}$ for -1 of the $(2n-5, 2n-4)$ -element, so that it becomes

$$k_{n-1}k_{n-2}x_{n-1}y_{n-2}\tilde{H}_{n-1} \quad (6c)$$

where

$$\tilde{H}_{n-1} = \begin{vmatrix} (H_{n-2}) & \vdots & -1 & 0 \\ & \vdots & -y_{n-3} & 0 \\ \cdots & \cdots & \cdots & \cdots \\ x_{n-2} & \vdots & 1 & -x_{n-2} \\ 0 & \vdots & (1 + k_{n-2}^{-1})y_{n-2} & -k_{n-2}^{-1} \end{vmatrix} \quad (6d)$$

We see by comparing (6d) with (6b) that \tilde{H}_{n-1} is equal to H_{n-1} with k_{n-2} replaced by k_{n-2}^{-1} . Hence we have the recurrence formula of the form

$$H_n = H_{n-1} + k_{n-1}k_{n-2}x_{n-1}y_{n-2}\tilde{H}_{n-1}, \quad n \geq 3 \quad (7)$$

For the sake of simplicity, we shall use hereafter the notation

$$\tilde{H}_{n-1} = H_{n-1}(k_1, \dots, k_{n-3}, k_{n-2}^{-1}), \quad n \geq 3 \quad (8)$$

Similarly, we get the following recurrence formula:

$$G_n = G_{n-1} + k_{n-1}k_{n-2}x_{n-1}y_{n-2}\tilde{G}_{n-1}, \quad n \geq 3 \quad (9)$$

where

$$\tilde{G} = G_{n-1}(k_1, \dots, k_{n-3}, k_{n-2}^{-1}), \quad n \geq 3 \quad (10)$$

where, by (4),

$$N_n = G_n \prod_{j=1}^{n-1} a_j \quad (11)$$

From equation 2, 5, and 11 it follows that

$$\Delta_n = D_n \prod_{j=1}^{n-1} a_j \quad (12)$$

where

$$D_n = H_n - G_n \quad (13)$$

Hence by (7) and (9) we find that

$$D_n = D_{n-1} + k_{n-1}k_{n-2}x_{n-1}y_{n-2}\tilde{D}_{n-1}, \quad n \geq 3 \quad (14)$$

where

$$\tilde{D}_{n-1} = D_{n-1}(k_1, \dots, k_{n-3}, k_{n-2}^{-1}), \quad n \geq 3. \quad (15)$$

Finally, if we define

$$T_n = H_n + G_n \quad (16)$$

we get the recurrence formula

$$T_n = T_{n-1} + k_{n-1}k_{n-2}x_{n-1}y_{n-2}\tilde{T}_{n-1}, \quad n \geq 3 \quad (17)$$

where

$$\tilde{T}_{n-1} = T_{n-1}(k_1, \dots, k_{n-3}, k_{n-2}^{-1}), \quad n \geq 3 \quad (18)$$

The recurrence formulas (7), (9), (14), and (17) are very useful for the study of the property of the kernel function, and the advantage of these formulas as compared with those of Flathe lies in their distinct recurrent relation.

General formula for the kernel function. By the recurrence formulas (7) and (9), H_n and G_n can be calculated by a method of successive sub-

stitutions, since the direct solution of the two-boundary problem shows that

$$H_2 = \tilde{H}_2 = 1 \quad (19)$$

$$G_2 = k_1 x_1 \quad (20)$$

$$\tilde{G}_2 = k_1^{-1} x_1 \quad (21)$$

Thus, for $n = 3$ and 4, we can easily obtain

$$H_3 = H_2 + k_2 k_1 x_2 y_1 \tilde{H}_2 = 1 + k_2 k_1 x_2 y_1 \quad (22)$$

$$G_3 = G_2 + k_2 k_1 x_2 y_1 \tilde{G}_2 = k_2 x_2 + k_1 x_1 \quad (23)$$

$$\begin{aligned} H_4 &= H_3 + k_3 k_2 x_3 y_2 \tilde{H}_3 \\ &= 1 + k_3 k_2 x_3 y_2 + k_3 k_1 x_3 y_1 + k_2 k_1 x_2 y_1 \quad (24) \end{aligned}$$

where $\tilde{H}_3 = 1 + k_2^{-1} k_1 x_2 y_1$, and

$$\begin{aligned} G_4 &= G_3 + k_3 k_2 x_3 y_2 \tilde{G}_3 \\ &= k_3 x_3 + k_2 x_2 + k_1 x_1 + k_3 k_2 k_1 x_3 y_2 x_1 \quad (25) \end{aligned}$$

where $\tilde{G}_3 = k_2^{-1} x_2 + k_1 x_1$.

Making use of the notation

$$\begin{cases} s_1^0 = 1 \\ s_1^1 = k_1 x_1 \\ s_2^0 = 1 \\ s_2^1 = k_2 x_2 + k_1 x_1 \\ s_2^2 = k_2 k_1 x_2 y_1 \end{cases}$$

and

$$\begin{cases} s_3^0 = 1 \\ s_3^1 = k_3 x_3 + k_2 x_2 + k_1 x_1 \\ s_3^2 = k_3 k_2 x_3 y_2 + k_3 k_1 x_3 y_1 + k_2 k_1 x_2 y_1 \\ s_3^3 = k_3 k_2 k_1 x_3 y_2 x_1 \end{cases}$$

it follows from (19), (20), (22), (23), (24), and (25) that

$$\begin{aligned} H_2 &= S_1^0 \\ G_2 &= S_1^1 \\ H_3 &= S_2^0 + S_2^2 \\ G_3 &= S_2^1 \\ H_4 &= S_3^0 + S_3^2 \end{aligned}$$

and

$$G_4 = S_3^1 + S_3^3$$

This process may be performed $(n - 2)$ times until H_n is known. If $S_1^0 = 1$ and $S_n^j (j \geq 1)$ is the sum of all possible terms formed as the products of j of the k 's and the first j members of the repeated product xy (each group with descending subscripts not above n), then specifically,

$$\begin{aligned} S_{n-1}^0 &= 1 \\ S_{n-1}^1 &= k_{n-1} x_{n-1} + k_{n-2} x_{n-2} + \cdots \\ &\quad + k_2 x_2 + k_1 x_1 \\ S_{n-1}^2 &= k_{n-1} k_{n-2} x_{n-1} y_{n-2} + k_{n-1} k_{n-3} x_{n-1} y_{n-3} \\ &\quad + \cdots + k_{n-1} k_2 x_{n-1} y_2 + k_{n-1} k_1 x_{n-1} y_1 \\ &\quad + \cdots + k_3 k_2 x_3 y_2 + k_3 k_1 x_3 y_1 + k_2 k_1 x_2 y_1 \\ &\text{and so on to} \\ S_{n-1}^{n-1} &= k_{n-1} k_{n-2} k_{n-3} \cdots \\ &\quad k_3 k_2 k_1 x_{n-1} y_{n-2} x_{n-3} \cdots z_1 \end{aligned} \quad (26)$$

where $z_1 = x_1$ for n even and $z_1 = y_1$ for n odd, and a much simpler representation for H_n is obtained as

$$\begin{aligned} H_n &= S_{n-1}^0 + S_{n-1}^2 + \cdots + S_{n-1}^{2i}, \\ 0 &\leq 2i \leq n - 1 \end{aligned} \quad (27)$$

which is the sum of even-numbered functions in (26). This can be proved by mathematical induction as is shown in the Appendix.

The analogous expression for G_n may be written in the form

$$\begin{aligned} G_n &= S_{n-1}^1 + S_{n-1}^3 + \cdots + S_{n-1}^{2i+1}, \\ 1 &\leq 2i + 1 \leq n - 1 \end{aligned} \quad (28)$$

which is the sum of odd-numbered functions in (26).

Equations 14 and 17 are expressed by

$$\begin{aligned} D_n &= S_{n-1}^0 - S_{n-1}^1 + S_{n-1}^2 + \cdots \\ &\quad + (-1)^{n-1} S_{n-1}^{n-1} \end{aligned} \quad (29)$$

and

$$\begin{aligned} T_n &= S_{n-1}^0 + S_{n-1}^1 + S_{n-1}^2 + \cdots \\ &\quad + S_{n-1}^{n-1} \end{aligned} \quad (30)$$

Consequently, by substituting (27), (28), and (29), with the help of equations (5), (11), and (12), into (2), the kernel function for the gen-

eral case of the n -layer resistivity problem is given by the general formula

$$K_n(k_i, h_i; \lambda) = \frac{G_n}{D_n} = \frac{G_n}{H_n - G_n} \quad (31)$$

where

$$H_n = \sum_{i=0}^m S_{n-1}^{2i}, \quad (32)$$

$$G_n = \sum_{i=0}^m S_{n-1}^{2i+1}, \quad 1 \leq 2i+1 \leq n-1 \quad (33)$$

and

$$D_n = \sum_{i=0}^{n-1} (-1)^i S_{n-1}^i \quad (34)$$

The variable index of summation in (32) and (33) is defined by

$$m = \begin{cases} \frac{n}{2} - 1, & \text{if } n \text{ is even} \\ \frac{n-1}{2}, & \text{if } n \text{ is odd} \end{cases}$$

Slichter's kernel investigated by Pekeris [1940] is expressed by the formula (notation is the same as above)

$$k_n(\lambda) = \frac{T_n}{D_n} = \frac{\sum_{i=0}^{n-1} S_{n-1}^i}{\sum_{i=0}^{n-1} (-1)^i S_{n-1}^i}$$

If we put

$$P_n(\lambda) = G_n/H_n$$

then we obtain from (31)

$$K_n(k_i, h_i; \lambda) = \frac{P_n(\lambda)}{1 - P_n(\lambda)}$$

This is Maeda's expression, but there are some errata in the formula for $P_n(\lambda)$ in his original paper, and both the derivation and the proof are omitted [Maeda, 1949, p. 66].

The number of terms in the numerator and denominator of the kernel function. It is easily verified that the number of terms in S_{n-1}^i is $\binom{n-1}{i}$ the number of combinations of $n-1$ elements taken i at a time. Hence the number of

terms in H_n is

$$\binom{n-1}{0} + \binom{n-1}{2} + \dots + \binom{n-1}{2i} = 2^{n-2} \quad (35)$$

where i is the largest integer in $(n-1)/2$. Similarly the number of terms in G_n is

$$\binom{n-1}{1} + \binom{n-1}{3} + \dots + \binom{n-1}{2i+1} = 2^{n-2} \quad (36)$$

where i is the largest integer in $(n/2) - 1$. Taking the sum of terms in H_n and G_n , the total number of terms in the denominator of the kernel function is given by

$$2^{n-1} \quad (37)$$

The numbers of terms are of use in checking the kernel function in the course of calculation.

Example. The solution of the kernel function in the 7-layer resistivity problem follows.

Setting $n = 7$ in (26), we obtain the following expressions:

$$S_6^0 = 1 \quad (38)$$

$$S_6^1 = k_6x_6 + k_5x_5 + k_4x_4 + k_3x_3 + k_2x_2 + k_1x_1 \quad (39)$$

$$S_6^2 = k_6k_5x_6y_5 + k_6k_4x_6y_4 + k_5k_4x_5y_4 + k_6k_3x_6y_3 + k_5k_3x_5y_3 + k_4k_3x_4y_3 + k_6k_2x_6y_2 + k_5k_2x_5y_2 + k_4k_2x_4y_2 + k_6k_1x_6y_1 + k_5k_1x_5y_1 + k_4k_1x_4y_1 + k_3k_2x_3y_2 + k_3k_1x_3y_1 + k_2k_1x_2y_1 \quad (40)$$

$$S_6^3 = k_6k_5k_4x_6y_5x_4 + k_6k_5k_3x_6y_5x_3 + k_6k_5k_2x_6y_5x_2 + k_6k_5k_1x_6y_5x_1 + k_6k_4k_3x_6y_4x_3 + k_5k_4k_3x_5y_4x_3 + k_6k_4k_2x_6y_4x_2 + k_5k_4k_2x_5y_4x_2 + k_6k_4k_1x_6y_4x_1 + k_5k_4k_1x_5y_4x_1$$

$$\begin{aligned}
& + k_6 k_2 k_2 x_6 y_3 x_2 + k_5 k_3 k_2 x_5 y_3 x_2 \\
& + k_6 k_3 k_1 x_6 y_3 x_1 + k_5 k_3 k_1 x_5 y_3 x_1 \\
& + k_6 k_2 k_1 x_6 y_2 x_1 + k_5 k_2 k_1 x_5 y_2 x_1 \\
& + k_4 k_3 k_2 x_4 y_3 x_2 \\
& + k_4 k_3 k_1 x_4 y_3 x_1 \\
& + k_4 k_2 k_1 x_4 y_2 x_1 + k_3 k_2 k_1 x_3 y_2 x_1 \quad (41)
\end{aligned}$$

$$\begin{aligned}
S_6^4 = & k_6 k_5 k_4 k_3 x_6 y_5 x_4 y_3 \\
& + k_6 k_5 k_4 k_2 x_6 y_5 x_4 y_2 \\
& + k_6 k_5 k_4 k_1 x_6 y_5 x_4 y_1 \\
& + k_6 k_5 k_3 k_2 x_6 y_5 x_3 y_2 \\
& + k_6 k_5 k_3 k_1 x_6 y_5 x_3 y_1 \\
& + k_6 k_5 k_2 k_1 x_6 y_5 x_2 y_1 \\
& + k_6 k_4 k_3 k_2 x_6 y_4 x_3 y_2 + k_5 k_4 k_3 k_2 x_5 y_4 x_3 y_2 \\
& + k_6 k_4 k_3 k_1 x_6 y_4 x_3 y_1 + k_5 k_4 k_3 k_1 x_5 y_4 x_3 y_1 \\
& + k_6 k_4 k_2 k_1 x_6 y_4 x_2 y_1 + k_5 k_4 k_2 k_1 x_5 y_4 x_2 y_1 \\
& + k_6 k_3 k_2 k_1 x_6 y_3 x_2 y_1 + k_5 k_3 k_2 k_1 x_5 y_3 x_2 y_1 \\
& + k_4 k_3 k_2 k_1 x_4 y_3 x_2 y_1 \quad (42)
\end{aligned}$$

$$\begin{aligned}
S_6^5 = & k_6 k_5 k_4 k_3 k_2 x_6 y_5 x_4 y_3 x_2 \\
& + k_6 k_5 k_4 k_3 k_1 x_6 y_5 x_4 y_3 x_1 \\
& + k_6 k_5 k_4 k_2 k_1 x_6 y_5 x_4 y_2 x_1 \\
& + k_6 k_4 k_3 k_2 k_1 x_6 y_4 x_3 y_2 x_1 \\
& + k_5 k_4 k_3 k_2 k_1 x_5 y_4 x_3 y_2 x_1 \quad (43)
\end{aligned}$$

$$S_6^6 = k_6 k_5 k_4 k_3 k_2 k_1 x_6 y_5 x_4 y_3 x_2 y_1 \quad (44)$$

Then (32) and (33) are expressed in the forms

$$H_7 = S_6^0 + S_6^2 + S_6^4 + S_6^6 \quad (45)$$

and

$$G_7 = S_6^1 + S_6^3 + S_6^5 \quad (46)$$

Hence the required result is obtained by substituting (45) and (46) into (31) by virtue of equations (38), (39), (40), (41), (42), (43),

and (44). The explicit expression for the kernel function in the 7-layer resistivity problem has not yet been given in the literature.

This expression also applies to the 6-layer case if $k_6 = 0$, and the result obtained coincides with *Slichter's* [1933, pp. 318-319] schematic representation.

APPENDIX

The object of this Appendix is to prove new formulas given by (27) or (32), (28) or (33), (29) or (34), and (30). The lemmas necessary for the proof of these formulas are also of interest in themselves.

Lemma 1. If we write \bar{S}_{n-1}^{i-1} for S_{n-1}^{i-1} with x_j and y_j ($j = 1, 2, \dots, n-1$) interchanged, the following formula holds

$$S_n^i = S_{n-1}^i + k_n x_n \bar{S}_{n-1}^{i-1} \quad (i)$$

Proof. The right member of (i) may be written in the form

$$\begin{aligned}
& S_{n-1}^i + k_n x_n \bar{S}_{n-1}^{i-1} \\
& = (\dots + k_i k_{i-1} \dots k_2 k_1 x_i y_{i-1} \dots z_1) \\
& + (\dots k_n k_{i-1} k_{i-2} \dots k_2 k_1 x_n y_{i-1} x_{i-2} \dots z_1)
\end{aligned}$$

where $z_1 = x_1$ for i odd and $z_1 = y_1$ for i even. This is equal to the sum of all possible terms of the form $K_i L_i$, where K_i is all possible products of k_n, \dots, k_1 taken i at a time in decreasing order and L_i is the alternating products of $x_\gamma y_\beta \dots$ beginning with x where $\gamma, \beta \dots$ are the same as the subscripts of k 's in K_i in decreasing order. Hence the result gives S_n^i . This completes the proof.

Lemma 2.

$$\bar{S}_n^i = \bar{S}_{n-1}^i + k_n y_n S_{n-1}^{i-1} \quad (ii)$$

The proof proceeds as in lemma 1, by interchange of x and y in each term of lemma 1.

Lemma 3.

$$\begin{aligned}
S_n^i = & S_{n-1}^i + k_n x_n \bar{S}_{n-2}^{i-1} \\
& + k_n k_{n-1} x_n y_{n-1} S_{n-2}^{i-2} \quad (iii)
\end{aligned}$$

Proof. We may easily prove this lemma by lemmas 2 and 1 as follows:

The right member of (iii)

$$\begin{aligned}
& = S_{n-1}^i + k_n x_n (\bar{S}_{n-2}^{i-1} + k_{n-1} y_{n-1} S_{n-2}^{i-2}) \\
& = S_{n-1}^i + k_n x_n \bar{S}_{n-1}^{i-1} = S_n^i
\end{aligned}$$

Let us prove formula (32). Suppose that (32) is true. From the recurrence formula of (7) we obtain

$$H_{n+1} = H_n + k_n k_{n-1} x_n y_{n-1} \tilde{H}_n \quad (iv)$$

If, in (32), we write \tilde{S}_{n-1}^{2i} for S_{n-1}^{2i} with k_{n-1} replaced by k_{n-2}^{-1} , we get

$$\tilde{H}_n = \sum_{i=0}^m \tilde{S}_{n-1}^{2i} \quad (v)$$

The substitution of (32) and (v) into (iv) reduces to

$$H_{n+1} = \sum_{i=0}^m S_{n-1}^{2i} + k_n k_{n-1} x_n y_{n-1} \sum_{i=0}^m \tilde{S}_{n-1}^{2i} \quad (vi)$$

Applying lemma 1 to the summation in the second term of the right member of (vi), we obtain

$$\begin{aligned} \sum_{i=0}^m \tilde{S}_{n-1}^{2i} &= S_{n-1}^0 \\ &+ (S_{n-2}^2 + \tilde{S}_{n-2}^1 k_{n-1}^{-1} x_{n-1}) \\ &+ (S_{n-2}^4 + \tilde{S}_{n-2}^3 k_{n-1}^{-1} x_{n-1}) \\ &+ \dots \\ &+ (S_{n-2}^{2i-2} + \tilde{S}_{n-2}^{2i-3} k_{n-1}^{-1} x_{n-1}) \\ &+ (S_{n-2}^{2i} + \tilde{S}_{n-2}^{2i-1} k_{n-1}^{-1} x_{n-1}) \quad (vii) \end{aligned}$$

Multiplying each side of (vii) by $k_n k_{n-1} x_n y_{n-1}$ and substituting into (vi), we get, by lemma 3,

$$H_{n+1} = 1 + S_n^2 + S_n^4 + \dots + S_n^{2i-2} + S_n^{2i} + k_n k_{n-1} x_n y_{n-1} S_{n-2}^{2i} \quad (viii)$$

Since the last term of the right member of (viii) becomes

$$k_n k_{n-1} x_n y_{n-1} S_{n-2}^{2i} = \begin{cases} S_n^{2i}, & \text{for } i = \frac{n}{2} - 1 \\ 0, & \text{for } i = \frac{n-1}{2} \end{cases}$$

we have

$$H_{n+1} = \sum_{i=0}^m S_n^{2i}$$

which is exactly the same as equation 32 with n replaced by $n+1$.

However (32) asserts that $H_2 = 1$ for $n = 2$. Hence we can conclude by mathematical induction

that the formula (32) is true for all positive integral values of n greater than 2.

Similarly we can prove (33). As a conclusion of (32) and (33), formulas (34) and (30) may be justified.

For a more fundamental treatment of the material in this section, see Onodera [1959].

Acknowledgments. I wish to express my sincere thanks to Professor Yosiro Oono, Department of Communication Engineering, Kyushu University, and Professor Takashi Noguchi, Mining Department, for their many interesting discussions and suggestions during the course of work.

The writer is greatly indebted to Dr. Irwin Roman for help in preparing this article for publication.

REFERENCES

- Flathe, H., A practical method of calculating geoelectrical model graphs for horizontally stratified media, *Geophys. Prospecting*, 3, 269-294, 1955.
- King, L. V., On the flow of electric current in semi-infinite stratified media, *Proc. Roy. Soc. London, A.*, 139, 237-277, 1933.
- King, L. V., On the flow of electric current in semi-infinite media in which the specific resistance is a function of the depth, *Phil. Trans. Roy. Soc. London, A.*, 233, 327-359, 1934.
- La Compagnie Générale de Géophysique, Abaques de sondage électrique, *Geophys. Prospecting*, 3, Suppl. 3, 1955.
- Maeda, K., Denki-Teiko-Shiki Chishitsu-Tyosa no Keisan-Hoho, *Bull. Railway Tech. Lab. (Japanese Natl. Railways)*, 6, nos. 6-7, p. 66, 1949 (in Japanese).
- Maeda, K., Direct method of calculation in resistivity prospecting, *Butsuri-Tankô*, 3, 8-11, 1950 (in Japanese).
- Mooney, H. M., and W. W. Wetzel, *The Potentials about a Point Electrode and Apparent Resistivity Curves for a Two-, Three-, and Four-Layered Earth*, Univ. Minnesota Press, Minneapolis, 1956.
- Muskat, Morris, Potential distribution about an electrode on the surface of the earth, *Physics*, 4, 129-147, 1933.
- Onodera, S., Generalized expression for kernel function in integral representation of electric potential function at the surface of horizontally stratified media, *Technol. Repts. Kyushu Univ.*, 31, 22-25, 1958 (in Japanese).
- Onodera, S., On the recurrence relation of the elementary symmetric expression in commutative domain of integrity, *Technol. Repts. Kyushu Univ.*, 32, 174-178, 1959 (in Japanese).
- Onodera, S., General formula for the kernel function in the formal electric potential equation for n -layer resistivity problem, *J. Mining and Met. Inst. Japan*, 76, 159-166, 1960 (in Japanese).
- Pekeris, C. L., Direct method of interpretation in resistivity prospecting, *Geophysics*, 5, 31-42, 1940.

- Slichter, L. B., The interpretation of the resistivity prospecting method for horizontal structures, *Physics*, 4, 307-332 and 407, 1933.
- Stefanescu, S., en collaboration avec C. et M. Schlumberger, sur la distribution électrique potentielle autour d'une prise de terre ponctuelle dans un terrain a couches horizontales, homogènes et isotopes, *J. Phys. radium* 7, 132-141, 1930.
- Stevenson, A. F., On the theoretical determination of earth resistance from surface potential measurements, *Physics*, 5, 114-124, 1934.
- Wetzel, W. W., and H. V. McMurry, A set of curves to assist in the interpretation of the three layer resistivity problem, *Geophysics*, 2, 329-341, 1937.

(Manuscript received March 23, 1960; revised July 25, 1960.)

A Technique for the Numerical Solution of Geophysical Problems¹

I. M. LONGMAN

*Institute of Geophysics, University of California
Los Angeles, California*

Abstract. The theoretical analysis of problems in geophysics, and particularly in seismology, leads in many cases to solutions expressed in terms of integrals that cannot be evaluated by conventional numerical methods. The usual difficulties are connected with the oscillatory nature of the integrand and with the presence of one or more poles in the path of integration. In the simpler problems these difficulties can sometimes be circumvented by appropriate transformations in the complex plane, though this often involves lengthy analysis.

A method is presented for the direct and accurate evaluation of such solutions with a minimal use of algebraic manipulations. By way of illustration the method is applied to Lamb's problem with an oscillatory source.

Introduction. In previous publications, Longman [1956, 1957] has shown how infinite oscillatory integrals can readily be evaluated numerically by converting them into alternating series and then summing by Euler's transformation [Bromwich, 1942]. This method has recently been extended [Longman, 1960] to deal with finite oscillatory integrals. The numerical evaluation of integrals having poles on the path of integration can also be carried out quite simply by a method developed by Longman [1958]. By a combination of these methods it is possible to evaluate directly many integrals which occur in the solution of geophysical problems. For convenience these methods are briefly summarized below. For full details the reader is referred to the references quoted above.

Theory. Euler's transformation provides a method for transforming a slowly convergent alternating series into a rapidly convergent series. According to this transformation, if we have a series

$$S = v_0 - v_1 + v_2 - v_3 + \dots$$

where

$$v_n > 0, \quad v_{n+1} < v_n \quad \text{for all } n$$

and if we write

$$\Delta v_n = v_{n+1} - v_n, \quad \Delta^{r+1} v_n = \Delta^r v_{n+1} - \Delta^r v_n$$

then

$$S = (1/2)v_0 - (1/4)\Delta v_0 + (1/8)\Delta^2 v_0 - \dots$$

where the series on the right can be shown to be convergent whenever the original series is. In the (usual) case in which the higher differences of the v 's decrease rapidly with r , our new series is very rapidly convergent. If we now have an oscillatory integral to evaluate,

$$I = \int_a^\infty f(x) dx$$

we can convert this to an alternating series by expressing I as the sum of integrals between successive zeros of $f(x)$. Evaluating these successive integrals by numerical quadrature and then applying Euler's transformation to the resulting series provides a convenient means of computing the integral. This method is particularly suitable for programming on an electronic computer.

The other essential difficulty associated with the evaluation of integrals in geophysical problems is the numerical evaluation of the Cauchy principal value of an integral

$$I = P \int_{-a}^a f(x) dx$$

where without loss of generality we have supposed the singularity to be at the origin, and the range of integration to be symmetrical about the origin. This difficulty is resolved by splitting up the function $f(x)$ into its odd and even components

¹ Institute of Geophysics Publication No. 189.

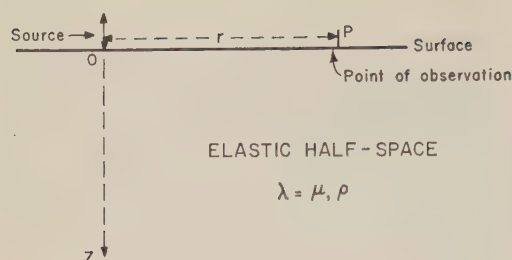


Fig. 1. Schematic illustration of Lamb's problem.

$$\begin{aligned}
 f(x) &= [f(x) - f(-x)]/2 \\
 &+ [f(x) + f(-x)]/2 \\
 &= g(x) + h(x), \text{ say.}
 \end{aligned}$$

Then $g(x)$ being odd gives no contribution, and

$$I = 2 \int_0^a h(x) dx$$

In this expression $h(x)$ has no singularity at the origin, since the singularity due to the pole is an odd one.

The technique is best illustrated by an example; and for the sake of simplicity Lamb's problem is chosen.

Example. We choose as our example the problem of the excitation of an elastic half-space by a point source. This problem was first formulated by *Lamb* [1904], who obtained expressions in the form of infinite integrals for its solution. Later *Pekeris* [1955a] obtained closed expressions for the motion of the surface of the solid when the point source is on the surface and has a time variation proportional to Heaviside's unit function. The case in which this type of source is buried beneath the surface was treated by *Pekeris* [1955b], and the solution was obtained in the form of definite integrals suitable

for evaluation on an electronic computer. This evaluation was carried out by *Pekeris and Lifson* [1957].

We shall treat here the case in which the source is oscillatory and lies on the surface. The problem is illustrated schematically in Figure 1. At a point 0 on the surface of an elastic half-space an oscillatory point source of pressure is located. For the sake of definiteness we shall suppose that the surface is horizontal, although of course this is immaterial to the problem. We seek to determine the motion of any point P on the surface. Since the problem has rotational symmetry, we employ cylindrical coordinates. Taking the origin at 0, we measure z vertically downwards and r radially. The nature of the source is specified as follows: we suppose that at 0 a vertical force of intensity $Ze^{i\omega t}$ is applied to the surface. By this we mean that a pressure p is applied to the surface, satisfying the conditions:

$$p = 0 \quad r > 0$$

$$p = \infty \quad r = 0$$

and

$$\int_S p dS = -Ze^{i\omega t}$$

is the force applied to the surface S (Z positive corresponds to a downward pressure at time $t = 0$).

The elastic half-space is supposed to be homogeneous and isotropic and to have Lamé elastic parameters λ , μ , which we shall assume to be equal. The density of the medium will be denoted by ρ . Then, following *Lamb* [1904] or *Pekeris* [1955a], the solution for the components of displacement w vertically downwards, q radially outwards can be put in the form

$$w = -e^{i\omega t} \cdot \frac{Zk}{2\pi\mu} \int_0^\infty \frac{J_0(krx)x \sqrt{x^2 - 1/3} dx}{(2x^2 - 1)^2 - 4x^2 \sqrt{x^2 - 1/3} \sqrt{x^2 - 1}} \quad (1)$$

$$q = e^{i\omega t} \cdot \frac{Zk}{2\pi\mu} \int_0^\infty \frac{J_1(krx)x^2(2x^2 - 1 - 2\sqrt{x^2 - 1/3} \sqrt{x^2 - 1}) dx}{(2x^2 - 1)^2 - 4x^2 \sqrt{x^2 - 1/3} \sqrt{x^2 - 1}} \quad (2)$$

where $k = \omega/c$, and $c = (\mu/\rho)^{1/2}$ is the velocity of S waves in the medium. The velocity of P waves in the medium is

$$c_p = [(\lambda + 2\mu)/\rho]^{1/2} = \sqrt{3} c$$

Also J_0 and J_1 denote respectively the Bessel functions (of the first kind) of orders 0 and 1.

take the path of integration parallel to the real axis and just above it (Fig. 2). An equivalent contour is that shown in Figure 3, where the pole is avoided by a semicircle of vanishingly small radius. The contribution of the semicircle can be calculated in each case by Cauchy's theorem, and with this formulation we find

$$= -\frac{e^{i\omega t} Zk}{2\pi\mu} \left[P \int_0^\infty \frac{J_0(krx)x \sqrt{x^2 - 1/3} dx}{(2x^2 - 1)^2 - 4x^2 \sqrt{x^2 - 1/3} \sqrt{x^2 - 1}} + \frac{\pi i}{8} \sqrt{3\gamma^2 - 1} J_0(R\gamma) \right] \quad (3)$$

$$= \frac{e^{i\omega t} Zk}{2\pi\mu} \left[P \int_0^\infty \frac{J_1(krx)(2x^2 - 1 - 2 \sqrt{x^2 - 1/3} \sqrt{x^2 - 1})x^2}{(2x^2 - 1)^2 - 4x^2 \sqrt{x^2 - 1/3} \sqrt{x^2 - 1}} dx + \frac{\pi i}{8} \gamma J_1(R\gamma) \right] \quad (4)$$

A few words of comment on the integrals (1) and (2) are necessary. In the first place, they are to a certain extent indeterminate as they stand, owing to the presence of a pole at $x = \frac{1}{2} [3 + (3)^{1/2}]^{1/2} = 1.087 \dots$ on the path of integration. This indeterminateness is associated [Lamb, 1904] with the possible existence of free surface waves, as distinct from the (forced) waves radiating away from the source. The former are Rayleigh waves which can travel in any direction over the surface with their own characteristic velocity of c/γ . In order to obtain the correct solution to our problem it is necessary to take that value of each integral which corresponds to diverging waves from the source. This kind of indeterminateness is common in physical problems of this nature, and the correct procedure [Morse and Feshbach, 1953] is to

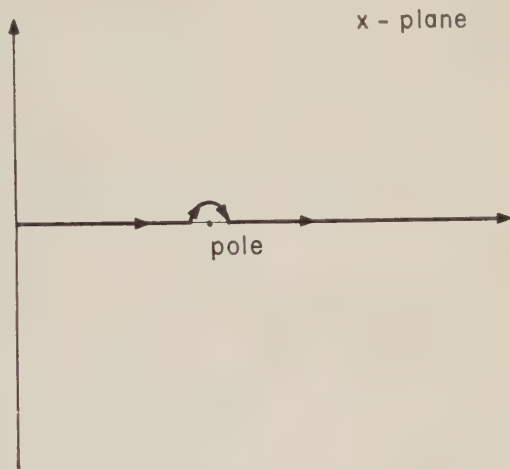


Fig. 3. Modified path of integration in the x plane.

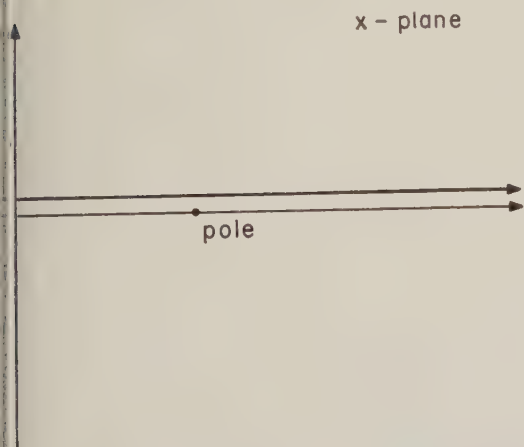


Fig. 2. Path of integration in the x plane showing the Rayleigh pole.

where P denotes that the Cauchy principal value is to be taken, and R is defined in equation 8 below. The radicals are defined to be positive when they are real and positive imaginary otherwise.

Now the main purpose of this paper is not to derive equations 3 and 4, which are standard, but rather to demonstrate a novel treatment of them. As they stand they are difficult to evaluate numerically owing to the pole and to the oscillatory nature of the integrand in each case. However, application of the methods developed in the form

$$w = \frac{Ze^{i\omega t}}{2\pi\mu r_0} [\alpha_1 e^{-i\beta_1}] \quad (5)$$

$$q = \frac{Ze^{i\omega t}}{2\pi\mu r_0} [\alpha_2 e^{-i\beta_2}] \quad (6)$$

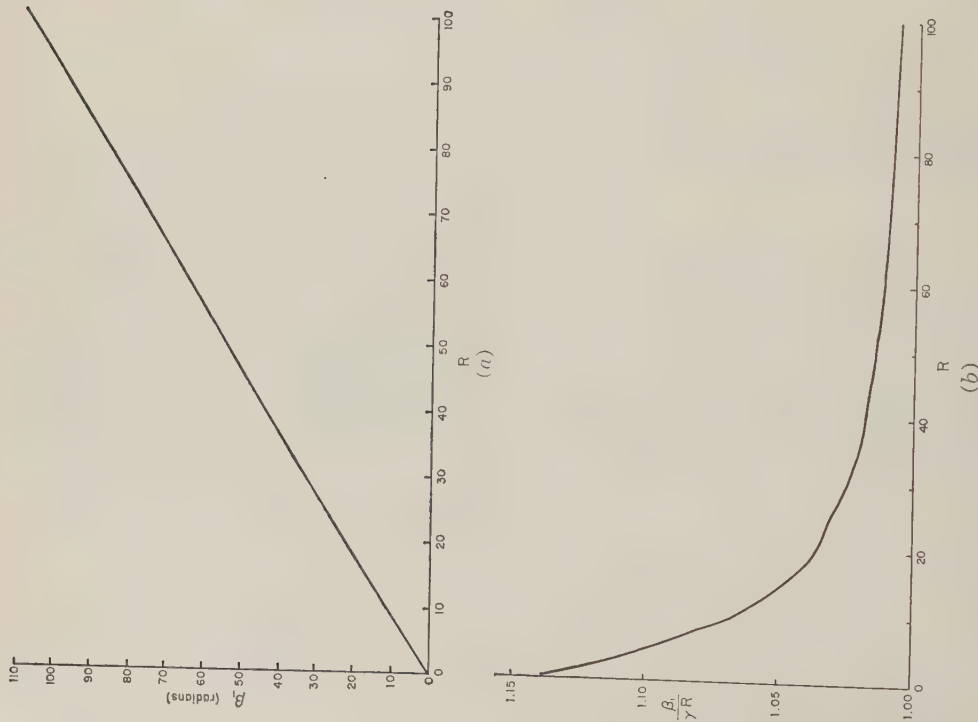


Fig. 4. Plot of phase change β_1 , in radians as a function of dimensionless range R for the vertical component of displacement. (a) Direct plot of β_1 against R . (b) Plot of $\beta_1/(\gamma R)$ against R .

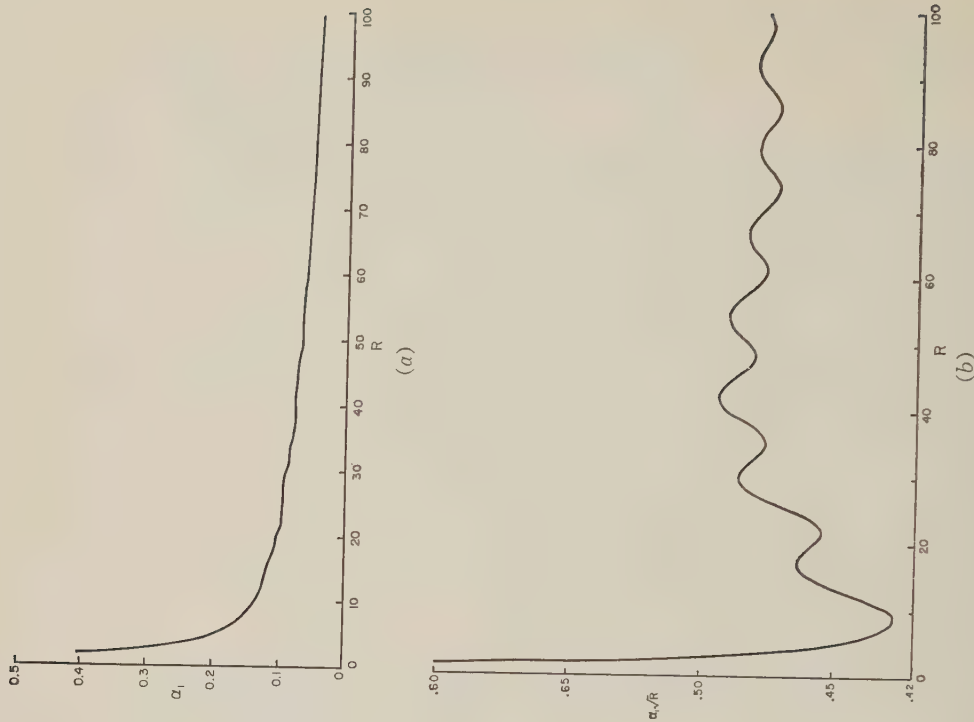


Fig. 5. Plot of amplitude factor α_1 , as a function of dimensionless range R for the vertical component of displacement. (a) Direct plot of α_1 , against R . (b) Plot of α_1/R against R .

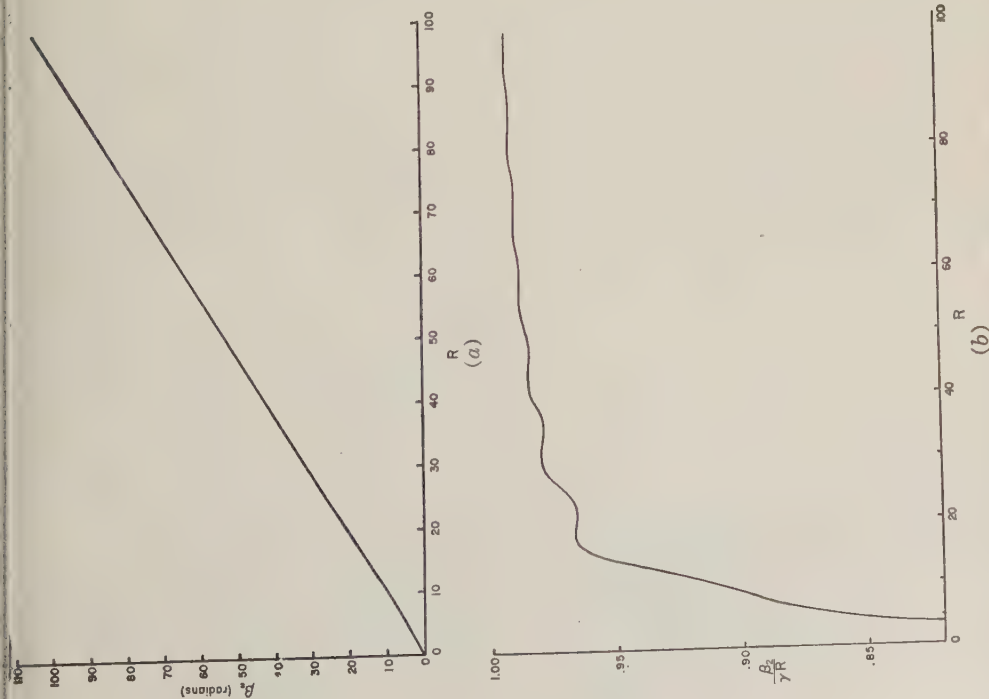


Fig. 6. Plot of phase change β_2 in radians as a function of dimensionless range R for the horizontal component of displacement. (a) Direct plot of β_2 against R . (b) Plot of $\beta_2/(\gamma R)$ against R .

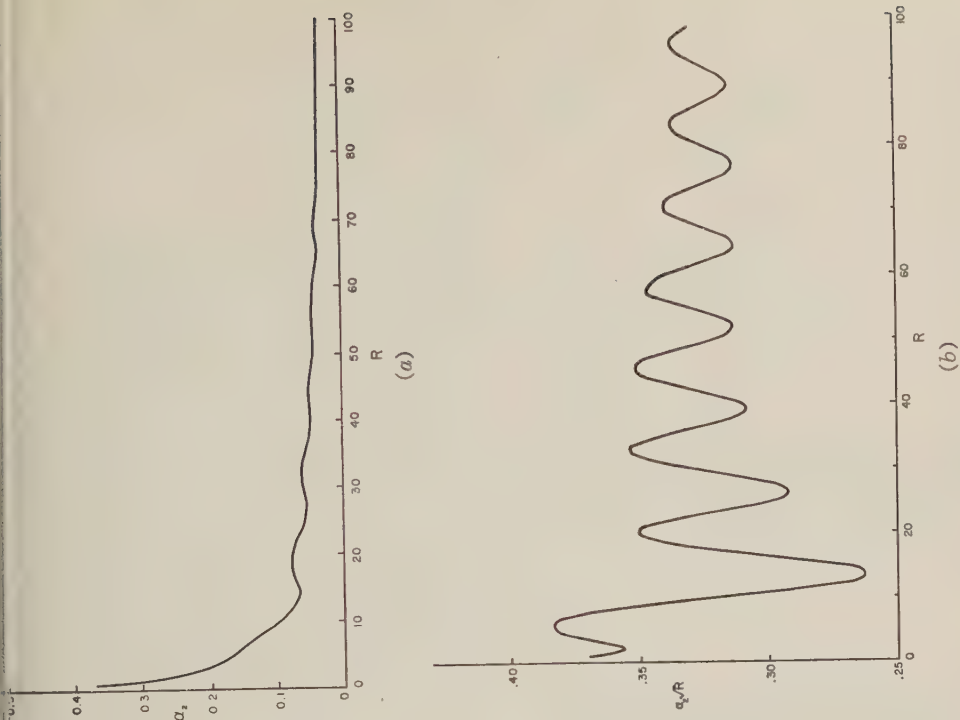


Fig. 7. Plot of amplitude factor α_2 as a function of dimensionless range R for the horizontal component of displacement. (a) Direct plot of α_2 against R . (b) Plot of $\alpha_2 R$ against R .

where $r_0 = c/\omega$ is a characteristic length of the system. Here the α 's are proportional to the amplitude of the response, and the β 's give the phase change. If we combine the exponentials by Longman [1956, 1958] enables us to evaluate (3) and (4) readily on a computer. It is true that by transformation in the complex plane (3) and (4) can be reduced to a form more amenable to numerical integration, but in the more complicated problems to which our method can be applied with equal facility this would be by no means simple and might be impossible.

The expressions in brackets in (3) and (4) have been evaluated with an IBM 709 electronic computer for a number of cases by the method described in the introduction to this paper. The results are discussed in the next section.

Results. Equations 3 and 4 can be evaluated we obtain expressions of the form

$$\frac{Z\alpha}{2\pi\mu r_0} e^{i\omega(t-\beta/\omega)} \quad (7)$$

showing that the β/ω represents the delay time. The expressions were calculated for ranges r which were various multiples R of r_0 .

$$R = r/r_0 = \omega r/c \quad (8)$$

Thus R is a nondimensional form of the range. In terms of R , then, we have as a kind of average velocity

$$r/(\beta/\omega) = (R/\beta)c$$

where β is measured in radians.

At large ranges the amplitude factor decreases as $R^{-1/2}$. This is because at large ranges the Rayleigh wave predominates. For the same reason we have the approximate relation

$$(R/\beta)c = c/\gamma$$

or

$$\beta = \gamma R$$

at large ranges.

The results are shown in Figures 4, 5, 6, and 7. In these figures the phase change and amplitude factor are shown plotted as functions of the range R , for both the vertical and horizontal components of the displacement. In Figures 4a and 6a the departures from linearity are not very obvious, but Figures 4b and 6b show in

more detail how $\beta/(\gamma R)$ approaches 1 in each case for large ranges. Similarly, Figures 5b and 7b show how $\alpha R^{1/2}$ approaches a constant value in each case for large ranges. In view of the definition of R , the results can also be regarded as giving the frequency response of our system at any fixed range.

Conclusion. Techniques of numerical integration developed by the author have been applied to a simple problem in geophysics. It is proposed to show in a future publication how the steady-state response obtained here can be used to obtain an approximation to the known response [Pekeris, 1955a] to a point source whose time variation is that of the Heaviside unit function. A technique will then be available for handling seismic problems of a complex nature.

Acknowledgments. I wish to record my appreciation of the computing facilities made available to me at the Western Data Processing Center of the University of California at Los Angeles. I also wish to thank the referee for some comments which helped me to improve the presentation.

REFERENCES

- Bromwich, T. J. I'A., *An Introduction to the Theory of Infinite Series*, The Macmillan Co., New York, 1942.
- Lamb, H., On the propagation of tremors over the surface of an elastic solid, *Phil. Trans. Roy. Soc. London, A*, 203, 1-42, 1904.
- Longman, I. M., Note on a method for computing infinite integrals of oscillatory functions, *Proc. Cambridge Phil. Soc.*, 52, 764-768, 1956.
- Longman, I. M., Tables for the rapid and accurate numerical evaluation of certain infinite integrals involving Bessel functions, *Math. Tables and Other Aids to Computation*, 11, 166-180, 1957.
- Longman, I. M., On the numerical evaluation of Cauchy principal values of integrals, *Math. Tables and Other Aids to Computation*, 12, 205-207, 1958.
- Longman, I. M., A method for the numerical evaluation of finite integrals of oscillatory functions, *Mathematics of Computation*, 14, 53-59, 1960.
- Morse, P. M. and H. Feshbach, *Methods of Theoretical Physics, I*, McGraw-Hill Book Co., 850, 1953.
- Pekeris, C. L., The seismic surface pulse, *Proc. Natl. Acad. Sci. U. S.*, 41, 469-480, 1955a.
- Pekeris, C. L., The seismic buried pulse, *Proc. Natl. Acad. Sci. U. S.*, 41, 629-639, 1955b.
- Pekeris, C. L., and H. Lifson, Motion of the surface of a uniform elastic half-space produced by a buried pulse, *J. Acoust. Soc. Am.*, 29, 1233, 1957.

(Manuscript received June 30, 1960; revised August 26, 1960.)

The Interpolation of Earth-Tide Records¹

I. M. LONGMAN

*Institute of Geophysics, University of California
Los Angeles, California*

Abstract. A method is presented whereby earth-tide gravity records can conveniently be interpolated. It is based on the theoretical rigid-earth gravity tide $g_0(t)$ and its time derivative. The possibility is envisaged that earth-tide gravity records for any station may be generated in their entirety by this method for any station for which a pair of constants has been determined.

Introduction. During the International Geophysical Year (IGY, 1958) earth-tide gravity recordings were made at a number of stations around the world. (This work was undertaken by the Institute of Geophysics of the University of California at Los Angeles, and will be reported on in detail separately.) A Lacoste and Lomborg gravity meter was used for the measurements, this meter being capable of recording changes in the vertical component of gravity of as little as $1 \mu\text{gal}$. The gravity variations were recorded continuously and the data from each station were reduced to numerical form by reading off the charts at half-hourly intervals. These readings were punched on IBM cards for convenient processing in an IBM 709 electronic digital computer.

The average length of record at each station was about 1 month, but in some instances power or component failures caused gaps in the records, and in order to facilitate their analysis a method of interpolation was developed by the author.

Theory. According to Love [1909], for an elastic earth having a spherically symmetrical distribution of mass and of elastic parameters, the deformation of the surface under tidal forces can be characterized by two constants which he denoted by h , k . Later Shida and Matsuyama [1912] showed that a third number is necessary. In terms of these numbers there is a gravimetric factor G defined by

$$G = 1 + h - 3k/2 \quad (1)$$

It can be shown that, under the above assumptions, the vertical component g of the measured gravity tide is proportional to the vertical component g_0 of the tidal acceleration due to the sun and moon (assumed to be acting on a rigid earth) and that in fact

$$g = Gg_0 \quad (2)$$

The value of G is in reality dependent upon tidal frequency, but since the period (12 hours) of the large semidiurnal tide is far removed from the largest period (approx. 1 hour) of free oscillation of the earth [Alterman, Jarosch, and Pekeris, 1959], it has approximately the statical value.

Equation 2 holds under the assumptions mentioned, but for the actual earth the situation is complicated by the presence of oceans and the possibility of nonelastic reactions within the earth. In the measurements taken during the IGY a relation of the form (2) was not found to hold too well at any of the stations, but on the other hand it was found empirically that a relation of the form

$$g(t) = \alpha g_0(t) + \beta(d/dt)g_0 \quad (3)$$

held with very great accuracy at each of the stations (with a different pair of values of α , β at each of the stations). Equation 3 was used for a very successful interpolation of those records having gaps, even when a gap extended over a period of several days.

Interpolation. The first step in the interpolation of a record was the computation of g_0 for the entire period of the record. This was accomplished on an IBM 709 computer with a special program based on a set of formulas

¹Institute of Geophysics Publication No. 193. This research was supported by the Office of Naval Research under Contract Nonr 233(19).

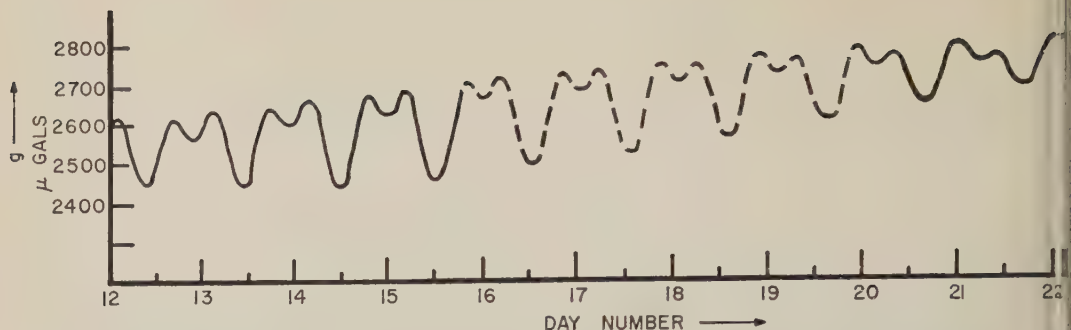


Fig. 1. Part of the earth-tide gravity record taken at Trieste, Italy. The solid line is actual record and the dashed line shows the interpolation. The day numbers correspond to 0 hr for each day. Day 1 was May 18, 1958.

summarized by Longman [1959]. Values of g_0 were computed at half-hourly intervals. Now a special difficulty encountered in the interpolation of records was caused by the instrumental drift. In each case it was found that the drift appeared to be superimposed upon recorded gravity changes. In most cases this drift was approximately linear. The first step, then, in the processing of the data from each station was the removal of the drift by some suitable numerical filter. This was found to be conveniently accomplished by a method due to Pertzev [1957]. According to Pertzev, if we measure t in hours, we can calculate meter drift M from the formula

$$\begin{aligned}
 M = & [g(t) + g(t-2) + g(t+2) \\
 & + g(t-3) + g(t+3) + g(t-5) \\
 & + g(t+5) + g(t-8) + g(t+8) \\
 & + g(t-10) + g(t+10) + g(t-13) \\
 & + g(t+13) + g(t-18) \\
 & + g(t+18)]/15
 \end{aligned} \quad (4)$$

Accordingly then,

$$g'(t) = g(t) - M \quad (5)$$

should represent fairly well the measured tide with the meter drift removed. Of course this process, which amounts to a numerical high pass filter, also removes the long-period tides, but these are relatively small in magnitude. In order to render $g'(t)$ and $g_0(t)$ more comparable, the same filtering process was applied to $g_0(t)$. We shall denote the resulting filtered tide by $g_0'(t)$.

An IBM 709 computer program was written which fitted the function

$$\alpha g_0'(t) + \beta(d/dt)g_0'(t)$$

to $g'(t)$ (at the half-hour points at which $g(t)$ was read off the original records) by the method of least squares. That is to say, a least-squares determination of α , β was made. The fit obtained in this way was usually very good, the root mean square deviation of about 3 μ gal being obtained over a record of a month or so.

The goodness of fit obtained suggested a method of interpolation for those records having gaps. The above procedure was applied to the various parts of a record (between gaps) and a value of α , β obtained for each section. These were usually found to agree fairly well among themselves, but a mean α and a mean β were taken to apply to the whole record. In this way the function

$$\alpha g_0'(t) + \beta(d/dt)g_0'(t)$$

was computed for the whole record. Then the drift curve, represented by $M(t)$, was interpolated by least-squares fitting of a straight line or straight lines, and an appropriate value of $M(t)$ was calculated for the complete record. Finally the record was simulated as the function

$$\alpha g_0'(t) + \beta(d/dt)g_0'(t) + M(t)$$

The result of an application of this technique to the interpolation of a gap in a record taken at Trieste, Italy, is shown in Figure 1. The heavy line illustrates the actual record, and the

dashed line is the interpolation for the gap. The instrumental drift is clearly seen in the figure. The values of α , β obtained for Trieste were

$$\alpha = 1.15, \quad \beta = -0.19 \text{ hr.}$$

The question immediately arises whether α and β are truly constant for each station or merely change little in the course of a month's observations. It is hoped that further work will shed more light on this question. If α , β do prove to be true constants for each station, it will be possible to determine once and for all the pair appropriate to any station of interest. Then the gravity tide starting at any epoch can be simply computed with the aid of an electronic computer.

Conclusion. A method for the interpolation of earth-tide measurements has been presented and its efficiency demonstrated. Mention has been made of a possibility that the method may extend itself to the complete prediction of the gravity tide at any station for which a pair of constants has been determined.

Acknowledgments. I am grateful to Professor L. B. Slichter, Director of the Institute of Geophysics, for encouragement and advice. It is also a pleasure to acknowledge the excellent computing facilities made available to me by the Western Data Processing Center of the University of California at Los Angeles.

REFERENCES

- Alterman, Z., H. Jarosch, and C. L. Pekeris, Oscillations of the earth, *Proc. Roy. Soc. A*, 252, 80-95, 1959.
- Longman, I. M., Formulas for computing the tidal accelerations due to the moon and the sun, *J. Geophys. Research*, 64, 2351-2355, 1959.
- Love, A. E. H., The yielding of the earth to disturbing forces, *Proc. Roy. Soc. London, A*, 82, 73, 1909.
- Pertzev, B. P., on the calculation of the drift curve in observations of bodily tides, *Bulletin d'informations no. 5 commission pour l'étude des marées terrestres*, Uccle, 71-72, 1957.
- Shida, T., and M. Matsuyama, Change of plumb-line referred to the axis of the earth as found from international latitude observations, *Mem. Coll. Sci. Eng. Kyoto Imp. Univ.*, 4 pt. 6, 277-284, 1912.

(Manuscript received July 15, 1960; revised August 22, 1960.)

Particle Amplitude Profiles for Rayleigh Waves on a Heterogeneous Earth¹

JAMES DORMAN AND DAVID PRENTISS

*Lamont Geological Observatory
(Columbia University)
Palisades, New York*

Abstract. The relationship between vertical and horizontal particle amplitude and depth for Rayleigh waves was obtained for several models of a heterogeneous, solid half-space using a new computing program for the IBM 650. The data show how the well-known characteristics of Rayleigh wave motion on a homogeneous half-space are modified in the common case in which compressional and shear velocities increase downward in the earth and also in the case in which a low-velocity region such as the mantle or asthenospheric low-velocity channel exists.

Theoretical particle amplitude profiles and dispersion curves, computed on the basis of bore hole measurements of compressional and shear velocities made by Dobrin, Simon, and Lawrence, are compared with data on explosion-generated Rayleigh waves of 4 to 8 cps recorded by them in the bore hole. Observed particle trajectories and computed amplitude profiles are in good agreement except in the upper 10 feet, where the very large horizontal amplitudes predicted by theory, particularly for short periods, are not shown in the field observations.

Particle amplitude profiles based on Gutenberg's model of the mantle are given for a broad spectrum of mantle Rayleigh wave and long-period crustal Rayleigh wave frequencies. These data show that the heterogeneous character of the mantle cannot be neglected in the problem of crustal Rayleigh wave dispersion. They also show that no 'captured waves' or 'channelled waves' of unusual character exist in the Rayleigh mode. Instead, particle motion profiles for the heterogeneous earth differ only slightly from the profile for Rayleigh waves on a homogeneous half-space throughout the spectrum of this mode.

Introduction. A computing program used by Dorman, Ewing, and Oliver [1960] for computing phase velocities of Rayleigh waves for a layered half-space has been adapted for computing the associated distributions of particle amplitude versus depth. The phase velocity and distribution of particle motion of Rayleigh waves on a homogeneous half-space are obtained by well-known methods from the theory of elastic disturbances confined to the region of the free surface [see Bullen, 1947, p. 90]. Also, a few examples of particle amplitude distribution on models with simple heterogeneity are available [see, for instance, Stoneley and Hochstrasser, 1957]. The new particle amplitude program combined with the previously existing phase velocity program makes particle amplitude data as well as dispersion data readily available for structures of great complexity.

In general, when phase velocity is a function of frequency, the distribution of orbital motion

is a function of frequency also. The close relationship between velocity dispersion and distribution of orbital motion for Rayleigh waves usually means that, when a method exists for calculating one of these properties, there is also a closely related method for calculating the other. In practical calculations, one usually can be obtained as a by-product of the other. For example, Sato [1959] calculated the particle motion distribution for a heterogeneous half-space by numerical integration on the basis of an assumed dispersion solution (phase velocity vs. period) and used the convergence of the particle amplitude functions to test the validity of the assumed dispersion solution. The calculation of particle motion versus depth is also implicit in the method which Haskell [1953] gave for solving the phase-velocity problem for a half-space consisting of solid homogeneous layers. Haskell's method, which is used in the present work, is practical for solving dispersion and particle trajectory problems for very complicated layered structures.

Field observations of particle trajectories of

¹ Lamont Geological Observatory Contribution No. 443.

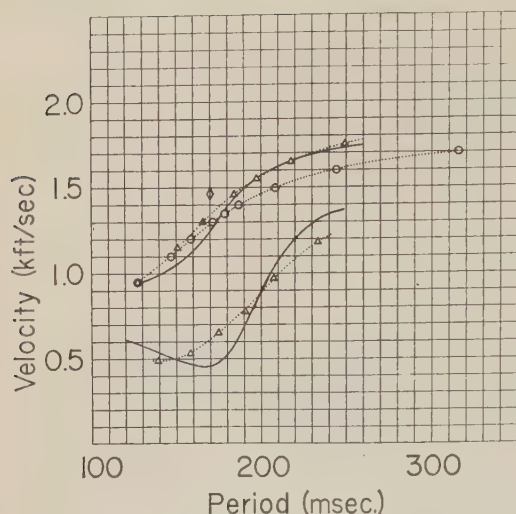


Fig. 1. Observed and computed dispersion data for the small-scale problem. Solid curves are phase velocity (upper curve) and group velocity (lower curve) observed in the field by *Dobrin, Simon, and Lawrence* [1951]. Computed phase velocity points: case 8300, open circles; case 8300A, triangles; case 8301, diamond symbol. The long-period points of case 8300A show that a shear velocity of about 2200 ft/sec is the optimum choice for depths greater than 100 feet. (See Fig. 2 for velocity structures used in these computations).

Rayleigh waves at depth of a significant portion of a wavelength are possible only for relatively short wavelengths. Thus, most earthquake-generated Rayleigh waves are ruled out because of the great wavelengths involved. In this paper computations of particle amplitude profiles are related to a small-scale problem involving observable particle trajectories and a large-scale problem involving particle amplitude profiles too deep in the earth to be observable. The former group is designed for comparison with the field observations of *Dobrin, Simon, and Lawrence* [1951] on explosion-generated Rayleigh waves of 4 to 8 cps recorded on the surface over a 3000-foot range and down to 100 feet in a bore hole 1900 feet from the shot (see Figs. 1, 2, and 3). The latter are based on Gutenberg's model of the mantle of the earth and cover the period range 53 to 275 sec (see Figs. 4, 5, 6, and 7).

In the work of *Dobrin, Simon, and Lawrence*, phase velocity and group velocity were measured directly from the seismograms. The

bore hole recordings at a distance of 1900 feet from the shot were made with a 3-component seismometer assembly at depth intervals of 10 feet down to 100 feet. Profiles of compressional and shear velocity were measured in the same bore hole to the same depth. The bore hole recordings made it possible to determine the particle trajectory in the Rayleigh wave train at various depths. These data, which were originally compared with the theoretical profiles of particle amplitude for a homogeneous half-space, are here compared with amplitude profiles based on a 20-layer model of the bore hole profiles of compressional and shear velocity. Since the minimum wavelength studied is about 100 feet, the 5-foot thickness of each layer is small enough so that the shape of the computed dispersion curve is the same as would be found if the variation of properties were smooth. However, the 100-foot depth to which layering extends is limited by the depth of available bore hole measurements, and it is less than the maximum depth at which elastic parameters are important for the longest wavelength (about 400 feet). Thus, as is shown below, it was necessary to choose empirically a single value of shear velocity for the region below 100 feet which gave the best agreement between observed and computed dispersion. With this procedure, reasonably good agreement between the features of the theoretical and experimental particle motion profiles is also obtained (Fig. 3). Even the very large horizontal amplitude which theoretically is expected in weak near-surface material is seen to a limited extent in the experimental data. Systematic differences confined primarily to the shortest periods and shallowest depths observed which still remain between the theoretical and experimental particle motion profiles are ascribed mainly to the difficulty of making accurate bore hole velocity measurements and amplitude observations in the near-surface material and possibly to the effect of air coupling, which was neglected in the theoretical computations.

In the present study the calculations of particle motion indicate that the unconsolidated zone is a region in which further refinement of theoretical and experimental techniques for study of both body and surface waves is desirable.

In the second part of this paper, in which

computations of particle amplitudes based on Gutenberg's model [see Bullard, 1957, p. 25] of the mantle are presented, direct comparison with observation is impossible. These data are of interest because they show the great depths to which the disturbance due to Rayleigh waves penetrates. Data of this type based on a sufficiently detailed model of the earth's mantle are hitherto lacking. The present data have world-wide significance because it has been shown that the Rayleigh mode group-velocity dispersion curve based on this model [see Dorman, Ewing, and Oliver, 1960] is in good agreement with mantle Rayleigh wave observations for periods less than 200 sec [Ewing and Press, 1954a, 1954b]. The profiles apply strictly only to continental areas, since a continental model is used, but for periods greater than 75 sec the profiles are probably quite accurate below a few hundred kilometers for oceanic areas as well.

One of the important results of the computations of particle amplitudes in the mantle is to show that no unusual particle amplitude distributions such as might constitute the so-called channel waves, for instance, exist in the Rayleigh mode. Instead, amplitudes of particle motion for Rayleigh waves in the mantle of the earth decay more rapidly with depth and have relatively larger horizontal components near the surface than amplitudes for Rayleigh waves of identical wavelengths on a homogeneous half-space, but otherwise the two cases are similar.

The calculations of particle amplitudes conclusively prove that for purposes of the analytical precision desired at present the properties of Rayleigh waves of a given wavelength must be considered to depend on the elastic properties of all the material down to a depth greater than 1 wavelength. Approximations which relate waves in a given portion of the spectrum to earth properties in a more limited range of depths are no longer exact enough to be useful for studying the earth. Numerous papers [e.g., Ewing and Press, 1954a, b; Oliver and Ewing, 1958, p. 33] have amply demonstrated the value of considering the entire surface wave train as a dispersed train. More recently, an attempt to analyze the exact shape of the dispersion curve for mantle Rayleigh waves in terms of mantle structure [Dorman, Ewing, and Oliver, 1960] has yielded such encouraging results as to emphasize the need for more precise analytical methods.

Method of computation.

Let T be wave period.

c be phase velocity.

\dot{u} be horizontal particle velocity.

\dot{w} be vertical particle velocity.

σ be stress normal to a horizontal plane.

τ be stress tangential to a horizontal plane in the direction of wave propagation.

a_m be the solid layer matrix [see Haskell, 1953, p. 21].

In the present problem a_m is a function of depth or, more strictly, a function of the layer index, m . It is desired to find u and w as functions of depth. According to Haskell [1953, equation 2.15],

$$\mathbf{v}_m = a_m \mathbf{v}_{m-1} \quad (1)$$

where $\mathbf{v}_m = (\dot{u}_m/c, \dot{w}_m/c, \sigma_m, \tau_m)$ is the motion-stress vector and m is the layer index or interface index. The free surface is interface 0. For Rayleigh waves we may take the motion-stress vector for the free surface to be $\mathbf{v}_0 = (R, 1, 0, 0)$ where R is an imaginary number whose magnitude is the ratio of horizontal to vertical amplitude of Rayleigh wave motion at the free surface. R can be found from the solution of the phase velocity-period equation [Haskell, 1953, equation 2.21]. Starting with its initial value, \mathbf{v}_m is computed as a function of m by iterative use of (1). A very detailed profile can be obtained by using additional interfaces spaced as closely as necessary between the interfaces which are the discontinuities in physical properties.

A program for the IBM 650 was written in which the matrices, a_m , for a layered solid are computed, (1) is applied iteratively, and the current value of \mathbf{v}_m is punched out after each iteration. The necessary starting point (R, c, T) for each profile is obtained by solving the phase-velocity-period equation by a 650 program previously written [see Dorman, Ewing, and Oliver, 1960]. Theoretical group-velocity data are obtained by numerical differentiation of the phase-velocity curves.

A remark is appropriate about the divergence of some of the particle amplitude profiles downward below a depth of 1 to 2 wavelengths, as found in Figures 2 and 6. This phenomenon is always to be expected since the particle amplitude profiles are extrapolations or integrations based on surface values of the amplitudes ob-

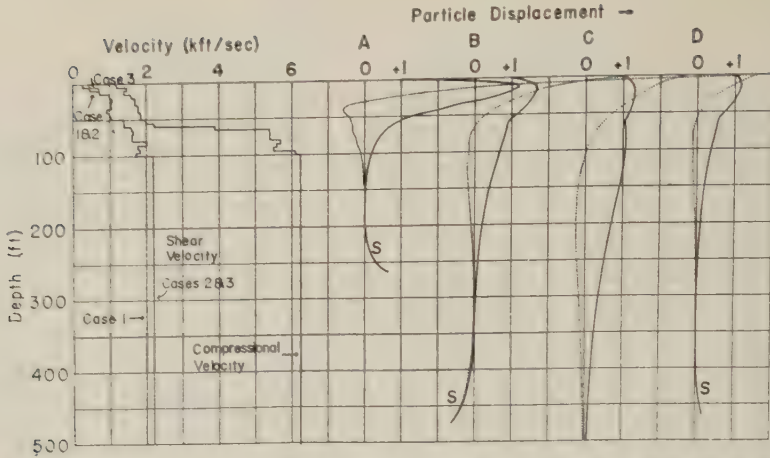


Fig. 2. Velocity structures and computed particle amplitude profiles. Shear velocity structure for case S301 differs from that for cases S300 and S300.A in the two upper layers. Shear velocity structure for cases S300.A and S301 differs from that for case S300 below 100-foot depth. Compressional velocity structure is the same for all cases. Particle displacement profiles: A is computed for case S300.A, $c = 950$ ft/sec, $T = 127$ msec; B, case S300.A, $c = 1460$ ft/sec, $T = 184$ msec; C, case S300.A, $c = 1750$ ft/sec, $T = 249$ msec; D, case S301, $c = 1460$ ft/sec, $T = 170$ msec. Solid curves are vertical displacement; dotted curves are horizontal displacement. Surface orbital motion is retrograde in all cases. The striking difference between the horizontal motion profiles for B and D are due to structural differences in the upper 10 feet of the model, since phase velocities are the same for both profiles. The symbol S indicates specific portions of the numerical solutions (see text).

tained from a dispersion solution. In these cases, inaccuracies in the dispersion solutions which are of the order of 1 part in 10^5 or 10^6 result in particle amplitude profiles which diverge at depths of 1 to 2 wavelengths. These inaccuracies are negligible with respect to the dispersion curve, and the corresponding errors in the amplitude values are negligible for depths shallower than that at which the amplitudes decay to about 1/100 or 1/1000 of surface values.

Comparison of computed amplitude profiles with the field observations of Dobrin, Simon, and Lawrence. In the small-scale problem the layer parameters of three slightly different models used for the theoretical dispersion and particle motion computations are based on a 100-foot bore hole velocity profile [Dobrin, Simon, and Lawrence, 1951, Fig. 3]. In each model twenty layers, each of 5-foot thickness, overlying a half-space are used. Compressional and shear velocity of the layers are the values which were logged for 5-foot intervals. Density, which was not given in the published report, is assumed to be 2.0 g/cm³ between the depths of 0 and 15 feet, 2.25 g/cm³ between 15 and 60 feet, 2.5 g/cm³ between 60 and 100 feet, and 2.6 g/cm³ below 100 feet. It is necessary to assume elastic

TABLE 1a. Layer Parameters, Case S300

H , ft	α , kft/sec	β , kft/sec	ρ , g/cm
5.0	1.204453	0.259784*	2.00
5.0	1.487854	0.448718†	2.00
5.0	1.393387	0.732119	2.00
5.0	1.605938	1.000000	2.25
5.0	1.700404	1.086370	2.25
5.0	1.700404	1.062753	2.25
5.0	1.794872	1.062753	2.25
5.0	1.794872	0.944669	2.25
5.0	1.865722	1.000000	2.25
5.0	1.865722	1.062753	2.25
5.0	2.000000	1.417004	2.25
5.0	2.243590	1.417004	2.25
5.0	3.896761	1.605938	2.50
5.0	5.408232	1.653171	2.50
5.0	5.408232	1.629555	2.50
5.0	5.408232	1.629555	2.50
5.0	5.691633	2.031039	2.50
5.0	5.597166	1.771255	2.50
5.0	5.502699	1.842105	2.50
5.0	6.116734	1.724022	2.50
Inf.	6.234818	2.000000‡	2.60

* For case S301, $\beta = 0.448718$ kilofeet/sec.

† For case S301, $\beta = 0.732119$ kilofeet/sec.

‡ For cases S300.A and S301, $\beta = 2.200$ kilofeet/sec.

TABLE 1b. Computed Rayleigh Wave Dispersion

Case	Period, msec	Phase Velocity, kft/sec	Group Velocity, kft/sec
8300	391.54	1.750	
	315.27	1.700	
	243.49	1.600	
	208.65	1.500	
	187.05	1.400	
	178.72	1.350	
	171.41	1.300	
	158.63	1.200	
	146.82	1.100	
	127.28	0.950	
8304	127.05	0.950	
	150.69	1.150	
	165.70	1.300	
	183.99	1.460	
	197.32	1.550	
	217.41	1.650	
	248.91	1.750	
	138.87	1.050	0.491
	158.19	1.225	0.533
	174.85	1.380	0.652
8301	207.36	1.600	0.972
	233.16	1.700	1.183
	170.01	1.460	

properties for the half-space below 100 feet, the maximum depth logged, since dispersion in the long-period portion of the observed spectrum is insensitive to these properties. An assumed shear velocity of 2000 ft/sec for all material below 100 feet used in case 8300 (Table 1) is found to be too low by comparison of the theoretical phase-velocity curve with the observed phase-velocity curve at long periods (see Fig. 1). An assumed shear velocity of 2200 ft/sec used in case 8300A is found to give good agreement between theoretical and experimental phase-velocity dispersion curves at the long-period end (Fig. 1) as well as reasonably good agreement over the rest of the spectrum. Therefore, particle motion calculations are based on the latter case.

Comparison of phase-velocity dispersion curves for cases 8300 and 8300A with the experimental curve thus provides a means of estimating the average values of shear velocity at depths greater than 100 feet. From Figure 2, where the particle motion profiles for case

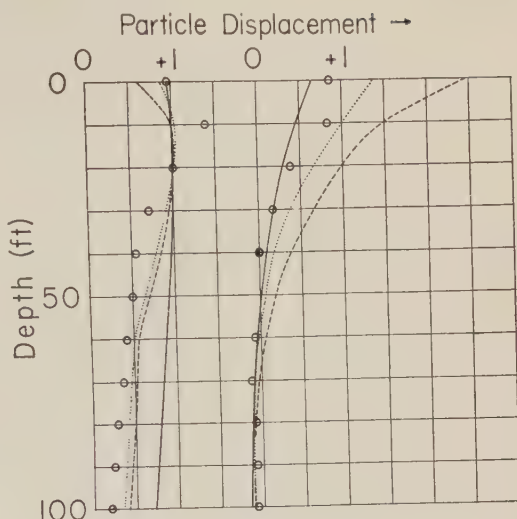


Fig. 3. Profiles of relative particle amplitudes for Rayleigh waves on homogeneous and heterogeneous structures. Vertical amplitude is set equal to unity at a depth of 20 feet. The left-hand set of curves are vertical particle displacements and the right-hand set of curves are horizontal displacements. Solid curves are computed for a wavelength of 268 feet on a homogeneous half-space; dashed curves, case 8300A, $c = 1460$ ft/sec; dotted curves, case 8301, $c = 1460$ ft/sec; open circles, field data of Dobrin, Simon, and Lawrence [1951]. Best experimental agreement with respect to particle amplitude profiles is given by case 8301, but case 8301 is not the best fit with respect to phase-velocity dispersion as shown by diamond-shaped point in Fig. 1.

8300A, period 249 msec, are given, it appears that material below 300 to 400 feet would not have an appreciable effect on waves of that period, and hence 2200 ft/sec can be taken as an approximate value for the shear velocity in the zone between depths of 100 and 300 to 400 feet. The compressional velocity for this region used in case 8300A should not be regarded as a precise estimate, because the Rayleigh wave velocity is more sensitive to shear velocity than to compressional velocity. However, the determination of shear velocity is relatively precise.

In Figure 2 four of the calculated particle motion profiles are plotted to a depth great enough to show the convergence of the solutions downward. Deeper 'tailing off' or divergence of the curves downward is due to very small initial errors. (See preceding section on method of computation.) The first three profiles of Figure 2 are based on case 8300A and the last is based

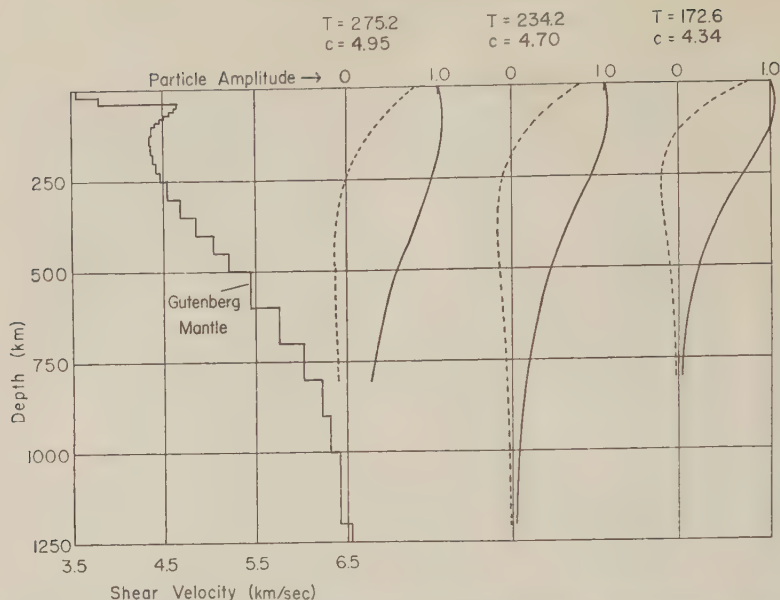


Fig. 4. Shear velocity structure and corresponding particle amplitude profiles for intermediate-period mantle Rayleigh waves. Solid line is vertical amplitude and dashed line is horizontal amplitude.

on case 8301, which will be described below. The first three profiles cover the frequency range of waves observed in the field. The second profile is for approximately the same period as the waves in the particle trajectory diagrams published by *Dobrin, Simon, and Lawrence*, [1951, Figs. 11 and 12]. Figure 3 shows the profile derived from these field observations plotted with the first 100 feet of computed particle motion profiles for cases 8300A, 8301, and a homogeneous half-space. For easiest comparison, all amplitudes in Figure 3 are scaled so that vertical amplitudes equal 1 at a depth of 20 feet.

From Figure 3 it is clear that the vertical component of case 8300A agrees better with the experimental data than does the vertical component for the homogeneous half-space but that the situation is reversed for the horizontal component. The most serious discrepancy between the experimental data and case 8300A is that a very large horizontal amplitude is computed for the near-surface zone but is not observed in the field. This feature of the computed profile may be understood as being due to the very low shear velocity of the upper two layers of case 8300A. Where the phase velocity exceeds the shear velocity at the surface by a large factor, the *S*-ray components of the Rayleigh wave system must have a very small angle of inci-

dence at the surface. This causes the computed particle motion for small depths to be largely horizontal.

There are several possible reasons why the relatively large near-surface amplitudes are almost absent in observations:

1. Seismometer coupling to the loose surface material may not have been satisfactory. This would probably affect the horizontal component the most and would cause observed values to be too low. In this event, agreement between the experimental data and case 8300A would be better than is indicated in Figure 3.

2. Bore hole measurements of shear velocity may have given values too low owing to the difficulty of making measurements in the loose surficial material.

3. Air coupling, which has not been taken into account in computations, may modify the results somewhat for phase velocities close to the velocity of sound in air.

4. Application of the exact elastic theory to the unconsolidated surface materials may not be valid. It is difficult to estimate either the magnitude or the sign of this effect on the computed result.

The last possibility was not examined because of lack of an adequate theoretical treatment.

The third possibility was not tested numeri-

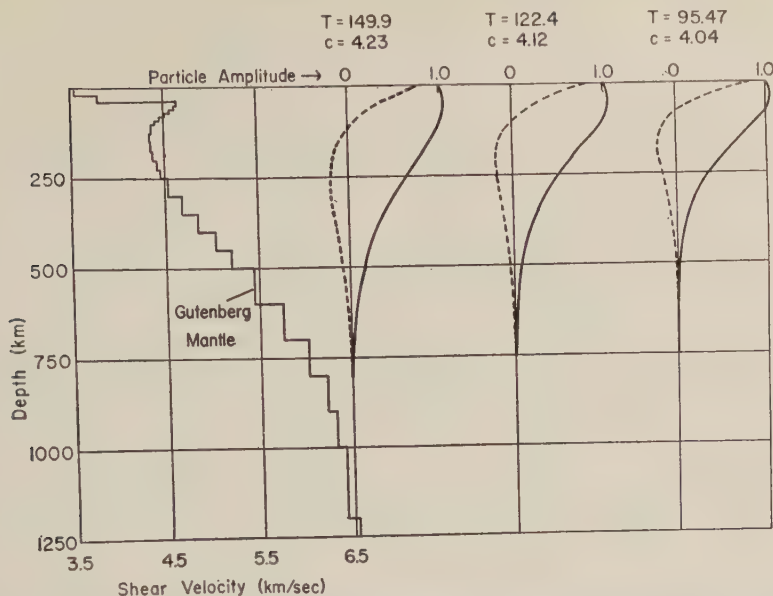


Fig. 5. Shear velocity structure and corresponding particle amplitude profiles for short-period mantle Rayleigh waves. Solid line is vertical amplitude and dashed line is horizontal amplitude.

ally because of lack of a computing program for taking the air into account as a fluid half-space extending upward. Air coupling would be appreciable only at phase velocities close to the velocity of sound in air, i.e., at the short-period end of the spectrum of present observation [see discussion in *Ewing, Jardetzky, and Press, 1957, p. 235*]. The possibility remains that better experimental agreement for short-period waves might be found by taking air into account, but only slight modification should be expected because of the great impedance contrast at the ground surface. In their original work, Dobrin, Simon, and Lawrence, distinguished carefully between trains of waves that are due to air coupling and those that are not. Thus there is no possibility that the field measurements used here are due to a branch of the dispersion curve which exists only in the presence of an air medium. The amplitude of these waves is minimized because both the explosion and the point of observation are in the same medium, i.e., the ground.

The second possibility was tested by comparing profiles for case 8301, which is identical to case 8300A except for higher shear velocities in the upper two layers. According to the above argument, case 8301 should have relatively smaller horizontal amplitude near the surface

because of the higher near-surface shear velocity. Such is the theoretical result obtained from the particle motion profiles for case 8301 at period 170 msec, shown as the fourth profile in Figure 3. However, it hardly seems likely that complete agreement could be obtained by further experimenting in this direction. In Figure 1 the dispersion solution for case 8301 does not fall as close to the experimentally observed phase velocity curve as does the curve computed for case 8300A. Thus, if the dispersion data are heavily weighted, it would seem more likely that the observations of the shallow particle trajectories are at fault; i.e., the first possibility is more important. Considering the difficulty of making precise bore hole measurements of body wave velocities and particle amplitudes, these computed profiles seem satisfactory in comparison with observed particle motion distribution. Clearly experimental observations agree better with the heterogeneous cases, 8300A or 8301, than with the case of the homogeneous half-space.

The comparison of calculated with observed particle amplitude profiles has enabled us to obtain more information in the present case than is obtainable from the ordinary surface wave observations made on the surface, observations which give the dispersion curve only. Us-

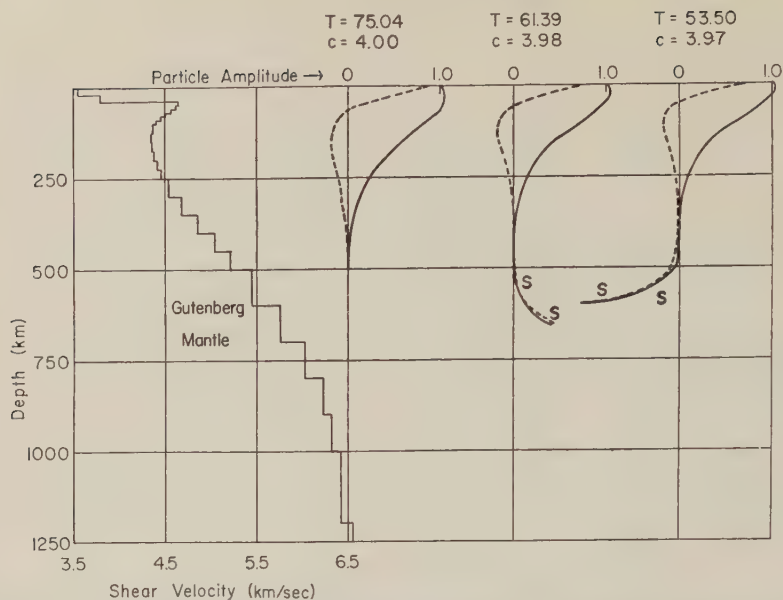


Fig. 6. Shear velocity structure and corresponding particle amplitude profiles for long-period crustal Rayleigh waves. The symbol *S* indicates spurious portions of the numerical solutions (see text). Solid line is vertical amplitude and dashed line is horizontal amplitude.

ing only the dispersion curve as a means of analysis would have left a more satisfactory picture of experimental agreement because the data to be satisfied would have been fewer, but some interesting points about the unconsolidated surface layer might have been missed entirely. However, as we have seen, with the addition of restricting criteria of various kinds, the choice of the exact model which will simultaneously satisfy all available data becomes more difficult. The problem is a familiar one in the use of surface wave data for studying the earth on any scale. To satisfy meager data, acceptable models can be found by a few trial and error steps. But to satisfy more comprehensive sets of data, for instance, dispersion data over a broad frequency range, dispersion data in several modes of propagation, or, as in this case, particle amplitude profiles as well, the number of acceptable models is greatly restricted and solutions become very difficult to find. A more systematic method of choosing the correct model is needed. This will be the subject of further work.

Particle motion for mantle Rayleigh waves. The particle amplitude profiles in Figures 4, 5, and 6 are computed on the basis of a model of the mantle given by Gutenberg [see Bullard, 1957]. The dispersion data, phase velocity

versus period, which correspond to each profile are noted in the figures. Complete parameters used for computing these profiles as well as more complete phase and group velocity dispersion data for this case are given by Dorman, Ewing, and Oliver [1960]. The shear velocity distribution, which is the most important factor governing dispersion and particle amplitude distribution, is also drawn in the present figures. The wavelengths represented by the profiles of Figures 4, 5, and 6 range from 1362 km for the first profile of Figure 4 to 212 km for the last profile of Figure 6. The 1362-km wavelength is about half the length of the longest mantle Rayleigh waves observed to date, and 212 km is well within the range of crustal Rayleigh waves. The other profiles cover the intervening spectrum quite closely.

Crustal Rayleigh waves were defined by Ewing and Press [1956] as Rayleigh waves with periods less than the period of the continental group velocity maximum which occurs at a period of about 70 sec. Group velocity in this range decreases sharply with decreasing period because of the low shear velocity of crustal rocks in comparison with the material of the upper mantle. However, long-period crustal Rayleigh waves, as represented by the profiles of Figure

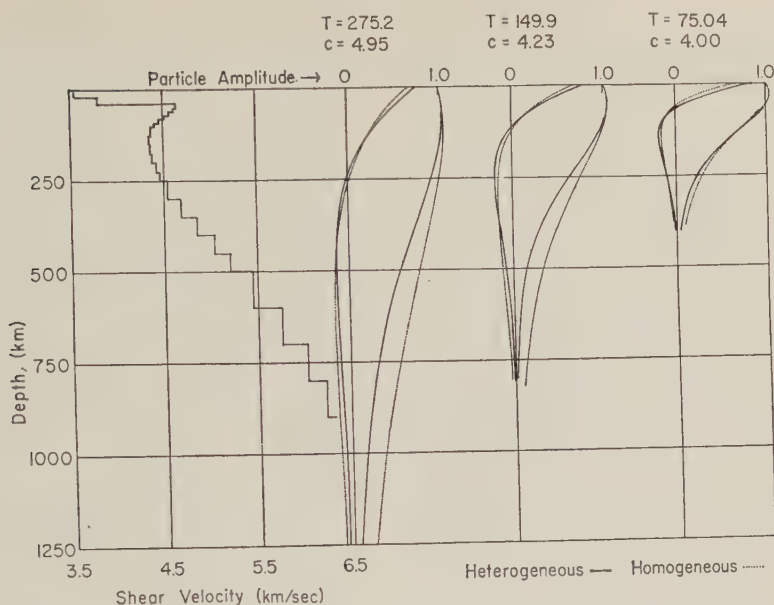


Fig. 7. Particle amplitude distributions for Rayleigh waves of long, intermediate, and short wavelengths on the heterogeneous earth plotted with the particle amplitude distribution of Rayleigh waves for the same respective wavelengths in homogeneous media. The structure in the heterogeneous cases is the Gutenberg structure, the shear velocity distribution of which is shown at left. Solid line is vertical amplitude and dashed line is horizontal amplitude.

6, have appreciable particle motion at a depth of several hundred kilometers in the mantle, and thus even for these waves the continental crust is relatively thin with respect to the range of depths in which large particle amplitudes exist. Therefore the properties of long-period crustal Rayleigh waves depend to a large extent on properties of the upper mantle. Accordingly, it would seem that the heterogeneity of the upper mantle should not be neglected in the interpretation of crustal Rayleigh waves when the best precision is desired. The reader is referred to *Oliver, Kovach, and Dorman* [in press] for precise numerical data on the effect of mantle heterogeneity on the dispersion of crustal Rayleigh waves. These data show that for periods less than 15 sec the mantle may be considered to be a homogeneous half-space without significant error but that for longer periods the phase-velocity curve for the heterogeneous mantle is systematically lower than it is for a homogeneous mantle with properties found immediately beneath the M discontinuity. The corresponding effect on the group-velocity curve is that higher group velocities are found between 20 and 60

or 70 sec for the model with heterogeneous mantle than are found for the model with the homogeneous mantle. Crustal thicknesses deduced from comparison of observed dispersion data with dispersion data computed for models with a homogeneous mantle must be revised accordingly. Interpretation based on the homogeneous mantle gives too great a thickness if the phase velocity method is used and too small a thickness if the group velocity method is used. Error in most cases would probably be about 10 per cent.

Comparison of the profiles in Figures 4 through 6 shows the regular way in which the amplitude distributions for mantle Rayleigh waves vary with wavelength. Amplitudes at all periods are largest near the free surface and decrease downward in a way roughly characteristic of Rayleigh waves on a homogeneous half-space. Departures of the amplitude distribution for Rayleigh waves on the heterogeneous earth from that for Rayleigh waves on a homogeneous medium are not apparent from examination of these profiles. Hence, it does not seem appropriate to speak of any part of the Rayleigh wave spectrum as a 'channel wave' except in the sense

that waves throughout the spectrum under discussion are waves in a channel whose upper boundary is the surface of the earth and whose lower boundary is the general positive velocity gradient in the crust and mantle. In Figure 7 three of the mantle Rayleigh wave profiles are compared with amplitude profiles for waves of the same wavelengths on a homogeneous medium. Reference to this method of illustration is necessary to bring out the rather small systematic differences in amplitude distribution which are due to the particular structure of the mantle. Consistently the amplitudes of both horizontal and vertical motion decay more rapidly with depth, and horizontal amplitude is relatively greater near the surface in the heterogeneous earth than in the homogeneous medium. These two effects can reasonably be attributed to the general rigidity gradient. We have already seen by comparing cases 8300 and 8300A with case 8301 how decreased rigidity in the near-surface zone is associated with relatively greater shallow horizontal amplitudes. The explanation offered above for this phenomenon may also be applied here; namely, that owing to the low shear velocity near the surface, *SV* rays have smaller angles of incidence in the near-surface layers and the motion associated with them is therefore more nearly horizontal.

In Figure 7 the first and second profiles for the heterogeneous earth would apparently fit profiles for a somewhat shorter wavelength of Rayleigh waves on a homogeneous earth better than they fit the profiles for waves of equal wavelength with which they are compared. According to the above discussion this is due to the general positive downward gradient of rigidity or shear velocity in the mantle. The third, or short-period, profile fits much better with a profile of equal wavelength for a homogeneous medium. This is probably due to the fact that the wavelength here is short enough so that the particle motion is mainly in the region of the low-velocity channel and is not affected by the strong positive velocity gradient deeper in the mantle. Thus, for cases in which a positive velocity gradient is present, the effective depth of exploration is decreased somewhat for Rayleigh waves of a given wavelength.

The present data show that material between about 40 and 250 km (the low-velocity channel

according to the Gutenberg model) has an important effect on waves of all periods here considered, i.e., 53 to 275 sec. From the profile presented here it can be roughly estimated that only Rayleigh waves shorter than 40 km, i.e., period of about 12 to 15 sec, would be independent of conditions below a depth of 40 km. Thus the properties of Rayleigh waves in any limited period range cannot be directly related to conditions in any limited range of depths in the crust or mantle. The problem is considerably more complicated, requiring consideration of conditions over a surprisingly large range of depths in order to determine the velocity or other property of Rayleigh waves at any particular period. Oversimplification of the problem leads to approximate ideas or results which are not precise enough to be useful for obtaining further information about the earth at the present state of knowledge.

Since the velocity relationship of the shallow crustal or sedimentary zone to the deeper parts of the crust is roughly the same as the relationship of the crust to the upper mantle, except for a scale factor, it is clear that the remarks made above with reference to the spectrum of periods from 53 to 275 sec apply approximately to shorter-period Rayleigh waves, although no amplitude calculations have been made here for shorter periods.

The present data do not explain observations at Uppsala [Báth, 1959] and at Palisades (G. H. Sutton, personal communication) that the particle orbit of long-period Rayleigh waves is an ellipse with the major axis horizontal. The theoretical surface orbits, according to the Gutenberg case, are about $R = 0.8$. This ratio is also nearly the same for somewhat different models of the mantle [see Dorman, Ewing, and Oliver, 1960, Tables 1, 2, 4, 5]. Rough calculations show that the longitudinal acceleration due to tilt associated with the Rayleigh waves is in phase with the acceleration due to longitudinal particle displacement but is not large enough in the period range in question to account for the observed flattening of the orbital shapes. More data on R as a function of period and geographical position are needed and will be forthcoming now that carefully matched sets of long-period vertical and horizontal instruments are more widely distributed.

Conclusions. In the comparison of theoretical computations with the field data of Dobrin, Simon, and Lawrence [1951], computed and observed dispersion are in agreement when computations are based on the bore hole velocity log measured in the field combined with a substratum (below a depth of 100 feet) having shear velocity of 2200 feet/sec (case 8300A or 301). The particle amplitude profile computed for the heterogeneous structures agrees with the observed particle trajectories much better than the corresponding profile for a homogeneous half-space, except that computed horizontal amplitudes in the shallow, unconsolidated zone are much greater than the observed amplitudes. If the assumed shear velocity of the unconsolidated zone is arbitrarily increased (case 301), the computed horizontal particle amplitude agrees better with that observed, but agreement between observed and computed phase velocity dispersion is poorer at short periods. The data indicate that difficulty may have been encountered in the field either in coupling seismometers to the unconsolidated surface material or in making bore hole velocity measurements in this material. The possibility that the elastic theory does not strictly apply to this material was not investigated. Because of the difficulty of finding a layered model that satisfies a comprehensive set of surface wave data, further work is being done on a systematic general method of reaching such a solution.

Calculation of particle amplitude profiles for mantle Rayleigh waves has led to a clearer understanding of the factors that govern the properties of these waves and the type of information that may be obtained from them, even though observation of them at a significant depth in the earth is not possible. In all cases, consideration of properties of the crust and mantle down to depths of at least 1 wavelength is necessary in order to explain the properties of these waves. Thus, waves of periods greater than 15 sec depend to some extent on the properties of the mantle, whereas long crustal Rayleigh waves, i.e., periods of 50 to 75 sec, are governed primarily by the properties of the mantle. In the latter case, neglecting the effect of heterogeneity in the mantle leads to errors in deductions based on Rayleigh wave dispersion concerning the thickness and structure of

the crust. The shape of relative particle amplitude curves for Rayleigh waves on the heterogeneous earth is similar to that for Rayleigh waves on a homogeneous half-space and does not vary markedly with wavelength. Thus, in the Rayleigh mode between periods of 53 and 275 sec, there are no waves that can be called channel waves on the basis of particle amplitude distribution. From simple considerations it is clear that the same conclusion applies to Rayleigh waves of shorter period.

Comparison of theoretical particle amplitude profiles with particle trajectory observations, when possible, increases the amount of information obtainable from surface waves by increasing the number of criteria which must be satisfied. Such computations, as well as dispersion computations for multilayered media, are easily made with the programs written for the IBM 650 which were used in this work.

Acknowledgment. We are indebted to Dr. Jack Oliver and Dr. Maurice Ewing, who reviewed the manuscript critically and offered several useful suggestions. This work was supported by contracts Nonr 266 (53), AF 19 (604) 4144, and NSF-G 3485.

REFERENCES

- Båth, Markus, Ultra-long-period motions from the Alaska earthquake of July 10, 1958, *Geofis. pura e appl.*, **41**, 91-100, 1959.
- Bullard, E. C., The density within the earth, *Verhandel. Ned. Geol. Mijubouw. Genoot. Geol. Ser.*, **18**, 23-41, 1957.
- Bullen, K. E., *An Introduction to the Theory of Seismology*, Cambridge Univ. Press, Cambridge, 1947.
- Dobrin, M. B., R. F. Simon, and P. L. Lawrence, Rayleigh waves from small explosions, *Trans. Am. Geophys. Union*, **32**, 822-832, 1951.
- Dorman, James, Maurice Ewing, and Jack Oliver, Study of shear velocity distribution in the upper mantle by mantle Rayleigh waves, *Bull. Seism. Soc. Am.*, **50**, 87-115, 1960.
- Ewing, Maurice, W. S. Jardetzky, and Frank Press, *Elastic Waves in Layered Media*, McGraw-Hill Book Co., New York, 1957.
- Ewing, Maurice, and Frank Press, An investigation of mantle Rayleigh waves, *Bull. Seism. Soc. Am.*, **44**, 121-147, 1954a.
- Ewing, Maurice, and Frank Press, Mantle Rayleigh waves from the Kamchatka earthquake of November 4, 1952, *Bull. Seism. Soc. Am.*, **44**, 471-479, 1954b.
- Ewing, Maurice, and Frank Press, Rayleigh wave

- dispersion in the period range 10 to 500 seconds, *Trans. Am. Geophys. Union*, 37, 213-215, 1956.
- Haskell, N. A., The dispersion of surface waves on multilayered media, *Bull. Seism. Soc. Am.*, 43, 17-34, 1953.
- Oliver, Jack, and Maurice Ewing, Normal modes of continental surface waves, *Bull. Seism. Soc. Am.*, 48, 33-49, 1958.
- Oliver, Jack, Robert Kovach, and James Dorman, Crustal structure of the New York-Pennsylvania area, *Bull. Geol. Soc. Am.*, in press.
- Satô, Y., Numerical integration of the equation of motion for surface waves in a medium with arbitrary variation of material constants, *Bull. Seism. Soc. Am.*, 49, 57-77, 1959.
- Stoneley, Robert, and Urs Hochstrasser, The attenuation of Rayleigh waves with depth in a medium with two surface layers, *Monthly Notices Roy. Astron. Soc., Geophys. Suppl.*, 7, 279-288, 1957.

(Manuscript received July 22, 1960.)

PS Converted Waves from Large Explosions¹

JOSEPH J. SCHWIND, JOSEPH W. BERG, JR., AND KENNETH L. COOK

*Department of Geophysics, University of Utah
Salt Lake City, Utah*

Abstract. Four seismograms obtained during 1958 and 1959 from large quarry blasts at Promontory (1,221,000 and 2,138,000 lb of explosive) and Lakeside, Utah (1,500,000 lb), and the underground Blanca nuclear explosion (38,000,000 lb equivalent) near Mercury, Nevada, were studied to ascertain whether converted waves of *PS* type were recorded and, if so, whether they could be used in an analysis of earth crustal layering, as proposed by Andreev in 1957. The *PS* converted wave is presumed to be composed principally of the *SV*-type wave (vertically polarized shear wave) and to result from the conversion of energy from the parent compressional *P* wave at the interface between two crustal layers of contrasting seismic velocity.

The method of analysis consisted in computing theoretical times of arrival for *PS* converted waves based on crustal layering and velocities in the area as determined from refraction seismic studies by Berg, Cook, and Narans [1959], by plotting the radial horizontal component versus the vertical component of velocity of ground motion over appropriate time intervals, and by comparing amplitudes and frequencies of the *PS* converted waves with the amplitude and frequency of the parent *P* wave.

Arrivals, provisionally interpreted as *PS* converted waves, were detected on the traces of both the radial horizontal-component seismometers (2 cps natural frequency) and the vertical-component seismometers (2 cps). The amplitude of the *PS* converted waves was usually several times greater than that of the first arrival of the *P* wave. The successively later arrivals of *PS* converted waves from successively deeper horizons showed progressively greater ground-velocity amplitudes, as found by Andreev on earthquake seismograms, but some variance from this generalization was found. The frequencies of the various *PS* converted wave arrivals were approximately the same as those of the parent *P* wave, between 5 and 10 cps.

The crustal layering, which was determined by using the times of arrival of the *PS* converted waves, compared favorably with that given by Berg, Cook, and Narans for this area. The computed depths of the successive layers were: 5.5, 9.7, 16, and 26 km at Neola, Utah (epicentral distance of about 245 km from Lakeside blast); 12, 26, and 31 km at Gold Hill, Utah (173 km from Promontory); 8.6, 24, and 29 km, also at Gold Hill (379 km from Blanca); and 12, 22, and 31 km at Elko, Nevada (279 km from Promontory).

INTRODUCTION

During the period 1956 to 1959, large quarry blasts provided material for a causeway across the Great Salt Lake, Utah, for the Southern Pacific Railroad. Seismograms from quarry blasts at Promontory, Utah, and Lakeside, Utah (see Fig. 1), involving from 50,000 to 2,138,000 lb of explosive were obtained with portable seismic equipment by the University of Utah to distances of 278 km from the blasts. Three seismograms obtained from these blasts, one from Lakeside and two from Promontory, and one seismogram obtained from the Blanca nuclear explosion, near Mercury, Nevada, were studied to determine (1) whether *PS* converted

waves were recorded and, if so, (2) whether a set of criteria could be established for the systematic and reliable identification and analysis of such waves.

PREVIOUS WORK

Knott [1899] first presented energy distribution equations for the general case in which either a compressional wave (*P*) or a transverse wave (*S*) impinges upon a boundary separating two media. He showed that a wave of either type, incident upon a boundary, will result in the generation of a reflected and a refracted *P* wave and a reflected and a refracted *S* wave.

Andreev [1957] proposed a method for the study of the layering of the earth's crust using earthquake seismograms and the theory of the conversion of incident *P*-wave energy at a

¹ Contribution No. 31, Department of Geophysics, University of Utah.

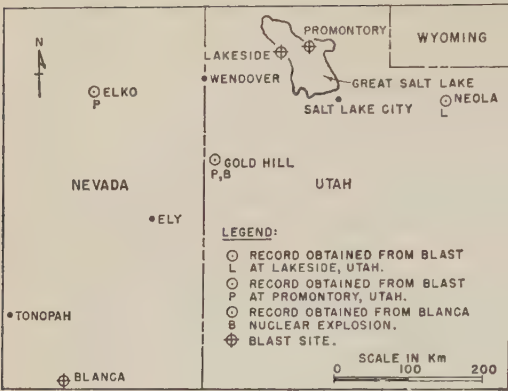


Fig. 1. Map showing locations of blasts and temporary seismograph stations where seismograms were obtained.

boundary within the crust to refracted *S*-wave energy (thought to be vertically polarized shear, *SV*). The refracted *S* wave has been designated by him as a *PS*-type exchange wave. The terminology of *PS* converted, in preference to exchange wave is to be understood throughout this paper. Advantages advanced for this method are that the analysis is not dependent on a knowledge of the exact position of the source of the seismic energy, time of origin of the energy, and/or absolute times of wave arrivals. In a later paper, *Andreev and Shebalin* [1957] gave additional results of crustal layering which were

obtained from 'bursts' as well as from earthquakes.

A *PS* converted wave formed at the base of the *n*th layer in the earth's crust is designated as *PS_n*. If a four-layer section is assumed, the formation of a *PS* converted wave system would be as shown in Figures 2*a*, 2*b*, and 2*c*, which illustrate the formation of the waves *PS₁*, *PS₂*, and *PS₃* from the same incident *P* wave. According to Andreev, if the first *P* arrival traveled in the top of the layer immediately below the crust, using the four-layer section as the example, *PS₁* would be the first to arrive because of the shorter distance that *PS₁* travels as a transverse wave compared with either *PS₂* or *PS₃*. The next wave arrival would be that of *PS₂*, and *PS₃* would follow. From the time delays, designated as Δt_n , between the arrival of the *P* wave and the *PS* converted waves, together with a knowledge of the angles of refraction from layer to layer, it is possible to calculate the thicknesses of the three top layers.

The equations are:

(a) for the two-layer case,

$$\Delta t_1 = h_1 \left[\frac{\cos a_1}{V_{S_1}} - \frac{\cos i_1}{V_{P_1}} \right] \quad (1)$$

where (Fig. 2*d*) Δt_1 is the delay time through the upper layer; h_1 is the thickness of the layer; i_1 is the angle of refraction of the compressional

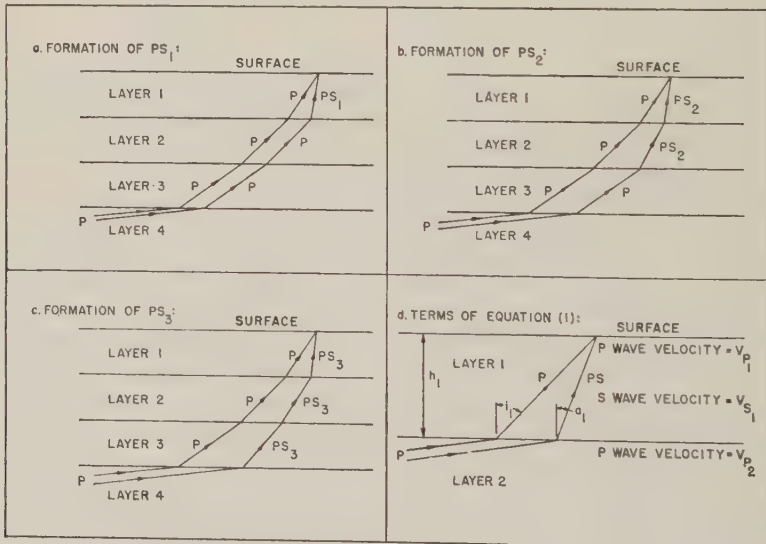


Fig. 2. Formation of *PS* converted waves in assumed four-layer section: (a) *PS₁*, (b) *PS₂*, (c) *PS₃*, (d) two-layer section with terms used in equation 1.

TABLE 1. Summary of Data from Quarry Blasts at Promontory and Lakeside, Utah, and Underground Blanca Nuclear Explosion

Location of Temporary Station	Neola, Utah	Gold Hill, Utah	Elko, Nevada	Gold Hill, Utah
Date of Blast	Feb. 8, 1959	Feb. 4, 1958	Jan. 5, 1958	Oct. 30, 1958
Location of Blast	Lakeside, Utah	Promontory, Utah (No. 1 Quarry)	Promontory, Utah (No. 2 Quarry)	AEC Proving Grounds, Nevada
Size of Blast, lb. of explosive	1,500,000	1,221,000	2,138,000	38,000,000 (equivalent lb)
Distance, km	245.3	173.3	279.4	379.5

ave; a_1 is the angle of refraction of the transverse wave; V_{S_1} is the velocity of the transverse wave and V_{P_1} is the velocity of the compressional wave in the upper layer; and

(b) for the general case of $(n + 1)$ layers,

$$t_n = h_1 \left[\frac{\cos a_1}{V_{S_1}} - \frac{\cos i_1}{V_{P_1}} \right] + \dots \\ \dots + h_n \left[\frac{\cos a_n}{V_{S_n}} - \frac{\cos i_n}{V_{P_n}} \right] \quad (2)$$

where Δt_n is the total delay time through n layers. For the derivations of equations 1 and 2 it is assumed that the angle of incidence of the apparent P wave upon the lowermost boundary is approximately 90° ; that is, that the ray path of P is essentially parallel to the boundary. When the P wave is incident upon the lowermost boundary at angles for which this approximation is not valid, the apparent velocity of the incident P wave has to be considered, and equations 1 and 2 are not valid.

For a quantitative analysis, all the PS converted waves must be formed from the same P wave, and a velocity cross section is required so that the various angles of refraction of the P and PS converted waves may be determined.

EXPERIMENTAL DATA

Figure 1 shows the locations of the three temporary seismograph stations (Neola, Gold Hill, and Elko) where the observations were made. Table 1 gives other relevant information.

The instrumentation for the field work consisted of low-frequency seismometers (2 cps) manufactured by the Houston Technical Laboratories; amplifiers of the conventional seismic reflection type, modified to pass frequencies between approximately 3 and 50 cps; and conventional seismic prospecting oscillographs with

a paper speed of about 30 cm/sec. Usually, a radial horizontal-component seismometer, and a vertical-component seismometer were placed within a few meters of each other. Additional vertical seismometers were placed in line with the blast at intervals ranging between a few tens of meters and about 1 km. All seismometers were placed on, or within a few meters of, bed-rock.

For ease of reference the four seismograms used in this research have been designated as Neola-Lakeside, Gold Hill-Promontory, Elko-Promontory, and Gold Hill-Blanca. In selecting records from the many that were available, the following criteria were considered:

(a) Since, according to Andreev, the PS converted waves are believed to be characterized by SV ground motion, it is advisable to have a horizontal seismometer (oriented in the direction to the blast) and a vertical-component seismometer to provide a complete description of the PS converted wave.

(b) Sufficient epicentral distance must be maintained to insure that the first wave to arrive is that which has traveled in the top of the medium immediately below the deepest layer whose thickness is required. Moreover, this dis-

TABLE 2. Velocity Model as Determined from Promontory and Lakeside Blasts and Blanca Underground Nuclear Explosion by Berg, Cook, and Narans [1959]

Layer	Thickness, km	Compressional Wave Velocity, km/sec
1	9	5.7
2	16	6.3
3	...	7.6

Total section thickness: 25 km.

TABLE 3. Summary of Velocity Models Used and Layering Determined from *PS* Converted Wave Analysis

Neola-Lakeside Seismogram		Gold Hill-Promontory Seismogram		Elko-Promontory Seismogram		Gold Hill-Blanca Seismogram	
Velocity of Compressional Wave in Layer, km/sec	Thickness of Layer, km	Velocity of Compressional Wave in Layer, km/sec	Thickness of Layer, km	Velocity of Compressional Wave in Layer, km/sec	Thickness of Layer, km	Velocity of Compressional Wave in Layer, km/sec	Thickness of Layer, km
4.3	5.5	4.3	12	4.3	12	4.3	8.6
5.2	4.2
5.7	5.9	5.7	14	5.7	10	5.7	15
6.3	10	6.3	5.2	6.3	9.4	6.3	5.3
7.6	...	7.6	...	7.6	...	7.6	...
Total	26 km		31 km		31 km		29 km

tance must be sufficiently large so that the motion of other arrivals does not interfere with the motion of the *PS* converted wave arrivals.

(c) Since the frequencies of the first arrivals from large explosions at the distances involved could be expected to be between 1 and 15 cps, only records obtained with instruments capable of recording this range would be relevant.

Except as noted below, the four seismograms studied conformed to these requirements.

The velocity data of *Berg, Cook, and Narans* [1959], obtained from seismic studies of the Promontory and Lakeside blasts, and the Blanca underground nuclear explosion, were considered to be appropriate. These data are summarized in Table 2. However, other data were used when available. In all instances, a value of 1.7 was used for the ratio of the velocity of the compressional wave to the velocity of the shear wave when these waves traveled in the same medium.

ANALYSIS

The steps adopted for the identification of *PS* converted wave arrivals were as follows:

(a) It was first necessary to make calculations, based on the velocity model given in Table 2, of the theoretical delay times between the first arrival, a *P* wave, and the expected arrival of the *PS* converted waves. These delay times were used to indicate the possible arrival times of *PS* converted waves on the seismograms studied.

(b) The phase relationship of the arrivals

that were picked as possible *PS* converted waves was such as to conform to *SV* motion. Thus, if the recording instruments were such that the horizontal and vertical components of the compressional wave were in phase, the shear wave arrival would show these components to be out of phase.

(c) A comparison of the amplitudes of the observed arrivals as measured directly on the seismograms was made, as Andreev had reported that 'these waves have a larger amplitude the later they arrive.'

(d) A comparison was also made between the frequencies of the possible *PS* converted waves and of the first-arrival *P* waves.

(e) Finally, plots of horizontal versus vertical ground motion were constructed to give an indication of the type of wave involved in any particular arrival.

RESULTS

Neola-Lakeside seismogram. It is believed that four *PS* converted wave arrivals were identified on the Neola-Lakeside seismogram. An adjustment was made in the velocity cross section because the layering appeared to be more than that shown in Table 2. Reliable velocity data were made available for this area by oil companies, and these data showed that, near the surface, material was present having an average velocity of 4.2 km/sec for compressional waves. Immediately under this material, a velocity of 5.2 km/sec was assumed. The remaining velocity

TABLE 4. Summary of Additional Information Obtained from Seismograms

Station and Blast	Arrival	Galvanometer Deflection, inch		Frequency, cps	
		Vertical Trace	Horizontal Trace	Vertical Trace	Horizontal Trace
Neola-Lakeside	<i>P</i>	0.2	0.2	5.6	6.0
	<i>PS</i> ₁	0.8	0.6	6.2	5.6
	<i>PS</i> ₂	0.9	0.7	6.7	5.4
	<i>PS</i> ₃	2.7	1.5	6.7	6.1
	<i>PS</i> ₄	2.4	1.4	5.9	5.6
Gold Hill-Promontory	<i>P</i>	0.3	0.7	6.4	6.7
	<i>PS</i> ₁	0.8	1.7	13.7	10.8
	<i>PS</i> ₂	0.8	1.8	10.0	10.0
	<i>PS</i> ₃	0.5	2.1	11.1	11.9
Elko-Promontory	<i>P</i>	0.1	0.2	5.6	6.2
	<i>PS</i> ₁	0.4	0.5	5.9	7.7
	<i>PS</i> ₂	0.4	1.9	8.0	7.6
	<i>PS</i> ₃	0.6	0.8	8.2	10.0
Gold Hill-Blanca	<i>P</i>	0.2	...	5.3	...
	<i>PS</i> ₁	1.2	...	7.3	...
	<i>PS</i> ₂	1.0	...	7.5	...
	<i>PS</i> ₃	0.5	...	6.7	...

section, beginning with 5.7 km/sec, was taken from Table 2.

Substitution into equation 2 of the observed delay times and the assumed velocities resulted in crustal layers with individual thicknesses of 5.5, 4.2, 5.9, and 10 km, from the top to the bottom of the section, respectively. The total section thickness becomes, therefore, about 26 km.

Any differences between the velocities assumed and the velocities actually existing in the layers would, of course, alter the calculated section. In this case, if each of the assumed velocities were increased by 0.2 km/sec, the total depth would be increased by less than 5 per cent.

Figure 3, from the Neola-Lakeside seismogram, shows the arrival of the possible *PS*₁, *PS*₂, *PS*₃, and *PS*₄ converted waves. The exact times of onset of the waves are probably earlier than are shown on this figure.

Ground-motion graphs were plotted for all arrivals picked as possible *PS* converted waves on all seismograms used in this research, and all plots showed ground motion of shear type. This was one of the criteria used in evaluating arrivals.

Gold Hill-Promontory seismogram. The seis-

monometer arrangement used to obtain the Gold Hill-Promontory seismogram was similar to that used at Neola (Fig. 3). Three arrivals were interpreted as *PS* converted waves on this seismogram. Adjustment was made in the velocity cross section by eliminating the 5.2 km/sec layer from the section used in the Neola-Lakeside analysis because of geological considerations. The velocity model then was 4.2, 5.7, 6.3, and 7.6 km/sec, from top to bottom, respectively. The thicknesses of the corresponding layers of the resulting section were 12, 14, and 5.2 km, from top to bottom, respectively, and the total thickness becomes about 31 km.

Elko-Promontory seismogram. For the Elko-Promontory measurements, the horizontal-component seismometer was separated from the vertical seismometer by a horizontal distance of 800 meters in a direction toward the blast. Assuming that the compressional wave from which the *PS* converted waves would be formed was that *P* wave which was traveling in the top of the 7.6 km/sec layer, the seismogram tracings were moved relative to each other by the amount of time required for the *P* wave to travel the distance of 800 meters between the vertical- and horizontal-component seismometers, or 0.11 sec. Using this method, three ar-

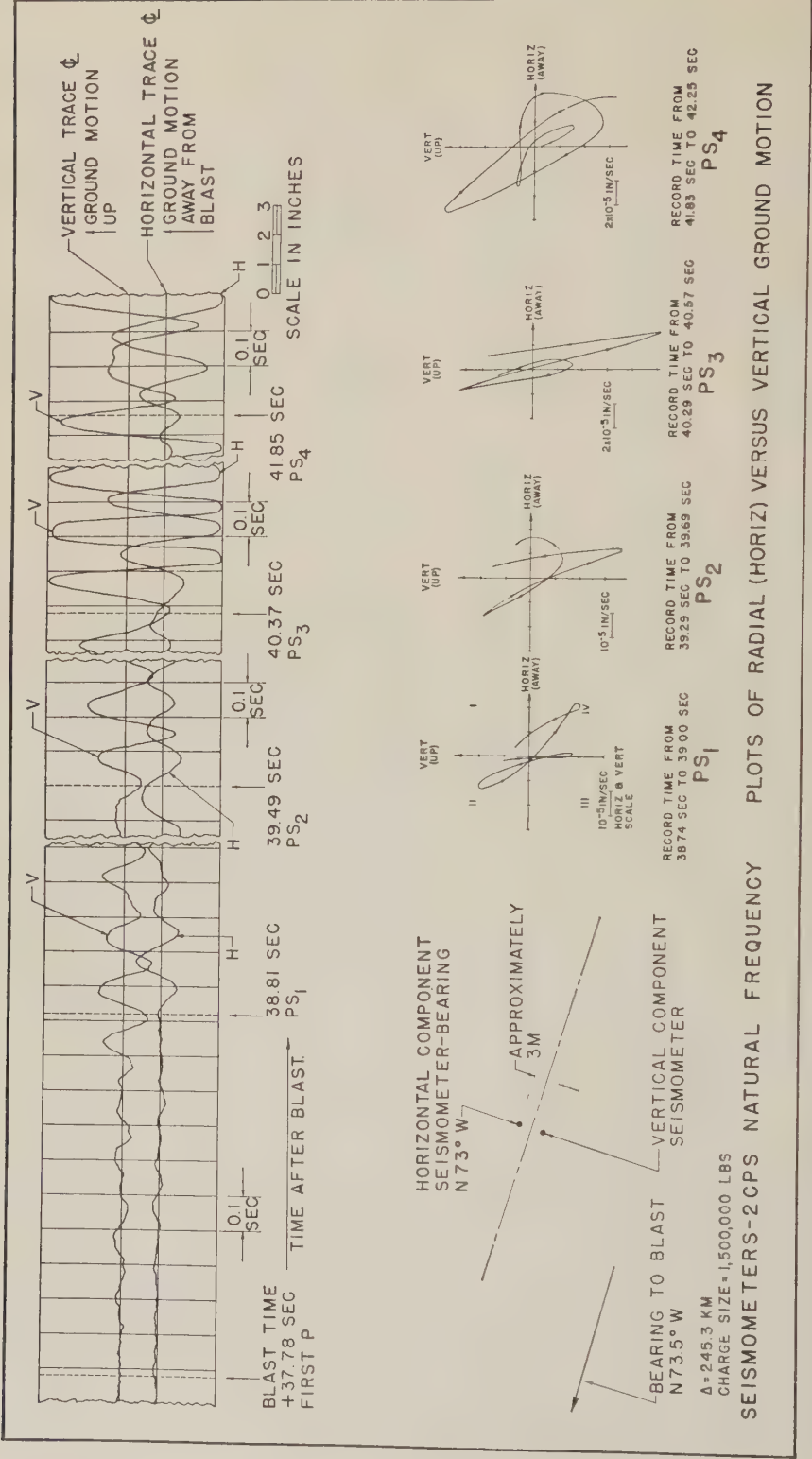


Fig. 3. Neola-Lakeside seismogram (at top) showing arrivals of possible PS converted waves from 1,500,000-lb Lakeside blast, distance 245.3 km. Direction of ground motion (upper right) is shown by arrows. Plan view (lower left) of seismometer spread and plots (lower right) of horizontal versus vertical ground motion. For these arrivals, the graphs show the ground motion to be predominantly in and between quadrants II and IV indicating SV motion.

ivals were identified as possible *PS* converted waves. The same velocity cross section as that used for the Gold Hill-Promontory calculations was used for these computations, and the individual layer thicknesses for the section became 2, 10, and 9.4 km, from top to bottom, respectively; the resulting total thickness is about 11 km.

Gold Hill-Blanca Seismogram. The Gold Hill-Blanca seismogram, which was obtained at the same location as the Gold Hill-Promontory seismogram, afforded an excellent opportunity for determining the repeatability of the results at Gold Hill, since the converted waves are a function of the observation site only. Unfortunately, the trace of the horizontal component of ground motion was not usable, but the seismogram contained two traces of the vertical component from two seismometers that were separated by a distance of 460 meters towards the blast.

Utilizing the apparent velocity, which was about the same as that of the parent *P* wave, between the two vertical-component traces and the direction of ground motion, three possible *PS* converted wave arrivals were noted, and application of the delay times and the velocities from the velocity section used for the Gold Hill-Promontory analysis yielded a section with layer thicknesses of 8.6, 15, and 5.3 km, from top to bottom, respectively; the total thickness became about 29 km. It is seen that these results compare favorably with those obtained from the Gold Hill-Promontory seismogram.

The velocity models and layering determined for the four seismograms studied are summarized in Table 3.

Trace amplitudes and frequencies of the possible *PS* converted wave arrivals are summarized in Table 4. The amplitude of the *PS* converted waves was usually several times greater than that of the first arrival of the *P* wave. From this table it can be seen that the amplitudes of the *PS* converted waves generally increase with the lateness of the arrival; but there is some variance from this generalization. Except for the Gold Hill-Promontory arrivals, the frequencies of the possible *PS* converted waves compare favorably with the frequency of the *P* wave.

CONCLUSIONS

The results of this research indicate that *PS*

converted waves were probably recorded on the seismograms analyzed. In future experiments, it would be more useful and diagnostic to use, instead of one vertical seismometer and one horizontal seismometer, a line of vertical seismometers with a horizontal seismometer at either or, preferably, both ends of the array. The apparent velocity of the seismic pulse across the array would be a criterion for analysis.

For purposes of analyzing the records for *PS* converted waves, the following criteria have been found useful in this research.

(a) The phase relationship between the vertical and horizontal components of the arrivals that were picked as possible *PS* converted waves were such as to indicate a shear wave arrival of the *SV* type.

(b) The amplitude of the *PS* converted waves was usually several times greater than that of the first arrival of the *P* wave.

(c) A general trend of increasing ground motion amplitudes was observed with increasing lateness of arrival of the *PS* converted waves. This criterion must be used cautiously, however, as there was some variance from it.

(d) The frequencies of the various *PS* converted wave arrivals were approximately the same as the frequency of the parent *P* wave.

In view of the findings of this research, the sections summarized in Table 3 probably have significance.

Acknowledgments. The Continental Oil Company provided a fellowship for the first author during the academic year 1959-1960, while he was compiling much of the material presented in this paper for an M. S. thesis. The seismograms and other data were obtained during the course of a project sponsored by the National Science Foundation under research grants G-4645 and G-9192 and the University Research Fund of the University of Utah.

Final Note. After the completion of this paper, the English translation of a paper by Kuz'mina [1959] became available. Besides giving, to date, the most comprehensive discussion, as well as bibliography, on *PS* converted waves, Kuz'mina, using earthquake data for crustal studies, presents results from which he concludes that the waves recorded in 1953 from crustal layers in the Main Caucasus Range region were *PS* converted waves. He states that (1) the amplitude of the *PS* converted waves is, on the average, 2 to 5 times greater than that of the first arrival of the parent *P* wave; (2) the amplitude of the displacement of

the *PS* converted wave increases with the depth to successively deeper horizons (this result agrees with theory, according to both Andreev [1957] and Kuz'mina [1959]); and (3) the oscillation periods of the *PS* converted waves are 1.3 to 1.7 times larger than those of the parent *P* wave. Except for the last observation, the results presented here are comparable with those of Kuz'mina. It should be noted, however, that the epicentral distances of Kuz'mina's work were generally much smaller than those in this research, and that his seismograms were obtained from earthquakes instead of quarry blasts; perhaps for these reasons, or because of different structural conditions, or for other reasons now unknown, the results are not entirely comparable.

REFERENCES

- Andreev, S. S., A study of the plutonic structure of the earth's crust using *PS* exchange waves recorded during earthquakes, *Bull. Acad. Sci. USSR, Geophys. Ser. (English Translation)*, **1**, 22-31, 1957.
- Andreev, S. S., and Shebalin, N. V., The use of short-period seismographs for isolating exchange waves on traces of distant earthquakes, *Bull. Acad. Sci. USSR, Geophys. Ser. (English Translation)*, **7**, 109-112, 1957.
- Berg, J. W., Jr., Cook, K. L., and Narans, H. D., Jr., Seismic studies of crustal structure in the eastern Basin and Range province (abstract), *Bull. Geol. Soc. Am.*, **70**, 1709, 1959.
- Knott, C. G., Reflexion and refraction of elastic waves with seismological application, *Phil. Mag.*, **5th series**, **48**, 64-97, 1899.
- Kuz'mina, N. V., The use of converted waves in the study of the structure of the earth's crust in the southeastern portion of the Main Caucasus Range, *Bull. Acad. Sci. USSR, Geophys. Ser. (English Translation)*, **7**, 734-743, 1959.

(Manuscript received July 6, 1960; revised August 29, 1960.)

SELECTED GEOMAGNETIC AND SOLAR DATA (Compiled by J. Virginia Lincoln)
Kp, Ci, Cp, Ap, K_{Fr}, Rz and Selected Days
 January 1960

Day ¹	3-hr Range Indices Kp^2								Sum	Prel. ³ C_i	Cp^4	Ap^5	3-hr Range Indices K_{Fr}^6		Prov. ⁷ R_z
	1	2	3	4	5	6	7	8					Values	Sum	
1	5-	4+	5-	3o	3+	3o	4+	3o	30+	1.2	1.2	26	5443 3343	29	167
2	4-	3o	4o	4-	3+	2o	2o	2-	23+	0.9	0.9	16	3343 3222	22	154
3	2o	3-	2+	3o	2+	3+	3+	3+	22+	0.8	0.8	13	2323 2343	22	161
4	4o	3+	4+	3+	3o	4-	3o	3o	28-	1.0	1.0	20	4454 3334	30	203
5	3+	3-	3+	4o	3+	2o	3+	3-	25-	0.9	0.9	16	3344 3233	25	168
6	4-	2+	2+	4o	3o	2o	2-	1+	20+	0.6	0.7	12	3323 2222	19	139
7 Q	1-	1o	2-	2-	1-	2-	1o	1+	10-	0.2	0.2	5	1122 0212	11	119
8 Q	1+	1o	1-	1o	1-	1-	0+	1-	6+	0.0	0.1	3	1100 0001	03	124
9 Q	1-	1-	1+	2-	1-	1-	1-	1+	8-	0.1	0.1	4	1022 0012	08	120
10 q	3-	2o	2o	2-	1+	2+	3-	2+	17o	0.5	0.5	8	3231 1232	17	97
11	3-	2+	1+	3-	2o	3o	3-	3-	19+	0.8	0.6	10	2323 2333	21	93
12	3-	2+	3o	2+	3o	2o	2-	2o	19o	0.7	0.6	10	3332 3122	19	74
13	3-	3o	3o	2o	2+	3+	3o	2+	22-	0.7	0.7	12	3333 2332	22	83
14 D	1+	4-	3+	4o	4-	6o	5o	6+	33+	1.4	1.4	40	1433 3556	30	93
15 D	3o	4-	4-	5o	6+	7+	8-	8o	45-	1.8	1.9	93	3445 4566	37	105
16 D	8+	7-	6-	5o	4+	5+	5-	4o	44o	1.7	1.8	77	9564 3443	38	138
17	5+	5-	4+	3-	2o	3+	3-	3+	28+	1.2	1.2	24	5553 2233	28	131
18	3o	3-	3o	3-	3+	4o	2o	2-	22+	0.9	0.8	14	4332 3412	22	122
19 D	1-	3-	5o	6o	4o	4o	5o	4+	32-	1.4	1.4	35	1365 4335	30	143
20	4o	2o	2+	4-	5o	4o	4+	5-	30o	1.2	1.2	26	5224 4344	28	137
21	2+	4-	2+	1+	3o	2o	2-	2o	18+	0.6	0.6	10	3432 2123	20	139
22	2+	3o	2+	2o	3-	2-	2o	3+	19+	0.6	0.6	10	2332 2223	19	135
23 q	5-	2o	2o	1-	1o	1o	1+	2-	14+	0.6	0.5	9	4221 1122	15	127
24 q	2+	2o	3-	2+	3-	3-	2o	2+	19o	0.7	0.5	10	2332 2222	18	105
25 Q	1-	1+	1-	0+	0+	1-	1+	2-	7o	0.0	0.1	4	1210 1122	10	111
26 q	1+	1+	1o	1+	2+	2-	2o	4o	15o	0.5	0.5	8	1211 2234	16	92
27 Q	2+	1+	2+	1+	2-	1o	1o	1-	12-	0.3	0.3	6	3122 2112	14	90
28 q	0o	1+	1+	2o	3-	1o	2-	2+	12+	0.4	0.3	6	0122 2122	12	73
29	5-	4+	4o	3-	3o	5o	5-	4-	32o	1.3	1.3	29	5441 3344	28	94
30	5-	4+	3-	5o	5+	3o	3o	3-	31-	1.2	1.3	29	4444 4233	28	82
31 D	6-	4+	5+	5o	4-	4+	3o	4-	35o	1.3	1.4	37	5364 3333	30	83
Means:										0.82	0.82	20			119.4
No. of days:										31	31	31			31

¹ Five quiet days (Q), ten quiet days (Q or q), five disturbed days (D), selected by Committee on Characterization of Magnetic Disturbances, J. Veldkamp, Kon. Nederlandsch Meteorologisch Instituut, DeBilt, Holland.

² Geomagnetic planetary 3-hr-range indices *Kp* prepared by Committee on Characterization of Magnetic Disturbances, J. Bartels, Chairman, University, Göttingen, Germany.

³ Preliminary magnetic character figures, *Ci*, prepared by J. Veldkamp.

⁴ Magnetic character figures, *Cp*, prepared by J. Bartels.

⁵ Average amplitudes *Ap* (unit 2γ), prepared by J. Bartels.

⁶ Fredericksburg 3-hr-range indices *K* (*K*₉ = 500γ); scale values of variometers in γ/mm: *D* = 2.7; *H* = 2.5, *Z* = 3.1, prepared by Robert E. Gebhardt, Observer-in-Charge, Fredericksburg Magnetic Observatory, Corbin, Virginia.

⁷ Provisional sunspot-numbers (dependent on observations at Zurich Observatory and its stations at Locarno and Arosa) prepared by M. Waldmeier, Swiss Federal Observatory, Zurich, Switzerland.

Letters to the Editor

The Gyromagnetic Ratio of the Proton

J. H. NELSON

*Chairman, Committee on Magnetic Instruments
International Association of Geomagnetism and Aeronomy
U. S. Coast and Geodetic Survey, Washington, D. C.*

In order that all measurements of the intensity of the geomagnetic field, made by investigators and observers throughout the world, might be referred to the same fundamental physical constant, the following resolution was adopted by the Association of Geomagnetism and Aeronomy, International Union of Geodesy and Geophysics, at the XII General Assembly of the Union in Helsinki, Finland, during the period July 25 to August 6, 1960:

L'Association de Géomagnétisme et d'Aéronomie considérant la nécessité d'un accord général sur la valeur à adopter pour le rapport gyromagnétique du proton intervenant dans les mesures du champ magnétique terrestre, demande que, dans l'attente d'une décision sur la valeur définitive qui sera adoptée éventuellement par un organisme international compétent, la valeur 2.67513×10^4 radians/gauss seconde soit celle

revenue pour toutes les mesures du champ magnétique terrestre faites au moyen d'un magnétomètre à proton à précession libre, utilisant de l'eau pure comme source de protons.

The International Association of Geomagnetism and Aeronomy, considering the need for a universal agreement regarding the value of the gyromagnetic ratio of the proton for measurements of the geomagnetic field, strongly recommends that, pending the agreement and specification by an appropriate international scientific organization of a final value, all measurements of the geomagnetic field with a proton free-precession magnetometer, using pure water as a proton sample, shall be based on the following value of the gyromagnetic ratio:

$$2.67513 \times 10^4 \text{ radians/gauss second.}$$

(Received September 14, 1960.)

Bright 21-Centimeter Solar Regions and Geomagnetic Storms in 1952-1953

RICHARD T. HANSEN

*High Altitude Observatory of the University of Colorado
Boulder, Colorado*

Numerous attempts have been made to relate the nonsolar flare associated geomagnetic storms, which are most characteristic of periods of declining solar activity, to specific solar features. Representative of these are investigations by Allen [1944], who studied sunspots; Bell and Glazer [1957] and Warwick [1959], bright coronal regions; Babcock and Babcock [1955], unipolar magnetic fields; Hansen [1959], filaments; and Mustel [1959], chromospheric plagues. The purpose of this letter is to report the results of still another investigation based upon solar regions producing enhanced radio flux in the decimeter range.

In June 1952 the Commonwealth Scientific and Industrial Research Organization (CSIRO) of Australia put into operation a radioheliograph, providing a one-dimensional, east-west scan of the solar disk at the wavelength 21 cm [Christiansen, Warburton, and Davies, 1957]. The angular resolution of the interferometer

was 3', sufficient to discriminate localized regions on the sun that are high emitting at this wavelength.

The dates of central meridian position (CMP) of the brightest regions at 21 cm were selected from the CSIRO's published tracings of daily interferometer scans of the sun. A list of 13 such days, chosen on the basis of the regions emitting at least 10 per cent of the quiet sun flux, is given in Table 1. Because of occasional gaps in the observations, it was necessary in some cases to interpolate values from a day or two before or after the actual CMP of the region.

As a first test of the association between these regions and geomagnetic storms, superposed epoch plots were made of K_p and A_p , the planetary geomagnetic indices, around the 13 CMP dates. The average values are shown in Figure 1 in the usual way for 14 days before through 14 days after the CMP's. The most striking feature about both plots is the sharp increase in geomagnetic indices on the sixth day after CMP of solar regions highly emissive at 21 cm. The K_p value is 30 and the A_p nearly 34. A student's t test was applied to determine the chance probabilities of deviations as high as or higher than these from the means [Hoel, 1958, p. 222] and in both cases they were 0.008, or about 1 chance in 100.

As a second test of this association, a comparison was made between the dates given in Table 1 with the dates of the beginnings of geomagnetic storms during the same time intervals (Table 2). Greenwich-Abinger [Greenwich, 1955] recorded these 15 storms, using the criterion that deviations in the earth's magnetic field exceeded 30' in declination or 150 gammas in the horizontal or vertical component. It is seen that in 6 instances the CMP of an intense 21-cm region was followed by the start of a geomagnetic storm within 3-6 days.

A straightforward probability test of this

TABLE 1. Dates Localized Regions, Emitting at least 10 per cent of the Quiet Sun Flux, Passed Central Meridian Position (CMP)

1952	June 29*
	July 15
	August 26
	September 2*
	September 10
	September 23*
	October 11
	October 26*
	November 22*
1953	May 1
	June 6
	June 20
	August 17*

Taken from the CSIRO daily 21 cm solar scans for the following intervals: June 20-July 24, 1952; August 22-November 30, 1952; May 4-June 26, 1953; July 7-September 5 1953; October 13-December 5, 1953.

* Followed by geomagnetic storm.

TABLE 2. Starting times of Geomagnetic Storms, Reported by Greenwich Corresponding to Periods of 21-cm Solar Observations by CSIRO.

1952	June 29.8
	July 5.0
	September 7.7
	September 25.8
	September 28.6
	October 3.7
	October 25.7
	October 29.5
	November 26.8
	December 1.7
1953	May 15.5
	August 23.0
	September 3.7
	October 15.4
	November 12.5

result is to consider the likelihood of 6 or more successes in 13 attempts where a 'success' is denoted by a CMP date falling 3–6 days before one of the 15 storm dates. Thus there are 60 'success' possibilities. Since a total of 321 calendar dates was included in the intervals for which CSIRO obtained 21-cm solar observations, the probability of an individual success is 60/321. The calculation for exactly 6 successes in 13 attempts is given by application of the binomial frequency function [Hoel, 1958, p. 63] as shown below:

$$P(6) = \frac{n!}{x!(n-x)!} p^x q^{n-x}$$

$$= \frac{13!}{6!7!} \left(\frac{4 \times 15}{321}\right)^6 \left(\frac{321-60}{321}\right)^7 = 0.017$$

The probability of 6 or more successes is determined by successively substituting $x = 6, 7, \dots, 13$ into the formula above and summing up the individual probabilities. This result is 0.022, or, only about 1 chance in 50 that the association between the solar regions and geomagnetic storms was accidental.

The result of this study, namely the discovery of a marked tendency for geomagnetic storminess to increase 5–7 days after CMP passage of solar regions characterized by strong radio emission at 21 cm, is not very different from that found by others who have examined active solar region phenomena. *Mustel and Mitropolskaya* [1959] emphasized the increase in storminess 5–10 days after CMP of sunspots and plages; *Roberts and Pecker* [1955] showed a similar

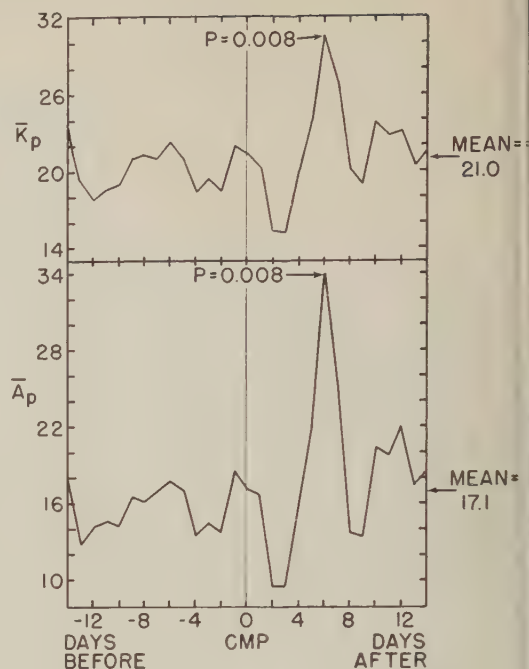


Fig. 1. The trends of geomagnetic indices K_p (above) and A_p (below) around zero days of CMP of bright 21-cm solar regions (13 cases, 1952–1953).

increase in the distribution of magnetically disturbed days after CMP of active regions (their Fig. 1). The similarity is not surprising in view of the positional association of many of the solar features. The 21-cm radio flux is attributed to thermal radiation from regions in the corona having about twice the normal electron density and occurring above chromospheric plages [Newkirk, 1959; Christiansen and Mathewson, 1959; Waldmeier, 1959]. Furthermore, *Babcock and Babcock* [1955] and *Leighton* (1959) have shown plages to be identical with regions of enhanced solar magnetic fields. To the extent that the present study reveals a more pronounced solar-geomagnetic association than previous ones, decimetric radio emission may be considered a particularly sensitive indication of the likelihood of an active solar region producing a geomagnetic disturbance.

REFERENCES

- Allen, C. W., Relation between magnetic storms and solar activity, *Monthly Notices Roy. Astron. Soc.*, 104, 13–21, 1944.
 Babcock, H. W., and H. D. Babcock, The sun's

- magnetic field, 1942-1954, *Astrophys. J.*, 121, 349-366, 1955.
- ell, B., and H. Glazer, Geomagnetism and the emission-line corona, 1950-1953, *Smithsonian Inst. Contrib.*, 2, 51-107, 1957.
- Christiansen, W. N., J. A. Warburton, and R. D. Davies, The distribution of radio brightness on the solar disk at a wavelength of 21 centimeters, IV, The slowly varying component, *Australian J. Phys.*, 10, 491, 1957.
- Christiansen, W. N., and D. S. Mathewson, 'The origin of the slowly varying component,' *Paris Symposium on Radio Astronomy* (IAU Symposium No. 9 and URSI Symposium No. 1), Stanford University Press, 1959, p. 108.
- Greenwich Royal Observatory, *Sunspots and Geomagnetic Storm Data, 1874-1954*, Her Majesty's Stationery Office, London, 1955.
- Hansen, Richard T., Recurrent geomagnetic storms and solar prominences, *J. Geophys. Research*, 64, 23-25, 1959.
- Hoel, Paul G., *Introduction to Mathematical Statistics*, John Wiley & Sons, New York, 1958.
- Leighton, Robert B., Observations of solar magnetic fields in plage regions, *Astrophys. J.*, 130, 366-380, 1959.
- Mustel, E. R., and O. N. Mitropolskaya, On certain statistical effects in the problem of the origin of geomagnetic disturbances, *Observatory*, 79, 15, 1959.
- Newkirk, G., A model of the electron corona with reference to radio observations, *Paris Symposium on Radio Astronomy* (IAU Symposium No. 9 and URSI Symposium No. 1), Stanford University Press, 1959, p. 149.
- Roberts, W. O., and J. C. Pecker, Solar corpuscles responsible for geomagnetic disturbances, *J. Geophys. Research*, 60, 33-44, 1955.
- Waldmeier, M., A Comparison between radio-heliograms and optical observations of the solar corona, *Paris Symposium on Radio Astronomy* (IAU Symposium No. 9 and URSI Symposium No. 1), Stanford University Press, 1959, p. 118.
- Warwick, C., Green coronal line intensity and geomagnetism, *J. Geophys. Research*, 64, 527, 1959.

(Received April 13, 1960; revised
August 29, 1960.)

Auroral Noise at HF

R. D. EGAN AND A. M. PETERSON

*Radioscience Laboratory
Stanford University
Stanford, California*

Auroral noise has been the subject of extensive private discussion. Very little has been published, however, because it has proved exceedingly difficult to identify positively the observed effects as pure noise and not as anomalously propagated signals distorted beyond intelligibility by the aurora. The initial reference to possible auroral noise appears to have been made by Covington [1947] in reporting 3000 Mc/s observations during periods of strong magnetic activity. Additional reports of microwave noise were made a few years later [Forsyth, Petrie, and Currie, 1949; Covington, 1950; Chapman and Currie, 1953], although the possible connection between microwave noise and the high-frequency noise described here is not obvious. In the latter reference a negative result was obtained, which was considered attributable to the decrease in sunspot activity. Since then a number of reports of vhf noise associated with auroral or magnetic disturbances have appeared [Harang and Landmark, 1954; Hartz, Reid, and Vogan, 1956; Chivers and Wells, 1959].

Shortly after reduction of the IGY fixed-frequency backscatter sounder [Peterson, Egan, and Pratt, 1959] records began, a persistent appearance of noise on the records preceding strong auroral disturbances was observed. The backscatter sounders utilize a rotating antenna with approximately a 60°-beamwidth, and hence it is possible to infer directional characteristics of incoming signals provided the angle of arrival is not too high. Noise, as the term is used with reference to the backscatter sounder observations, refers to the noiselike character of the signal. From this one measurement, however, there is little assurance that the 'noise' is not due to signals which have been made noiselike as a result of propagation through the aurora. The noise observed on the backscatter PPI oscilloscope always appeared in the magnetic north sector and would then spread more or less uni-

formly around in the east and west directions with the maximum azimuthal extent from the north dependent on the strength of the magnetic disturbance. A typical example of the noise as it appears in the PPI photograph is shown in Figure 1. Noise amplitude comparisons between the north and south directions (at both 18 and 30 Mc/s) indicate that during magnetically quiet periods the noise amplitude from the south is between 10 and 15 db stronger than noise from the north. On the night of March 31, during which the K_p index rose to 8+, the noise from the north exceeded the noise from the south by 3 db. It is apparent from this observation that the aurorally associated noise cannot be explained in terms of aurorally propagated atmospheric noise which originates at low latitudes.

Measurements made with the swept-frequency riometer [Little and Leinbach, 1959] very nearly eliminate the possibility of propagated interference causing the apparent rise in noise level. This device with approximately a 10-kc bandwidth, sweeps through a 100-kc frequency band in about 1 minute. Interfering signals, if they are present, give rise to a characteristic varying trace as the riometer frequency sweeps through the frequency of the interfering signal. Simultaneous observation of this same 100-kc frequency band, plus the 100 kc on either side on a spectrum analyzer, has not revealed a discernable CW or modulated signal.

Riometer records during the large magnetic storm of November 27-28, 1959, recorded intense aurorally associated absorption at Meenook, Alberta. The absorption is plotted on a logarithmic amplitude scale in Figure 2a as a function of 120°W time (PST) and represents a record typical of a station in or just below the auroral zone. Figures 2b and 2c are replots of similar data taken at Pullman, Washington, and Stanford, California. Auroral absorption is seldom seen at Stanford, but negative absorption

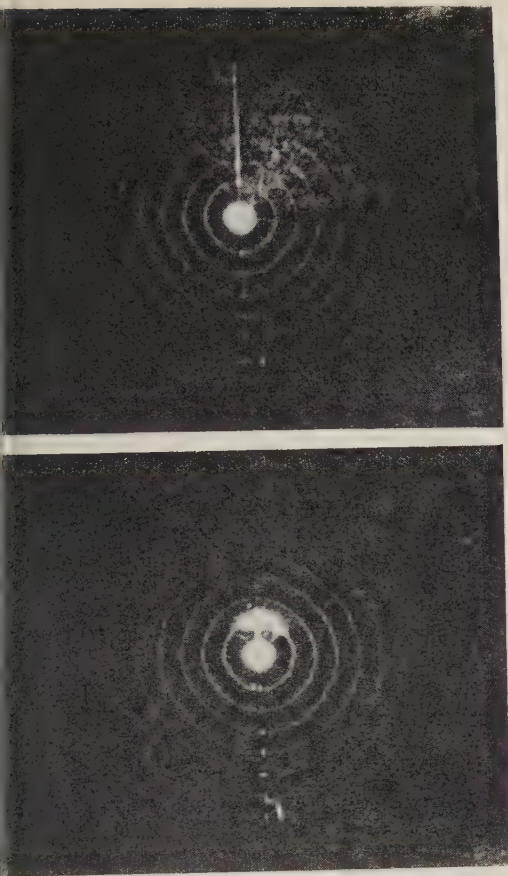


Fig. 1. Aurorally associated noise as it appears in the fixed-frequency backscatter sounder PPI records at 0257/22 Jan. 58. At 0308/22 Jan. 58, a strong field-aligned irregularity echo appeared. (Times given in Pacific Standard, 120°W.)

or excess noise) is quite frequently observed. On the particular night of November 27-28 a low-latitude red aurora was present. The 3-hour K_p index reached a maximum value of 8. There is a close correlation apparent between the noise peaks at Stanford and absorption peaks at Meanook. The records taken at Pullman indicate that both absorption and noise are present, and consequently only the net effect was measured. More recent measurements at Stanford with modified riometer equipment and extensive spectrum analysis to identify interference, if it is present, have confirmed the absence of interference and the existence of aurorally associated noise. These observations are now being studied and will be reported in the near future.

Possible mechanisms for the generation of

auroral noise include radiation from accelerated electrons in the Van Allen belt. Dyce and Nakada [1959] have examined the possibility of observing synchrotron radiation from the inner Van Allen belt at the magnetic equator. Synchrotron radiation from trapped electrons in the outer Van Allen region that are mirrored at a lower height as a result of a magnetic disturbance is regarded as the most likely mechanism for the noise observed at Stanford. Calculations following Schwinger's work [Schwinger, 1949] indicate that an integrated flux density of $10^8 \text{ cm}^{-2} \text{ sec}^{-1}$ of electrons with energies greater than approximately 1 Mev, or $5 \times 10^{11} \text{ cm}^{-2} \text{ sec}^{-1}$ of electrons with energies greater than 200 keV, would produce the 10-db increase in noise observed on the modified riometer equipment at 27 megacycles. Reasonable assumptions regarding the electron energy spectrum suggest that the amount of noise may be sharply reduced at higher frequencies. For example, synchrotron radiation at 50 Mc/s may be down by more than 10 db, and consequently may not be observable above the cosmic noise background. During dis-

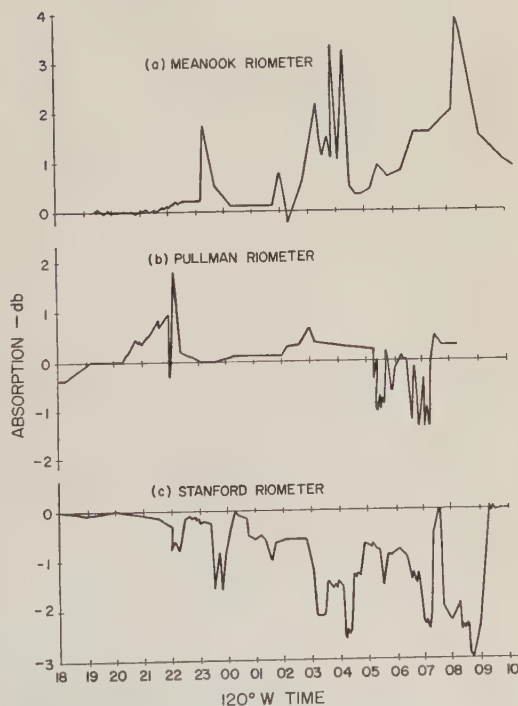


Fig. 2. Absorption or noise observed during the night of November 27-28, 1959, at (a) Meanook, (b) Pullman, (c) Stanford.

turbances, higher energy electrons which may be guided by the magnetic field but not necessarily trapped could result in vhf noise bursts as seen by Chivers and Wells [1959] at 80 Mc/s and occasional bursts at frequencies of 3000 Mc/s or more.

The only direct measurement of the flux density in the outer Van Allen belt as a function of energy was made on July 7, 1959, by Walt, Chase, Cladis, Imhof, and Knecht [1960]. Their experiment consisted of flying a magnetic spectrometer from Wallops Island with an upward trajectory very nearly along a magnetic field line into the outer radiation belt. The payload reached a peak altitude of 1040 km, at which point the flux density was on the order of 10^7 electrons $\text{cm}^{-2} \text{sec}^{-1}$. The higher energy electrons (1.5 Mev and up) are estimated to constitute 1 per cent or less of the total flux observed, giving a maximum particle flux density of higher energy electrons at 1000 km of $10^5 \text{ cm}^{-2} \text{sec}^{-1}$. This value is 10^8 less than that required to explain the noise observations; it was obtained, however, during a very quiet magnetic period. A recent value of electron flux density over the equatorial region in the outer belt, also during a magnetically quiet period, has been provided by Arnoldy, Hoffman, and Winkler [1960] from Explorer VI data. X-ray calibration of the radiation unit indicated a value of 50 Kev for the mean energy of the X-rays and from this value the maximum electron-particle flux was estimated to be $1.2 \times 10^{11} \text{ cm}^{-2} \text{sec}^{-1}$ during the week of August 7, 1959. The necessary several orders of magnitude reduction of this number for spatial position and energy spectrum does not appear to be inconsistent with our present observations.

Recent measurements of the auroral noise reveal that it does not correlate with daily magnetic indices, although there is a general overall storm-period correlation. If the behavior of the outer radiation region following a magnetic storm onset can be generally assumed to follow the pattern illustrated by Explorer VI, then there is better agreement between the presence of noise and higher counting rates. The noise generally comes up strongly at the onset of the magnetic storm and then decays in amplitude relatively slowly over the next 10 to 15 nights. This is unlike the magnetic activity, which may return to normal within a few days.

A quite good hour-by-hour correlation has also been observed between spread *F* and night time sporadic *E*, as observed on Seattle ionogram records, and the presence of noise on the modified riometer equipment. A good correlation is also observed with the field-aligned irregularity echoes observed on the Stanford fixed frequency backscatter sounder.

Acknowledgment. I wish to thank personnel of the Washington State University and the Meadbrook Magnetic Observatory for the continued operation of riometer equipment and the University of Washington for ionogram records. Dr. M. P. Nakada of the Lawrence Radiation Laboratory, University of California, has contributed helpful suggestions regarding the Van Allen radiation belts.

REFERENCES

- Arnoldy, R. L., R. A. Hoffman, and J. R. Winkler, Observations of the Van Allen regions during August and September, 1959, part 1, *J. Geophys. Research*, **65**, 1361-1376, 1960.
- Chapman, R. P., and B. W. Currie, Radio noise from aurora, *J. Geophys. Research*, **58**, 363-367, 1953.
- Chivers, H. J. A., and H. W. Wells, A new ionospheric phenomenon, *Nature*, **183**, 1178, 1959.
- Covington, A. E., Microwave sky noise, *J. Geophys. Research*, **52**, 339-341, 1947.
- Covington, A. E., Microwave sky noise, *J. Geophys. Research*, **55**, 33-37, 1950.
- Dyce, R. B., and M. P. Nakada, On the possibility of detecting synchrotron radiation from electrons in the Van Allen belts, *J. Geophys. Research*, **64**, 1163-1168, 1959.
- Forsyth, P. A., W. Petrie, and B. W. Currie, Auroral radiation in the 3000-Mc region, *Nature*, **164**, 453, 1949.
- Harang, L., and B. Landmark, Radio echoes observed during aurorae and geomagnetic storms using 35 and 74 Mc/s waves simultaneously, *J. Atmospheric and Terrest. Phys.*, **4**, 322-338, 1954.
- Hartz, T. R. G. C. Reid, and E. L. Vogan, VHF auroral noise, *Can. J. Phys.*, **34**, 728-729, 1956.
- Little C. G., and H. Leinbach, The riometer—a device for the continuous measurement of ionospheric absorption, *Proc. IRE*, **47**, 315-320, 1959.
- Peterson, A. M., R. D. Egan, and D. S. Pratt, The IGY three-frequency backscatter sounder, *Proc. IRE*, **47**, 300-315, 1959.
- Schwinger, J., On the classical radiation of accelerated electrons, *Phys. Rev.*, **75**, 1912-1925, 1949.
- Walt, M., L. F. Chase, Jr., J. B. Cladis, W. C. Imhof, and D. J. Knecht, *Energy spectra and altitude dependence of electrons trapped in the earth's magnetic field*, presented at the First International Space Science Symposium (COSPAR), Nice, France, 1960.

(Received August 23, 1960.)

The Distribution of Minor Ions in Electrostatic Equilibrium in the High Atmosphere

P. MANGE

U. S. Naval Research Laboratory
Washington 25, D. C.

The distribution of an atmospheric ionic constituent in electrostatic equilibrium with electrons is well known, having been described long ago by Pannekoek and Rosseland, as noted by van de Hulst [1953]. In an atmosphere of a given temperature the ionized constituent has a scale height twice that of its corresponding neutral form. We generalize the discussion for application to an atmosphere having more than one species of ion present, in accordance with a comment by P. J. Kellogg, of the University of Minnesota, that behavior of light minor ions in the atmosphere should be strongly affected by the presence of heavy ions.

In general, there is an electric field E in the ionized atmosphere that tends to restrain electrons from rising and also tends to draw the

heavier ions upward. The usual equation for the altitude dependence of the partial pressure, P_i , of the i^{th} ion species is then

$$kT d(\ln P_i)/dz = -m_i g + eE \quad (1)$$

where

k is Boltzmann's constant.

T is the local ion temperature.

z is the altitude measured positively upward.

m_i is the ion mass.

g is the gravitational acceleration.

e is the magnitude of the electronic charge.

Equation 1 follows from the perfect gas law and the law of static equilibrium, as does the analogous expression for the electrons present

$$kT d(\ln P_e)/dz = -m_e g - eE \quad (2)$$

Rewriting these equations in terms of n_i and n_e , the concentrations, taking $T_i(z) = T_e(z)$ for all i , and summing on i , expressions are obtained that, together with application of the condition of electrical neutrality, $\sum n_i = n_e$, permit one to solve for eE . The resulting ionic distributions are

$$d(\ln n_i)/dz = -\left[\frac{1}{1 - m_+/2m_i} H_i\right]^{-1} \quad (3)$$

where m_+ is the mean ionic mass and $H_i = kT/m_i g$ is the scale height of the neutral species corresponding to the ion species. Equation 3 can be simply integrated numerically (most easily with the aid of a computer) in step-by-step fashion for any given temperature distribution taking account of the variation of g with altitude.

At the 250-km level O^+ is the predominant ion in the earth's atmosphere [Johnson, Meadows, and Holmes, 1958]. It is of interest to examine the distribution of hydrogen ions where diffusive equilibrium is the controlling process. The re-

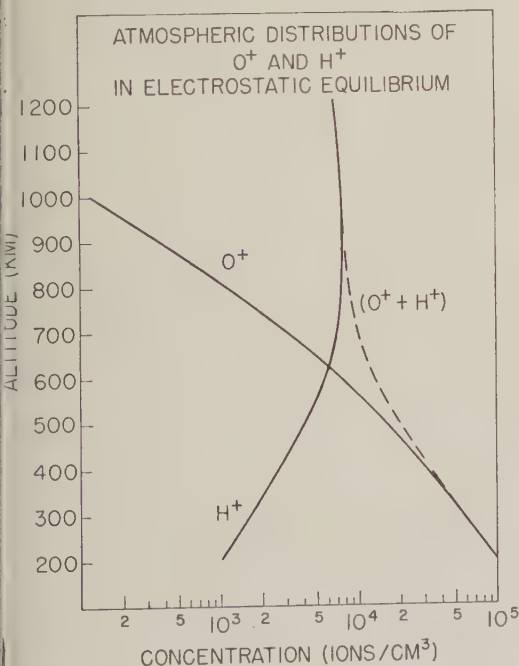


Fig. 1

sults of such calculations are shown in the accompanying figure. These results are based on a 1500°K atmosphere with constant g , commencing at the arbitrary altitude of 200 km with arbitrary concentrations of 10^3 and 10^5 cm^{-3} for the H^+ and O^+ ions, respectively. In the region where H^+ is a minor ion it increases rapidly with altitude and has a negative scale height whose magnitude is one-seventh that of neutral hydrogen.

The slopes of the extremities of such curves correspond to limiting cases depending on whether the constituent is major or minor, heavy or light. The curves are perfectly general in that (neglecting the variation of g) the whole pattern may be translated relative to the axes. Thus, for the same concentration of O^+ at the 200-km level reduction of the concentration of H^+ to 10^3 cm^{-3} raises the altitude of equal H^+ and O^+ concentration by some 200 km. It should be noted that 10^3 cm^{-3} is an upper limit for the concentration of H^+ at 200 km [Johnson and Holmes, 1960].

To summarize: (a) at sufficiently high altitudes light ionic constituents, such as H^+ or He^+ in the presence of a predominant heavy ion, such as O^+ , will increase with altitude; (b) the scale height of the predominant ion (light or heavy) approximates twice that of the corresponding neutral constituent; and (c) at levels where the heavy ion is a minor constituent its scale height approximates that of the corresponding neutral particle.

REFERENCES

- Van de Hulst, H. C., in *The Sun*, edited by G. F. Kuiper, The University of Chicago Press, Chicago, p. 306, 1953.
 Johnson, C. Y., E. B. Meadows, and J. C. Holmes, Ion composition of the Arctic ionosphere, *J. Geophys. Research*, **63**, 443-444, 1958.
 Johnson, C. Y., and J. C. Holmes, in *Proceedings of the First International Space Science Symposium, Nice, 1960*, edited by H. Kallmann (to be published).

(Received August 8, 1960.)

Seasonal and Day-to-Day Changes of the Central Position of the S_q Overhead Current System¹

S. MATSUSHITA

*High Altitude Observatory
University of Colorado
Boulder, Colorado*

The solar daily geomagnetic variation on quiet days, S_q , is due mainly to the overhead electric current system flowing in the lower ionosphere. Figure 1 gives the well-known diagrams of the S_q overhead current system in two seasons, obtained by Bartels [Bartels, 1928; Chapman and Bartels, 1940] from spherical harmonic analysis of geomagnetic data obtained at 18 stations in the sunspot-minimum year 1902.

The overhead current system consists of four sets of ovals, two each in the northern and southern hemispheres. In the present study the position of the center of the current system—that is, the location of the focus of a counter-clockwise oval current—for the daylight hours in the northern hemisphere was found to undergo a remarkable seasonal change. The center, on the average, was found to be in higher latitudes in summer than in winter. This is just opposite of the seasonal changes shown in Figure 1.

In order to find the central position of the S_q overhead current system in the North American zone, the IGY geomagnetic data were studied for three permanent stations, Fredericksburg (38°12'N, 77°22'W; geomagnetic 49.6°N), Tucson (32°14'N, 110°57'W; geomagnetic 40.4°N), and San Juan (18°23'N, 66°07'W; geomagnetic 29.9°N). Supplementary data were used from a net of seven stations in the continental United States [see Matsushita, 1960].

Before examining these data, it was ascertained that geomagnetic variations on quiet days at San Juan were almost identical with those at Teoloyucan (19°45'N, 99°11'W; geomagnetic 29.6°N). These two stations are located at nearly the same latitude, but differ about 33° in

longitude. This indicates that there is little change in the latitudinal location of the center between these two longitudes. Accordingly, we may infer that the longitudinal difference can be neglected as far as San Juan and stations in the continental United States are concerned, and that we may study the latitudinal location of the center from these stations as if they were on the same meridian. The longitudinal difference cannot be neglected for stations in widely different longitudes, however, as will be mentioned later.

For an approximation, it was assumed that two-thirds of the varying field is due to the overhead electric current, and that the induced current within the earth due to the overhead current does not have much effect on the central position of the overhead current system. For our purpose it was also assumed that the horizontal component H could be substituted for the northward component X . Under these assumptions, the average daily variations of the horizontal component were calculated on the 10 international quiet days in each month at Fredericksburg, Tucson, and San Juan. Examples are shown in Figure 2 for the three seasons: summer, equinoxes, and winter. It is well known that the indicated location for a station showing a V-shaped daily variation of the X (and therefore H) component is north of the central position, as illustrated in Figure 2 by the Fredericksburg station. The reversed V shape of the daily variation, shown by the San Juan curve in July 1957, indicates that the station is located south of the center. At the station near the central position, the daily variation shows a flat shape, such as seen at Tucson in July 1957 in Figure 2. It is easy to estimate from Figure 2, then, that on the average the central position was at a latitude near Tucson in summer, between Tucson and San Juan in equinoxes, and near San

¹ Presented at the Forty-First Annual Meeting of the American Geophysical Union, Washington, D. C., April 1960.

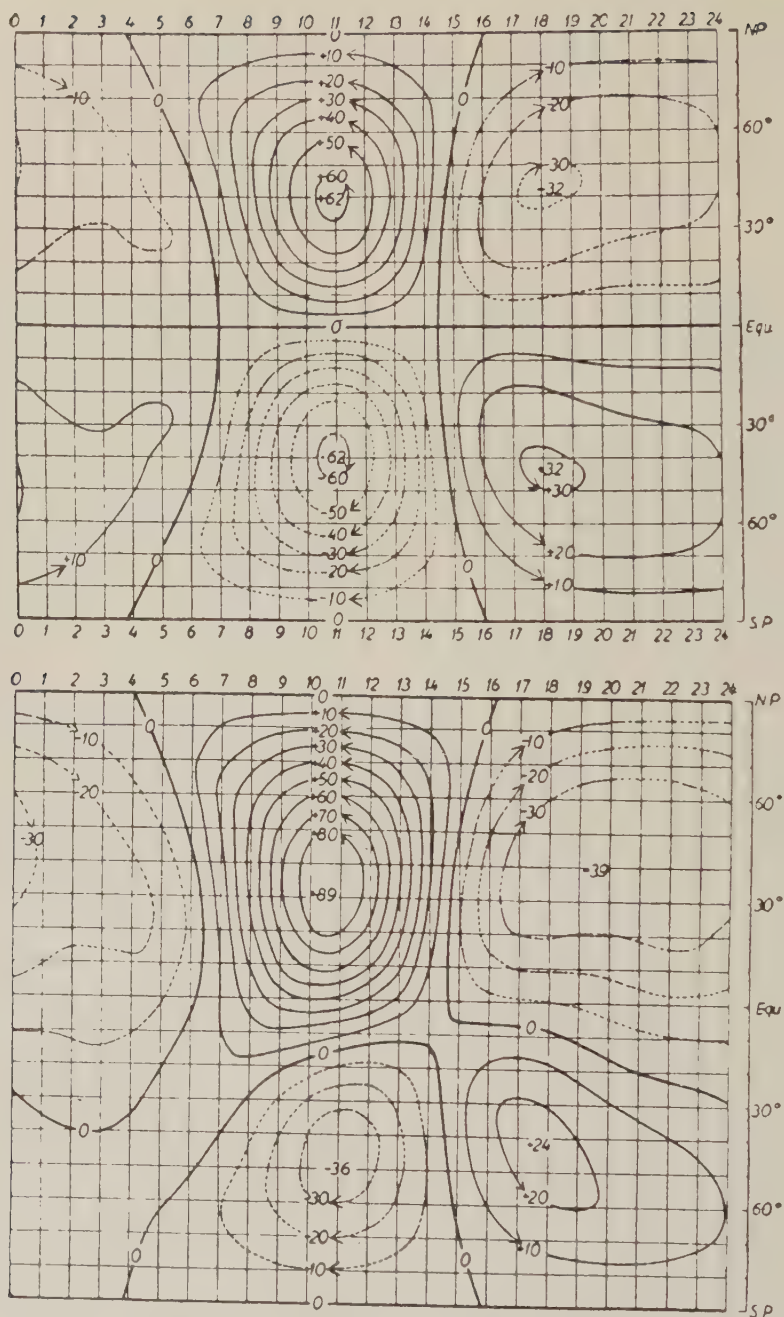


Fig. 1. The overhead electric current system for the solar daily geomagnetic variation on quiet days in the equinoxes (*above*), and in June (*below*), obtained by Bartels. The center of the oval current in the daytime is situated in lower latitudes in summer than in equinoxes and winter. The present result is opposite of this. (The ordinate is the geographic latitude, and the abscissa refers to local time.)

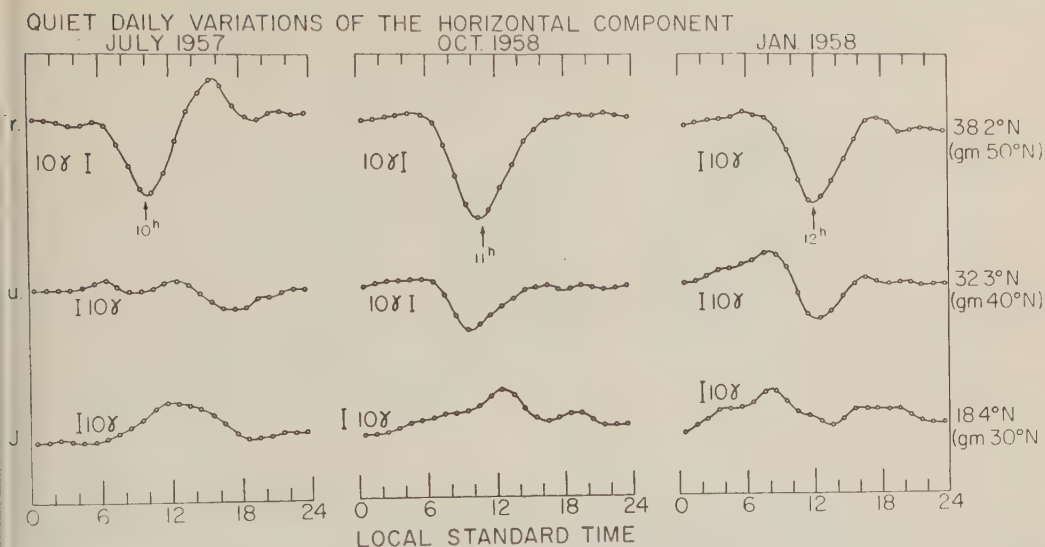


Fig. 2. Average daily variations of the geomagnetic horizontal component on quiet days in summer, equinoxes, and winter, at Fredericksburg, Tucson, and San Juan.

uan in winter. This demonstrates that in the North American zone the latitudinal location of the center is higher in summer than in winter. It can also be seen from Figure 2 that the local standard time at which the minimum daily variation of H occurs at Fredericksburg is different in the three seasons.

The seasonal change of the latitudinal location of the center is more clearly shown in Figure 3. The block diagrams in the figure indicate the occurrence frequencies of the central position on 10 quiet days in each month at six different latitudinal zones: (1) near Fredericksburg, (2) between Fredericksburg and Tucson, (3) near Tucson, (4) between Tucson and San Juan, (5) near San Juan, and (6) below San Juan. The 6 months from May to August during the IGY (July 1957–December 1958) were included in summer in Figure 3; November to February were included in winter, and the remaining months were treated as equinoctial. The seasonal change of the central position—that is, in higher latitude in summer than in winter—can be seen clearly in Figure 3.

The same type of seasonal variations of the latitudinal location of the center for the daylight hours can be seen in the European zone. Daily variations at San Fernando ($36^{\circ}27'N$, $06^{\circ}11'W$; geomagnetic $41.0^{\circ}N$) clearly indicate that in winter the center is at a little lower latitude

than San Fernando, and that in summer it is at a higher latitude, near L'Aquila ($42^{\circ}24'N$, $13^{\circ}19'E$; geomagnetic $42.9^{\circ}N$).

In the Far Eastern zone, the data tell the same story. The center is situated at a latitude near Kanoya ($31^{\circ}25'N$, $130^{\circ}53'E$; geomagnetic $20.7^{\circ}N$) in summer, and lower than Kanoya in winter.

The seasonal change obtained in all three zones is in opposite sense from that indicated in Figure 1, where the central position moves toward the equator in summer and toward the pole in winter. The present result seems more reasonable than the latter, because it seems to indicate that the central position of the dayside oval current system follows closely the change of position of the subsolar point in different seasons. The reversed result obtained by Bartels came from the assumption that there was no longitudinal inequality in the location of the center. Data used in the present study show that to the contrary there are remarkable longitudinal inequalities in the geomagnetic coordinates of the center, and that there are smaller, but still noticeable, inequalities in the geographic coordinates.

In order to show the S_e current system having minimum longitudinal inequalities, it can be concluded from the present study that the best ordinate for the current system is values of the vertical intensity H_e of the earth's main mag-

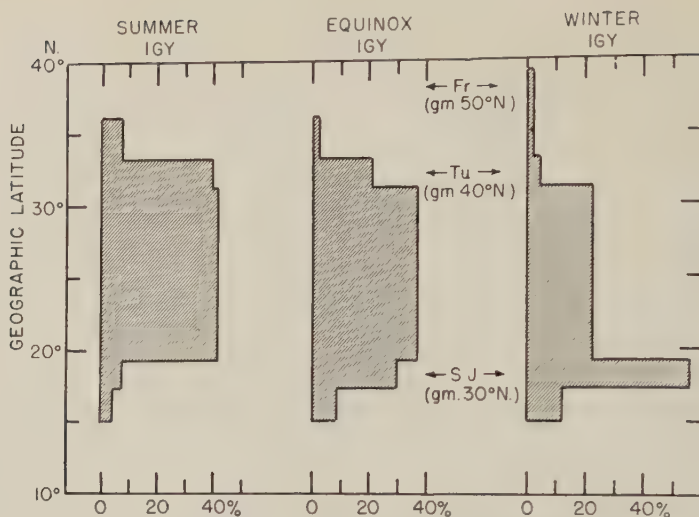


Fig. 3. Occurrence frequencies of the central position of the S_q overhead current system in three seasons during the IGY in the North American zone.

netic field. In other words, the pattern of the S_q current system is largely regulated by local time and H_z . The center of the daytime S_q current system is situated, on the average, at a certain line of equal H_z , where the value of H_z is about 0.36 gauss in summer, about 0.32 gauss in winter, and about 0.34 gauss in the equinoxes. Also the boundary between the daytime S_q current system in the northern hemisphere and that in the southern hemisphere seems to be another line of equal H_z , where $H_z = 0$, which is the magnetic equator (dip = 0°), in all seasons. The equatorial electrojet is then flowing at the boundary. These considerations indicate that in the dynamo theory the common assumption $|H_z| = 2/3 \cos \theta$ gauss, where θ is the colatitude, is oversimplified. We should use the expanded spherical harmonic series

$$P_n^m(\alpha_n^m \cos m\lambda + \beta_n^m \sin m\lambda)$$

for H_z . In all fairness it should be added that there still remains a very slight longitudinal inequality, even if we use H_z as the new ordinate. However this is understandable as a dynamo effect due to the distribution of wind and the electrical conductivity, both of which depend mainly on the geographic coordinates. The essential point is that the pattern of the S_q current system is regulated by H_z much more than by geographic latitude.

Hasegawa [1960] has recently published a summary of his studies in cooperation with Ota [1950] on the central position of the S_q , using geomagnetic data for the Second Polar Year and, in addition, for the first six months of the IGY. In his paper he introduced Ota's work on a seasonal change of the latitudinal location in the Far Eastern Zone during a part of the Second Polar Year and a part of the IGY. For the Polar Year, Ota obtained a remarkable seasonal change opposite in sense from the present study. From the IGY, Ota obtained no apparent seasonal change, although he used a similar method for both periods. The discrepancy between the results of these two studies and the present result would not be due to different solar activity in the Polar Year and the IGY but to differences in statistical methods used. In the present study, the seasonal change of the central position on quiet days was obtained by using only the 10 international quiet days. Ota, on the other hand, estimated the central position on quiet days from data for the entire month, including even stormy days, and 'calculated 30-day means to show the seasonal variation.' It is extremely difficult to estimate the central position of the quiet field on disturbed and stormy days because of additional current systems. In fact, the error introduced here leads to an incorrect result for the seasonal change. Thus Ota obtained a reversed seasonal change for the

Second Polar Year, and no apparent change at for the IGY.

The day-to-day variations of the latitudinal position of the center have been studied by Hasegawa [1936, 1960], Ota [1950] and Vestine, Laporte, Lange, and Scott [1947], using data from the Second Polar Year. The day-to-day variations in the present study were obtained from IGY data on consecutive quiet days in the North American, Far Eastern, and European zones. The average day-to-day shift was found to be several degrees of latitude (about 0.15 gauss on H_z). It was also found that an unusually high or low central position in one zone did not necessarily have a corresponding high or low in other zones.

The day-to-day variations were compared with the daily solar flux at 2800 Mc/s observed at Ottawa, and also with the intensity of the equatorial electrojet. The complete paper will give full detail and theoretical discussion on both day-to-day and seasonal changes of center. A study on the S_q potential field during the IGY is in process.

Acknowledgments. I wish to express my sincere gratitude to Dr. W. O. Roberts, Mr. A. H. Shapley, and Mr. S.-I. Akasofu for their kind advice. I also wish to thank the Boulder Laboratories of the National Bureau of Standards for my appointment as guest worker and for extending me their facilities.

The work reported here was supported by the National Academy of Sciences under grant NSF-G9427.

REFERENCES

- Bartels, J., Periodische variationen aktivität *Handbuch der Experimental-physik*, 25, 624-665, Akademische Verlagsgesellschaft M. B. H., Leipzig, 1928.
- Chapman, S., and J. Bartels, *Geomagnetism*, I, p. 229, Clarendon Press, Oxford, 1940.
- Hasegawa, M., A statistical study of the type of diurnal variations of terrestrial magnetism on quiet days, *Proc. Imp. Acad. Tokyo*, 12, 185-188, 1936.
- Hasegawa, M., On the progressive change of the field of diurnal variations of terrestrial magnetism, *Proc. Imp. Acad. Tokyo*, 12, 277-280, 1936.
- Hasegawa, M., On the position of the focus of the geomagnetic S_q current system, *J. Geophys. Research*, 65, 1437-1447, 1960.
- Matsushita, S., Studies on sudden commencements of geomagnetic storms using IGY data from United States stations, *J. Geophys. Research*, 65, 1423-1435, 1960.
- Ota, M., The position and motion of the focus of the electric current vortex equivalent to the variation-field of the terrestrial magnetism at middle latitude, Transactions of Oslo Meeting, 1948, *IATME Bull.* 13, 438-442, 1950.
- Vestine, E. H., L. Laporte, I. Lange, and W. E. Scott, *The Geomagnetic Field, Its Description and Analysis*, Carnegie Inst. Wash. Publ. 580, chap. VII, 1947.

(Received August 4, 1960.)

Traveling Wave Amplification of Whistlers

N. M. BRICE

Stanford University
Stanford, California

Traveling wave amplification has been postulated by *Helliwell* [1956] and by *Gallet* [1959] as a possible generation mechanism for audio-frequency ionospheric emissions. The present note discusses the application of the theory of the traveling wave tube [*Chodorow and Suskind*, 1960] to these frequencies with particular reference to whistlers and whistler echo trains.

In a traveling wave tube, the magnitude and direction of the electric field initially seen by the particle depends on the phase of the wave when the particles are injected, so that some of them will be speeded up and some slowed down. Bunching tends to occur in a range around the point where the field is passing through zero from accelerating to decelerating, as seen when moving forward through the wave.

If the electrons have a slightly greater average velocity than the wave, then the particles bunched around the point of zero field will tend to drift forward into the region of retarding potential, so that they are slowed and lose energy. This energy is transferred to the electromagnetic field, increasing the amplitude of the wave. Conversely, if the particles have a slightly smaller average velocity than the wave, then the latter will be decreased in amplitude.

We now consider these principles as they are applied to audio-frequency waves in the ionosphere for particles with constant velocity in the direction of the magnetic field. The wave, in general, will have a component of electric field in the direction of the magnetic field [*Helliwell*, 1956] so that particles moving through the wave will be accelerated and decelerated. On the average, they will neither gain nor lose energy. If, however, the wave phase velocity becomes matched to the particle velocity, then bunching of the particles will occur. The matching condition is that these velocities are sufficiently close for the acceleration or deceleration during one-half cycle of the wave to make them equal.

At the time of trapping the particles have, on the average, the same velocity as the wave. Thus for a fixed frequency wave in a homogeneous medium, no change in amplitude of the wave would occur due to this mechanism. We may expect the wave to be amplified or absorbed according as the phase velocity is decreasing or increasing, respectively, at the point in the wave at which the particles are trapped. This change in velocity may be due to change in the properties of the medium, or, for a wave whose frequency changes with time, to the change in frequency of the wave where the particles are trapped. It will, in general, be a combination of both of these effects. The change in particle velocity may be expressed as

$$dv = \left. \frac{\partial v_p}{\partial s} \right|_f ds + \left. \frac{\partial v_p}{\partial f} \right|_s df \quad (1)$$

where

v_p = the wave phase velocity.

v = the particle velocity.

f = the wave frequency.

s = distance measured in the direction of particle travel.

The necessary condition for possible amplification, then, is that dv be negative so the particles are decelerated.

The change in frequency df is illustrated in Figure 1 and arises as follows. For whistler mode propagation, the wave phase and group velocities will, in general, be different.

$$v_g = 2v_p(1 - f/f_H) \quad (2)$$

where

v_g = the wave group velocity.

f_H = the electron gyrofrequency

The particles traveling at the phase velocity are thus continually moving through the wave (except where $f = \frac{1}{2}f_H$), so that if the fre-

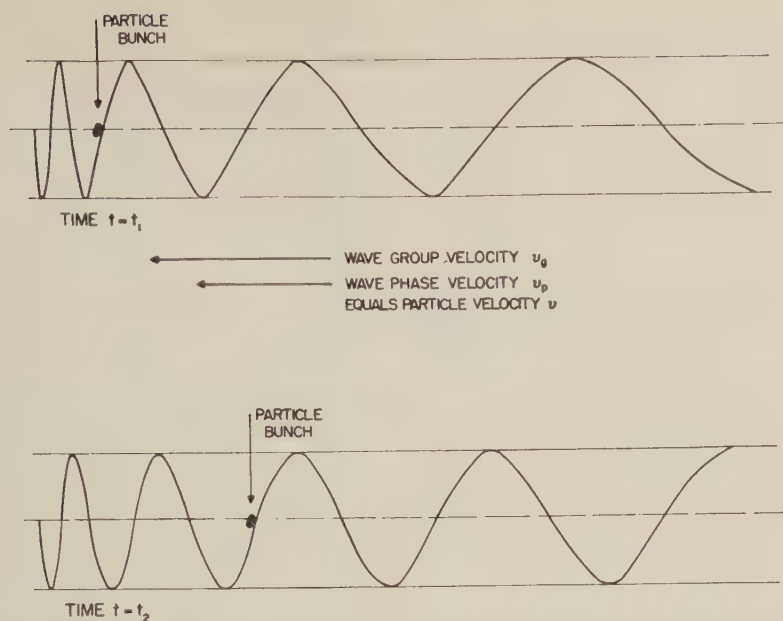


Fig. 1. A schematic diagram of the electric field of a whistler and a trapped bunch of particles at two different times, illustrating that the particles move with respect to the wave group while remaining bunched at a zero crossing of the field.

frequency of the wave is changing, so also is the frequency where the particles are trapped.

In traveling a distance Δs , the particles will be delayed with respect to the wave by an amount

$$\Delta t = \frac{\Delta s}{v_p} - \frac{\Delta s}{v_g} \quad (3)$$

so that the corresponding change in frequency is given by

$$\begin{aligned} \Delta f &= \left(\frac{1}{v_p} - \frac{1}{v_g} \right) \frac{\partial f}{\partial t} \Delta s \\ &= \frac{(1 - 2f/f_H)}{2v_p(1 - f/f_H)} \frac{\partial f}{\partial t} \Delta s \end{aligned} \quad (4)$$

Now v_p may be expressed as

$$v_p = cf^{\frac{1}{2}}(f_H - f)^{\frac{1}{2}}/f_0 \quad (5)$$

so that

$$\frac{\partial v_p}{\partial f} = \frac{v_p(1 - 2f/f_H)}{2f(1 - f/f_H)} \quad (6)$$

From (4) and (6) we obtain

$$\frac{\partial v_p}{\partial f} df = \frac{(1 - 2f/f_H)^2}{4f(1 - f/f_H)^2} \frac{\partial f}{\partial t} ds \quad (7)$$

Note that the sign of this expression is dependent only on the sign of $\partial f/\partial t$ so that if the wave frequency decreases with increasing time, then in a homogeneous medium any trapped particles may amplify the wave via the traveling wave mechanism.

For a whistler, the trapping conditions depend on the magnitude of the wave frequency compared with the instantaneous nose frequency [Helliwell, Crary, Pope, and Smith, 1956] and half the electron gyrofrequency, both of which vary during the propagation. It is not proposed to consider all possible situations here. In the simplest and most common case, the wave frequency is below both the nose and half the gyrofrequency. Then the wave group velocity exceeds the phase velocity, the latter decreasing with frequency. Particles with velocities in the range of interest move back with respect to the wave until they reach a frequency where they are trapped. The bunching process then begins. For a medium that is symmetrical about the top of the path, those frequencies with $\partial f/\partial t$ negative will have a bias in favor of amplification. Further, in a whistler train, $|\partial f/\partial t|$ decreases with increasing number of hops; the asymmetry in dv , or bias in favor of amplification,

decreases accordingly. This feature offers an explanation for the increase of amplitude of the first few echoes of a train [Storey, 1953].

Detailed calculations have been made for a model electron-density distribution in which the electron density is proportional to the magnetic field. These results and evidence of amplification in a whistler train will be published at a later date.

Acknowledgment. I wish to express my thanks to Dr. R. A. Helliwell of this department for helpful criticism of this work, which was sponsored by U. S. Air Force research contract AF 18(603)-126.

REFERENCES

Chodorow, M., and C. Susskind, *Fundamentals of*

Microwave Tubes, McGraw-Hill, New York (in press).

Helliwell, R. A., Low frequency propagation studies, part I: Whistlers and related phenomena: Final report, Contract AF 19(604)7953, June 15, 1953, to September 30, 1956 (revised May 28, 1958), AFCRC-TR-56-189, ASTIA Document AD 110184, 1956.

Helliwell, R. A., J. H. Crary, J. H. Pope, and R. L. Smith, The 'nose' whistler—a new high latitude phenomenon, *J. Geophys. Research*, **61**, 139-142, 1956.

Gallet, R. M., The very low frequency emissions generated in the ionosphere, *Proc. IRE*, **47**, 211-231, 1959.

Storey, L. R. O., An investigation of whistling atmospherics, *Phil. Trans. Roy. Soc. London, A*, **246**, 113-141, 1953.

(Received August 1, 1960.)

I-Xe Dating of Meteorites

J. H. REYNOLDS

Miller Institute for Basic Research in Science

and

*Department of Physics, University of California
Berkeley, California*

In previous letters [Reynolds, 1960a, b] we have reported that there are two kinds of isotopic anomaly encountered in studying xenon dissolved in stone meteorites. First, there can be a large excess of Xe^{129} . In the Richardton stone, xenon from the larger samples studied (5–7 grams) has a $\text{Xe}^{129}/\text{Xe}^{132}$ ratio of 1.5 in contrast to the terrestrial value of 0.98. Similar results on Richardton have been obtained by Signer [1960] and by Zähringer and Gentner [1960]. The effect is especially striking in the enstatite chondrite Indarch; there the $\text{Xe}^{129}/\text{Xe}^{132}$ ratio is 3.4. Second, there are recurrent secondary differences between the isotopic composition of xenon from the atmosphere and from many of the meteorites studied. A comparison of the results of rare gas studies for Richardton and for the carbonaceous chondrite Murray [Reynolds, 1960b] indicated that the secondary anomalies are primordial and are unrelated to cosmic-ray exposure of the stones. Other carbonaceous chondrites recently examined are, like Murray, xenon-rich and exhibit the secondary anomalies. Table 1 contains the isotopic composition of the anomalous component of xenon from the carbonaceous chondrites Murray, Mighei, and Orgueil. The anomalous component is here defined as that which remains after a subtraction of terrestrial xenon, based on the assumption that all Xe^{136} is from a component of terrestrial composition. Xe^{136} is the only isotope which can be used in this way if all the anomalous abundances are to be positive. Table 1 also contains the $\text{Xe}^{129}/\text{Xe}^{132}$ ratio for the total xenon in the stones.

Most of the excess Xe^{129} is from decay of 17.2 million-year I^{129} incorporated in the meteorite at the time of formation. We assume that at a time Δt after the end of nucleosynthesis the iodine-bearing minerals of the meteorite began

TABLE 1. Xenon in Carbonaceous Chondrites

Isotope	Per cent Abundance in Anomalous Component		
	Murray	Mighei	Orgueil
124	0.64 ± 0.05	0.62 ± 0.11	0.72 ± 0.24
126	0.56 ± 0.10	0.52 ± 0.10	0.52 ± 0.25
128	6.52 ± 0.25	6.05 ± 0.50	6.45 ± 0.41
129	46.6 ± 3.4	54.3 ± 4.4	49.4 ± 4.4
130	7.33 ± 0.81	5.67 ± 0.60	6.08 ± 0.68
131	25.12 ± 2.7	22.5 ± 2.9	24.03 ± 3.0
132	11.59 ± 3.4	9.52 ± 3.37	11.63 ± 2.5
134	1.69 ± 1.3	0.83 ± 1.30	1.16 ± 1.31
136
Isotope Ratio	Value for total xenon in stone		
129/132	1.056	1.077	1.062

abruptly to retain radiogenic xenon. Then

$$\Delta t = \frac{17.2}{0.693} [\ln (\text{I}^{127}/\text{Xe}^{129*})_{\text{met}} + \ln (\text{I}^{129}/\text{I}^{127})_0] \text{my}$$

where Xe^{129*} is the amount of Xe^{129} attributed to iodine decay in the meteorite and $(\text{I}^{129}/\text{I}^{127})_0$ is the ratio of these isotopes at the end of nucleosynthesis. The experimental quantity to be evaluated is $(\text{I}^{127}/\text{Xe}^{129*})$. Estimates of Δt published hitherto have been based on a guess of the abundance of iodine in meteorites.

A convenient and precise way to measure $(\text{I}^{127}/\text{Xe}^{129*})_{\text{met}}$ is to irradiate a piece of the meteorite with thermal neutrons. I^{127} undergoes neutron capture to form 25 minute I^{128} , which decays to Xe^{128} . A mass spectrometric analysis of xenon extracted from the irradiated meteorite gives directly the quantity $(\text{Xe}^{128*}/\text{Xe}^{130*})_{\text{met}}$ where Xe^{128*} is the Xe^{128} produced by the irradiation. A KI monitor is irradiated in the same capsule with the meteorite. There is relatively

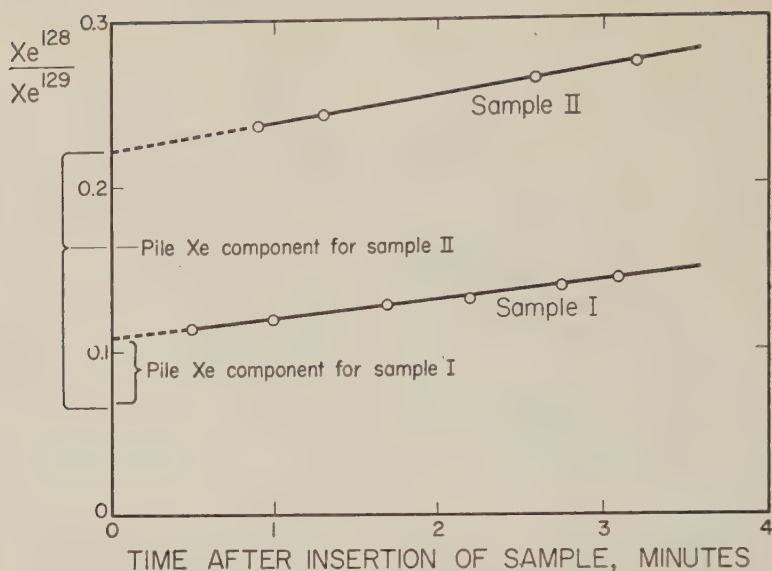


Fig. 1. Influence of mass spectrometer memory on $\text{Xe}^{128}/\text{Xe}^{129}$ ratio.

TABLE 2. Component Analysis of the Xenon

Sample	A/P	M/P	X/P
I	42	32	15
II	12	6.7	3.4

copious production of Xe^{128} in the monitor; the concentration of Xe^{128} there is easily determined by isotope dilution with atmospheric xenon from a McLeod gauge. From this we calculate $(\text{I}^{127}/\text{Xe}^{128*})_{\text{met}}$. Then

$$(\text{I}^{127}/\text{Xe}^{129*})_{\text{met}} = (\text{I}^{127}/\text{Xe}^{128*})_{\text{met}} \cdot (\text{Xe}^{128*}/\text{Xe}^{129*})_{\text{met}}$$

The method has the great advantage that the required ratio is determined almost directly and for a single sample.

We have applied this method to two 1-gram fragments of Richardton that were irradiated at different times in the Livermore Pool-Type Reactor. Specimen I was from a stone from the Nininger collection (museum no. 100.69); it received a 24-hour irradiation at a slow neutron flux of about 2×10^{12} (S1 position). Specimen II was from the American Museum of Natural History (AMNH no. 3884) and received a 143-hour irradiation at a slow neutron flux of about 3×10^{12} (S4 position). As determined from KI monitors $(\text{I}^{127}/\text{Xe}^{128})_{\text{I}} = 8.78 \times 10^6$ and $(\text{I}^{127}/\text{Xe}^{128})_{\text{II}} = 1.052 \times 10^6$.

So as to make a complete analysis of the xenon isotopic data, four xenon components were identified: 'P' xenon is Xe^{128} from the pile neutrons on I^{127} ; 'M' xenon is meteorite xenon with isotopic composition like that found for 5-7 gram samples of Richardton [Reynolds, 1960a] but minus all Xe^{130} ; 'X' xenon is Xe^{129} , in part primordial and in part radiogenic (this is best considered independently from the 'M' component since the iodine content of the stone may be variable from one sample to another); finally, 'A' xenon is from the atmosphere (and must be taken into account since xenon from 1-gram samples has always contained both 'M' and 'A' (blank) xenon in our experiments). The $\text{Xe}^{130}/\text{Xe}^{132}$ ratio can be used to determine the relative amounts of 'M' and 'A' xenon. The $\text{Xe}^{131}/\text{Xe}^{132}$ ratio can also be used for this purpose but with less accuracy. The $\text{Xe}^{136}/\text{Xe}^{132}$ and $\text{Xe}^{134}/\text{Xe}^{132}$ ratios can then be used to find the relative amounts of 'M,' 'P,' and 'X' xenon. Results are listed in Table 2.

The total meteoritic xenon is the sum of the 'M' and 'X' components. Amounts of several of the isotopes are listed in Table 3 in units of the amount of the 'P' component.

To evaluate $(\text{Xe}^{128*}/\text{Xe}^{129*})_{\text{met}}$ we must decide what fraction of Xe^{128}/P is due to iodine decay. If, as in the past, we perform the 'Xe' subtraction we find

TABLE 3. Isotopic Analysis of the 'M' plus 'X' Xenon

Sample	Xe ¹²⁸ /Xe ^{128*}	Xe ¹²⁹ /Xe ^{128*}	Xe ¹³⁰ /Xe ^{128*}	Xe ¹³² /Xe ^{128*}	Xe ¹³⁶ /Xe ^{128*}
I	0.98	14.6	1.86	11.5	3.70
II	0.21	3.35	0.39	2.42	0.78

$$(\text{Xe}^{128*}/\text{Xe}^{129*})_{\text{I}} = 0.28 \pm .04$$

$$(\text{Xe}^{128*}/\text{Xe}^{129*})_{\text{II}} = 0.97 \pm .10$$

Multiplying these by the $(\text{I}^{127}/\text{Xe}^{128*})$ factors determined from the KI monitors we obtain:

$$(\text{I}^{127}/\text{Xe}^{129*})_{\text{I}} = (2.5 \pm 0.4) \times 10^5$$

$$(\text{I}^{127}/\text{Xe}^{129*})_{\text{II}} = (1.02 \pm 0.11) \times 10^5$$

These ratios are about an order of magnitude less than previous estimates [Reynolds, 1960a] based on an assumed 1 ppm for the iodine content of chondrites. The discrepancy between samples I and II is not understood at present. It cannot be reduced significantly by other types of xenon subtraction. It could arise from contamination of sample I by terrestrial iodine. Another possibility is that there are iodine bearing minerals in the stone having different values of Δt and that these minerals are sampled differently in samples I and II. In this connection, it will be very interesting in the future to see if Δt is the same for the chondrules as for the matrix of a stone. Experimental error is certainly possible, especially in the determination of the Xe¹²⁸/Xe¹²⁹ ratio, on which attention was focused during the early part of the mass spectrometer runs. This ratio rose rapidly during the runs due to memory of previous large samples heavily spiked with Xe¹²⁸ and could only be evaluated by the extrapolation indicated in Figure 1. It is possible that the true value of Xe¹²⁸/Xe¹²⁹ is less than that given by the extrapolation for sample I; an error of this type would have had much less influence on the result obtained for the more heavily irradiated sample II, so that the latter result must be preferred until the discrepancy is resolved. More experiments on Richardton—using heavier irradiations—are planned.

If, as is generally believed, nucleosynthesis has been a prolonged process, $(\text{I}^{129}/\text{I}^{127})_0$ will be the ratio of the mean life of I¹²⁹ to the duration T of nucleosynthesis. Fowler and Hoyle [1960] place

this at about 10¹⁰ years. If stellar activity has declined significantly in the galaxy over this period, the effective value of T will be even longer. Cameron (private communication) chooses 2×10^{10} as a reasonable value for T_{eff} . In this case $(\text{I}^{129}/\text{I}^{127})_0$ is 0.00125. The result for sample II is then $\Delta t = 120$ million years. The $(\text{I}^{127}/\text{Xe}^{129*})$ ratio for Indarch seems to be even lower than 10⁵. A preliminary value by us for the Xe^{129*} content of Indarch is $2.5 \pm 1.0 \times 10^{-9}$ ccSTP/g. Preliminary values for the iodine content of Indarch by neutron activation and counting of I¹²⁹ [Goles and Anders, 1960] are 283 and 455 ppb. Combining these preliminary values gives a tentative value of $(\text{I}^{127}/\text{Xe}^{129*}) = 2.6 \times 10^4$ for Indarch or $\Delta t = 86$ million years. Formation of our solar system is usually seen as a condensation of cold gas and dust, which included debris from recent and past supernovae. Present results indicate that this process of collapse was relatively swift. The only alternative—formation of I¹²⁹ by some special process in the solar corona shortly before meteorite formation—seems less likely now that such high values of the Xe^{129*}/I¹²⁷ ratio have been seen in meteorites.

Earlier work on a sample of Richardton [Reynolds, 1960a] gave 0.13×10^{-9} ccSTP/g for Xe^{129*}. Combining this with the $(\text{I}^{127}/\text{Xe}^{129*})$ ratio for sample II leads to a value of 76 ppb for the iodine content of the earlier sample of Richardton. This is in general if not good agreement with values of 37 ± 8 and 57 ± 10 ppb obtained earlier by Goles and Anders [1960].

Kuroda [1960] has argued that the terrestrial Xe subtraction should be based on Xe¹³⁰, which is the most abundant Xe isotope shielded in fission. When this subtraction is applied to meteoritic xenon, isotopes Xe¹³¹, Xe¹³³, Xe¹³⁴, and Xe¹³⁶ are deficient in the meteorite, or, in other words, are in excess terrestrially. This is not unreasonable, if they are attributed to fission, since the terrestrial Xe/U ratio is probably less than that for Richardton. The relative abun-

dances of these isotopes in this presumed fission component do not fit the fission yields for any known type of fission, but Kuroda considers it possible that spontaneous fission of extinct Pu^{244} may have the very high fission yield at mass 132 required to fit the data. If the Xe^{130} subtraction is repeated using the original isotope ratios and the errors in these quantities, which have not been published directly, the meteoritic anomalies have the same values calculated by Kuroda, but the errors at masses 128, 129, 131, and 132 are reduced by almost an order of magnitude. This makes the 'misfit' at mass 132 much more striking (and the result very different if the other shielded isotope, Xe^{129} , is used as the basis for the subtraction). Nevertheless, the Xe^{130} subtraction may be preferable on some grounds in estimating amounts of excess Xe^{129} . Making use of it, we find alternatively

$$(\text{I}^{127}/\text{Xe}^{129*})_{\text{I}} = 3.4 \times 10^5$$

$$(\text{I}^{127}/\text{Xe}^{129*})_{\text{II}} = 1.3 \times 10^5$$

These values are not appreciably different from those based on the Xe^{130} subtraction but the discrepancy between samples I and II is widened.

Acknowledgment. I wish to thank Mr. Sidney Putnam for skillful assistance with the raregas extraction apparatus and Mr. Robert Pepin for help in calibration of the KI monitors. Staff members of the Lawrence Radiation Laboratories at Berke-

ley and Livermore have been very cooperative in furnishing the required pile irradiations. I am grateful to Dr. Brian Mason of the American Museum of Natural History for many of the samples used. Drs. Gordon Goles and Edward Anders of Chicago have been most generous in encouragement and in letting me use some of their unpublished data on the iodine content of meteorites. Especially I would like to thank Dr. Earl Hyde and a group of his radiochemical colleagues at the Berkeley Radiation Laboratory for a discussion in which they persuaded me that a mass spectrometer might be the best detector for activated iodine in meteorites. Subsequent work has borne out their good judgment.

The work reported by this paper is supported in part by the U. S. Atomic Energy Commission.

REFERENCES

- Fowler, W. A., and F. Hoyle, Nuclear cosmochronology, *Annals of Physics*, 10, 280, 1960.
 Goles, G., and E. Anders, Iodine content of meteorites and their I^{129} - Xe^{129} Ages, *J. Geophys. Research*, in press, 1960.
 Kuroda, P. K., Nuclear fission in the early history of the earth, *Nature*, 187, 36, 1960.
 Reynolds, J. H., Determination of the age of the elements, *Phys. Rev. Letters*, 4, 8, 1960a.
 Reynolds, J. H., Isotopic composition of primordial xenon, *Phys. Rev. Letters*, 4, 351, 1960b.
 Signer, P., Bestätigung des abnormal hohen gehaltes an Xe^{129} in Richardton, *Z. Naturforsch.*, in press, 1960.
 Zähringer, J., and W. Gentner, Uredelgase in einigen steinmeteoriten, *Z. Naturforsch.*, in press, 1960.

(Received September 3, 1960.)

Discussion of Paper by J. N. Luthin and J. W. Holmes, 'An Analysis of the Flow of Water in a Shallow, Linear Aquifer, and of the Approach to a New Equilibrium after Intake'

MAHDI S. HANTUSH

*New Mexico Institute of Mining and Technology
Socorro, New Mexico*

A valuable study has been presented in this paper. More work of this nature should be encouraged. Some ground-water engineers still believe that studies such as this have no practical application because of the limiting conditions involved and the fact that naturally occurring heterogeneous aquifers depart from the assumed ideal homogeneous porous media. Considerable work has been carried out in Europe and America on this subject, and there is no doubt that the scientific approach employed in this study can play an important part in the elucidation of ground-water problems.

Luthin and Holmes [1960] have developed their solution with a specific case in mind. The writer is certain that they are aware of the fact that their equations involve much more than a reader will appreciate without considerable thought. With suitable transformations, the equations can be put into a form more suitable for computation for large values of time, and/or they can be modified so that they can be used to describe the flow in systems under more relaxed conditions than those assumed by the authors. For the benefit of those who may be unfamiliar with the mathematical development and/or with the appropriate adjustment required to relax the limitation on the author's equations, the following observations are made:

1. If the inverse Laplace transform of equation 5 is found by integrating the inversion integral in the complex plane [Churchill, 1944], a solution equivalent to that given by equation 6, but more suitable for computation when the time is large, can be obtained as

$$\phi = \phi_L [x/l + (2/\pi) \sum_{n=1}^{\infty} (1/n) \sin(n\pi x/l) \cdot \exp(-n^2 \pi^2 Kt/l^2)] - (\alpha/2)x(l-x)$$

$$+ (4\alpha l^2/\pi^3) \sum_{n=0}^{\infty} [1/(2n+1)^3] \cdot \sin[(2n+1)\pi x/l] \cdot \exp[-(2n+1)^2 \pi^2 Kt/l^2] \quad (8)$$

The solution that corresponds to (7) is obtained from (8) by taking α as zero.

2. The fact that the initial water-table surface is plane is a good indication that the rate of loss either by evapotranspiration or by deep seepage is very small. If such a rate is not small, and if the flow system is in a state of dynamic equilibrium, the water-table profile would be some function of distance rather than a plane surface. However, the fact that the initial water table is a plane surface does not exclude the possibility that the rate of loss may be appreciable as the water table rises. If it is assumed that the rate of loss will be proportional to the hydraulic head above lake level for $t > 0$ [Hantush, 1955], the counterparts of equations 1, 6, and 8 will be

$$\frac{\partial^2 \phi}{\partial x^2} - \beta^2 \phi = \frac{1}{K} \frac{\partial \phi}{\partial t} \quad (9)$$

$$\phi = (\phi_L/2) \sum_{n=0}^{\infty} \left\{ \exp(-(2n+1)l-x)\beta) \cdot \operatorname{erfc}\left(\frac{(2n+1)l-x}{\sqrt{4Kt}} - \beta \sqrt{Kt}\right) + \exp([(2n+1)l-x]\beta) \cdot \operatorname{erfc}\left(\frac{(2n+1)l-x}{\sqrt{4Kt}} + \beta \sqrt{Kt}\right) + \exp(-[(2n+1)l+x]\beta) \cdot \operatorname{erfc}\left(\frac{(2n+1)l+x}{\sqrt{4Kt}} - \beta \sqrt{Kt}\right) \right\}$$

$$+ \exp([(2n+1)l+x]\beta) \cdot \operatorname{erfc}\left(\frac{(2n+1)l+x}{\sqrt{4Kt}} + \beta\sqrt{Kt}\right)\} \quad (10)$$

$$\phi = \phi_L \left\{ \sinh \beta x / \sinh \beta l \right. \\ \left. + (2/l) \sum_{n=1}^{\infty} \frac{(-)^n (n\pi/l) \sin(n\pi x/l)}{\beta^2 + (n\pi/l)^2} \right. \\ \left. \cdot \exp(-[\beta^2 + (n\pi/l)^2]Kt) \right\} \quad (11)$$

where $\beta^2 = (E+L)/km$, and E and L are the rates of loss per unit area per unit rise of water table due to evapotranspiration and deep seepage, respectively.

3. Equations 1 and 9 are derived basically for artesian flows in an aquifer of thickness m or for free aquifer flow with $l \gg m \gg \Phi_L$ [Jacob, 1950; Maasland, 1959]. Consequently, equations 6 through 11 describe the flow in an artesian aquifer without limitation, and in free aquifers if $\Phi_L/(\Phi_L + m) \leq 0.02$ [Jacob, 1950], provided, of course, that the usual assumptions with regard to uniformity and homogeneity of the aquifer and constancy of the formation coefficients obtain.

4. If Φ_L is not small compared with m , the equations of motion can be shown to take, instead of (1) and (9), the form

$$\frac{\partial^2}{\partial x^2} (h^2 - m^2) - \alpha_w = \frac{1}{K_w} \frac{\partial}{\partial t} (h^2 - m^2) \quad (12)$$

$$\frac{\partial^2}{\partial x^2} (h^2 - m^2) - \beta_w^2 (h^2 - m^2)$$

$$= \frac{1}{K_w} \frac{\partial}{\partial t} (h^2 - m^2) \quad (13)$$

where $h = \phi + m$, $\alpha_w = 2A/k$, $\beta_w^2 = 4(E+L)/k(\phi_L + 4m)$, $K_w = k(\phi_L \text{ plus } 2m)/2\phi_L$, and $\phi_L/(\phi_L + m) < 0.25$.

Equations 12 and 13 are analogous to equations 1 and 9; they are linear second-order differential equations. The boundary conditions imposed on ϕ in (1) and (9) are analogous to those imposed on $(h^2 - m^2)$ in (12) and (13). It is clear, therefore, that the solutions of (1) and (9) as given by (6) through (11) are applicable to (12) and (13); it is only required that ϕ be replaced by $(h^2 - m^2)$, ϕ_L by $(h^2 - m^2)$, α by α_w , β by β_w , and K by K_w .

The constant term in (1) should be A/km rather than A/k ; also, q^2 should be p/K rather than p/k —obviously typographical errors.

REFERENCES

- Churchill, R. V., *Modern Operational Mathematics in Engineering*, McGraw-Hill Book Co., New York, 1944.
- Hantush, M. S., Preliminary quantitative study of the Roswell ground-water reservoir, New Mexico Institute of Mining and Technology, 1955.
- Jacob, C. E., *Engineering Hydraulics*, John Wiley & Sons, New York, ch. 5, 1950.
- Luthin, J. N., and J. W. Holmes, An analysis of the flow of water in a shallow, linear aquifer, and of the approach to a new equilibrium after intake, *J. Geophys. Research* 65, 1573-1576, 1960.
- Maasland, Marinus, Water table fluctuations induced by intermittent recharge, *J. Geophys. Research*, 64, 549-559, 1959.

(Received May 31, 1960.)

Discussion of Paper by J. N. Luthin and J. W. Holmes, An Analysis of the Flow of Water in a Shallow, Linear Aquifer, and of the Approach to a New Equilibrium after Intake

MORTON W. BITTINGER

*Colorado State University
Fort Collins, Colorado*

This paper [Luthin and Holmes, 1960] represents another significant contribution to the rapidly growing literature in the field of transient ground-water hydraulics.

It is worthy of note, however, that the complement of the error function sufficiently describes water-table levels in the aquifer from time zero until the water begins to flow from the outlet end of the aquifer for the conditions set forth by the authors.

A solution of the differential equation 1, neglecting the term A/k , for an aquifer of infinite extent is

$$\begin{aligned} &= \phi_L \frac{2}{\sqrt{\pi}} \int_{x'/\sqrt{4Kt}}^{\infty} e^{-u^2} du \\ &= \phi_L \operatorname{erfc} \frac{x'}{\sqrt{4Kt}} \quad (8) \end{aligned}$$

where $x' = l - x$ in the authors' notation.

Equation 8 meets the following initial and boundary conditions:

$$\phi = 0, \quad 0 < x' < \infty, \quad t = 0$$

$$\begin{aligned} \phi &= \phi_L, & x' &= 0, & t &> 0 \\ \phi &= 0, & x' &= \infty, & t &> 0 \end{aligned}$$

Up until the moment the water reaches the discharge point at distance l from the intake end, the aquifer may be considered infinite in length, and equation 8 be used to estimate the water-table surface with time. The ratio ϕ/ϕ_L may be computed with two-place agreement using equation 8 when the parameter $l/\sqrt{4Kt} \geq 2.0$. When t becomes large enough for $l/\sqrt{4Kt} < 2.0$, equation 7 of the authors' paper becomes more appropriate than equation 8 above. However, for the authors' example this situation is reached only after some 476 years.

REFERENCE

- Luthin, J. N., and J. W. Holmes, An analysis of the flow of water in a shallow, linear aquifer, and of the approach to a new equilibrium after intake, *J. Geophys. Research*, 65, 1573-1576, 1960.

(Received July 8, 1960.)

A Note on the Interception Loss Equation

ROBERT A. MERRIAM

*Pacific Southwest Forest and Range Experiment Station
Glendora, California*

Interception is the process in which precipitation is caught by a vegetative canopy and redistributed to the ground, to the atmosphere, or into the plant. Interception loss is that portion of the precipitation which is returned to the atmosphere through evaporation from plant surfaces or is absorbed into the plant. Thus, it is the difference between the precipitation actually occurring over an area and that which reaches the ground.

Horton [1919] presented the first comprehensive discussion of the interception process and summarized data collected by himself as well as data published by others. He observed that interception loss was the sum of (1) the water stored on the plant surfaces at the end of a storm (and subsequently returned to the atmosphere by evaporation) and (2) the evaporation from wet plant surfaces during a storm. Horton expressed this relation in an equation of the form

$$L = S + RET \quad (1)$$

where

L is interception loss in inches depth over the projected area of the canopy.

S is the water stored on the vegetation in inches depth over the projected area of the canopy.

R is the ratio of vegetation surface area to the projected area of the canopy.

E is the evaporation rate in inches depth per hour during the storm.

T is the duration of the storm in hours.

Horton also presented results in the form

$$L = S + KP \quad (2)$$

where

$K (= RET/P)$ is the fraction of the precipitation lost by evaporation and absorption during the storm.

P is the storm precipitation in inches, and L and S are defined as above. He further stated that this formula applies only when P is greater than S , otherwise $L = P$, nearly.

Kittredge [1948] summarized available data on the interception process. Many individual studies have also been conducted which present data in the form of equation 2.

Linsley, Kohler, and Paulhus [1949] pointed out that equation 1 yields a value of interception which is independent of the amount of precipitation and that in this equation it is assumed that the rainfall in each storm completely fills interception storage. They suggest that if we can assume that the interception loss given by (1) is approached exponentially as the amount of rainfall is increased from zero to some high value (for a specified duration), then

$$L = (S + RET)(1 - e^{-cP}) \quad (3)$$

where

e is the base of the Napierian logarithms,
 c is a constant,

and all other terms are defined as before. Since the interception loss should approach the rainfall for very small storms, dL/dP will approach unity when P is near zero.

Application of the exponential factor to the storage term S in equation 3 seems justified. A buildup of the amount of rainfall held as storage has been observed and demonstrated [Horton, 1919; Grah and Wilson, 1944; Rowe and Hendrix, 1951]. Data plotted by these authors show that an equation of the exponential growth form is a reasonable expression of the buildup of storage. However, application of the exponential factor to the RET portion of the equation seems open to question. There seems to be no reason why the evaporation during the storm should be included as an exponential function.

This reasoning leads this author to suggest the equations

$$L = S(1 - e^{-cP}) + RET \quad (4)$$

$$L = S(1 - e^{-cP}) + KP \quad (5)$$

with all terms as before.

When either equation is differentiated with respect to P , and dL/dP is equated to unity as P approaches zero, then

$$c = 1/S$$

and the general equations become

$$L = S(1 - e^{-P/S}) + RET \quad (6)$$

$$L = S(1 - e^{-P/S}) + KP \quad (7)$$

These equations seem to describe the known behavior of the interception process. When values for S , R , E , and T or S and K are known or can be estimated, curves relating interception loss to precipitation can be prepared.

Most publications of interception loss data have related loss to storm precipitation, irrespective of storm duration. A linear regression is calculated for storms greater than some small amount, commonly 0.50 inch. *Hamilton and Rowe* [1949] provide several examples of this calculation. A 'best fit' curve is then fitted by eye to the data for storms smaller than the minimum used in the regression.

As an example, interception loss for storms greater than 0.50 inch in the chaparral on the San Dimas Experimental Forest¹ has been estimated [*Hamilton and Rowe*, 1949] from the equation

$$L = 0.083 + 0.062 P \quad (8)$$

The proposed new equation is

$$L = 0.083(1 - e^{-P/0.083}) + 0.062 P \quad (9)$$

The experimental and calculated values for storms of less than 0.50 inch are compared in Figure 1. Also shown is the eye-fitted curve currently in use. For storms greater than 0.50 inch there is no difference between the new equation and the one in use, since the value $(1 - e^{-P/0.083})$ has become nearly equal to unity at that amount.

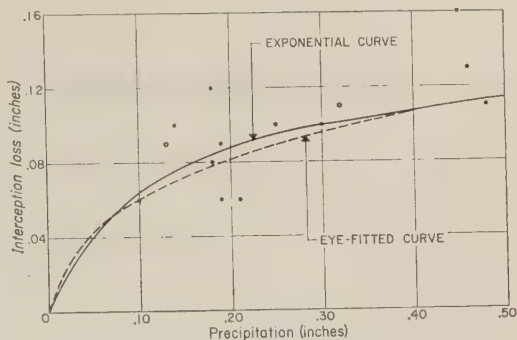


Fig. 1. Comparison of experimentally derived interception loss and eye-fitted and exponential curves for mature chaparral on the San Dimas Experimental Forest.

The exponential interception loss equation proposed here describes the observed relationship between interception loss and total storm rainfall over the entire range of precipitation values. It has been found to closely approximate experimental data for evergreen and deciduous chaparral published by *Hamilton and Rowe* [1949]. It also closely approximates the curve for ponderosa pine given by *Rowe and Hendricks* [1951]. With few exceptions, the calculated curve values came within ± 0.03 inch of the measured value.

Whether the equation is applicable to all types of vegetation and conditions of precipitation remains to be seen. We hope that others who have interception data available will test the application of the equation presented here. Such tests will strengthen present knowledge of the interception process.

REFERENCES

- Grah, R. F., and C. C. Wilson, Some components of rainfall interception, *J. Forestry*, 42, 890-898, 1944.
- Hamilton, E. L., and P. B. Rowe, *Rainfall Interception by Chaparral in California*, Calif. Dept. of Nat. Resources, Div. Forestry, 43 pp., 1949.
- Horton, R. E., Rainfall interception, *Monthly Weather Rev.*, 47, 603-623, 1919.
- Kittredge, J., *Forest Influences*, McGraw-Hill Book Co., New York, 394 pp., 1948.
- Linsley, R. K., Jr., M. A. Kohler, and J. L. Paulhus, *Applied Hydrology*, McGraw-Hill Book Co., New York, 689 pp., 1949.
- Rowe, P. B., and T. M. Hendrix, Interception of rain and snow by second-growth ponderosa pine, *Trans. Am. Geophys. Union*, 32, 903-908, 1951.

(Received June 29, 1960.)

¹ Maintained by the Pacific Southwest Forest and Range Experiment Station, U. S. Forest Service, in cooperation with the California Department of Natural Resources, Division of Forestry.

Some Physical Aspects of Earthquake Mechanism

M. A. CHINNERY

*Geophysics Laboratory, University of Toronto
Toronto, Ontario, Canada*

There has been considerable discussion in recent years of the kind of stress changes that occur at the focus of an earthquake as fracture takes place. Two mechanisms consisting of stress patterns in the form of a single couple with moment (nucleus I) and a double couple without moment (nucleus II) were first proposed by Nakano [1923]. (Here we use the notation of Honda [1957].) Nakano showed that the distributions of first motions of earthquake wave arrivals can be used to investigate the mechanism concerned, since the *P*-wave distributions for the nuclei are identical but the *S*-wave distributions are different.

The importance of distinguishing between these two mechanisms has arisen in connection with the fault-plane solutions of earthquakes which have been carried out by Hodgson and others. If only *P*-wave arrivals are considered, the fault-plane solution defines two possible planes, corresponding to the two kinds of nuclei, and to remove the ambiguity, further information is necessary. Investigations of *S*-wave arrivals have confused, rather than clarified, the situation. Several Russian seismologists [e.g., Kohan, 1954] have obtained results that indicate a nucleus I, and others [e.g., Honda and Masatsuka, 1952] have found a nucleus II. Recently, Aki [1960] suggested that Love waves may be used to investigate the mechanism, and preliminary results suggest the presence of a nucleus II.

I propose to consider the physical implications of these two nuclei and to show that there is a relationship between the mechanism and the properties of the material around the focus. To do this, we shall have to consider the processes that occur while fracture is in progress. It should be noted that in the arguments that follow we are concerned only with those stresses that are changed by the fracture. With the exception of the small region close to the fracture surface,

these stresses will have little or no relation to the total stress distribution existing before failure.

The first point to be made is that, whatever happens during the faulting, the over-all stress change due to the fracture must satisfy the equilibrium conditions. Hence, if we are to represent this stress change by couples, a double couple is necessary [Steketee, 1958]. The physical significance of such a double couple depends on how it is derived. Thus it can represent either those stresses that are reduced to zero by the break, or it can represent the stresses that would be produced if such a fracture were introduced artificially into an unstressed medium (this is the approach of dislocation theory). These two definitions are, of course, equivalent, but some clarification of the processes involved in the dynamic case is often reached by considering both aspects of the problem.

Let us suppose that the first motions of the waves emitted by a fracture conform to a dynamic nucleus II. This implies that the impulse delivered by the break to the surrounding medium is in equilibrium. This may occur in two ways: Either the stresses relieved at each instant of fracture are balanced, or the stresses relieved are unbalanced, but the break occurs in such a way that the medium has time to adjust itself to an equilibrium state as fracture proceeds. The first of these does not seem physically realistic when applied to a shear fracture. Steketee [1958] has proposed a mechanism for the second. He suggests that the plane of the fracture should rotate, thus producing compressions and dilatations which will maintain equilibrium.

Now consider the implications of the presence of a nucleus I. Here the impulse transmitted by the break is definitely unbalanced, and the equilibrium state must have been reattained at some time later than the first emission of seismic

waves. It also implies that the process of re-attaining equilibrium must take considerably longer than the time for fracture to occur.

We have to decide which of these two possibilities is more likely to occur in practice. In an elastic solid, as Steketee points out, there is no *a priori* reason, mathematically, to choose between them, for an elastic solid cannot fracture in the first place. In this case the problem becomes a question of whether the equilibrium equations are satisfied or not. The work of Knopoff and Gilbert [1959] and Kasahara [1958] shows that, if the displacement field is assumed to obey Navier's equations at all times, the radiation from a dynamic displacement discontinuity follows the distribution of a nucleus II. On the other hand, nonequilibrium states of the material around the fracture are also possible, and it is conceivable that some of these may result in the distribution of a nucleus I. However, in the case of a physically realistic solid, such as the crust of the earth, we can say rather more, for the speed at which the sides of a fracture surface move is severely limited by frictional effects. It seems that typical observations would show a relative displacement of a few meters taking place in a few seconds. As this 'velocity' is so much slower than the velocity of seismic waves, it is difficult to see any reason why equilibrium should not be maintained as the faces of the fault move. I therefore suggest that if a fracture occurs in a reasonably rigid solid, the observed first motions should correspond to the distribution of a nucleus II.

Conversely, if a nucleus I is observed, this must indicate a nonequilibrium situation that is only explainable if we assume some plasticity in the material around the focus, and since we are here concerned with such a short time scale, this plasticity will be of the utmost importance in geological processes. Certainly, it would seem that, if a nucleus I is present, the material at the focus may not be regarded (even approximately) as an elastic solid. Extending this suggestion further, if equilibrium is reattained shortly after fracture ceases, indicating a small degree of plasticity, it may be possible that observations of seismic waves of period comparable to the time of fracture will indicate an unbalanced nucleus, while similar observations of waves of long period may indicate an equilibrium nucleus.

These arguments suggest two points. First, as the crust of the earth is rigid for small time intervals, surface faults should emit the distributions of a nucleus II. If this is the case, evidence of the equilibrium process, which involves a rotation of the material at the focus, should be observed in the immediate area of the fault. An excellent example of such evidence is afforded by the Tango earthquake of 1927 in Japan [Tsuboi, 1930]. The main fault in this case was the Gomura fault, and this was observed to consist of numerous *en échelon* cracks. The orientation of these cracks was such that rotation of the ground took place as faulting occurred, tending to maintain equilibrium. At the same time as the Gomura fault and at right angles to it, the Yamada fault was produced, and this too is oriented so as to preserve equilibrium. These facts must be interpreted as indicating that equilibrium was maintained during the fracture process and that therefore the distribution of waves of a nucleus II must have been emitted.

Second, we must conclude that for deep earthquakes, the nature of the mechanism is a reflection of the properties of the mantle at the focus. In particular, considering present ideas of the mantle, if the distribution of a nucleus I is observed at all, it should be only for waves below some critical wavelength. If this wavelength can be determined from seismic records, it will be a qualitative indication of the departure of the mantle from the properties of an elastic solid. This would provide valuable information for studies of the interior of the earth. It may be possible later to put this argument on a quantitative basis, but this has not yet been attempted. However, this could provide the reason for the apparent conflict between the data obtained from long wavelength Love waves and that from some of the studies on shorter wavelength *S* waves.

The resolution of these problems will have to wait until better *S*-wave data are available. In general, it would seem much more likely that nuclei II are present than nuclei I, and I disagree with Hodgson [1957] who says, 'On grounds of geological plausibility the idealised mathematical model (nucleus II) is unacceptable.' Alternatively, if nuclei I are really present to any extent, the revision of those theories that treat the mantle as an elastic solid may be necessary.

REFERENCES

- Aki, K., The use of Love waves for the study of earthquake mechanism, *J. Geophys. Research*, 65, 323-331, 1960.
- Hodgson, J. H., Nature of faulting in large earthquakes, *Bull. Geol. Soc. Am.*, 68, 611-652, 1957.
- Honda, H., The mechanism of the earthquakes, *Sci. Repts. Tohoku Univ., Fifth Ser.*, 9, 1-46, 1957.
- Honda, H., and Masatsuka, A., On the mechanism of the earthquakes, and the stresses producing them in Japan and vicinity, *Sci. Repts. Tohoku Univ., Fifth Ser.*, 8, 30-49, 1952.
- Kasahara, K., The nature of seismic origins as inferred from seismological and geodetic observations, *Bull. Earthquakes Research Inst., Tokyo Univ.*, 36, 21-53, 1958.
- Knopoff, L., and Gilbert, F., Radiation from a strike-slip fault, *Bull. Seism. Soc. Am.*, 49, 163-178, 1959.
- Kohan, S. D., The question of research on the mechanism of deep earthquakes, *Doklady Akad. Nauk SSSR*, 99, 385-388, 1954.
- Nakano, H., Notes on the nature of the forces which give rise to the earthquake motions, *Seism. Bull. Central Meteorol. Obs. Japan*, 1, 92-120, 1923.
- Steketee, J. A., Some geophysical applications of the elasticity theory of dislocations, *Can. J. Phys.*, 36, 1168-1198, 1958.
- Tsuboi, C., Investigation on the deformation of the earth's crust in the Tango district connected with the Tango earthquake of 1927, *Bull. Earthquake Research Inst. Tokyo Univ.*, 8, 153-221, 1930.

(Received May 16, 1960; revised August 5, 1960.)

Elastic Constants of Rutile—A Correction to a Paper by R. K. Verma, 'Elasticity of Some High-Density Crystals'

FRANCIS BIRCH

*Division of Geological Sciences
Harvard University
Cambridge, Massachusetts*

Elastic constants for synthetic rutile have been published by *Vick and Hollander* [1960], *Sachman, Tefft, and Lam* [1960] and *Verma* [1960a]. Appreciable discrepancies exist for some of the constants, especially between those of Verma and those of the other investigators. The discrepancies are largely removed, however, when Verma's measurements are recalculated on the assumption that the direction which he took for [100] was in fact [110], and vice versa. Although Dr. Verma has returned to India, one of his samples is still available, and this assumption has been confirmed by an X-ray examination. The measurements on this sample have also been repeated, and found to be in good agreement with Verma's values.

The observational data are then as shown in Table 1, which replaces Verma's Table 4. Three independent determinations of C_{44} furnish an indication of the consistency of the measurements. There are four measurements to determine the three constants, C_{11} , C_{12} , and C_{66} . C_{41} and C_{66} have been taken from the relations giving them directly; there are then two values for C_{12} , 1.79 and 1.73 (all in 10^{12} dyne/cm²). However, one may eliminate C_{12} , obtaining two values, 4.67 and 4.64, for the sum $C_{11} + C_{66}$. There is consequently a slight discrepancy,

either in orientations or in the measurements of velocity. The value taken for C_{12} is 1.76, the mean of the two values given above; this is not necessarily the best solution, but the coefficients given in Table 2 satisfy all the measurements to within 1 per cent or better.

Besides the velocities for pulses in various directions, given in Verma's published paper, there are determinations in Verma's thesis [1960b] of Young's modulus from resonant frequencies of thin bars cut in two directions. One of these directions is parallel to [001], and the measurement furnishes

$$1/s_{33} = C_{33} - 2C_{13}^2/(C_{11} + C_{12}) = 3.85_3 \cdot 10^{12}$$

This has been used for the determination of C_{13} . The other direction was intended to be the [100] direction, which would have given s_{11} ; as it is actually the [110] direction, it gives

$$(s_{11} + s_{12})/2 + s_{66}/4$$

The measured reciprocal of this is $3.69 \cdot 10^{12}$, and we find from Table 2, $3.72 \cdot 10^{12}$.

Further verification may be obtained from the velocities in the direction A. This is the direction intended by Verma to be inclined at 45° to the [001] and [100] directions. Substi-

TABLE 1. Observational Data

Direction of Propagation	Mode	Direction of Displacement	Velocity, km/sec	Coefficient Determined
[001]	Compressional	[001]	10.65	C_{33}
[001]	Shear	any	5.41	C_{44}
[100]	Compressional	[100]	8.00	C_{11}
[100]	Shear	[010]	6.74	C_{66}
[100]	Shear	[001]	5.41	C_{44}
[110]	Compressional	[110]	9.89	$(C_{11} + C_{12} + 2C_{66})/2$
[110]	Shear	[001]	5.42	C_{44}
[110]	Shear	[110]	3.32	$(C_{11} - C_{12})/2$
A	Compressional		9.98	see text
A	Shear		5.95	see text

TABLE 2. Elastic Parameters of Rutile
(C_{pq} in 10^{12} dyne/cm²; s_{pq} in 10^{-13} cm²/dyne)

	Vick and Hollander [1960]	Wachtman, Tefft, and Lam [1960]	Verma [1960], recalc.	Bridgman [1928]
C_{11}	2.48	3.6	2.73	
C_{33}	4.52	4.8	4.84	
C_{44}	1.20	1.26	1.25	
C_{66}	1.6	1.47	1.94	
C_{12}	2.0	2.7	1.76	
C_{13}	1.4	1.7	1.49	
s_{11}	12	6.47	6.55	
s_{33}	3	2.59	2.59	
s_{44}	8	8.01	8.00	
s_{66}	6	6.8	5.16	
s_{12}	-9	-4.5	-3.76	
s_{13}	-1	-0.70	-0.86	
$s_{11} + s_{12} + s_{13}$	2*	1.27	1.93	1.90
$s_{33} + 2s_{13}$	1*	1.19	0.87	1.05
$2s_{11} + s_{33} + 2s_{12} + 4s_{13}$	5	3.73	4.73	4.83

*Assumed.

tuting [110] for [100] we find the direction cosines of direction A to be $l = \frac{1}{2}$, $m = \frac{1}{2}$, $n = 1/\sqrt{2}$, and the velocities are the roots of

oriented with faces normal to [110] instead of to [100], and to Professor C. S. Hurlbut, Jr., for verifying this conjecture.

$(C_{11} + C_{66} + 2C_{44})/4 - \rho c^2$

$(C_{12} + C_{66})/4$

$(C_{13} + C_{44})/2 \sqrt{2}$

$(C_{12} + C_{66})/4$

$(C_{11} + C_{66} + 2C_{44})/4 - \rho c^2$

$(C_{13} + C_{44})/2 \sqrt{2}$

$(C_{13} + C_{44})/2 \sqrt{2}$

$(C_{13} + C_{44})/2 \sqrt{2}$

$(C_{44} + C_{33})/2 - \rho c^2$

$= 0$

This is cumbersome for an algebraic solution, but it is not difficult to substitute the values of the constants from Table 2 for a numerical solution; the three roots correspond to the velocities 9.99, 5.93, and 4.50, all in km/sec. The two observed velocities are 9.98 and 5.95 km/sec, in excellent agreement with the first two roots.

The recalculated values, with various derived quantities, are shown in Table 2, together with the comparable values from other authors. The linear and volume compressibilities are little changed by this correction, and still compare relatively well with the directly measured values of Bridgman [1928] for a natural rutile crystal. The agreement with the theoretical values of Dayal and Appalanarsimham [1950] is now greatly improved except for C_{33} , as noted by the other authors.

I am greatly indebted to Mr. Wayne Tefft for the suggestion that Verma's samples were

REFERENCES

Bridgman, P. W., The linear compressibility of thirteen natural crystals, *Am. J. Sci.*, 10, 287-296, 1928.

Dayal, B., and N. Appalanarsimham, The evaluation of the elastic constants of rutile from spectroscopic data, *J. Sci. Research, Benares Hindu Univ.*, 1, 26-30, 1950-1951.

Verma, R. K., Elasticity of some high-density crystals, *J. Geophys. Research*, 65, 757-766, 1960a.

Verma, R. K., Elasticity of several high-density crystals and relationship to velocities in ultrabasic rocks, Thesis, Harvard University, 1960b.

Vick, G. L., and L. E. Hollander, Ultrasonic measurement of the elastic moduli of rutile, *J. Acoust. Soc. Am.*, in press, 1960; see also Vick, G. L., L. E. Hollander, and A. E. Brown, Elastic moduli of single-crystal rutile (TiO₂) (Abstract), *Bull. Am. Phys. Soc.* 4-8, 463, 1959.

Wachtman, J. B., Jr., W. E. Tefft, and D. G. Lam, Jr., Elastic constants of rutile (TiO₂) (Abstract), *Bull. Am. Phys. Soc.*, 5-4, 278, 1960.

(Received September 30, 1960.)

Auxiliary Publications Program

MALCOLM RIGBY¹

American Meteorological Society Abstracts
Box 1736, Washington 13, D. C.

For a quarter of a century the American Documentation Institute has maintained a valuable service for scientists and editors who are faced with the age-old publication dilemma: whether to omit useful supporting data from published articles or to publish these data at great expense of time and money—perhaps at the sacrifice of other articles of equal importance. With many editors the answer is unequivocal—no supporting data may ever be published. At best, the supporting data are provided in a highly concentrated form or only the conclusions are given.

The Auxiliary Publications Program, which was started in the early history of the American Documentation Institute as a service to journal editors who felt a need for an archive for material of scholarly character which could not be published in full, provides a compromise solution to this dilemma. It consists of a central depository or archives in the Photoduplication Service of the Library of Congress where prompt and

efficient processing of both incoming documents and service requests is maintained. Materials for deposit may include extensive statistical tabulations, large charts, raw experimental data, graphical analyses, etc. Such material may be submitted by any editor of a scientific, technical, scholarly, or abstracting journal or publication. Those wishing to order documents thus deposited need only send in a request stating the author's name, the title of the article, and the document number which has been assigned to it, and the microfilm or photoprint copy of the document will be furnished at the usual nominal charge for this type of service. The document number, price, and availability of the material must be published as a footnote to the article itself. Only material supporting a published article may be thus deposited.

(Received August 17, 1960.)

NOTE: We believe that this service of the American Documentation Institute provides an excellent solution to the data publication problem and hope that it will find wide use among the contributors to this Journal.

The Editors

¹Chairman, Auxiliary Publications Program, American Documentation Institute.

Corrigenda

• Professor J. A. Lockwood has called to attention the following error which appeared in 'A Comparison of the Cosmic-Ray Intensity at High Altitudes with the Nucleonic Component at Ground Elevation' by J. E. Henkel, J. A. Lockwood, and J. H. Trainor, published in vol. 64, no. 10, (October 1959) of this *Journal*. On page 1427, the last sentence of the abstract should read "It is found that the hemispherical average unidirectional intensity above the atmosphere derived from the counting rate at the Pfofzer maximum has decreased by a factor of 2 from 1954 to 1958 at $\lambda = 53^\circ$ N, and this change is compared with results at other latitudes."

On page 1432 line 4 in the second column should be changed to read "... has decreased by a factor of 21." The fifth line, second column of the same page should read "... smaller than the decrease of a factor of 4 measured by Neher."

On page 1437, the last sentence of text should read, "It was found that the intensity had decreased by a factor of 4 from 1954 to 1958."

On page 1430, the first column, line 16 should be "... for the intensity in 1947." In column 2 on the same page, line 5 should read "... 1958 as for 1947."

• The author, J. R. Winckler, has called attention to an error in 'Balloon Study of High Altitude Radiations during the International Geophysical Year,' in the May 1960 issue of the *Journal* (vol. 65, no. 5). On page 1336, line 3 of text, the sentence should be changed to read: " R is the normalized chamber rate in pulses/sec, and dp the pressure increment measured in millibars."

• Attention has been called to two errors in 'Some Characteristics of Ionospheric Backscatter at 440 Mc/s,' by V. C. Pinco, L. G. Kraft, and H. W. Briscoe, in the September 1960 issue of the *Journal* (vol. 65, no. 9). On page 2631, column 1, line 3, the reference should be to Figure 6 instead of Figure 5.

At the top of column 1, page 2632, the scattering coefficient $N\bar{\sigma}$ in equation 1 is erroneously shown as an exponent. Equation 1 corrected is

$$\bar{P}_r = (P_i A / 4\pi R^2) (c\tau/2) (1/L) N\bar{\sigma}.$$



AMERICAN GEOPHYSICAL UNION

1515 Massachusetts Avenue, N.W., Washington 5, D. C.

Established by the National Research Council in 1919 for the development of the science of geophysics through scientific publication and the advancement of professional ideals.

QUALIFICATIONS FOR MEMBERSHIP

The membership of the AGU shall consist of Members, Associate Members, Student Members, and Corporation Members.

Those eligible as candidates for election to the grade of MEMBER shall be:

MEMBER (a) Persons who have made an active contribution to geophysical research through observation, publication, teaching, or administration. Definite evidence should be presented to the Membership Committee. "Publication" may include books, articles, unpublished manuscripts, inventions, or development of geophysical instruments.

(b) Persons who have made active practical application of geophysical research. It should be shown that the nominee's work has not been purely routine, but that it has tended to create new knowledge of, or to broaden or strengthen the application of, geophysical research. In general, the minimum qualifications for membership will be not less than three years of professional experience in some phase of geophysics.

(Continued on next page)

Cut along this line

APPLICATION FOR MEMBERSHIP

Please refer to qualifications on reverse side and designate below type of membership desired:

Member (\$10) ☐

Associate (\$10) ☐

Student (\$4.50) ☐
(1960)

Application forms for Corporation Membership are available upon request.

1.

<u>Surname</u>	<u>First Name</u>	<u>Middle Name</u>
----------------	-------------------	--------------------
2. Preferred mailing address for publications
- Permanent address
3.

<u>Place</u>	<u>Month</u>	<u>Day</u>	<u>Year of Birth</u>	4. <u>Country of citizenship/naturalization</u>
--------------	--------------	------------	----------------------	-------------------------------------------------
5. Nature of work and title and/or military rank; name and address of organization with which you are associated.
6. Check section or sections with which affiliation is desired.

<input type="checkbox"/> Geodesy	<input type="checkbox"/> Oceanography
<input type="checkbox"/> Seismology	<input type="checkbox"/> Volcanology, Geochemistry, and Petrology
<input type="checkbox"/> Meteorology	<input type="checkbox"/> Hydrology
<input type="checkbox"/> Geomagnetism and Aeronomy	<input type="checkbox"/> Tectonophysics

7. EXPERIENCE (List below, use added sheets as necessary)

Dates: From To Name and address of organization Title, duties, nature of work

8. EDUCATION (List Below, use added sheets as necessary)

Dates: From To School Address Major Subject Degree, if any; year

(over)

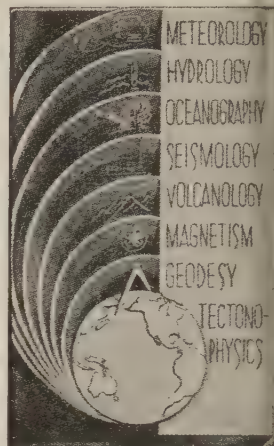
(Continued from previous page)

Those eligible as candidates for election to the grade of ASSOCIATE MEMBER shall be:

ASSOCIATE MEMBER Persons who have an active interest in physical processes of the Earth or technical assistance in the application of geophysics. In general, the minimum qualification for associate membership will be acceptable training or experience in some field of geophysics or allied science.

CORPORATION MEMBER Corporations and other interested organizations shall be eligible as candidates for election to CORPORATION MEMBERSHIP. They shall have the privilege of designating a representative who has the rights and privileges of Members (use special form).

STUDENT MEMBER Those eligible as candidates for election to the grade of STUDENT MEMBER shall be persons who are graduate or undergraduate students in residence at least half-time and who are specializing in the geophysical sciences. Teaching or research assistants enrolled in more than half of a full-time academic program may also be eligible for Student Membership. Student Members shall have all the privileges of Members except that they shall not vote or hold office.



Cut along this line

*9. References: Please list below names and addresses of two or three references; include members of the AGU or others who know you well.

*10. Titles of technical contributions or publications, particularly those in the geophysical sciences, and where published.

*11. Brief statement of any special interests or qualifications in the geophysical sciences.

Date _____

Written Signature _____

12. (STUDENT MEMBERS ONLY) The person whose signature appears above is known to me and is a student majoring in _____ (subject) at _____

(Name of college or university) expected to graduate in _____ (year) with the degree of _____

☐ He is a full-time student, or ☐ a teaching or research assistant enrolled in more than half of a full-time academic program.

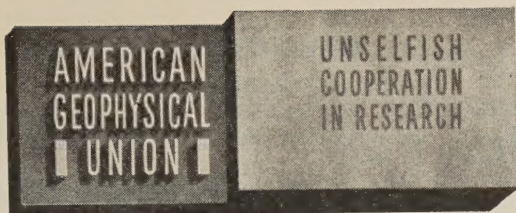
(Signature of faculty sponsor) _____

☐ Check here if faculty sponsor is a member of AGU and willing to act as a regular sponsor for associate membership as well.

(Typed or printed name of sponsor) _____

(Title) _____

* Applicants for student membership may omit Questions 9, 10, and 11, but must fill in Question 12. Please return form with check or money order payable to American Geophysical Union, 1515 Massachusetts Ave., N.W., Washington 5, D. C.



INFORMATION CONCERNING CORPORATION MEMBERSHIP

The American Geophysical Union is a non-profit scientific organization established by the National Research Council. It is the American National Committee of the International Union of Geodesy and Geophysics, and its Executive Committee is the Committee on Geophysics of the National Research Council.

Extracts from the Statutes:

Article 3. Membership—The membership of the American Geophysical Union shall be as follows:

- (e) *Corporation Members*—Corporations and other organizations interested in geophysics elected by the Executive Committee of the Union. The designated representative of each such organization shall enjoy the privileges of a Member.

(Continued on next page)

Cut along this line

American Geophysical Union

PROPOSAL FOR CORPORATION MEMBERSHIP

To the Executive Committee, American Geophysical Union
1515 Massachusetts Ave., N.W., Washington 5, D. C.

Gentlemen:

As an indication of our interest in the aims and activities of the American Geophysical Union, and to assist in maintaining and extending its program of publication and other work in the development of the geophysical sciences, the undersigned applies for Corporation Membership in the AGU and, until further notice, agrees to pay annual dues, currently at the rate of \$100 per unit of corporation membership, in accordance with the information set forth above.

Company or Organization _____

By _____ Title _____

(Signature)

(over)

(Continued from previous page)

Extracts from the By-Laws:

- (2) . . . Members of class (e) shall pay dues of not less than \$100 for each calendar year; . . .
- (21) One copy of each issue of (a) the *Transactions*, (b) *Journal of Geophysical Research*, (c) any published *List of Members and Officers*, and (d) any other publication which may be approved for *free distribution* to the membership by the Executive Committee of the Union, shall be sent to each . . . Corporation Member. . . Each . . . organization in good standing may purchase any available publication of the Union at a discount from printed price list to nonmembers. The General Secretary is authorized to establish discounts for sales of publications.

Action of the Executive Committee, November 29, 1946:

- (1) A list of corporation members shall be published on one or more pages immediately after the final page of text in each issue of the *Transactions*.
- (2) A list of corporation members shall be included in the Membership Directory as a distinct unit.

AMERICAN GEOPHYSICAL UNION

1515 Massachusetts Ave., N.W.
Washington 5, D. C.

Cut along this line

Address _____

City _____ State _____

General fields of activity _____

The following person is designated as our representative in this membership _____
_____ Title _____

Number of units of membership desired (this will be taken as one unless otherwise indicated) _____

Place _____

Date _____

Contents

(Continued from back cover)

	PAGE
Correlations between Soil-Moisture Depletion, Solar Radiation, and Other Environmental Factors <i>Forest W. Stearns and Charles A. Carlson</i>	3727
Operational Characteristics of the Laterals near the Edge of a Tile Drainage System <i>Ben L. Grover, James T. Ligon, and Don Kirkham</i>	3733
Angular Distributions for the Analysis of Multiple-Fluid Flow through Porous Media <i>G. de Josselin de Jong</i>	3739
Distribution of Excessive Rainfall Amounts over an Urban Area... <i>F. A. Huff and S. A. Changnon</i>	3759
Method of Estimating Basin Temperatures in New England and New York <i>Charles D. Hopkins, Jr.</i>	3767
Investigations of the Radioisotopes Be^7 , P^{32} , and S^{35} in Rain Water..... <i>Rama</i>	3773
Proposed Automatic Standard Magnetic Observatory..... <i>L. R. Alldredge</i>	3777
The Kernel Function in a Multiple-Layer Resistivity Problem..... <i>Seibe Onodera</i>	3787
Technique for the Numerical Solution of Geophysical Problems..... <i>I. M. Longman</i>	3795
The Interpolation of Earth-Tide Records..... <i>I. M. Longman</i>	3801
Particle Amplitude Profiles for Rayleigh Waves on a Heterogeneous Earth <i>James Dorman and David Prentiss</i>	3805
S Converted Waves from Large Explosions <i>Joseph J. Schwind, Joseph W. Berg, Jr., and Kenneth L. Cook</i>	3815
Selected Geomagnetic and Solar Data..... <i>J. Virginia Lincoln</i>	3825
Letters to the Editor:	
The Gyromagnetic Ratio of the Proton..... <i>J. H. Nelson</i>	3826
Bright 21-Centimeter Solar Regions and Geomagnetic Storms in 1952-1953.. <i>Richard T. Hansen</i>	3827
Auroral Noise at HF..... <i>R. D. Egan and A. M. Peterson</i>	3830
The Distribution of Minor Ions in Electrostatic Equilibrium in the High Atmosphere <i>P. Mange</i>	3833
Seasonal and Day-to-Day Changes of the Central Position of the S_q Overhead Current System <i>S. Matsushita</i>	3835
Traveling Wave Amplification of Whistlers..... <i>N. M. Brice</i>	3840
I-Xe Dating of Meteorites..... <i>J. H. Reynolds</i>	3843
Discussion of Paper by J. N. Luthin and J. W. Holmes, 'An Analysis of the Flow of Water in a Shallow, Linear Aquifer, and of the Approach to a New Equilibrium after Intake' <i>Mahdi S. Hantush</i>	3847
Discussion of Paper by J. N. Luthin and J. W. Holmes, 'An Analysis of the Flow of Water in a Shallow, Linear Aquifer, and of the Approach to a New Equilibrium after Intake' <i>Morton W. Bittinger</i>	3849
A Note on the Interception Loss Equation..... <i>Robert A. Merriam</i>	3850
Some Physical Aspects of Earthquake Mechanism..... <i>M. A. Chinnery</i>	3852
Elastic Constants of Rutile—A Correction to a Paper by R. K. Verma, 'Elasticity of Some High-Density Crystals'..... <i>Francis Birch</i>	3855
Auxiliary Publications Program..... <i>Malcolm Rigby</i>	3857
Erratum..... <i>J. E. Henkel, J. A. Lockwood, and J. H. Trainor</i>	3858
Erratum..... <i>J. R. Winckler</i>	3858
Erratum..... <i>V. C. Pineo, L. C. Kraft, and H. W. Briscoe</i>	3858

Contents

	PAGE
Balloon Observation of Artificial Radioactivity at the Base of the Stratosphere <i>H. T. Mantis and J. R. Winckler</i>	3515
Balloon Observations of X Rays in the Auroral Zone II. <i>K. A. Anderson and D. C. Enemark</i>	3521
The Cosmic-Ray Equator and the Earth's Magnetic Field <i>Martin A. Pomerantz, Vasant R. Potnis, and Arne E. Sandström</i>	3535
The Secular Variation and the Geomagnetic Theory of Cosmic Radiation. <i>Ruth Gall</i>	3545
The Interaction of the Terrestrial Magnetic Field with the Solar Corpuscular Radiation <i>David B. Beard</i>	3559
Radiation from Protons of Auroral Energy in the Vicinity of the Earth <i>W. B. Murcray and J. H. Pope</i>	3569
The Height of Maximum Luminosity in an Auroral Arc <i>F. E. Roach, J. G. Moore, E. C. Bruner, Jr., H. Cronin, and S. M. Silverman</i>	3575
Some Statistics of Solar Radio Bursts at Sunspot Maximum <i>A. Maxwell, W. E. Howard, III, and G. Garmire</i>	3581
The Cause of Magnetic Storms and Bays. <i>R. A. Duncan</i>	3589
Hydromagnetic Waves in the Ionosphere. <i>W. E. Francis and Robert Karplus</i>	3593
Electron Densities in the <i>F</i> Region of the Ionosphere from Rocket Measurements. Part 1. Methods of Analysis. <i>John S. Nisbet and S. A. Bowhill</i>	3601
Electron Densities in the <i>F</i> Region of the Ionosphere from Rocket Measurements. Part 2. Results of Analysis. <i>John S. Nisbet and S. A. Bowhill</i>	3609
The Geomorphology of Spread <i>F</i> <i>D. G. Singleton</i>	3615
The <i>D</i> ₁ , <i>D</i> ₂ Layers and the Absorption of Radio Waves. <i>G. C. Rumi</i>	3625
Scattering of Electromagnetic Waves from a Nondegenerate Ionized Gas. <i>Jacques Renau</i>	3631
Water Vapor Distribution above 90,000 Feet <i>David G. Murcray, Frank H. Murcray, Walter J. Williams, and Frank E. Leslie</i>	3641
Atmospheric Net Radiation Flux during Winter in the Thule Area, Greenland <i>Robert W. Fenn and Helmut K. Weickmann</i>	3651
The Economical Net Radiometer. <i>C. B. Tanner, J. A. Businger, and P. M. Kuhn</i>	3657
Infrared Radiometer Soundings on a Synoptic Scale. <i>P. M. Kuhn and Verner E. Suomi</i>	3669
An Improved Technique for Obtaining Atmospheric Ion Mobility Distributions. . <i>E. C. Whipple, Jr.</i>	3679
Internal Gravity-Vorticity Lee Waves over Mountains. <i>Louis Berkofsky</i>	3685
A Low-Frequency Microbarograph. <i>Wm. G. Van Dorn</i>	3693
Estimates of Bowen's Ratio by the Heat Budget Measurements of a Cornfield <i>J. F. Gerber and W. L. Decker</i>	3699
The Exceptional Advances of the Muldrow, Black Rapids, and Susitna Glaciers. . . <i>Austin S. Post</i>	3793
Modification of the Theory of Leaky Aquifers. <i>Mahdi S. Hantush</i>	3713

(Continued inside back cover)